

AN ABSTRACT OF A DISSERTATION

ANALYSIS AND CONTROL OF A MICROGRID WITH CONVERTER FED DISTRIBUTED ENERGY SOURCES

Hossein Karimi-Davijani

Doctor of Philosophy in Engineering

The past few decades has seen rapid growth of renewable energy sources for electric power generation. The main driving forces for this growth are due to the adverse environmental impacts of conventional power plants, their huge costs and losses in long transmission lines. The aforementioned concerns encourage the use of distributed generation (DG) in which the energy sources are installed close to the end users. Renewable energies with their infinite sources (like sun and wind) and the lowest impact on the environment are the first choice for the primary power of distributed generation units.

In a microgrid with renewable energy sources, the objective is to transfer the maximum possible power. In grid connected mode, since the voltage magnitude and frequency are adapted from the main grid, the controller objectives are different from autonomous operation mode. In grid connected mode the output active and reactive power or input DC-link voltage magnitude can be controlled. In autonomous mode, along with the power balance between the loads and the sources, the voltage magnitude and frequency should be controlled.

To have the same controller strategy in both grid connected and autonomous modes of operation, the droop control is proposed. To verify the proposed controllers, the dynamic simulation of the system is performed using MATLAB/Simulink and validated through laboratory scale experiment. The designed experimental system consists of a microgrid with two different sources: a nonlinear PV source and a battery source. In addition it includes three different power electronic converters: a unidirectional DC-DC boost converter, a bidirectional buck and boost converter and a three phase inverter. Each converter has its own controller signals coming from different control structure, drivers, sensor boards and digital signal processor (DSP) unit.

Permanent magnet (PM) machines are one of the most popular synchronous machines in wind turbine applications. In the interior permanent magnet (IPM) structure, the equivalent air gap is not uniform and it makes saliency effect obvious. Therefore, both magnetic and reluctance torque can be produced by IPM machine. In this research the dynamic model of interior permanent magnet machine as a wind turbine generator connected to the grid is studied. The control parts are designed to get maximum power from the wind, keep DC link voltage constant and guarantee unity power factor operation. Loss minimization of the generator is also analyzed. In addition the controllability of the system is studied using the analysis of its open-loop stability and

zero phase behaviors. The zero dynamics of the grid connected IPM generator using both the L and the LCL filter are investigated. The controllability analysis for the IPM generator system suggests that the topological structure of the interface filter and the controlled variables have significant effects on the phase behavior of the system. It is shown that the generator fitted with the L filter has a stable zero dynamics while the system connected through the LCL filter is non-minimum phase.

**ANALYSIS AND CONTROL OF A MICROGRID WITH CONVERTER FED
DISTRIBUTED ENERGY SOURCES**

A Dissertation

Presented to

The Faculty of the Graduate School

Tennessee Technological University

by

Hossein Karimi-Davijani

In Partial Fulfillment

of the Requirements for the Degree

DOCTOR OF PHILOSOPHY

Engineering

December 2012

CERTIFICATE OF APPROVAL OF DISSERTATION

**ANALYSIS AND CONTROL OF A MICROGRID WITH CONVERTER FED
DISTRIBUTED ENERGY SOURCES**

by

Hossein Karimi-Davijani

Graduate Advisory Committee:

Joseph O. Ojo, Chairperson Date

Ghadir Radman Date

Ahmed Kamal Date

Omar Elkeelany Date

Yung-Way Liu Date

Approved for the Faculty:

Francis Otuonye
Associate Vice President
for Research and Graduate Studies

Date

DEDICATION

To my wife, Shiva and my parents, Parvin and Alireza.

ACKNOWLEDGEMENTS

I would like to express my gratitude to the chairperson of my advisory committee, Dr. Joseph Ojo for his guidance and encouragement during the course of the research. I would like to thank the other members of my committee, Dr. Ghadir Radman, Dr. Omar Elkeelany, Dr. Ahmed Kamal and Dr. Yung-Way Liu for their wonderful courses and their efforts in evaluating my research works.

I would like to thank the office of Center for Energy Systems Research (CESR) and the Department of Electrical and Computer Engineering for the financial support. I also would like to express my gratitude to my lab members, Sosthenes Karugaba, Melaku Mihret, Kennedy Aghana, Dr. Jianfu Fu, Will Mefford, Mehdi Ramezani, Mehdi Khayami, Adineyi Babalola, Bule Mehari and Manideep Angirekula.

I would like to thank my parents for a lifetime support, selfless love, endless patience and encouragement.

Finally, I would like to give my most sincere thanks to my wife Shiva for her moral support, invaluable help and encouragement during the course of my PhD Program.

TABLE OF CONTENTS

	Page
LIST OF TABLES.....	xiii
LIST OF FIGURES.....	xiv
INTRODUCTION AND LITERATURE REVIEW	1
1.1 Introduction	1
1.2 Literature Review	3
1.2.1 DG Units Control Structures in the Microgrid	3
1.2.2 Photovoltaic as a Renewable Source	15
CONTROLLER DESIGN, BIFURCATION ANALYSIS AND SIMULATION OF ISOLATED MICROGRID.....	21
2.1 Introduction	21
2.2 Autonomous Operation of One Converter System.....	23
2.3 Controller Design of One Converter System	27
2.3.1 Droop Control.....	27
2.3.2 Voltage Control.....	29
2.3.3 Current Control	31
2.4 Equilibrium Curves of One Converter System.....	36
2.5 Autonomous Operation of Two Converter System.....	40

2.5.1	Dynamic Model	41
2.5.2	Controller Unit of Two Converter System.....	44
2.5.3	Droop Control.....	45
2.5.4	Voltage Control.....	47
2.5.5	Current control.....	49
2.5.6	Phase Lock Loop.....	52
2.5.7	Simulation of Two Converter System	53
2.6	Conclusion.....	58
STEADY STATE ANALYSIS AND DYNAMIC CONTROL OF PHOTOVOLTAIC		
SYSTEM.....		59
3.1	Introduction	59
3.2	Dynamic Model of the Stand-Alone System.....	60
3.2.1	Nonlinear Model and MPP Operation of PV System.....	61
3.2.2	Boost Converter Connected to the PV System	64
3.2.3	Bidirectional Boost Converter of Battery	66
3.2.4	DC Link Equations	67
3.2.5	Dynamic Model of the Battery	67
3.2.6	Load Equation.....	67
3.2.7	Three Phase Converter Equations.....	68
3.2.8	Linear Load of DG1 (L1) Equations.....	68

3.2.9	Capacitor of DG1 Equations.....	69
3.3	Steady-State Operation.....	69
3.4	Control Unit Design	72
3.4.1	Load Voltage Control	72
3.4.2	AC Inverter Current Control.....	74
3.4.3	PV Voltage Control.....	76
3.4.4	PV Converter Current Control.....	77
3.4.5	DC Link Voltage Control.....	78
3.4.6	Current Control of Battery Converter.....	79
3.4.7	Voltage Control of PV in Disabled Battery	80
3.4.8	PV Converter Current Control in Disabled Battery	81
3.4.9	DC Link Voltage Control in Disabled Battery	82
3.4.10	Droop Control.....	82
3.4.11	Phase Locked Loop.....	84
3.5	Simulation Results.....	86
3.6	Conclusions	89
STEADY STATE ANALYSIS AND DYNAMIC CONTROL OF PV SYSTEM		
CONNECTED TO THE MAIN GRID.....		
4.1	Introduction	92
4.2	Dynamic Model of the System.....	93

4.3	Steady-State Operation.....	97
4.4	Bifurcation Analysis.....	104
4.5	Controller Design	110
4.5.1	DC Link Voltage Control.....	112
4.5.2	Reactive Power Control	116
4.5.3	Current Control	117
4.5.4	State Space Model.....	118
4.6	Simulation Results.....	121
4.1	Conclusions	126
EXPERIMENTAL SETUP AND DYNAMIC CONTROL OF PV SYSTEM		129
5.1	Introduction	129
5.2	Design and Open Loop Test of the Boost Converter for PV System Applications	129
5.2.1	Input Capacitor Design	132
5.2.2	The Switch Design.....	133
5.2.3	The Diode Design	134
5.2.4	Output Capacitor Design.....	135
5.2.5	The Inductor Design	135
5.2.6	PCB Model and Open Loop Test of the Boost Converter	138

5.3	Closed Loop Experimental Design of Maximum Power Point Tracking Algorithm in PV System Applications	141
5.3.1	Design of the Current and Voltage Sensors	143
5.3.2	Design of the Driver Circuit	145
5.3.3	Design of the Power Supply	148
5.3.4	Controller Design and Closed Loop Test.....	148
5.4	Closed Loop Test of Battery System Converter.....	158
5.5	Design and Open Loop Test of Three Phase Inverter	159
5.5.1	Study System	160
5.5.2	The Experimental Setup.....	166
5.6	Phase Lock Loop.....	168
5.7	Connection of Three Phase Inverter to the Grid.....	172
5.7.1	Study System	174
5.7.2	Power Control of Inverter in Grid Connected Mode	181
5.8	Comparison of PLL and EPLL.....	188
5.9	Connection of the PV, Battery and Three Phase Inverter	209
5.10	Conclusions	215
DYNAMIC OPERATION AND CONTROL OF GRID COONECTED INTERIOR		
PERMANENT MAGNET WIND TURBINE GENERATOR.....		
6.1	Introduction	219

6.2	Study System.....	221
6.3	Wind Turbine Model.....	222
6.3.1	Defining MPP in Wind Turbine.....	224
6.3.2	Pitch Angle Effect.....	225
6.4	Dynamic Model and Steady State Operation region.....	229
6.4.1	Steady State Operation under Constant Generator Speed after Nominal Wind Speed	240
6.4.2	Steady state operation under constant pitch angle.....	244
6.5	Operation Regions of the Permanent Magnet Machine.....	244
6.5.1	Voltage and Current Constraints of PM Machine.....	248
6.5.2	Maximum Torque per Ampere (MTPA) Operation ($\omega \leq \omega_b$).....	251
6.5.3	Maximum Torque per Voltage (MTPV) Operation (Flux Weakening) ($\omega_b \leq \omega \leq \omega_{c1}$)	255
6.5.4	Flux Weakening with Stator Current Operation ($\omega \geq \omega_{c1}$).....	256
6.6	Machine Side Converter Controller Design.....	261
6.6.1	Loss Minimization and Rotor Speed Control.....	264
6.6.2	Current Control.....	267
6.7	Grid Side Converter Controller Design.....	270
6.7.1	DC Link Voltage and Reactive Power Control.....	270
6.7.2	Current Control.....	273

6.8	Simulation Results.....	274
6.9	Conclusions	275
CONTROLLABILITY ANALYSIS OF RENEWABLE ENERGY SOURCES		
CONNECTED TO THE GRID		
7.1	Introduction	279
7.2	Zero Dynamics of the Nonlinear System	282
7.2.1	First Method.....	284
7.2.2	Second Method	285
7.3	Controllability of Wind Turbine Connected through L filter to the Grid.....	286
7.3.1	Steady State and Stable Operation Region	288
7.3.2	Zero Dynamic Analysis	292
7.4	Controllability of Wind Turbine Connected through LCL filter to the Grid	294
7.4.1	Steady State and Stable Operation Region	295
7.4.2	Zero Dynamic Analysis	301
7.5	Controllability and Stability Analysis of PV System Connected to Current Source Inverter.....	308
7.5.1	Steady State and Stability Analysis of the System	310
7.5.2	Zero Dynamics Analysis of PV	313
7.6	Conclusions	321
CONCLUSION AND FUTURE WORKS		
		323

8.1	Introduction	323
8.2	Conclusions	323
8.3	Future Work	327
	REFERENCES	329
	APPENDIX.....	344
	PUBLICATIONS.....	358
	VITA.....	359

LIST OF TABLES

	Page
Table 2.1 System parameters of DG	54
Table 2.2 Parameters of the designed controllers	54
Table 3.1 Parameters of PV system	62
Table 3.2 Parameters of power system	86
Table 3.3 Parameters of the battery	86
Table 3.4 PI controllers' coefficients.....	86
Table 4.1 System parameters of DG connected to the grid	98
Table 5.1 Parameters of the designed inductor	137
Table 5.2 Coefficients of the low pass Hamming digital filter.....	154
Table 5.3 The study system parameters.....	175
Table 6.1 Wind turbine parameters.....	223
Table 6.2 Parameters of the IPM machine and the grid.....	236
Table 6.3 Designed parameters of the controllers	271
Table 7.1 Parameters of the IPM machine for controllability analysis.....	287

LIST OF FIGURES

	Page
Figure 1.1 Different structures of PV system.	18
Figure 2.1 Standalone one converter system schematic diagram	23
Figure 2.2 Block diagram of controlled unit beside power stage	29
Figure 2.3 Frequency of the system	36
Figure 2.4 Output active power of converter	37
Figure 2.5 Output reactive power of converter	37
Figure 2.6 Modulation index magnitude of converter	38
Figure 2.7 Load voltage magnitude	38
Figure 2.8 Active power of linear RL load	39
Figure 2.9 Reactive power of linear RL load	39
Figure 2.10 Schematic diagram of study system	41
Figure 2.11 Control unit diagram	44
Figure 2.12 Droop control unit	46
Figure 2.13 Schematic diagram of voltage control and inner current control units	48
Figure 2.14 Block diagram of phase locked loop	52
Figure 2.15 Active and reactive powers reference of first and second converters constant load, (a) and (b) are active and reactive powers of DG1 constant load, (c) and (d) are active and reactive powers of DG2 constant load	55

Figure 2.16 Output active and reactive powers of first and second converters, (a) and (b) are active and reactive powers of DG1, (c) and (d) are active and reactive powers of DG2.....	55
Figure 2.17 Actual local frequency (blue) and reference frequency (red) of the system, a) local frequency of DG1, b) local frequency of DG2.....	56
Figure 2.18 Local load voltages, a) q-axis load voltage of DG1, b) d-axis load voltage of DG1, c) q-axis load voltage of DG2, d) d-axis load voltage of DG2.	57
Figure 2.19 Modulation indices of converters, a) q-axis modulation index of first converter, b) d-axis modulation index of first converter, c) q-axis modulation index of second converter, d) d-axis modulation index of second converter.	57
Figure 3.1 Schematic diagram of the stand-alone PV, battery inverter power system.	61
Figure 3.2 Current and power characteristics of PV system in per unit	63
Figure 3.3 PV curve characteristics in different irradiation level.....	65
Figure 3.4 Calculated optimum voltage at MPP in different irradiation level.....	65
Figure 3.5 DC link voltage versus active power of constant load, blue(S = 1), red(S = 0.7)	70
Figure 3.6 Battery voltage versus active power of constant load, blue (S = 1), red(S = 0.7)	70
Figure 3.7 Inverter output active power versus active power of constant load, blue(S =1), red(S = 0.7)	70
Figure 3.8 Inverter output reactive power versus active power of constant load, blue(S=1), red(S = 0.7)	70

Figure 3.9 Battery output current versus active power of constant load, blue($S=1$), red($S=0.7$).....	71
Figure 3.10 Battery output power versus active power of constant load, blue($S=1$), red($S=0.7$).....	71
Figure 3.11 PV converter modulation index versus active power of constant load, blue($M=0.91$), red($M=0.61$).....	71
Figure 3.12 Battery converter modulation index versus active power of constant load, blue($M=0.91$), red($M=0.61$).....	71
Figure 3.13 Block diagram of DC-AC three phase converter control part.....	73
Figure 3.14 Block diagram of PV DC-DC boost converter control part.....	76
Figure 3.15 Block diagram of Battery DC-DC converter control part.....	79
Figure 3.16 Block diagram of PV DC-DC boost converter control part if battery converter is disabled.....	81
Figure 3.17 Droop control unit.....	82
Figure 3.18 Block diagram of phase locked loop.....	85
Figure 3.19 Constant load and inverter output active powers.....	87
Figure 3.20 Battery converter modulation index.....	87
Figure 3.21 Battery output current.....	87
Figure 3.22 DC link voltage.....	87
Figure 3.23 PV system output current.....	88
Figure 3.24 Inverter modulation index magnitude.....	88
Figure 3.25 PV converter modulation index.....	88
Figure 3.26 Load voltage magnitude.....	88

Figure 3.27 Operation under different irradiation level. (a) irradiation level, (b) reference and actual PV voltage, (c) PV output current, (d) battery output current, (e) Dc link voltage.....	90
Figure 4.1 Schematic diagram of a DG system with PV source connected to the grid	93
Figure 4.2 Nonlinear characteristic of PV source.....	99
Figure 4.3 Load and capacitor voltage.....	100
Figure 4.4 Modulation index magnitude.....	100
Figure 4.5 Active power of the main grid (negative means power flows into the main grid).....	101
Figure 4.6 Reactive power of the main grid	101
Figure 4.7 Reactive power of the converter.....	101
Figure 4.8 Modulation index magnitude of converter	102
Figure 4.9 Load and capacitor voltage.....	102
Figure 4.10 q-axis voltage of main grid.....	102
Figure 4.11 d-axis voltage of main grid.....	102
Figure 4.12 Active power of main grid.....	103
Figure 4.13 Reactive power of main grid	103
Figure 4.14 q-axis output converter current.....	103
Figure 4.15 Output converter current magnitude.....	103
Figure 4.16 Equilibrium curve of PV DC voltage when constant load active power (P1) is an active parameter for different q-axis modulation indices. H (Hopf Bifurcation Point), LP (Limit Point).	105

Figure 4.17 Equilibrium curve of the main grid active power (P_s) when constant load active power (P_1) is an active parameter for different q-axis modulation indices.	105
Figure 4.18 Equilibrium curve of the main grid reactive power (Q_s) when constant load active power (P_1) is an active parameter for different q-axis modulation indices.	106
Figure 4.19 Equilibrium curve of the input power (P_{in}) when constant load active power (P_1) is an active parameter for different q-axis modulation indices.	106
Figure 4.20 Equilibrium curve of the load voltage magnitude when constant load active power (P_1) is an active parameter for different q-axis modulation indices.	107
Figure 4.21 Equilibrium curve of the total load active power when constant load active power (P_1) is an active parameter for different q-axis modulation indices.	107
Figure 4.22 Equilibrium curve of the total load reactive power when constant load active power (P_1) is an active parameter for different q-axis modulation indices.	108
Figure 4.23 Equilibrium curve of the per unit q-axis load voltage (V_{qm}) when constant load active power (P_1) is an active parameter for different q-axis modulation indices.	108
Figure 4.24 Equilibrium curve of the converter output voltage magnitude when constant load active power (P_1) is an active parameter for different q-axis modulation indices.	109
Figure 4.25 Block diagram of DC voltage and reactive power control	113
Figure 4.26 Block diagram of DC voltage and reactive power control after removing the effect of PV source.	115
Figure 4.27 Change irradiation level and DC link voltage response for MPPT of PV...	122

Figure 4.28 Change of active reactive power of the inverter due to the change of irradiation level	122
Figure 4.29 Change of active reactive power of the main grid due to the change of irradiation level	123
Figure 4.30 Reference and actual qd-axis currents of inverter	123
Figure 4.31 qd-axis modulation indices of the inverter	124
Figure 4.32 system dynamic under the change of constant load, a) constant load active power, b) constant load reactive power, c) active power of the main grid, d) reactive power of the main grid, e) reactive power of the inverter f) q-axis load voltage g) d-axis load voltage h) DC link voltage.....	127
Figure 5.1 Schematic diagram of a boost converter	131
Figure 5.2 The actual shape and PCB model of the capacitor ALS30.	132
Figure 5.3 The actual shape and PCB model of the MOSFET FCH76N60NF.	133
Figure 5.4 The actual shape and PCB model of the diode STTH30L06.	134
Figure 5.5 The designed inductor	139
Figure 5.6 Input and output voltage in 50kHz switching frequency and duty ratio of 0.5	139
Figure 5.7 PCB design of Boost converter circuit a) top layer, b) bottom layer	140
Figure 5.8 Designed PV boost converter	142
Figure 5.9 Experimental open circuit test of the Boost converter	142
Figure 5.10 Designed PCB board for current sensor	144
Figure 5.11 Designed PCB board for voltage sensor.....	144
Figure 5.12 Designed PCB board for driver of the MOSFET	145

Figure 5.13 The output of TLP250 driver under the load.....	147
Figure 5.14 The output of UCC27134 driver and IL710 isolator under the load	147
Figure 5.15 The output of MC33151 driver and IL710 isolator under the load	149
Figure 5.16 Designed PCB board for the power supply	149
Figure 5.17 Output voltage ripple of the boost converter in terms of change of duty ratio in any predefine duty ratio set point.....	151
Figure 5.18 Programmed current versus voltage characteristic of experimental PV source	152
Figure 5.19 Programmed output power versus voltage characteristic of experimental PV source	152
Figure 5.20 Change of duty ratio versus output power of PV system connected to linear resistive load	153
Figure 5.21 Schematic of the P&O algorithm for MPPT of the PV system.....	154
Figure 5.22 The experimental setup of the Boost converter for PV MPPT.....	155
Figure 5.23 Experimental dynamic behavior of the load voltage of PV system using P&O MPP algorithm	156
Figure 5.24 Experimental steady state operation of the input power versus PV voltage in MPPT	156
Figure 5.25 The output of the driver at 50kHz and duty ratio of 0.24.....	157
Figure 5.26 Experimental dynamic behavior of the load voltage of PV with step change of irradiation level.....	157
Figure 5.27 the bidirectional battery converter.....	158

Figure 5.28 Experimental closed loop response of the bidirectional converter, Ch1: Vin, Ch3:Vdc	159
Figure 5.29 Three phase inverter simulated in MATLAB connected to the load.....	160
Figure 5.30 Experimental switching signals of produced by DSP in typical SPWM converter	162
Figure 5.31 Modulation waveform after adding zero sequence to the typical SPWM in DSP	164
Figure 5.32 Phase voltage of the inverter using imported DSP SPWM switching signals	164
Figure 5.33 Phase voltage of the simulated capacitor using imported DSP SPWM switching signals.....	165
Figure 5.34 Designed interface circuit to connect the DSP to the inverter drivers	165
Figure 5.35 Experimental set up of the three phase inverter and interface driver circuit	166
Figure 5.36 Experimental inverter output phase voltage of a resistive load with input DC voltage of 200V and modulation index $M=0.8$	167
Figure 5.37 Experimental inverter output phase voltage and phase current of a RL load with input DC voltage of 200V and modulation index $M=0.8$	167
Figure 5.38 PLL system diagram in the experiment.....	168
Figure 5.39 Experimental PLL measured frequency and angle of the sample voltage ..	173
Figure 5.40 Original and reproduced voltage from the PLL angle and frequency	173
Figure 5.41 Transformed qd-axis of the sample voltage using PLL angle.....	174
Figure 5.42 Three phase inverter connected to the grid and resistive load.....	175
Figure 5.43 Single line diagram of the study system in connection to the grid.....	177

Figure 5.44 Designed PCB board for AC voltage sensor.....	177
Figure 5.45 The measure angular frequency of the grid using PLL.....	178
Figure 5.46 The measured line to line grid voltage transformed to qd-axis.....	178
Figure 5.47 Schematic diagram of AC current sensor.....	179
Figure 5.48 PCB board of three AC current sensors.....	180
Figure 5.49 Experimental measured voltages on two sides of the switch before connection. (Ch1: Vm1 Ch4:Vm2 Ch3:Is1c).....	180
Figure 5.50 Effect of dead-time in a fixed frequency and different V_{dc} and M_a	181
Figure 5.51 Reduced dead-time in the output of DSP PWM signals to $2\mu s$	182
Figure 5.52 Experimental measured open loop voltages after applying correction. (Ch1: Vm1 Ch4:Vm2 Ch3:Is1c).....	182
Figure 5.53 Inverter current control structure.....	184
Figure 5.54 The experimental grid voltage (Ch1) and inverter output phase current (Ch3), $P_{ref} = 50W, Q_{ref} = 5Var$	186
Figure 5.55 The experimental grid voltage (Ch1) and inverter output phase current (Ch3), $P_{ref} = 100W, Q_{ref} = 10Var$	186
Figure 5.56 Experimental active and reactive power of the inverter in closed loop control. ($V_{dc}=100 V$ and $V_{m1-rms}=36 V$).....	187
Figure 5.57 Experimental active and reactive power of the inverter at higher voltage. ($V_{dc}=200 V$ and $V_{m1-rms}=90 V$).....	187
Figure 5.58 Harmonic spectrum of line to line inverter voltage at $f_{sw}=5KHz$, fundamental frequency is 20 times reduced scale.....	189

Figure 5.59 Harmonic spectrum of line to line inverter voltage at $f_{sw}=4860$ Hz, fundamental frequency is 20 times reduced scale.....	189
Figure 5.60 EPLL system diagram	195
Figure 5.61 EPLL structure for three phase system.....	197
Figure 5.62 Experimental output voltage of digital filter	203
Figure 5.63 Experimental output voltage of EPLL.....	204
Figure 5.64 Experimental output current of digital filter.....	204
Figure 5.65 Experimental output current of EPLL	205
Figure 5.66 Experimental qd-axis voltage output of PLL and EPLL.....	205
Figure 5.67 Experimental qd-axis voltage output of PLL and EPLL.....	206
Figure 5.68 Experimental voltage frequency output of PLL and EPLL.....	206
Figure 5.69 Harmonic spectrum of phase current of the digital filter for PLL, fundamental frequency is 20 times reduced scale.....	207
Figure 5.70 Harmonic spectrum of output phase current of EPLL, fundamental frequency is 20 times reduced scale.....	207
Figure 5.71 Hardware experimental setup	208
Figure 5.72 Relay driver PCB board.....	208
Figure 5.73 Experimental closed loop inverter voltage and current controller response	210
Figure 5.74 Experimental active and reactive power of the inverter in both autonomous and grid connected modes.....	210
Figure 5.75 Experimental active and reactive power of the grid in both autonomous and grid connected modes.	212

Figure 5.76 Experimental active and reactive power of the grid in both autonomous and grid connected modes.	212
Figure 5.77 Experimental qd-axis load voltages in both autonomous and grid connected modes.	213
Figure 5.78 Experimental qd-axis inverter currents in both autonomous and grid connected modes.	213
Figure 5.79 Experimental voltage and current of the inverter with changing of the PV source in grid connected mode, Ch1: Vmab, Ch3:Is1a	214
Figure 5.80 Experimental DC-link voltage after connection to the grid and change of reference power.....	214
Figure 5.81 Experimental output voltage and current of the PV source.....	216
Figure 5.82 Experimental output voltage and current of the battery source.....	216
Figure 6.1 Schematic diagram of IPM wind turbine connected to the main grid.....	221
Figure 6.2 Power coefficient versus tip speed ratio at zero pitch angle	226
Figure 6.3 Power coefficient versus tip speed ratio at zero pitch angle	226
Figure 6.4 Tip speed ratio versus power coefficient at different pitch angle	228
Figure 6.5 Output power of wind turbine versus generator rotor speed at different pitch angle and $V_w=10(m/s)$	228
Figure 6.6 Pitch angle versus generator rotor speed at constant turbine power and wind speed	229
Figure 6.7 Wind speed versus pitch angle at the rated output power and rated rotor speed	230
Figure 6.8 Equivalent circuits of IPM Machine.....	236

Figure 6.9 Wind turbine speed versus wind speed	241
Figure 6.10 Machine side converter modulation index versus wind speed	241
Figure 6.11 qd-axis stator current magnitudes versus wind speed	242
Figure 6.12 Stator voltage and current magnitude versus wind speed	242
Figure 6.13 Power of wind turbine and output active power of generator versus wind speed	243
Figure 6.14 Efficiency versus wind speed	243
Figure 6.15 Wind turbine speed versus wind speed	245
Figure 6.16 Stator voltage and current magnitude versus wind speed	245
Figure 6.17 Converter modulation index versus wind speed.....	246
Figure 6.18 Power of wind turbine and output active power of generator versus wind speed	246
Figure 6.19 Efficiency versus wind speed	247
Figure 6.20 Power and torque characteristics of PM machine	247
Figure 6.21 Voltage and current constraints characteristics a) Interior permanent magnet machine b) Surface mounted permanent magnet machine	250
Figure 6.22 Operation region of PM machine a) Interior permanent magnet machine ($\lambda_m / L_{sd} \geq I_{s \max}$), b) Interior permanent magnet machine ($\lambda_m / L_{sd} \leq I_{s \max}$), c) Surface mounted permanent magnet machine.	257
Figure 6.23 The qd-axis and magnitude of the IPM stator current.....	260
Figure 6.24 The qd-axis and magnitude of the IPM stator voltage	260
Figure 6.25 The output power and torque of the IPM generator	261
Figure 6.26 Machine side converter controller	265

Figure 6.27 Grid side converter controller.....	271
Figure 6.28 Dynamic operation of generator and MSC. a) wind speed, b) generator rotor speed, c) output active power, d) stator current magnitude	276
Figure 6.29 Pitch angle and power coefficient of wind turbine. a) pitch angle, b) power coefficient	276
Figure 6.30 Dynamic operation of grid side converter. a) Dc link voltage, b) output reactive power, c) GSC output current magnitude.....	277
Figure 7.1 Schematic diagram of IPM wind turbine connected to the main grid with L type filter.....	286
Figure 7.2 Steady state operation region of the system. a) output active power of the generator (W), b) output reactive power of the generator (Var), c) stator current (A), d) stator voltage (V), e) modulation index magnitude of machine side converter f) modulation index magnitude of grid side converter	290
Figure 7.3 Stability region based on Routh–Hurwitz criteria. The last coefficient of the characteristic equation.....	293
Figure 7.4 The IPM machine as a wind turbine generator connected through LCL filter.	294
Figure 7.5 Output active power of IPM generator.....	296
Figure 7.6 Output reactive power of IPM generator.....	296
Figure 7.7 Stator current magnitude of IPM generator.....	297
Figure 7.8 Stator voltage magnitude of IPM generator.	297
Figure 7.9 Modulation index magnitude of the machine side inverter.....	298
Figure 7.10 Modulation index magnitude of the grid side inverter.....	298

Figure 7.11 Active power flowing into the grid.	299
Figure 7.12 Two of the coefficients of the linearized zero dynamics characteristic equation (46). (a) the last coefficient (n_0), (b) second coefficient (n_2).	308
Figure 7.13 An IPM machine as a wind turbine generator connected through LCL filter.	309
Figure 7.14 PV output voltage at MPP with in different irradiation level.....	313
Figure 7.15 PV output current at MPP with in different irradiation level	313
Figure 7.16 Inverter modulation index magnitude at different irradiation level	313
Figure 7.17 q-axis capacitor voltage at different irradiation level.....	313
Figure 7.18 Two of the coefficients of the linearized PV zero dynamics characteristic	320

CHAPTER 1

INTRODUCTION AND LITERATURE REVIEW

1.1 Introduction

The environmental effects and the cost of central power plants are causing a large focus on renewable energies. The power plants are using fossil fuels which result in greenhouse gas emissions. These greenhouse gas emissions have a significant effect on the planet especially with the growth of the population and the corresponding increase of energy consumption. The power plants need to send the electricity to the customers using long transmission and distribution lines because they have been installed concentrated in one place and also out of the big cities. A lot of power is lost along the lines which creates the need for power substations to increase the voltage level at the point of transmission and reduce it at the point of consumption to minimize these losses. In addition to the environmental issues, the sources of fossil fuels are limited and depleting quickly.

The aforementioned concerns encourage the use of distributed generation (DG) with which the energy sources are installed close to the end users. In particular, for consumers that are far from the transmission lines or main power plants and small customers for whom sending energy using transmission lines is not economical, use of DGs are recommended.

Renewable energies with their essentially infinite source (like sun and wind) and low impact on the environment are the first choice for the primary power of distribution

generation units. Thus the distribution generation can be combined with renewable energies as their sources to get both the advantages of environmental friendliness and cost effectiveness. The types of Distributed Generation (DG) units based on renewable energy which have the fastest growing amount of usage are employing either photovoltaic cells or wind turbine sources, the choice of which is based on availability, location, amount of power needed, and feasibility.

When we choose a renewable energy as our input source, we need to consider the fact that it is typically unpredictable and uncontrollable; therefore, to use these kinds of sources either in connection to the main grid, or in feeding local loads, the concept of control and power electronic inverters as an interface should be kept in mind.

Wind turbines produce AC voltage using different kinds of generators and are normally connected with an AC-DC-AC back-to-back inverter. In this condition, the input AC voltage is converted to DC voltage and is then converted to an AC voltage with a desirable voltage magnitude and frequency. In addition, the active and reactive power in both sides can also be controlled.

The PV system as a DC source can be connected to the loads in either single stage or double stage mode. In single stage mode, the PV system is connected to the grid using a three phase or single phase inverter which directly converts the input DC to AC. The other combination, due to the non-linear characteristics of the PV system, uses a DC/DC converter to control and normally boost the input source voltage while another inverter converts the DC voltage to AC voltage.

There are many reasons and a lot of efforts to develop new types of the controllers which enable optimum operation of DG units:

- Normally nonlinear characteristics of the renewable sources
- Tend to get maximum power from the renewable energies.
- Unpredictable amount of input power.
- Parallel operation of different DG units and power sharing between them.
- The control structure in autonomous mode, grid connected mode and transient condition between these two modes.

This chapter has a short review of the works that have been done in literature to solve or improve upon the current solutions to the mentioned problems in using DG systems.

1.2 Literature Review

1.2.1 DG Units Control Structures in the Microgrid

Distributed sources are usually connected to the load or the main grid through an interface power electronic inverter to control their output voltage and power. They can work in either autonomous mode or grid connected mode. Usually, distributed sources are working as a current source in grid connected mode. However, they use a voltage source inverter (VSI) to maintain voltage and frequency stability, ride-through capability, and islanding operation. Using two different control structures in autonomous mode and grid connected modes, distributed sources need to have a fast islanding detection to switch in one mode to another and increase the performance. In addition, the two operation modes adhere to different and somewhat conflicting dynamics and steady-state

characteristics [1]. Due to aforementioned constraint, the control of the DG is arguably the most important part of their implementation.

In the control of output power and load sharing of DG units, conventional droop control of the synchronous generators of power plants is the concept most commonly used in literature. The prevalent method is drooping frequency versus active power and drooping voltage magnitude versus reactive power. Reference [2] uses droop control for parallel connection of Uninterruptable Power Supply (UPS) systems using droop control in both autonomous and grid connected mode. The real and reactive power management strategies of electronically interfaced DG units using droop control in the context of a multiple-DG microgrid system is addressed in [3], which uses eigenvalue analysis to investigate the microgrid dynamic behavior and select control parameters.

The voltage-power droop/frequency-reactive power boost (VPD/FQB) control scheme, is proposed in [4], allows current controlled voltage source converters (VSCs) to operate in parallel on the same microgrid, both in islanded and grid connected modes. This controller droops the voltage reference against its real power output and boosts the frequency reference against its reactive power.

A frequency locked loop based on the second order generalized integrator (SOGI-FLL) on both voltage and current in the PCC is used in [5] to estimate grid impedance. Using the estimated grid impedance magnitude and angle, the active and reactive powers are transformed to values independent from the grid impedance. A droop control is designed to control the calculated independent powers using two compensator controllers. The parameters of these controllers are defined based on the root locus criteria for stability of the system in the operation region.

To minimize the circulating current between parallel DG units, several control strategies have been adopted to achieve this goal. These strategies include the concentrated control technique [6], the master–slave control method [7-9], the power deviation control method [10-11], and the frequency and voltage droop method [12-14].

The conventional droop method cannot achieve efficient power sharing in the case of a system with complex impedance condition due to the coupled active and reactive power characteristic of the system [15-17], which causes circulating current. The transient and steady-state behaviors of the droop method also highly depend on the system mismatches which can affect the inverter output impedance accuracy and the line impedance of the wires. The inverter output impedance also depends on the adopted inverter control strategy and the system parameters [18-19].

In [20], the inverters are controlled by droop schemes in both grid connected and autonomous modes. These inverters are controlled as voltage sources even if they are connected to the grid, so that typical control algorithms that inject the inverter output current in phase with the grid voltage (current source algorithms) developed in grid connection mode are discarded. To enhance the power loop dynamics, droop control combined with a derivative controller is used in islanded mode. In grid-connected mode, to strictly control the power factor at the point of common coupling (PCC), a droop method combined with an integral controller is adopted. In the other words, a proportional derivative (PD) control is applied to the active power droop control and a proportional integral (PI) control is applied to the reactive power droop control. Reference [21] uses islanding detection to switch between autonomous control mode and grid connected mode control of the microgrid.

In a paralleled AC system, such as a multi-inverter microgrid, circulating currents may occur due to differences in voltage magnitude, frequency, phase angle or DC offset. Minor fluctuations in the voltage magnitudes will cause circulating currents and will also influence the reactive power supplied by the inverters to deviate from the desired values. DC offsets may also occur due to a measurement offset in the inverter controllers, irregular switching of inverter legs, or fluctuations in the DC-bus voltage of the inverter [22]. The DC components in the voltages will be limited only by the resistances of the cables and, therefore, the DC components in the currents between the inverters will be large, even for small differences in the DC components in output voltages. This causes malfunction of droop control and loss in the grid. Reference [22] provides a mathematical model that predicts the effect of voltage-magnitude offsets on reactive power sharing between inverters and a simple capacitor emulation control law implemented in software to eliminate DC-circulating currents.

To avoid the communication between multi DG units the droop control is adopted in [23] for a single phase PV system connected to the grid. The droop coefficient of active power control is a PI controller. While the droop coefficient for reactive power is a proportional gain related to voltage sag percentage in order to control the voltage magnitude. The grid is considered mainly inductive.

The load sharing capability of the droop method may be degraded if the load changes or the line impedance changes. Taking advantage of fast inverter operation while avoiding large transients during mode transfer is very important for paralleling inverter-based DG units in a microgrid system. The intent of [24] is to present a controller intended for using supervisory control and communication between DGs in a single-

phase inverter-based microgrid system that ensures smooth mode transfer between islanding and grid-tie modes.

Two important classes of autonomous load-sharing techniques that have been proposed are the frequency/voltage droop technique, and the signal injection technique. In the signal injection technique each VSC injects a non-60-Hz signal and uses it as a means of sharing a common load with other VSCs on the network [25]. However, the circuitry required to measure the small real power output variations due to the injected signal adds to the complexity of the control.

We can use droop real power/angle control instead of frequency to avoid limiting frequency regulation due to allowable range of frequency droop gain. Moreover, a PI controller is used in [26] for droop reactive power/voltage droop control to achieve the desired speed of response without affecting voltage regulation. The angle droop control is also presented in [27] instead of frequency. Although High gain angle droop control ensures proper load sharing, especially under weak system conditions, it has a negative impact on overall stability. A supplementary loop based on evolutionary technique optimization is proposed around a conventional droop control of each DG converter in order to stabilize the system while using high angle droop gains.

In [28], in addition to the converter of any DC or renewable energy source, another back to back converter is used to connect the whole microgrid to the grid. With this it is trying to isolate each side of the inverter from the fault and voltage fluctuations of the other side. It is shown that the real power/voltage angle is superior to conventional real power/frequency droop control from the frequency control point of view because the change of frequency is less in the suggested control method.

It should be noted that although the standard deviation of frequency with angle droop is much smaller than standard deviation of frequency with frequency droop, for the measurement of angles with respect to a common reference, GPS communications are needed with angle droop control [29].

The conventional droop method also has several drawbacks including a slow transient response, a trade-off between power-sharing accuracy and voltage deviation, unbalanced harmonic current sharing, and a high dependency on the inverter output impedance [4]. Power sharing of parallel DGs is mostly based on inductive line assumption; however, when implemented in a low voltage microgrid, the different DG output impedances and the high line impedance ratio lead to various impedances (inductive or resistive) among DG units, and the traditional droop method is subject to more severe real and reactive power control coupling and deteriorated system stability. The mainly resistive line impedance in low voltage systems, the unequal impedance among distributed generation (DG) units, the uncertainty of the inverter output impedance related to the control strategy [30], and the microgrid load locations make the conventional frequency and voltage droop method unpractical.; in addition, this output impedance is neither possible to measure nor easy to estimate.

In order to realize decoupled power control and improve the system stability, a number of different variations of the traditional droop control are proposed [31-32]. In some references [33-34] the opposite droop control (active power/voltage magnitude and reactive power/frequency) is used. The only advantage of this method is direct voltage control in islanded mode, but the connection of the microgrid to the network will cause

counteracting with the valid normal droop control of synchronous generators and no active power dispatch will be possible; also, voltage deviation will remain in the grid.

Among the methods that have been used in the literature, using the virtual impedance is the most practical one for decoupled active and reactive power control especially in the resistive distribution line systems [35]. It has been shown in the literature that if resistive output impedance is virtually imposed, it improves the damping of the system and harmonic current-sharing ability [33]. The most important benefit from utilizing virtual output impedance is that the magnitude and phase angle of the output impedance can be controllable variables. The limitation of virtual impedance is that it is too dependent on the voltage loop bandwidth and it may increase the reactive power control and sharing error due to the increased impedance voltage drops.

The virtual DG output inductance, which can effectively decouple the power flows and at the same time maintain good system dynamics and stability. The design of the virtual inductance is a challenging issue. Extension of the virtual frequency and voltage frame power control scheme is done in [36] by proposing a virtual frame operation range control strategy [37]. Its relationship to the actual operation limits is conducted to avoid operating beyond the actual frequency and voltage limits so the microgrid power quality is not affected.

Reference [16] details a virtual inductor at the interfacing inverter output and reactive power control and sharing algorithm with consideration of impedance voltage drop and DG local load effects. Considering the complex locations of loads in a multibus microgrid, the reactive power control accuracy is further improved by employing an online estimated reactive power offset to compensate the effects of DG local load power

demands. A virtual resistive output impedance is used in [38] to maintain the harmonic contents at the output voltage within the desired limit, and instead of a set of bandpass filters, a voltage-regulation PR control loop with resonant peaks at the desired frequencies is used.

A trade-off between voltage control and reactive power sharing is considered in [39] using two methods. The first method is an extension of conventional droop control with virtual impedance. The second is based on an optimization method using a genetic algorithm to enhance the load voltages and minimize the circulating reactive power between buses.

The possible grid-impedance variations have a significant influence on the system stability. In [40] an H_∞ controller with explicit robustness in terms of grid-impedance variations is proposed to incorporate the desired tracking performance and the stability margin.

H_2 control considers white noise disturbances and H_∞ control considers energy bounded L_2 disturbances. In contrast, L_1 theory considers persistent bounded uncertain disturbances (L_∞ disturbances) [41-43]. The droop constants are optimized in [44] by PSO with power-electronic-switch level simulations. For the inverter-output controllers, a robust controller design scheme has been proposed. To deal with persistent voltage and frequency disturbances in a microgrid, an L_1 robust control theory with PSO algorithm has been proposed.

Normally power factor correction (PFC) capacitors are used in power systems to reduced electric utility bills, losses, heating in lines and transformers, and most importantly, elimination of utility power-factor penalties [45]. Adding PFC may cause

voltage and current resonance and also system parameter variations. The authors in [46] investigate the effective shunt-filter-capacitance variation and resonance phenomena in a microgrid due to a connection of a PFC capacitor. To compensate the capacitance-parameter variation, an H_∞ controller is applied to VSI.

Optimal design of LC filters, controller parameters, and damping resistance is carried out in case of grid-connected mode. On the other hand, controller parameters and power sharing coefficients are optimized in the case of autonomous mode. The control problem is formulated as an optimization problem in [47] where particle swarm optimization is employed to search for optimal settings of the parameters in each mode.

Reference [48] analyzes the stability of a microgrid and its sensitivity to changes in its parameters. It linearizes the model around an operating point and the resulting system matrix is used to derive the eigenvalues. The eigenvalues indicate the frequency and damping of oscillatory components in the transient response. It was observed that the dominant low-frequency modes are highly sensitive to the network configuration and the parameters of the power sharing droop controller DGs. The high frequency modes are largely sensitive to the inverter inner loop controllers, network dynamics, and load dynamics.

Microgrid stability margin decreases with increase in the droop controller gains and the system finally becomes unstable for large values of active power/frequency droop gain [49-50]. It has also been shown that the stability results are strongly dependent on the loading conditions of the microgrid and on network parameters. Reference [51] considers only the effect of the droop control gains and the topology of the microgrid with some assumptions to reduce the complexity and computational burden.

Along with the control of output power and voltage, compensation of power quality problems like voltage unbalance can also be achieved through proper control strategies in Microgrid. Voltage unbalance is mostly due to the utility grid (under grid-connection mode) and the connection of unbalanced loads such as unevenly distributed single phase loads within its own network. There are negative impacts due to voltage unbalance on some equipment such as induction motors, power electronic converters, and adjustable speed drives.

An accurate power-flow analysis is needed for the control, protection, and power management of the power system. Most of the work done for this purpose is applied to large power systems based on the system positive-sequence representation. Reference [52] used a sequence-frame power-flow solver in a Microgrid containing DG units and unbalanced loads. Using the sequence-components frame in the power-flow analysis effectively reduces the problem size and the computational burden when compared to the phase-frame approach. Due to the weak coupling between the three sequence networks, the system equations can be solved using parallel programming

Various imbalance compensation solutions have been proposed in the literature for the control of Microgrid under unbalanced voltage. A synchronous-reference-frame (SRF)-PI controller on the positive-sequence component of the inverter voltage is presented in [53]. The integration of a positive and a negative sequence SRF-PI controller of inverter output voltage is proposed in [54]. The negative-sequence current compensation with a shunt converter is presented in [55-56], and that with a series converter is introduced in [57].

The voltage unbalance compensation is done using negative voltage injection to the power system either in series [58-60] or in parallel [61-62]. Injection of negative sequence current by the DG is proposed in [31] which needs a large power converter in severe conditions. The method proposed in [63] and [64] is based on controlling the DG as a negative sequence conductance to compensate for the voltage unbalance at the microgrid DG's terminal. Two references, [65-66], use two different control structures. A primary local controller mainly consists of power, voltage and current controllers, and a virtual impedance control loop. A secondary central controller is also used to manage the compensation of voltage unbalance at the point of common coupling (PCC) instead of local voltage in an islanded Microgrid which needs communication between DGs.

Reference [67] introduces the potential function based control as secondary controller of a Microgrid. It considered three levels of control for the system, primary, secondary and tertiary. The potential function has been exploited in the secondary control part which is slower than the primary controller and needs communication between Microgrid components and DGs. It uses a centralized controller to manage the output power and voltage of the distributed resources.

For the control of Microgrid in grid connected mode, in [68-69] the DGs are operating in constant current mode to feed a constant power to the grid and the loads. During the intentional islanding mode, the controller mode changes to constant voltage mode and the load shedding is applied for power balance between the source and the load. A voltage and frequency range was chosen for islanding detection.

Synchronous reference frame control needs accurate angle and frequency identification and more computational power to transform the ac quantities to dc values

to be controlled and then return back them to ac parameters. To control a grid connected three phase inverter in stationary reference frame, the PI controller causes steady state error. Although PR controller is more applicable in unbalanced conditions due to the simultaneous control of both positive and negative sequence, it also has a slow transient response because its dominant poles are close to the imaginary axis. Reference [70] proposes a proportional complex integral (PCI) controller for this purpose. A constant voltage source as the input is considered and assumed the controllers are always working in linear operation region.

In [71] the power synchronization control is used to control the voltage source converter (VSC) in connection to the weak grid. This method usually controls the power transfer to the grid directly so it does not have current controllers and current limitations and avoids using a PLL. The author added the current limitation controller and also a PLL for synchronization in case of emergencies.

For reducing the complexity and avoiding cascaded AC-system outages spreading from one system to another, the High-voltage DC (HVDC) transmission is introduced in [72] as a good solution for connection of renewable energy sources to the grid. This chapter uses Jacobian matrix and power synchronization control to increase power transmission between two weak AC systems. It is shown that the increase of load angle causes the zeros of the system to move closer to the origin and limit the bandwidth so that a higher DC capacitance value is needed. Power synchronization control uses AC voltage and active power control loops that make the VSC operation like a synchronous machine which supports the weak AC systems.

Some authors believe that the adaptive control in which the controller's parameters are tuned based on the estimation of the unknown parameters is not a reliable approach to be used in the power electronics/systems applications [73]. In [73] current controllers in grid connected mode and voltage controllers in autonomous mode are designed based on the transfer function of the dynamic model of Microgrid.

Reference [74] introduces the conventional qd-axis current control strategy of DG unit in grid connected mode. In autonomous mode, the control system switches to voltage control with an internal oscillator to determine the voltage magnitude and frequency of the system. In addition, [75] tries to provide seamless transfer of microgrid between grid connected mode and autonomous mode. The current controller forces the current to zero with a short transient and the voltage controller maintains the voltage after transition.

1.2.2 Photovoltaic as a Renewable Source

One of the advantages of the Microgrid is its flexibility of using renewable energies as its primary source. The photovoltaic is one of the most popular methods for producing electricity directly from the irradiation of the sun. It is environmental friendly, renewable, and free after initial production. At most times, the goal is to get the maximum possible power from the photovoltaic. For maximum power point (MPP) tracking of solar cells, two main algorithms are suggested: open loop and closed loop control. The open loop control is the simplest but the effect of solar irradiance variations is not taken into account and the efficiency may not be satisfactory.

In closed loop control, due to nonlinear characteristic of the solar cells and unpredictable environmental conditions and their effect of on the output of the PV panel, designing a precise controller is very complex and sometimes not completely applicable. The most popular methods for close MPP control of PV systems are incremental conductance (INC) and the perturbation and observation (P&O) algorithm.

Three techniques have been proposed in the literature for implementing the P&O algorithm: reference voltage perturbation [76-78], reference current perturbation [79-80], and direct duty ratio perturbation [77] and [81-82]. Reference current perturbation has slow transient response to irradiance changes and high susceptibility to noise and PI controller oscillation. Reference [83] compares voltage perturbation and direct duty ratio perturbation on the basis of system stability, performance characteristics, and energy utilization for standalone PV pumping systems. In reference voltage perturbation, the system has a faster response to irradiance and temperature transients; however, it loses stability if operated at a high perturbation rate or if low pass filters are used for noise rejection. Direct duty ratio control offers better energy utilization and better stability characteristics at a slower transient response and worse performance at rapidly changing irradiance. System stability is not affected by using low-pass feedback filters and it allows the use of high perturbation rates

Perturb and observe (P&O) techniques still suffer from several disadvantages, such as sustained oscillation around the MPP, fast tracking versus oscillation trade-offs, and user predefined constants. A short review of previous conventional (voltage or current perturbation) and modified (duty ratio perturbation) P&O with and without adaptive perturb as well as an introduction of new conventional adaptive P&O is done in

[84]. In that paper, the change of array power is utilized as an error signal manipulated by a PI controller to generate an adaptive perturb. Two PI controllers are used which need tuning.

Reference [85] introduces optimization of perturbation and observation method parameters in MPPT of the PV system. The considered parameters are amplitude of duty cycle perturbation and the sampling time. Lowering duty cycle perturbation reduces the oscillation around MPP which reduces the steady-state losses but it makes the algorithm less efficient in the case of rapidly changing atmospheric conditions. The sampling interval should be set higher than a proper threshold in order to avoid instability of the MPPT and reduce oscillations around the MPP in steady state. It should be based on the dynamic of the system in a way that the system reaches the steady state before the next measurement otherwise very high sampling time confuses the control algorithm.

Partial-shading condition exhibits multiple local maximum power points (MPPs). In [86] a new method to track the global MPP is presented. It scans the PV curve every 1-15 minutes and finds the global MPP. In the meantime after finding the MPP the P&O method tracks that operating point.

The usual method for maximum power point tracking in PV systems is called maximum power point tracking (MPPT); however, this is not a good solution for large PV farms due to different orientations of PV modules belonging to the same PV field.

Shadowing effects, manufacturing tolerances, and nonuniformity of ambient temperature of the PV field may have more than one peak and MPPT. Reference [87]

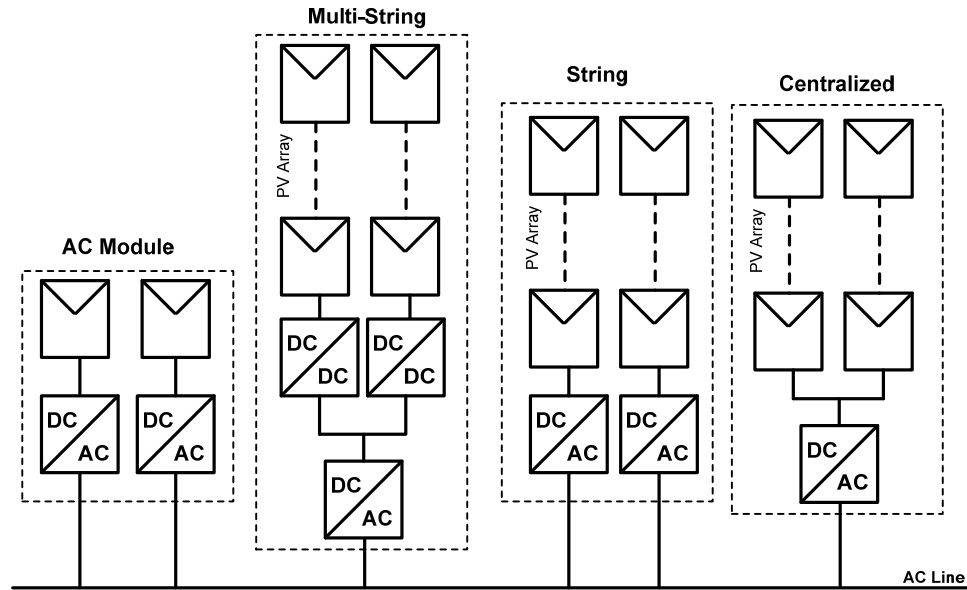


Figure 1.1 Different structures of PV system.

introduces distribute maximum power point tracking (DMPPT) which is based on the adoption of a DC/DC converter dedicated to each PV module. It is focuses on the design of a DC/DC converter for this purpose as well as a trade-off between performance and the cost.

The reliability of the various techniques adopted in grid-connected inverters in preventing non-intentional operation in islanding mode and the reliability of maximum power point tracking (MPPT) schemes in PV system applications is studied in [88].

There are four topologies used in PV generation systems as shown in Figure 1.1 [89] including centralized, string, multi string and AC module. Multi-string and AC module topology are more common [90].

In Multi-string topology not only can the modular DC/DC converters and DC/AC converters be connected through a DC bus, but also the energy storage devices and local

multifunctional power converters are developed to integrate batteries as the backup for PV generation systems [91-92]. PV generation and batteries are coordinated to feed utility grid or plug-in hybrid electric vehicle loads [93-95]. In these papers, different power conditions and battery capacity limits are taken into account, but the islanding operation is not considered. The upper/lower limits of state of charge (SoC) for batteries are usually ignored [96-97]. For smooth energy production in [98-99] not only batteries, but fuel cells are also employed.

In [100-101], the study of PV system equipped with batteries and super capacitors grid-connected power flow is not taken into account.

The objective of this dissertation is to improve the control of Microgrid for both autonomous and grid conned modes. The droop control is applied to the maintain voltage and frequency. Frequency droops against output active power of converter while voltage magnitude droops against reactive power. The PI load voltage control and inner current control are designed based on complex format of dynamic equations. Along with considering both modes of operation, the locally available control parameters of each DG unit are used, so that communication among DG units can be avoided in order to improve the system reliability and reduce the costs. The three phase PLL is designed and added to each converter in order to measure instantaneous local frequency and prepare reference frequency for qd-axis transformation. Instead of a constant DC source for the input of the inverter, in this dissertation a photovoltaic source with its nonlinear characteristic is used. The DG unit is connected to the main grid through the three phase inverter. The load voltage magnitude and frequency are adapted from the main grid. The DC link voltage is controlled for maximum power point operation of the PV. In autonomous operation of the

microgrid, the limitation of the source power for feeding the loads is included. A battery with a bidirectional DC-DC converter is added. To verify the proposed controllers, the laboratory scale experiment is implemented in addition to the dynamic simulation of the system. The designed experimental system consists of a microgrid with two different sources, a nonlinear PV source and a battery source. Along with the programmed PLL, the enhanced phase lock loop (EPLL) also is designed and the experimental results of both systems are compared. EPLL is used to define the reference frequency and angle of the load voltage. It is operated as a band pass filter for the other parameters.

This dissertation is organized into seven major chapters which follow this introduction. Chapter 2 discusses the concept of microgrid and also the use of droop control in power sharing among different sources. Chapter 3 describes the autonomous PV system. The proposed controlled is applied to the PV system. A battery is added to control DC link voltage and also balance the power between the source and the loads. In Chapter 4 the grid connected operation of the PV system is investigated. In Chapter 5 the experimental setup design is explained and the proposed method for both autonomous mode and grid connected mode is applied. Chapter 6 describes the use of interior permanent magnet (IPM) generator in wind turbine applications. The steady state and dynamic operations of IPM generator under variable wind speed are studied. The controllability analysis of both wind turbine and PV systems are investigated in Chapter 7. Finally Chapter 8 presents conclusions and recommendations for future research.

CHAPTER 2

CONTROLLER DESIGN, BIFURCATION ANALYSIS AND SIMULATION OF ISOLATED MICROGRID

2.1 Introduction

Distribution networks are not always connected to each other or to a higher voltage level power system. There is always an area of the electrical network which operates autonomously with its own generation units. This may happen for larger areas like a city, state, or just a small village far from the main network.

Usually distributed generation (DG) units are smaller than conventional power plants and use renewable energy sources such as wind turbine, PV systems, or fuel cells. Besides the clear benefits gained from these sources like clean characteristics and availability of renewable energy sources, cost reduction and improvement of technologies such as power electronic converters has recently made them even more attractive.

A Microgrid is a combination of local loads with their own DG units that can operate autonomously or connected to the main grid. In grid connected mode, the frequency and voltage magnitude is dictated by the main grid and the DG unit is feeding the total load or part of it. While in autonomous mode, besides feeding total active and reactive powers of the loads, frequency and voltage magnitude should also be controlled by DG units. Total loads should be shared between DG units based on their rated capacity when there is more than one unit in order to avoid over loading the sources.

In [102-103] a single converter connected to the grid is considered therefore the frequency of the system is assumed to be constant. The angle droop control and frequency droop control are proposed in [104-105] respectively to share total load between DG units in autonomous operation mode. The state space model of a multi-converter autonomous system is defined in [106] and droop control is applied to share total loads. The frequency of the first converter is used to convert all system equations in the same qd-axis reference frame, but the dynamic of a phase locked loop for synchronization and frequency measurement is not considered. A virtual inductor is added to the control system in [107] to decouple active and reactive power sharing in low voltage systems, but controller designs are not included. In [108] the voltage is drooping against active power and the frequency is boosting versus reactive power in a two converter system, but the dynamics of converters are not included and they are assumed as current sources. Reference [109] studies the Microgrid operation from stability points of view and shows controller dominant eigenvalues are caused by the droop controller.

In this chapter, a dynamic model of one converter system including their control parts designed in complex format is explained. A droop controller is added to maintain voltage and frequency and also to feed the loads. Bifurcation analysis is applied to the system to find equilibrium curves of parameters and bifurcation points in the operation region. Then, a general dynamic model of a multi converter system is derived. Control unit for a two converter system in separated qd-axis format for this system is designed. To share active and reactive power between converters in autonomous operation, a droop controller is added to the control part. A PLL is designed and its dynamic is added to the

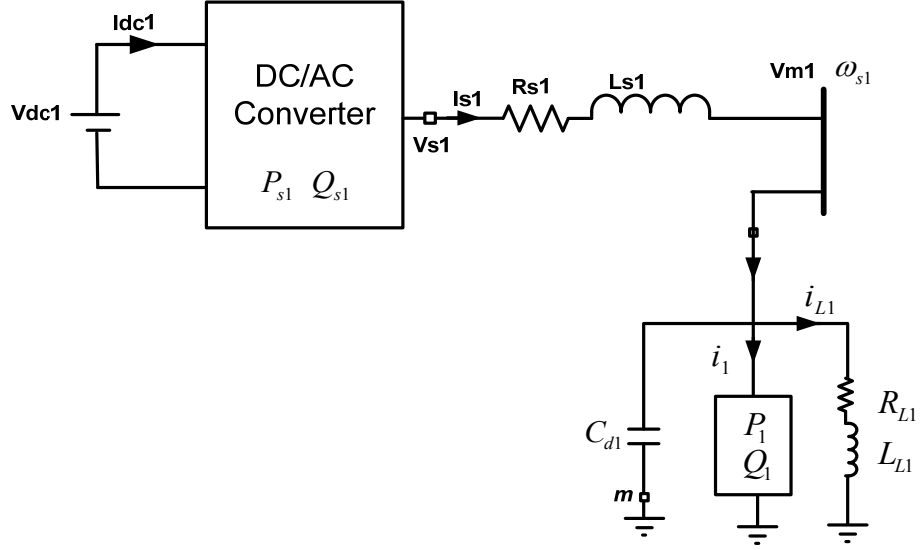


Figure 2.1 Standalone one converter system schematic diagram

power system. The controlled system is simulated in MATLAB software and dynamic operation of the converters is studied.

2.2 Autonomous Operation of One Converter System

Figure 2.1 represents the block diagram of a typical standalone converter base power system. A voltage source converter converts DC input to AC output voltage. A linear RL load and a constant load are connected to the converter through transmission line. A capacitor is connected across the load to smooth its voltage.

The dynamic equations of the system in three phase abc frame are as follows:

Transmission line dynamic equations

$$\begin{cases} V_{s1a} = V_{m1a} + L_{s1}pI_{s1a} + R_{s1}I_{s1a} \\ V_{s1b} = V_{m1b} + L_{s1}pI_{s1b} + R_{s1}I_{s1b} \\ V_{s1c} = V_{m1c} + L_{s1}pI_{s1c} + R_{s1}I_{s1c} \end{cases} \quad (2.1)$$

The three phase inverter equations are

$$\begin{cases} V_{s1a} + V_{no} = \frac{V_{dc1}}{2}(2s_{ap} - 1) \\ V_{s1a} + V_{no} = \frac{V_{dc1}}{2}(2s_{bp} - 1) \\ V_{s1a} + V_{no} = \frac{V_{dc1}}{2}(2s_{cp} - 1) \end{cases} \quad (2.2)$$

where V_{s1abc} , I_{s1abc} and s_{abc} are output phase voltages, phase currents and switching functions of DG1 (VSC1).

Linear load of DG1 (L1) equations are

$$\begin{cases} V_{m1a} = R_{L1}I_{L1a} + L_{L1}pI_{L1a} \\ V_{m1b} = R_{L1}I_{L1b} + L_{L1}pI_{L1b} \\ V_{m1c} = R_{L1}I_{L1c} + L_{L1}pI_{L1c} \end{cases} \quad (2.3)$$

where I_{L1abc} are phase currents of linear load (L1) of DG1

Capacitor of DG1 equations are

$$\begin{cases} C_{d1}pV_{m1a} = I_{s1a} - I_{L1a} - I_{1a} \\ C_{d1}pV_{m1b} = I_{s1b} - I_{L1b} - I_{1b} \\ C_{d1}pV_{m1c} = I_{s1c} - I_{L1c} - I_{1c} \end{cases} \quad (2.4)$$

where I_{1abc} are the phase currents of constant load of DG1.

For converting abc to qdo reference frame we can use a transformation matrix

$$\begin{bmatrix} f_q \\ f_d \\ f_0 \end{bmatrix} = K_s \begin{bmatrix} f_a \\ f_b \\ f_c \end{bmatrix}, \quad K_s = \frac{2}{3} \begin{bmatrix} \cos(\theta) & \cos(\theta - \frac{2\pi}{3}) & \cos(\theta + \frac{2\pi}{3}) \\ \sin(\theta) & \sin(\theta - \frac{2\pi}{3}) & \sin(\theta + \frac{2\pi}{3}) \\ \frac{1}{2} & \frac{1}{2} & \frac{1}{2} \end{bmatrix}, \quad \theta = \omega t + \theta_0 \quad (2.5)$$

The inverse transformation matrix is

$$\begin{bmatrix} f_a \\ f_b \\ f_c \end{bmatrix} = K_s^{-1} \begin{bmatrix} f_q \\ f_d \\ f_0 \end{bmatrix}, \quad K_s^{-1} = \begin{bmatrix} \cos(\theta) & \sin(\theta) & 1 \\ \cos(\theta - \frac{2\pi}{3}) & \sin(\theta - \frac{2\pi}{3}) & 1 \\ \cos(\theta + \frac{2\pi}{3}) & \sin(\theta + \frac{2\pi}{3}) & 1 \end{bmatrix} \quad (2.6)$$

qd-axis dynamic equations of the system in local frequency reference frame are as follows:

$$\begin{cases} M_{q1} = M_1 \cos((\omega_1 - \omega_{s1})t + (\theta_{10} - \theta_{s10})) \\ M_{d1} = -M_1 \sin((\omega_1 - \omega_{s1})t + (\theta_{10} - \theta_{s10})) \end{cases} \quad (2.7)$$

where ω_1 and θ_{10} are frequency and initial angle of converter. ω_{s1} and θ_{s10} are instantaneous frequency and initial angle of the system that is measured by a phase locked loop (PLL). M_1 , M_{q1} and M_{d1} are modulation index magnitude, q-axis modulation index and d axis modulation index of the converter.

Load voltage equations

$$\begin{cases} V_{qm1} = V_{m1} \cos((\omega_{s1} - \omega_{s1})t + (\theta_{s10} - \theta_{s10})) = V_{m1} \\ V_{dm1} = 0 \end{cases} \quad (2.8)$$

where V_{m1} is the load voltage magnitude.

$$\begin{cases} pI_{s1q} = \frac{1}{L_{s1}} (M_{q1} \frac{V_{dc1}}{2} - V_{qm1} - R_{s1} I_{s1q} - L_{s1} \omega_{s1} I_{s1d}) \\ pI_{s1d} = \frac{1}{L_{s1}} (M_{d1} \frac{V_{dc1}}{2} - V_{dm1} - R_{s1} I_{s1d} + L_{s1} \omega_{s1} I_{s1q}) \end{cases} \quad (2.9)$$

where I_{s1qd} , R_{s1} and L_{s1} are qd-axis current, resistance and inductance of transmission

$$\text{line } p = \frac{d}{dt}.$$

Linear Load of DG1 (L1) equations

$$\begin{cases} pI_{L1q} = \frac{1}{L_{L1}}(V_{qm1} - R_{L1}I_{L1q} - L_{L1}\omega_{s1}I_{L1d}) \\ pI_{L1d} = \frac{1}{L_{L1}}(V_{dm1} - R_{L1}I_{L1d} + L_{L1}\omega_{s1}I_{L1q}) \end{cases} \quad (2.10)$$

where I_{L1qd} , R_{L1} and L_{L1} are qd-axis current, resistance and inductance of the linear load.

Constant load of DG1 equations

$$I_{1q} = \frac{2}{3} \frac{P_1 V_{qm1} - Q_1 V_{dm1}}{V_{qm1}^2 + V_{dm1}^2} \quad \text{and} \quad I_{1d} = \frac{2}{3} \frac{P_1 V_{dm1} + Q_1 V_{qm1}}{V_{qm1}^2 + V_{dm1}^2} \quad (2.11)$$

where I_{1qd} , P_1 and Q_1 are qd-axis current, active power and reactive power of constant load.

Capacitor of DG1 Equations

$$\begin{cases} pV_{qm1} = \frac{1}{C_{d1}}(I_{s1q} - I_{L1q} - I_{1q} - C_{d1}\omega_{s1}V_{dm1}) \\ pV_{dm1} = \frac{1}{C_{d1}}(I_{s1d} - I_{L1d} - I_{1d} + C_{d1}\omega_{s1}V_{qm1}) \end{cases} \quad (2.12)$$

Where C_{d1} is the capacitance of parallel capacitor connected to the loads.

2.3 Controller Design of One Converter System

2.3.1 Droop Control

The droop control method is being used in conventional generators of power plants. In autonomous operation of converter based DG systems, this method can be adopted to share total load and also control voltage magnitude and frequency in a special range. In this control unit we can share active power of total load by drooping the frequency as a function of output active power of converter. We can also droop output voltage magnitude of the converter against its output reactive to share total load reactive power. As it is shown in (2.13) two coefficients control the slope of change of frequency and voltage against active and reactive power respectively.

$$\begin{cases} \theta_1 = \frac{\omega_1}{p} = \frac{1}{p}(\omega_n - m_p P_{s1}) \\ V_{m1} = V_n - n_q Q_{s1} \end{cases} \quad (2.13)$$

where ω_n and V_n are rated frequency and rated voltage of the system. m_p , n_q , P_{s1} and Q_{s1} are active power droop coefficient, reactive power droop coefficient, output active power and output reactive power of the converter.

To remove fluctuations and produce an average value of output power, both calculated instantaneous powers passed through a low pass filter with cut of frequency of ω_c that is assumed to be 10% of nominal frequency.

$$\begin{cases} \tilde{P}_{s1} = \frac{3}{2}(V_{qm1}I_{qs1} + V_{dm1}I_{ds1}) \\ \tilde{Q}_{s1} = \frac{3}{2}(V_{qm1}I_{ds1} - V_{dm1}I_{qs1}) \end{cases} \quad (2.14)$$

and

$$\begin{cases} P_{s1} = \frac{\omega_c}{p + \omega_c} \tilde{P}_{s1} = \frac{\omega_c}{p + \omega_c} \frac{3}{2}(V_{qm1}I_{qs1} + V_{dm1}I_{ds1}) \\ Q_{s1} = \frac{\omega_c}{p + \omega_c} \tilde{Q}_{s1} = \frac{\omega_c}{p + \omega_c} \frac{3}{2}(V_{qm1}I_{ds1} - V_{dm1}I_{qs1}) \end{cases} \quad (2.15)$$

Therefore

$$\begin{cases} pP_{s1} = \frac{3\omega_c}{2}(V_{qm1}I_{qs1} + V_{dm1}I_{ds1}) - \omega_c P_{s1} \\ pQ_{s1} = \frac{3\omega_c}{2}(V_{qm1}I_{ds1} - V_{dm1}I_{qs1}) - \omega_c Q_{s1} \end{cases} \quad (2.16)$$

The outputs of droop control are voltage magnitude and angular frequency which define the reference angle of the load voltage using an integrator. Thus qd axis reference voltage can be determined as follows:

$$\begin{cases} V_{qm1}^* = V_{m1} \cos(\theta_1 - \theta_{s1}) \\ V_{dm1}^* = -V_{m1} \sin(\theta_1 - \theta_{s1}) \end{cases} \quad (2.17)$$

where θ_{s1} comes from PLL.

$$\begin{cases} \theta_1 = \omega_n t - \frac{m_p P_{s1}}{p} \\ \theta_{s1} = \omega_{s1} t + \theta_{s10} \end{cases} \quad (2.18)$$

Therefore

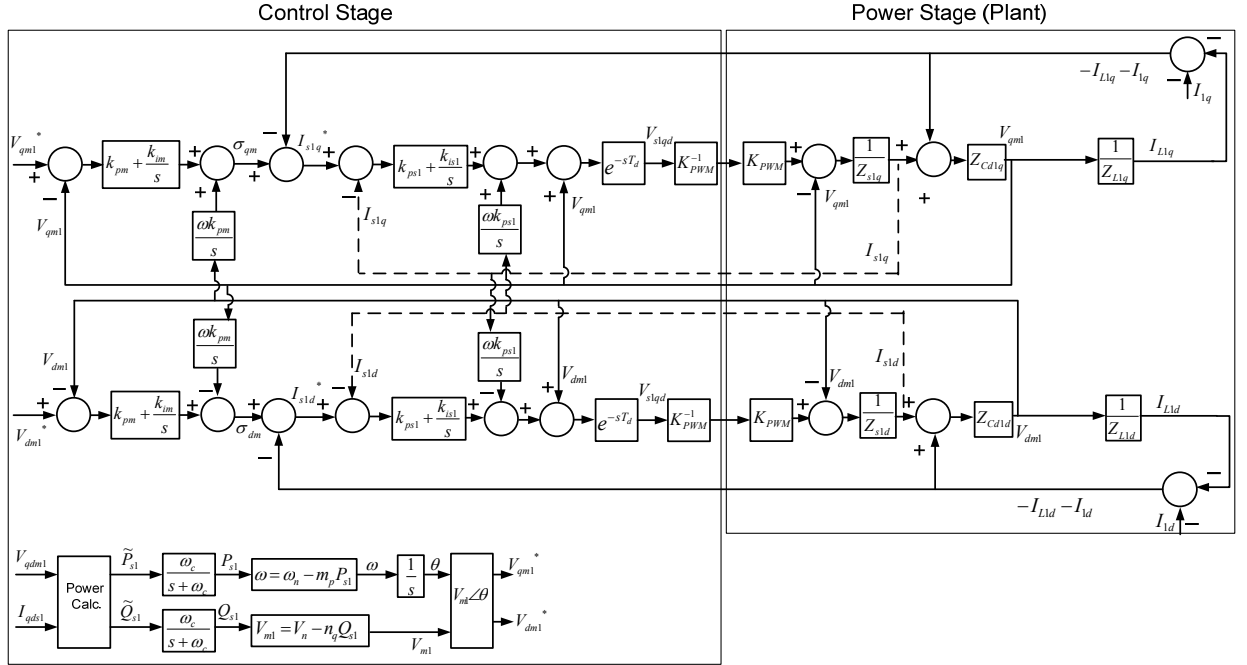


Figure 2.2 Block diagram of controlled unit beside power stage

$$\begin{cases} V_{qd1}^* = (V_n - n_q Q_{s1}) \cos\left((\omega_n - \omega_{s1})t - \frac{m_p P_{s1}}{p} - \theta_{s10}\right) \\ V_{dm1}^* = -(V_n - n_q Q_{s1}) \sin\left((\omega_n - \omega_{s1})t - \frac{m_p P_{s1}}{p} - \theta_{s10}\right) \end{cases} \quad (2.19)$$

2.3.2 Voltage Control

Figure 2.2 illustrates block diagram of the controlled system. To follow reference voltage, produced from droop control, a PI voltage controller is designed. From Figure 2.2 and complex Dynamic equations of the system in laplace format

$$C_{d1}pV_{qdm1} - jC_{d1}\omega_{s1}V_{qdm1} = I_{s1qd} - I_{L1qd} - I_{\lambda qd} = \sigma_{qdm} = k_m(p)(V_{qdm1}^* - V_{qdm1}) \quad (2.20)$$

The transfer function of voltage control

$$\frac{V_{qdm1}}{V_{qdm1}^*} = \frac{k_m(s)}{C_{d1}s - jC_{d1}\omega_{s1} + k_m(p)} \text{ and } k_m(s) = k_{pm} + \frac{k_{im} - j\omega k_{pm}}{p} \quad (2.21)$$

Therefore

$$\frac{V_{qdm1}}{V_{qdm1}^*} = \frac{pk_{pm} + k_{im} - j\omega_{s1}k_{pm}}{C_{d1}p^2 + (k_{pm} - jC_{d1}\omega_{s1})p + k_{im} - j\omega_{s1}k_{pm}} \Rightarrow \text{if we choose } k_{im} = 0 \quad (2.22)$$

$$\frac{V_{qdm1}}{V_{qdm1}^*} = \frac{k_{pm}(p - j\omega_{s1})}{C_{d1}p^2 + (k_{pm} - jC_{d1}\omega_{s1})p - j\omega_{s1}k_{pm}} = \frac{k_{pm}(p - j\omega_{s1})}{(C_{d1}p + k_{pm})(p - j\omega_{s1})} = \frac{k_{pm}}{(C_{d1}p + k_{pm})} \quad (2.23)$$

So the parameter of PI voltage controller can be defined as

$$\begin{cases} k_m(s) = k_{pm} + \frac{k_{im} - j\omega_{s1}k_{pm}}{p} \\ k_{im} = 0 \end{cases} \quad (2.24)$$

and

$$I_{s1qd}^* = \sigma_{qdm} + I_{L1qd} + I_{1qd} \quad (2.25)$$

where the σ_{qdm} is the output of voltage controller

$$\sigma_{qdm} = (V_{qqm1} + jV_{ddm1})\left(k_{pm} + \frac{k_{im} - j\omega_{s1}k_{pm}}{p}\right) \text{ and } \begin{cases} V_{qqm1} = V_{qm1}^* - V_{qm1} \\ V_{ddm1} = V_{dm1}^* - V_{dm1} \end{cases} \quad (2.26)$$

So

$$\begin{cases} \sigma_{qm} = V_{qqm1}\left(k_{pm} + \frac{k_{im}}{p}\right) + V_{ddm1}\left(\frac{\omega_{s1}k_{pm}}{p}\right) \\ \sigma_{dm} = V_{ddm1}\left(k_{pm} + \frac{k_{im}}{p}\right) - V_{qqm1}\left(\frac{\omega_{s1}k_{pm}}{p}\right) \end{cases} \quad (2.27)$$

$$\begin{cases} I_{s1q}^* = (V_{qm1}^* - V_{qm1})(k_{pm} + \frac{k_{im}}{s}) + (\frac{\omega_{s1}k_{pm}}{s})(V_{dm1}^* - V_{dm1}) + I_{L1q} + I_{1q} \\ I_{s1d}^* = (V_{dm1}^* - V_{dm1})(k_{pm} + \frac{k_{im}}{s}) - (\frac{\omega_{s1}k_{pm}}{s})(V_{qm1}^* - V_{qm1}) + I_{L1d} + I_{1d} \end{cases} \quad (2.28)$$

Adding one state variable due to integral function

$$\begin{cases} \dot{\gamma}_{q1} = (V_{qm1}^* - V_{qm1}) = (V_n - n_q Q_{s1}) \cos\left((\omega_n - \omega_{s1})t - \frac{m_p P_{s1}}{p} - \theta_{s10}\right) - V_{qm1} \\ \dot{\gamma}_{d1} = (V_{dm1}^* - V_{dm1}) = -(V_n - n_q Q_{s1}) \sin\left((\omega_n - \omega_{s1})t - \frac{m_p P_{s1}}{p} - \theta_{s10}\right) - V_{dm1} \end{cases} \quad (2.29)$$

Thus

$$\begin{cases} \gamma_{q1} = (V_{qm1}^* - V_{qm1})\left(\frac{1}{p}\right) \\ \gamma_{d1} = (V_{dm1}^* - V_{dm1})\left(\frac{1}{p}\right) \end{cases} \quad (2.30)$$

And the output reference currents are

$$\begin{cases} I_{s1q}^* = (V_{qm1}^* - V_{qm1})(k_{pm}) + k_{im} \gamma_{q1} + (\omega_{s1}k_{pm})\gamma_{d1} + I_{L1q} + I_{1q} \\ I_{s1d}^* = (V_{dm1}^* - V_{dm1})(k_{pm}) + k_{im} \gamma_{d1} - (\omega_{s1}k_{pm})\gamma_{q1} + I_{L1d} + I_{1d} \end{cases} \quad (2.31)$$

2.3.3 Current Control

As an inner current control, from the equations of the system in complex format

$$L_{s1}pI_{s1qd} + R_{s1}I_{s1qd} - jL_{s1}\omega I_{s1qd} = M_{qd1} \frac{V_{dc1}}{2} - V_{qdm1} = \sigma_{s1} = k_{s1}(p)(I_{s1qd}^* - I_{s1qd}) \quad (2.32)$$

Where $k_{s1}(s)$ is the current controller, therefore current transfer function is

$$\frac{I_{s1qd}}{I_{s1qd}^*} = \frac{k_{s1}(p)}{L_{s1}s + R_{s1} - jL_{s1}\omega + k_{s1}(p)} \text{ and } k_{s1}(p) = k_{ps1} + \frac{k_{is1} - j\omega k_{ps1}}{p} \quad (2.33)$$

where k_{ps1} and k_{is1} are proportional and integral parameters of current controller.

$$\frac{I_{s1qd}}{I_{s1qd}^*} = \frac{pk_{ps1} + k_{is1} - j\omega k_{ps1}}{L_{s1}p^2 + (k_{ps1} + R_{s1} - jL_{s1}\omega)p + k_{is1} - j\omega k_{ps1}} \Rightarrow \text{if we choose } k_{is1} = \frac{R_{s1}}{L_{s1}}k_{ps1} \quad (2.34)$$

Transfer function of current control

$$\frac{I_{s1qd}}{I_{s1qd}^*} = \frac{(p + \frac{R_{s1}}{L_{s1}} - j\omega)k_{ps1}}{(pL_{s1} + k_{ps1})(p + \frac{R_{s1}}{L_{s1}} - j\omega)} = \frac{k_{ps1}}{pL_{s1} + k_{ps1}} \quad (2.35)$$

Thus parameters of current control can be defined as

$$\begin{cases} k_{s1}(p) = k_{ps1} + \frac{k_{is1} - j\omega k_{ps1}}{p} \\ k_{is1} = \frac{R_{s1}}{L_{s1}}k_{ps1} \end{cases} \quad (2.36)$$

And modulation indices as the output of inner current controller are

$$M_{qd1} = \frac{2}{V_{dc1}}(\sigma_{qd} + V_{qdm1}) \quad (2.37)$$

$$\sigma_{s1} = (I_{s1qq} + jI_{s1dd})(k_{ps1} + \frac{k_{is1} - j\omega k_{ps1}}{p}) \text{ and } \begin{cases} I_{s1qq} = I_{s1q}^* - I_{s1q} \\ I_{s1dd} = I_{s1d}^* - I_{s1d} \end{cases} \quad (2.38)$$

So for separating qd-axis

$$\begin{cases} \sigma_{qs1} = I_{s1qq} \left(k_{ps1} + \frac{k_{is1}}{s} \right) + I_{s1dd} \left(\frac{\omega k_{ps1}}{s} \right) \\ \sigma_{ds1} = I_{s1dd} \left(k_{ps1} + \frac{k_{is1}}{s} \right) - I_{s1qq} \left(\frac{\omega k_{ps1}}{s} \right) \end{cases} \quad (2.39)$$

Inputs and outputs of current controller are I_{s1qd} and M_{qd1} respectively, therefore we need to define I_{s1q}^* and I_{s1d}^* .

$$\begin{cases} V_{qs1} = \left(I_{s1q}^* - I_{s1q} \right) \left(k_{ps1} + \frac{k_{is1}}{s} \right) + \left(I_{s1d}^* - I_{s1d} \right) \left(\frac{\omega_{s1} k_{ps1}}{s} \right) + V_{qm1} \\ V_{ds1} = \left(I_{s1d}^* - I_{s1d} \right) \left(k_{ps1} + \frac{k_{is1}}{s} \right) - \left(I_{s1q}^* - I_{s1q} \right) \left(\frac{\omega_{s1} k_{ps1}}{s} \right) + V_{dm1} \end{cases} \quad (2.40)$$

Adding one state variable due to integral function

$$\begin{cases} \dot{\phi}_{q1} = \left(I_{s1q}^* - I_{s1q} \right) = (V_{qm1} - V_{qm1})(k_{pm}) + k_{im} \gamma_{q1} + (\omega_{s1} k_{pm}) \gamma_{d1} + I_{L1q} + I_{1q} - I_{s1q} \\ \dot{\phi}_{d1} = \left(I_{s1d}^* - I_{s1d} \right) = (V_{dm1} - V_{dm1})(k_{pm}) + k_{im} \gamma_{d1} - (\omega_{s1} k_{pm}) \gamma_{q1} + I_{L1d} + I_{1d} - I_{s1d} \end{cases} \quad (2.41)$$

$$\begin{cases} \dot{\phi}_{q1} = \left\{ \begin{array}{l} -k_{pm} V_{qm1} - I_{s1q} + I_{L1q} + k_{im} \gamma_{q1} + (\omega_{s1} k_{pm}) \gamma_{d1} - k_{pm} n_q \cos \left((\omega_n - \omega_{s1}) t - \frac{m_p P_{s1}}{p} - \theta_{s10} \right) \mathcal{Q}_{s1} \\ + I_{1q} + (k_{pm} V_n) \cos \left((\omega_n - \omega_{s1}) t - \frac{m_p P_{s1}}{p} - \theta_{s10} \right) \end{array} \right\} \\ \dot{\phi}_{d1} = \left\{ \begin{array}{l} -k_{pm} V_{dm1} - I_{s1d} + I_{L1d} + k_{im} \gamma_{d1} - (\omega_{s1} k_{pm}) \gamma_{q1} + k_{pm} n_q \sin \left((\omega_n - \omega_{s1}) t - \frac{m_p P_{s1}}{p} - \theta_{s10} \right) \mathcal{Q}_{s1} \\ + I_{1d} + (-k_{pm} V_n) \sin \left((\omega_n - \omega_{s1}) t - \frac{m_p P_{s1}}{p} - \theta_{s10} \right) \end{array} \right\} \end{cases} \quad (2.42)$$

Therefore

$$\begin{cases} \phi_{q1} = (I_{s1q}^* - I_{s1q}) \left(\frac{1}{p} \right) \\ \phi_{d1} = (I_{s1d}^* - I_{s1d}) \left(\frac{1}{p} \right) \end{cases} \quad (2.43)$$

$$\begin{cases} V_{qs1} = (I_{s1q}^* - I_{s1q})(k_{ps1}) + k_{is1} \phi_{q1} + (\omega_{s1} k_{ps1}) \phi_{d1} + V_{qm1} \\ V_{ds1} = (I_{s1d}^* - I_{s1d})(k_{ps1}) + k_{is1} \phi_{d1} - (\omega_{s1} k_{ps1}) \phi_{q1} + V_{dm1} \end{cases} \quad (2.44)$$

$$\begin{cases} V_{qs1} = \left\{ \begin{aligned} & \left((V_{qm1}^* - V_{qm1})(k_{pm}) + k_{im} \gamma_{q1} + (\omega_{s1} k_{pm}) \gamma_{d1} + I_{L1q} + I_{1q} - I_{s1q} \right) (k_{ps1}) \\ & + k_{is1} \phi_{q1} + (\omega_{s1} k_{ps1}) \phi_{d1} + V_{qm1} \end{aligned} \right\} \\ V_{ds1} = \left\{ \begin{aligned} & \left((V_{dm1}^* - V_{dm1})(k_{pm}) + k_{im} \gamma_{d1} - (\omega_{s1} k_{pm}) \gamma_{q1} + I_{L1d} + I_{1d} - I_{s1d} \right) (k_{ps1}) \\ & + k_{is1} \phi_{d1} - (\omega_{s1} k_{ps1}) \phi_{q1} + V_{dm1} \end{aligned} \right\} \end{cases} \quad (2.45)$$

with substituting (2.19) into (2.45)

$$\begin{cases} V_{qs1} = \left\{ \begin{aligned} & \left((V_n - n_q Q_{s1}) \cos \left((\omega_n - \omega_{s1})t - \frac{m_p P_{s1}}{s} - \theta_{s10} \right) - V_{qm1} \right) (k_{pm}) + k_{im} \gamma_{q1} + (\omega_{s1} k_{pm}) \gamma_{d1} \\ & + I_{L1q} + I_{1q} - I_{s1q} \end{aligned} \right\} (k_{ps1}) \\ & + k_{is1} \phi_{q1} + (\omega_{s1} k_{ps1}) \phi_{d1} + V_{qm1} \\ V_{ds1} = \left\{ \begin{aligned} & \left(-(V_n - n_q Q_{s1}) \sin \left((\omega_n - \omega_{s1})t - \frac{m_p P_{s1}}{s} - \theta_{s10} \right) - V_{dm1} \right) (k_{pm}) + k_{im} \gamma_{d1} - (\omega_{s1} k_{pm}) \gamma_{q1} \\ & + I_{L1d} + I_{1d} - I_{s1d} \end{aligned} \right\} (k_{ps1}) \\ & + k_{is1} \phi_{d1} - (\omega_{s1} k_{ps1}) \phi_{q1} + V_{dm1} \end{cases}$$

So the qd-axis output voltages of converter are

$$\left. \begin{aligned}
V_{qs1} &= \left\{ \begin{aligned}
&(1 - k_{pm}k_{ps1})V_{qm1} - k_{ps1}I_{s1q} + k_{ps1}I_{L1q} + k_{im}k_{ps1}\gamma_{q1} + \omega_{s1}k_{pm}k_{ps1}\gamma_{d1} + k_{is1}\phi_{q1} \\
&+ (\omega_{s1}k_{ps1})\phi_{d1} - k_{pm}k_{ps1}n_q \cos\left((\omega_n - \omega_{s1})t - \frac{m_p P_{s1}}{s} - \theta_{s10}\right) Q_{s1} \\
&+ k_{ps1}I_{1q} + (k_{pm}k_{ps1}V_n) \cos\left((\omega_n - \omega_{s1})t - \frac{m_p P_{s1}}{s} - \theta_{s10}\right)
\end{aligned} \right\} \\
V_{ds1} &= \left\{ \begin{aligned}
&(1 - k_{pm}k_{ps1})V_{dm1} - k_{ps1}I_{s1d} + k_{ps1}I_{L1d} - (\omega_{s1}k_{pm}k_{ps1})\gamma_{q1} + k_{im}k_{ps1}\gamma_{d1} \\
&- (\omega_{s1}k_{ps1})\phi_{q1} + k_{is1}\phi_{d1} - k_{pm}k_{ps1}n_q \sin\left((\omega_n - \omega_{s1})t - \frac{m_p P_{s1}}{s} - \theta_{s10}\right) Q_{s1} \\
&+ k_{ps1}I_{1d} - (k_{pm}k_{ps1}V_n) \sin\left((\omega_n - \omega_{s1})t - \frac{m_p P_{s1}}{s} - \theta_{s10}\right)
\end{aligned} \right\}
\end{aligned} \right. \quad (2.46)$$

And state space equations of the converter output currents

$$\left. \begin{aligned}
pI_{s1q} &= \frac{1}{L_{s1}} \left\{ \begin{aligned}
&(-k_{pm}k_{ps1})V_{qm1} - (k_{ps1} + R_{s1})I_{s1q} - L_{s1}\omega_{s1}I_{s1d} + k_{ps1}I_{L1q} + k_{im}k_{ps1}\gamma_{q1} \\
&+ k_{is1}\phi_{q1} + (\omega_{s1}k_{ps1})\phi_{d1} - k_{pm}k_{ps1}n_q \cos\left((\omega_n - \omega_{s1})t - \frac{m_p P_{s1}}{s} - \theta_{s10}\right) Q_{s1} \\
&+ \omega_{s1}k_{pm}k_{ps1}\gamma_{d1} + k_{ps1}I_{1q} + (k_{pm}k_{ps1}V_n) \cos\left((\omega_n - \omega_{s1})t - \frac{m_p P_{s1}}{s} - \theta_{s10}\right)
\end{aligned} \right\} \\
pI_{s1d} &= \frac{1}{L_{s1}} \left\{ \begin{aligned}
&(-k_{pm}k_{ps1})V_{dm1} + L_{s1}\omega_{s1}I_{s1q} - (k_{ps1} + R_{s1})I_{s1d} + k_{ps1}I_{L1d} - (\omega_{s1}k_{pm}k_{ps1})\gamma_{q1} \\
&- (\omega_{s1}k_{ps1})\phi_{q1} + k_{is1}\phi_{d1} - k_{pm}k_{ps1}n_q \sin\left((\omega_n - \omega_{s1})t - \frac{m_p P_{s1}}{s} - \theta_{s10}\right) Q_{s1} \\
&+ k_{im}k_{ps1}\gamma_{d1} + k_{ps1}I_{1d} - (k_{pm}k_{ps1}V_n) \sin\left((\omega_n - \omega_{s1})t - \frac{m_p P_{s1}}{s} - \theta_{s10}\right)
\end{aligned} \right\}
\end{aligned} \right. \quad (2.47)$$

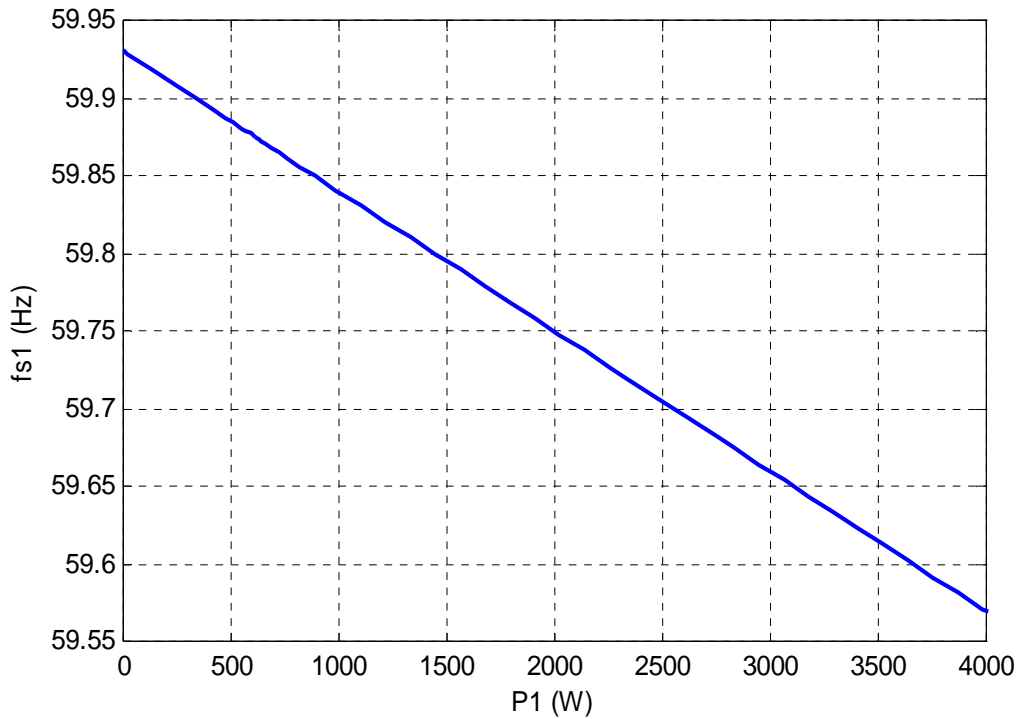


Figure 2.3 Frequency of the system

2.4 Equilibrium Curves of One Converter System

In this section to draw the equilibrium curve of the one converter standalone system and define steady state operation points without linearization, the CL_MATCONT software package [110] along with MATLAB is used. Figure 2.3 shows trend of frequency with change of active power of constant load. With increase of constant load active power from zero to 4000W, droop control reduces frequency till 59.57Hz. Output active power of the converter increases to about 4800W to feed the loads in Figure 2.4.

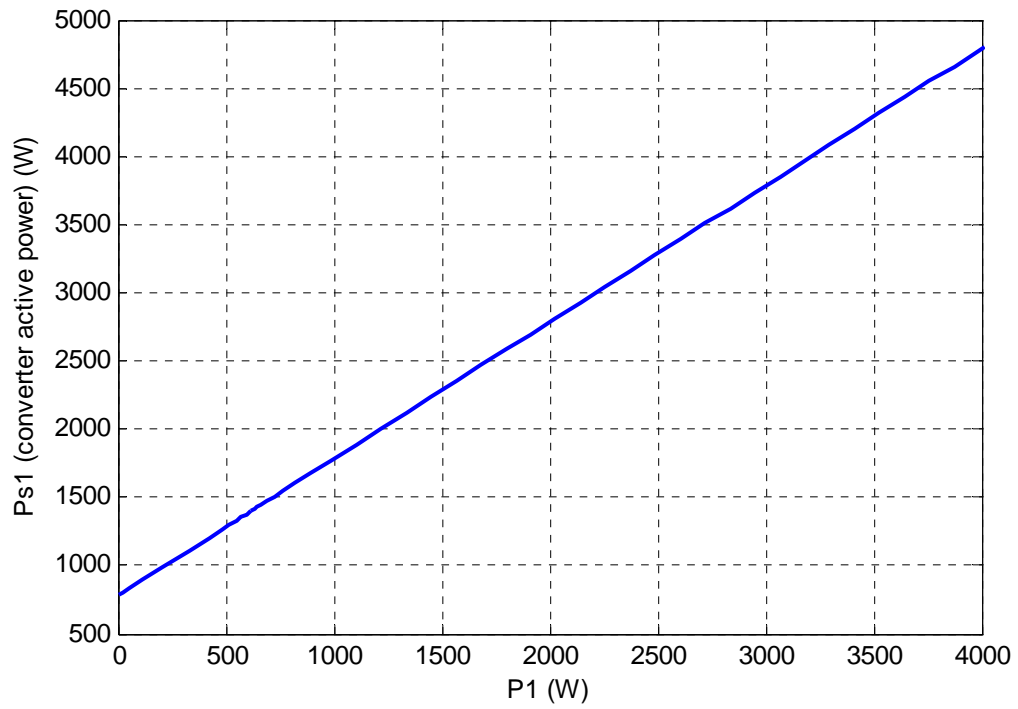


Figure 2.4 Output active power of converter

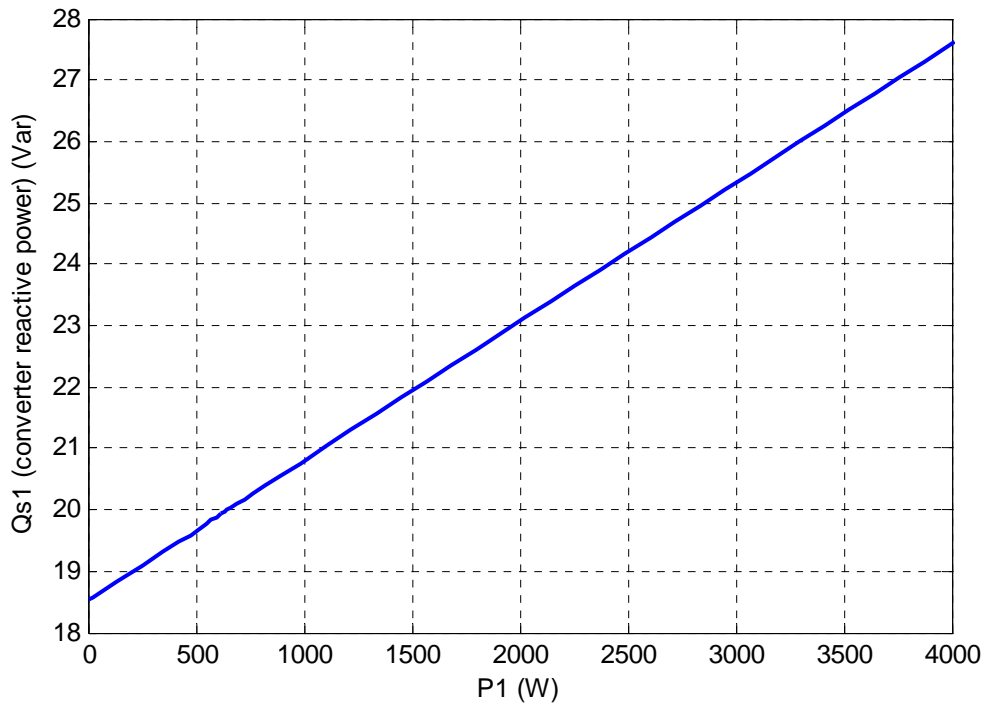


Figure 2.5 Output reactive power of converter

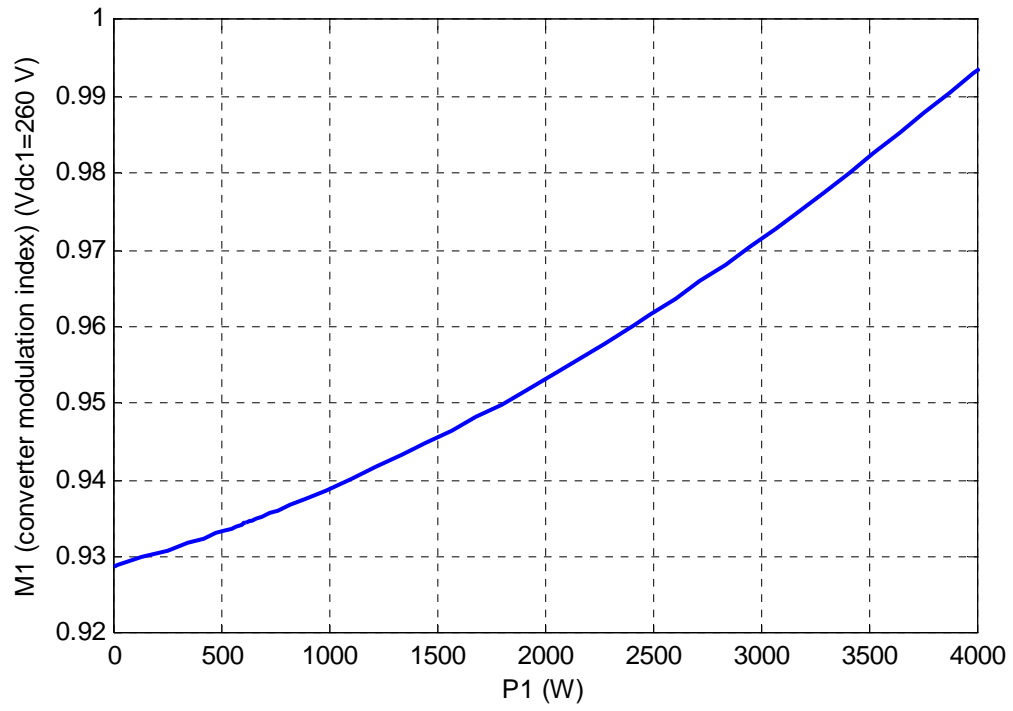


Figure 2.6 Modulation index magnitude of converter

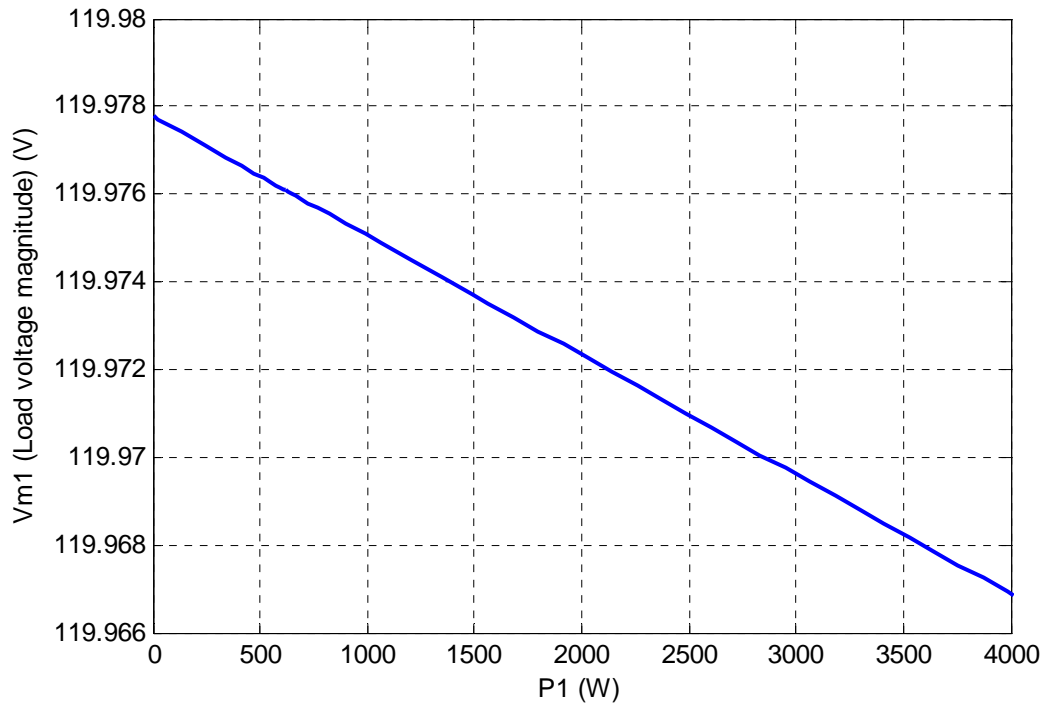


Figure 2.7 Load voltage magnitude

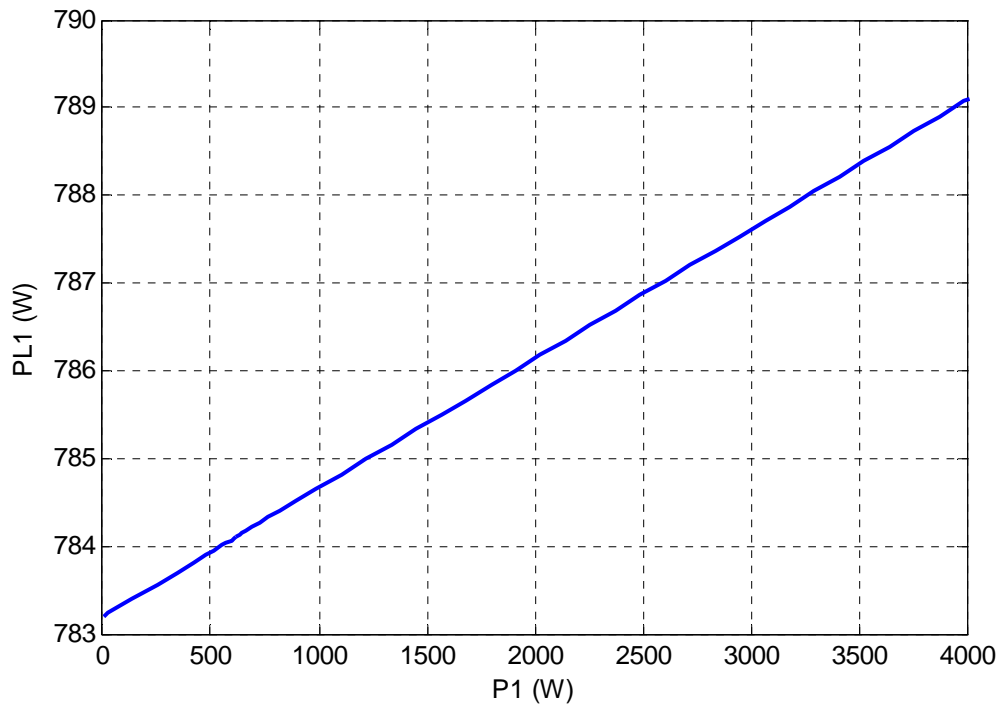


Figure 2.8 Active power of linear RL load

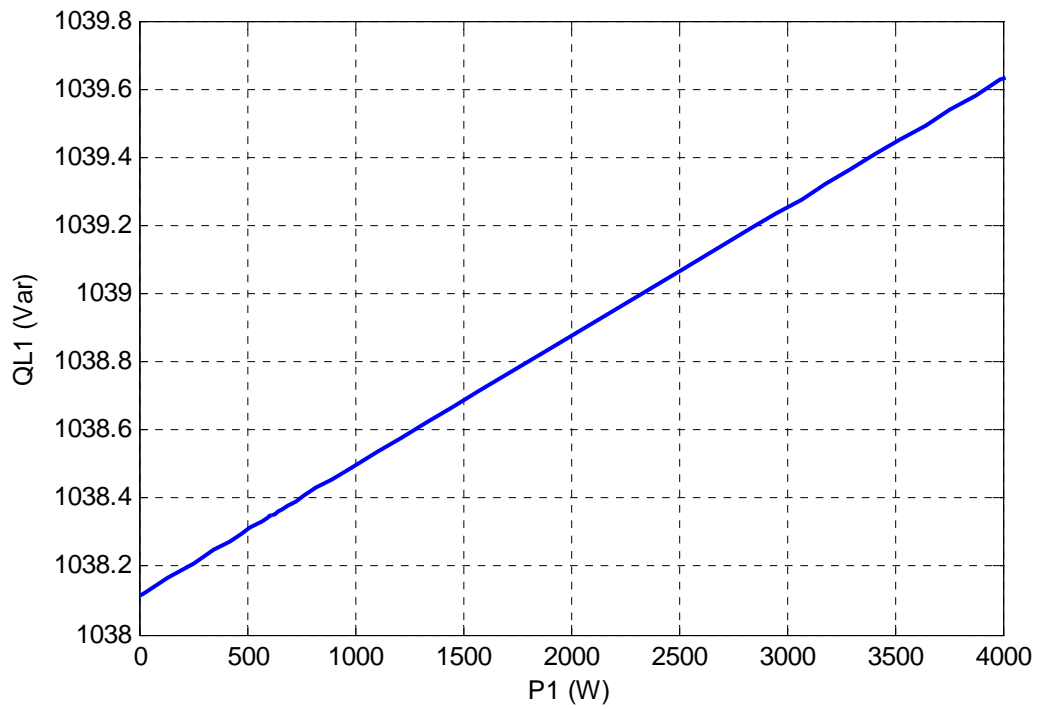


Figure 2.9 Reactive power of linear RL load

modulation index magnitude of the converter in Figure 2.6 increases and is always less than unity. Change of frequency affects the amount of inductance of transmission lines and linear load so there is a small change in voltage magnitude and active power of linear load that is related to it; in addition, reactive power of linear load has a small change in reactive power. It should be noted that change of voltage and consequently active and reactive of the linear load due to the change of constant load and frequency are small and almost negligible.

2.5 Autonomous Operation of Two Converter System

To describe how droop control shares total load in a multi converter system, a two converter system is represented in this part. The dynamic model of the system is described as a general case of a multi converter system. Control units are designed in separated qd-axis format with a phase locked loop (PLL) for each converter. The system is simulated in MATLAB software.

Figure 2.10 represents a single line diagram of a two converter system. The whole system is working autonomously. Microgrid consists of two DG units which have their own local loads which are connected to each other. Three different types of loads are used, a linear RL load, a constant load and a nonlinear load that is related to voltage magnitude and frequency. A transmission line connects local loads to the converters. Its resistance includes transmission line loss and converter switching loss. A capacitor is added at the point of load connection to remove output noise and voltage fluctuations of

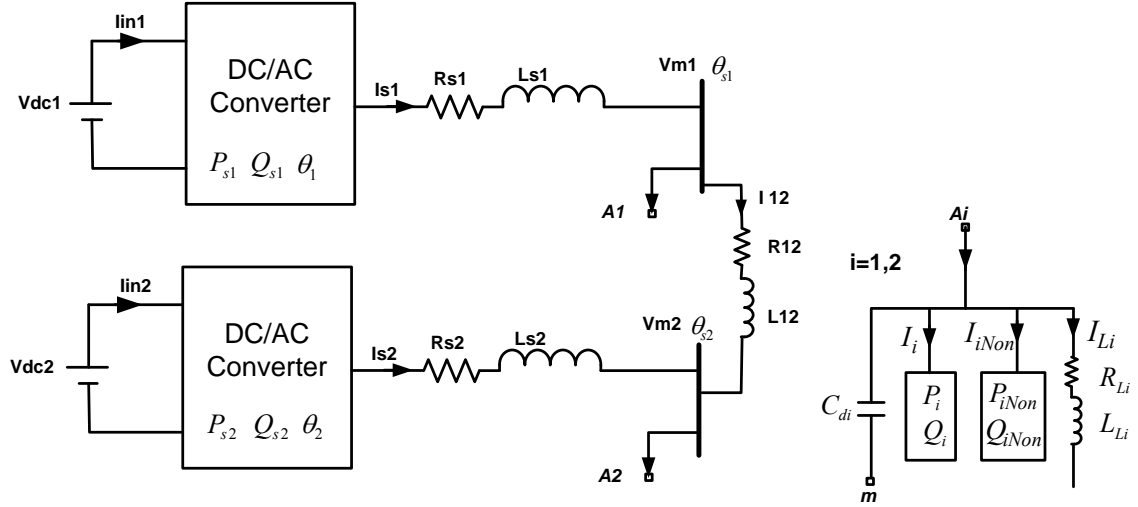


Figure 2.10 Schematic diagram of study system

the converter and prepare a smooth load voltage. The input sources are assumed to have enough capacity to feed the loads and both converters are sharing total load.

2.5.1 Dynamic Model

A droop control is applied to each converter to share total load based on local measurement so each DG unit is considered with its own local frequency which is measured using a phase lock loop (PLL). Dynamic equations of the system are as follows

$$\left(p = \frac{d}{dt} \text{ and } i = 1, 2 \right)$$

$$V_{si} = V_{mi} - L_{si} p I_{si} - R_{si} I_{si} = M_i \frac{V_{dci}}{2} \quad (2.48)$$

where V_{si} , I_{si} , and M_i are output phase voltage, phase current, and modulation index of converters. V_{mi} , R_{si} and L_{si} are load voltage, transmission line resistance and inductance of DG_i respectively.

Linear loads equation

$$V_{mi} = R_{Li}I_{Li} + L_{Li}pI_{Li} \quad (2.49)$$

where I_{Li} , R_{Li} and L_{Li} are phase current, resistance and inductance of linear load respectively.

Transmission line between two converters equation

$$V_{mi} - V_{mj} = R_{12}I_{ij} + L_{12}pI_{ij} \quad (2.50)$$

Where R_{12} and L_{12} are resistance and inductance of connection line.

Capacitor voltage equations

$$C_{di}pV_{mi} = I_{si} - I_{ij} - I_{Li} - I_i - I_{iNon} \quad (2.51)$$

where I_i , I_{iNon} and C_{di} are phase currents of constant load and nonlinear load and capacitance of DG_i.

Nonlinear load equations

$$P_{iNon} = P_{i0} \left(\frac{V_{mi}}{V_n} \right)^2 \left(\frac{f_{si}}{f_n} \right)^2 \quad (2.52)$$

$$Q_{iNon} = Q_{i0} \left(\frac{V_{mi}}{V_n} \right)^2 \left(\frac{f_{si}}{f_n} \right)^2 \quad (2.53)$$

Where P_{i0} and Q_{i0} are initial active and reactive powers of nonlinear loads. V_{mi} and f_{si} are local load voltage magnitude and frequency. V_n and f_n are nominal voltage and frequency of the system.

For each converter its own local frequency as synchronous reference frame is used to transform dynamic equations of the system to qd reference frame and produce time invariant variables.

Dynamic equations of the converter in qd-axis reference frame

$$V_{siq} = V_{miq} - L_{si} pI_{siq} - R_{si} I_{siq} - \omega_{si} L_{si} I_{sid} = M_{iq} \frac{V_{dci}}{2} \quad (2.54)$$

$$V_{sid} = V_{mid} - R_{si} I_{sid} - L_{si} pI_{sid} + \omega_{si} L_{si} I_{siq} = M_{id} \frac{V_{dci}}{2} \quad (2.55)$$

Linear loads equations

$$V_{miq} = R_{Li} I_{Liq} + L_{Li} pI_{Liq} + \omega_{si} L_{Li} I_{Lid} \quad (2.56)$$

$$V_{mid} = R_{Li} I_{Lid} + L_{Li} pI_{Lid} - \omega_{si} L_{Li} I_{Liq} \quad (2.57)$$

Transmission line between two converters equations

$$V_{miq} - V_{mjg} = R_{12} I_{ijq} + L_{12} pI_{ijq} + \omega_{si} L_{12} I_{ijd} \quad (2.58)$$

$$V_{mid} - V_{mjd} = R_{12} I_{ijd} + L_{12} pI_{ijd} - \omega_{si} L_{12} I_{ijq} \quad (2.59)$$

Capacitor voltage equations

$$C_{di} pV_{miq} = I_{siq} - I_{ijq} - I_{Liq} - I_{iq} - I_{iNonq} - \omega_{si} C_{di} V_{mid} \quad (2.60)$$

$$C_{di} pV_{mid} = I_{sid} - I_{ijd} - I_{Lid} - I_{id} - I_{iNond} + \omega_{si} C_{di} V_{miq} \quad (2.61)$$

Nonlinear load current equation

$$I_{iNonq} = \frac{2}{3} \frac{P_{iNon} V_{miq} - Q_{iNon} V_{mid}}{V_{miq}^2 + V_{mid}^2} \quad (2.62)$$

$$I_{iNond} = \frac{2}{3} \frac{P_{iNon} V_{mid} + Q_{iNon} V_{miq}}{V_{miq}^2 + V_{mid}^2} \quad (2.63)$$

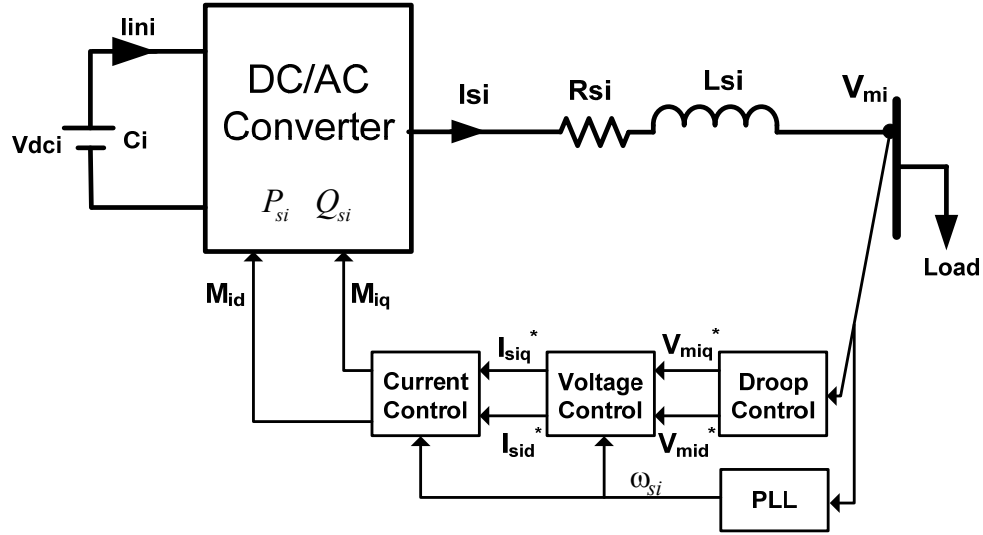


Figure 2.11 Control unit diagram

Constant load current equation

$$I_{iq} = \frac{2 P_i V_{miq} - Q_i V_{mid}}{3 V_{miq}^2 + V_{mid}^2} \quad (2.64)$$

$$I_{id} = \frac{2 P_i V_{mid} + Q_i V_{miq}}{3 V_{miq}^2 + V_{mid}^2} \quad (2.65)$$

2.5.2 Controller Unit of Two Converter System

Since microgrid is works autonomously, voltage magnitude and frequency of each DG unit should be defined along with the feed of the total load. This is illustrated in Figure 2.11 the control unit of each converter consists of four main parts, a droop control to share the load between converters, a voltage and an inner current control. A phase lock loop (PLL) is added to align load voltage in q-axis reference frame and measure local frequency.

2.5.3 Droop Control

Like one converter system, in a multi converter system

$$\omega_i^* = \omega_n - m_{pi} P_{si} \quad (2.66)$$

$$V_{mi}^* = V_n - n_{qi} Q_{si} \quad (2.67)$$

where ω_n and V_n are rated frequency and rated voltage of the

In (2.68) and (2.69) the amount of droop coefficients are defined. The active power droop coefficient is based on maximum change of frequency that is considered 1% against maximum change of active power of converter which is nominal power of converter.

$$m_{pi} = \frac{\Delta\omega}{\Delta P_{si\max}} \quad (2.68)$$

$$n_{qi} = \frac{\Delta V}{\Delta Q_{si\max}} \quad (2.69)$$

For reactive power droop coefficient, the maximum tolerance of voltage is considered 2%. It should be noted that to have the same frequency in the whole system

$$\omega_n - m_{p1} P_{s1} = \omega_n - m_{p2} P_{s2} \quad (2.70)$$

Therefore

$$\frac{m_{p1}}{m_{p2}} = \frac{P_{s2}}{P_{s1}} \quad (2.71)$$

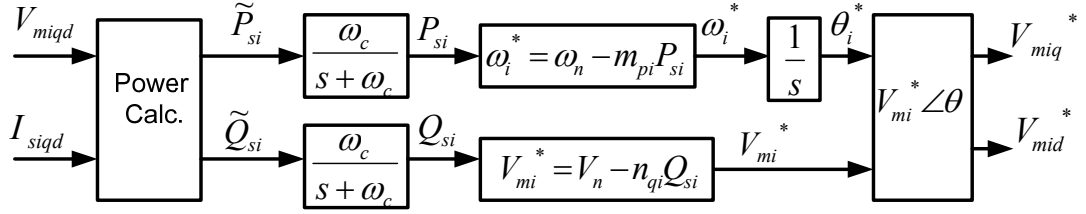


Figure 2.12 Droop control unit

It means if for instance, nominal power of second converter is two times that of the first converter, the active power droop coefficient of second converter should be chosen as half of the first converter.

Figure 2.12 shows the droop control unit in detail. First instantaneous output active and reactive power of converter is calculated using measured output current of converter and load voltage.

$$\tilde{P}_{si} = \frac{3}{2}(V_{miq}I_{siq} + V_{mid}I_{sid}) \quad (2.72)$$

$$\tilde{Q}_{si} = \frac{3}{2}(V_{miq}I_{sid} - V_{mid}I_{siq}) \quad (2.73)$$

To remove fluctuations and produce an average value of output power, both calculated instantaneous powers passed through a low pass filter with cut off frequency of ω_c that is assumed to be 10% of nominal frequency.

$$P_{si} = \frac{\omega_c}{s + \omega_c} \tilde{P}_{si} \quad (2.74)$$

$$Q_{si} = \frac{\omega_c}{s + \omega_c} \tilde{Q}_{si} \quad (2.75)$$

The outputs of droop control are voltage magnitude and angular frequency which define the reference angle of the load voltage using an integrator. Thus qd axis reference voltage can be determined as follows:

$$V_{miq}^* = V_{mi}^* \cos(\theta_i^* - \theta_{si}) \quad (2.76)$$

$$V_{mid}^* = -V_{mi}^* \sin(\theta_i^* - \theta_{si}) \quad (2.77)$$

where θ_{si} is the reference angle for transformation to qd axis reference frame. This angle is local frequency of each converter that is the output of PLL.

2.5.4 Voltage Control

To follow reference voltage, produced from droop control, a PI voltage controller is designed. From Figure 2.13 and dynamic equation of the system in laplace format

$$C_{di} p V_{miq} = I_{siq} - I_{ijq} - I_{Liq} - I_{iq} - I_{iNonq} - \omega_{si} C_{di} V_{mid} \quad (2.78)$$

$$C_{di} p V_{mid} = I_{sid} - I_{ijd} - I_{Lid} - I_{id} - I_{iNond} + \omega_{si} C_{di} V_{miq} \quad (2.79)$$

$$C_{di} p V_{miq} = k_{miq}(s)(V_{miq}^* - V_{miq}) = \sigma_{miq} \quad (2.80)$$

$$C_{di} p V_{mid} = k_{mid}(s)(V_{mid}^* - V_{mid}) = \sigma_{mid} \quad (2.81)$$

where PI voltage controllers are

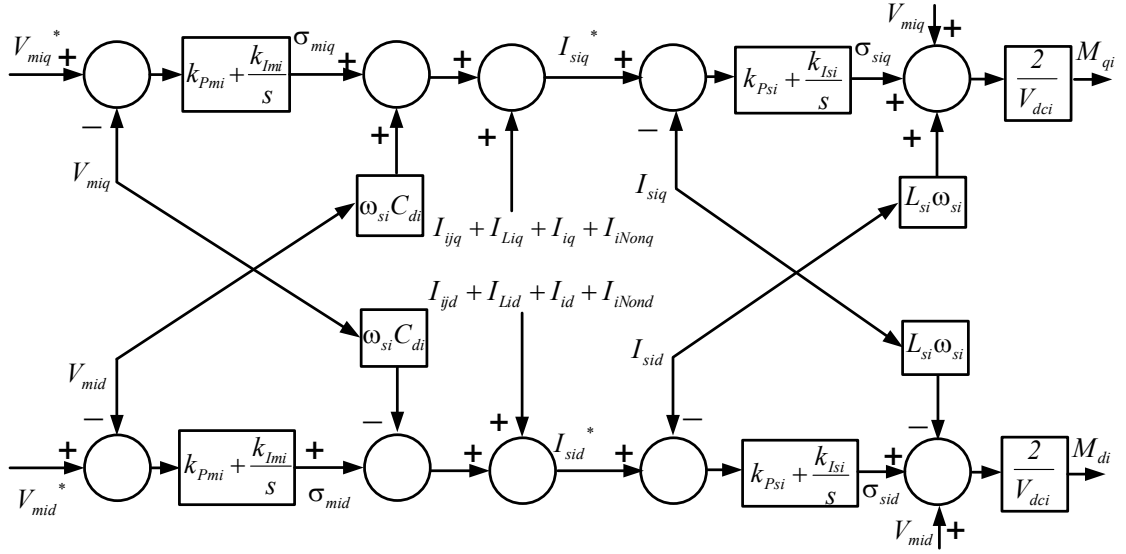


Figure 2.13 Schematic diagram of voltage control and inner current control units

$$k_{miq}(p) = k_{mid}(p) = k_{Pmi} + \frac{k_{Lmi}}{p} \quad (2.82)$$

Substituting (2.82) into (2.80) and (2.81) we can define the transfer function of voltage control and compare it with a standard first order transfer function with a time constant of τ_{mi} .

$$\frac{V_{miq}}{V_{miq}^*} = \frac{k_{miq}(p)}{sC_{di}k_{miq}(p)} = \frac{1}{1 + \tau_{mi}p} = \frac{1}{1 + \frac{pC_{di}}{k_{miq}(p)}} \quad (2.83)$$

$$\frac{V_{mid}}{V_{mid}^*} = \frac{k_{mid}(p)}{pC_{di}k_{mid}(p)} = \frac{1}{1 + \tau_{mi}p} = \frac{1}{1 + \frac{pC_{di}}{k_{mid}(p)}} \quad (2.84)$$

Therefore we can calculate PI controller parameters of PI controller using the time constant of controller and capacitance of load capacitor

$$k_{miq}(p) = k_{miq}(p) = \frac{p C_{di}}{p \tau_{mi}} = k_{pmi} + \frac{k_{lmi}}{p} \quad (2.85)$$

$$k_{pmi} = \frac{C_{di}}{\tau_{mi}} \text{ and } k_{lmi} = 0 \quad (2.86)$$

For a fast voltage control response we need a small time constant but should still be much larger than the switching time interval. It is chosen as ten times of switching time interval

$$\tau_{si} = 10 \frac{1}{2\pi f_{swi}} \quad (2.87)$$

where f_{swi} is the switching frequency of converter of DG_i.

Using the output of the voltage controller the reference output current of converter can be defined as

$$I_{siq}^* = \sigma_{miq} + I_{ijq} + I_{Liq} + I_{iq} + I_{iNonq} + \omega_{si} C_{di} V_{mid} \quad (2.88)$$

$$I_{sid}^* = \sigma_{mid} + I_{ijd} + I_{Lid} + I_{id} + I_{iNond} - \omega_{si} C_{di} V_{miq} \quad (2.89)$$

Where σ_{miq} and σ_{mid} are output voltage PI controller.

2.5.5 Current control

After controlling the load voltage magnitude and defining current reference, the current controller will follow its reference. The advantage of inner current control is that we can put a limiter in the reference current so we will apply an inherent current protection to the system which is especially good for the power electronic converter which has a limited rated capacity.

To design the inner current controller, using qd axis dynamic equations of the system

$$L_{si} p I_{siq} + R_{si} I_{siq} = M_{qi} \frac{V_{dci}}{2} - V_{miq} - L_{si} \omega_{si} I_{sid} \quad (2.90)$$

$$L_{si} p I_{sid} + R_{si} I_{sid} = M_{di} \frac{V_{dci}}{2} - V_{dmi} + L_{si} \omega_{si} I_{siq} \quad (2.91)$$

and

$$L_{si} p I_{sid} + R_{si} I_{sid} = k_{sid}(p)(I_{sid}^* - I_{sid}) = \sigma_{sid} \quad (2.92)$$

$$L_{si} p I_{siq} + R_{si} I_{siq} = k_{siq}(p)(I_{siq}^* - I_{siq}) = \sigma_{siq} \quad (2.93)$$

where PI current controller are

$$k_{siq}(p) = k_{sid}(p) = k_{Psi} + \frac{k_{Isi}}{p} \quad (2.94)$$

With substituting (2.94) into (2.92) and (2.93) we can define the transfer function of current controller and compare it with a standard first order transfer function with a time constant of τ_{si} .

$$\frac{I_{siq}}{I_{siq}^*} = \frac{k_{siq}(p)}{pL_{si} + R_{si} + k_{siq}(p)} = \frac{1}{1 + \tau_{si} p} = \frac{1}{1 + \frac{pL_{si} + R_{si}}{k_{siq}(p)}} \quad (2.95)$$

$$\frac{I_{sid}}{I_{sid}^*} = \frac{k_{sid}(p)}{pL_{si} + R_{si} + k_{sid}(p)} = \frac{1}{1 + \tau_{si} p} = \frac{1}{1 + \frac{pL_{si} + R_{si}}{k_{sid}(p)}} \quad (2.96)$$

Therefore we can calculate PI controller parameters of the current PI controller using the time constant of the controller, and the resistance and inductance of the output transmission line of converters

$$k_{siq}(p) = k_{siq}(p) = \frac{pL_{s1} + R_{s1}}{\tau_{si}p} = k_{Psi} + \frac{k_{Isi}}{p} \quad (2.97)$$

$$k_{Psi} = \frac{L_{si}}{\tau_{si}} \text{ and } k_{Isi} = \frac{R_{si}}{\tau_{si}} \quad (2.98)$$

Because the current controller is the most inner control unit, it should be the fastest controller. Its time constant is chosen as half of the voltage controller or five times the switching frequency time intervals

$$\tau_{mi} = 5 \frac{1}{2\pi f_{swi}} \quad (2.99)$$

The modulation indices of the outputs of the controller will be

$$M_{qi} = \frac{2}{V_{dci}} (\sigma_{siq} + V_{miq} + L_{si} \omega_{si} I_{sid}) \quad (2.100)$$

$$M_{di} = \frac{2}{V_{dci}} (\sigma_{sid} + V_{mid} - L_{si} \omega_{si} I_{siq}) \quad (2.101)$$

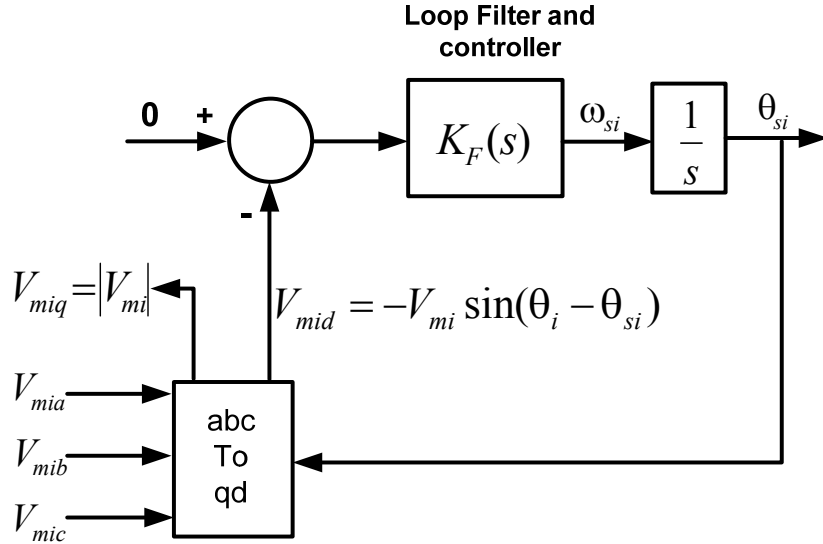


Figure 2.14 Block diagram of phase locked loop

2.5.6 Phase Lock Loop

To measure the frequency of the system and define a reference frequency for qd transformation, a phase lock loop is designed and applied to each DG unit. Its dynamic is added to the system equations to be more realistic. As it is shown in Figure 2.14 the three phase PLL uses measured local load voltages and converts them to qd-axis frame then compares d-axis voltage with zero as a reference. The error passes through a controller and then through a low pass filter to remove noises. The idea of the PLL is to align voltage to the q-axis and makes d-axis voltage zero, therefore

$$V_{mid} = -V_{mi} \sin(\theta_i - \theta_{si}) \quad (2.102)$$

$$\text{If } V_{mid} = 0 \Rightarrow \sin(\theta_i - \theta_{si}) = 0 \Rightarrow \theta_{si} = \theta_i$$

$$e = 0 - V_{mid} = V_{mi} \sin(\theta_i - \theta_{si}) \quad (2.103)$$

If $(\theta_i - \theta_{si})$ is very small we can assume

$$\sin(\theta_i - \theta_{si}) \approx (\theta_i - \theta_{si}) \quad (2.104)$$

$$V_{mi}(\theta_i - \theta_{si}) \frac{K_F(p)}{p} = \theta_{si} \quad (2.105)$$

Therefore we can define the closed loop transfer function and compare it with second order standard Butterworth filter

$$\frac{\theta_{si}}{\theta_i} = \frac{V_{mi}K_F(p)}{p + V_{mi}K_F(p)} \quad (2.106)$$

$$\frac{\theta_{si}}{\theta_i} = \frac{pV_{mi}k_{Ppll} + V_{mi}k_{Ipll}}{p^2 + pV_{mi}k_{Ppll} + V_{mi}k_{Ipll}} = \frac{2\zeta\omega_{n1} p + \omega_{n1}^2}{s^2 + 2\zeta\omega_{n1} p + \omega_{n1}^2} \quad (2.107)$$

$$k_{Ppll} = \frac{2\zeta\omega_{n1}}{V_{mi}} \text{ and } k_{Ipll} = \frac{\omega_{n1}^2}{V_{mi}} \quad (2.108)$$

where ζ is damping factor and is usually chosen as critical damping factor which is 0.707 and ω_{n1} is natural frequency which is chosen as $377(\text{rad}/s)$.

2.5.7 Simulation of Two Converter System

To verify the operation of the system and controllers, the autonomous system of Figure 2.10 with two converters as DG units is simulated in MATLAB software. Table 2.1 shows the system parameters for simulation and the designed controller parameters

Table 2.1 System parameters of DG

V_n	120V	R_{Li}	10 Ω
ω_n	377(rad/s)	L_{Li}	0.0352H
R_{si}	0.1 Ω	P_{10}	200W
L_{si}	4e ⁻³ H	Q_{10}	100Var
R_{12}	0.04 Ω	ω_c	37.7(rad/s)
L_{12}	1e ⁻³ H	f_{sw}	5KHz
C_{di}	200e ⁻⁶ F	V_{dci}	300V

Table 2.2 Parameters of the designed controllers

k_{Pmi}	0.628	k_{Imi}	0
k_{Psi}	25.13	k_{Lsi}	628.32
k_{Ppll}	4.44	k_{Ipll}	1184
m_{p1}	0.0038	m_{p2}	0.0019
n_{q1}	0.0012	n_{q2}	0.0012

are shown in Table 2.2. To show the process of load sharing when DG units have different nominal powers, the rated power of second converter is assumed to be two times that of the first converter. As a result, the active droop coefficient of the second converter is selected as half of that of the first converter. Figure 2.15 shows the reference of constant load active and reactive power of the first and second converter. More over Figure 2.16 illustrates output active and reactive power of converters and the process of load sharing between two DG units. At 0.3s, 1.1s and 1.9s we have change of reference active power and at 0.7s and at 5s reactive power references are changed. At 0.3s the first constant load active power changes from 150W to 2000W. We can see that both active powers of the converters change to feed the load. Output active power of DG1 changes from 600W to 1250W and DG2 output active power, due to higher capacity and lower active power coefficient, produces twice the previous power. Output active powers of DG1 and DG2 also increase from 1250W and 2500W to 1900W and 3800W respectively when the active power of second constant load rises to 2000W. In other regions active power converter units are almost constant. Because we have the same frequency in the whole system, both converters are sharing total active power based on their rated capacity

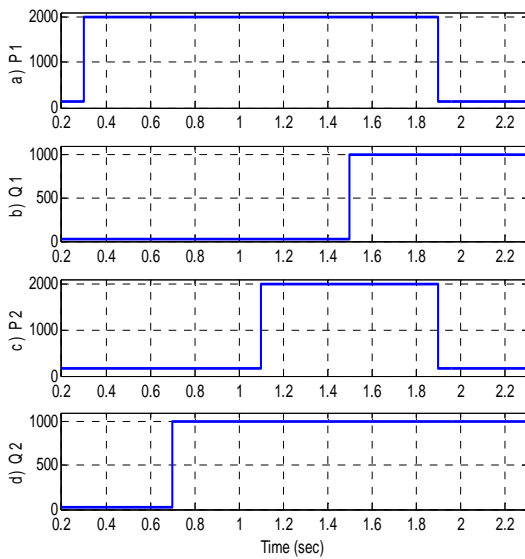


Figure 2.15 Active and reactive powers reference of first and second converters constant load, (a) and (b) are active and reactive powers of DG1 constant load, (c) and (d) are active and reactive powers of DG2 constant load.

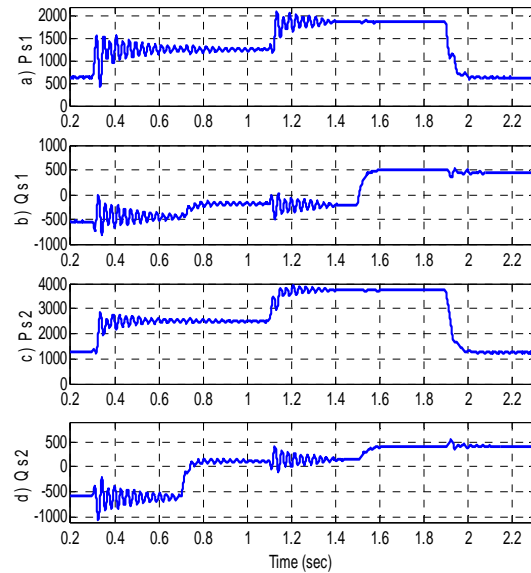


Figure 2.16 Output active and reactive powers of first and second converters, (a) and (b) are active and reactive powers of DG1, (c) and (d) are active and reactive powers of DG2.

when either first or second local load active power changes. With change of first and second load reactive powers, the output reactive powers of both converters are varied. The sharing of reactive power is not exactly based on reactive power droop coefficient. Because we can have different voltage magnitudes in different points of the power system, reactive power change of each load more affects the output reactive power of its local DG unit. Instead of some fluctuation, we can see small change in reactive power with increase of active output power of the converters. Increase of active power droops frequency so the reactive power of capacitor load capacitors and inductances changes and causes the output reactive power of the converters to change in order to make the power of total system balanced. Due to the small change of frequency, this effect on reactive power is small.

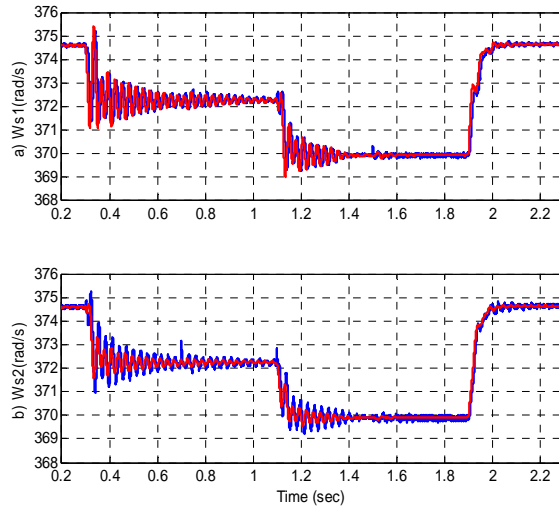


Figure 2.17 Actual local frequency (blue) and reference frequency (red) of the system, a) local frequency of DG1, b) local frequency of DG2

In Figure 2.17 the trend of measured local frequencies from the PLL and their references from the output of the droop control and in different load conditions is illustrated. Frequency of both converters reduces when the active power of the loads increase. Different droop coefficient affects the output active power of converters base on their rated power and both local frequencies are changing together so always total system has the same frequency. Moreover control system follows the reference frequency fast so the frequency ordered by droop control is always the same as the actual frequency of the system. Change of reactive power doesn't affect frequency.

Figure 2.18 shows qd-axis local load voltage of converters. Local frequency of each converter is used for the qd reference frame transformation therefore both voltages aligned with q-axis and d-axis voltages are almost zero. The voltage magnitude of both converters changes with change of reactive power based on the droop control output. With change of the second load reactive power the biggest effect is on the output reactive

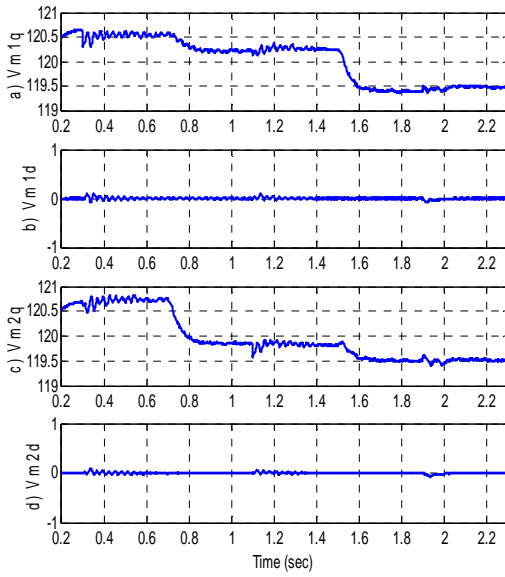


Figure 2.18 Local load voltages, a) q-axis load voltage of DG1, b) d-axis load voltage of DG1, c) q-axis load voltage of DG2, d) d-axis load voltage of DG2.

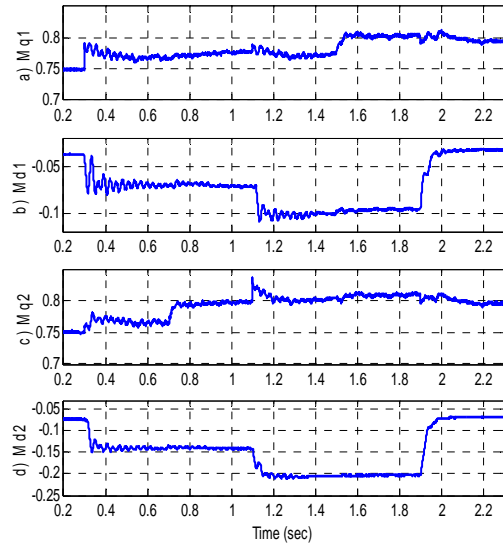


Figure 2.19 Modulation indices of converters, a) q-axis modulation index of first converter, b) d-axis modulation index of first converter, c) q-axis modulation index of second converter, d) d-axis modulation index of second converter.

power of DG2, and consequently on the voltage magnitude of second converter local load. During the change of active power, voltage magnitudes are almost constant.

In Figure 2.19 modulation indices of the first and second converters are shown to display the effects of the dynamics of the power system and control unit on the converters. The sinusoidal pulse width modulation (SPWM) voltage source converters are used to convert DC voltage to AC voltage. qd-axis modulation indices convert to abc frame in the local synchronous frequency of each converter. Comparing modulation indices with a triangular waveform of 5KHz switching frequency will produce switching time intervals of each phase to convert DC input voltage to three phase AC output. qd-axis modulation indices change with output active power of converters. With increase of active power, the d-axis modulation indices' magnitudes increase. The biggest effect of

reactive power and voltage change is on q-axis modulation index. In the process of changing loads, modulation indices' magnitudes never saturate and they are always less than unity.

2.6 Conclusion

In this chapter the dynamic model of a stand-alone single converter system is presented. The droop control is applied to maintain voltage and frequency. Frequency droops against output active power of converter and voltage magnitude droops against reactive power. The PI load voltage control and inner current control are designed based on the complex format of dynamic equations. Using bifurcation analysis, equilibrium curves of one converter system are illustrated. Operation points of the controlled system in different active power of constant load are shown.

The dynamic model of the two converter system as a multi-converter system is explained as well as the droop control based on the rated capacity applied in order to share total active and reactive power of the loads. Inner voltage and current controllers based on separated qd-axis equations of the system are designed. The three phase PLL is designed and added to each converter to measure instantaneous local frequency and prepare the reference frequency for qd-axis transformation. The system is simulated in MATLAB software. Simulation results show, based on rated capacity of each converter and their droop coefficient, the active and reactive power of total load is shared between them and change of frequency and voltage are related to active and reactive power respectively.

CHAPTER 3

STEADY STATE ANALYSIS AND DYNAMIC CONTROL OF PHOTOVOLTAIC SYSTEM

3.1 Introduction

Renewable energies are already playing important roles in the operation of electric power systems. Most distributed generation (DG) units use renewable energies such as solar (PV) and wind as their sources. Power electronic converters control the output power and the voltage magnitude of the DG units.

In grid connected mode, the frequency and voltage magnitude of the load in the Microgrid are adopted from the main grid. With control, it is possible to deliver the maximum power of the sources to the grid or autonomous load. PV systems have a non-linear output voltage and current relationship [111-112].

There are situations in which power systems with renewable energy sources are normally operated in stand-alone modes. In such situations, there must be dedicated power systems for rural areas, moveable military bases and facilities requiring premium power quality. For the proper calculation and control operation of autonomous generation systems, the dynamics of the power sources and the loads must be properly taken into account through adequate system modeling. In autonomous mode, due to the power balance between sources and loads, the PV system as the input source may not always operate at the maximum power point. Under this condition of potential variation of PV

operating point, the control of the system should naturally consider the nonlinear characteristics of the input source [113] in order to meet load requirements which could be a combination of linear and non-linear loads. Alternatively, there should be another source, like a battery, to maintain operation at the PV maximum power extraction strategy. Under this condition, the steady state operation region of the system under different loads, which define the currents, will be affected.

In this chapter, an autonomous (stand-alone) microgrid with a PV system as the primary source is considered. In addition, a battery is connected to control DC link voltage. The nonlinear characteristic of PV systems is added and the steady state operation region of the system without linearization for different load conditions is studied with MATLAB software.

3.2 Dynamic Model of the Stand-Alone System

Figure 3.1 shows a schematic diagram of the studied isolated power system. A PV source and a battery are connected to the three phase DC/AC inverter. A boost DC/DC converter increases the input PV voltage magnitude, and hence, controls the output power of the source. A bidirectional DC/DC converter charges or discharges the battery to fix DC link voltage. The inverter converts input DC voltage to AC and controls the voltage magnitude of the load. A linear RL (resistance-inductance) load and a constant apparent load are used. A capacitor is connected in parallel to the load to remove voltage fluctuations. As shown, the structure of the battery consists of a constant dc source, and internal capacitances and resistances.

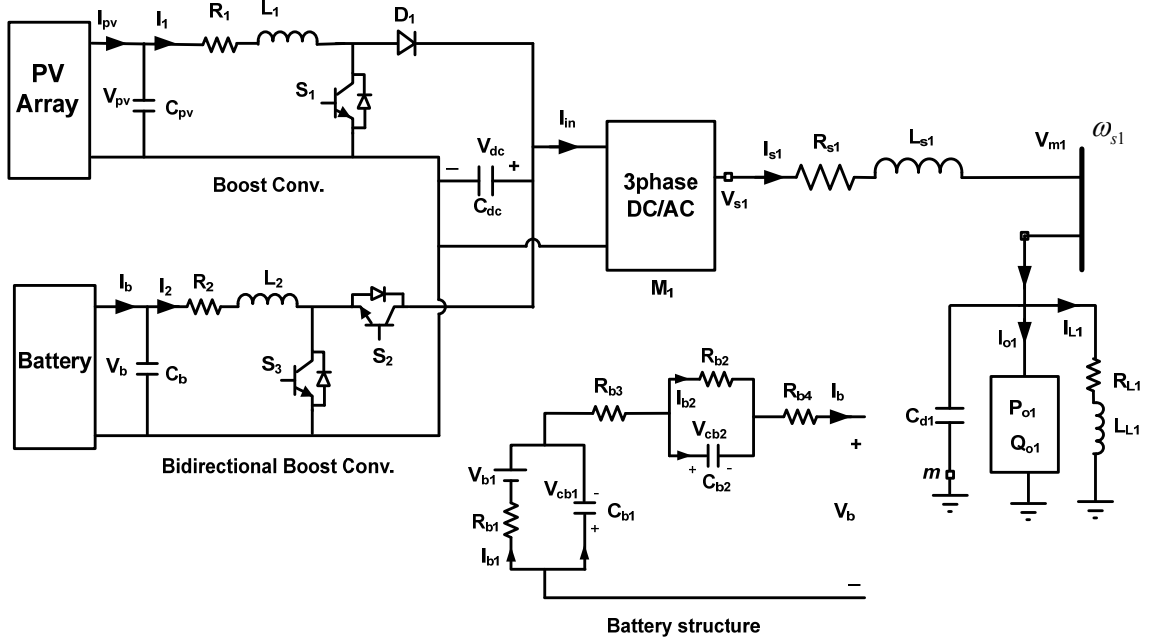


Figure 3.1 Schematic diagram of the stand-alone PV, battery inverter power system.

To study dynamic behavior and calculate steady state operation region of the system, dynamic equations of each part are defined in detail.

3.2.1 Nonlinear Model and MPP Operation of PV System

The nonlinear model of the PV system relating the current flowing out of the PV and the terminal voltage is defined as follows [113]:

$$I_{pv} = n_p I_{ph} - n_p I_{rs} \left[\exp\left(\frac{q}{k \theta A n_s} \frac{V_{pv}}{n_s}\right) - 1 \right] \quad (3.1)$$

$$I_{ph} = \left[I_{src} + k_{\theta} (\theta - \theta_r) \right] \frac{S}{100} \quad (3.2)$$

Table 3.1 Parameters of PV system

I_{rs}	$1.2e^{-7}$	θ_r	$300^\circ k$
q	$1.602e^{-19} C$	I_{src}	$8.03 A$
k	$1.38e^{-23} J / K$	k_θ	0.0017
θ	$298^\circ k$	n_s	225
A	1.92	n_p	250
S	1		

In (3.1), I_{rs} and θ are the reverse saturation current and the temperature of $p-n$ junction. I_{src} is the short-circuit current of one PV cell, n_s and n_p are the number of series and parallel PV cells in a string, respectively. A is the ideality factor and S is solar irradiation level. θ_r is the cell reference temperature and k_θ is the temperature coefficient. $q(=1.602e^{-19} C)$ and $k(=1.38e^{-23} J / K)$ are the unit electric charge and Boltzmann's constant. Table 3.1 shows parameters of PV system.

Figure 3.2 illustrates per unit output current and power of the PV system where $P_b = 2000W$ and $V_b = 120V$ are selected as base values. At around $V_{pv} = 1.01 pu$ we have maximum power point at unity irradiation level ($S = 1$).

To define maximum power point in each solar irradiation level

$$P_{pv} = V_{pv} n_p I_{ph} - V_{pv} n_p I_{rs} \left[\exp\left(\frac{q}{k \theta A} \frac{V_{pv}}{n_s}\right) - 1 \right] \quad (3.3)$$

$$P_{pv} = V_{pv} n_p \left[I_{src} + k_\theta (\theta - \theta_r) \right] \frac{S}{100} - V_{pv} n_p I_{rs} \left[\exp\left(\frac{q}{k \theta A} \frac{V_{pv}}{n_s}\right) - 1 \right] \quad (3.4)$$

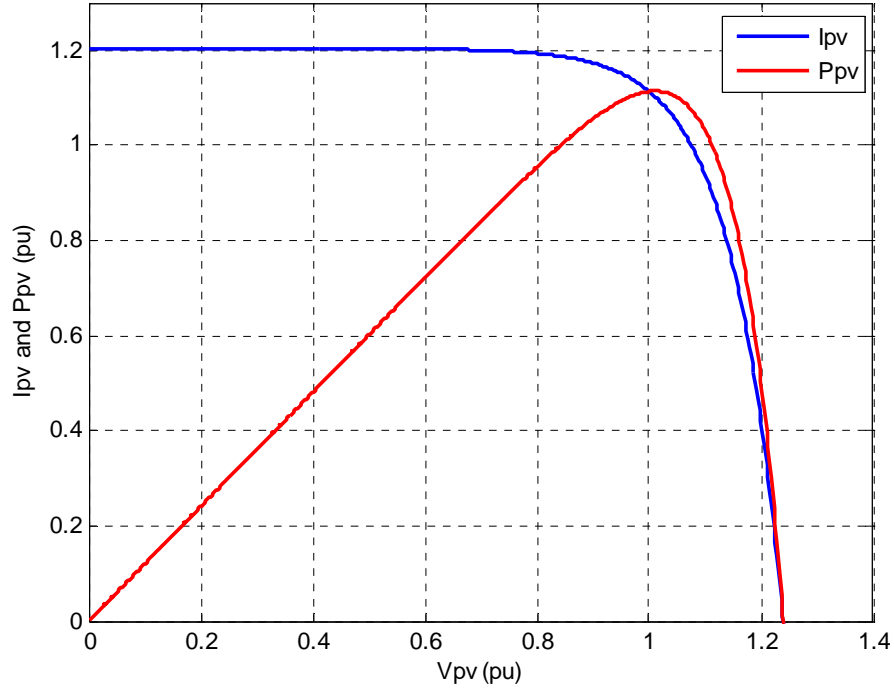


Figure 3.2 Current and power characteristics of PV system in per unit

$$\frac{dP_{pv}}{dV_{pv}} = n_p \left[I_{src} + k_\theta (\theta - \theta_r) \right] \frac{S}{100} + n_p I_{rs} - n_p I_{rs} \left(\frac{q}{k \theta A n_s} V_{pv} + 1 \right) \left[\exp\left(\frac{q}{k \theta A n_s} V_{pv} \right) \right] = 0 \quad (3.5)$$

$$\frac{dP_{pv}}{dV_{pv}} = \left[I_{src} + k_\theta (\theta - \theta_r) \right] \frac{S}{I_{rs} 100} + 1 - \left(\frac{q}{k \theta A n_s} V_{pv} + 1 \right) \left[\exp\left(\frac{q}{k \theta A n_s} V_{pv} \right) \right] = 0 \quad (3.6)$$

If $xe^x = y \Leftrightarrow x = W(y)$ and W is the Lambert function.

$$W(y) = \sum_{n=1}^{\infty} \frac{(-n)^{n-1}}{n!} x^n = x - x^2 + \left(\frac{3}{2}\right)x^3 - \left(\frac{8}{3}\right)x^4 + \left(\frac{125}{24}\right)x^5 - \dots \quad (3.7)$$

$$\frac{dP_{pv}}{dV_{pv}} = a - (bV_{pv} + 1)e^{bV_{pv}} \text{ where } \begin{cases} a = \left[I_{src} + k_\theta (\theta - \theta_r) \right] \frac{S}{I_{rs} 100} + 1 \\ b = \frac{q}{k \theta A n_s} \end{cases} \quad (3.8)$$

$$\frac{dP_{pv}}{dV_{pv}} = a - (bV_{pv} + 1)e^{bV_{pv}} = 0 \quad (3.9)$$

$$(bV_{pv} + 1)e^{bV_{pv}} = a \quad (3.10)$$

$$(bV_{pv} + 1)e^{(bV_{pv}+1)} = a e^1 \quad (3.11)$$

$$(bV_{pv} + 1) = W(a e^1) \quad (3.12)$$

$$V_{pv-opt} = \frac{W(a e^1) - 1}{b} \quad (3.13)$$

Figure 3.3 shows PV curve characteristics and calculated maximum power points in 10 different irradiation levels from 0.01 to 1. In Figure 3.4 trend of PV output voltage at maximum power point (MPP) based on solar irradiation level is shown.

3.2.2 Boost Converter Connected to the PV System

The model of the PV, DC-DC converter is given as ($p = \frac{d}{dt}$)

When S_1 is ON ($S_1 = 1$)

$$C_{pv} pV_{pv} = I_{pv} - I_1 \quad (3.14)$$

$$V_{pv} = L_1 pI_1 + R_1 I_1 \quad (3.15)$$

When S_1 is Off ($D_1 = 1$)

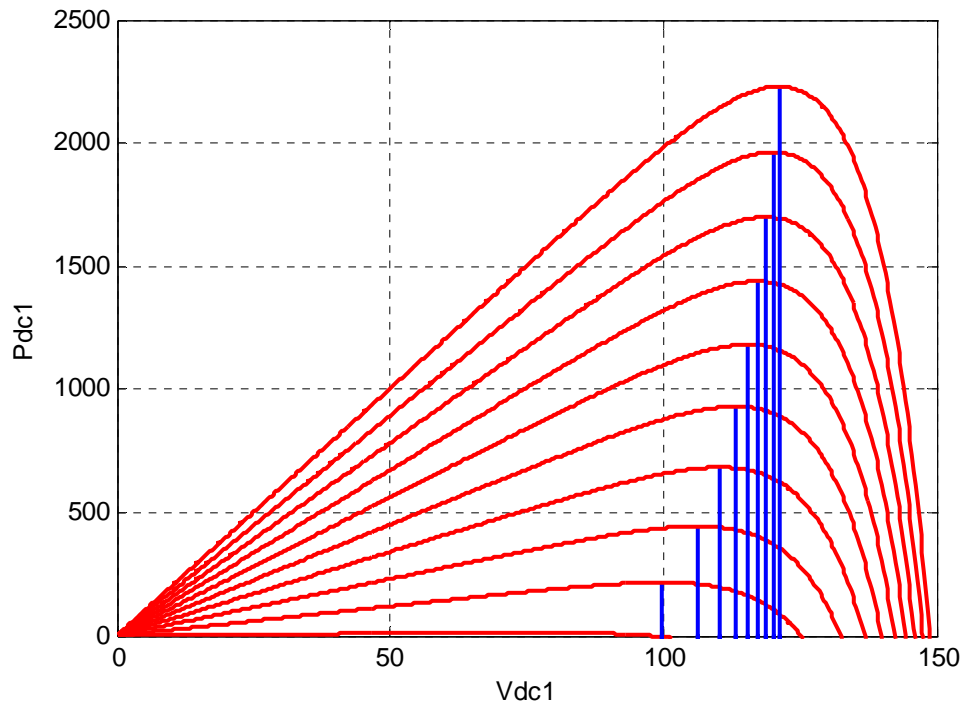


Figure 3.3 PV curve characteristics in different irradiation level

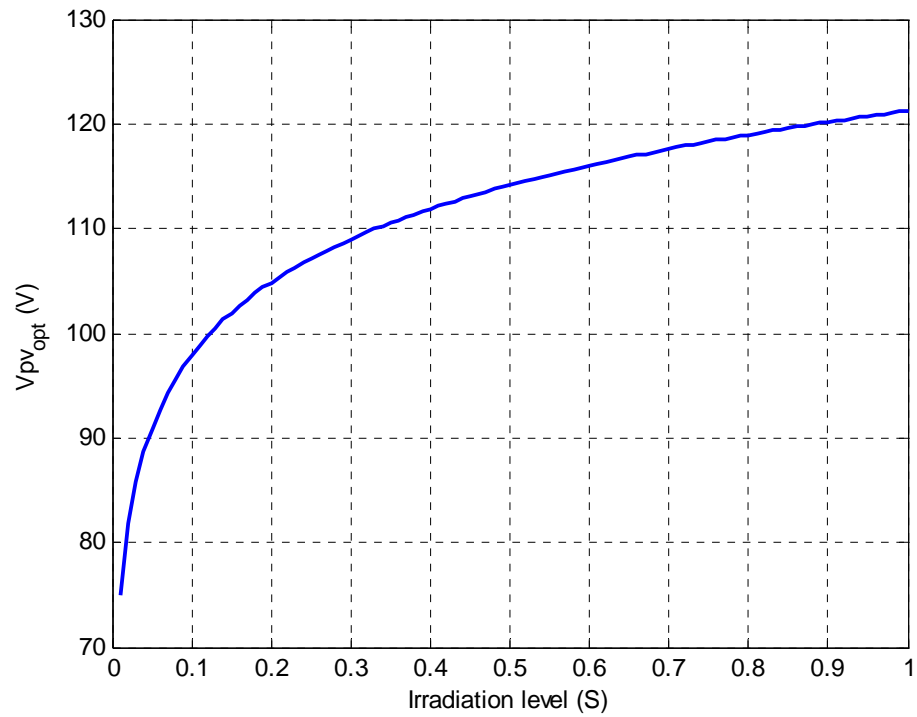


Figure 3.4 Calculated optimum voltage at MPP in different irradiation level

$$C_{pv}pV_{pv} = I_{pv} - I_1 \quad (3.16)$$

$$V_{pv} = L_1pI_1 + R_1I_1 + V_{dc} \quad (3.17)$$

Therefore with combination of two modes ($D_1 = 1 - S_1$)

$$C_{pv}pV_{pv} = I_{pv} - I_1 \quad (3.18)$$

$$V_{pv} = L_1pI_1 + R_1I_1 + (1 - S_1)V_{dc} \quad (3.19)$$

3.2.3 Bidirectional Boost Converter of Battery

In the bidirectional boost converter, when S_2 is on ($S_2 = 1, S_3 = 0$)

$$C_b pV_b = I_b - I_2 \quad (3.20)$$

$$L_2 pI_2 + R_2 I_2 = V_b - V_{dc} \quad (3.21)$$

When S_2 is off ($S_2 = 0, S_3 = 1$)

$$C_b pV_b = I_b - I_2 \quad (3.22)$$

$$L_2 pI_2 + R_2 I_2 = V_b \quad (3.23)$$

Therefore with combination of two modes ($S_3 = 1 - S_2$)

$$C_b pV_b = I_b - I_2 \quad (3.24)$$

$$L_2 pI_2 + R_2 I_2 = V_b - S_2 V_{dc} \quad (3.25)$$

3.2.4 DC Link Equations

The dynamic equation of the DC link voltage

$$C_{dc}pV_{dc} = (1 - S_1)I_1 + S_2I_2 - I_{in} = (1 - S_1)I_1 + S_2I_2 - \frac{3}{4}(M_{q1}I_{s1q} + M_{d1}I_{s1d}) \quad (3.26)$$

3.2.5 Dynamic Model of the Battery

The model of the battery is expressed (Figure 3.1) as

$$\begin{cases} R_{b1}I_{b1} - V_{b1} - V_{cb1} = 0 \\ R_{b2}I_{b2} - V_{cb2} = 0 \\ V_{cb1} + V_{cb2} + (R_{b3} + R_{b4})I_b + V_b = 0 \\ I_{b1} = I_b - C_{b1}pV_{cb1} \\ I_{b2} = I_b - C_{b2}pV_{cb2} \end{cases} \quad (3.27)$$

$$\begin{cases} R_{b1}(I_b - C_{b1}pV_{cb1}) - V_{b1} - V_{cb1} = 0 \\ R_{b2}(I_b - C_{b2}pV_{cb2}) - V_{cb2} = 0 \\ V_b = -V_{cb1} - V_{cb2} - (R_{b3} + R_{b4})I_b \end{cases} \quad (3.28)$$

$$\begin{cases} R_{b1}C_{b1}pV_{cb1} = R_{b1}I_b - V_{b1} - V_{cb1} \\ R_{b2}C_{b2}pV_{cb2} = R_{b2}I_b - V_{cb2} \\ V_b = -V_{cb1} - V_{cb2} - (R_{b3} + R_{b4})I_b \end{cases} \quad (3.29)$$

3.2.6 Load Equation

The equations for the constant load currents expressed in the qd-axis synchronous reference frame in terms of the constant real and imaginary powers are given as

$$I_{olq} = \frac{2}{3} \frac{P_{o1}V_{m1q} - Q_{o1}V_{m1d}}{V_{m1q}^2 + V_{m1d}^2} \quad (3.30)$$

$$I_{old} = \frac{2}{3} \frac{P_{o1}V_{m1d} + Q_{o1}V_{m1q}}{V_{m1q}^2 + V_{m1d}^2} \quad (3.31)$$

Where P_{o1} and Q_{o1} are active and reactive power of the constant load.

3.2.7 Three Phase Converter Equations

The voltage source converter as illustrated in Figure 3.1 is modeled in the qd reference frame below, where M_{q1} and M_{d1} are the q and d modulation indices

$$\begin{cases} pI_{s1q} = \frac{1}{L_{s1}} (M_{q1} \frac{V_{dc1}}{2} - V_{m1q} - R_{s1}I_{s1q} - L_{s1}\omega_{s1}I_{s1d}) \\ pI_{s1d} = \frac{1}{L_{s1}} (M_{d1} \frac{V_{dc1}}{2} - V_{m1d} - R_{s1}I_{s1d} + L_{s1}\omega_{s1}I_{s1q}) \end{cases} \quad (3.32)$$

3.2.8 Linear Load of DG1 (L1) Equations

The qd- synchronous reference frame equations of the resistance-inductance load at the angular frequency ω_{s1} at the terminal of the voltage source inverter are given as

$$\begin{cases} pI_{L1q} = \frac{1}{L_{L1}} (V_{m1q} - R_{L1}I_{L1q} - L_{L1}\omega_{s1}I_{L1d}) \\ pI_{L1d} = \frac{1}{L_{L1}} (V_{m1d} - R_{L1}I_{L1d} + L_{L1}\omega_{s1}I_{L1q}) \end{cases} \quad (3.33)$$

3.2.9 Capacitor of DG1 Equations

The qd equations of the load capacitors are given as

$$\begin{cases} pV_{m1q} = \frac{1}{C_{d1}}(I_{s1q} - I_{L1q} - I_{01q} - C_{d1}\omega_{s1}V_{m1d}) \\ pV_{m1d} = \frac{1}{C_{d1}}(I_{s1d} - I_{L1d} - I_{01d} + C_{d1}\omega_{s1}V_{m1q}) \end{cases} \quad (3.34)$$

3.3 Steady-State Operation

The steady state operation variables of the stand-alone power system operating at an angular frequency of ω_{s1} are obtained when the derivatives of the states in the dynamic equations in Section 3.2 are set equal to zero. The operation region is studied by changing the active power of the constant load when $M_{q1}=0.9$, $M_{d1}=-0.16$, $Q_{o1} = 200\text{Var}$, $V_{m1} = 120\text{V}$, and the PV is providing maximum output power. Two different solar irradiations $S = 1$ and $S = 0.7$, and therefore two different PV system voltages $V_{pv} = 121.25\text{V}$ and $V_{pv} = 117.6\text{V}$, are considered respectively. By increasing the load's active power, the DC link voltage in Figure 3.5 increases and the battery starts to discharge. In Figure 3.6, the discharge of the battery reduces its output voltage. In Figure 3.7, the inverter's output active power increases gradually to meet the load requirement and ensure the power balance. Due to the constant load voltage, active and reactive powers of the linear load are constant. Thus with the constant reactive power of the other load, the total inverter output reactive shown power in Figure 3.8, is constant.

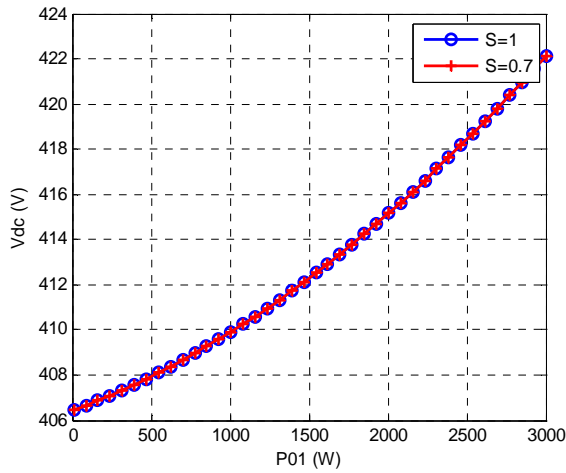


Figure 3.5 DC link voltage versus active power of constant load, blue($S = 1$), red($S = 0.7$)

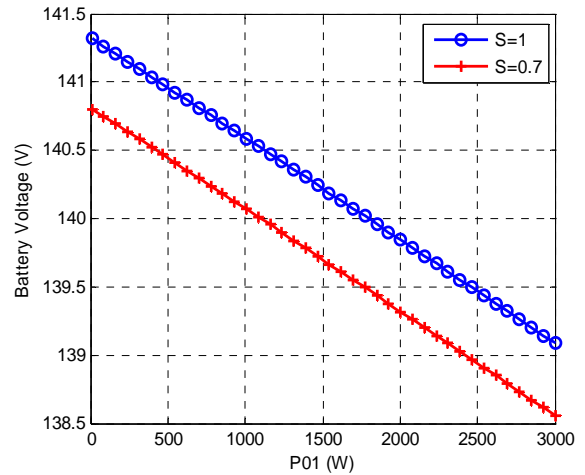


Figure 3.6 Battery voltage versus active power of constant load, blue ($S = 1$), red($S = 0.7$)

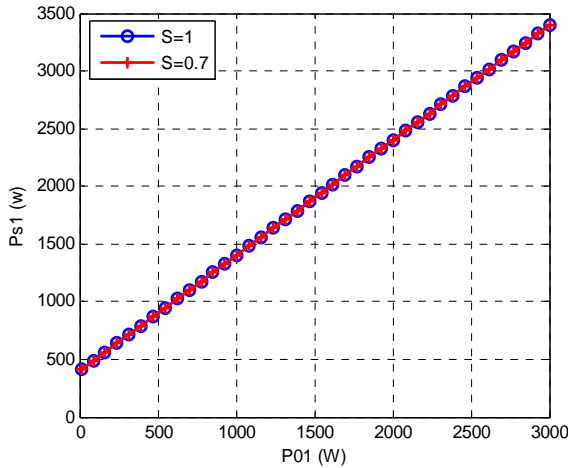


Figure 3.7 Inverter output active power versus active power of constant load, blue($S = 1$), red($S = 0.7$)

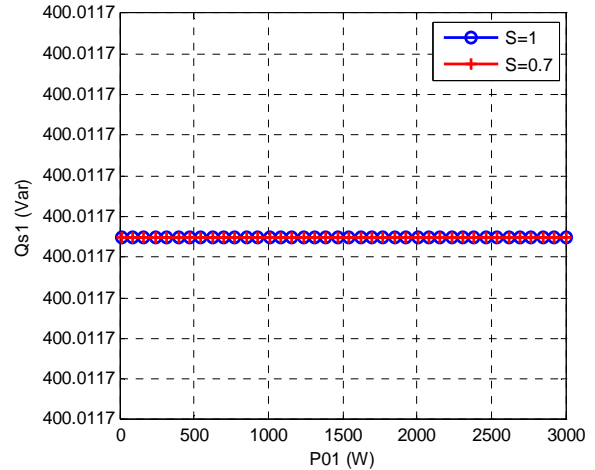


Figure 3.8 Inverter output reactive power versus active power of constant load, blue($S = 1$), red($S = 0.7$)

Figure 3.9 and Figure 3.10 illustrate the output current and power of the battery. When total load is less than the maximum power supplied by the PV system, the excessive power charges the battery. After approximately 1800W for unity irradiation level ($S=1$), the total load exceeds the maximum power of PV system and the battery starts to discharge, releasing power to the load. When the irradiation level of the PV system decreases from 1 to 0.7, the maximum power decreases from 2229W to 1510W.

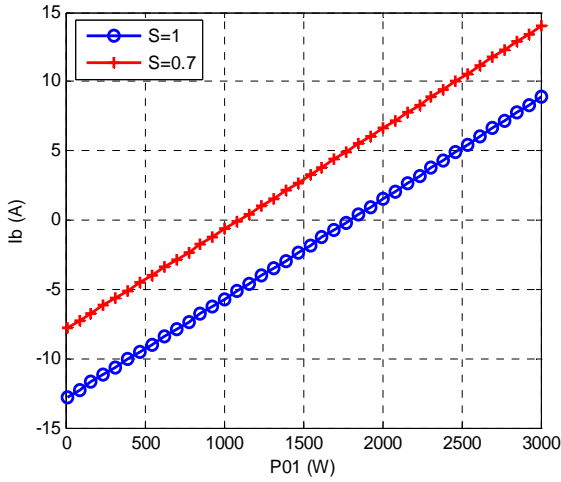


Figure 3.9 Battery output current versus active power of constant load, blue($S=1$), red($S=0.7$)

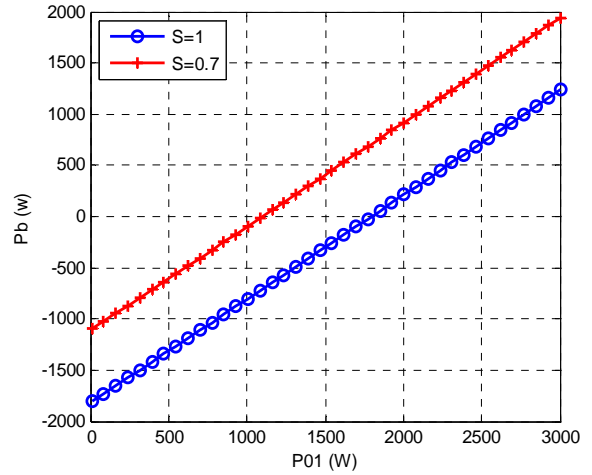


Figure 3.10 Battery output power versus active power of constant load, blue($S=1$), red($S=0.7$)

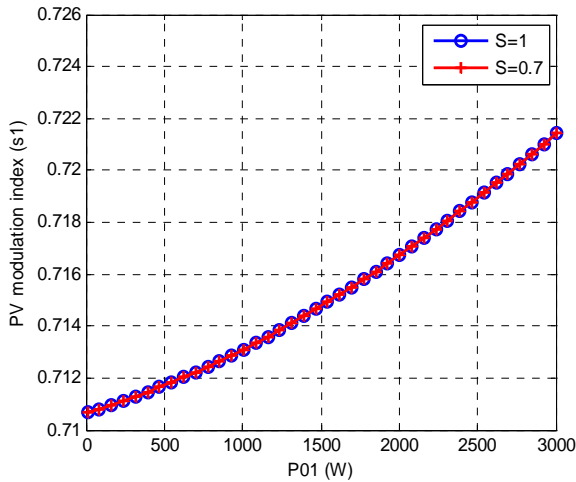


Figure 3.11 PV converter modulation index versus active power of constant load, blue($M=0.91$), red($M=0.61$)

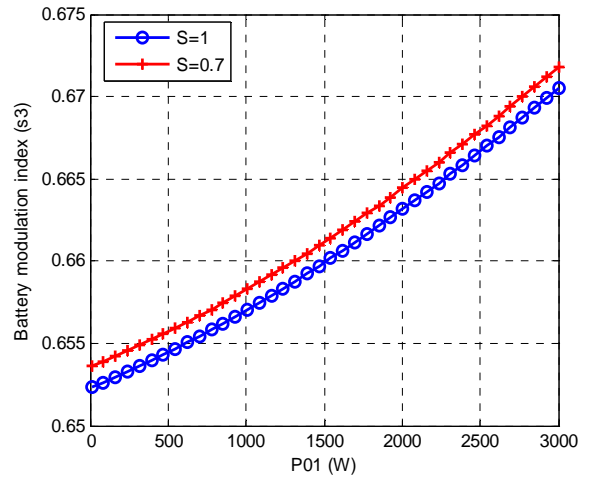


Figure 3.12 Battery converter modulation index versus active power of constant load, blue($M=0.91$), red($M=0.61$)

The largest effect is on the battery since the PV source is decreased and the battery discharges even for smaller load demand. Thus the battery starts to discharge when the constant load power is about 1000W. Figure 3.11 shows the duty ratio of the

DC-DC converter connected to the PV to meet the load demand. The battery converter's corresponding duty ratio is shown in Figure 3.12

3.4 Control Unit Design

3.4.1 Load Voltage Control

To follow the load reference voltage at rated value, a PI voltage controller is designed. From Figure 3.13 and the dynamic equations of the system in Laplace format given as

$$C_{d1}pV_{m1q} = I_{s1q} - I_{L1q} - I_{1oq} - \omega_{s1}C_{d1}V_{m1d} = k_{m1q}(s)(V_{m1q}^* - V_{m1q}) = \sigma_{m1q} \quad (3.35)$$

$$C_{d1}pV_{m1d} = I_{s1d} - I_{L1d} - I_{1od} + \omega_{s1}C_{d1}V_{m1q} = k_{m1d}(s)(V_{m1d}^* - V_{m1d}) = \sigma_{m1d} \quad (3.36)$$

where the PI voltage controllers are

$$k_{m1q}(s) = k_{m1d}(s) = k_{pm1} + \frac{k_{im1}}{s} \quad (3.37)$$

Substituting (3.37) into (3.35) and (3.36) we can define the transfer function of voltage control and compare it with a standard first order transfer function with a time constant of τ_{m1} as.

$$\frac{V_{m1q}}{V_{m1q}^*} = \frac{k_{m1q}(s)}{sC_{d1}k_{m1q}(s)} = \frac{1}{1 + \tau_{m1}s} = \frac{1}{1 + \frac{sC_{d1}}{k_{m1q}(s)}} \quad (3.38)$$

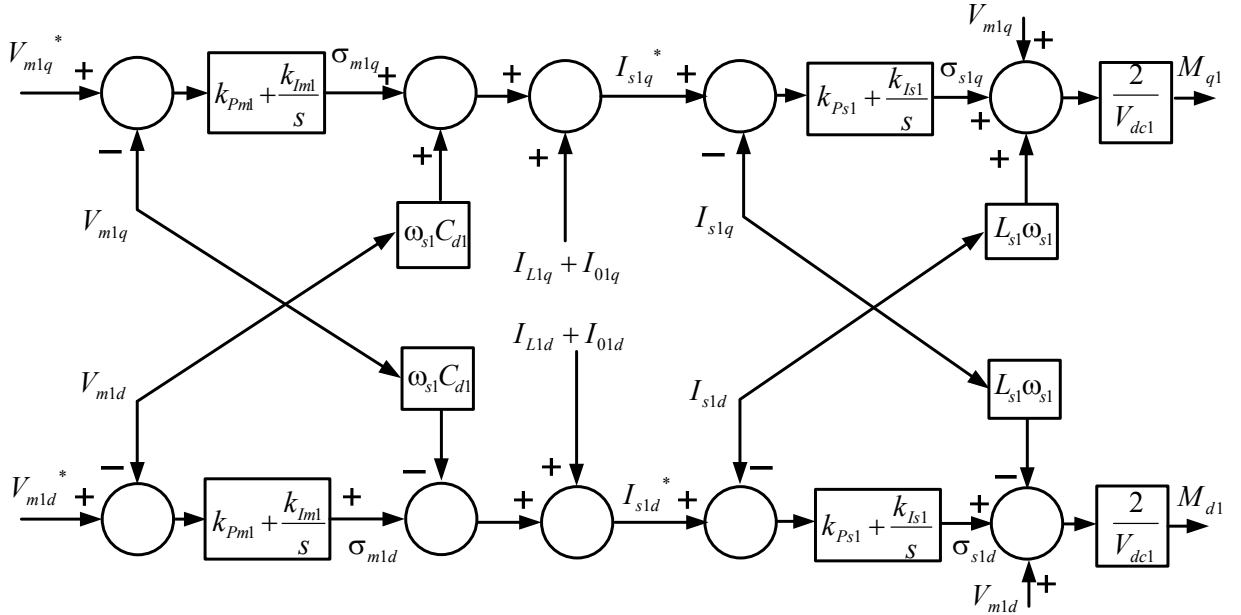


Figure 3.13 Block diagram of DC-AC three phase converter control part

$$\frac{V_{m1d}^*}{V_{m1d}} = \frac{k_{m1d}(s)}{sC_{d1}k_{m1d}(s)} = \frac{1}{1 + \tau_{m1}s} = \frac{1}{1 + \frac{sC_{d1}}{k_{m1d}(s)}} \quad (3.39)$$

Therefore the PI controller parameters can be calculated using the time constant of the controller and capacitance of the load capacitor as

$$k_{m1q}(s) = k_{m1q}(s) = \frac{s C_{d1}}{s \tau_{m1}} = k_{Pm1} + \frac{k_{Im1}}{s} \quad (3.40)$$

$$k_{Pm1} = \frac{C_{d1}}{\tau_{m1}} \text{ and, } k_{Im1} = 0 \quad (3.41)$$

For a fast voltage control response, a small time constant is needed. It shouldn't be very small, but must be bigger than the switching time interval. It is therefore chosen to be about ten times the switching time interval

$$\tau_{m1} = 10 \frac{1}{2\pi f_{sw}} \quad (3.42)$$

where f_{sw} is the switching frequency of the converter for the DG₁ (5kHz).

Using the output of voltage controller, the reference output current of converter can be defined as

$$I_{s1q}^* = \sigma_{m1q} + I_{L1q} + I_{1oq} + \omega_{s1} C_{d1} V_{m1d} \quad (3.43)$$

$$I_{s1d}^* = \sigma_{m1d} + I_{L1d} + I_{1od} - \omega_{s1} C_{d1} V_{m1q} \quad (3.44)$$

where σ_{m1q} and σ_{m1d} are output voltages of the PI controllers.

3.4.2 AC Inverter Current Control

After controlling the load voltage magnitude and defining the current reference, the current controller will follow its reference. The advantage of inner current control is that one can put a limiter in the reference current so as to apply an inherent current protection to the system. This is especially necessary for the power electronic converter which has a limited KVA rated capacity.

The inner current controller is designed using the qd axis dynamic equations of the system as follows:

$$L_{s1} s I_{s1q} + R_{s1} I_{s1q} = M_{q1} \frac{V_{dc1}}{2} - V_{m1q} - L_{s1} \omega_{s1} I_{s1d} = k_{s1q}(s)(I_{s1q}^* - I_{s1q}) = \sigma_{s1q} \quad (3.45)$$

$$L_{s1} s I_{s1d} + R_{s1} I_{s1d} = M_{d1} \frac{V_{dc1}}{2} - V_{dm1} + L_{s1} \omega_{s1} I_{s1q} = k_{s1d}(s)(I_{s1d}^* - I_{s1d}) = \sigma_{s1d} \quad (3.46)$$

where the PI current controller is given by

$$k_{s1q}(s) = k_{s1d}(s) = k_{ps1} + \frac{k_{Is1}}{s} \quad (3.47)$$

Substituting (3.47) into (3.45) and (3.46), one can define the transfer function of the current controller and compare it with a standard first order transfer function with a time constant of τ_{s1} as follows:

$$\frac{I_{s1q}}{I_{s1q}^*} = \frac{k_{s1q}(s)}{sL_{s1} + R_{s1} + k_{s1q}(s)} = \frac{1}{1 + \tau_{s1}s} = \frac{1}{1 + \frac{sL_{s1} + R_{s1}}{k_{s1q}(s)}} \quad (3.48)$$

$$\frac{I_{s1d}}{I_{s1d}^*} = \frac{k_{s1d}(s)}{sL_{s1} + R_{s1} + k_{s1d}(s)} = \frac{1}{1 + \tau_{s1}s} = \frac{1}{1 + \frac{sL_{s1} + R_{s1}}{k_{s1d}(s)}} \quad (3.49)$$

Therefore the PI controller parameters of the current controller can be calculated using the time constant of the controller, the resistance, and the inductance of the output transmission line of converters

$$k_{s1q}(s) = k_{s1d}(s) = \frac{sL_{s1} + R_{s1}}{\tau_{s1}s} = k_{ps1} + \frac{k_{Is1}}{s} \quad (3.50)$$

$$k_{ps1} = \frac{L_{s1}}{\tau_{s1}} \text{ and } k_{Is1} = \frac{R_{s1}}{\tau_{s1}} \quad (3.51)$$

Being the inner most control unit, the current controller must have fastest response. Therefore, its time constant is chosen to be half of the voltage controller or five times the switching period

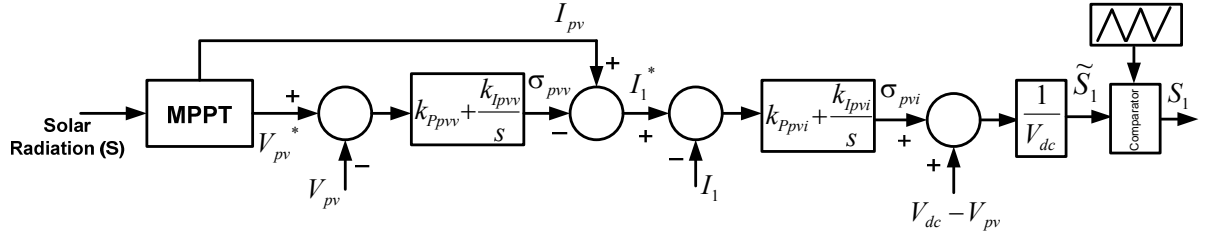


Figure 3.14 Block diagram of PV DC-DC boost converter control part

$$\tau_{si} = 5 \frac{1}{2\pi f_{sw}} \quad (3.52)$$

The modulation indices which are the outputs of the controllers will be

$$M_{q1} = \frac{2}{V_{dc1}} (\sigma_{s1q} + V_{m1q} + L_{s1} \omega_{s1} I_{s1d}) \quad (3.53)$$

$$M_{d1} = \frac{2}{V_{dc1}} (\sigma_{s1d} + V_{m1d} - L_{s1} \omega_{s1} I_{s1q}) \quad (3.54)$$

3.4.3 PV Voltage Control

As illustrated in Figure 3.14, the objective of the PV control is to follow maximum power point. The output voltage controller is therefore designed using (3.18) as

$$C_{pv} s V_{pv} = I_{pv} - I_1 = k_{pvv}(s)(V_{pv}^* - V_{pv}) = \sigma_{pvv} \quad (3.55)$$

where PV voltage reference (V_{pv}^*) comes from maximum power point tracking (MPPT).

$$\frac{V_{pv}}{V_{pv}^*} = \frac{k_{pvv}(s)}{sC_{pv} + k_{pvv}(s)} = \text{and } k_{pvv}(s) = k_{Ppvv} + \frac{k_{Ipvv}}{s} \quad (3.56)$$

$$\frac{V_{pv}}{V_{pv}^*} = \frac{sk_{Ppvv} + k_{Ipvv}}{s^2C_{pv} + sk_{Ppvv} + k_{Ipvv}} \quad (3.57)$$

Comparing denominator of transfer function with denominator of second order Butterworth filter

$$s^2C_{pv} + sk_{Ppvv} + k_{Ipvv} = s^2 + 2\zeta\omega_n s + \omega_n^2 \quad (3.58)$$

The coefficients of outer voltage PI controller and the reference current for the inner controller are defined as

$$\begin{cases} k_{Ppvv} = 2\zeta\omega_n C_{pv} \\ k_{Ipvv} = \omega_n^2 C_{pv} \end{cases} \quad (3.59)$$

$$I_1^* = I_{pv} - \sigma_{pvv} \quad (3.60)$$

The controller parameters are chosen as $\zeta = 0.7$ and $\omega_{n1} = 0.2\pi f_{swdc}$, where f_{swdc} is the switching frequency of the DC-DC converter which is chosen to be 5kHz for both DC-DC converters.

3.4.4 PV Converter Current Control

To follow the reference current of the PV, based on the dynamic equation of the converter interface inductor in (3.19)

$$L_1 s I_1 + R_1 I_1 = V_{pv} - (1 - \tilde{S}_1) V_{dc} = k_{pvi}(s)(I_1^* - I_1) = \sigma_{pvi} \quad (3.61)$$

where \tilde{S}_1 is the average duty ratio of the converter.

$$\frac{I_1}{I_1^*} = \frac{k_{pvi}(s)}{sL_1 + R_1 + k_{pvi}(s)} \quad \text{and} \quad k_{pvi}(s) = k_{ppvi} + \frac{k_{lpvi}}{s} \quad (3.62)$$

$$\frac{I_1}{I_1^*} = \frac{sk_{ppvi} + k_{lpvi}}{s^2 L_1 + (R_1 + k_{ppvi})s + k_{lpvi}} \quad (3.63)$$

$$s^2 L_1 + (R_1 + k_{ppvi})s + k_{lpvi} = s^2 + 2\zeta\omega_n s + \omega_n^2 \Rightarrow \begin{cases} k_{ppvi} = 2\zeta\omega_n L_1 - R_1 \\ k_{lpvi} = \omega_n^2 L_1 \end{cases} \quad (3.64)$$

$$\tilde{S}_1 = 1 - \frac{V_{pv} - \sigma_{pvi}}{V_{dc}} \quad (3.65)$$

For faster inner current controller $\omega_{n2} = 0.4\pi f_{swdc}$.

3.4.5 DC Link Voltage Control

The battery DC-DC converter should control the DC link voltage. Figure 3.15 and Table 3.3 show the block diagram of battery converter control unit and battery parameters. From the dynamics of the DC link voltage in (3.26) if the aforementioned method is used

$$C_{dc} s V_{dc} = (1 - \tilde{S}_1) I_1 + \tilde{S}_2 I_2 - \frac{3}{4} (M_{q1} I_{s1q} + M_{d1} I_{s1d}) = k_{dc}(s)(V_{dc}^* - V_{dc}) = \sigma_{dc} \quad (3.66)$$

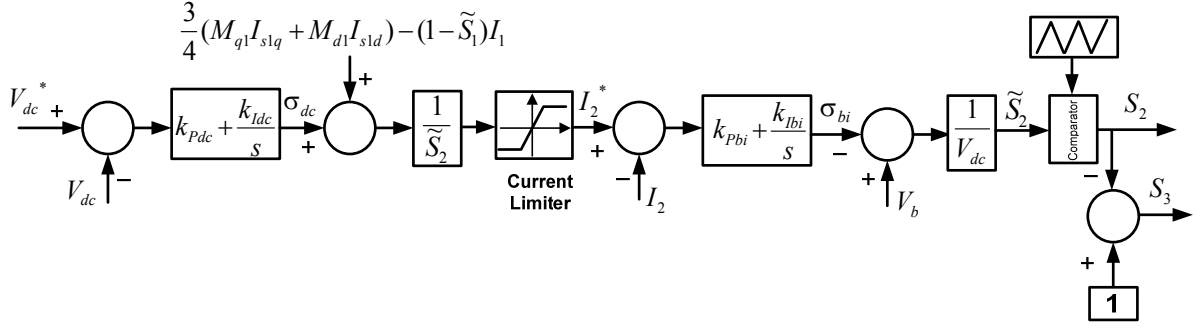


Figure 3.15 Block diagram of Battery DC-DC converter control part

$$\frac{V_{dc}}{V_{dc}^*} = \frac{k_{dc}(s)}{sC_{dc} + k_{dc}(s)} \quad \text{and} \quad k_{dc}(s) = k_{Pdc} + \frac{k_{Idc}}{s} \quad (3.67)$$

$$\frac{V_{dc}}{V_{dc}^*} = \frac{sk_{Pdc} + k_{Idc}}{s^2C_{dc} + sk_{Pdc} + k_{Idc}} \quad (3.68)$$

$$s^2C_{dc} + sk_{Pdc} + k_{Idc} = s^2 + 2\zeta\omega_n s + \omega_n^2 \Rightarrow \begin{cases} k_{Pdc} = 2\zeta\omega_n C_{dc} \\ k_{Idc} = \omega_n^2 C_{dc} \end{cases} \quad (3.69)$$

$$I_2^* = \frac{\sigma_{dc} + \frac{3}{4}(M_{q1}I_{s1q} + M_{d1}I_{s1d}) - (1 - \tilde{S}_1)I_1}{\tilde{S}_2} \quad (3.70)$$

3.4.6 Current Control of Battery Converter

The utilization of the battery inner current loop controller in addition to fault protection, can limit the charge and the discharge current of the battery which is a key factor in the determination of the battery life time. From (3.25)

$$L_2 s I_2 + R_2 I_2 = V_b - \tilde{S}_2 V_{dc} = k_{bi}(s)(I_2^* - I_2) = \sigma_{bi} \quad (3.71)$$

$$\frac{I_2}{I_2^*} = \frac{k_{bi}(s)}{sL_2 + R_2 + k_{bi}(s)} \text{ and } k_{bi}(s) = k_{pbi} + \frac{k_{lbi}}{s} \quad (3.72)$$

$$\frac{I_2}{I_2^*} = \frac{sk_{pbi} + k_{lbi}}{s^2L_2 + (R_2 + k_{pbi})s + k_{lbi}} \quad (3.73)$$

$$s^2L_2 + (R_2 + k_{pbi})s + k_{lbi} = s^2 + 2\zeta\omega_n s + \omega_n^2 \Rightarrow \begin{cases} k_{pbi} = 2\zeta\omega_n L_2 - L_2 \\ k_{lbi} = \omega_n^2 L_2 \end{cases} \quad (3.74)$$

$$\tilde{S}_2 = \frac{V_b - \sigma_{bi}}{V_{dc}} \quad (3.75)$$

3.4.7 Voltage Control of PV in Disabled Battery

If the battery is disabled, DC link voltage should be regulated by PV converter.

To follow the reference voltage of the PV (V_{pv}^*) system that comes from MPPT

$$C_{pv}sV_{pv} = I_{pv} - I_1 = k_{pvv}(s)(V_{pv}^* - V_{pv}) = \sigma_{pvv} \quad (3.76)$$

$$\frac{V_{pv}}{V_{pv}^*} = \frac{k_{pvv}(s)}{sC_{pv} + k_{pvv}(s)} = \frac{sk_{ppvv} + k_{lpvv}}{s^2C_{pv} + sk_{ppvv} + k_{lpvv}} \quad (3.77)$$

$$\begin{cases} k_{ppvv} = 2\zeta\omega_n C_{pv} \\ k_{lpvv} = \omega_n^2 C_{pv} \end{cases} \quad (3.78)$$

$$I_1^* = I_{pv} - \sigma_{pvv} \quad (3.79)$$

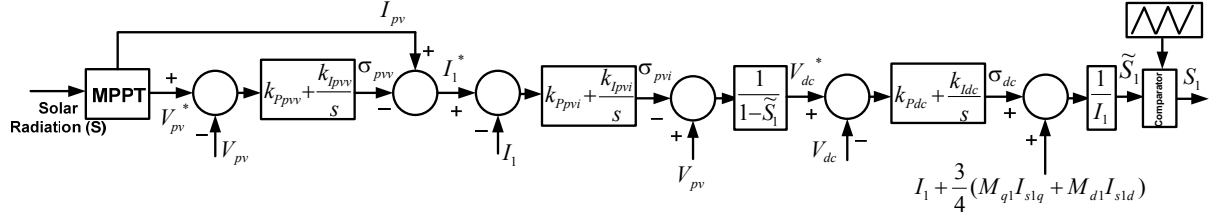


Figure 3.16 Block diagram of PV DC-DC boost converter control part if battery converter is disabled

3.4.8 PV Converter Current Control in Disabled Battery

In disabled battery mode, the dynamic equation of the PV current and therefore its controller structure is changed as

$$L_1 s I_1 + R_1 I_1 = V_{pv} - (1 - \tilde{S}_1) V_{dc} = k_{pvi}(s)(I_1^* - I_1) = \sigma_{pvi} \quad (3.80)$$

The transfer function for current controller is

$$\frac{I_1}{I_1^*} = \frac{k_{pvi}(s)}{sL_1 + R_1 + k_{pvi}(s)} = \frac{sk_{Ppvi} + k_{Ipvi}}{s^2L_1 + (R_1 + k_{Ppvi})s + k_{Ipvi}} \quad (3.81)$$

$$\begin{cases} k_{Ppvi} = 2\zeta\omega_n L_1 - R_1 \\ k_{Ipvi} = \omega_n^2 L_1 \end{cases} \quad (3.82)$$

$$V_{dc}^* = \frac{V_{pv} - \sigma_{pvi}}{1 - \tilde{S}_1} \quad (3.83)$$

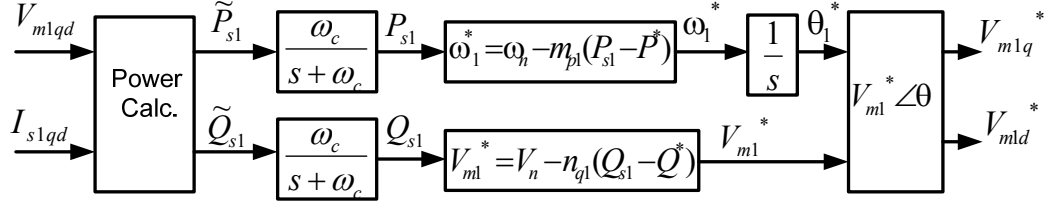


Figure 3.17 Droop control unit

3.4.9 DC Link Voltage Control in Disabled Battery

To control the DC-link voltage

$$C_{dc}sV_{dc} = (1 - \tilde{S}_1)I_1 - \frac{3}{4}(M_{q1}I_{s1q} + M_{d1}I_{s1d}) = k_{dc}(s)(V_{dc}^* - V_{dc}) = \sigma_{dc} \quad (3.84)$$

$$\frac{V_{dc}}{V_{dc}^*} = \frac{k_{dc}(s)}{sC_{dc} + k_{dc}(s)} = \frac{sk_{Pdc} + k_{Idc}}{s^2C_{dc} + sk_{Pdc} + k_{Idc}} \quad (3.85)$$

$$\begin{cases} k_{Pdc} = 2\zeta\omega_n C_{dc} \\ k_{Idc} = \omega_n^2 C_{dc} \end{cases} \quad (3.86)$$

$$\tilde{S}_1 = \frac{-\sigma_{dc} + I_1 + \frac{3}{4}(M_{q1}I_{s1q} + M_{d1}I_{s1d})}{I_1} \quad (3.87)$$

3.4.10 Droop Control

To guarantee total power balance either if total power of converter and battery is less than total load or total load is less than produced power, a droop control is used.

The droop control droops frequency and voltage against output active and reactive power of the three phase converter respectively.

$$\omega_1^* = \omega_n - m_{p1}(P_{s1} - P^*) \quad (3.88)$$

$$V_{m1}^* = V_n - n_{q1}(Q_{s1} - Q^*) \quad (3.89)$$

where ω_n and V_n are rated frequency and rated voltage of the system. m_{p1} , n_{q1} , P_{s1} and Q_{s1} are active power droop coefficients, reactive power droop coefficient, output active power and output reactive power of converter, respectively. P^* and Q^* are desired active and reactive powers of the converter. In this case P^* is maximum power of PV system that comes from MPPT and Q^* is considered zero.

In (3.90) and (3.91) the amount of droop coefficients are defined. The active power droop coefficient and reactive power droop coefficient are based on maximum change of frequency and voltage respectively.

$$m_{p1} = \frac{\Delta\omega}{\Delta P_{s1\max}} \quad (3.90)$$

$$n_{q1} = \frac{\Delta V}{\Delta Q_{s1\max}} \quad (3.91)$$

Figure 3.17 shows the droop control unit in detail. First the instantaneous output active and reactive powers of the converter are calculated using measured output current of the converter and load voltage.

$$\tilde{P}_{s1} = \frac{3}{2}(V_{m1q}I_{s1q} + V_{m1d}I_{s1d}) \quad (3.92)$$

$$\tilde{Q}_{s1} = \frac{3}{2}(V_{m1q}I_{s1d} - V_{m1d}I_{s1q}) \quad (3.93)$$

To remove fluctuations and produce average values of output powers, both calculated instantaneous powers are passed through a low pass filter with a cut off frequency of ω_c .

$$P_{s1} = \frac{\omega_c}{s + \omega_c} \tilde{P}_{s1} \quad (3.94)$$

$$Q_{s1} = \frac{\omega_c}{s + \omega_c} \tilde{Q}_{s1} \quad (3.95)$$

The outputs of droop control are voltage magnitude and angular frequency which define the reference angle of the load voltage using an integrator. Thus the qd-axis reference voltage can be determined as follows:

$$V_{m1q}^* = V_{m1}^* \cos(\theta_1^* - \theta_{s1}) \quad (3.96)$$

$$V_{m1d}^* = -V_{m1}^* \sin(\theta_1^* - \theta_{s1}) \quad (3.97)$$

3.4.11 Phase Locked Loop

To measure the frequency of the system and define reference frequency for qd transformation a phase lock loop (PLL) is designed and applied to each DG unit.

$$V_{m1d} = -V_{m1} \sin(\theta_1 - \theta_{s1}) \quad (3.98)$$

$$\text{If } V_{m1d} = 0 \Rightarrow \sin(\theta_1 - \theta_{s1}) = 0 \Rightarrow \theta_{s1} = \theta_1$$

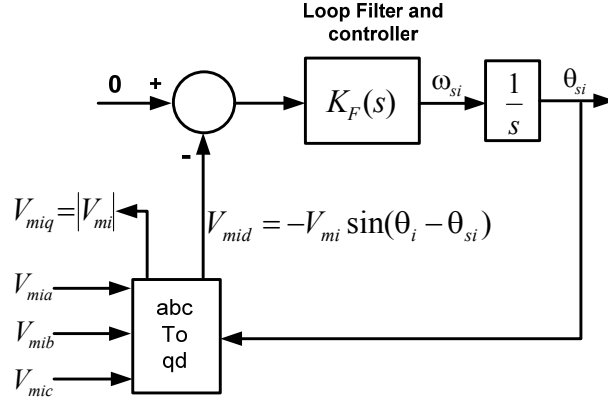


Figure 3.18 Block diagram of phase locked loop

$$e = 0 - V_{m1d} = V_{m1} \sin(\theta_1 - \theta_{s1}) \quad (3.99)$$

If $(\theta_1 - \theta_{s1})$ is very small we can assume

$$\sin(\theta_1 - \theta_{s1}) \approx (\theta_1 - \theta_{s1}) \quad (3.100)$$

$$V_{m1} (\theta_1 - \theta_{s1}) \frac{K_F(s)}{s} = \theta_{s1} \quad (3.101)$$

Therefore one can define the closed loop transfer function and compare its denominator with that of the second order standard Butterworth filter transfer function

$$\frac{\theta_{s1}}{\theta_1} = \frac{V_{m1} K_F(s)}{s + V_{m1} K_F(s)} = \frac{s V_{m1} k_{Ppll} + V_{m1} k_{Ipll}}{s^2 + s V_{m1} k_{Ppll} + V_{m1} k_{Ipll}} = \frac{2\zeta\omega_{n1} s + \omega_{n1}^2}{s^2 + 2\zeta\omega_{n1} s + \omega_{n1}^2} \quad (3.102)$$

$$k_{Ppll} = \frac{2\zeta\omega_{n1}}{V_{mi}} \text{ and } k_{Ipll} = \frac{\omega_{n1}^2}{V_{mi}} \quad (3.103)$$

$$e = 0 - V_{m1d} = V_{m1} \sin(\theta_1 - \theta_{s1}) \quad (3.104)$$

Table 3.2 Parameters of power system

R_{s1}	0.1Ω	R_1	0.2Ω
L_{s1}	$4e^{-3}H$	L_1	$2e^{-3}H$
R_{L1}	10Ω	C_{pv}	$100e^{-6}F$
L_{L1}	$0.0352H$	R_2	0.2Ω
C_{d1}	$200e^{-6}F$	L_2	$2e^{-3}H$
C_{dc}	$5e^{-3}F$	C_b	$100e^{-6}F$

Table 3.3 Parameters of the battery

R_{b1}	0.05Ω	V_b	$48V$
C_{b1}	$54000F$	R_{b3}	0.002Ω
R_{b2}	0.001Ω	R_{b4}	0.05Ω
C_{b2}	$1F$		

Table 3.4 PI controllers' coefficients

k_{pm1}	0.377	k_{Im1}	0
k_{ps1}	25.13	k_{Is1}	628.32
k_{ppvv}	0.053	k_{Ippv}	14.21
k_{ppvi}	0.866	k_{Ipvi}	284.26
k_{pdc}	2.66	k_{Idc}	710.6
k_{pbi}	0.866	k_{Ibi}	284.26
k_{ppll}	4.44	k_{Ipll}	1184
m_{p1}	$38e^{-4}$	n_{q1}	$12e^{-4}$

$$e = 0 - V_{m1d} = V_{m1} \sin(\theta_1 - \theta_{s1}) \quad (3.105)$$

where ζ is damping factor and is usually chosen as critical damping factor which is 0.707.

3.5 Simulation Results

To show the performance of the designed controllers, the studied system is simulated in MATLAB software. Table 3.2 gives the parameters of the system in Figure 3.1.

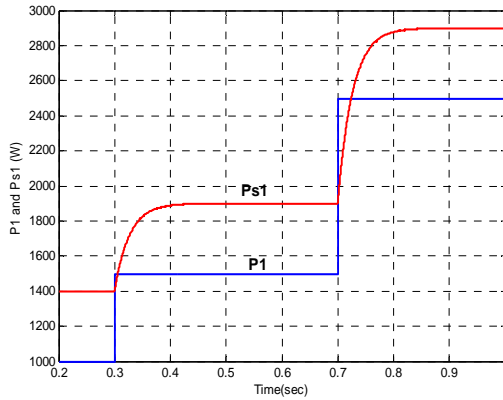


Figure 3.19 Constant load and inverter output active powers

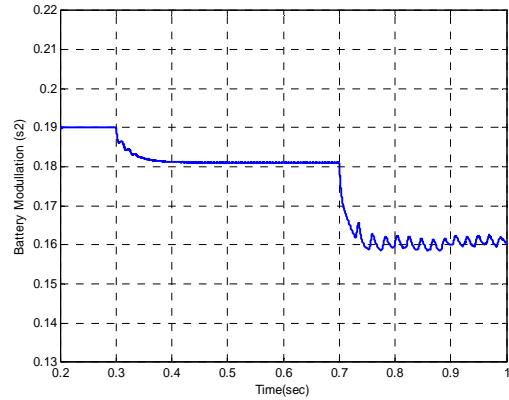


Figure 3.20 Battery converter modulation index

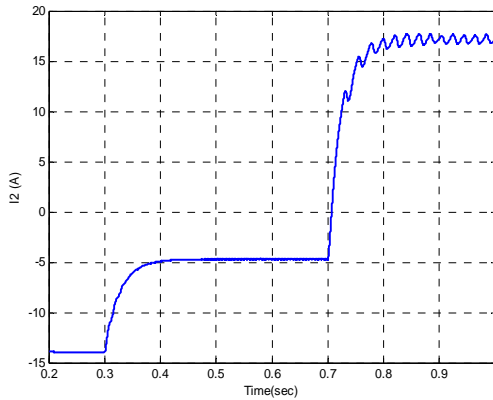


Figure 3.21 Battery output current

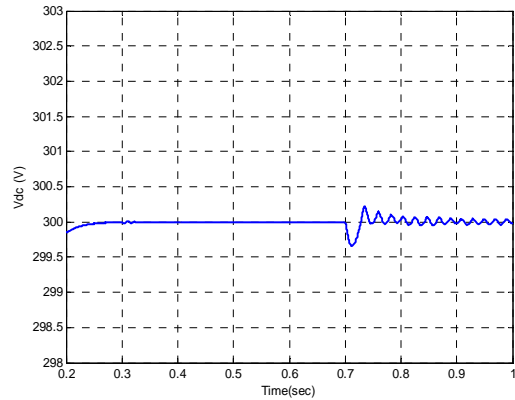


Figure 3.22 DC link voltage

Parameters of the battery and PI controllers' coefficients are presented in Table 3.3 and Table 3.4 respectively. The PV system is always working in maximum power point and the battery converter tries to control DC link voltage and limit maximum charge or discharge currents of the battery that are chosen 300V and 20A respectively. Figure 3.19 shows the constant active load power changes at 0.3s and 0.7s from the lower to the higher than rated power of PV system (2300W at unity irradiation level) with constant reactive load power of 20Var. With a change of constant load active power, the output active power of the inverter changes to feed both the linear and the constant loads.

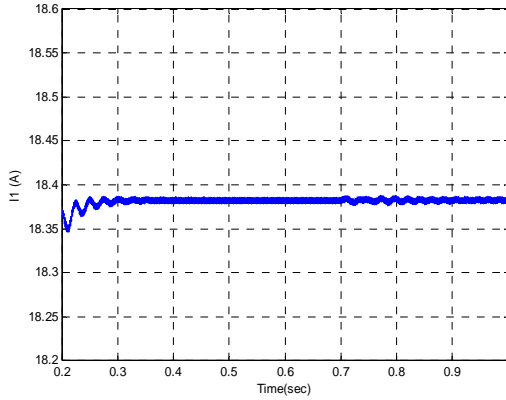


Figure 3.23 PV system output current

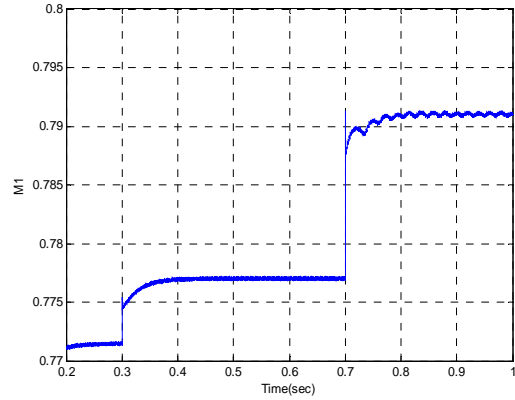


Figure 3.24 Inverter modulation index magnitude

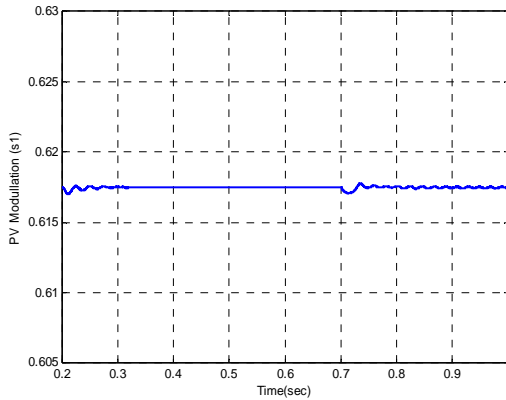


Figure 3.25 PV converter modulation index

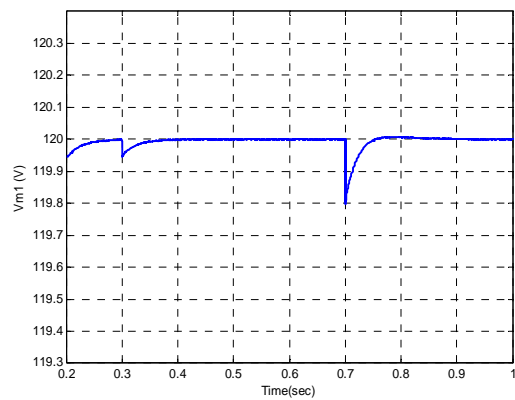


Figure 3.26 Load voltage magnitude

Therefore total load will be 1900W and 2900W respectively. The nominal power of the PV system at the maximum point is about 2300W. As illustrated in Figure 3.20, based on the total load power, the battery is charging or discharging. When the total load is less than the nominal power of PV system as primary source, excessive power charges the battery and makes the current of the battery negative. After 0.7s total load is more than MPP of PV and the battery is discharged to feed the load. The modulation index of the battery converter changes in Figure 3.21 based on output current. Due to the performance of the battery converter controller unit, DC link voltage remains almost constant in Figure 3.22. In a constant DC voltage, the PV system works in MPP mode without any special

change in its output current and modulation index as shown in Figure 3.23 and Figure 3.24 respectively. With increase of the load active power, modulation index of the three phase inverter increases in Figure 3.25 and is always less than unity. In Figure 3.26, load voltage magnitude experiences a small voltage sag in the instant of load change but it reaches nominal value and remains constant for less than 50ms using a three phase inverter controller.

To show the effect of array shading, the irradiation level at 0.5s is changed from unity to 0.7, when the total load is kept constant at 2000W. Based on the proven equation of optimum PV voltage, to follow maximum power point, the reference PV voltage changes from 121.25V to 117.6V and the corresponding maximum output power of the PV changes from 2300W to 1500W. Figure 3.27b shows that the PV controller follows the reference voltage perfectly to produce maximum possible active power. Because the total load is more than the maximum power of the PV system, the battery will discharge. In Figure 3.27, with decrease of output PV current due to irradiation level reduction, the battery produces positive current to meet the load requirement and keep the DC link voltage constant.

3.6 Conclusions

In this chapter, the model and steady state performance characteristics of an autonomous power system fed by a PV source and battery are set forth. The nonlinearities of the PV and load are included in the model. At steady-state, when the PV system is working at the maximum power point, it is observed that with an increase of the load, the dc link voltage

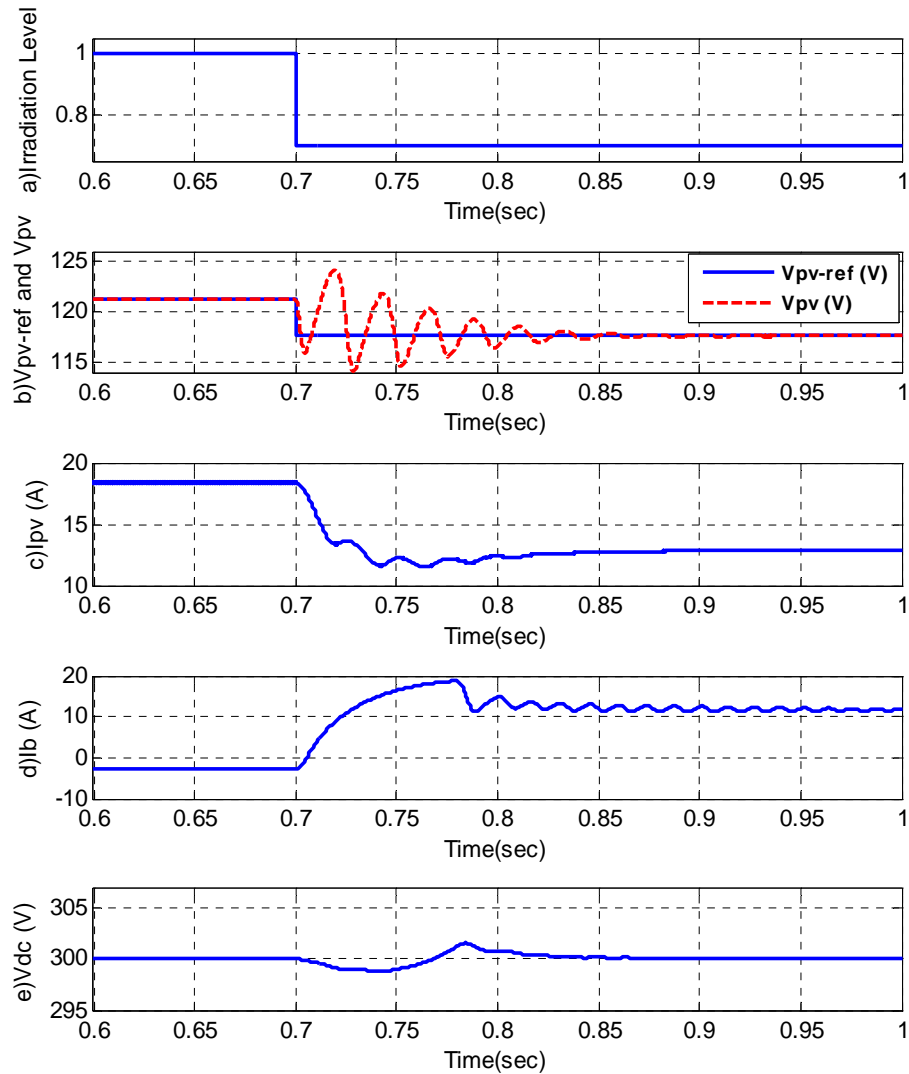


Figure 3.27 Operation under different irradiation level. (a) irradiation level, (b) reference and actual PV voltage, (c) PV output current, (d) battery output current, (e) Dc link voltage

increases to meet the constant load voltage when the voltage source converter operates at a constant modulation index. The battery discharges when total load is more than maximum power of the PV system. Under a lower irradiation level, the maximum power of PV system decreases, thus the battery discharges even under reduced load demand. With reduction of the inverter modulation index magnitude, to meet constant load

voltage, the input DC link voltage and the duty ratios of the two boost converters interfacing the sources are increased.

Controller parts of DC/AC inverter and DC/DC converters are designed. The objectives of the inverter and battery converter are to control load voltage and DC link voltage respectively. PV converter tries to operate in maximum power point. If load power is more than the maximum power of PV system and the battery is discharged, droop control manages frequency and load voltage to guarantee total load balance. The three phase inverter controls the frequency and voltage magnitude of the load. Simulation results prove that with the change of load or irradiation level, controllers enable following of the reference and meet load requirements in standalone mode condition.

CHAPTER 4

STEADY STATE ANALYSIS AND DYNAMIC CONTROL OF PV SYSTEM CONNECTED TO THE MAIN GRID

4.1 Introduction

The goal for the microgrid with renewable energy sources is to transfer the maximum possible power in grid connected mode. Since the voltage magnitude and frequency are adapted from the main grid, the controller objectives are different in this mode than in autonomous mode operation.

In grid connected mode the output active and reactive power or input DC-link voltage magnitude can be controlled. In this chapter, a controller for grid connected operation of a microgrid with a photovoltaic (PV) system as an input source has been designed.

In the first section a single converter as a DG unit connected to a local linear RL and a non-linear voltage dependent load along with a capacitor to remove harmonics and stabilize load voltage is considered. The system equations are transformed from abc to qd0 in synchronous reference frame and dynamic equations are defined.

Two different control algorithms are considered. First the objective is to control input DC voltage and assume load voltage is constant because it is connected to the main grid. Secondly, with assumption of constant input DC voltage source, the load voltage is controlled. In both algorithms we have an inner current control loop which controls qd-axis output current of the converter separately.

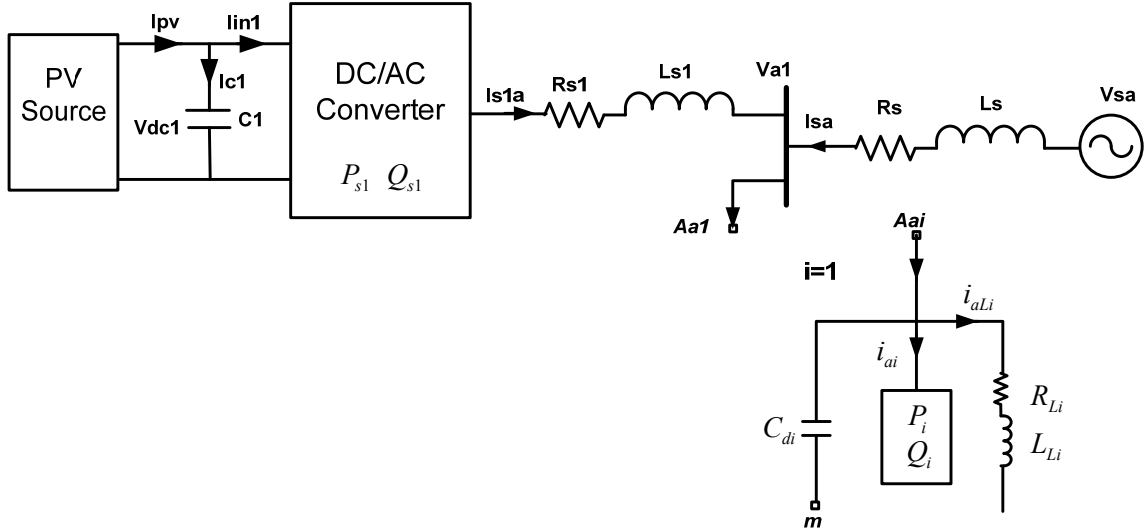


Figure 4.1 Schematic diagram of a DG system with PV source connected to the grid

After designing controllers, a state space model of the whole system is defined and bifurcation analysis is applied to the system to find equilibrium curves of parameters and bifurcation points in the operation region. The simulation results prove the performance of the designed controllers.

4.2 Dynamic Model of the System

Figure 4.1 shows the block diagram of a grid connected distributed generation (DG) system. A voltage source converter converts DC input to AC output voltage. A linear RL load and a constant load are connected to the converter through a transmission line. A capacitor is connected to remove the high frequency voltage harmonics out of the three phase inverter and smooth the load voltage. Another transmission line connects the system to the main network with constant voltage magnitude and frequency.

The dynamic equations of the system in three phase abc frame are as follows:

The inverter transmission line dynamic equations

$$\begin{cases} V_{s1a} = V_{m1a} + L_{s1}pI_{s1a} + R_{s1}I_{s1a} \\ V_{s1b} = V_{m1b} + L_{s1}pI_{s1b} + R_{s1}I_{s1b} \\ V_{s1c} = V_{m1c} + L_{s1}pI_{s1c} + R_{s1}I_{s1c} \end{cases} \quad (4.1)$$

The three phase inverter equations

$$\begin{cases} V_{s1a} + V_{no} = \frac{V_{dc1}}{2}(2s_{ap} - 1) \\ V_{s1b} + V_{no} = \frac{V_{dc1}}{2}(2s_{bp} - 1) \\ V_{s1c} + V_{no} = \frac{V_{dc1}}{2}(2s_{cp} - 1) \end{cases} \quad (4.2)$$

where V_{s1abc} , I_{s1abc} and s_{abc} are output phase voltages, phase currents and switching functions of DG1 (VSC1).

Linear Load of DG1 (L1) equations

$$\begin{cases} V_{m1a} = R_{L1}I_{L1a} + L_{L1}pI_{L1a} \\ V_{m1b} = R_{L1}I_{L1b} + L_{L1}pI_{L1b} \\ V_{m1c} = R_{L1}I_{L1c} + L_{L1}pI_{L1c} \end{cases} \quad (4.3)$$

where I_{L1abc} are phase currents of linear load (L1) of DG1

The main grid equations

$$\begin{cases} V_{sa} - V_{m1a} = L_s pI_{sa} + R_s I_{sa} \\ V_{sb} - V_{m1b} = L_s pI_{sb} + R_s I_{sb} \\ V_{sc} - V_{m1c} = L_s pI_{sc} + R_s I_{sc} \end{cases} \quad (4.4)$$

Capacitor of DG1 Equations

$$\begin{cases} C_{d1}pV_{m1a} = I_{s1a} + I_{sa} - I_{L1a} - I_{1a} \\ C_{d1}pV_{m1b} = I_{s1b} + I_{sb} - I_{L1b} - I_{1b} \\ C_{d1}pV_{m1c} = I_{s1c} + I_{sc} - I_{L1c} - I_{1c} \end{cases} \quad (4.5)$$

where I_{1abc} are the phase currents of second (nonlinear) load of DG1.

The input DC current of DG1

$$C_1pV_{dc1} = I_{pv} - I_{in1} = I_{pv} - (I_{s1a}s_{ap} + I_{s1b}s_{bp} + I_{s1c}s_{cp}) \quad (4.6)$$

where s_{abc} are modulation signals of three phase inverter. qd-axis dynamic equations of the system in grid frequency synchronous reference frame are as follows:

$$\begin{cases} M_{q1} = M_1 \cos((\omega_1 - \omega_{s1})t + (\theta_{10} - \theta_{s10})) \\ M_{d1} = -M_1 \sin((\omega_1 - \omega_{s1})t + (\theta_{10} - \theta_{s10})) \end{cases} \quad (4.7)$$

where ω_1 and θ_{10} are frequency and initial angle of converter and ω_{s1} and θ_{s10} are instantaneous frequency and initial angle of the system that is measured by a phase locked loop (PLL). M_1 , M_{q1} and M_{d1} are modulation index magnitude, q-axis modulation index and d axis modulation index of the converter respectively.

Load voltage equations

$$\begin{cases} V_{qm1} = V_{m1} \cos((\omega_{s1} - \omega_{s1})t + (\theta_{s10} - \theta_{s10})) = V_{m1} \\ V_{dm1} = 0 \end{cases} \quad (4.8)$$

where V_{m1} is the load voltage magnitude.

$$\begin{cases} pI_{s1q} = \frac{1}{L_{s1}} (M_{q1} \frac{V_{dc1}}{2} - V_{qm1} - R_{s1}I_{s1q} - L_{s1}\omega_{s1}I_{s1d}) \\ pI_{s1d} = \frac{1}{L_{s1}} (M_{d1} \frac{V_{dc1}}{2} - V_{dm1} - R_{s1}I_{s1d} + L_{s1}\omega_{s1}I_{s1q}) \end{cases} \quad (4.9)$$

where I_{s1qd} , R_{s1} and L_{s1} are qd-axis current, resistance and inductance of converter side transmission line respectively ($p = \frac{d}{dt}$).

Linear Load of DG1 (L1) equations

$$\begin{cases} pI_{L1q} = \frac{1}{L_{L1}}(V_{qm1} - R_{L1}I_{L1q} - L_{L1}\omega_{s1}I_{L1d}) \\ pI_{L1d} = \frac{1}{L_{L1}}(V_{dm1} - R_{L1}I_{L1d} + L_{L1}\omega_{s1}I_{L1q}) \end{cases} \quad (4.10)$$

where I_{L1qd} , R_{L1} and L_{L1} are qd-axis current, resistance and inductance of the linear load respectively.

The second load is considered as constant load therefore its current equations are

$$I_{1q} = \frac{2}{3} \frac{P_1 V_{qm1} - Q_1 V_{dm1}}{V_{qm1}^2 + V_{dm1}^2} \quad (4.11)$$

$$I_{1d} = \frac{2}{3} \frac{P_1 V_{dm1} + Q_1 V_{qm1}}{V_{qm1}^2 + V_{dm1}^2} \quad (4.12)$$

Capacitor of DG1 equations

$$\begin{cases} pV_{qm1} = \frac{1}{C_{d1}}(I_{s1q} + I_{sq} - I_{L1q} - I_{1q} - C_{d1}\omega_{s1}V_{dm1}) \\ pV_{dm1} = \frac{1}{C_{d1}}(I_{s1d} + I_{sd} - I_{L1d} - I_{1d} + C_{d1}\omega_{s1}V_{qm1}) \end{cases} \quad (4.13)$$

where C_{d1} is the capacitance of parallel capacitor connected to the loads.

The input DC current of DG1

$$I_{pv} = I_{in1} = \frac{3}{4}(M_{q1}I_{s1q} + M_{d1}I_{s1d}) \quad (4.14)$$

$$I_{pv} = I_{in1} = \frac{3}{4}(M_{q1}I_{s1q} + M_{d1}I_{s1d}) \quad (4.15)$$

The nonlinear model of the PV system relating the current flowing out of the PV and the terminal voltage is defined as follows:

$$I_{pv} = n_p I_{ph} - n_p I_{rs} \left[\exp\left(\frac{q}{k \theta} \frac{V_{pv}}{A n_s}\right) - 1 \right] \quad (4.16)$$

$$I_{ph} = \left[I_{src} + k_\theta (\theta - \theta_r) \right] \frac{S}{100} \quad (4.17)$$

4.3 Steady-State Operation

At steady state the derivatives of the states in the dynamic equations are set equal to zero. The converter equations of DG1

$$\begin{cases} V_{s1q} = V_{qm1} + R_{s1}I_{s1q} + L_{s1}\omega I_{s1d} = M_{q1} \frac{V_{dc1}}{2} \\ V_{s1d} = V_{dm1} + R_{s1}I_{s1d} - L_{s1}\omega I_{s1q} = M_{d1} \frac{V_{dc1}}{2} \end{cases} \quad (4.18)$$

Linear Load of DG1 (L1) equations

$$\begin{cases} V_{qm1} = R_{L1}I_{L1q} + L_{L1}\omega I_{L1d} \\ V_{dm1} = R_{L1}I_{L1d} - L_{L1}\omega I_{L1q} \end{cases} \quad (4.19)$$

Capacitor of DG1 equations

Table 4.1 System parameters of DG connected to the grid

V_s	120V	ω_s	377(rad/s)
R_s	0.05 Ω	L_s	0.002H
R_{s1}	0.1 Ω	L_{s1}	0.004H
R_{L1}	10 Ω	L_{L1}	0.0352H
C_{d1}	200e ⁻⁶ F	C_1	0.005F

$$\begin{cases} C_{d1}\omega V_{dm1} = I_{s1q} + I_{sq} - I_{L1q} - I_{1q} \\ -C_{d1}\omega V_{qm1} = I_{s1d} + I_{sd} - I_{L1d} - I_{1d} \end{cases} \quad (4.20)$$

The parameters of the power system are presented in Table 4.1. The parameters of the PV system are the same as Table 3.1 instead of number of parallel and series cells (n_p and n_s). Since there is no boost converter and the PV is directly connected to three phase inverter and DC link voltage magnitude should be considered at least two times of the magnitude of the grid voltage in the AC side at the operation point, the number of parallel cells has been considered one and a half times of previous case in this chapter. To have the same output power, the number of series cells is divided by three to cause lower current with higher output voltage. Figure 4.2 illustrates the used nonlinear characteristic of the PV in per unit. The base values are the same ($S_b=2000W$ and $V_b=120V$).

From the system equations, the known variables for steady state calculation are the grid voltage magnitude and the irradiation level of the sun for PV ($S=1$). The DC link voltage and current are calculated based on the operation of the PV system in maximum power point.

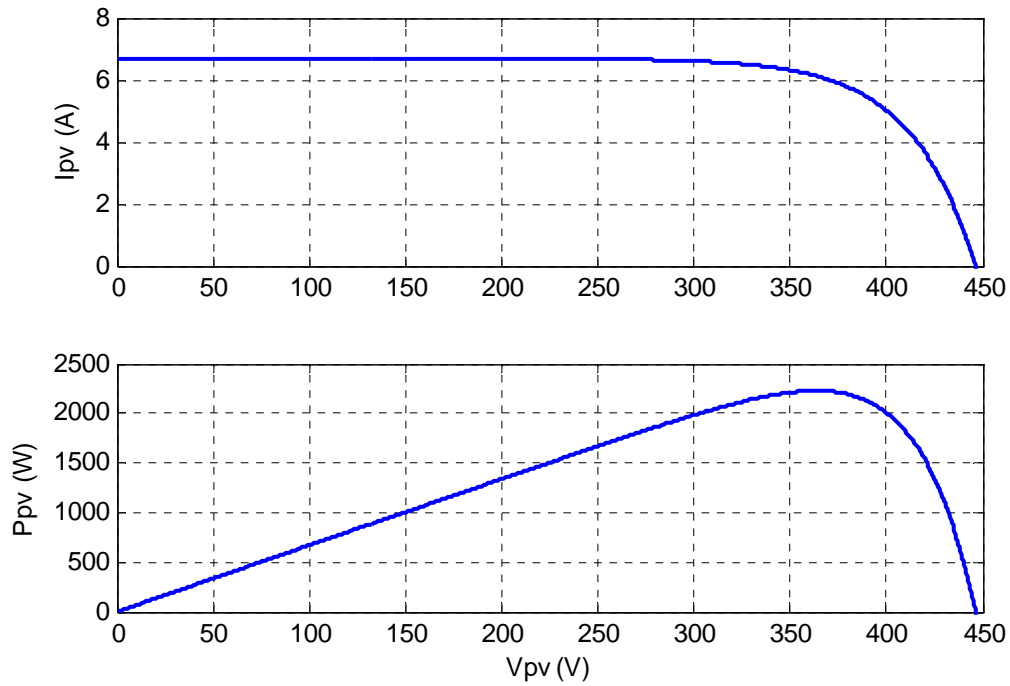


Figure 4.2 Nonlinear characteristic of PV source

4.2.2.1 Operation under different values of q-axis grid voltage (V_{qs}) and four different constant loads ($V_{md1}=0$). Since the load (capacitor) voltage is considered as the reference for qd axis transformation the qd axis grid voltage are free to be changed. In this study, the parameters of the system have been defined in four different constant load values.

In this condition because we have two more variables than equations, in transforming equations from abs to qdo reference frame, we considered $V_{dm1} = 0$ which is d-axis load and capacitor voltage. V_{qs} is a known variable, so with change of it from negative to positive nominal value (-120V to 120V) we can calculate other parameters to see the operation region of the system.

These figures just show the logical operation region in which we have real answers for other parameters and the modulation index is less than one. As illustrated in

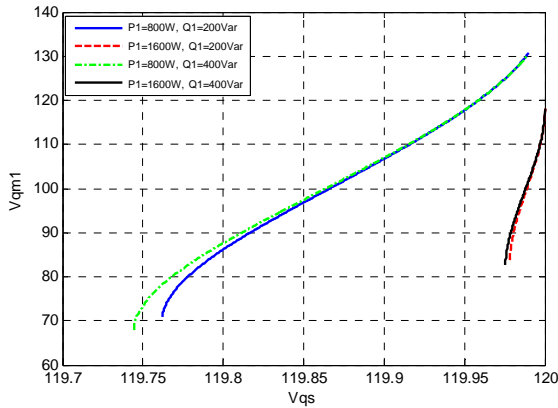


Figure 4.3 Load and capacitor voltage

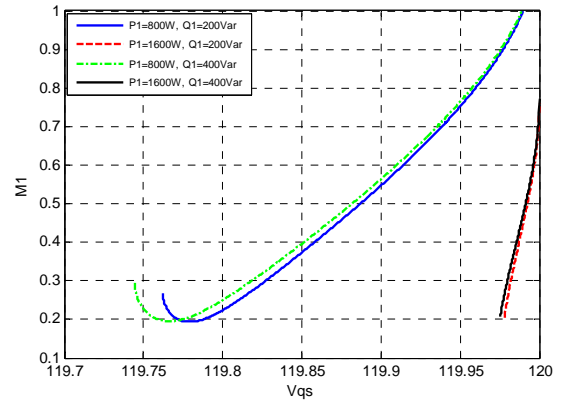


Figure 4.4 Modulation index magnitude

Figure 4.3, the operation region of the system based on predefined values of the loads and grid impedances is in a narrow range of q-axis main grid voltage in which with change of V_{qs} from 118V to 120V, load voltage (V_{qm1}) changes from 70V to 140V. Figure 4.4 shows with increasing grid and load voltage, modulation index of the converter increases gradually. Active power of the converter is constant because its input DC voltage and current are assumed to be constant. In low constant load, because output active power of the converter is more than total load, excessive power flows into the grid. In addition because the range of the change of V_{qs} is small but V_{qm1} is increasing, the difference between them decreases gradually which causes reduction in active power consumed by line resistances although active power of the linear load due to increase of its voltage increases, therefore active power that is flowing into the main grid in Figure 4.5 (magnitude) first starts to increase then it reduces.

As can be seen from the figures, change of the constant load active power has more effect than change of the constant load reactive power on operation region. With

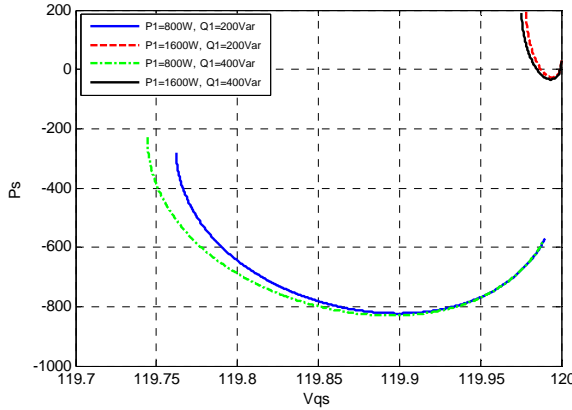


Figure 4.5 Active power of the main grid (negative means power flows into the main grid)

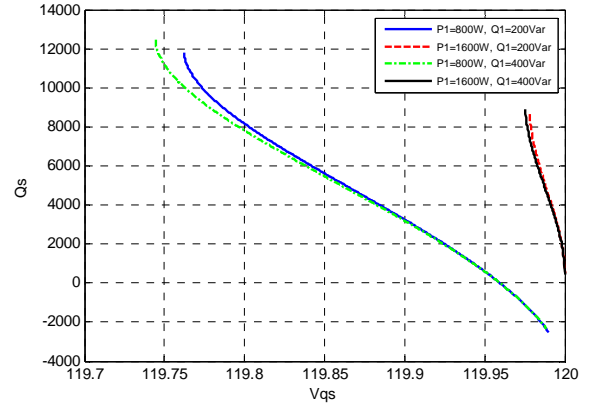


Figure 4.6 Reactive power of the main grid

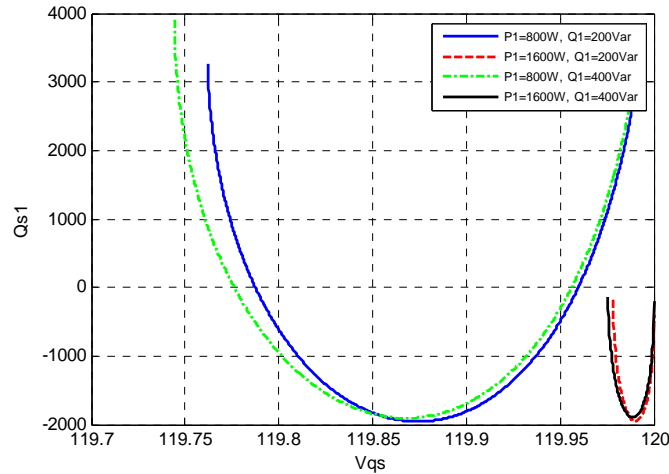


Figure 4.7 Reactive power of the converter

increasing of the constant load active power, the limit and rate of the load voltage change will be smaller and sharper respectively. Furthermore active and reactive power of the grid increases to feed the load in Figure 4.5 and Figure 4.6.

4.2.2.1 Operation under zero output reactive power of converter ($Q_{s1}=0$) and change of constant load. In this part also we considered $V_{dm1} = 0$ but V_{qs} is unknown, instead we assumed output reactive power of converter (Q_{s1}) is zero (unity power factor operation) which adds another equation which makes eleven equations and eleven

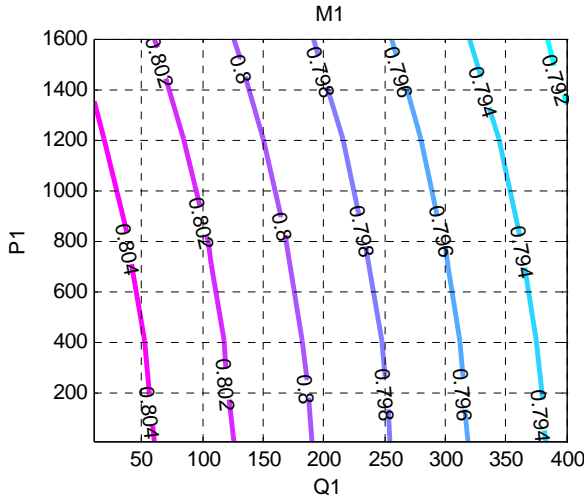


Figure 4.8 Modulation index magnitude of converter

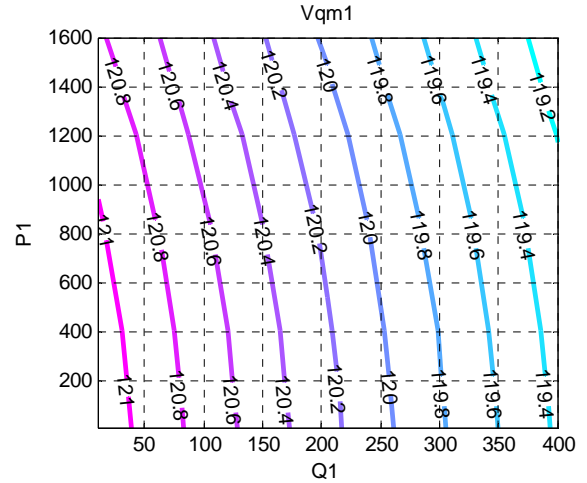


Figure 4.9 Load and capacitor voltage

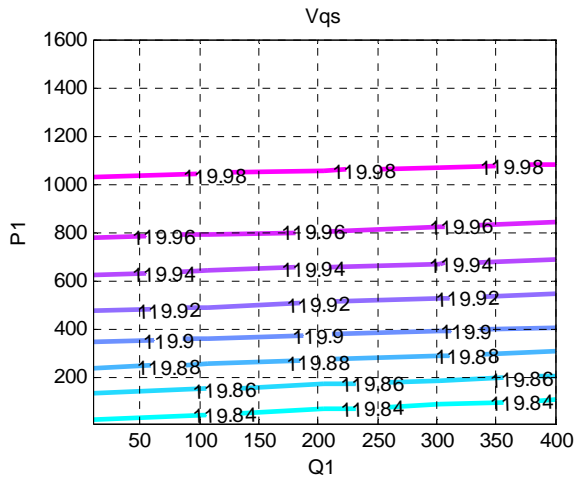


Figure 4.10 q-axis voltage of main grid

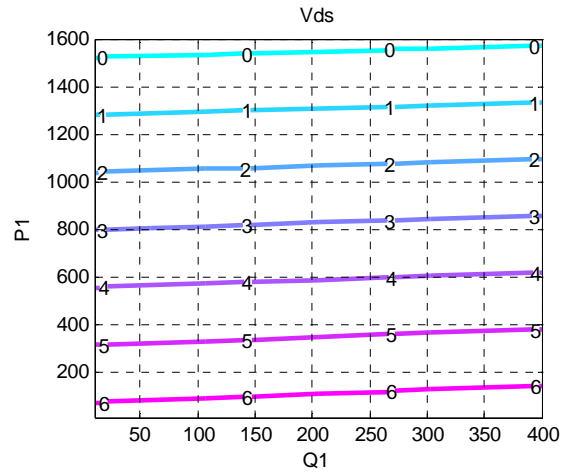


Figure 4.11 d-axis voltage of main grid

variables. The contours of change of system parameters with change of active and reactive power of constant load are presented. The active and reactive powers of the constant load have been changed from 10W to 1600W and 10Var to 400Var respectively.

With a load voltage close to rated value, the modulation index is high in Figure 4.8 (about 0.8) and the output current of the converter to feed the load is small. The Load voltage magnitude ($V_{ml}=V_{mlq}$) and q-axis voltage of the grid in Figure 4.9 and Figure 4.10 are close to nominal value (120V) and d-axis voltage of the main grid in Figure 4.11 is small.

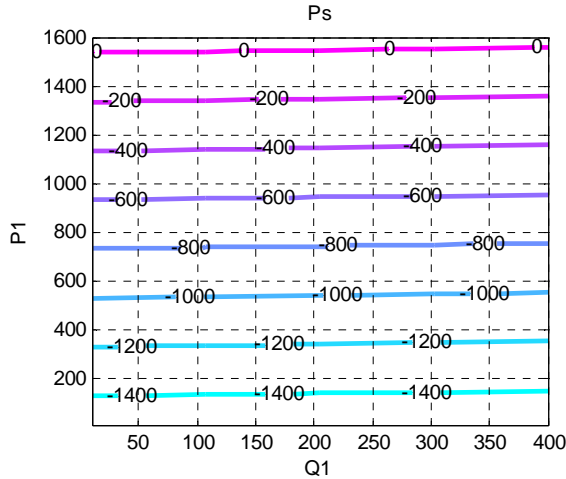


Figure 4.12 Active power of main grid

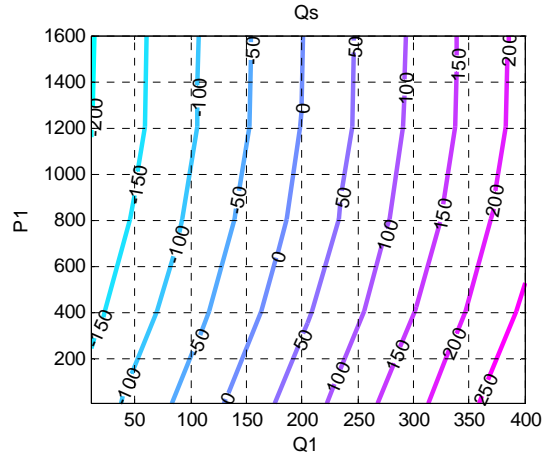


Figure 4.13 Reactive power of main grid

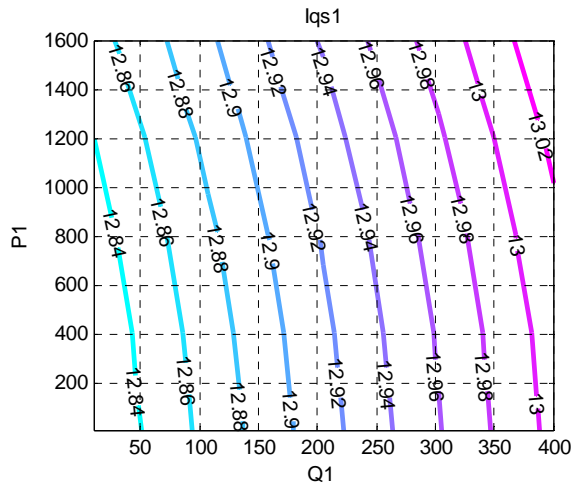


Figure 4.14 q-axis output converter current

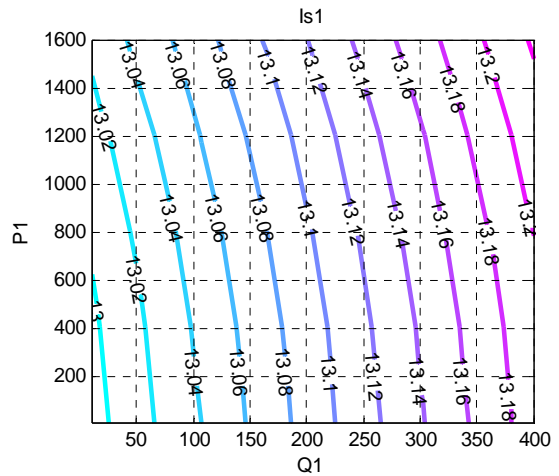


Figure 4.15 Output converter current magnitude

The change of the load voltage and therefore the modulation index and converter current magnitude is small in this range of the load change. With increasing active and reactive power of the constant load, active and reactive power of the main grid in Figure 4.12 and Figure 4.13 increase from negative to positive values because in small loads, output power of the converter is more than total loss and loads but with increasing the total load will finally be more than the power of the converter and excessive load should be fed from the main grid.

Output reactive power of the converter is always zero and output active power of the converter is always at maximum power point operation of the PV source. Output current of the inverter in Figure 4.15 is about 13A which is mostly aligned with q-axis in Figure 4.14.

4.4 Bifurcation Analysis

Power systems consist of nonlinear elements. The dynamics of these systems are usually represented by dynamic and algebraic equations of generators or sources, loads and transmission lines. Therefore we have a set of nonlinear differential equations where change of some parameters of the system like loads may cause qualitative changes at bifurcation points. Hopf bifurcation and saddle node bifurcation are the typical bifurcations. The saddle node bifurcation point results in instability. Hopf bifurcation causes oscillatory behavior of a power system [116].

In this part, the CL_MATCONT software package [110] along with MATLAB is used. The equilibrium curve and bifurcation points of a PV system with consideration of nonlinear behavior of input source are investigated. For this purpose all of the parameters are transformed to per unit values. The base values for calculating parameter values in per unit are as follows:

$$S_b = 2000VA, V_b = 120V, I_b = \frac{2}{3} \left(\frac{S_b}{V_b} \right), Z_b = \frac{3}{2} \left(\frac{V_b^2}{S_b} \right), \omega_b = 377(rad/s) \quad (4.21)$$

Figure 4.16 shows DC voltage of a PV source versus active power of constant load (P_1) as an active parameter for different q-axis converter modulation indices. With

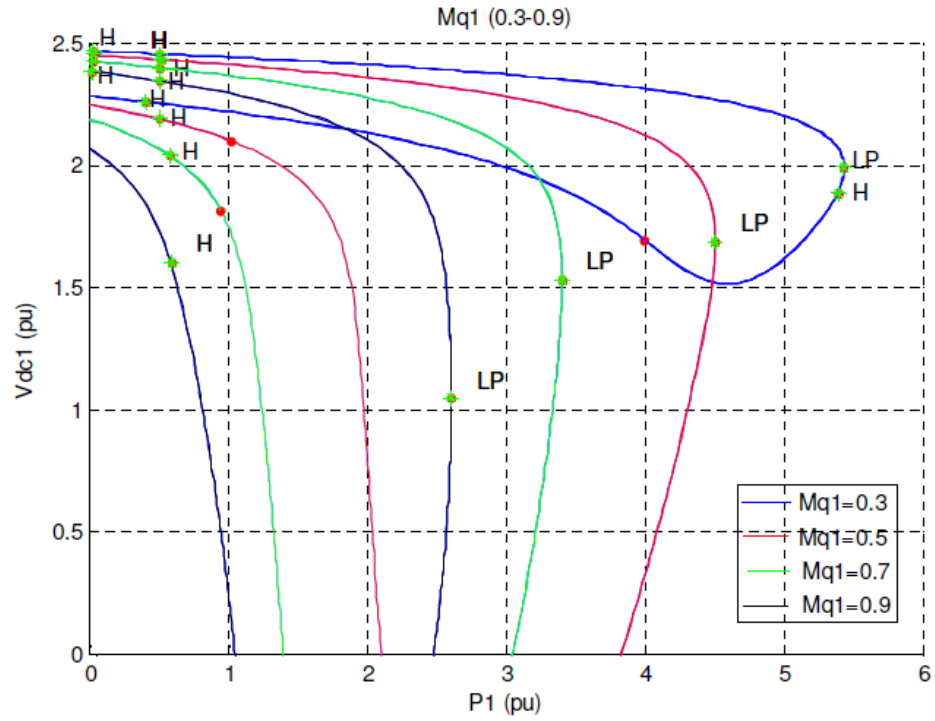


Figure 4.16 Equilibrium curve of PV DC voltage when constant load active power (P_1) is an active parameter for different q-axis modulation indices. H (Hopf Bifurcation Point), LP (Limit Point).

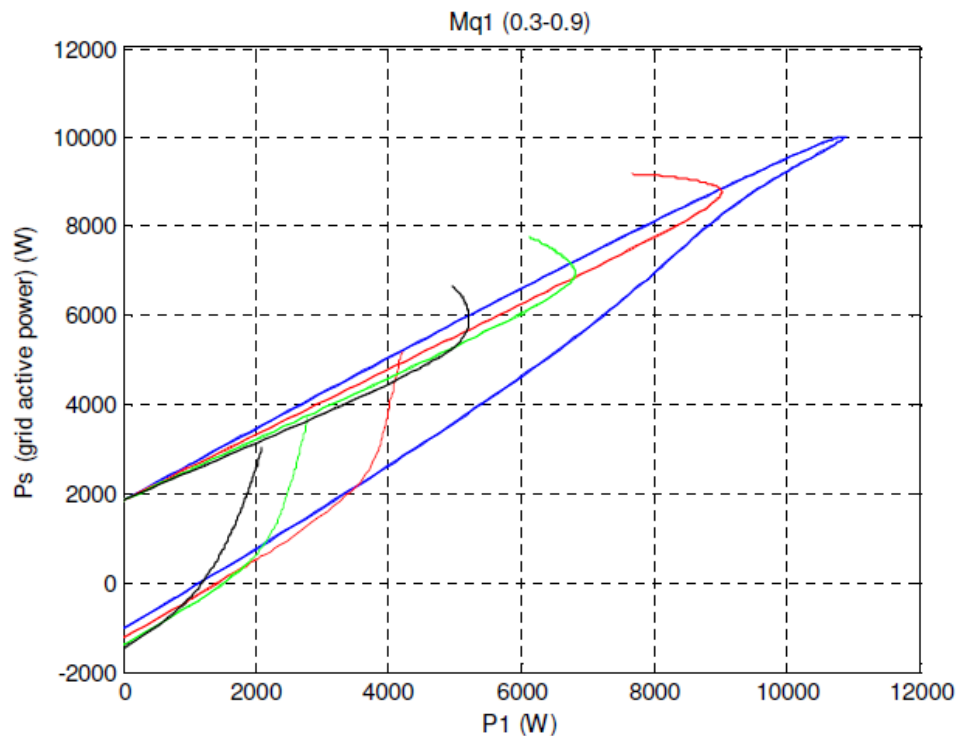


Figure 4.17 Equilibrium curve of the main grid active power (P_s) when constant load active power (P_1) is an active parameter for different q-axis modulation indices.

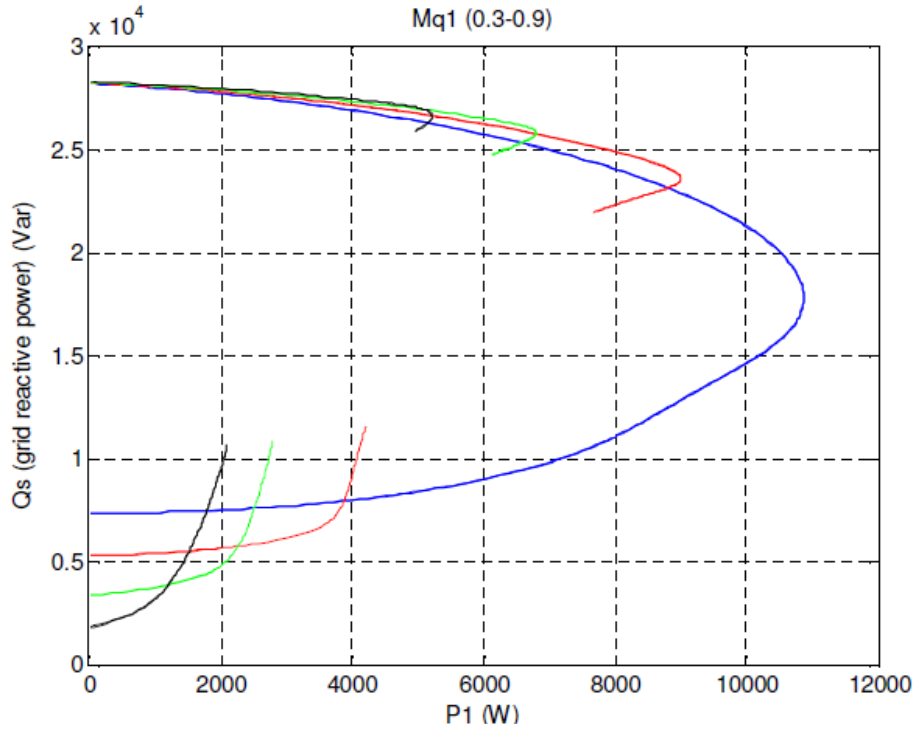


Figure 4.18 Equilibrium curve of the main grid reactive power (Q_s) when constant load active power (P_1) is an active parameter for different q-axis modulation indices.

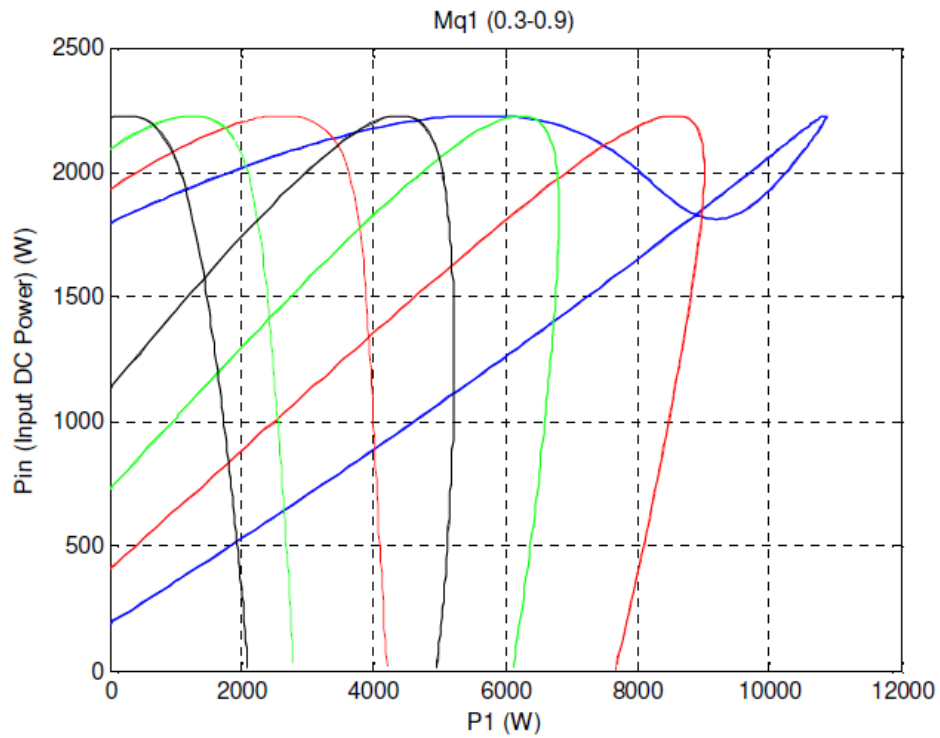


Figure 4.19 Equilibrium curve of the input power (P_{in}) when constant load active power (P_1) is an active parameter for different q-axis modulation indices.

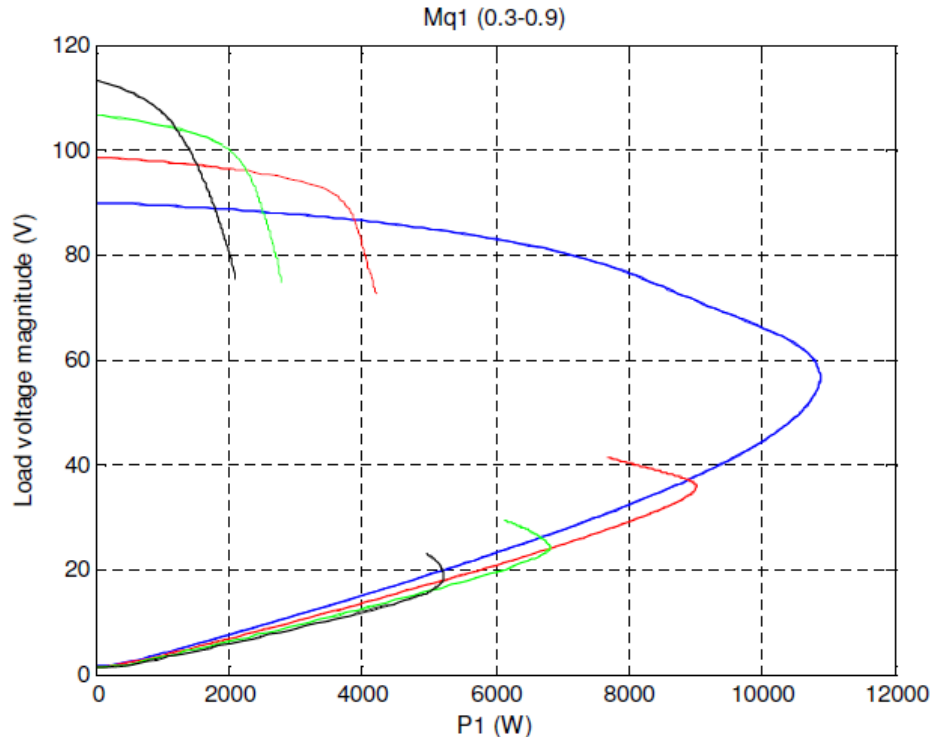


Figure 4.20 Equilibrium curve of the load voltage magnitude when constant load active power (P_1) is an active parameter for different q-axis modulation indices.

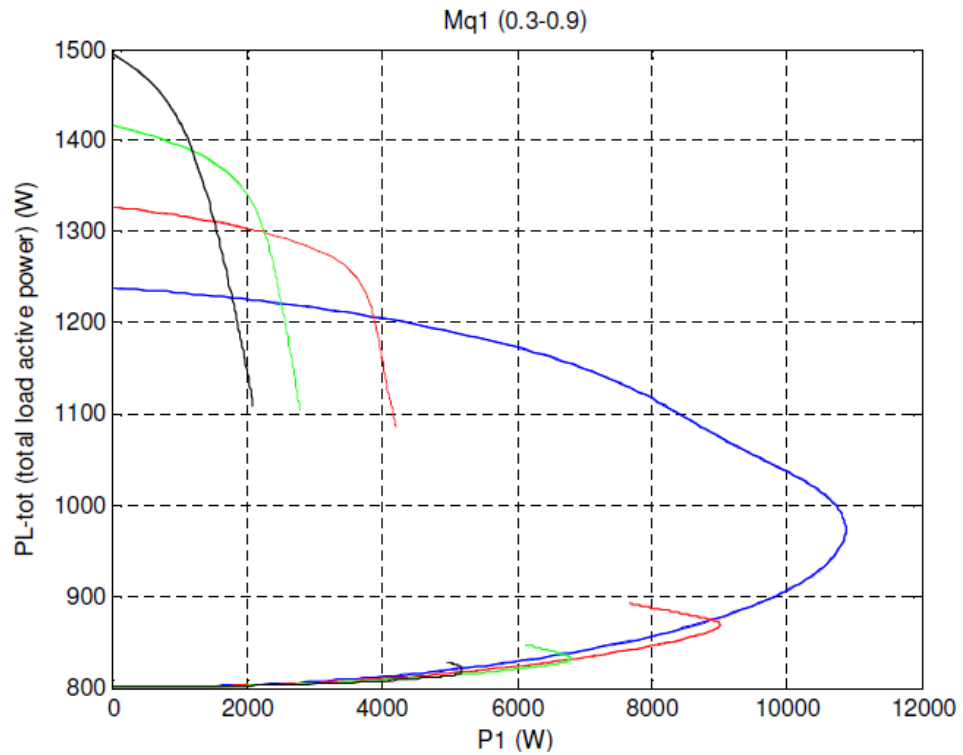


Figure 4.21 Equilibrium curve of the total load active power when constant load active power (P_1) is an active parameter for different q-axis modulation indices.

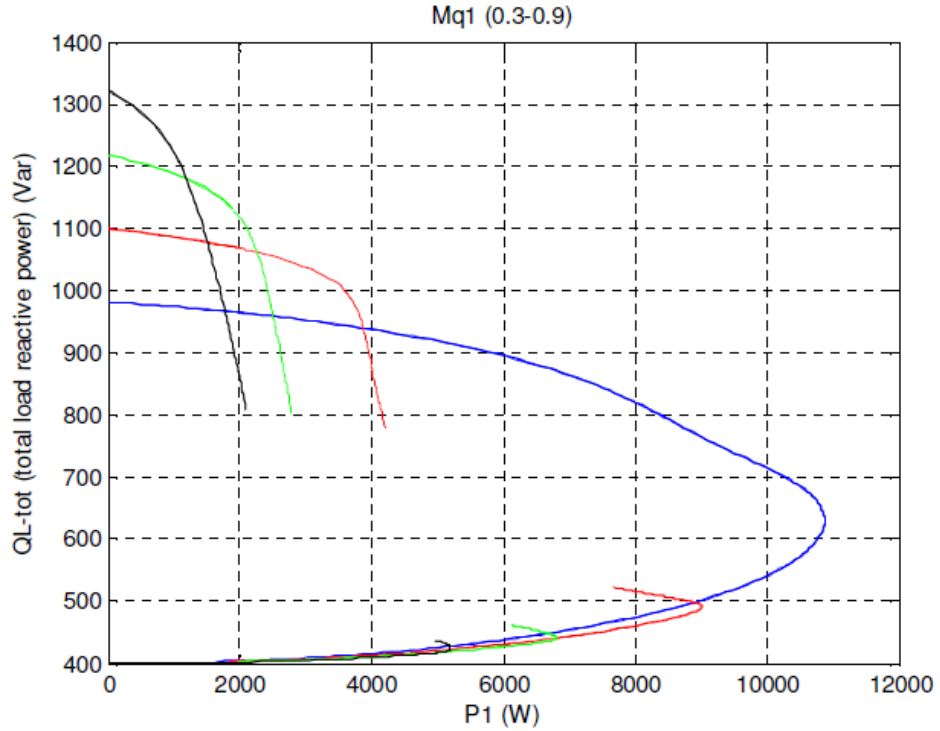


Figure 4.22 Equilibrium curve of the total load reactive power when constant load active power (P_1) is an active parameter for different q -axis modulation indices.

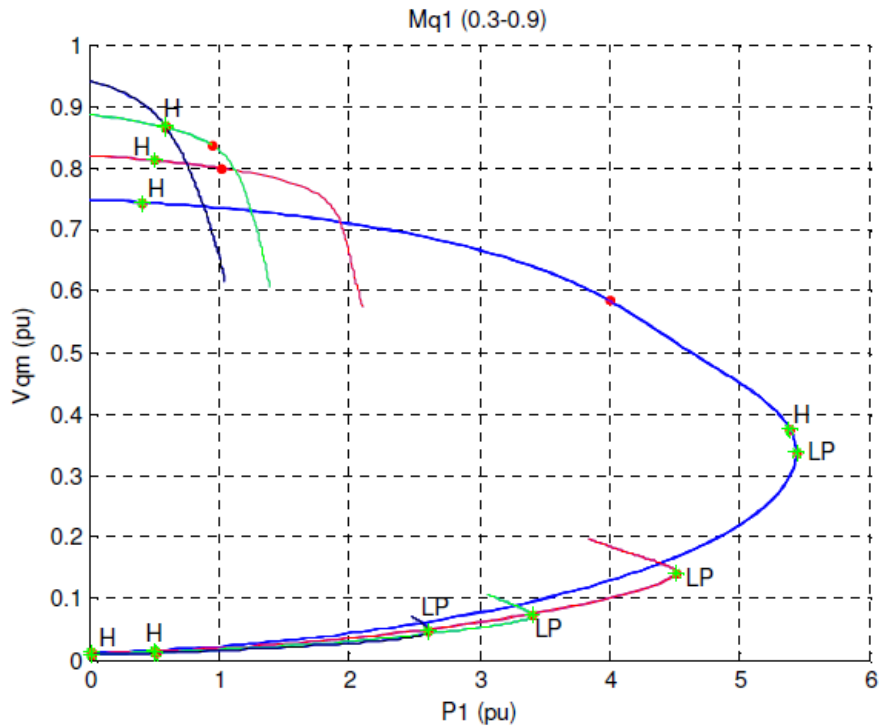


Figure 4.23 Equilibrium curve of the per unit q -axis load voltage (V_{qm}) when constant load active power (P_1) is an active parameter for different q -axis modulation indices.

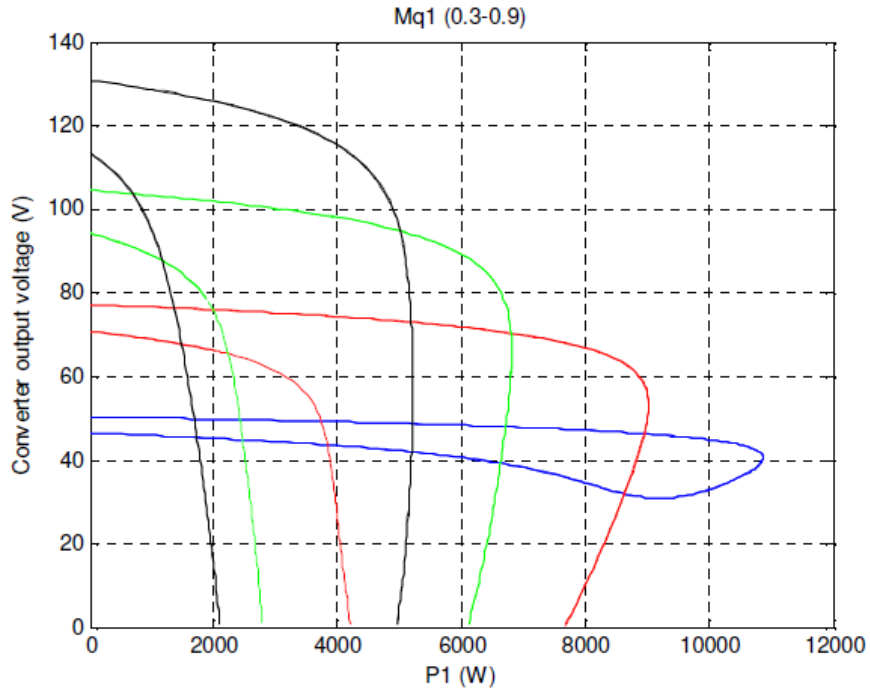


Figure 4.24 Equilibrium curve of the converter output voltage magnitude when constant load active power (P_1) is an active parameter for different q-axis modulation indices.

increase of load active power with a constant PV DC voltage more modulation index is needed and with increase of DC voltage in a constant load active power, modulation index is reduced. Moreover with a higher modulation index, the operation region of PV DC voltage increases and operation region of load active power is decreased. Hopf bifurcation and limit points in equilibrium curves are defined.

Figure 4.17 and Figure 4.18 illustrate equilibrium curves of the main grid's active and reactive powers versus load active power. The grid is always producing reactive power. With lower active power of load, excessive power of the converter flows into the main grid and makes it active power negative.

In Figure 4.19 we can get maximum power from the input source in all modulation indices with different combinations of load active power and therefore PV

DC voltage. Figure 4.20 shows the operation region can be either in less active power of the load and higher load voltage or in more load active power and lower load voltage.

Because the active and reactive power of the RL load are just related to its voltage, the trend of powers of total load in Figure 4.21 and Figure 4.22 that are a combination of linear RL load and constant load are like voltage magnitude. In higher load voltage, near nominal value that is usually acceptable operation region, with increase of constant load active, power active and reactive power of RL load and therefore total load is reduced.

Figure 4.23 shows per unit q-axis voltage of the load versus active power of the constant load. The trend of change of this figure is similar to Figure 4.20 because d-axis voltage of load is always small. Also in this figure, bifurcation points are defined. Figure 4.24 illustrates converter output voltage equilibrium curves. In each iteration PV DC voltage is a state variable and modulation index is constant therefore trend of output converter voltage is like DC voltage. As it is shown, in a constant load, with increase of modulation index we have more converter output converter voltage. In a constant output voltage with reduction of modulation index we can feed more load because we are increasing output converter current with a constant voltage indirectly.

4.5 Controller Design

Since the DG system is connected to the main grid and the voltage magnitude and frequency are adapted from it, two objectives can be considered for the controller design purposes.

First the output active and reactive power of three phase inverter can be controlled. In this case the assumption is that the input power of the DG is always equal or bigger than the reference so it can send the demand power from the reference all the time. In this case

$$I_{s1q}^* = \frac{2}{3} \frac{P_{s1}^* V_{qm1} - Q_{s1}^* V_{dm1}}{V_{qm1}^2 + V_{dm1}^2} \quad (4.22)$$

$$I_{s1d}^* = \frac{2}{3} \frac{P_{s1}^* V_{dm1} + Q_{s1}^* V_{qm1}}{V_{qm1}^2 + V_{dm1}^2} \quad (4.23)$$

where P_{s1}^* and Q_{s1}^* are the reference of output active and reactive power respectively which producing the reference of the output qd-axis current of the inverter (I_{s1qd}^*).

In most of real conditions and also in the studied system in this chapter, the input source has a limit rated power. We also prefer to transfer the maximum possible power from a renewable source like PV. Due to aforementioned reasons, the objective of the controller is considered to control input DC link voltage and output reactive power of the inverter.

With the control of the DC link voltage which is the same as the PV output voltage illustrated in Figure 4.25, maximum power point tracking can be applied to extract the maximum power from the PV system at any irradiation level of the sun. The reactive power control can be used for unity power factor operation. If the local load power is less than the PV source power at MPP, the excessive power will flow into the grid and if the load is more than the PV source or it needs reactive power, the rest will be delivered from the grid.

4.5.1 DC Link Voltage Control

The maximum power point operation produces the reference for the DC link voltage. To control the DC link voltage, from its dynamic equation

$$sC_1V_{dc1} = I_{pv} - \frac{3}{4}(M_{q1}I_{s1q} + M_{d1}I_{s1d}) \quad (4.24)$$

With substitution of modulation index equations

$$sC_1V_{dc1} = I_{pv} - \frac{3}{2V_{dc1}} \left((\sigma_q + V_{qm1} + L_{s1}\omega I_{s1d})I_{s1q} + (\sigma_d + V_{dm1} - L_{s1}\omega I_{s1q})I_{s1d} \right) \quad (4.25)$$

$$sC_1V_{dc1} = I_{pv} - \frac{3}{2V_{dc1}} \left((\sigma_q + V_{qm1})I_{s1q} + (\sigma_d + V_{dm1})I_{s1d} \right) \quad (4.26)$$

$$V_{dc1}C_1sV_{dc1} = I_{pv}V_{dc1} - \frac{3}{2} \left((\sigma_q + V_{qm1})I_{s1q} + (\sigma_d + V_{dm1})I_{s1d} \right) \quad (4.27)$$

$$\frac{C_1}{2}sV_{dc1}^2 = P_{pv} - \frac{3}{2} \left((\sigma_q + V_{qm1})I_{s1q} + (\sigma_d + V_{dm1})I_{s1d} \right) = \sigma_{pv} = k_v(s)(V_{dc1}^{2*} - V_{dc1}^2) \quad (4.28)$$

Where $k_v(s)$ is the DC voltage controller, therefore DC voltage transfer function is

$$\frac{V_{dc1}^2}{V_{dc1}^{2*}} = \frac{k_v(s)}{\frac{C_1}{2}s + k_v(s)} \quad (4.29)$$

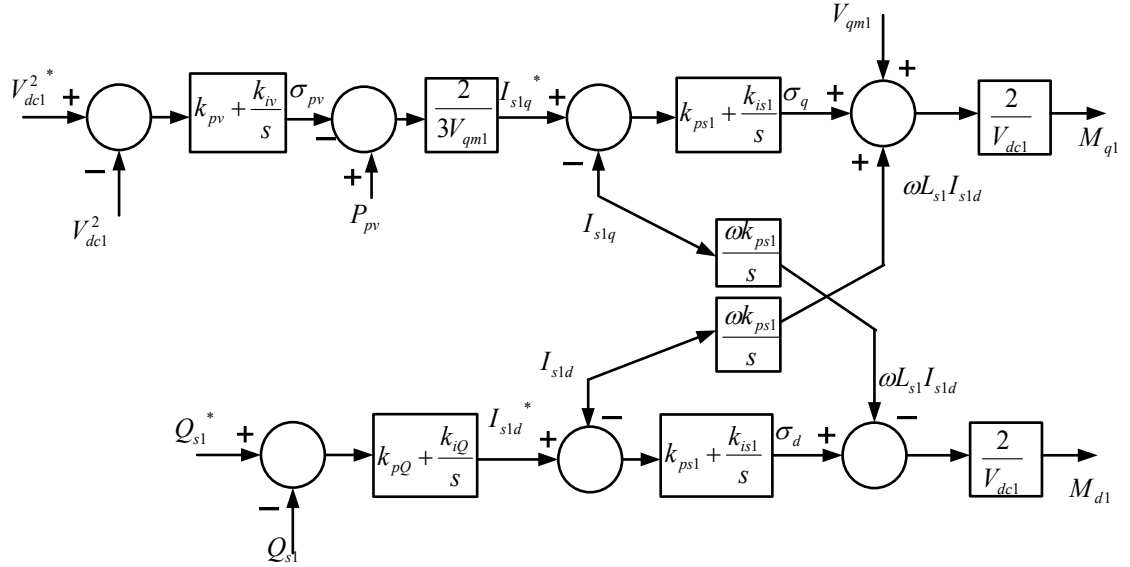


Figure 4.25 Block diagram of DC voltage and reactive power control

If we consider a PI controller

$$k_v(s) = k_{pv} + \frac{k_{iv}}{s} \quad (4.30)$$

Then

$$\frac{V_{dc1}^2}{V_{dc1}^{2*}} = \frac{2}{C_1} \frac{sk_{pv} + k_{iv}}{s^2 + \frac{2k_{pv}}{C_1}s + \frac{2k_{iv}}{C_1}} \quad (4.31)$$

With comparison to the denominator of a second order Butterworth transfer function

$$s^2 + \frac{2k_{pv}}{C_1}s + \frac{2k_{iv}}{C_1} = s^2 + 2\zeta\omega_n s + \omega_n^2 \Rightarrow \begin{cases} k_{iv} = \frac{C_1\omega_n^2}{2} \\ k_{pv} = C_1\zeta\omega_n \end{cases} \quad (4.32)$$

Therefore with selecting natural frequency (ω_n) and damping factor (ζ) we can define coefficients of the PI controller.

If the current controller works correctly $I_{s1qd}^* = I_{s1qd}$ and $\sigma_{qd} = 0$ therefore

$$\frac{C_1}{2} s V_{dc1}^2 = \sigma_{pv} = P_{pv} - \frac{3}{2} (V_{qm1} I_{s1q}^* + V_{dm1} I_{s1d}^*) \quad (4.33)$$

For converting from abc to qd reference frame (using PLL) we can align voltage in q-axis reference frame and put $V_{dm1} = 0$

$$\frac{C_1}{2} s V_{dc1}^2 = \sigma_{pv} = P_{pv} - \frac{3}{2} (V_{qm1} I_{s1q}^*) \quad (4.34)$$

$$I_{s1q}^* = \frac{2}{3V_{qm1}} (P_{pv} - \sigma_{pv}) \quad (4.35)$$

In the other word, we define q-axis reference current by controlling V_{dc1} .

If dynamics of the PV system is taken into account, DC voltage control is related to active power of PV source that is nonlinear and also related to V_{dc1} . Therefore assumption of (4.28) may not be true and control system of DC voltage is nonlinear.

To remove this nonlinearity we can apply new control input (γ) that can be zero or unity

$$\frac{C_1}{2} s V_{dc1}^2 = P_{pv} - \frac{3}{2} (V_{qm1} I_{s1q}^*) \quad (4.36)$$

$$\frac{C_1}{2} s V_{dc1}^2 = (1 - \gamma) P_{pv} - \frac{3}{2} V_{qm1} u_v \quad (4.37)$$

Thus

$$P_{pv} - \frac{3}{2} (V_{qm1} I_{s1q}^*) = (1 - \gamma) P_{pv} - \frac{3}{2} V_{qm1} u_v \quad (4.38)$$

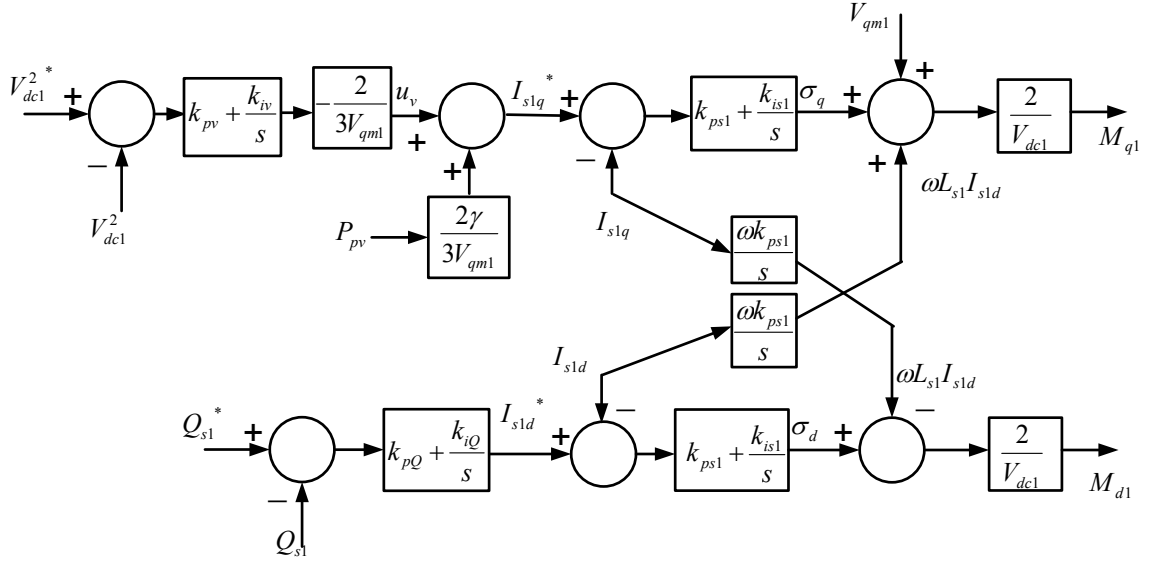


Figure 4.26 Block diagram of DC voltage and reactive power control after removing the effect of PV source

$$I_{s1q}^* = u_v + \frac{2\gamma}{3V_{qm1}} P_{pv} \quad (4.39)$$

If we choose $\gamma = 1$, DC voltage control is independent of active power of PV system and the control diagram will be

$$I_{s1q}^* = u_v + \frac{2\gamma}{3V_{qm1}} P_{pv} \quad (4.40)$$

$$\frac{C_1}{2} s V_{dc1}^2 = (1-\gamma) P_{pv} - \frac{3}{2} V_{qm1} u_v = k_v(s) (V_{dc1}^{2*} - V_{dc1}^2) \quad (4.41)$$

And if $\gamma = 1$

$$\frac{C_1}{2} s V_{dc1}^2 = -\frac{3}{2} V_{qm1} u_v = k_v(s) (V_{dc1}^{2*} - V_{dc1}^2) \quad (4.42)$$

$$\text{If } k_v(s) = k_{pv} + \frac{k_{iv}}{s} \text{ then } \frac{V_{dc1}^2}{V_{dc1}^{2*}} = \frac{2}{C_1} \frac{sk_{pv} + k_{iv}}{s^2 + \frac{2k_{pv}}{C_1}s + \frac{2k_{iv}}{C_1}} \quad (4.43)$$

$$\text{If } k_v(s) = \frac{\alpha_1 s + \alpha_2}{s(s + \alpha_3)} \text{ then } \frac{V_{dc1}^2}{V_{dc1}^{2*}} = \frac{2}{C_1} \frac{\alpha_1 s + \alpha_2}{s^3 + \alpha_3 s^2 + \frac{2\alpha_1}{C_1}s + \frac{2\alpha_2}{C_1}} \quad (4.44)$$

4.5.2 Reactive Power Control

Output reactive power of the inverter after the filter at PCC

$$Q_{s1} = \frac{3}{2}(V_{qm1}I_{s1d} - V_{dm1}I_{s1q}) \quad (4.45)$$

If it is assumed that $V_{dm1} = 0$

$$I_{s1d}^* = k_Q(s)(Q_{s1}^* - Q_{s1}) = (k_{pQ} + \frac{k_{iQ}}{s})(Q_{s1}^* - Q_{s1}) \quad (4.46)$$

A new variable can be defined as

$$s x_{qs} = (Q_{s1}^* - Q_{s1}) \quad (4.47)$$

Thus

$$I_{s1d}^* = k_{pQ}(Q_{s1}^* - Q_{s1}) + k_{iQ}x_{qs} \quad (4.48)$$

Therefore d-axis reference current can be defined using reference reactive power (Q_{s1}^*).

Usually V_{dc1}^* is kept constant or defined by maximum power point tracking

(MPPT) of PV system and for unity power factor $Q_{s1}^* = 0$

4.5.3 Current Control

After defining the qd-axis current references from the outer DC link voltage and reactive power controllers, the inner current controller can be designed. From the dynamic equation of the inverter transmission line in complex format

$$L_{s1}sI_{s1qd} + R_{s1}I_{s1qd} - jL_{s1}\omega I_{s1qd} = M_{qd1} \frac{V_{dc1}}{2} - V_{qdm1} = \sigma_{s1} = k_{s1}(s)(I_{s1qd}^* - I_{s1qd}) \quad (4.49)$$

where $k_{s1}(s)$ is the current controller, therefore current transfer function is

$$\frac{I_{s1qd}}{I_{s1qd}^*} = \frac{k_{s1}(s)}{L_{s1}s + R_{s1} - jL_{s1}\omega + k_{s1}(s)} \quad (4.50)$$

And

$$k_{s1}(s) = k_{ps1} + \frac{k_{is1} - j\omega k_{ps1}}{s} \quad (4.51)$$

where k_{ps1} and k_{is1} are proportional and integral parameters of current controller.

$$\frac{I_{s1qd}}{I_{s1qd}^*} = \frac{sk_{ps1} + k_{is1} - j\omega k_{ps1}}{L_{s1}s^2 + (k_{ps1} + R_{s1} - jL_{s1}\omega)s + k_{is1} - j\omega k_{ps1}} \quad (4.52)$$

If it is chosen

$$k_{is1} = \frac{R_{s1}}{L_{s1}} k_{ps1} \quad (4.53)$$

then

$$\frac{I_{s1qd}}{I_{s1qd}^*} = \frac{(s + \frac{R_{s1}}{L_{s1}} - j\omega)k_{ps1}}{(sL_{s1} + k_{ps1})(s + \frac{R_{s1}}{L_{s1}} - j\omega)} = \frac{k_{ps1}}{sL_{s1} + k_{ps1}} \quad (4.54)$$

From (4.49)

$$M_{qd1} = \frac{2}{V_{dc1}} (\sigma_{qd} + V_{qdm1}) \quad (4.55)$$

and

$$\sigma_{s1} = (I_{s1qq} + jI_{s1dd})(k_{ps1} + \frac{k_{is1} - j\omega k_{ps1}}{s}) \quad (4.56)$$

$$\begin{cases} I_{s1qq} = I_{s1q}^* - I_{s1q} \\ I_{s1dd} = I_{s1d}^* - I_{s1d} \end{cases} \quad (4.57)$$

So for separated qd-axis from the complex format

$$\begin{cases} \sigma_{qs1} = I_{s1qq} (k_{ps1} + \frac{k_{is1}}{s}) + I_{s1dd} (\frac{\omega k_{ps1}}{s}) \\ \sigma_{ds1} = I_{s1dd} (k_{ps1} + \frac{k_{is1}}{s}) - I_{s1qq} (\frac{\omega k_{ps1}}{s}) \end{cases} \quad (4.58)$$

The outputs of current controller are modulation indices (M_{qd1}) that produce the output voltage of the three phase inverter connected to the grid.

4.5.4 State Space Model

To define the state space model of the system, the dynamic equations and also the designed controller parameters have been used. From the control part

$$\left(\left(P_{pv} - (V_{dc1}^2 - V_{dc1}^2) k_v(s) \right) \frac{2}{3V_{qm1}} - I_{s1q} \right) k_{s1}(s) + V_{qm1} + \frac{\omega k_{ps1}}{s} I_{s1d} = V_{s1q} = M_{q1} \frac{V_{dc1}}{2} \quad (4.59)$$

$$\left((Q_{s1}^* - Q_{s1})k_Q(s) - I_{s1d} \right) k_{s1}(s) - \frac{\omega k_{ps1}}{s} I_{s1q} = V_{s1d} = M_{d1} \frac{V_{dc1}}{2} \quad (4.60)$$

And from the dynamic equations of the system

$$\begin{cases} sI_{s1qd} = \frac{1}{L_{s1}} \left(M_{qd1} \frac{V_{dc1}}{2} - V_{qdm1} - R_{s1} I_{s1qd} + jL_{s1} \omega I_{s1qd} \right) \\ sV_{qdm1} = \frac{1}{C_{d1}} \left(I_{s1qd} + I_{sqd} - I_{L1qd} - I_{1qd} + jC_{d1} \omega V_{qdm1} \right) \\ sI_{L1qd} = \frac{1}{L_{L1}} \left(V_{qdm1} - R_{L1} I_{L1qd} + jL_{L1} \omega I_{L1qd} \right) \\ sI_{sqd} = \frac{1}{L_s} \left(V_{sqd} - V_{qdm1} - R_s I_{sqd} + jL_s \omega I_{sqd} \right) \\ sV_{dc1}^2 = \frac{2}{C_1} \left(P_{pv} - \frac{3}{2} (V_{qm1} I_{s1q} + V_{dm1} I_{s1d}) \right) \end{cases} \quad (4.61)$$

In separated qd-axis format and with assumption of $V_{dm1} = 0$ that is considered in

control part for decouple control of reactive power

$$\begin{cases} sI_{s1q} = \frac{1}{L_{s1}} \left(M_{q1} \frac{V_{dc1}}{2} - V_{qm1} - R_{s1} I_{s1q} - L_{s1} \omega I_{s1d} \right) \\ sI_{s1d} = \frac{1}{L_{s1}} \left(M_{d1} \frac{V_{dc1}}{2} - R_{s1} I_{s1d} + L_{s1} \omega I_{s1q} \right) \\ sI_{L1q} = \frac{1}{L_{L1}} \left(V_{qm1} - R_{L1} I_{L1q} - L_{L1} \omega I_{L1d} \right) \\ sI_{L1d} = \frac{1}{L_{L1}} \left(-R_{L1} I_{L1d} + L_{L1} \omega I_{L1q} \right) \\ sI_{sq} = \frac{1}{L_s} \left(V_{sq} - V_{qm1} - R_s I_{sq} - L_s \omega I_{sd} \right) \\ sI_{sd} = \frac{1}{L_s} \left(V_{sd} - R_s I_{sd} + L_s \omega I_{sq} \right) \\ sV_{qm1} = \frac{1}{C_{d1}} \left(I_{s1q} + I_{sq} - I_{L1q} - I_{1q} \right) \\ sV_{dc1}^2 = \frac{2}{C_1} \left(P_{pv} - P_{s1} \right) \end{cases} \quad (4.62)$$

With substituting control part equations in the first two equations of plant

$$\begin{cases} sI_{s1q} = \frac{1}{L_{s1}} \left((V_{dc1}^2)k_v(s)k_{s1}(s) \left(\frac{2}{3V_{qm1}} \right) - V_{dc1}^2 k_v(s)k_{s1}(s) \left(\frac{2}{3V_{qm1}} \right) + P_{pv} \frac{2}{3V_{qm1}} k_{s1}(s) \right) \\ - I_{s1q} (k_{s1}(s) + R_{s1}) + \left(\frac{\omega k_{ps1}}{s} - L_{s1}\omega \right) I_{s1d} \\ sI_{s1d} = \frac{1}{L_{s1}} \left((-Q_{s1})k_Q(s)k_{s1}(s) + Q_{s1} k_Q(s)k_{s1}(s) - I_{s1d} (k_{s1}(s) + R_{s1}) + \left(L_{s1}\omega - \frac{\omega k_{ps1}}{s} \right) I_{s1q} \right) \end{cases} \quad (4.63)$$

In general, the state space model

$$\dot{X} = AX + BU + EU_d \quad \text{and} \quad X = (sI - A)^{-1}(BU + EU_d) \quad (4.64)$$

$$Y = CX + DU + FU_d \quad (4.65)$$

where X , U , U_d and Y are state variable, input, disturbance input and output matrices respectively. The complete state space model of the system is as follows:

$$\begin{bmatrix} \dot{I}_{s1q} \\ \dot{I}_{s1d} \\ \dot{I}_{L1q} \\ \dot{I}_{L1d} \\ \dot{I}_{sq} \\ \dot{I}_{sd} \\ \dot{V}_{qm1} \\ \dot{V}_{dc1}^2 \end{bmatrix} = \begin{bmatrix} -\frac{(k_{s1}(s) + R_{s1})}{L_{s1}} & \left(\frac{\omega k_{ps1}}{sL_{s1}} - \frac{L_{s1}\omega}{L_{s1}} \right) & 0 & 0 & 0 & 0 & 0 & k_v(s)k_{s1}(s) \left(\frac{2}{3L_{s1}V_{qm1}} \right) \\ \left(\frac{L_{s1}\omega}{L_{s1}} - \frac{\omega k_{ps1}}{sL_{s1}} \right) & -\frac{(k_{s1}(s) + R_{s1})}{L_{s1}} & 0 & 0 & 0 & 0 & 0 & 0 \\ 0 & 0 & -\frac{R_{L1}}{L_{L1}} & -\frac{L_{L1}\omega}{L_{L1}} & 0 & 0 & \frac{1}{L_{L1}} & 0 \\ 0 & 0 & \frac{L_{L1}\omega}{L_{L1}} & -\frac{R_{L1}}{L_{L1}} & 0 & 0 & 0 & 0 \\ 0 & 0 & 0 & 0 & -\frac{R_s}{L_s} & -\frac{L_s\omega}{L_s} & -\frac{1}{L_s} & 0 \\ 0 & 0 & 0 & 0 & \frac{L_s\omega}{L_s} & -\frac{R_s}{L_s} & 0 & 0 \\ \frac{1}{C_{d1}} & 0 & -\frac{1}{C_{d1}} & 0 & \frac{1}{C_{d1}} & 0 & 0 & 0 \\ 0 & 0 & 0 & 0 & 0 & 0 & 0 & 0 \end{bmatrix} \begin{bmatrix} I_{s1q} \\ I_{s1d} \\ I_{L1q} \\ I_{L1d} \\ I_{sq} \\ I_{sd} \\ V_{qm1} \\ V_{dc1}^2 \end{bmatrix}$$

$$\begin{aligned}
& + \begin{bmatrix} 0 & 0 & 0 & 0 & \frac{2}{3L_{s1}V_{qm1}}k_{s1}(s) & 0 \\ 0 & 0 & 0 & -\frac{k_Q(s)k_{s1}(s)}{L_{s1}} & 0 & 0 \\ 0 & 0 & 0 & 0 & 0 & 0 \\ 0 & 0 & 0 & 0 & 0 & 0 \\ \frac{1}{L_s} & 0 & 0 & 0 & 0 & 0 \\ 0 & \frac{1}{L_s} & 0 & 0 & 0 & 0 \\ 0 & 0 & 0 & 0 & 0 & -\frac{1}{C_{d1}} \\ 0 & 0 & -\frac{2}{C_1} & 0 & \frac{2}{C_1} & 0 \end{bmatrix} \begin{bmatrix} V_{sq} \\ V_{sd} \\ P_{s1} \\ Q_{s1} \\ P_{pv} \\ I_{1q} \end{bmatrix} + \begin{bmatrix} 0 & -k_v(s)k_{s1}(s)\frac{2}{3L_{s1}V_{qm1}} \\ \frac{k_Q(s)k_{s1}(s)}{L_{s1}} & 0 \\ 0 & 0 \\ 0 & 0 \\ 0 & 0 \\ 0 & 0 \\ 0 & 0 \end{bmatrix} \begin{bmatrix} Q_{s1}^* \\ V_{dc1}^* \end{bmatrix}
\end{aligned}$$

4.6 Simulation Results

To study the dynamic behaviour and verify the performance of the controller parts design, the dynamic model of the system is simulated in MATLAB software. The nonlinear characteristic of the PV is included. To see the dynamic response two different tests have been applied. In the first case irradiation level of the sun is changed to investigate the response and performance of the DC link voltage controller for maximum power tracking of the PV source. In the second case, the constant load is varied suddenly to analyze the robustness of the controllers and power sharing between the DG unit and the main grid.

In Figure 4.27 the irradiation level of the sun has been changed from 1 to 0.8 at 0.6 second. Therefore the DC link voltage reference which is the same as PV output voltage at maximum power point operation of the PV in each irradiation level is varied. The DC link voltage controller tracks the reference and reaches steady state in less than 0.1s.

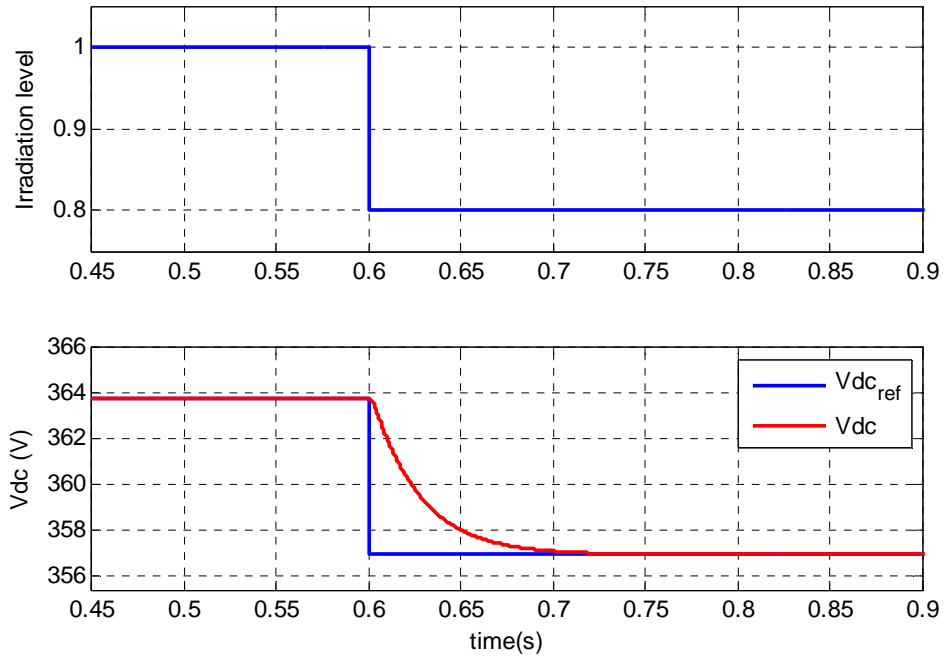


Figure 4.27 Change irradiation level and DC link voltage response for MPPT of PV

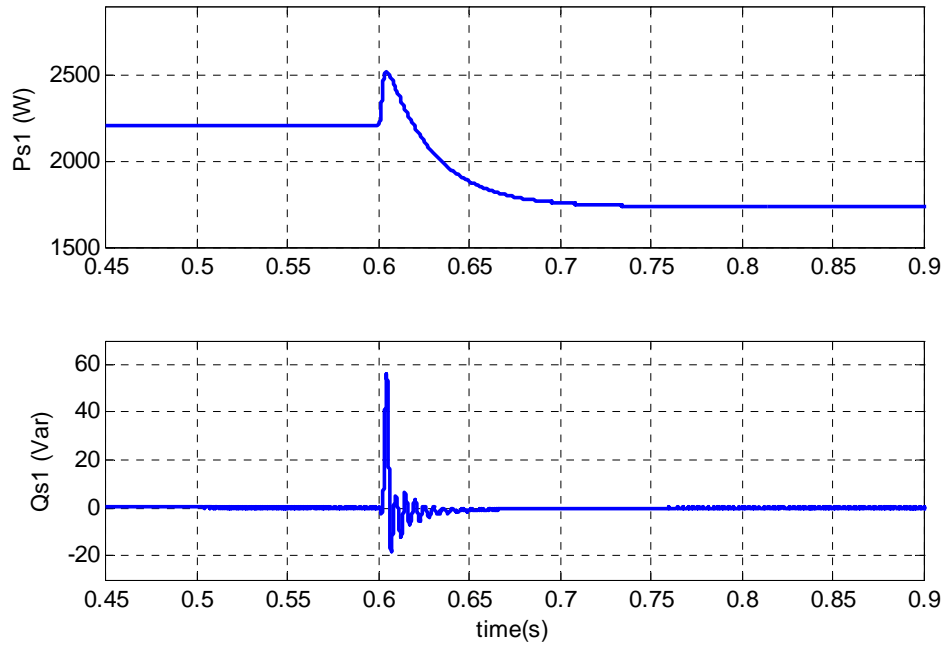


Figure 4.28 Change of active reactive power of the inverter due to the change of irradiation level

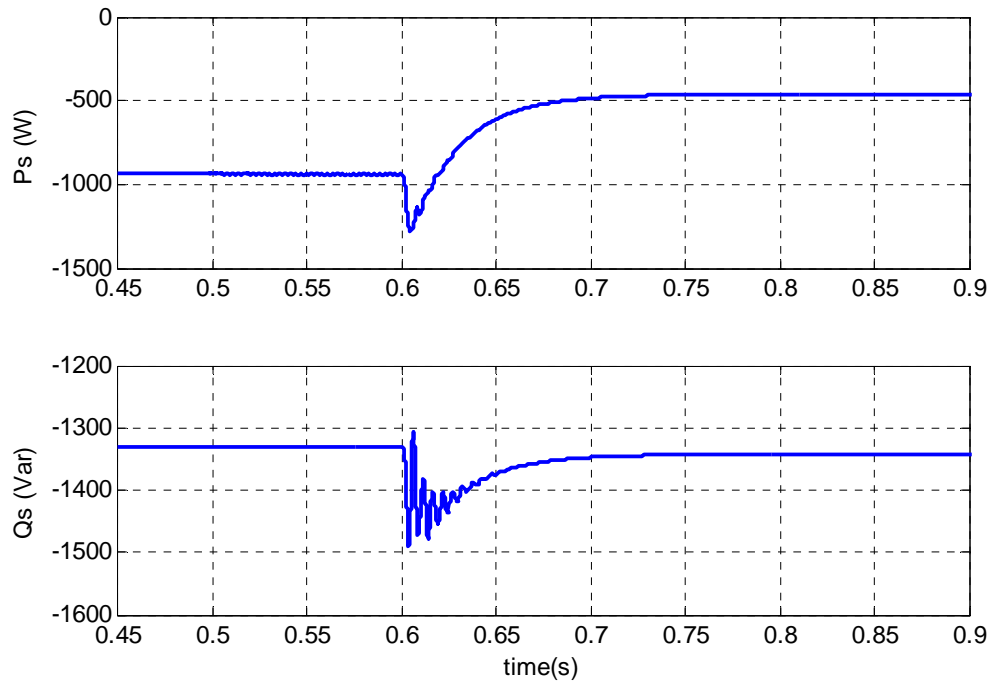


Figure 4.29 Change of active reactive power of the main grid due to the change of irradiation level

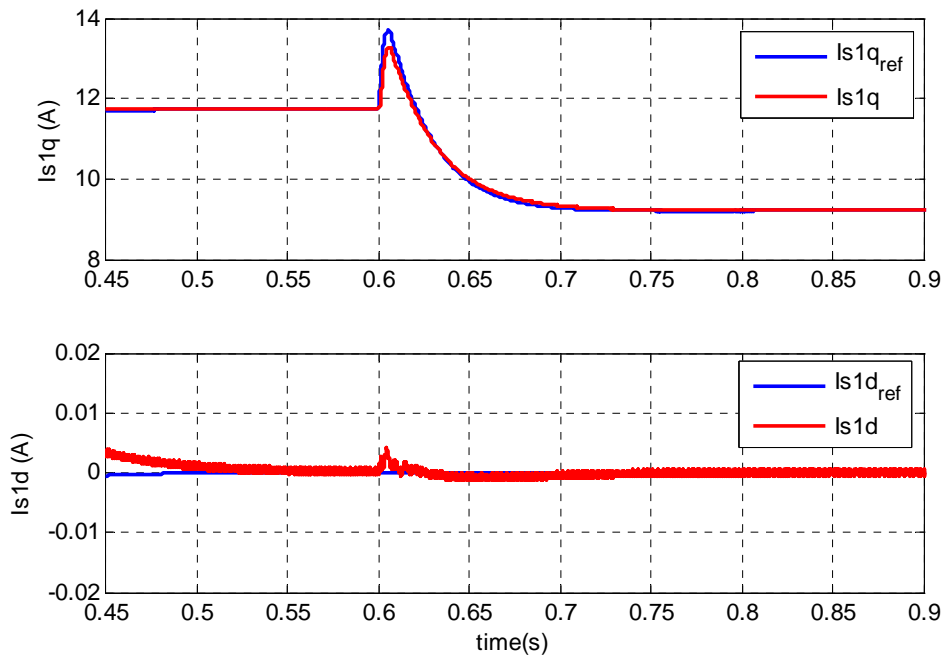


Figure 4.30 Reference and actual qd-axis currents of inverter

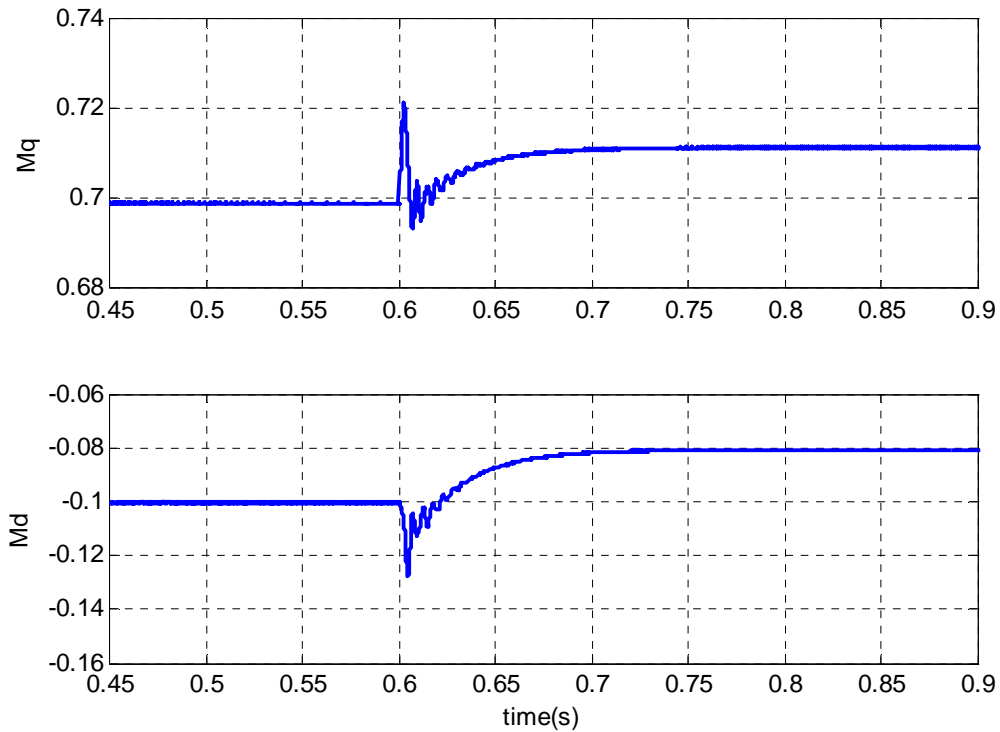


Figure 4.31 qd-axis modulation indices of the inverter

Figure 4.28 illustrates the output active and reactive power of the inverter. The active power reduces due to the reduction of irradiation level but still extracts the maximum possible power from the sun. The reference for reactive power controller is chosen to be zero for unity power factor operation of the PV system. Instead of small fluctuations in the instant of the irradiation level change, the output reactive power is always kept at zero. Since the loads are less than the output power of the DG unit, the power of the main grid is negative in Figure 4.29. It means the excessive power is transferred to the main network.

Although the inverter is not producing reactive power, the big value of capacitor is the reason of negative reactive power of the grid. With reduction of the irradiation level and consequently the output power of the DG, the transferred power to the grid in the constant load is also reduced. Figure 4.30 shows how the current controllers are trying to

follow qd-axis reference currents. The d-axis reference current corresponding to the reactive power is zero for all time. The q-axis reference current is changing based on the output of DC link voltage controller. The faster speed of the inner current controllers for tracking the references compared to outer controller is shown in this figure. In Figure 4.31 the modulation indices of the three phase inverter are presented. It shows that due to the performance of the controllers the inverter is always operating in linear region without saturation of the modulation index magnitude.

In the second case, the active and reactive powers of the constant load are changed in two different instances in Figure 4.32. The active power of the load is change from 800W to 2400W at 0.6s and reactive power is changed from 200Var to 600Var at 0.8s respectively. Due to the constant irradiation level and MPP operation, the output active power of the DG is constant. The additional power of the load when it is raised beyond the maximum power of the PV, should then come from the grid. The active power of the grid is changed from negative (absorbing power) to positive (producing power). Due to the increase of the load reactive power at 0.8s, the flow of the reactive power into the grid reduces and goes into the load instead. Although there is no load voltage control, load voltage magnitude is dictated by the grid and shows just a small change. The phase lock loop always tracks the frequency and the angle of the load voltage and makes the d-axis load voltage zero. DC link voltage is also tracking its reference even with a significant change in the load values.

4.1 Conclusions

In this chapter, the steady state operation region of a microgrid with a PV source connected to the main network is studied. First, with changing of the q-axis grid voltage, other parameters are calculated. The operation region of the grid voltage is small in that it is always close to rated value. With a small change in q-axis main grid voltage we will have a wide change in load voltage. With increasing the load and grid voltages, modulation index of the converter increases and it is always less than one. The change of the reactive power of the grid and converter are based on difference between the grid and the converter voltages as well as voltage of the capacitor which produces part of reactive power. For the second case, output reactive power of the converter is considered zero so we will have two operation regions based on the load voltage magnitude. For bigger load voltage, modulation index is also bigger and in constant input DC voltage and current, output converter current is smaller. With increasing active and reactive power of constant load, active and reactive power of the grid increases because output powers of the converter are assumed constant always operating at maximum power point of PV source in this condition.

The controllers are design and explained in detail for the system. The load voltage magnitude and frequency are adapted from the main grid. The DC link voltage is controlled for maximum power point operation of the PV. For unity power factor operation the second reference has been considered as output reactive power of the three phase inverter. Inner current control loops are designed to control qd-axis output currents of the converter separately. To control the DC link voltage, the nonlinear characteristic of

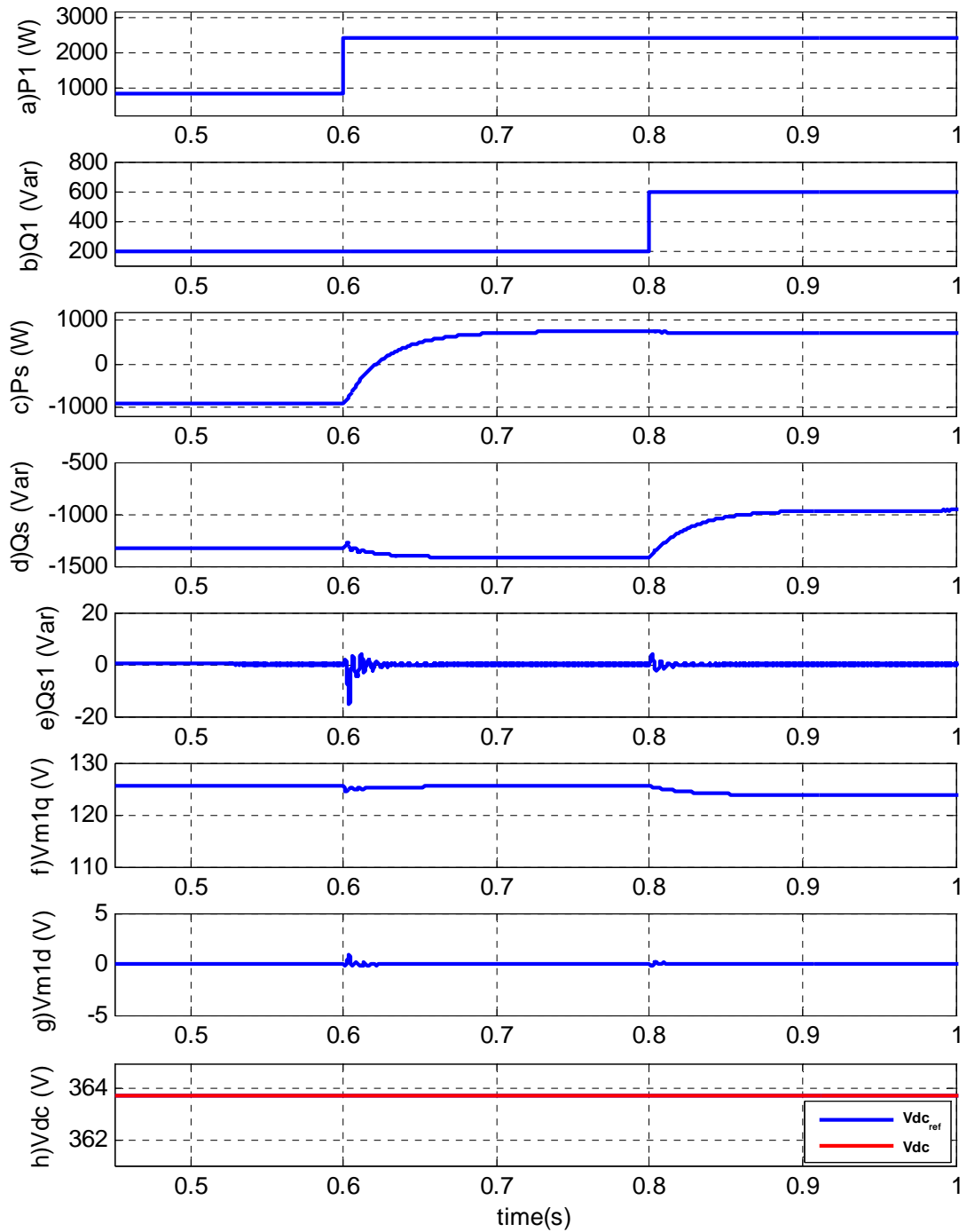


Figure 4.32 system dynamic under the change of constant load, a) constant load active power, b) constant load reactive power, c) active power of the main grid, d) reactive power of the main grid, e) reactive power of the inverter f) q-axis load voltage g) d-axis load voltage h) DC link voltage.

the PV system is considered and using a feed forward gain, its effect on the control part is removed. Effect of the main grid and both linear and constant loads are considered in an input output feedback linearization control. A state space model of whole system after applying controller parts is defined. The bifurcation analysis using MATCONT software is applied to the system. Equilibrium curves of parameters along with bifurcation points are defined.

The dynamic system is simulated in MATLAB software. With the change of irradiation level, DC link voltage and reactive power controllers follow their references precisely. Even during sudden change of the loads, the actual parameters of the system are still tracking their references well due to the fast response of the controllers. The DG unit is always operating in unity power factor and modulation indices of the inverter, even during transients, are less than unity.

CHAPTER 5

EXPERIMENTAL SETUP AND DYNAMIC CONTROL OF PV SYSTEM

5.1 Introduction

To verify the proposed controllers, besides the dynamic simulation of the system, the experimental setup has been built and tested. The system consists of a microgrid with two different sources, a nonlinear PV and a battery source. In addition it includes three different power electronic converters, a unidirectional DC/DC boost converter, a bidirectional buck and boost converter and a three phase inverter. Each converter has its own controller signals coming from different controller structures, drivers and sensor boards. Due to the complexity of the system, each part is investigated separately and the process of design and experimental results are shown in different sections.

5.2 Design and Open Loop Test of the Boost Converter for PV System Applications

Power electronic converters can be used to connect renewable energy sources to the load or the grid. Using DC/DC converters it is possible to control the output voltage magnitude and also, as a special case, obtain maximum power from renewable sources.

The photovoltaic is one the most popular methods for producing electricity from solar energy. It directly converts the solar irradiation to electric voltage. Renewable energies have two main advantages. First of all they are environmental friendly.

Secondly, there are no costs beyond manufacturing and installation. To get these benefits, renewable energies should be used to obtain the maximum possible power from them.

Even a series array of solar cells doesn't have enough voltage magnitude to be directly connected to the load; therefore, a boost converter can be used to increase the output voltage. In this section, a 3kW boost converter is designed in detail and the open loop test validates the performance of operation.

As it is shown in Figure 5.1, the boost converter consists of five major parts

- a) The Input capacitor
- b) The switch
- c) The diode
- d) The Output capacitor
- e) The inductor

Each of them should be designed and selected from the available equipment in the market. For designing the DC/DC converter, first the rated parameters of the converter should be defined. A 3kw DC/DC converter which operates in the switching frequency of 50kHz in considered. The output voltage is always kept constant at 300V and the input voltage can change from 50V to 200V.

$$\begin{cases} P = 3kW \\ f_{sw} = 50kHz \end{cases} \quad (5.1)$$

$$\begin{cases} V_{in} = 50V - 200V \\ V_{out} = 300V \end{cases} \quad (5.2)$$

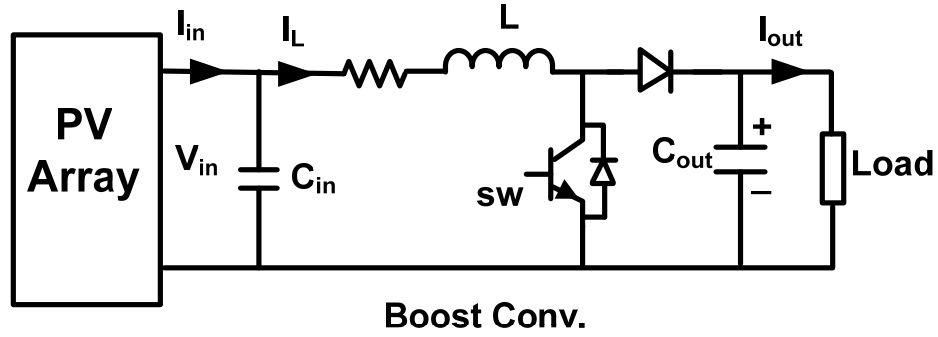


Figure 5.1 Schematic diagram of a boost converter

For the boost converter

$$\frac{V_{out}}{V_{in}} = \frac{1}{1-D} \quad (5.3)$$

Therefore, the maximum duty ratio is

$$D_{max} = 1 - \frac{V_{in(min)}}{V_{out}} = 1 - \frac{50}{300} \approx 0.84 \quad (5.4)$$

where D is the duty ratio of the boost converter.

The ripple of the current is considered as 10 percent of the input current and the maximum output current can be calculated as

$$\begin{cases} I_{in(max)} = 15A \\ I_{out(max)} = I_{in(max)} \frac{V_{in(max)}}{V_{out}} = 10A \\ \Delta I_{Lpp} = 0.1 I_{in(max)} = 1.5A \end{cases} \quad (5.5)$$

where ΔI_{Lpp} is the peak to peak ripple current. The design of the boost converter is given in the next section after all parameters are define.

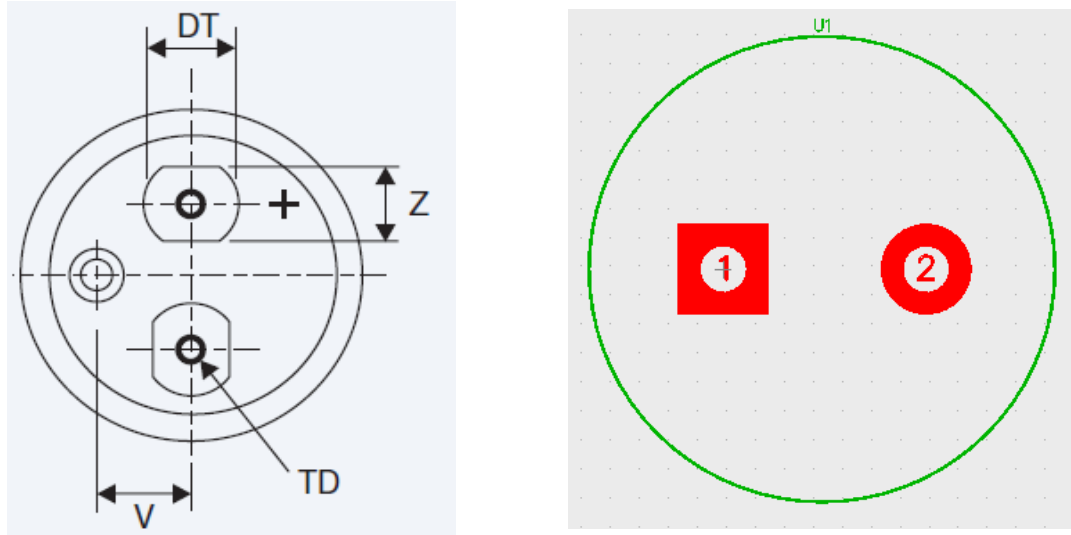


Figure 5.2 The actual shape and PCB model of the capacitor ALS30.

5.2.1 Input Capacitor Design

For safety purpose, the rated voltage of the capacitor is set as two times the output voltage. In this voltage range the only choices are electrolytic capacitors. The main concern with electrolytic capacitors is the equivalent series resistance (ESR) which causes heat and power loss. Furthermore, the ripple voltage is directly related to the current ripple and the ESR of the capacitor; the lower the resistance, the lower the ripple voltage. For a desirable voltage control, the ripple voltage of the capacitor should be less than the assumed change of the voltage at maximum power point of the PV which is the operating point and the critical point with the biggest change ratio based on the characteristic of the PV. The rated current of the input capacitor should be

$$\begin{cases} V_{cin} > 2V_{out} = 600V \\ I_{rms-Cin} > \frac{\Delta I_{Lpp}}{2\sqrt{3}} = 0.44A \\ \Delta V_{in} = r_{cin} \Delta I_{Lpp} < \Delta V_{MPP} \end{cases} \quad (5.6)$$

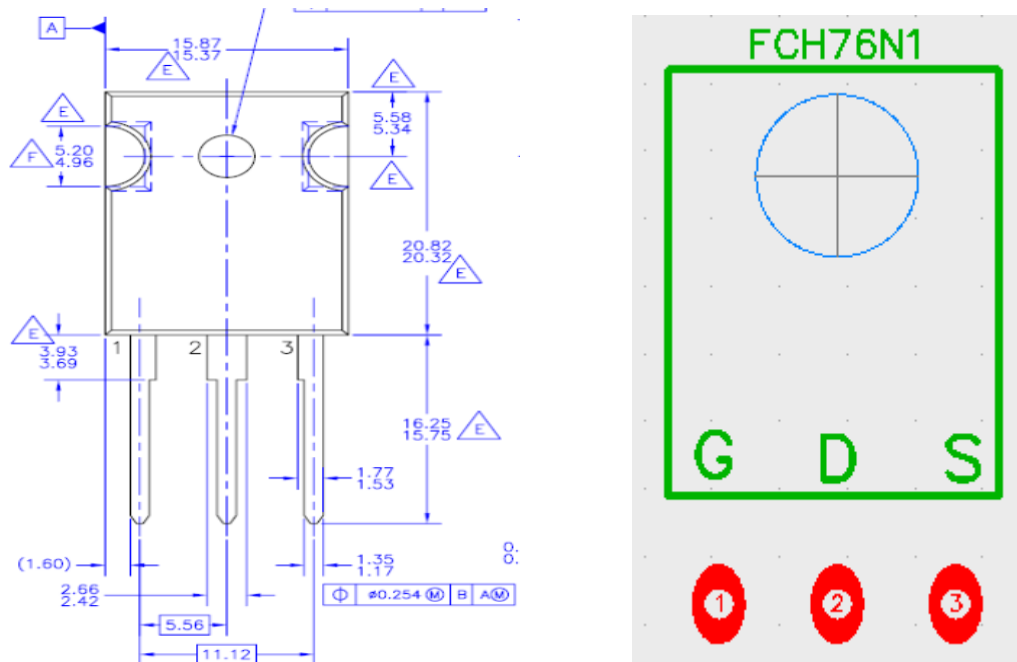


Figure 5.3 The actual shape and PCB model of the MOSFET FCH76N60NF.

Based on these parameters a capacitor from ALS30 series is chosen. Figure 5.2 shows the actual dimensions and designed PCB model of the capacitor.

5.2.2 The Switch Design

For the design or selection of the switch, it is necessary to consider at least three parameters, the switching frequency, the rated voltage and rated current. When working at higher frequencies the best choice is a MOSFET with the least series resistance. Series resistance has a large effect on conduction loss especially with higher currents. The current that passes through the switch is the maximum input average current in addition to the ripple current. Thus the voltage and current of the switch are considered as follows:

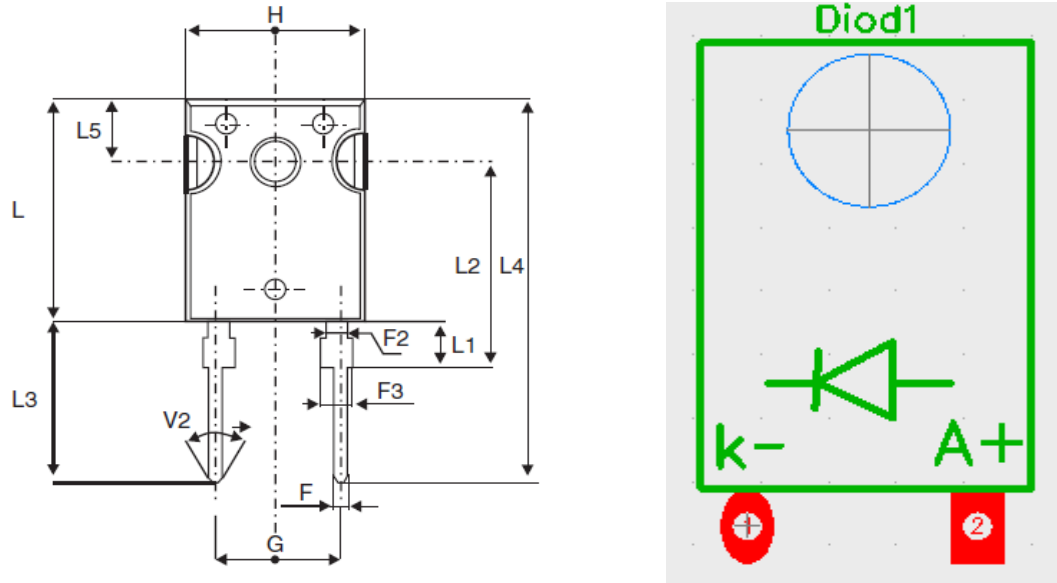


Figure 5.4 The actual shape and PCB model of the diode STTH30L06.

$$\begin{cases} V_{sw} > 2V_{out} = 600V \\ I_{sw} > I_{in(max)} + \frac{\Delta I_{Lpp}}{2} = 15.75A \end{cases} \quad (5.7)$$

For the highest efficiency the MOSFET FCH76N60NF from Fairchild semiconductor with low on resistance is chosen. The model of the MOSFET is presented in Figure 5.3.

5.2.3 The Diode Design

Diode should have the same voltage rating as the switch. The current passes through the diode is the maximum output current and the ripples. In the boost converter the output current is always less than the input current. The current and the voltage of the diode should be as follows:

$$\begin{cases} V_{diod} > 2V_{out} = 600V \\ I_{diod} > I_{out(max)} + \frac{\Delta I_{Lpp}}{2} = 10.75A \end{cases} \quad (5.8)$$

The STTH30L06, the selected diode is a fast high current and high voltage diode from STMicroelectronics. The designed model of the diode is illustrated in Figure 5.4.

5.2.4 Output Capacitor Design

Like the input capacitor, the rated and ripple voltages should be considered for the output capacitor. The ripple voltage of the output capacitor is transmitted to the output. So for higher waveform quality, the output ripple voltage is assumed to be around 2 percent of the output voltage which limits the selection of the capacitor with lowest ESR.

$$\begin{cases} V_{Cout} > 2V_{out} = 600V \\ \Delta V_{out} = r_{Cout} \Delta I_{Lpp} < 0.02V_{out} = 6V \\ I_{rms-Cout} > \max(I_{out} \sqrt{\frac{D}{1-D}}) \\ C_{out} = \frac{I_{out} D}{\Delta V_{out} f_{sw}} \end{cases} \quad (5.9)$$

The output capacitor is chosen identical to the input capacitor.

5.2.5 The Inductor Design

The inductor is the most difficult component to find in the market while fulfilling the design requirements. After defining the current rating and the inductance, the inductor needs to be designed and its core wounded like a transformer. Usually the inductor is assigned with the ripple current and amount of energy it can handle based on the time

step and current magnitude. The higher the inductance the lower the current ripple will be.

$$\begin{cases} L = \frac{V_{in(\min)} D_{\max}}{\Delta I_{Lpp} f_{sw}} = \frac{50 * 0.84}{1.5 * 50e^3} = 0.56mH \\ I_{L-sat} > (I_{in(\max)} + \frac{\Delta I_{Lpp}}{2}) = 15.75A \end{cases} \quad (5.10)$$

The selected core for this application is ferrite EE65/32/27, and the wire is a Litz wire with AWG36 and 200 strands. Based on the designed inductor parameters in

$$k_g = \frac{E^2}{\alpha k_e} = 2.4404 \text{ cm}^5 \quad (5.11)$$

The peak current

$$I_{pk} = I_{dc} + \frac{\Delta I_{dc}}{2} = 16A \quad (5.12)$$

The energy that the inductor can handle is

$$E = \frac{1}{2} L I_{pk}^2 = 0.07168 \text{ W / s} \quad (5.13)$$

The electrical condition coefficient

$$k_e = 0.145e^{-4} P_o B_m^2 = 2.1054e^{-3} \quad (5.14)$$

where B_m is the operating flux density.

The core geometry coefficient

$$k_g = \frac{E^2}{\alpha k_e} = 2.4404 \text{ cm}^5 \quad (5.15)$$

Table 5.1 Parameters of the designed inductor

L	0.00056H	I_{dc}	15A
ΔI_{dc}	2A	P_o	3000W
α	1%	f_{sw}	50KHz
B_m	0.3 tesla	k_u	0.4
T_r	25° c		

where α is regulation factor.

The core that is selected (based on k_g) that is EE65/32/27 has an area product (the product of window area and core cross section area)

$$A_p = 29.9 \text{ cm}^4 \quad (5.16)$$

The current density

$$J = \frac{2e^4 E}{B_m A_p k_u} = 400 \text{ A/cm}^2 \quad (5.17)$$

where k_u is window utilization.

The rms current

$$I_{rms} = \sqrt{I_{dc}^2 + \Delta I_{dc}^2} = 15.13 \quad (5.18)$$

The required bare wire area

$$A_w = \frac{I_{rms}}{J} = 0.03782 \text{ cm}^2 = 3.782 \text{ mm}^2 \quad (5.19)$$

The relationship between n AWG (American Wire Gauge) and diameter of the wire is

$$d = 0.127 * 92^{\frac{36-n}{39}} \text{ mm} \quad (5.20)$$

and the area is

$$A = \frac{\pi}{4} d^2 \quad (5.21)$$

Therefore the required AWG is

$$n = 13 \quad (5.22)$$

That is equivalent to Litz wire 36/200 for working in high frequencies. The effective window area of the core is

$$W_{a(eff)} = 0.75W_a = 5.54 * 0.75 = 4.15 \text{ mm}^2 \quad (5.23)$$

The number of turns is

$$N = \frac{0.6W_{a(eff)}}{A_w} = 65 \quad (5.24)$$

Figure 5.5 shows the designed inductor. After selecting all parts a sample setup is designed. A bulb is connected to the output as a load. A signal generator is connected to the gate of the MOSFET to turn it on and off. In Figure 5.6, the switching signal of 50kHz with 50 percent duty ratio is applied to the gate. The input voltage is around 25V and is boosted up around 50V based on the duty ratio.

5.2.6 PCB Model and Open Loop Test of the Boost Converter

After the design of the equipment, as illustrated in Figure 5.7, the body of the boost converter circuit is designed. This figure shows the connection of different parts



Figure 5.5 The designed inductor

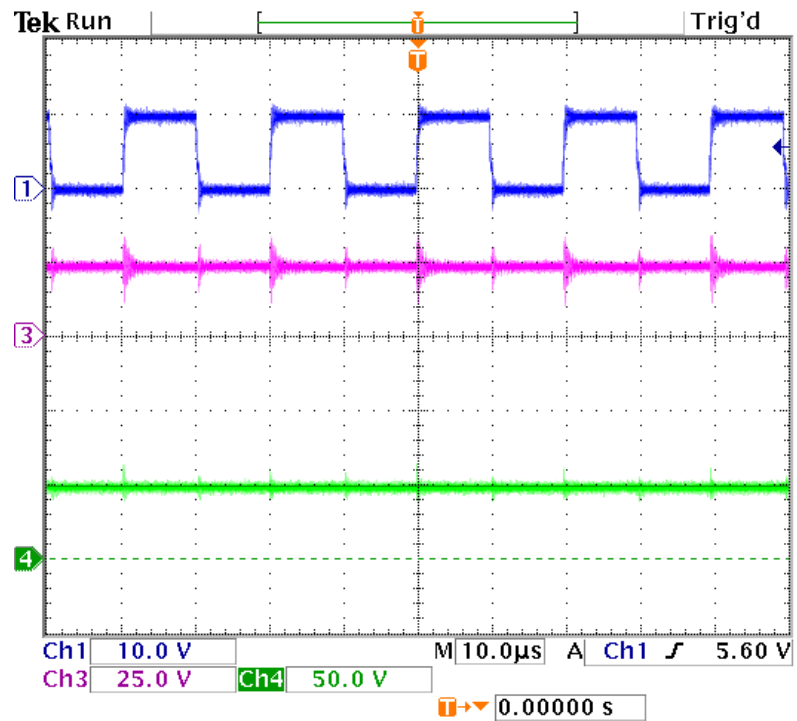


Figure 5.6 Input and output voltage in 50kHz switching frequency and duty ratio of 0.5

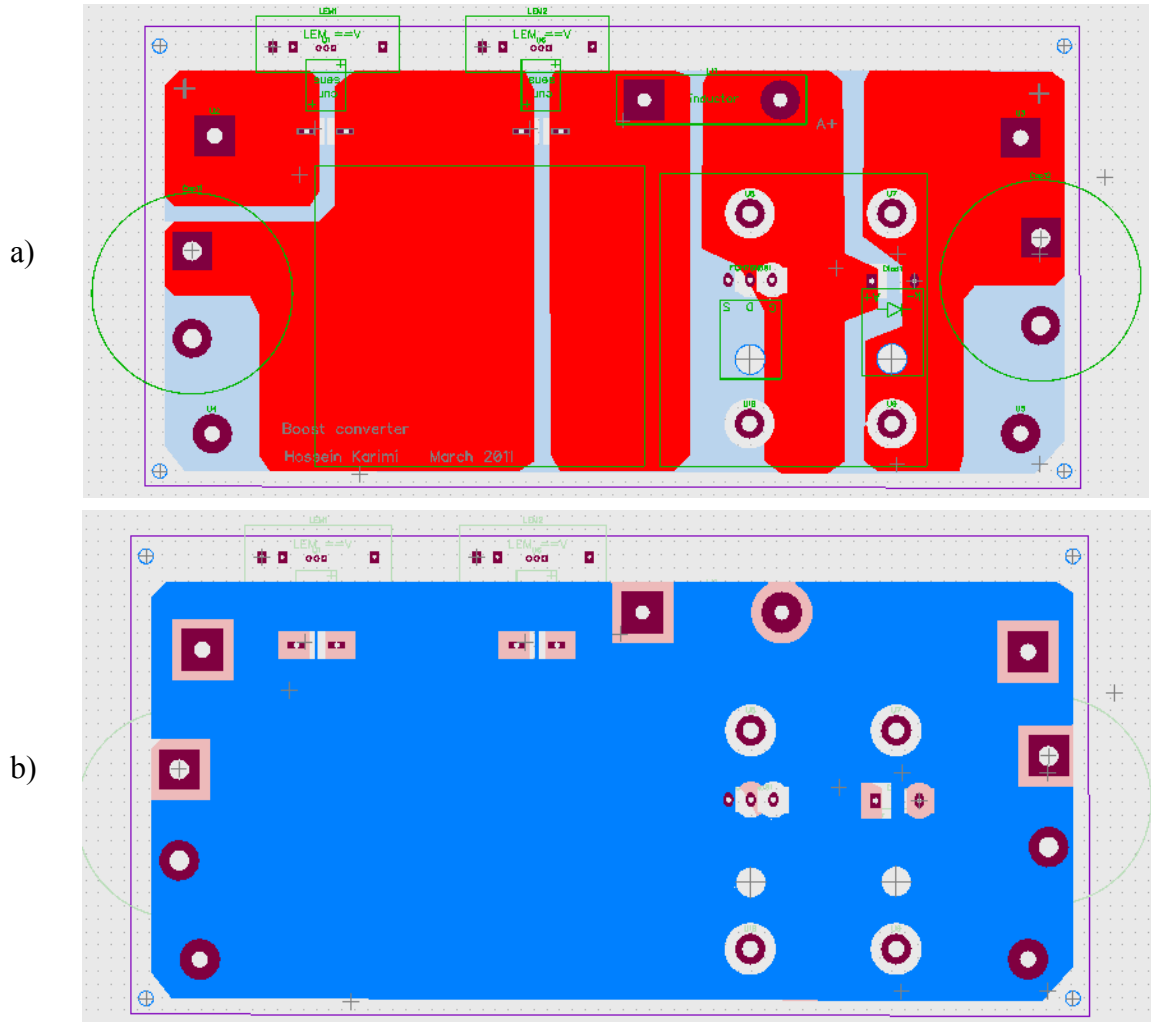


Figure 5.7 PCB design of Boost converter circuit a) top layer, b) bottom layer

besides current sensors on the board in both upper and lower sides. The completed and soldered open loop circuit is shown in Figure 5.8. The MOSFET and the diode are installed in the bottom connected to the heat sink for cooling and power dissipation.

The open circuit test is applied on the designed board in Figure 5.9. The duty ratio is selected to be around 60%. The input voltage is 68.3 V and the output voltage is 162 V.

$$D = 1 - \frac{V_{in}}{V_{out}} = 1 - \frac{68.3}{162} \approx 0.6 \quad (5.25)$$

5.3 Closed Loop Experimental Design of Maximum Power Point Tracking

Algorithm in PV System Applications

In closed loop control of the PV source output voltage, due to nonlinear characteristic of the solar cells and unpredictable environmental conditions and their effects on the output of the PV panel, designing a precise controller is very complex and sometimes not completely applicable. The most popular methods for close MPP control of PV systems are the incremental conductance (INC) and the perturbation and observation (P&O) algorithms.

The incremental conductance algorithm is implemented by periodically checking the slope of the P-V curve of a PV panel. If the slope becomes zero or equal to a defined small value, the perturbation is stopped and the PV panel is forced to work at this operating point.

The perturbation and observation (P&O) algorithm is based on making a perturbation in PV operation points of a PV panel in order to force the direction of tracking toward an MPP. In this method, based on the change of measured output power of PV in any time interval, a special amount is added to, or subtracted from the reference voltage or duty ratio of the converter. The advantages of these two closed loop methods are their simplicity in implementation and satisfactory accuracy without measuring solar irradiances and temperatures.

In this section, the perturbation and observation method as closed loop MPP controller is used to control the output power of the PV system. A programmable DC source is used to behave like a solar system. A DC/DC boost converter is designed and

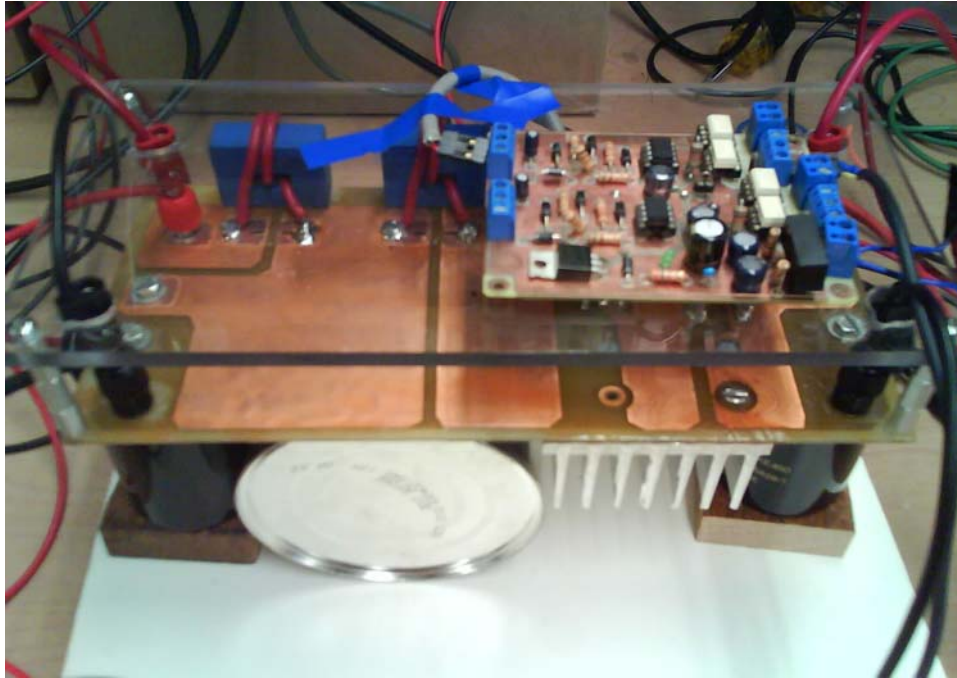


Figure 5.8 Designed PV boost converter

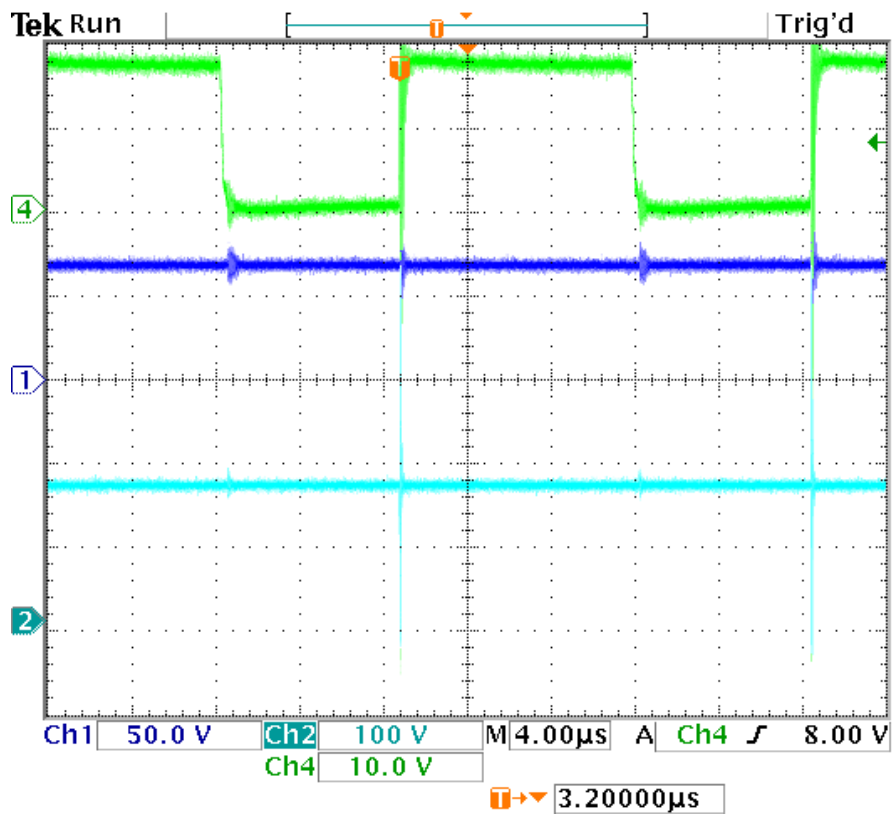


Figure 5.9 Experimental open circuit test of the Boost converter

built to connect the PV source to the resistive load. The ezDSPF28335 is used to control the closed loop system.

The system under study is shown in Figure 5.1. It includes a programmable DC power supply which is programmed to behave like a PV system. A DC/DC boost converter is designed to connect the PV source to the resistive load. The process of the design and open loop test of the boost converter is explained in previous section. . It is considered as a 3kw DC/DC converter which works at the switching frequency of 50kHz including input and output capacitors, a diode, a MOSFET as a switch and one high frequency inductor. Rated output voltage of the input and output sides are designed to be 300V.

5.3.1 Design of the Current and Voltage Sensors

For closed loop tests we need to measure the output power of the PV system. For this reason the voltage and current sensor circuits are designed. The output power is calculated from the measured voltage and current. For the current sensor the LEM50P is selected since its rating is up to 50 A. To increase the accuracy in lower currents two turns of wires are wound around it. It then produces the same output voltage in the lower (half) current magnitude. The current sensor is already mounted in series with the power circuit board.

An interface circuit is designed to supply an isolated power to the sensor as well as calibrate and filter the output. The designed PCB board of current sensor is presented in Figure 5.10.

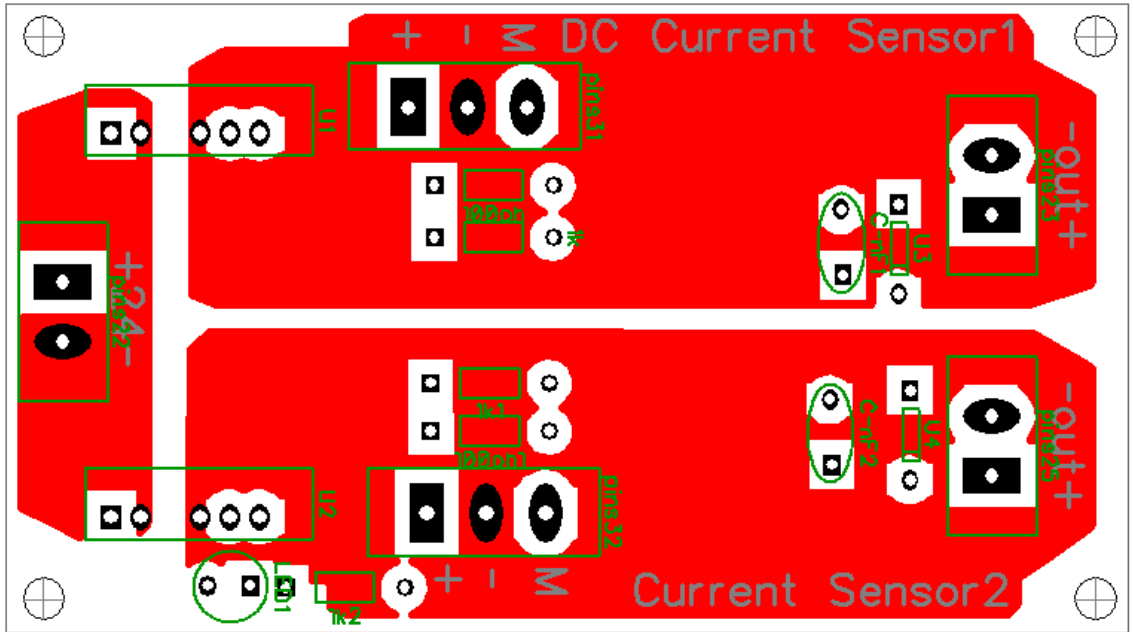


Figure 5.10 Designed PCB board for current sensor

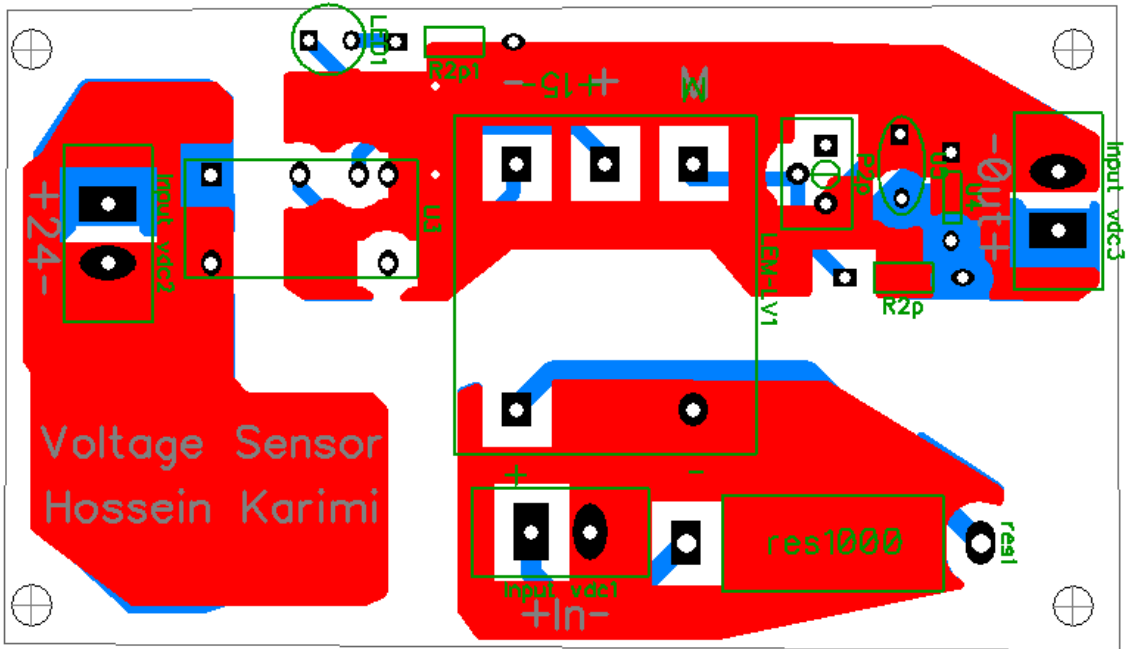


Figure 5.11 Designed PCB board for voltage sensor

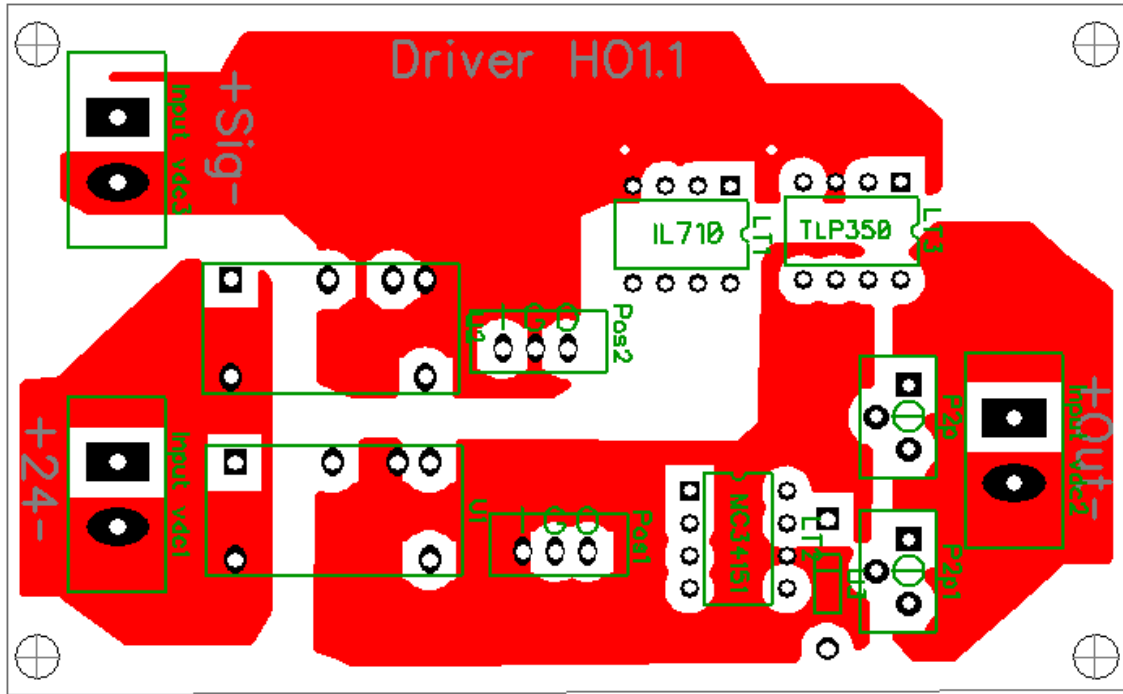


Figure 5.12 Designed PCB board for driver of the MOSFET

For a voltage sensor, the LV20P is used. The designed circuit is shown in Figure 5.11. It needs a $\pm 12\text{V}$ to $\pm 15\text{V}$ voltage supply. Based on the selected input and output resistance of the sensor, the output voltage range for importing to the control part (DSP) is zero to 3V for the actual input voltage of zero to 360V linearly.

5.3.2 Design of the Driver Circuit

One of the challenging parts for designing any converter is the driver circuit especially if we want to operate in high frequencies. In DC/DC converters to reduce the size of inductor, the switching frequency of the MOSFET is in a range of 10kHz to 100kHz. So a fast Driver with the least time delay, rise time, and fall time should be

selected. After reviewing characteristics of many available drivers in the market, the MC33151 is chosen.

For driving the MOSFET we need to increase the output voltage of the controller (DSP) from 3V to 15V and feed enough current to charge the capacitor between drain and source to force MOSFET to be on and off.

The control parts also need to be isolated from the power circuit in order to avoid drawing a high current and burning the DSP. An isolator is needed between DSP and the Driver. The isolator itself has a delay time so for this case also we should choose a fast isolator which has a sharp and stable output in high frequencies. The IL710, which is a high-speed digital isolator that is built based on Giant Magneto-resistive technology, is chosen for this purpose.

As shown in Figure 5.12, the driver circuit is designed based on the two selected ICs. The circuit is connected to the MOSFET and power circuit. It is tested under a load of 300V and switching frequency of 50 kHz. The result was acceptable. The other drivers which were also tested were the TLP250 and TLP350 which have opto-coupler isolator inside the IC. The MC33153 opto-coupler was also tested in addition to the TLP621. Even the UCC27134, one of the fastest drivers from Texas Instruments has been tried. Figure 5.13 to Figure 5.15 shows the output result of some tests. The light blue graph is the input signal, the red graph is the output and the dark blue graph is output voltage of the converter. It is worth mentioning that many of the drivers had satisfactory no load results but during the on load test which is our objective, the outputs fluctuate a lot or they have very long delay and rise time.

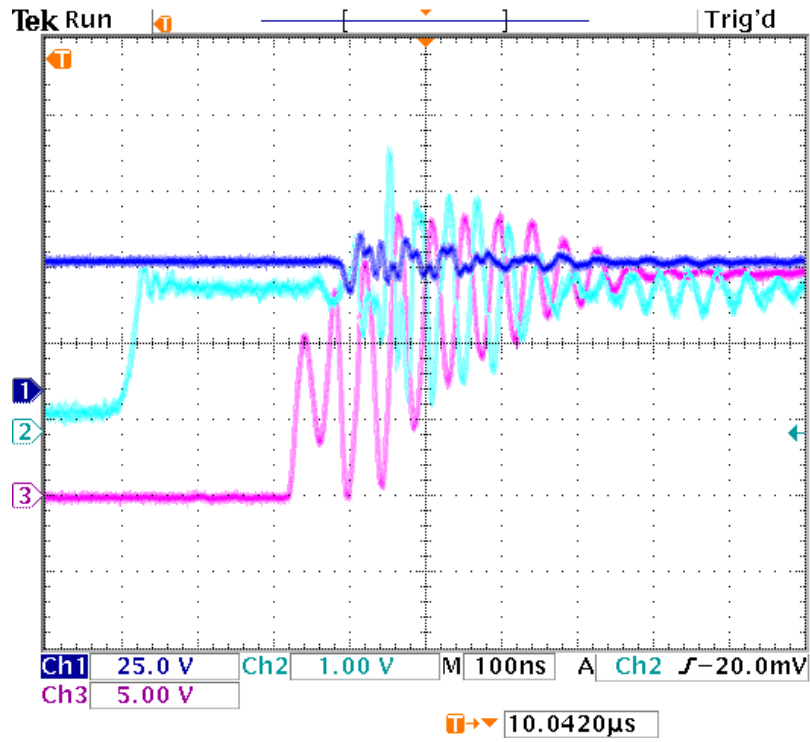


Figure 5.13 The output of TLP250 driver under the load

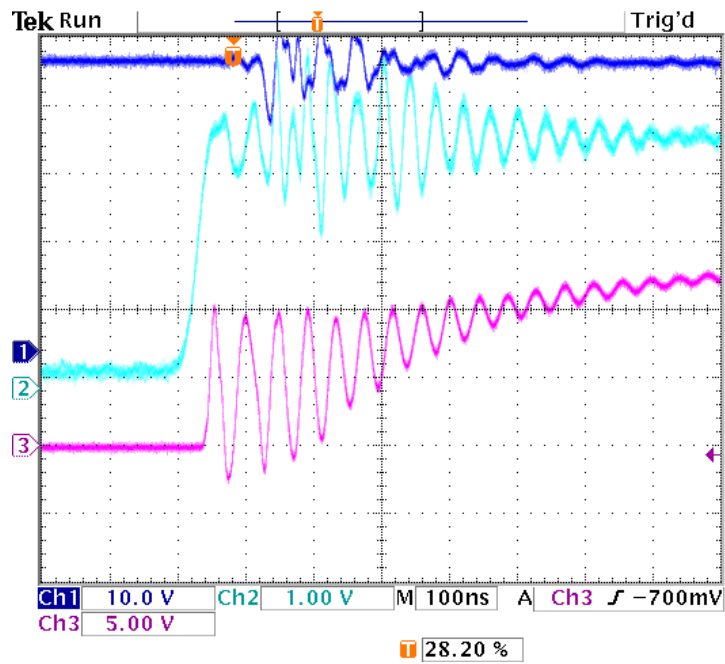


Figure 5.14 The output of UCC27134 driver and IL710 isolator under the load

After comparing all the results, the selected driver and isolator (MC33151 beside IL710) had the best results from the delay, rising time, falling time and fluctuation during turning on and off points of view.

5.3.3 Design of the Power Supply

All the designed boards including current and voltage sensors and the driver circuit need a 24V input source. For this reason another PCB board is designed. This board uses an AC 20VA, 115/48V transformer. The output of transformer is rectified, filtered and regulated to DC 24V as the output. Figure 5.16 shows the designed power supply circuit.

5.3.4 Controller Design and Closed Loop Test

The perturbation and observation (P&O) is selected for maximum power point tracking of the PV system. In this type of controller, choosing the perturbation step size which ensures a good matching between the tracking speed and the system dynamics is very important. Choosing a big step causes power and voltage oscillation around MPP in the steady-state while very small step size makes the controller dynamic slow. Therefore, the characteristic of a general DC/DC boost converter in terms of step change of duty ratio is studied. From the relationship between input and output voltage of the boost converter in two different duty ratio with change of ΔD

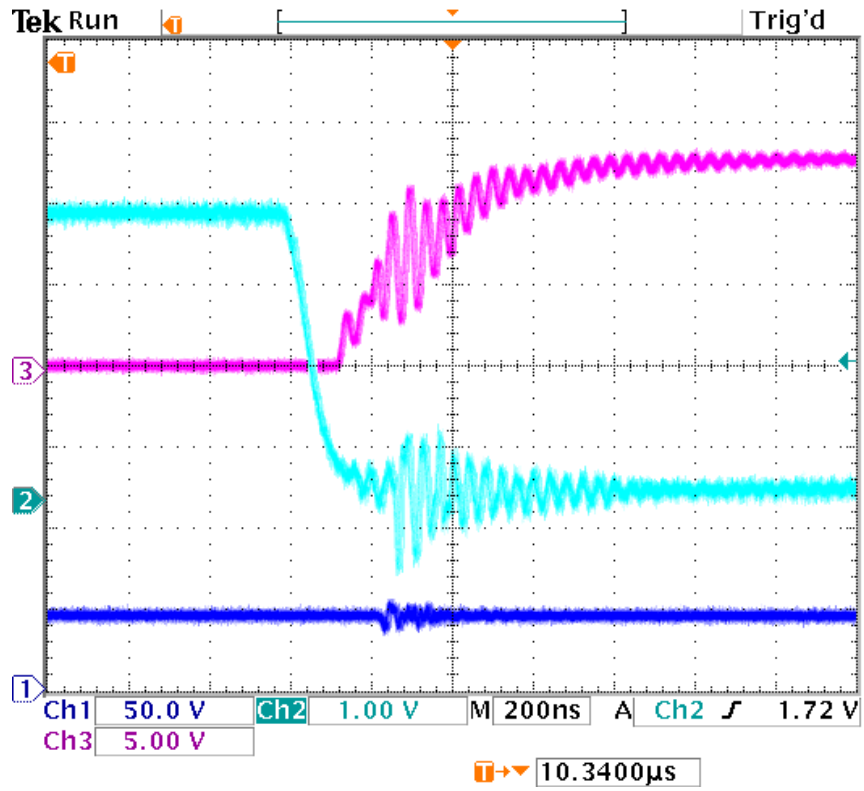


Figure 5.15 The output of MC33151 driver and IL710 isolator under the load

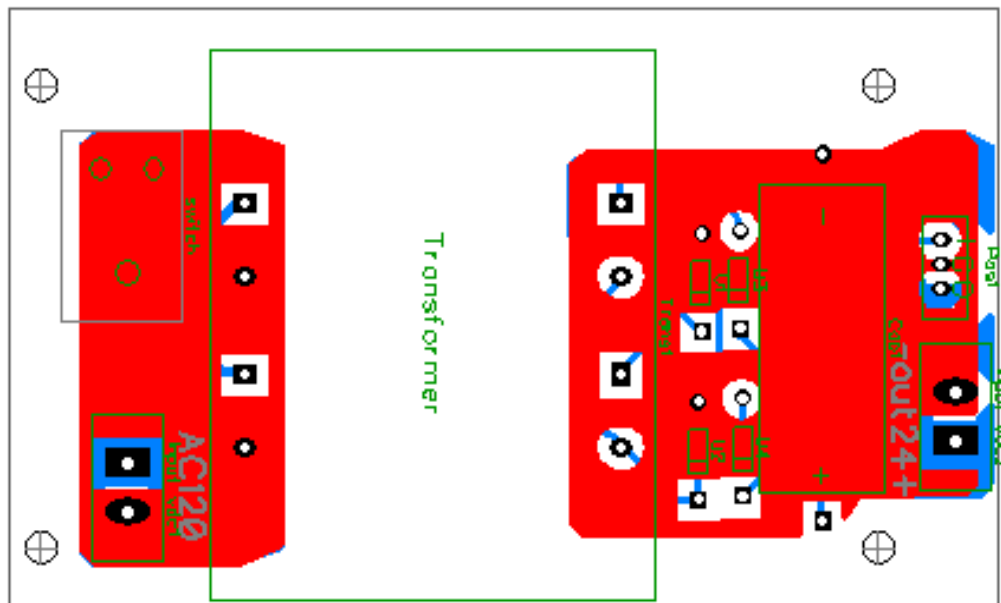


Figure 5.16 Designed PCB board for the power supply

$$V_{o1} = \frac{V_{in}}{1-D} \quad (5.26)$$

$$V_{o2} = \frac{V_{in}}{1-(D+\Delta D)} \quad (5.27)$$

$$\Delta V_o = V_{o2} - V_{o1} = V_{in} \left(\frac{1}{1-(D+\Delta D)} - \frac{1}{1-D} \right) \quad (5.28)$$

Thus we can define the relationship between amount of change of duty ratio and change of output voltage in a special duty ratio if the input voltage is kept constant.

$$\Delta D = \frac{-1}{\left(\frac{\Delta V_o}{V_{in}} + \frac{1}{1-D} \right)} + 1 - D \quad (5.29)$$

As it is shown in Figure 5.17, we can choose the desirable output voltage ripple of the boost converter due to step change of duty ratio and define the duty ratio set point (e.g., in maximum power point) and define the needed perturbation step size. Of course in the P&O method, the lower the desirable voltage ripple, the slower controller dynamic. For this purpose, 0.008 is selected for perturbation step size of the controller. The next step is to study the steady state behavior of the whole system when we connect a nonlinear PV system to a linear resistive load through a boost converter autonomously.

Figure 5.18 and Figure 5.19 show the characteristics of the programmed DC source to behave like a PV panel. This characteristic is under rated irradiation level (i.e. S=1). The experimental setup is based on this nonlinear PV characteristic. If the PV

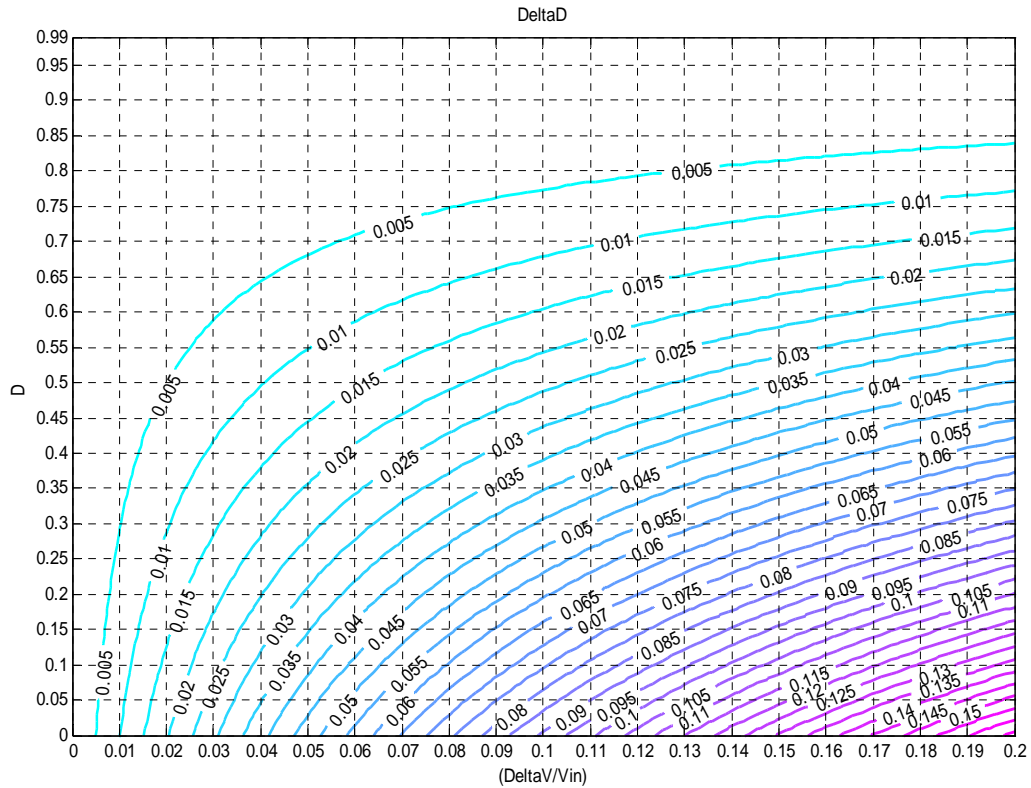


Figure 5.17 Output voltage ripple of the boost converter in terms of change of duty ratio in any predefined duty ratio set point

system is connected to the main grid with constant voltage which can absorb any power from the PV, from the boost converter characteristic we will have

$$V_{in} = V_{pv} = V_{o1}(1 - D) = V_{grid}(1 - D) \quad (5.30)$$

For increasing the output power of the PV we should increase the PV voltage, due to a constant voltage at the output so the duty ratio should be reduced.

In the case of connecting the PV source to an autonomous constant resistive load, the relationship between output voltage and current is linear and the relationship between voltage and power is quadratic. To have power balance and also operate always in MPP simultaneously, the output voltage can not be constant. From the power balance between

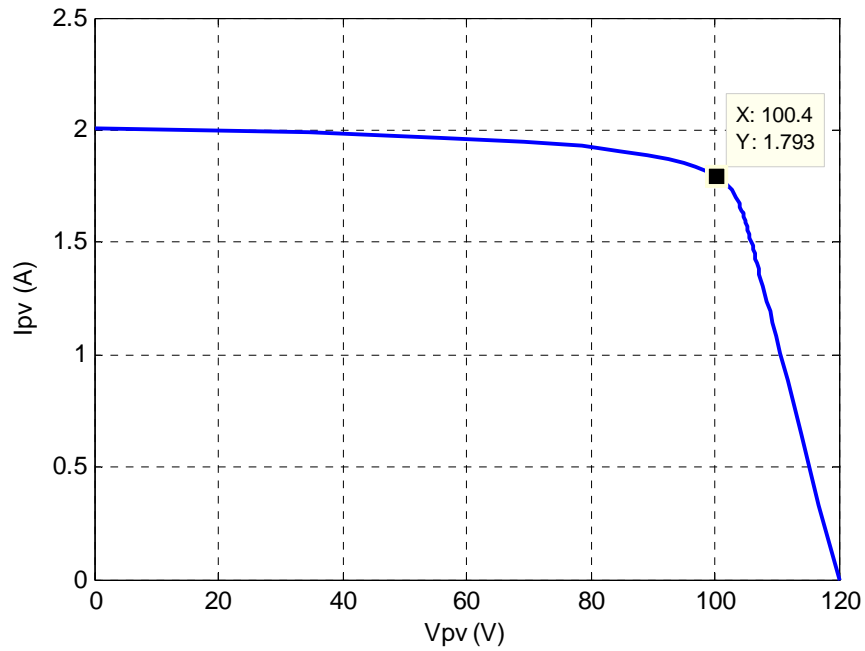


Figure 5.18 Programmed current versus voltage characteristic of experimental PV source

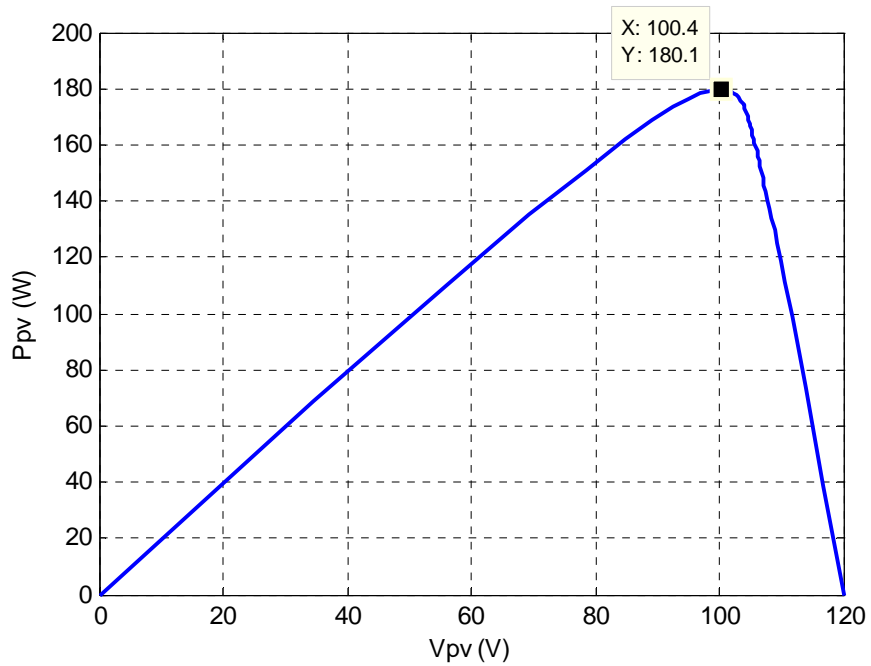


Figure 5.19 Programmed output power versus voltage characteristic of experimental PV source

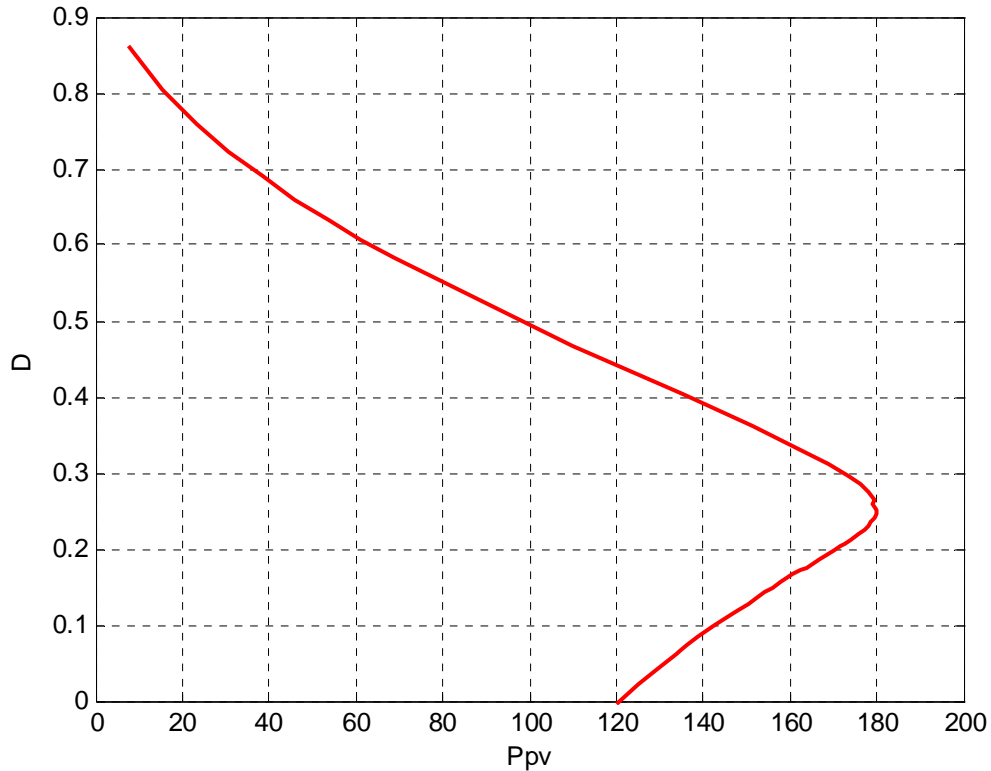


Figure 5.20 Change of duty ratio versus output power of PV system connected to linear resistive load

the nonlinear PV source and the resistive load of 100Ω , the relationship between the duty ratio of the boost converter and active power are illustrated in Figure 5.20. As shown in this figure, with reduction of the duty ratio, the power (input and output powers are almost the same) first starts to increase, it reaches to MPP and then reduces. Therefore the controller algorithm is designed based on Figure 5.21. In this diagram the power is calculated using measured voltage and current. It is compared with the previous interval calculated power. If the power is increasing the duty ratio is changing with the same trend (even increasing or reducing). If the power reduces, the change of duty ratio will be reversed. Therefore without the knowledge about the trend of the duty ratio, temperature

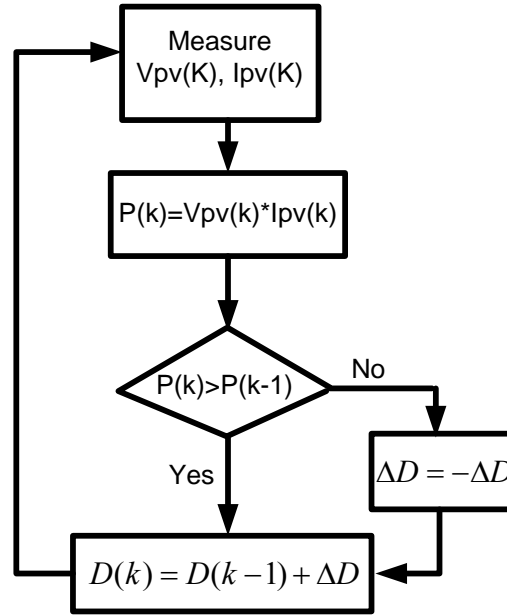


Figure 5.21 Schematic of the P&O algorithm for MPPT of the PV system

Table 5.2 Coefficients of the low pass Hamming digital filter

	a_0	a_1	a_2	a_3	a_4	a_5	a_6	a_7	a_8	a_9
Coefficients	0.0161	0.0379	0.0931	0.1559	0.197	0.197	0.1559	0.0931	0.0379	0.0161

or even irradiation level the maximum power point of the PV can be obtained.

For measurement of the voltage and current, an RC low pass filter is first added to the output of the sensors. Using coaxial cables the signals are transferred to the analog to digital (A/D) converter pins of the DSP. Inside the program 12 bit digital values are converter to floating point numbers and the measurements are calibrated to get the exact value of the actual signals. An inside PWM with a frequency (sampling rate) of 100kHz for the interrupt of A/D conversion is used. A 9th order Hamming digital low pass filter

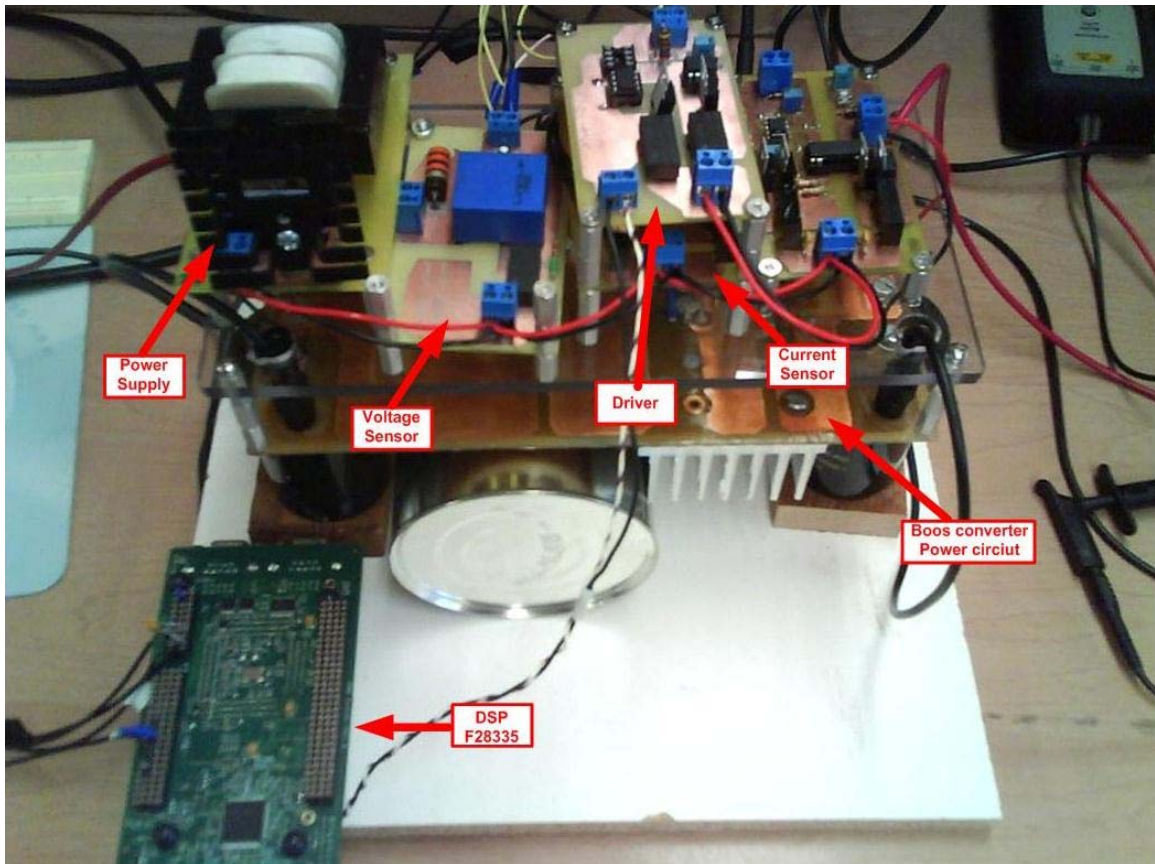


Figure 5.22 The experimental setup of the Boost converter for PV MPPT

with cut off frequency of 300Hz using filter design of the MATLAB is designed and applied to the measurements to remove the input noise of the DSP. The coefficients of the finite impulse response (FIR) Hamming low pass filter are presented in Table 5.2.

Figure 5.22 shows the experimental setup of the boost converter, sensors, and control part for maximum power point tracking of the PV system. This setup is connected to the nonlinear emulated PV source from one side and to the resistive load (constant at 100Ω). All of the algorithms for A/D conversion, digital filter, PWM generators and the main control algorithm are programmed and written directly in C language inside the DSP. Two main closed loop tests are shown in this report. As illustrated in Figure 5.23

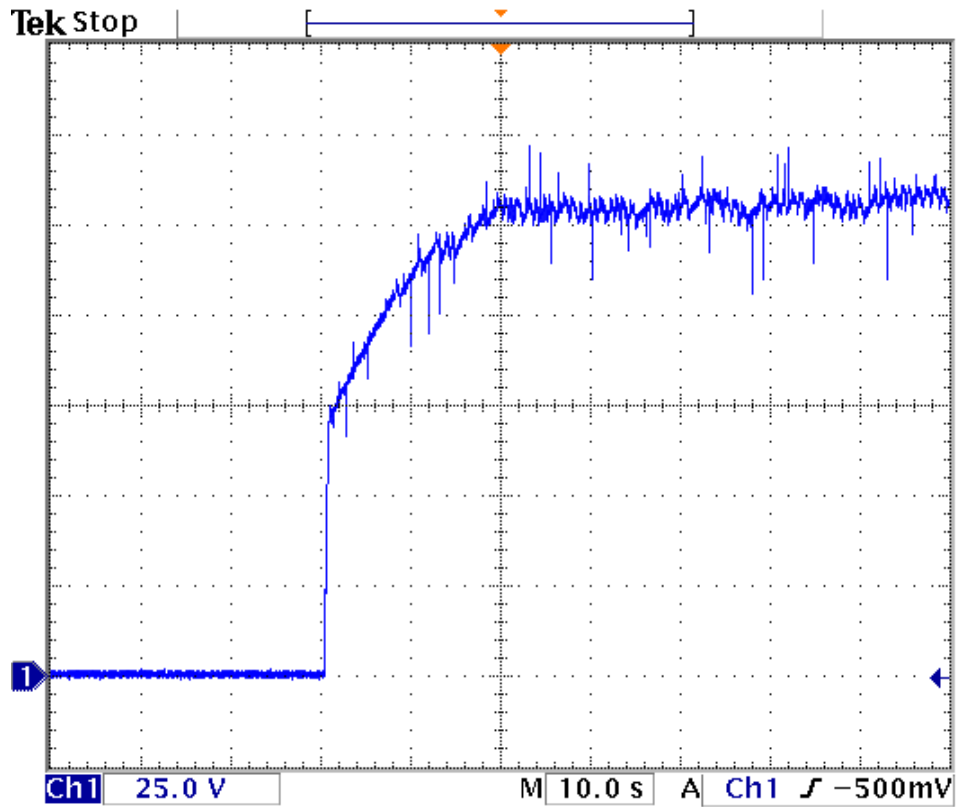


Figure 5.23 Experimental dynamic behavior of the load voltage of PV system using P&O MPP algorithm

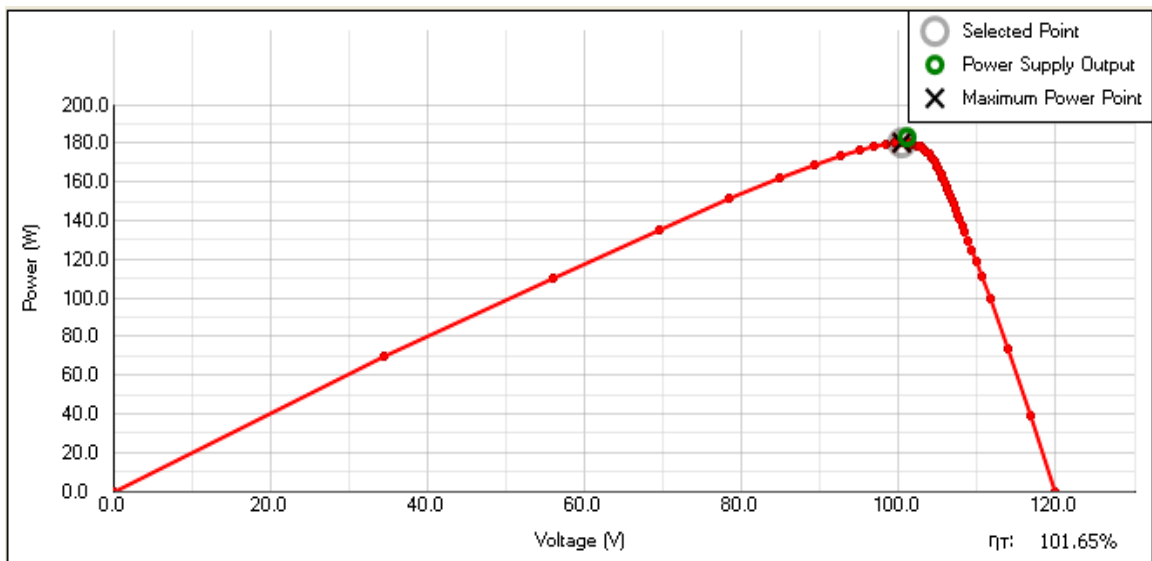


Figure 5.24 Experimental steady state operation of the input power versus PV voltage in MPPT

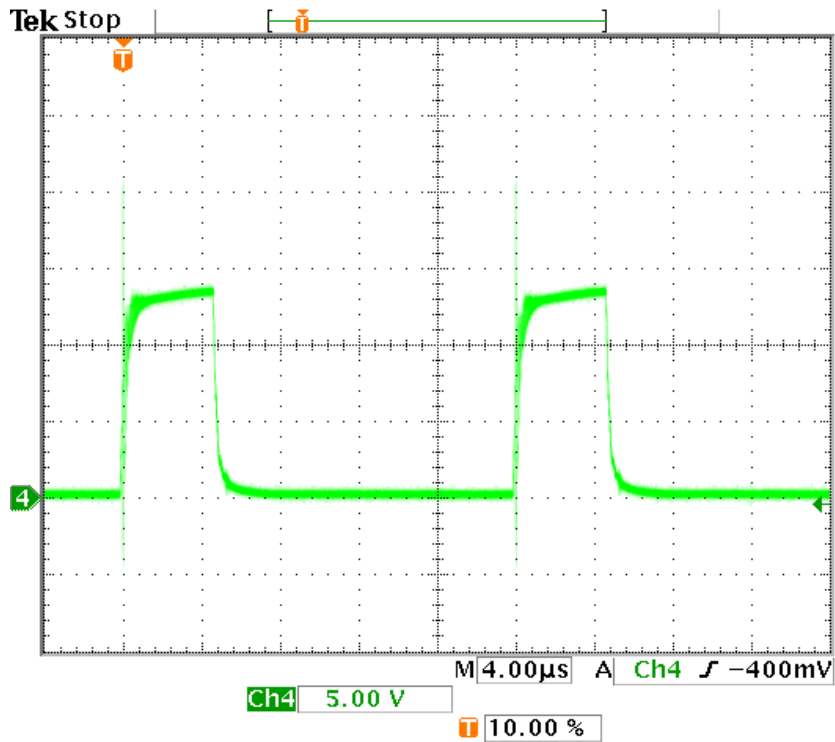


Figure 5.25 The output of the driver at 50kHz and duty ratio of 0.24

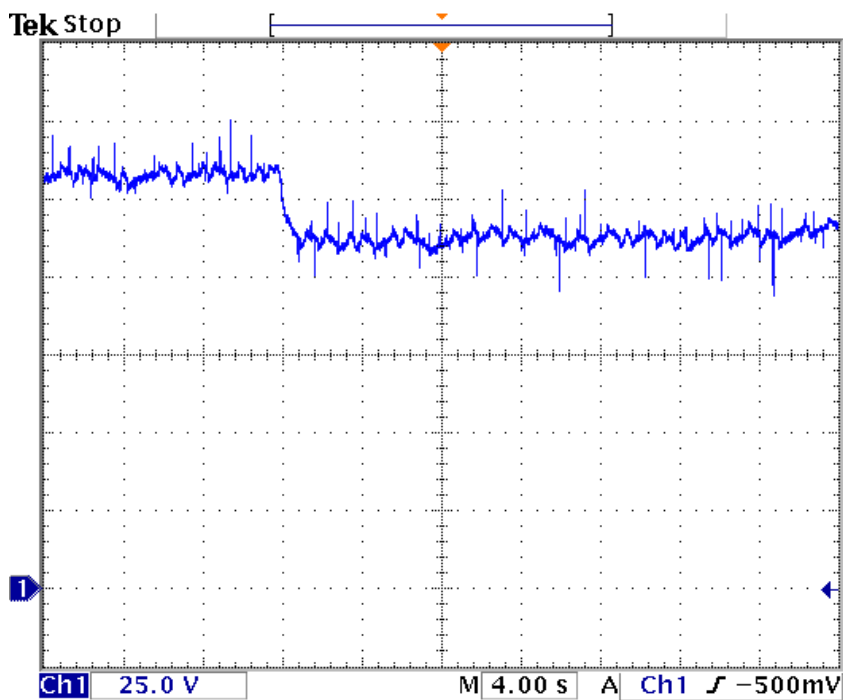


Figure 5.26 Experimental dynamic behavior of the load voltage of PV with step change of irradiation level

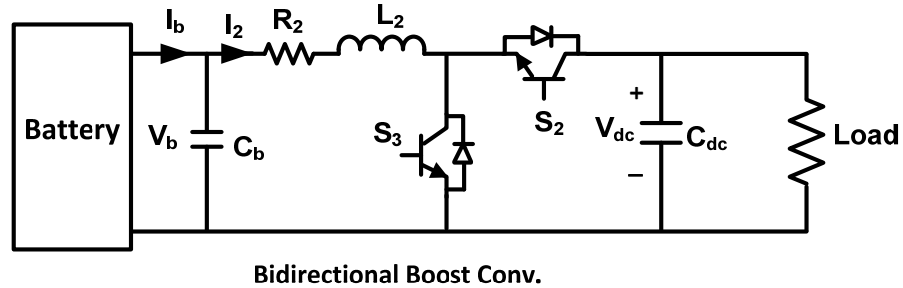


Figure 5.27 the bidirectional battery converter

the source is turned on from a zero set point at 30s. In this figure the dynamic response of the controller for finding the maximum power point in a constant irradiation level ($S=1$) is shown. After almost 20s the algorithm reaches the maximum power point which is shown in Figure 5.24 . This is obtained from the online measurement of programmable power source. After this moment it reaches steady state and has some small oscillations in MPP. Figure 5.25 shows the output of the driver at a 50kHz switching frequency with duty ratio of 0.24 which is the result of the PWM converter of the DSP controller program obtaining maximum power point.

In second test the irradiation level is changed suddenly from unity to 0.8 at 12s. As illustrated in Figure 5.26, the output voltage reaches the new steady state maximum power set point in less than 4s. These two test show even with a sudden change of the irradiation level of the sun, the perturbation and observation algorithm can find the maximum power point of the PV in a few seconds.

5.4 Closed Loop Test of Battery System Converter

For charging and discharging of the battery, the same process as PV system is followed to design the bidirectional buck and boost converter. As shown in Figure 5.27

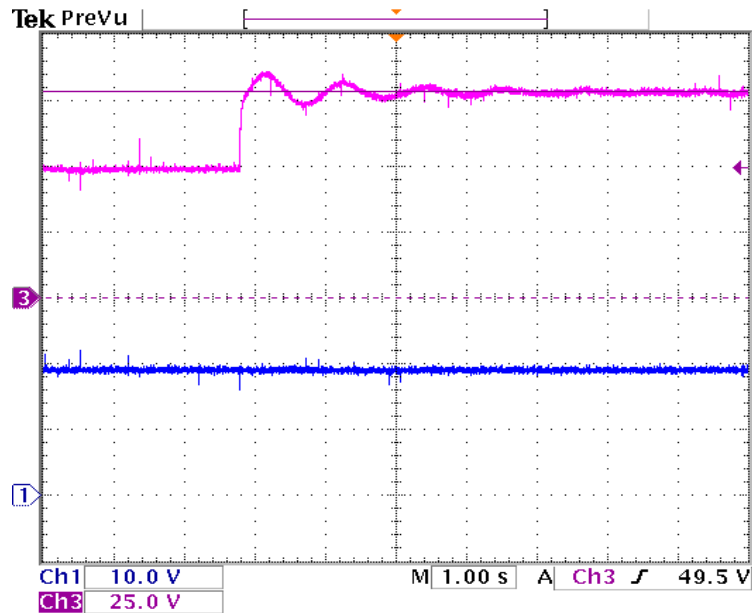


Figure 5.28 Experimental closed loop response of the bidirectional converter,
Ch1: V_{in} , Ch3: V_{dc}

the system is connected to a local DC load to verify the controller response of this system. This DC-DC converter from one side when feeding the load behaves as boost converter and in charging mode (if there exist another source on the other side) reduce the voltage level close to the rated voltage of the battery side like a buck converter. Therefore the current can follow in both directions. The objective of this converter is to control the DC link voltage. As illustrated in Figure 5.28, the reference of DC link voltage is changed from 50V to 80V in a constant input voltage. Even during drastical change of the reference voltage, the output tracks the reference with the lowest fluctuation and reaches to steady state precisely.

5.5 Design and Open Loop Test of Three Phase Inverter

Due to the fast response and controllability of power electronic devices, their use

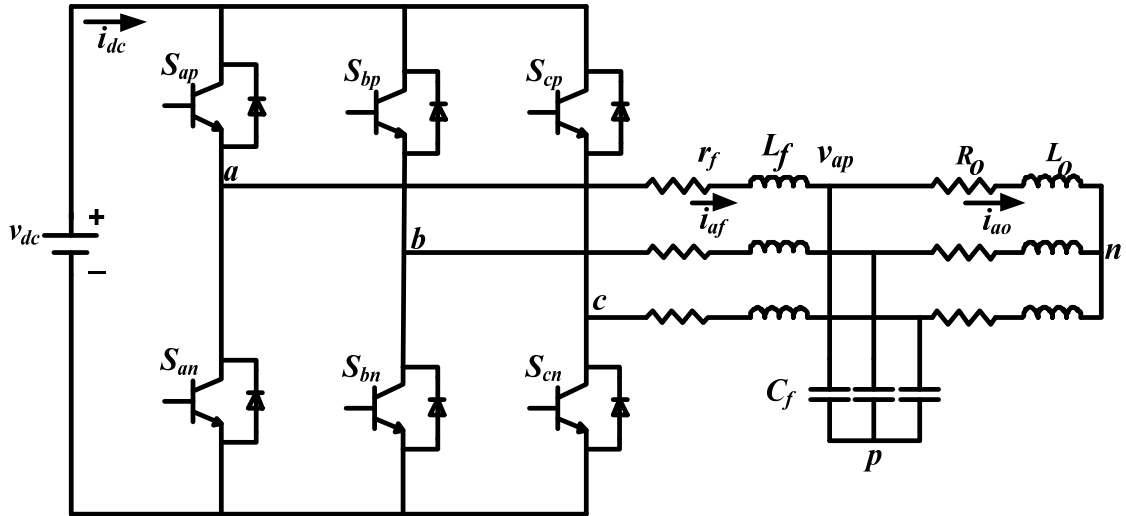


Figure 5.29 Three phase inverter simulated in MATLAB connected to the load

in electric power systems is growing fast. Most of the systems in the power system network are working as three phase systems resulting three phase converters being the most popular power electronic devices which are used in different topologies for a wide variety of applications. Inverters can control the output voltage magnitude and frequency. In this report the experimental setup for generating switching pulses using the sinusoidal pulse width modulation (SPWM) in the three phase inverter is shown. The DSP F28335 is used for generating the pulses. The zero sequence is added to the modulation signal to increase the linear modulation region. An interface circuit with isolators is designed to connect the DSP to the gate drivers of the three phase inverter for experimental testing of the system.

5.5.1 Study System

Figure 5.29 shows the study system which includes a three phase inverter connected to a linear RL load through a capacitor filter and transmission line. This

system is modeled with MATLAB software. The switching pulses are applied from imported DSP hardware. The model equations of the system are as follows:

The output voltage equations of inverter

$$\begin{cases} \frac{v_{dc}}{2}(2S_{ap} - 1) = R_f i_{af} + L_f p i_{af} + v_{ap} + v_{no} \\ \frac{v_{dc}}{2}(2S_{bp} - 1) = R_f i_{bf} + L_f p i_{bf} + v_{bp} + v_{no} \\ \frac{v_{dc}}{2}(2S_{cp} - 1) = R_f i_{cf} + L_f p i_{cf} + v_{cp} + v_{no} \end{cases} \quad (5.31)$$

where R_f and L_f are the resistance and inductance of the transmission line.

The load voltage equations

$$\begin{cases} v_{ap} = R_o i_{ao} + L_o p i_{ao} + v_{np} \\ v_{bp} = R_o i_{bo} + L_o p i_{bo} + v_{np} \\ v_{cp} = R_o i_{co} + L_o p i_{co} + v_{np} \end{cases} \quad (5.32)$$

where R_o and L_o are the resistance and inductance of the linear RL load.

Capacitor voltage equations

$$\begin{cases} C_f p v_{ap} = i_{af} - i_{ao} \\ C_f p v_{bp} = i_{bf} - i_{bo} \\ C_f p v_{cp} = i_{cf} - i_{co} \end{cases} \quad (5.33)$$

The C_f is the capacitor capacitance.

The input current equation of the system is

$$i_{dc} = S_{ap} i_{af} + S_{bp} i_{bf} + S_{cp} i_{cf} \quad (5.34)$$

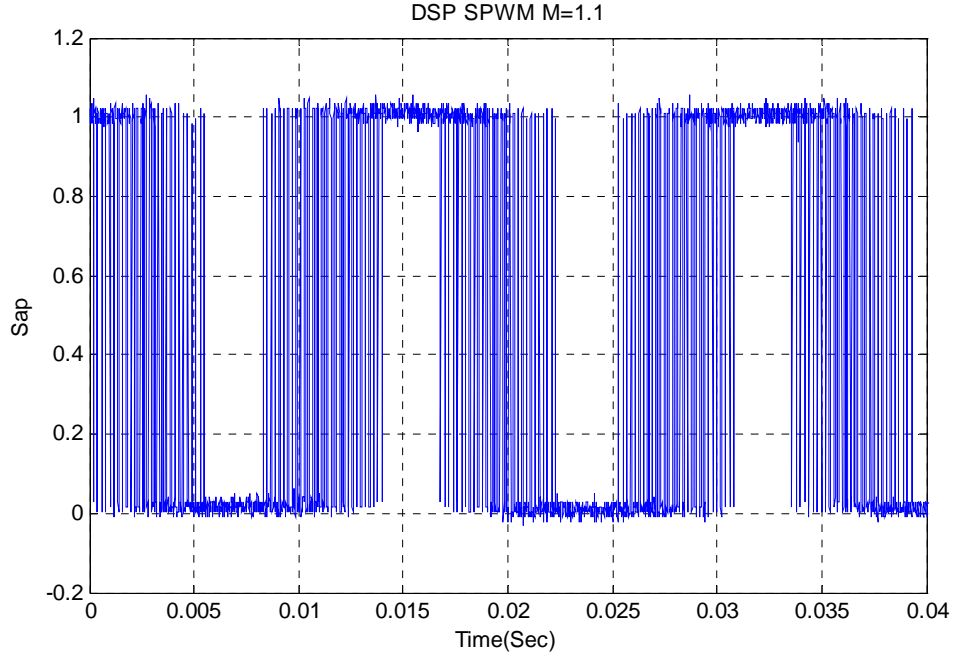


Figure 5.30 Experimental switching signals of produced by DSP in typical SPWM converter

If we apply the modulation index as more than unity we will go into the discontinuous region. As shown in Figure 5.30, with the modulation index $M = 1.1$ the switching signals are discontinuous in the typical SPWM converter.

To increase the SPMW modulation linear region we can add the zero sequence to the sinusoidal modulation waveform [117].

$$M_{ip} = \frac{2v_{in}^*}{v_{dc}} + \frac{2v_{no}}{v_{dc}} \quad (5.35)$$

where $i = a, b, c$. With defining

$$m_{ip}^* = \frac{2v_{in}^*}{v_{dc}}, \quad m_{oo} = \frac{2v_{no}}{v_{dc}} \quad (5.36)$$

$$M_{ip} = m_{ip}^* + m_{oo} \quad (5.37)$$

and

$$v_{no} = \frac{v_{dc}}{2}(1-2\alpha) - \alpha v_{\min} - (1-\alpha)v_{\max} \quad (5.38)$$

$$\frac{v_{no}}{\frac{v_{dc}}{2}} = (1-2\alpha) - \alpha \frac{v_{\min}}{\frac{v_{dc}}{2}} - (1-\alpha) \frac{v_{\max}}{\frac{v_{dc}}{2}} \quad (5.39)$$

$$m_{oo} = (1-2\alpha) - \alpha m_{\min} - (1-\alpha)m_{\max} \quad (5.40)$$

Where $m_{\min} = \frac{2v_{\min}}{v_{dc}}$, and $m_{\max} = \frac{2v_{\max}}{v_{dc}}$

Therefore the actual modulation

$$M_{ip} = m_{ip}^* + (1-2\alpha) - \alpha m_{\min} - (1-\alpha)m_{\max} \quad (5.41)$$

where $m_{\min} = \min(m_{ap}^*, m_{bp}^*, m_{cp}^*)$, $m_{\max} = \max(m_{ap}^*, m_{bp}^*, m_{cp}^*)$

The produced modulation waveform inside DSP is illustrated in Figure 5.31. The produced switching signals of the modulation index are imported into MATLAB software to be applied to the simulated system after adding the zero sequence waveform. The produced output voltages of the simulated system are presented in Figure 5.32 with no discontinuity in the waveform. The phase voltages of the capacitors are shown in Figure 5.33 as three sinusoidal waveforms with 120 degree phase shifts.

The 6MBP50RA060 inverter module with the nominal 600V, 50A input voltage and current ratings, consisting of six IGBTs and drivers is selected to convert the input

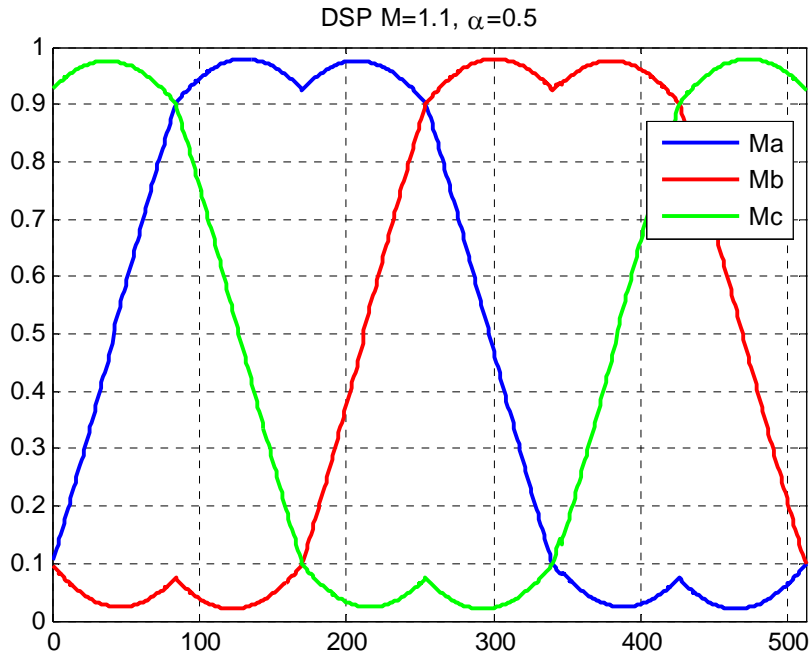


Figure 5.31 Modulation waveform after adding zero sequence to the typical SPWM in DSP

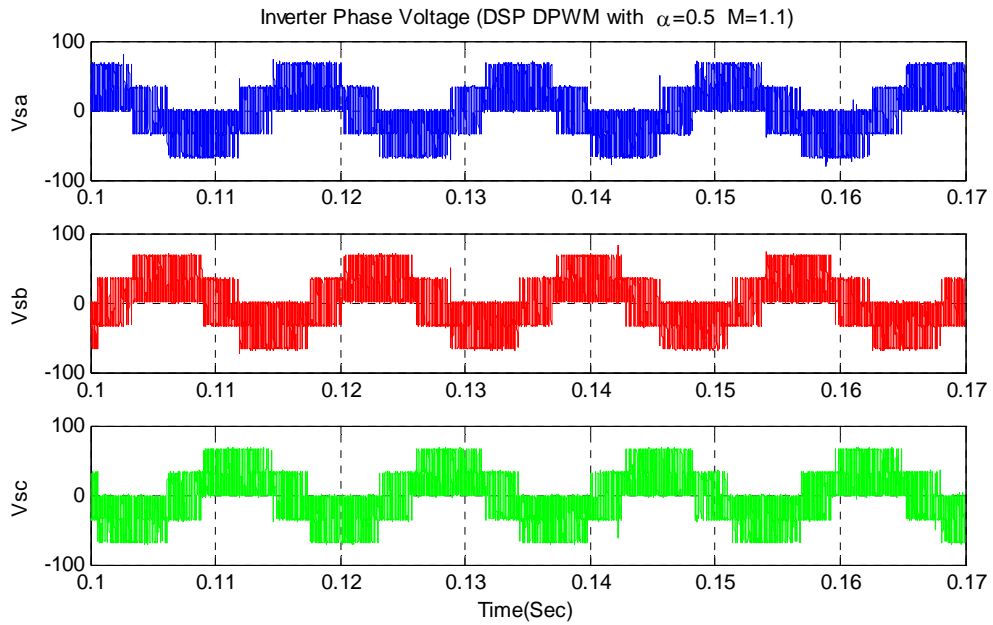


Figure 5.32 Phase voltage of the inverter using imported DSP SPWM switching signals

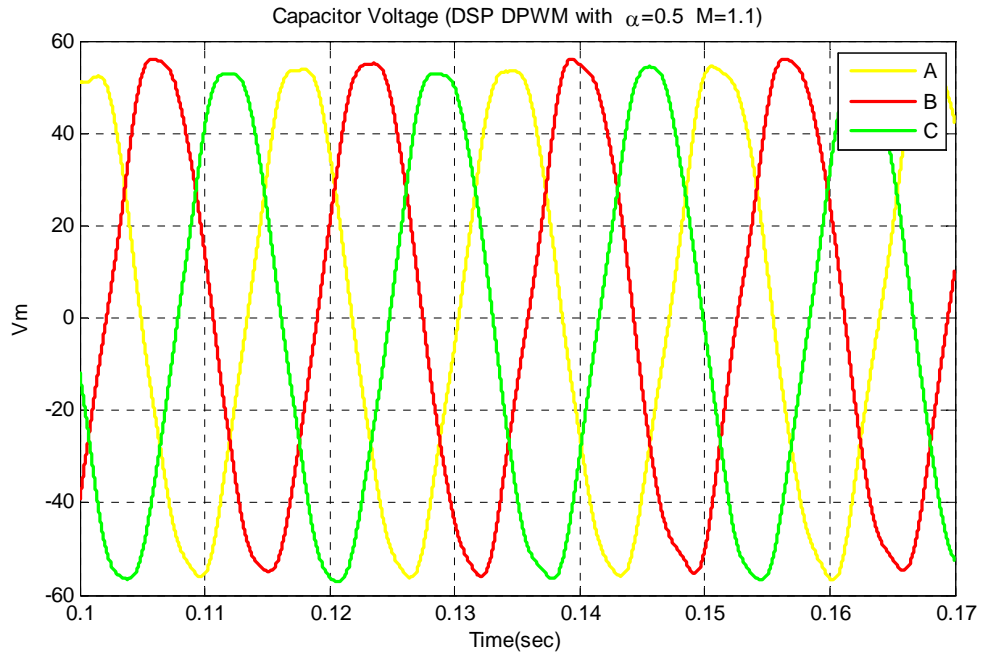


Figure 5.33 Phase voltage of the simulated capacitor using imported DSP SPWM switching signals

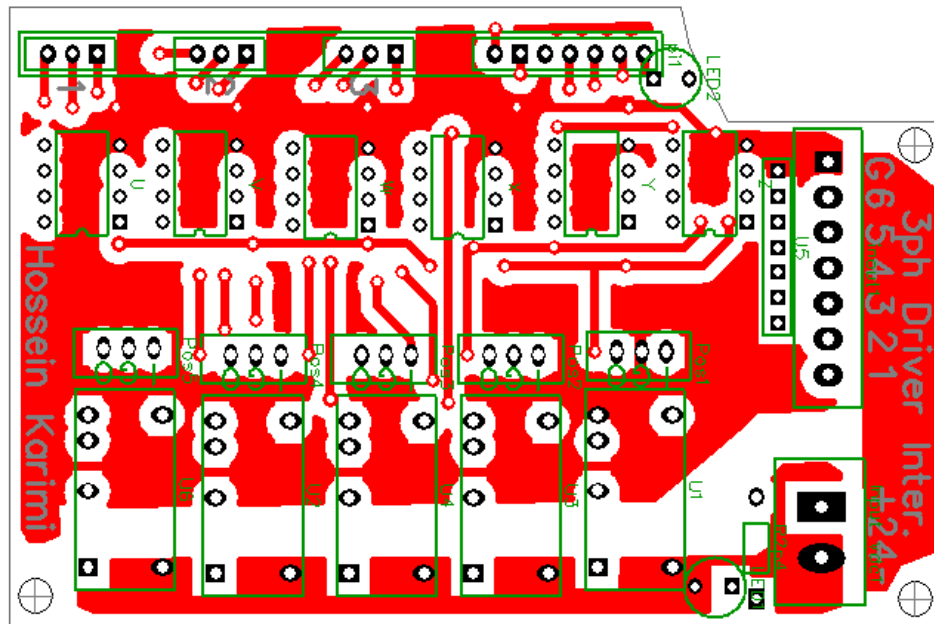


Figure 5.34 Designed interface circuit to connect the DSP to the inverter drivers

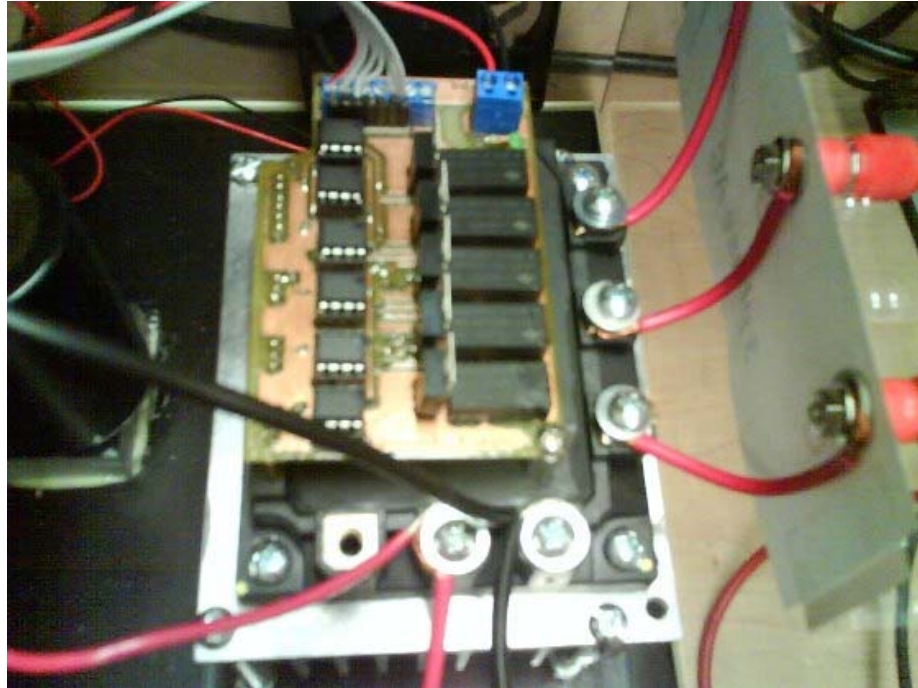


Figure 5.35 Experimental set up of the three phase inverter and interface driver circuit

DC voltage to the AC voltage. As shown in Figure 5.34, an interface circuit is designed to supply the drivers and isolate the DSP circuit from the drivers. This circuit has 3 isolated grounds for three top switches and one isolated ground for the lower switches.

5.5.2 The Experimental Setup

Figure 5.35 shows the experimental setup for three phase AC/DC inverter. A constant DC source is connected to the input and three resistors ($R = 42\Omega$) are star connected to the output. The three phase SPWM switching signals are produced inside the DSP to drive the IGBTs. The output voltage of phase A is shown in Figure 5.36. The input DC voltage of 200V and the modulation index of $M = 0.8$ are applied. The average of the output voltage is a sinusoidal waveform with the considered 60Hz frequency. It

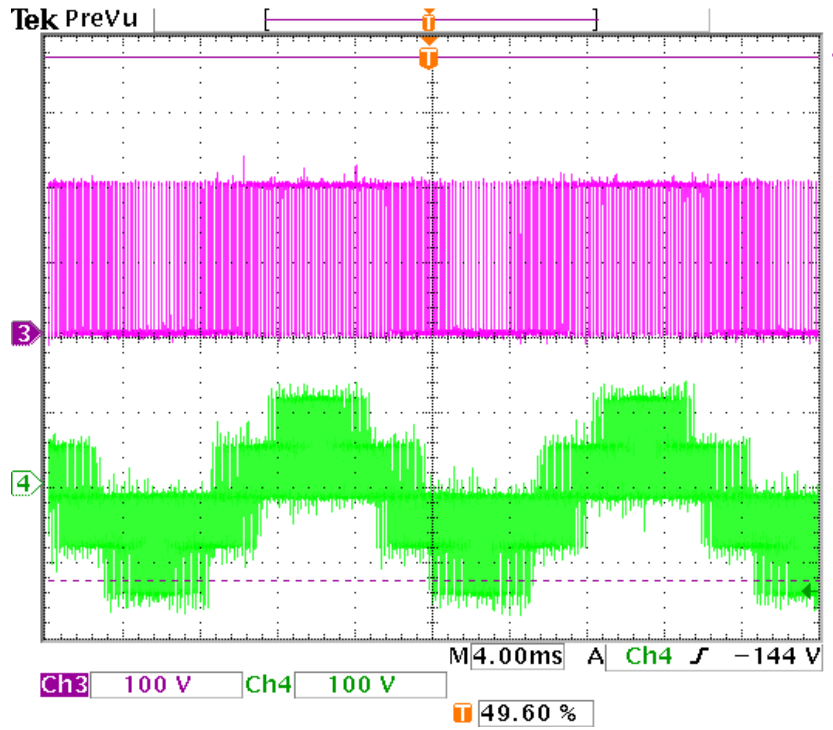


Figure 5.36 Experimental inverter output phase voltage of a resistive load with input DC voltage of 200V and modulation index $M=0.8$

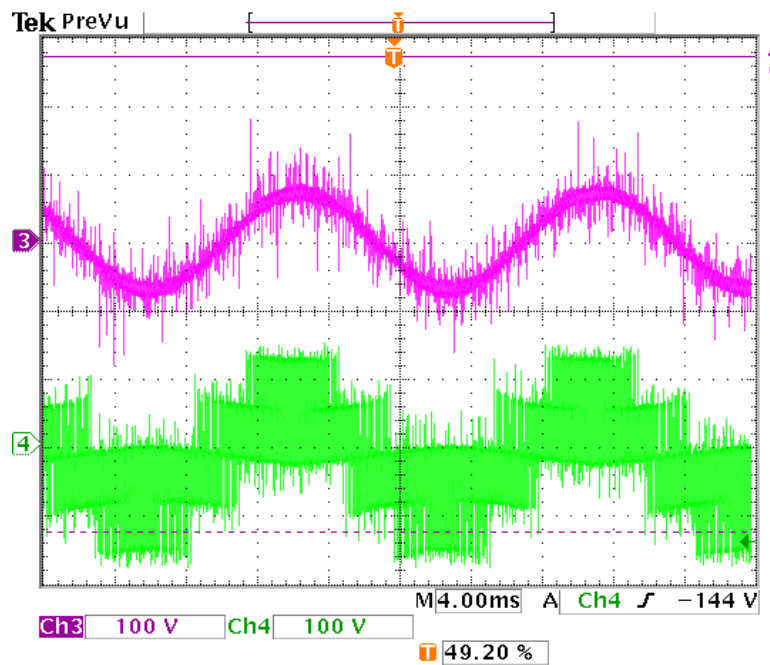


Figure 5.37 Experimental inverter output phase voltage and phase current of a RL load with input DC voltage of 200V and modulation index $M=0.8$

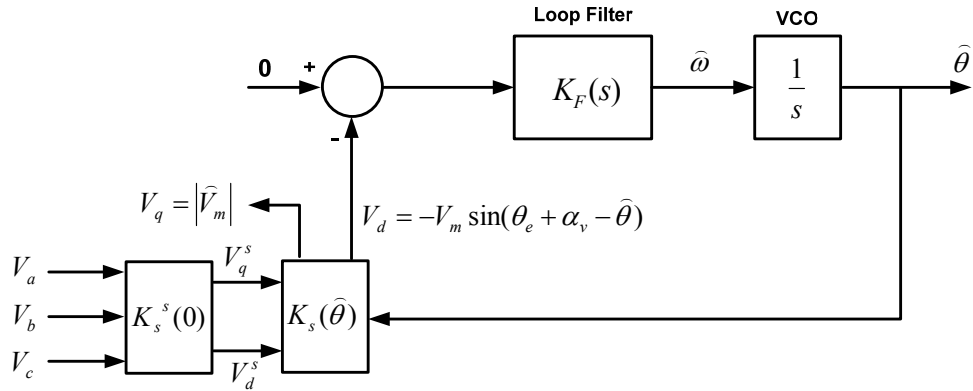


Figure 5.38 PLL system diagram in the experiment

should be noted that both frequency and the magnitude of output voltage can be controlled using the modulation index waveform.

For the second test under the load, an inductive load ($L = 10mH$) is added to the resistive load. As shown in Figure 5.37, channel 4 presents the phase voltage of the load and channel 3 presents the current waveform of the total RL load (the magnitude of the current is 42 times of the real value).

5.6 Phase Lock Loop

Due to high application of power electronic devices, especially three phase DC/AC inverters we want to connect them to the power system grid. For this purpose, like typical synchronous generators we need to synchronize the inverter with the grid voltage. This means we should produce the same frequency and voltage magnitude as the grid voltage. To define the frequency and the voltage phase angle of the grid a phase lock loop (PLL) is usually used. In addition the measured angle of the grid or load voltage can be used as the reference frequency for abc to qd-axis transformation of all three phase

parameters. As it is shown in Figure 5.38 the three phase PLL uses measured local load voltage and converts it to qd-axis frame then compares d-axis voltage with zero as a reference. The error passes through a controller and then through a low pass filter to remove noise. The idea of the PLL is to align the voltage to the q-axis and make the d-axis voltage zero; therefore

$$\begin{cases} V_a = V_m \cos(\theta_e + \alpha_v) \\ V_b = V_m \cos(\theta_e + \alpha_v - \frac{2\pi}{3}) \\ V_c = V_m \cos(\theta_e + \alpha_v + \frac{2\pi}{3}) \end{cases} \quad (5.42)$$

$$\begin{bmatrix} f_q \\ f_d \\ f_0 \end{bmatrix} = K_s \begin{bmatrix} f_a \\ f_b \\ f_c \end{bmatrix}, \quad K_s = \frac{2}{3} \begin{bmatrix} \cos(\theta) & \cos(\theta - \frac{2\pi}{3}) & \cos(\theta + \frac{2\pi}{3}) \\ \sin(\theta) & \sin(\theta - \frac{2\pi}{3}) & \sin(\theta + \frac{2\pi}{3}) \\ \frac{1}{2} & \frac{1}{2} & \frac{1}{2} \end{bmatrix}, \quad \theta = \omega t + \theta_0 \quad (5.43)$$

In stationary reference frame ($\theta = 0$)

$$K_s^s = \frac{2}{3} \begin{bmatrix} 1 & -\frac{1}{2} & -\frac{1}{2} \\ 0 & -\frac{\sqrt{3}}{2} & \frac{\sqrt{3}}{2} \end{bmatrix} \quad (5.44)$$

$$\begin{cases} V_q^s = \frac{2}{3}(V_a - \frac{V_b}{2} - \frac{V_c}{2}) \\ V_d^s = \frac{1}{\sqrt{3}}(V_c - V_b) \end{cases} \quad (5.45)$$

$$\begin{cases} V_q^s = \frac{2}{3}(V_a - V_b) + \frac{1}{3}(V_b - V_c) = \frac{2}{3}V_{ab} + \frac{1}{3}V_{bc} \\ V_d^s = -\frac{1}{\sqrt{3}}(V_b - V_c) = -\frac{1}{\sqrt{3}}V_{bc} \end{cases} \quad (5.46)$$

Therefore instead of measuring phase voltages we can measure just two line to line voltages. If transformation angle $\theta = \hat{\theta}$, for transforming from stationary reference frame to synchronous reference frame

$$K_s(\hat{\theta}) = \begin{bmatrix} \cos \hat{\theta} & -\sin \hat{\theta} \\ \sin \hat{\theta} & \cos \hat{\theta} \end{bmatrix} \Rightarrow \begin{cases} V_q = V_q^s \cos \hat{\theta} - V_d^s \sin \hat{\theta} \\ V_d = V_q^s \sin \hat{\theta} + V_d^s \cos \hat{\theta} \end{cases} \quad (5.47)$$

$$\begin{cases} V_q = V_m \cos(\theta_e + \alpha_v - \hat{\theta}) \\ V_d = -V_m \sin(\theta_e + \alpha_v - \hat{\theta}) \end{cases}, \quad \hat{\theta} = \hat{\omega} t + \hat{\theta}_0 \quad (5.48)$$

We assume ($\delta = \theta_e + \alpha_v - \hat{\theta}$)

$$\begin{cases} V_q = V_m \cos \delta \\ V_d = -V_m \sin \delta \end{cases} \quad (5.49)$$

$$\begin{cases} \frac{d\delta}{dt} = \omega_e - \hat{\omega} = \omega_x \\ \frac{d\hat{\theta}}{dt} = \hat{\omega} \end{cases} \quad (5.50)$$

If $V_d = 0 \Rightarrow \sin \delta = 0 \Rightarrow \delta = 0 \Rightarrow \hat{\theta} = \theta_e + \alpha_v$

The inverse qd transformation is

$$\begin{bmatrix} f_a \\ f_b \\ f_c \end{bmatrix} = K_s^{-1} \begin{bmatrix} f_q \\ f_d \\ f_0 \end{bmatrix}, \quad K_s^{-1} = \begin{bmatrix} \cos(\theta) & \sin(\theta) & 1 \\ \cos(\theta - \frac{2\pi}{3}) & \sin(\theta - \frac{2\pi}{3}) & 1 \\ \cos(\theta + \frac{2\pi}{3}) & \sin(\theta + \frac{2\pi}{3}) & 1 \end{bmatrix}, \quad \theta = \omega t + \theta_0 \quad (5.51)$$

$$K_s^{-1}(\hat{\theta}) = \begin{bmatrix} \cos \hat{\theta} & \sin \hat{\theta} \\ -\sin \hat{\theta} & \cos \hat{\theta} \end{bmatrix} \Rightarrow \begin{cases} V_q^s = V_q \cos \hat{\theta} + V_d \sin \hat{\theta} \\ V_d^s = -V_q \sin \hat{\theta} + V_d \cos \hat{\theta} \end{cases} \quad (5.52)$$

To define the abc reference frame voltages from the stationary reference frame values

$$K_s^{s-1} = \begin{bmatrix} 1 & 0 \\ -\frac{1}{2} & -\frac{\sqrt{3}}{2} \\ -\frac{1}{2} & \frac{\sqrt{3}}{2} \end{bmatrix} \Rightarrow \begin{cases} V_a = V_q^s \\ V_b = -\frac{1}{2} V_q^s - \frac{\sqrt{3}}{2} V_d^s \\ V_c = -\frac{1}{2} V_q^s + \frac{\sqrt{3}}{2} V_d^s \end{cases} \quad (5.53)$$

The d-axis voltage equation is

$$V_{mid} = -V_{mi} \sin(\theta_i - \theta_{si}) \quad (5.54)$$

$$\text{If } V_{mid} = 0 \Rightarrow \sin(\theta_i - \theta_{si}) = 0 \Rightarrow \theta_{si} = \theta_i$$

$$e = 0 - V_{mid} = V_{mi} \sin(\theta_i - \theta_{si}) \quad (5.55)$$

If $(\theta_i - \theta_{si})$ is very small we can assume

$$\sin(\theta_i - \theta_{si}) \approx (\theta_i - \theta_{si}) \quad (5.56)$$

$$V_{mi} (\theta_i - \theta_{si}) \frac{K_F(s)}{s} = \theta_{si} \quad (5.57)$$

Therefore one can define the closed loop transfer function and compare its denominator with that of the second order standard Butterworth filter transfer function

$$\frac{\theta_{si}}{\theta_i} = \frac{V_{mi}K_F(s)}{s + V_{mi}K_F(s)} \quad (5.58)$$

$$\frac{\theta_{si}}{\theta_i} = \frac{sV_{mi}k_{Ppll} + V_{mi}k_{Ipll}}{s^2 + sV_{mi}k_{Ppll} + V_{mi}k_{Ipll}} = \frac{2\zeta\omega_{n1} s + \omega_{n1}^2}{s^2 + 2\zeta\omega_{n1} s + \omega_{n1}^2} \quad (5.59)$$

$$k_{Ppll} = \frac{2\zeta\omega_{n1}}{V_{mi}} \quad \text{and} \quad k_{Ipll} = \frac{\omega_{n1}^2}{V_{mi}} \quad (5.60)$$

where ζ is the damping factor and is usually chosen as critical damping factor which is 0.707 and ω_{n1} is the natural frequency and it is chosen as $377(\text{rad}/s)$.

To examine the performance of the designed PLL, a three phase sinusoidal voltage waveform is produced inside the DSP using the sine look up table. The output of the PLL is stored inside the DSP and plotted in MATLAB. Figure 5.39 illustrates the measured frequency and angle of the sample waveform from DSP. In Figure 5.40, the original and the reproduced waveform from the measured frequency and angle of the PLL are compared. This figure shows that the PLL precisely tracks the reference.

Figure 5.41 shows the transformed qd-axis of the voltage. Since the original signal is purely sinusoidal, the q-axis voltage is exactly one per unit and d-axis voltage is zero constantly.

5.7 Connection of Three Phase Inverter to the Grid

The main objective of the inverter in grid connected mode is to control the output active and reactive power. The voltage magnitude and frequency is adopted from the

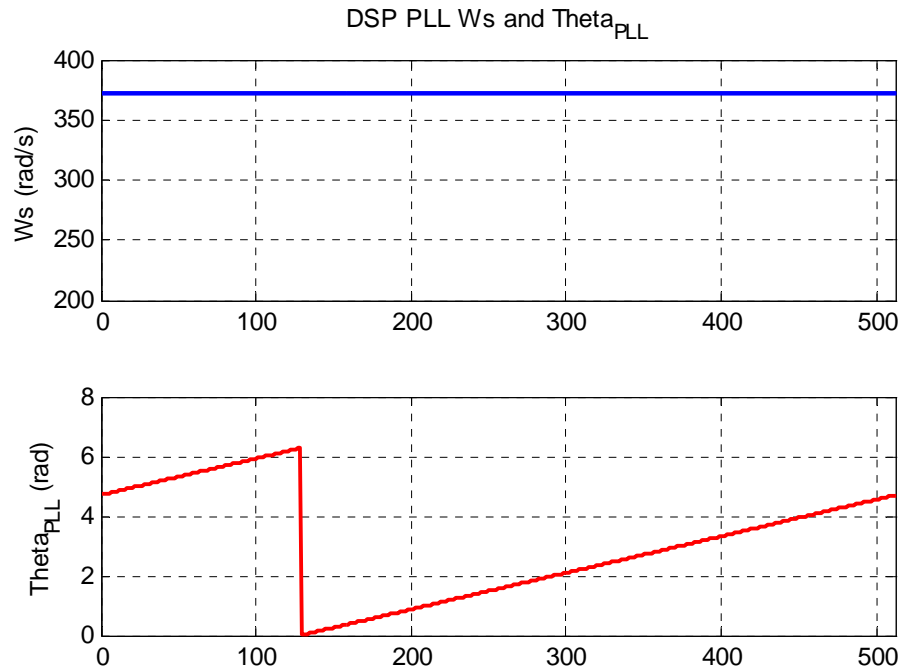


Figure 5.39 Experimental PLL measured frequency and angle of the sample voltage

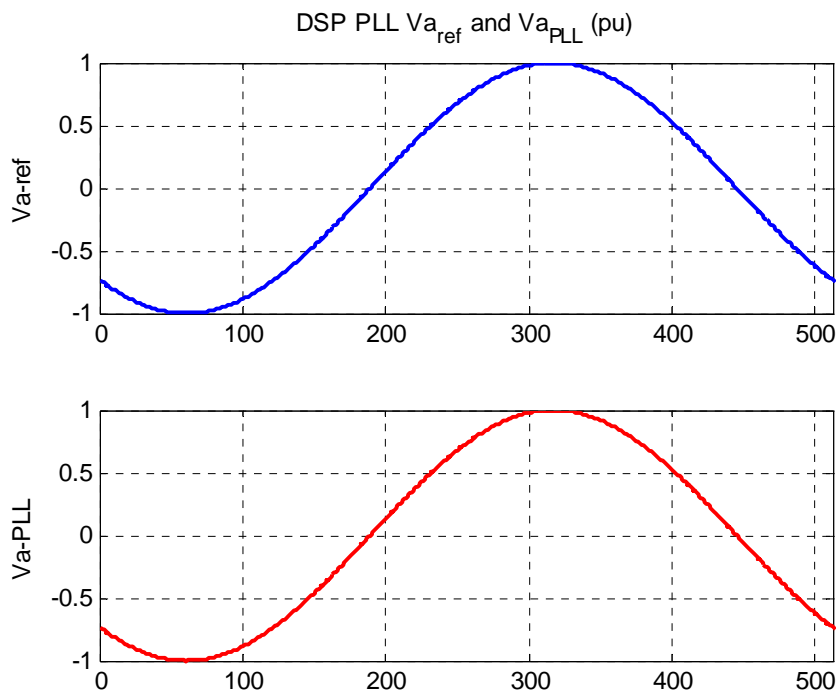


Figure 5.40 Original and reproduced voltage from the PLL angle and frequency

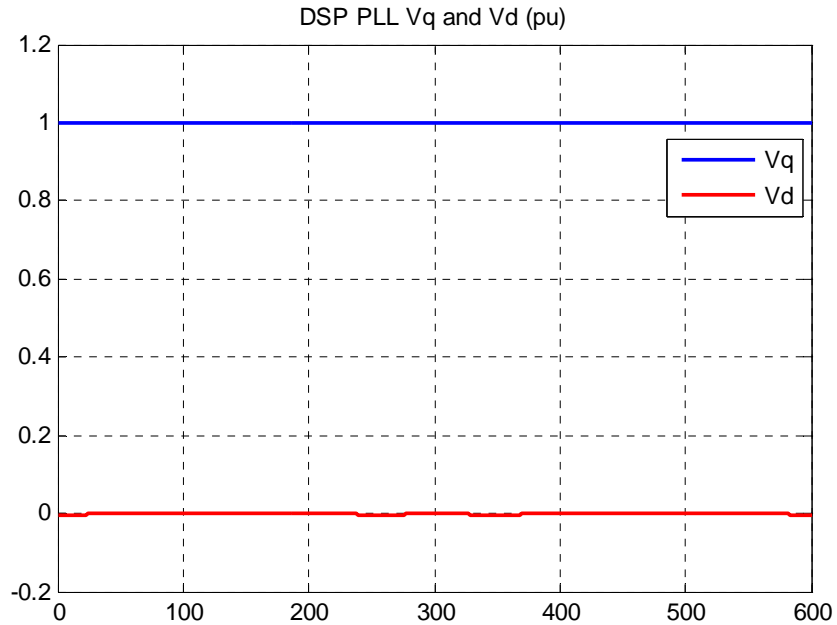


Figure 5.41 Transformed qd-axis of the sample voltage using PLL angle

grid. In this report the troubleshooting for abc-axis to qd-axis synchronous reference frame for the inverter current is investigated. Using the AC designed voltage sensors and digital signal processor analog to digital converter port, the actual voltage signals have been transferred into the DSP. The PLL measures and tracks the actual voltage frequency and angle. This angle is used as a reference for qd-axis conversion of all parameters. Furthermore the AC current sensors have been designed for this control purpose.

5.7.1 Study System

Figure 5.42 shows the study system which includes a three phase inverter connected to a linear RC load. This system is studied as experimental setup for testing the operation of the programmed software PLL inside DSP F28335. The switching pulses are

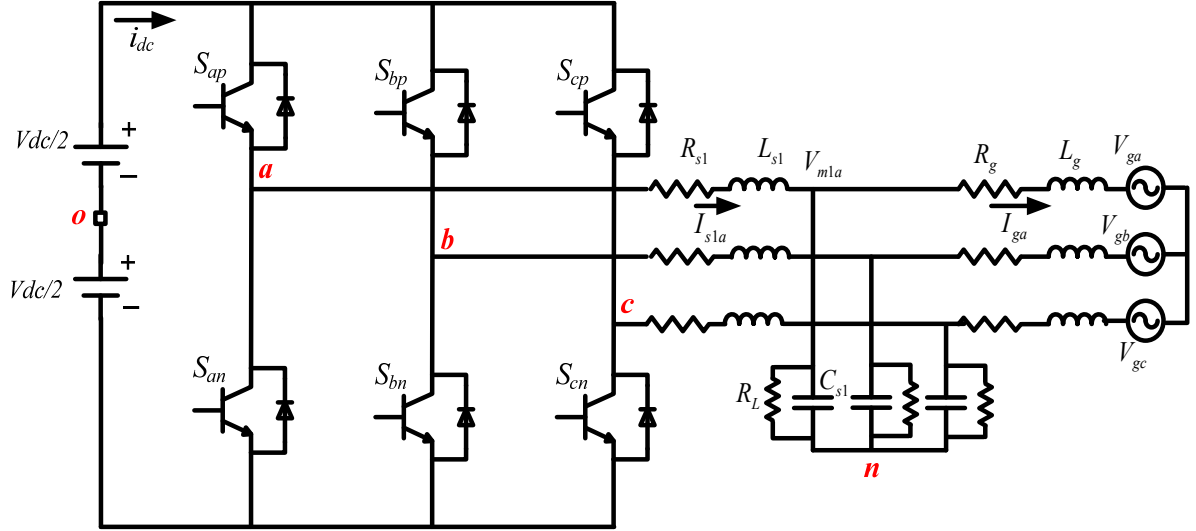


Figure 5.42 Three phase inverter connected to the grid and resistive load.

Table 5.3 The study system parameters

V_{dc}	100 V	C_{s1}	$30\mu F$
R_{s1}	0.15Ω	L_{s1}	$10mH$
R_L	42Ω	V_g	$20\sqrt{\frac{2}{3}} V$

applied from DSP hardware. Table 5.3 shows the parameters of the system. The model equations of the system are as follows: The output voltage equations of inverter

$$\begin{cases} \frac{V_{dc}}{2}(2S_{ap} - 1) = R_{s1}I_{s1a} + L_{s1}pI_{s1a} + V_{m1a} + V_{no} \\ \frac{V_{dc}}{2}(2S_{bp} - 1) = R_{s1}I_{s1b} + L_{s1}pI_{s1b} + V_{m1b} + V_{no} \\ \frac{V_{dc}}{2}(2S_{cp} - 1) = R_{s1}I_{s1c} + L_{s1}pI_{s1c} + V_{m1c} + V_{no} \end{cases} \quad (5.61)$$

where R_{s1} , L_{s1} and V_{m1abc} are resistance, inductance of the filter and phase voltage of the capacitor.

Capacitor voltage equations

$$\begin{cases} C_{s1}pV_{m1a} = I_{s1a} - \frac{V_{m1a}}{R_L} - I_{ga} \\ C_{s1}pV_{m1b} = I_{s1b} - \frac{V_{m1b}}{R_L} - I_{gb} \\ C_{s1}pV_{m1c} = I_{s1c} - \frac{V_{m1c}}{R_L} - I_{gc} \end{cases} \quad (5.62)$$

The grid equations are

$$\begin{cases} R_g I_{ga} + L_g pI_{ga} = V_{m1a} + V_{ga} \\ R_g I_{gb} + L_g pI_{gb} = V_{m1b} + V_{gb} \\ R_g I_{gc} + L_g pI_{gc} = V_{m1c} + V_{gc} \end{cases} \quad (5.63)$$

The input current equation of the system is

$$I_{dc} = S_{ap}I_{s1a} + S_{bp}I_{s1b} + S_{cp}I_{s1c} \quad (5.64)$$

In Figure 5.43 the single line diagram of the three phase inverter during the connection to the grid is shown. An AC voltage sensor is designed to measure and send the sensed line to line voltages (V_{m1}) to the digital signal processor (DSP) unit.

Figure 5.44 illustrates the structure of PCB board for the designed AC voltage sensor. Because the analog to digital converter of the DSP just accepts the positive voltages, the output of the voltage sensor which is between -1.5V to 1.5V should be increased to be between 0 to 3V. For this purpose a precise 1.5V DC offset is produced using a programmable shunt regulator (LM431). An opamp added this offset to the output of the voltage sensor. Therefore the input AC voltage magnitude of 0 to 250V is converted to 0 to 1.5V in the output of the voltage sensor.

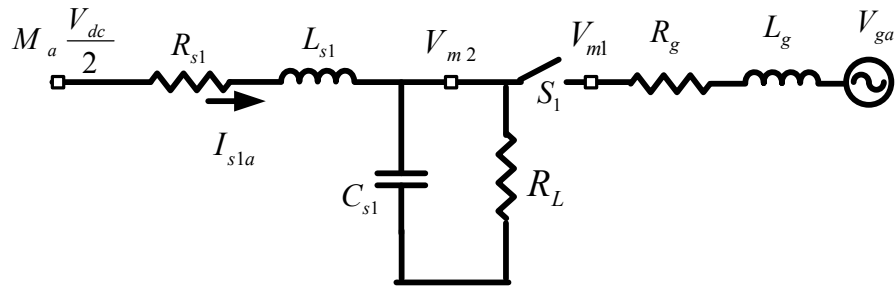


Figure 5.43 Single line diagram of the study system in connection to the grid.

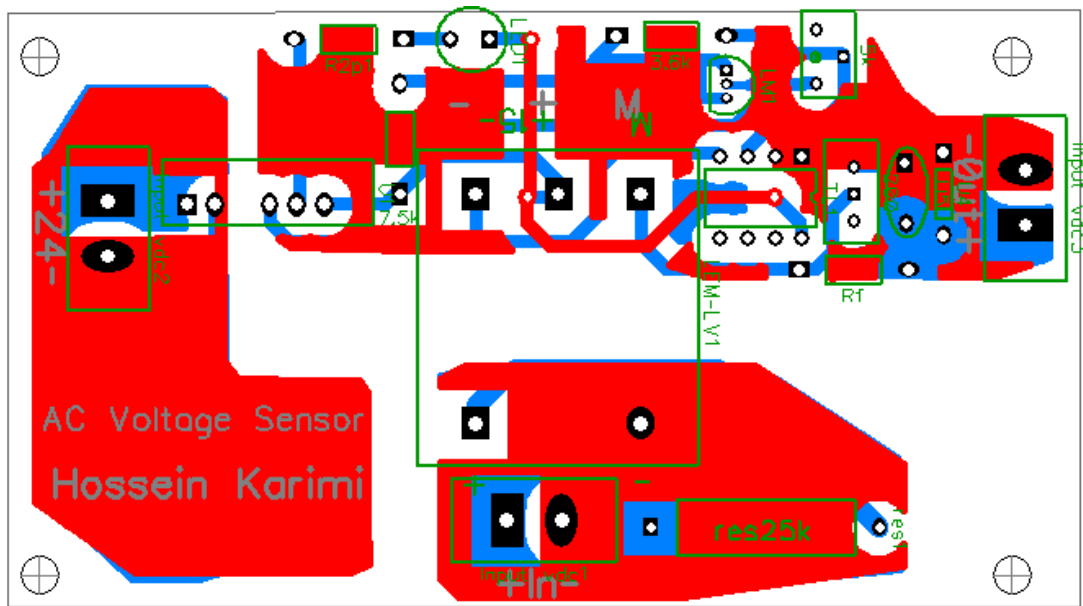


Figure 5.44 Designed PCB board for AC voltage sensor.

The measured frequency of the grid using a PLL is shown in Figure 5.45. In addition the transformed voltage of the grid to qd-axis format using the measures PLL angle and frequency is illustrated in Figure 5.46.

After defining the frequency and phase angle of the grid voltage, a DC voltage is applied to the input of the three phase inverter and the output voltage of the inverter is produced based on that angle and frequency. The RLC filter attenuates the high switching frequency ripples of the voltage and getting a sinusoidal waveform in the output of

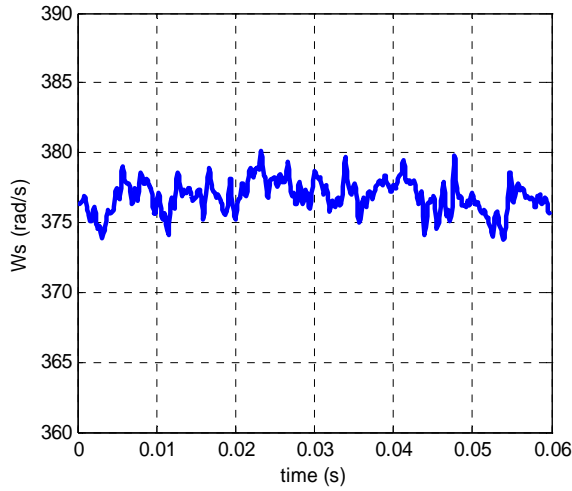


Figure 5.45 The measure angular frequency of the grid using PLL

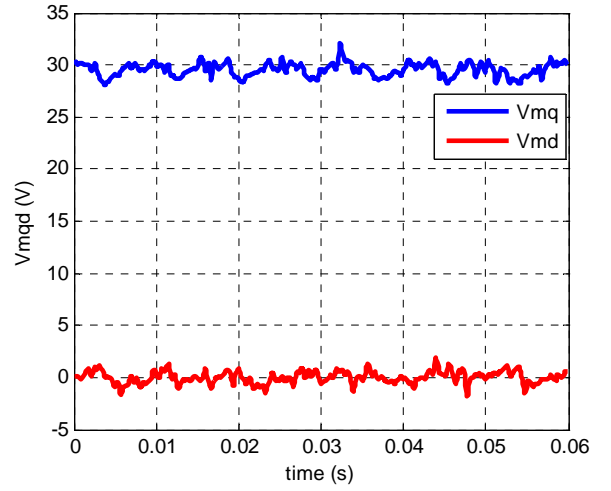


Figure 5.46 The measured line to line grid voltage transformed to qd-axis

inverter at the point of common coupling (PCC). To make two voltages of V_{m1} and V_{m2} on the two sides of the connection switch as close as possible in both magnitude and phase angle, the effect of filter is also included in calculation of inverter modulation indices. In qd-axis format

$$\begin{cases} M_{q1} = \frac{2}{V_{dc}} (V_{m1q} + L_1 \omega_s I_{s1d} + R_1 I_{s1q}) \\ M_{d1} = \frac{2}{V_{dc}} (V_{m1d} - L_1 \omega_s I_{s1q} + R_1 I_{s1d}) \end{cases} \quad (5.65)$$

We need to measure the current of the RL filter. A three phase AC current sensor is designed. Figure 5.47 shows the schematic of an AC current sensor with a 1.5V DC offset to produce positive output all of the time in the range of zero to 25 A input AC current. The designed PCB board of the three phase current sensor is shown in Figure 5.48.

In Figure 5.49 the voltage on both sides of the switch (S_1) are presented. As presented in Figure 5.49 using measured currents and voltages and (5.65). There is still a

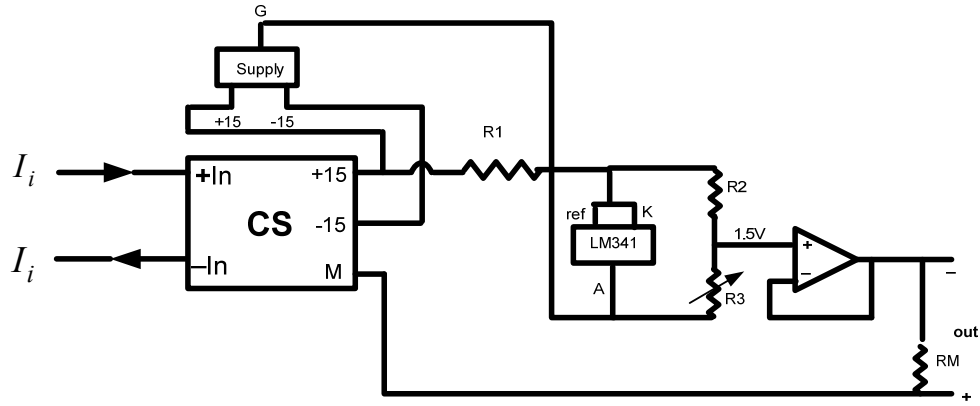


Figure 5.47 Schematic diagram of AC current sensor

slight difference between the voltage magnitude and phase angle in both sides of the connection switch at PCC. Besides the inaccurate values of the system parameters and tolerance in measurements two main issues are investigated. The first one is the delay due to sensors and especially the digital filter inside the DSP which affects the phase angle. The second one is the effect of dead-time applied to IGBT switches which is discussed as follows.

To avoid the short circuit in one leg and switch at zero voltage to reduce switching losses, the dead-time should be applied to power electronic switches. In Figure 5.50 the output voltage in a constant switching frequency and different modulation index and DC-link voltage is illustrated. The only difference of Figure 5.50(a) and (c) is the applied dead time. It can be seen that in the second case with dead time the output voltage is less. In Figure 5.50(b) and (d) half of the previous modulation index is applied to get the same voltage and (theoretically) the DC-link voltage is doubled. As it happens in the simulation, Figure 5.50(a) and (b) have the same output but Figure 5.50(d) with even with the same dead-time has less output from Figure 5.50(d). As a result, applying dead-time, not only reduces the output voltage magnitude but also result in higher DC-link

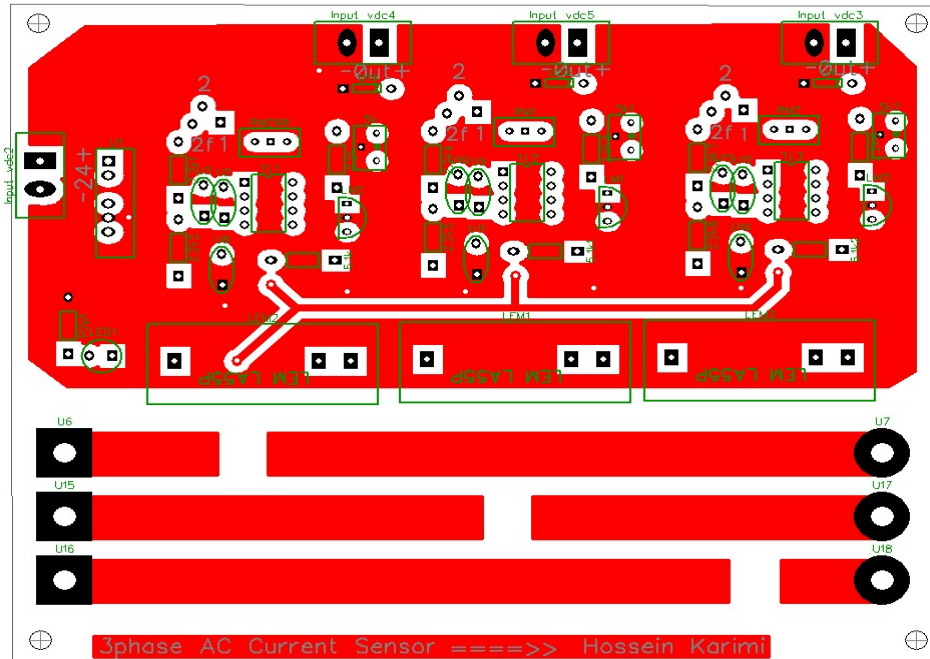


Figure 5.48 PCB board of three AC current sensors.

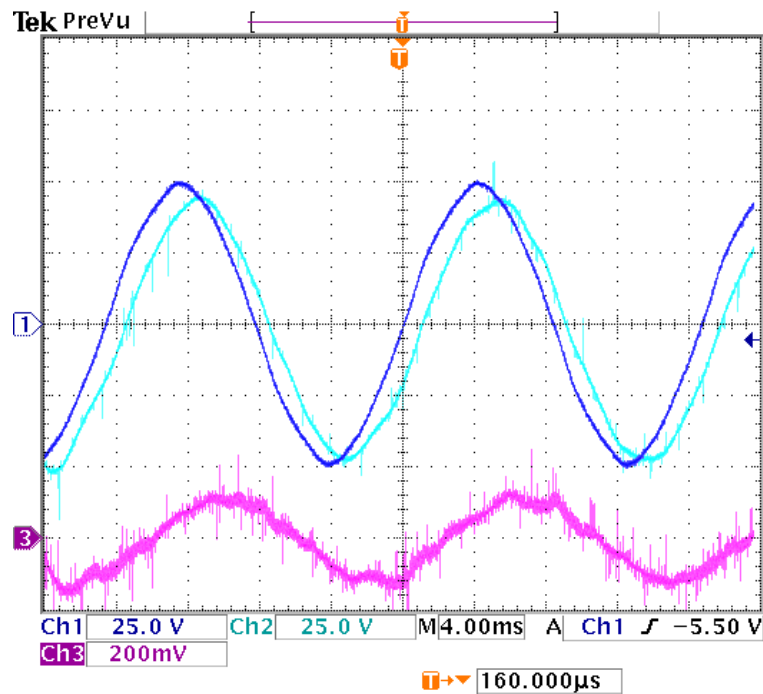


Figure 5.49 Experimental measured voltages on two sides of the switch before connection. (Ch1: Vm1 Ch4:Vm2 Ch3:Is1e)

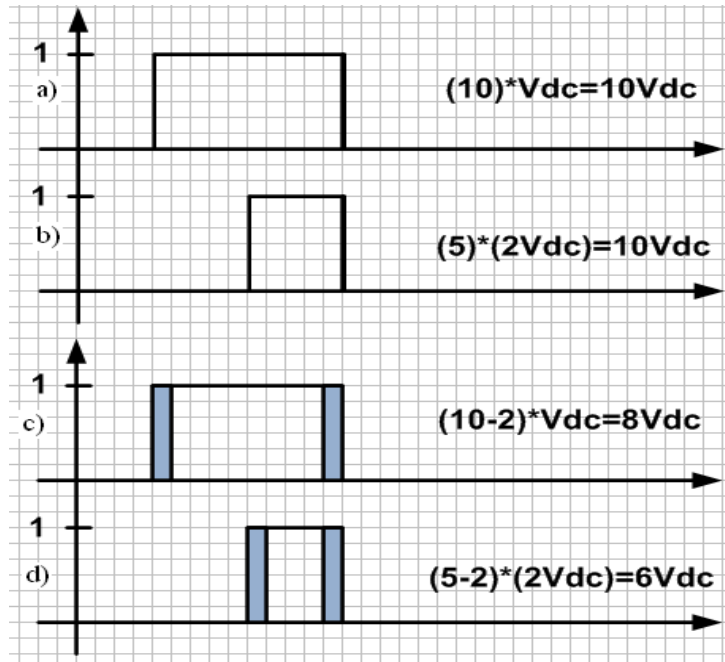


Figure 5.50 Effect of dead-time in a fixed frequency and different V_{dc} and M_a

voltage or higher frequencies. In this section, to reduce this effect, the dead-time is decreased from $4\mu\text{s}$ to the minimum recommended value for the selected IGBT to $2\mu\text{s}$ from each side as shown in Figure 5.51. It should be noted that the output of driver circuit is complement of the shown signals.

Figure 5.52 shows the result of the aforementioned two corrections even in higher DC-link voltage. So the two voltages are synchronized precisely.

5.7.2 Power Control of Inverter in Grid Connected Mode

After synchronization and connection of the inverter to the grid the output active and reactive power of the inverter can be controlled. The power equations of the inverter at PCC are as follows:

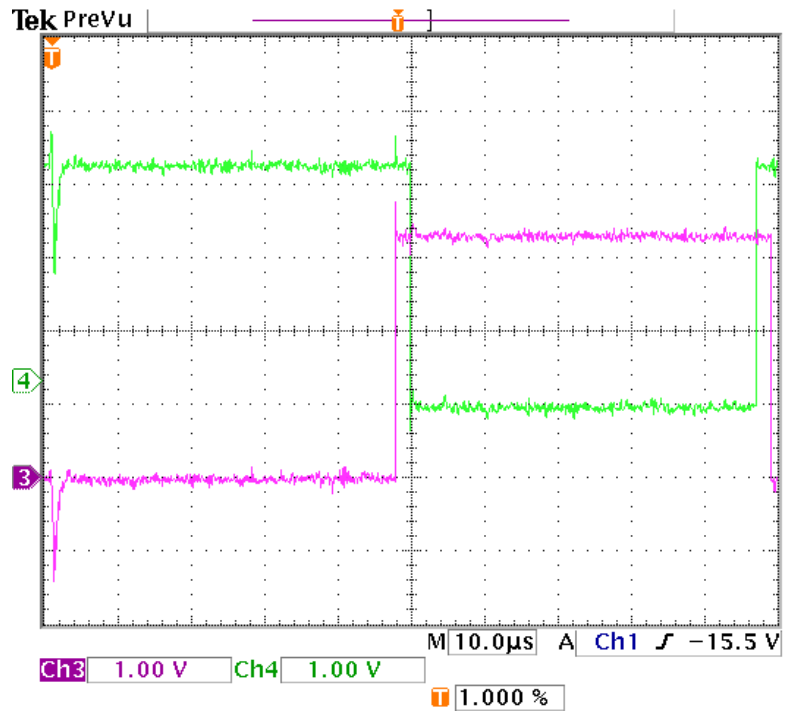


Figure 5.51 Reduced dead-time in the output of DSP PWM signals to $2\mu\text{s}$

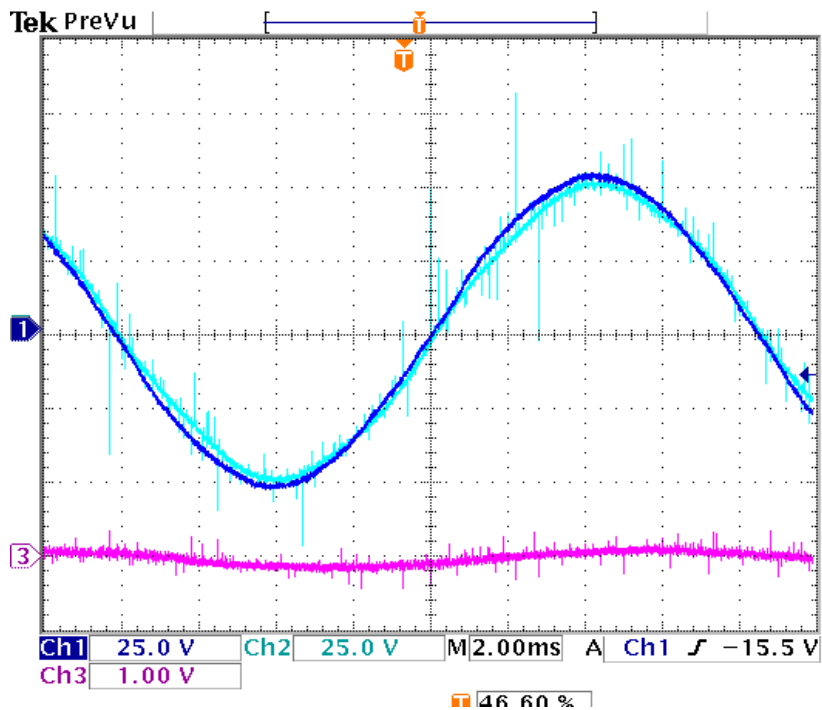


Figure 5.52 Experimental measured open loop voltages after applying correction.
 (Ch1: Vm1 Ch4: Vm2 Ch3: Is1c)

$$\begin{cases} P_{s1} = \left(\frac{3}{2}\right)(V_{m1q}I_{s1q} + V_{m1d}I_{s1d}) \\ Q_{s1} = \left(\frac{3}{2}\right)(V_{m1q}I_{s1d} - V_{m1d}I_{s1q}) \end{cases} \quad (5.66)$$

In grid connected mode the qd-axis of the voltage is known and adopted from the grid therefore we can define the current references from the output power references and measured qd-axis voltages.

$$\begin{cases} I_{s1q}^* = \frac{P_{ref}V_{m1q} - Q_{ref}V_{m1d}}{V_{m1q}^2 + V_{m1d}^2} \\ I_{s1d}^* = \frac{P_{ref}V_{m1d} + Q_{ref}V_{m1q}}{V_{m1q}^2 + V_{m1d}^2} \end{cases} \quad (5.67)$$

To design the current controller, from the dynamic equation of the system

$$\begin{cases} sL_{s1}I_{s1q} + R_{s1}I_{s1q} = \frac{M_{q1}}{2}V_{dc} - V_{m1q} - \omega_{s1}L_{s1}I_{s1d} = k_{s1q}(s)(I_{s1q}^* - I_{s1q}) = \sigma_{s1q} \\ sL_{s1}I_{s1d} + R_{s1}I_{s1d} = \frac{M_{d1}}{2}V_{dc} - V_{m1d} + \omega_{s1}L_{s1}I_{s1q} = k_{s1d}(s)(I_{s1d}^* - I_{s1d}) = \sigma_{s1d} \end{cases} \quad (5.68)$$

Applying the PI controller, the current controllers transfer functions are

$$\frac{I_{s1q}}{I_{s1q}^*} = \frac{k_{s1q}(s)}{sL_{s1} + R_{s1} + k_{s1q}(s)} = \frac{1}{1 + \tau_{s1}s} = \frac{1}{1 + \frac{sL_{s1} + R_{s1}}{k_{s1q}(s)}} \quad (5.69)$$

$$\frac{I_{s1d}}{I_{s1d}^*} = \frac{k_{s1d}(s)}{sL_{s1} + R_{s1} + k_{s1d}(s)} = \frac{1}{1 + \tau_{s1}s} = \frac{1}{1 + \frac{sL_{s1} + R_{s1}}{k_{s1d}(s)}} \quad (5.70)$$

where

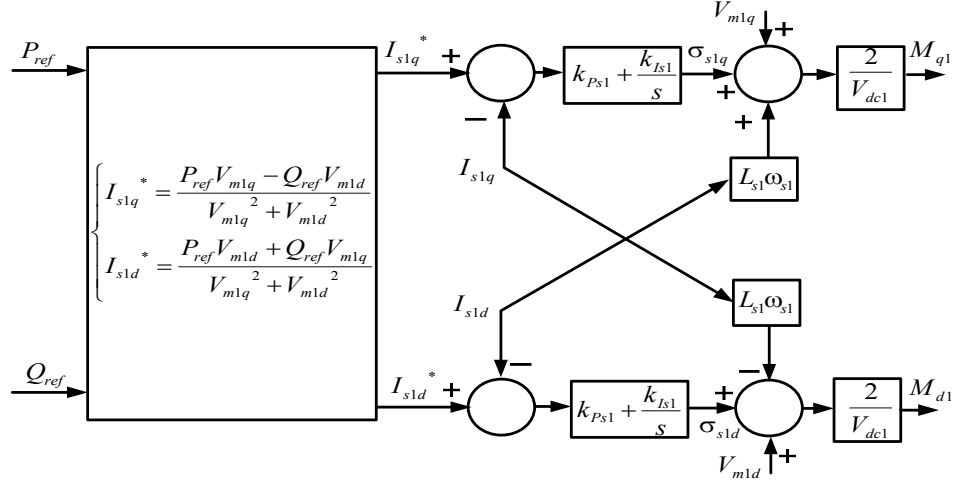


Figure 5.53 Inverter current control structure

$$k_{s1q}(s) = k_{s1q}(s) = \frac{sL_{s1} + R_{s1}}{\tau_{s1}s} = k_{Ps1} + \frac{k_{Is1}}{s} \quad (5.71)$$

So we can calculate the coefficients of PI current controller as

$$\begin{cases} k_{Ps1} = \frac{L_{s1}}{\tau_{s1}} = 81.68 \\ k_{Is1} = \frac{R_{s1}}{\tau_{s1}} = 942.47 \end{cases} \quad (5.72)$$

where for fast response the time constant is chosen to be five times of switching frequency time intervals

$$\tau_{s1} = 5 \frac{1}{2\pi f_{sw}} \quad (5.73)$$

The modulation indices which are the outputs of the controllers are given as

$$\begin{cases} M_{q1} = \frac{2}{V_{dc1}} (\sigma_{s1q} + V_{m1q} + L_{s1}\omega_{s1}I_{s1d}) \\ M_{d1} = \frac{2}{V_{dc1}} (\sigma_{s1d} + V_{m1d} - L_{s1}\omega_{s1}I_{s1q}) \end{cases} \quad (5.74)$$

The closed loop current and power control of the system is illustrated in Figure 5.53. After applying the controller inside DSP, Figure 5.54 shows the line to line voltage at PCC after connection and the phase current when the active power is set to 50W and reactive power is set to 5 Var.

In Figure 5.55, the values of active and reactive power references are changed to 100W and 10Var respectively. As it is shown, when the power output reference has been doubled the value of current magnitude drawn from the inverter is two times of the previous case. To show the dynamic response of the controller, 600 samples at the moment of power change is stored inside DSP. In Figure 5.56, the controller follows the reference active and reactive power in a very short transient. Due to the small amount of reactive power the transients are more significant.

Since the inverter and the whole setup is designed for higher voltage and power, the experiment is repeated in higher DC-link and grid voltages. The presented active and reactive powers in Figure 5.57 at higher voltage have more fluctuations. The amount of fluctuations in higher power isn't acceptable and makes the controller to fail tracking the references.

For solving the problem, the output of current sensors, inside the DSP after passing a low pass digital filter are studied. Therefore, in the first attempt the current sensors of the three phase have been calibrated. Even after calibration, the same problem occurred. Thus in the next step, the saved data was synthesized and transformed inside MATLAB software to be sure about the qd-axis transformation. Getting the same result as the experiment encouraged the study of the output line to line voltage data of the inverter from the oscilloscope inside MATLAB.

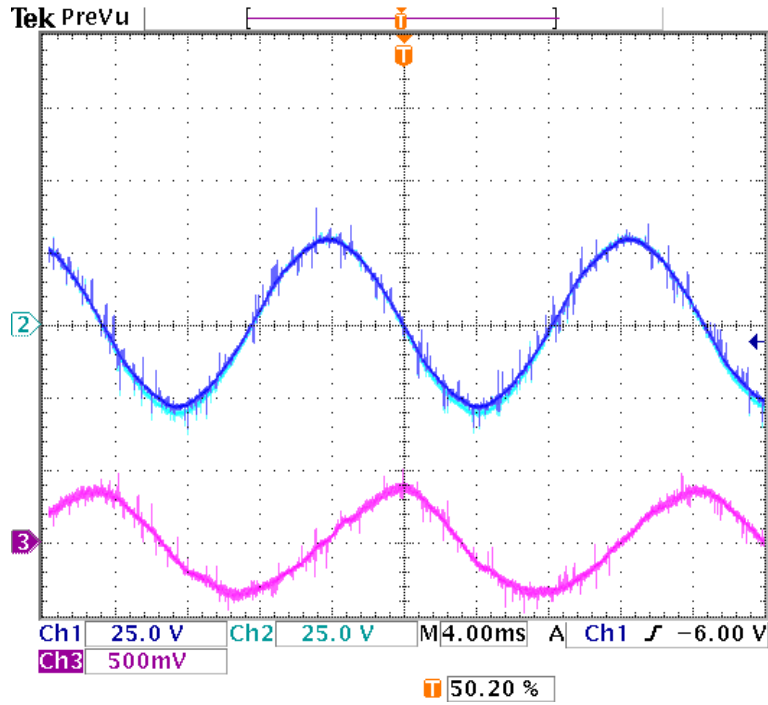


Figure 5.54 The experimental grid voltage (Ch1) and inverter output phase current (Ch3),
 $P_{ref} = 50W, Q_{ref} = 5Var$

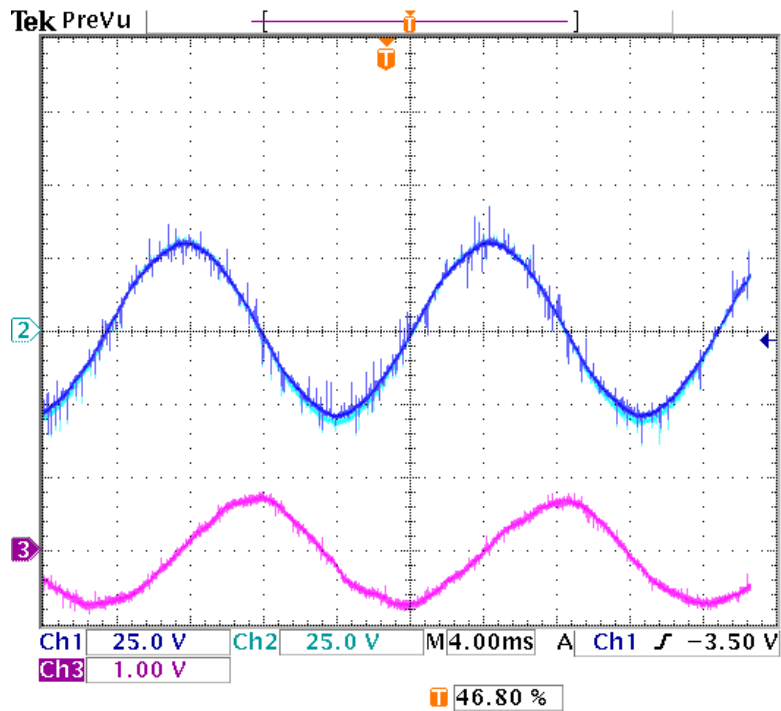


Figure 5.55 The experimental grid voltage (Ch1) and inverter output phase current (Ch3),
 $P_{ref} = 100W, Q_{ref} = 10Var$

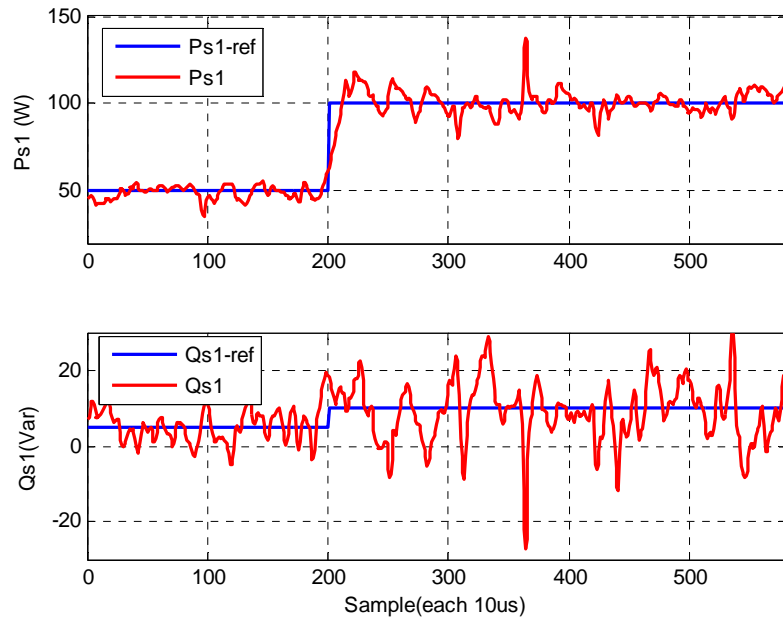


Figure 5.56 Experimental active and reactive power of the inverter in closed loop control.
 ($V_{dc}=100\text{ V}$ and $V_{m1-rms}=36\text{ V}$)

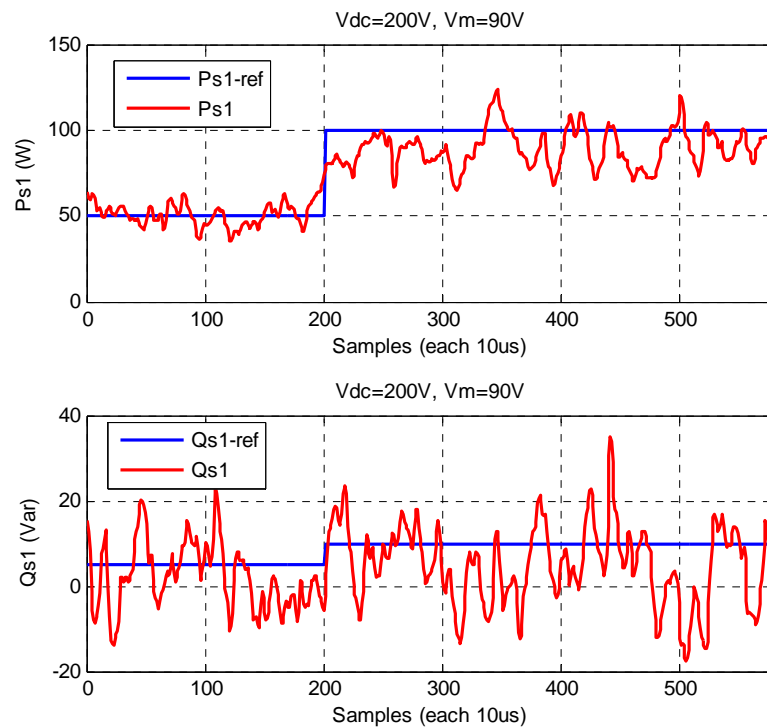


Figure 5.57 Experimental active and reactive power of the inverter at higher voltage.
 ($V_{dc}=200\text{ V}$ and $V_{m1-rms}=90\text{ V}$)

Figure 5.58 shows that this waveform has a fifth harmonic. To reduce the harmonic, the switching frequency of the inverter from asynchronous 5kHz is changed to synchronous 4860Hz (81×60) which is a multiply of three times the modulation signal (grid) frequency (60Hz). The result is presented in Figure 5.59 which shows fewer harmonics inside the voltage. Actually, harmonics in the second graph are spread around the switching frequency which can be removed with small low pass filters. The DC harmonics in the both last graphs are due to DC offset in the differential probes of oscilloscope.

5.8 Comparison of PLL and EPLL

In most power system applications the current and voltage magnitudes and angle should be measured and controlled. Those parameters are needed even to control the active and reactive power or the torque in the electrical machine.

Phase lock loop (PLL) has been used widely to define the frequency and the angle of the voltage either in single phase or three phase systems. This angle is used as a reference to convert the three phase parameters from abc reference frame to qd-axis synchronous reference frame. In qd-axis synchronous reference frame the parameters are DC quantities so the linear controllers can be applied to them.

One of the challenges for converting the parameters to qd-axis reference frame is the noise. Therefore, the output measured signals can not be constant as we expect in the experiment.

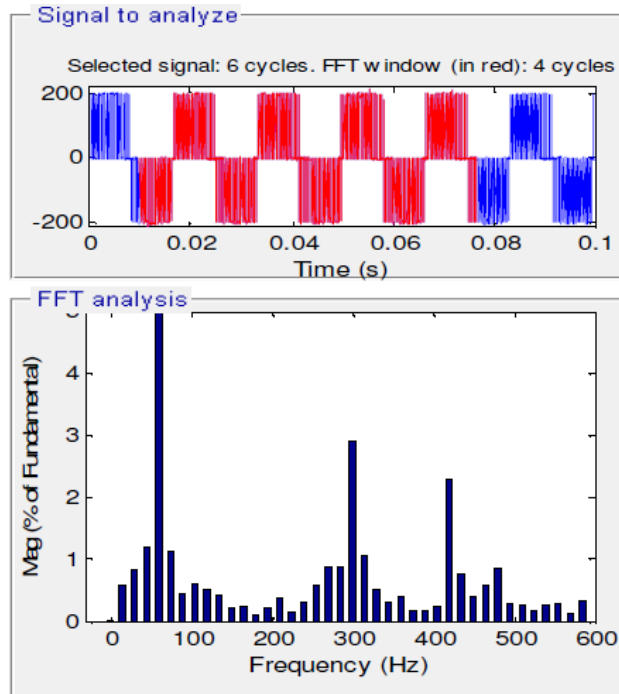


Figure 5.58 Harmonic spectrum of line to line inverter voltage at $f_{sw}=5\text{KHz}$, fundamental frequency is 20 times reduced scale.

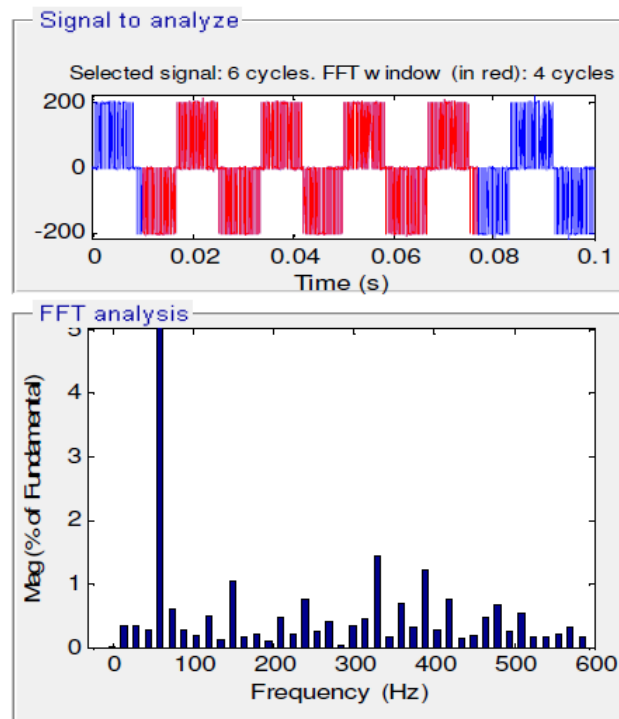


Figure 5.59 Harmonic spectrum of line to line inverter voltage at $f_{sw}=4860\text{ Hz}$, fundamental frequency is 20 times reduced scale.

In this section, two different solutions have been proposed. First, a digital low pass filter is added inside DSP program to remove the higher frequency noise. Then the typical phase lock loop (PLL) is applied. In the second solution, the enhanced phase lock loop (PLL) is applied to the actual signals of the experimental setup.

The structure and design process of the typical PLL inside the DSP are explained in section 5.6. Another type of PLL, adapted from signal processing concepts, which also operates as a band pass filter is called enhanced phase lock loop (EPLL).

Based on [118] the enhanced PLL is designed for single phase systems but using four of them we can define the frequency, ω , angle, θ , and amplitude of any three phase parameter, even in unbalanced condition. The advantage of EPLL is that, it follows the positive sequence of the input signal and in addition, it behaves like a band pass filter (BPF).

The controllers are trying to produce zero error

$$e = u(t) - y(t) \tag{5.75}$$

where the input and the output of the EPLL are

$$\begin{cases} u(t) = A_o \sin(\omega_o t + \delta_o) = A_o \sin(\theta_o) \\ y(t) = A \sin(\omega t + \delta) = A \sin(\theta) \end{cases} \tag{5.76}$$

From gradient decent method if the following is defined [118]

$$J = e^2 = (u(t) - y(t))^2 \tag{5.77}$$

The following criteria should me met to minimize the error

$$\begin{cases} pA = -\mu_{11} \left(\frac{\partial J}{\partial A} \right) \\ p\delta = -\mu_{21} \left(\frac{\partial J}{\partial \delta} \right) \\ p\theta = p \left(\int^t \omega(\tau) d\tau + \mu_{31} \delta \right) = \Delta\omega + \omega_o + \mu_{31} p\delta \end{cases} \quad (5.78)$$

$$\begin{cases} pA = \mu_{11} e \sin(\theta) \\ p\omega = \mu_{21} A e \cos(\theta) \\ p\theta = \mu_{21} \mu_{31} A e \cos(\theta) + \Delta\omega + \omega_o \end{cases} \quad (5.79)$$

To design the controller parameters of EPLL from the dynamic equations of the amplitude controller

$$pA = \mu_{11} e \sin(\theta) = \mu_{11} \sin(\theta) (A_o \sin(\theta_o) - A \sin(\theta)) \quad (5.80)$$

If we consider the angle control has already reached the reference

$$pA = \frac{\mu_{11}}{2} (A_o - A) - \frac{\mu_{11}}{2} \cos(2\theta_o) (A_o - A) \quad (5.81)$$

Therefore the linear approximation of the amplitude controller yields to

$$H_1 = \frac{A}{A_o} = \frac{\frac{\mu_{11}}{2}}{p + \frac{\mu_{11}}{2}} \quad (5.82)$$

To design the phase and frequency controllers, if we consider the amplitude control has already reached the reference, from their dynamic equations

$$\begin{cases} p\Delta\omega = A^2 \mu_{21} \cos(\theta) (\sin(\theta_o) - \sin(\theta)) \\ p\theta = \omega_o + \Delta\omega + A^2 \mu_{21} \mu_{31} \cos(\theta) (\sin(\theta_o) - \sin(\theta)) \end{cases} \quad (5.83)$$

$$\begin{cases} p\Delta\omega = \frac{A^2\mu_{21}}{2}(-\sin(\theta - \theta_o) + \sin(\theta + \theta_o) + \sin(2\theta)) \\ p\theta = \omega_o + \Delta\omega + \frac{A^2\mu_{21}\mu_{31}}{2}(-\sin(\theta - \theta_o) + \sin(\theta + \theta_o) + \sin(2\theta)) \end{cases} \quad (5.84)$$

Due to the closed loop control, the estimated and actual angles are very close thus

$\sin(\theta - \theta_o) \approx (\theta - \theta_o)$, in addition from the linear approximation of the above equation

$$\begin{bmatrix} p\Delta\omega \\ p\theta \end{bmatrix} = \begin{bmatrix} 0 & -\frac{A^2\mu_{21}}{2} \\ 1 & -\frac{A^2\mu_{21}\mu_{31}}{2} \end{bmatrix} \begin{bmatrix} \Delta\omega \\ \theta \end{bmatrix} + \begin{bmatrix} \frac{A^2\mu_{21}}{2} \\ \frac{A^2\mu_{21}\mu_{31}}{2} \end{bmatrix} \theta_o + \begin{bmatrix} 0 \\ \omega_o \end{bmatrix} \quad (5.85)$$

The characteristic equation is

$$|\lambda_1 I - A_1| = \lambda_1^2 + \frac{A^2\mu_{21}\mu_{31}}{2}\lambda_1 + \frac{A^2\mu_{21}}{2} = S^2 + 2\xi_1\omega_o + \omega_o^2 \quad (5.86)$$

Therefore two of the parameters of the EPLL can be defined as

$$\begin{cases} \mu_{21} = \frac{2\omega_o^2}{A^2} \\ \mu_{31} = \frac{4\xi_1\omega_o}{A^2\mu_{21}} \end{cases} \quad (5.87)$$

In a general case for a three phase system when the three phases are unbalanced

$$\begin{cases} pA_a = \mu_{11a}e_a \sin(\theta_a) \\ pA_b = \mu_{11b}e_b \sin(\theta_b) \\ pA_c = \mu_{11c}e_c \sin(\theta_c) \end{cases} \quad (5.88)$$

$$\begin{cases} p\omega_a = \mu_{21a}A_a e_a \cos(\theta_a) \\ p\omega_b = \mu_{21b}A_b e_b \cos(\theta_b) \\ p\omega_c = \mu_{21c}A_c e_c \cos(\theta_c) \end{cases} \quad (5.89)$$

$$\begin{cases} p\theta_a = \mu_{21a}\mu_{31a}A_a e_a \cos(\theta_a) + \Delta\omega_a + \omega_{oa} \\ p\theta_b = \mu_{21b}\mu_{31b}A_b e_b \cos(\theta_b) + \Delta\omega_b + \omega_{ob} \\ p\theta_c = \mu_{21c}\mu_{31c}A_c e_c \cos(\theta_c) + \Delta\omega_c + \omega_{oc} \end{cases} \quad (5.90)$$

The designed parameters for the unbalanced three phase system

$$\begin{cases} \mu_{2a} = \frac{2\omega_o^2}{A_a^2} \\ \mu_{2b} = \frac{2\omega_o^2}{A_b^2} \\ \mu_{2c} = \frac{2\omega_o^2}{A_c^2} \end{cases} \quad (5.91)$$

$$\begin{cases} \mu_{3a} = \frac{4\xi_1\omega_o}{A_a^2\mu_{21a}} \\ \mu_{3b} = \frac{4\xi_1\omega_o}{A_b^2\mu_{21b}} \\ \mu_{3c} = \frac{4\xi_1\omega_o}{A_c^2\mu_{21c}} \end{cases} \quad (5.92)$$

From (5.91) and (5.92), for the unbalanced three phase system first of all the frequency and angle controller parameters are coupled and secondly related to the magnitude of each phase. So in an unbalanced system different controllers should be applied. To solve this problem if the structure of the controller is changed and the dynamic equations of the EPLL are rewritten as follows:

$$\begin{cases} pA = \mu_1 e \sin(\theta) \\ p\omega = \mu_2 \frac{e}{A} \cos(\theta) \\ p\theta = \mu_3 \frac{e}{A} \cos(\theta) + \Delta\omega + \omega_o \end{cases} \quad \text{and} \quad \begin{cases} \mu_1 = \mu_{11} \\ \mu_2 = A^2 \mu_{21} \\ \mu_3 = A^2 \mu_{21} \mu_{31} \end{cases} \quad (5.93)$$

From (5.93) the redesigned structure of the EPLL for a single phase system is shown in Figure 5.60. It has three parameter controllers. The control of amplitude is almost independent of the phase angle and frequency control. To design the controller parameters of EPLL from the dynamic equations of the amplitude controller

$$pA = \mu_1 e \sin(\theta) = \mu_1 \sin(\theta)(A_o \sin(\theta_o) - A \sin(\theta)) \quad (5.94)$$

If we consider the angle control has already reached the reference

$$pA = \frac{\mu_1}{2}(A_o - A) - \frac{\mu_1}{2} \cos(2\theta_o)(A_o - A) \quad (5.95)$$

Therefore the linear approximation of the amplitude controller yields to

$$H_1 = \frac{A}{A_o} = \frac{\frac{\mu_1}{2}}{p + \frac{\mu_1}{2}} \quad (5.96)$$

To design the phase and frequency controllers, if we consider the amplitude control has already reached the reference, from their dynamic equations

$$\begin{cases} p\Delta\omega = \mu_2 \cos(\theta)(\sin(\theta_o) - \sin(\theta)) \\ p\theta = \omega_o + \Delta\omega + \mu_3 \cos(\theta)(\sin(\theta_o) - \sin(\theta)) \end{cases} \quad (5.97)$$

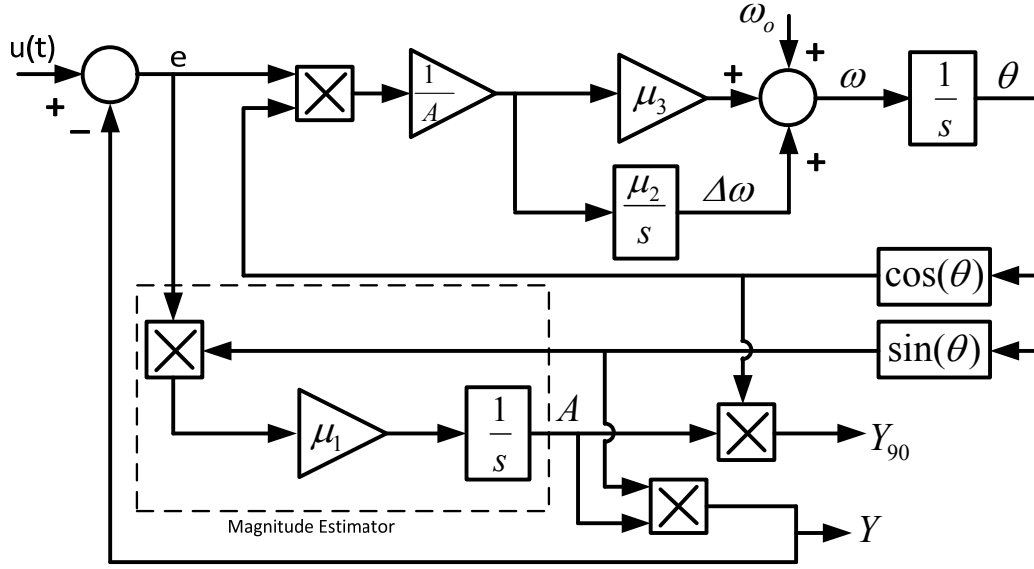


Figure 5.60 EPLL system diagram

$$\begin{cases} p\Delta\omega = \frac{\mu_2}{2}(-\sin(\theta - \theta_o) + \sin(\theta + \theta_o) + \sin(2\theta)) \\ p\theta = \omega_o + \Delta\omega + \frac{\mu_3}{2}(-\sin(\theta - \theta_o) + \sin(\theta + \theta_o) + \sin(2\theta)) \end{cases} \quad (5.98)$$

Due to the closed loop control, the estimated and actual angles are very close thus $\sin(\theta - \theta_o) \approx (\theta - \theta_o)$, in addition from the linear approximation of the above equation

$$\begin{bmatrix} p\Delta\omega \\ p\theta \end{bmatrix} = \begin{bmatrix} 0 & -\frac{\mu_2}{2} \\ 1 & -\frac{\mu_3}{2} \end{bmatrix} \begin{bmatrix} \Delta\omega \\ \theta \end{bmatrix} + \begin{bmatrix} \frac{\mu_2}{2} \\ \frac{\mu_3}{2} \end{bmatrix} \theta_o + \begin{bmatrix} 0 \\ \omega_o \end{bmatrix} \quad (5.99)$$

The characteristic equation is

$$|\lambda_1 I - A_1| = \lambda_1^2 + \frac{\mu_3}{2} \lambda_1 + \frac{\mu_2}{2} = S^2 + 2\xi_1 \omega_o + \omega_o^2 \quad (5.100)$$

Therefore two of the parameters of the EPLL can be defined as

$$\begin{cases} \mu_3 = 2\xi_1\omega_o \\ \mu_2 = \omega_o^2 \end{cases} \quad (5.101)$$

Therefore the controller parameters in the new structure are independent of the input signal magnitude and the same designed parameters can be applied to the unbalanced system.

If look at the whole system and define two new variables as

$$\begin{cases} x_1 = A\sin(\theta) \\ x_2 = A\cos(\theta) \end{cases} \quad (5.102)$$

$$\begin{cases} px_1 = \omega_o x_2 + (u - x_1)(\mu_1 \sin^2(\theta) + \mu_3 \cos^2(\theta)) \\ px_2 = -\omega_o x_1 + (u - x_1)\sin(\theta)\cos(\theta)(\mu_1 - \mu_3) \end{cases} \quad (5.103)$$

These equations are nonlinear so if we consider $\mu_1 = \mu_3$, it will be

$$\begin{aligned} \begin{bmatrix} px_1 \\ px_2 \end{bmatrix} &= \begin{bmatrix} -\mu_1 & \omega_o \\ -\omega_o & 0 \end{bmatrix} \begin{bmatrix} x_1 \\ x_2 \end{bmatrix} + \begin{bmatrix} \mu_1 \\ 0 \end{bmatrix} u \\ y &= \begin{bmatrix} 1 & 0 \end{bmatrix} \begin{bmatrix} x_1 \\ x_2 \end{bmatrix} \end{aligned} \quad (5.104)$$

Thus the transfer function is a second order band pass filter equation as follows:

$$\frac{u}{y} = \frac{\mu_1 s}{s^2 + \mu_1 s + \omega_o^2} = \frac{2\xi_2\omega_o s}{s^2 + 2\xi_2\omega_o s + \omega_o^2} \quad (5.105)$$

The EPLL is originally designed for a single phase system. The algorithm to define the angle, frequency and the amplitude of the three phase signal is illustrated in Figure 5.61. It includes four single phase EPLLs and a compensator unit. The first three

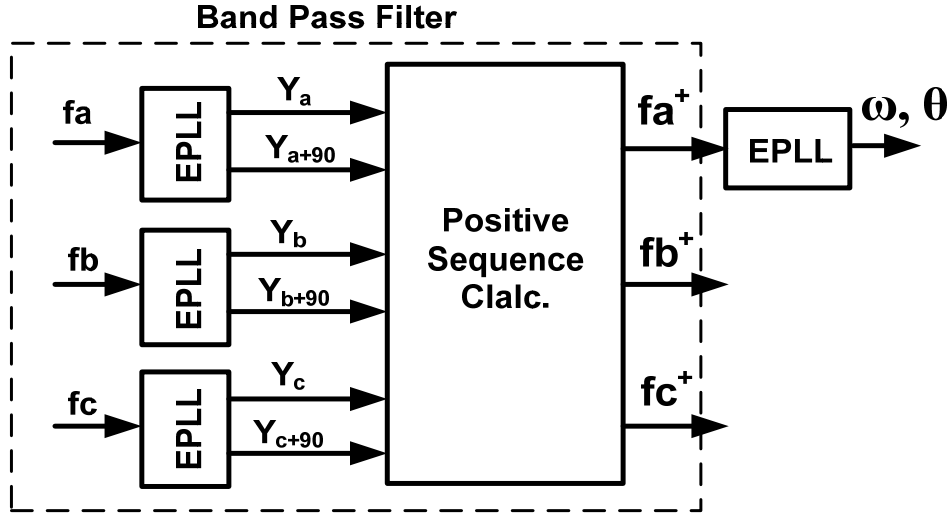


Figure 5.61 EPLL structure for three phase system

EPLLs, act like band pass filters when they follow the input signals (f_a, f_b, f_c) . Therefore they remove the noises. The compensator extracts the positive sequence (f_a^+, f_b^+, f_c^+) of the three phase filtered signals. Another advantage of EPLL is that it produces automatically both the filtered signal (y) and its 90 degree phase shifted one (y_{90}) which makes producing positive sequence easier.

$$\begin{bmatrix} V_a^+ \\ V_b^+ \\ V_c^+ \end{bmatrix} = \frac{1}{3} \begin{bmatrix} 1 & \beta & \beta^2 \\ \beta^2 & 1 & \beta \\ \beta & \beta^2 & 1 \end{bmatrix} \begin{bmatrix} V_a \\ V_b \\ V_c \end{bmatrix}, \quad \beta = e^{j120} \quad (5.106)$$

Or

$$\begin{cases} V_a^+ = \frac{1}{3}V_a - \frac{1}{6}(V_b + V_c) + \frac{1}{2\sqrt{3}}(V_{b_{-90}} - V_{c_{-90}}) \\ V_c^+ = \frac{1}{3}V_c - \frac{1}{6}(V_a + V_b) + \frac{1}{2\sqrt{3}}(V_{a_{-90}} - V_{b_{-90}}) \\ V_b^+ = -V_a^+ - V_c^+ \end{cases} \quad (5.107)$$

To look at the whole system of the EPLL, the magnitude, angle and frequency dynamic equations are

$$\begin{cases} pA_a = \mu_{1a}(U_a - Y_a) \sin(\theta_a) \\ pA_b = \mu_{1b}(U_b - Y_b) \sin(\theta_b) \\ pA_c = \mu_{1c}(U_c - Y_c) \sin(\theta_c) \end{cases} \quad (5.108)$$

$$\begin{cases} p\omega_a = \mu_{2a} \frac{(U_a - Y_a)}{A_a} \cos(\theta_a) \\ p\omega_b = \mu_{2b} \frac{(U_b - Y_b)}{A_b} \cos(\theta_b) \\ p\omega_c = \mu_{2c} \frac{(U_c - Y_c)}{A_c} \cos(\theta_c) \end{cases} \quad (5.109)$$

$$\begin{cases} p\theta_a = \mu_{3a} \frac{(U_a - Y_a)}{A_a} \cos(\theta_a) + \Delta\omega_a + \omega_{oa} \\ p\theta_b = \mu_{3b} \frac{(U_b - Y_b)}{A_b} \cos(\theta_b) + \Delta\omega_b + \omega_{ob} \\ p\theta_c = \mu_{3c} \frac{(U_c - Y_c)}{A_c} \cos(\theta_c) + \Delta\omega_c + \omega_{oc} \end{cases} \quad (5.110)$$

From the output equation of the EPLL

$$\begin{cases} Y_a = A_a \sin(\theta_a) = \mu_{1a}(Y_a - U_a) \sin(\theta_a) \sin\left(\mu_{3a} \frac{(Y_a - U_a)}{A_a} \cos(\theta_a) + \Delta\omega_a + \omega_{oa}\right) \\ Y_b = A_b \sin(\theta_b) = \mu_{1b}(Y_b - U_b) \sin(\theta_b) \sin\left(\mu_{3b} \frac{(Y_b - U_b)}{A_b} \cos(\theta_b) + \Delta\omega_b + \omega_{ob}\right) \\ Y_c = A_c \sin(\theta_c) = \mu_{1c}(Y_c - U_c) \sin(\theta_c) \sin\left(\mu_{3c} \frac{(Y_c - U_c)}{A_c} \cos(\theta_c) + \Delta\omega_c + \omega_{oc}\right) \end{cases} \quad (5.111)$$

Since $\frac{(Y-U)}{A}$ and $\Delta\omega$ are small and ω_o is the integer multiple of 2π , $\sin(\alpha) \approx \alpha$

$$\begin{cases} Y_a = \mu_{1a}(Y_a - U_a) \sin(\theta_a) \left(\mu_{3a} \frac{(Y_a - U_a)}{A_a} \cos(\theta_a) + \Delta\omega_a + \omega_{oa} \right) \\ Y_b = \mu_{1b}(Y_b - U_b) \sin(\theta_b) \left(\mu_{3b} \frac{(Y_b - U_b)}{A_b} \cos(\theta_b) + \Delta\omega_b + \omega_{ob} \right) \\ Y_c = \mu_{1c}(Y_c - U_c) \sin(\theta_c) \left(\mu_{3c} \frac{(Y_c - U_c)}{A_c} \cos(\theta_c) + \Delta\omega_c + \omega_{oc} \right) \end{cases} \quad (5.112)$$

$$\begin{cases} Y_a = \mu_{1a} \mu_{3a} \cos(\theta_a) \sin(\theta_a) \frac{(Y_a - U_a)^2}{A_a} + (\Delta\omega_a + \omega_{oa}) \mu_{1a} \sin(\theta_a) (Y_a - U_a) \\ Y_b = \mu_{1b} \mu_{3b} \cos(\theta_b) \sin(\theta_b) \frac{(Y_b - U_b)^2}{A_b} + (\Delta\omega_b + \omega_{ob}) \mu_{1b} \sin(\theta_b) (Y_b - U_b) \\ Y_c = \mu_{1c} \mu_{3c} \cos(\theta_c) \sin(\theta_c) \frac{(Y_c - U_c)^2}{A_c} + (\Delta\omega_c + \omega_{oc}) \mu_{1c} \sin(\theta_c) (Y_c - U_c) \end{cases} \quad (5.113)$$

Again when $\frac{(Y-U)}{A}$ is small, taking the linear part

$$\begin{cases} \frac{Y_a}{U_a} = \frac{(\Delta\omega_a + \omega_{oa}) \mu_{1a} \sin(\theta_a)}{1 + (\Delta\omega_a + \omega_{oa}) \mu_{1a} \sin(\theta_a)} \\ \frac{Y_b}{U_b} = \frac{(\Delta\omega_b + \omega_{ob}) \mu_{1b} \sin(\theta_b)}{1 + (\Delta\omega_b + \omega_{ob}) \mu_{1b} \sin(\theta_b)} \\ \frac{Y_c}{U_c} = \frac{(\Delta\omega_c + \omega_{oc}) \mu_{1c} \sin(\theta_c)}{1 + (\Delta\omega_c + \omega_{oc}) \mu_{1c} \sin(\theta_c)} \end{cases} \quad (5.114)$$

For the second input with 90 degree shift in the angle

$$\begin{cases} Y_{a+90} = A_a \cos(\theta_a) = \frac{A_a \sin(\theta_a) \cos(\theta_a)}{\sin(\theta_a)} = \frac{Y_a \cos(\theta_a)}{\sin(\theta_a)} \\ Y_{b+90} = A_b \cos(\theta_b) = \frac{Y_b \cos(\theta_b)}{\sin(\theta_b)} \\ Y_{c+90} = A_c \cos(\theta_c) = \frac{Y_c \cos(\theta_c)}{\sin(\theta_c)} \end{cases} \quad (5.115)$$

$$\begin{cases} \frac{Y_{a+90}}{U_a} = \frac{(\Delta\omega_a + \omega_{oa})\mu_{1a} \cos(\theta_a)}{1 + (\Delta\omega_a + \omega_{oa})\mu_{1a} \sin(\theta_a)} \\ \frac{Y_{b+90}}{U_b} = \frac{(\Delta\omega_b + \omega_{ob})\mu_{1b} \cos(\theta_b)}{1 + (\Delta\omega_b + \omega_{ob})\mu_{1b} \sin(\theta_b)} \\ \frac{Y_{c+90}}{U_c} = \frac{(\Delta\omega_c + \omega_{oc})\mu_{1c} \cos(\theta_c)}{1 + (\Delta\omega_c + \omega_{oc})\mu_{1c} \sin(\theta_c)} \end{cases} \quad (5.116)$$

Therefore in matrix form

$$\begin{bmatrix} Y_a \\ Y_{a+90} \\ Y_b \\ Y_{b+90} \\ Y_c \\ Y_{c+90} \end{bmatrix} = \begin{bmatrix} \frac{(\Delta\omega_a + \omega_{oa})\mu_{1a} \sin(\theta_a)}{1 + (\Delta\omega_a + \omega_{oa})\mu_{1a} \sin(\theta_a)} & 0 & 0 \\ \frac{(\Delta\omega_a + \omega_{oa})\mu_{1a} \cos(\theta_a)}{1 + (\Delta\omega_a + \omega_{oa})\mu_{1a} \sin(\theta_a)} & 0 & 0 \\ 0 & \frac{(\Delta\omega_b + \omega_{ob})\mu_{1b} \sin(\theta_b)}{1 + (\Delta\omega_b + \omega_{ob})\mu_{1b} \sin(\theta_b)} & 0 \\ 0 & \frac{(\Delta\omega_b + \omega_{ob})\mu_{1b} \cos(\theta_b)}{1 + (\Delta\omega_b + \omega_{ob})\mu_{1b} \sin(\theta_b)} & 0 \\ 0 & 0 & \frac{(\Delta\omega_c + \omega_{oc})\mu_{1c} \sin(\theta_c)}{1 + (\Delta\omega_c + \omega_{oc})\mu_{1c} \sin(\theta_c)} \\ 0 & 0 & \frac{(\Delta\omega_c + \omega_{oc})\mu_{1c} \cos(\theta_c)}{1 + (\Delta\omega_c + \omega_{oc})\mu_{1c} \sin(\theta_c)} \end{bmatrix} \begin{bmatrix} U_a \\ U_b \\ U_c \end{bmatrix} \quad (5.117)$$

$$\begin{bmatrix} Y_a^+ \\ Y_b^+ \\ Y_c^+ \end{bmatrix} = \begin{bmatrix} \frac{1}{3} & 0 & -\frac{1}{6} & \frac{1}{2\sqrt{3}} & -\frac{1}{6} & \frac{1}{2\sqrt{3}} \\ -\frac{1}{6} & \frac{1}{2\sqrt{3}} & \frac{1}{3} & 0 & -\frac{1}{6} & \frac{1}{2\sqrt{3}} \\ -\frac{1}{6} & \frac{1}{2\sqrt{3}} & -\frac{1}{6} & \frac{1}{2\sqrt{3}} & \frac{1}{3} & 0 \end{bmatrix} \begin{bmatrix} Y_a \\ Y_{a+90} \\ Y_b \\ Y_{b+90} \\ Y_c \\ Y_{c+90} \end{bmatrix} \quad (5.118)$$

In addition from the dynamic equations of the angle and frequency in (5.109) and (5.110)

$$p \begin{bmatrix} \theta_a \\ \omega_a \\ \theta_b \\ \omega_b \\ \theta_c \\ \omega_c \end{bmatrix} = \begin{bmatrix} \frac{\mu_{3a}}{A_a} \cos(\theta_a) & 0 & 0 \\ \frac{\mu_{2a}}{A_a} \cos(\theta_a) & 0 & 0 \\ 0 & \frac{\mu_{3b}}{A_b} \cos(\theta_b) & 0 \\ 0 & \frac{\mu_{2b}}{A_b} \cos(\theta_b) & 0 \\ 0 & 0 & \frac{\mu_{3c}}{A_c} \cos(\theta_c) \\ 0 & 0 & \frac{\mu_{2c}}{A_c} \cos(\theta_c) \end{bmatrix} \begin{bmatrix} Y_a^+ \\ Y_b^+ \\ Y_c^+ \end{bmatrix} + \begin{bmatrix} \Delta\omega_a + \omega_{oa} - \frac{\mu_{3a}}{A_a} Y_{ya^+} \cos(\theta_a) \\ -\frac{\mu_{2a}}{A_a} Y_{ya^+} \cos(\theta_a) \\ \Delta\omega_b + \omega_{ob} - \frac{\mu_{3b}}{A_b} Y_{yb^+} \cos(\theta_b) \\ -\frac{\mu_{2a}}{A_b} Y_{yb^+} \cos(\theta_b) \\ \Delta\omega_c + \omega_{oc} - \frac{\mu_{3c}}{A_c} Y_{yc^+} \cos(\theta_c) \\ -\frac{\mu_{2c}}{A_c} Y_{yc^+} \cos(\theta_c) \end{bmatrix} \quad (5.119)$$

If we consider

$$\begin{bmatrix} Y_a \\ Y_{a+90} \\ Y_b \\ Y_{b+90} \\ Y_c \\ Y_{c+90} \end{bmatrix} = \begin{bmatrix} a_1 & 0 & 0 \\ a_2 & 0 & 0 \\ 0 & a_3 & 0 \\ 0 & a_4 & 0 \\ 0 & 0 & a_5 \\ 0 & 0 & a_6 \end{bmatrix} \begin{bmatrix} U_a \\ U_b \\ U_c \end{bmatrix} \quad (5.120)$$

$$p \begin{bmatrix} \theta_a \\ \omega_a \\ \theta_b \\ \omega_b \\ \theta_c \\ \omega_c \end{bmatrix} = \begin{bmatrix} c_1 & 0 & 0 \\ c_2 & 0 & 0 \\ 0 & c_3 & 0 \\ 0 & c_4 & 0 \\ 0 & 0 & c_5 \\ 0 & 0 & c_6 \end{bmatrix} \begin{bmatrix} Y_a^+ \\ Y_b^+ \\ Y_c^+ \end{bmatrix} + \begin{bmatrix} \Delta\omega_a + \omega_{oa} - \frac{\mu_{3a}}{A_a} Y_{ya^+} \cos(\theta_a) \\ -\frac{\mu_{2a}}{A_a} Y_{ya^+} \cos(\theta_a) \\ \Delta\omega_b + \omega_{ob} - \frac{\mu_{3b}}{A_b} Y_{yb^+} \cos(\theta_b) \\ -\frac{\mu_{2a}}{A_b} Y_{yb^+} \cos(\theta_b) \\ \Delta\omega_c + \omega_{oc} - \frac{\mu_{3c}}{A_c} Y_{yc^+} \cos(\theta_c) \\ -\frac{\mu_{2c}}{A_c} Y_{yc^+} \cos(\theta_c) \end{bmatrix} \quad (5.121)$$

Substitute (5.118) and (5.120) into (5.121), the transfer function of the angle and frequency dynamic equations, from the output to input of the total EPLL for the three phase system is

$$\begin{aligned}
 P \begin{bmatrix} \theta_a \\ \omega_a \\ \theta_b \\ \omega_b \\ \theta_c \\ \omega_c \end{bmatrix} &= \begin{bmatrix} \frac{1}{3}c_1a_1 & -\frac{1}{6}c_1a_3 + \frac{1}{2\sqrt{3}}c_1a_4 & -\frac{1}{6}c_1a_5 + \frac{1}{2\sqrt{3}}c_1a_6 \\ \frac{1}{3}c_2a_1 & -\frac{1}{6}c_2a_3 + \frac{1}{2\sqrt{3}}c_2a_4 & -\frac{1}{6}c_2a_5 + \frac{1}{2\sqrt{3}}c_2a_6 \\ -\frac{1}{6}c_3a_1 + \frac{1}{2\sqrt{3}}c_3a_2 & \frac{1}{3}c_3a_3 & -\frac{1}{6}c_3a_5 + \frac{1}{2\sqrt{3}}c_3a_6 \\ -\frac{1}{6}c_4a_1 + \frac{1}{2\sqrt{3}}c_4a_2 & \frac{1}{3}c_4a_3 & -\frac{1}{6}c_4a_5 + \frac{1}{2\sqrt{3}}c_4a_6 \\ -\frac{1}{6}c_5a_1 + \frac{1}{2\sqrt{3}}c_5a_2 & -\frac{1}{6}c_5a_3 + \frac{1}{2\sqrt{3}}c_5a_4 & \frac{1}{3}c_5a_5 \\ -\frac{1}{6}c_6a_1 + \frac{1}{2\sqrt{3}}c_6a_2 & -\frac{1}{6}c_6a_3 + \frac{1}{2\sqrt{3}}c_6a_4 & \frac{1}{3}c_6a_5 \end{bmatrix} \begin{bmatrix} U_a \\ U_b \\ U_c \end{bmatrix} \\
 + \begin{bmatrix} \Delta\omega_a + \omega_{oa} - \frac{\mu_{3a}}{A_a} Y_{ya+} \cos(\theta_a) \\ -\frac{\mu_{2a}}{A_a} Y_{ya+} \cos(\theta_a) \\ \Delta\omega_b + \omega_{ob} - \frac{\mu_{3b}}{A_b} Y_{yb+} \cos(\theta_b) \\ -\frac{\mu_{2a}}{A_b} Y_{yb+} \cos(\theta_b) \\ \Delta\omega_c + \omega_{oc} - \frac{\mu_{3c}}{A_c} Y_{yc+} \cos(\theta_c) \\ -\frac{\mu_{2c}}{A_c} Y_{yc+} \cos(\theta_c) \end{bmatrix} & \quad (5.122)
 \end{aligned}$$

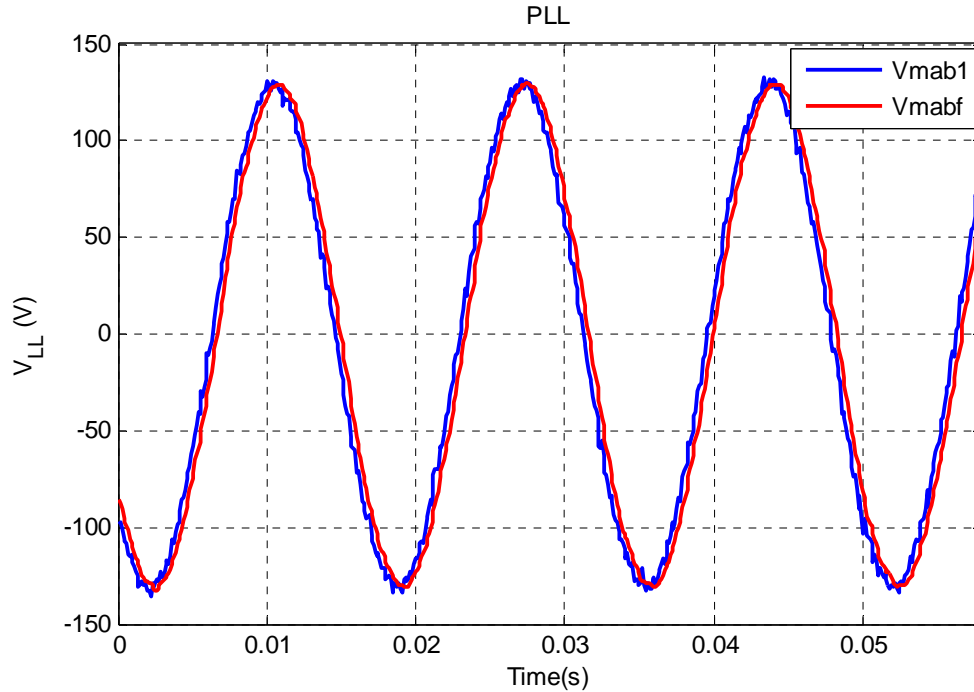


Figure 5.62 Experimental output voltage of digital filter

Using the same input signal, the output of typical PLL and EPLL are compared. In Figure 5.62 to Figure 5.65 the output of the EPLL as a band pass filter and a low pass digital filter are compared. The output of the EPLL has lower fluctuations in comparison with digital low pass filter. The output of the digital filter is applied to the typical PLL and the original signals are applied to the four EPLLs to define the frequency and angle of the three voltages and currents. Figure 5.66 and Figure 5.67 illustrate the converted qd-axis grid voltages and open loop currents of three phase inverter. In both cases the outputs of EPLL are more accurate with lowest fluctuations qd-axis parameters. In Figure 5.68, the measured grid frequency using PLL and EPLL are shown. The output of the EPLL defines the grid frequency more precisely. The harmonic spectrum of phase current from the output of digital filter for the PLL and also output of the EPLL are illustrated in Figure 5.69 and Figure 5.70 respectively.

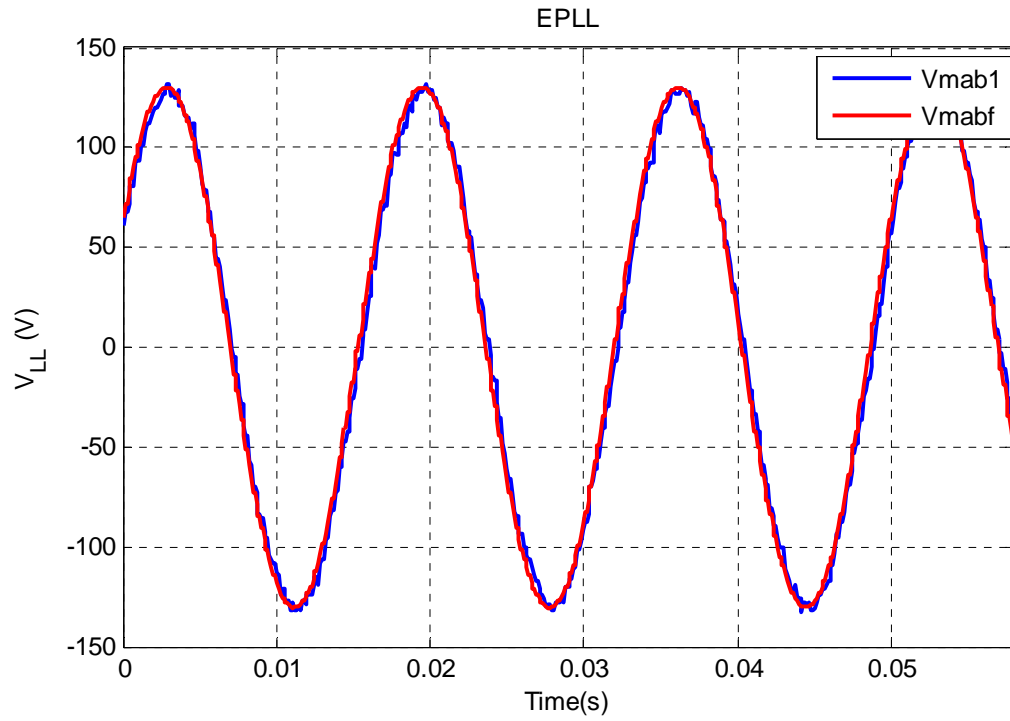


Figure 5.63 Experimental output voltage of EPLL

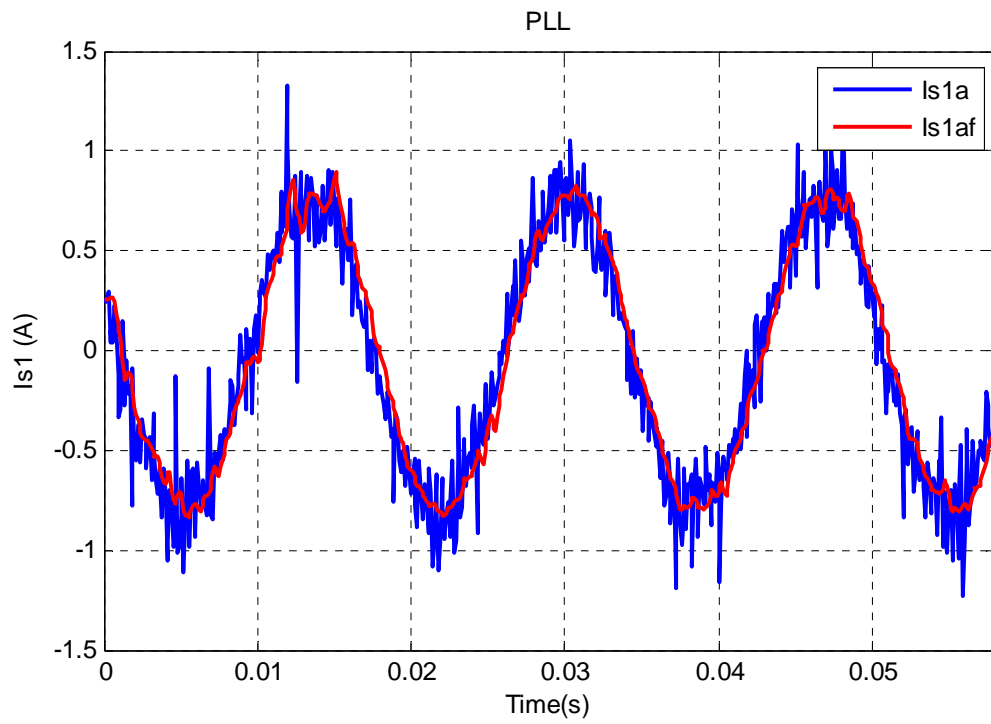


Figure 5.64 Experimental output current of digital filter

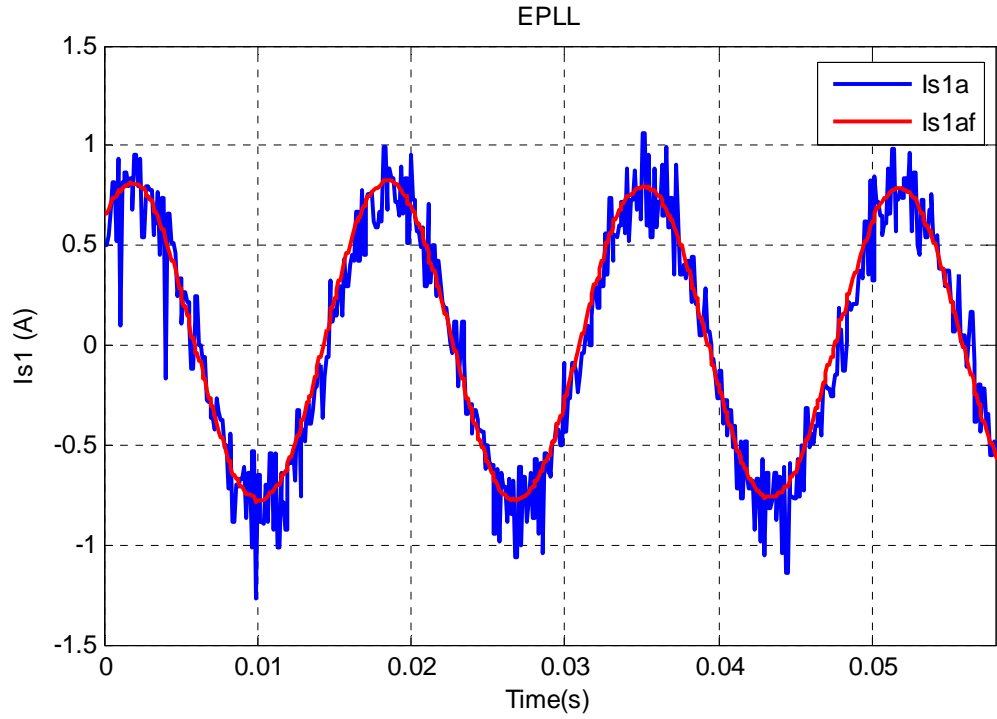


Figure 5.65 Experimental output current of EPLL

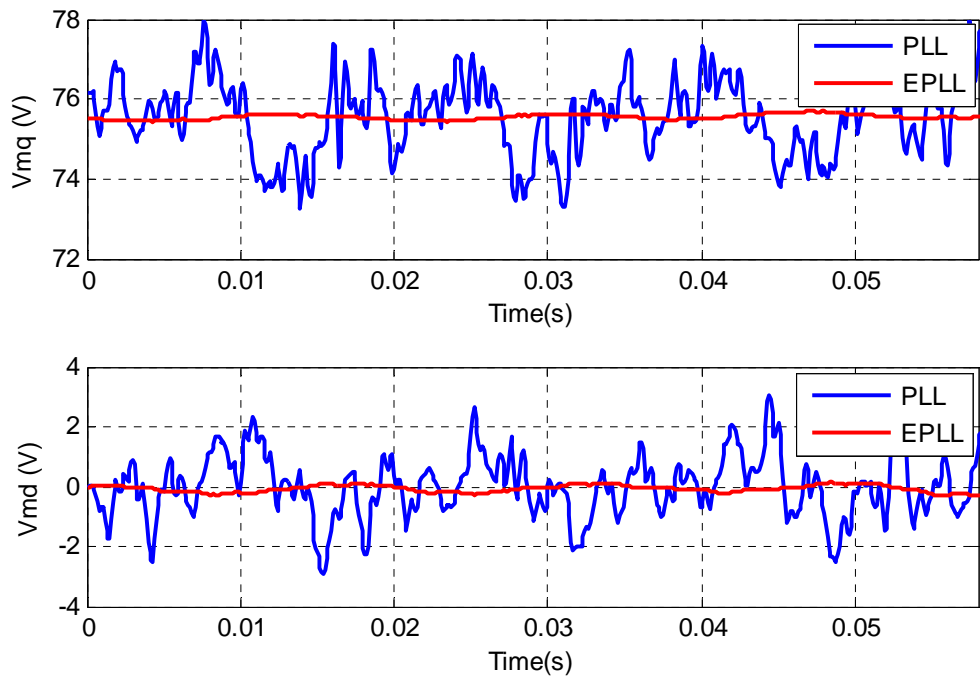


Figure 5.66 Experimental qd-axis voltage output of PLL and EPLL

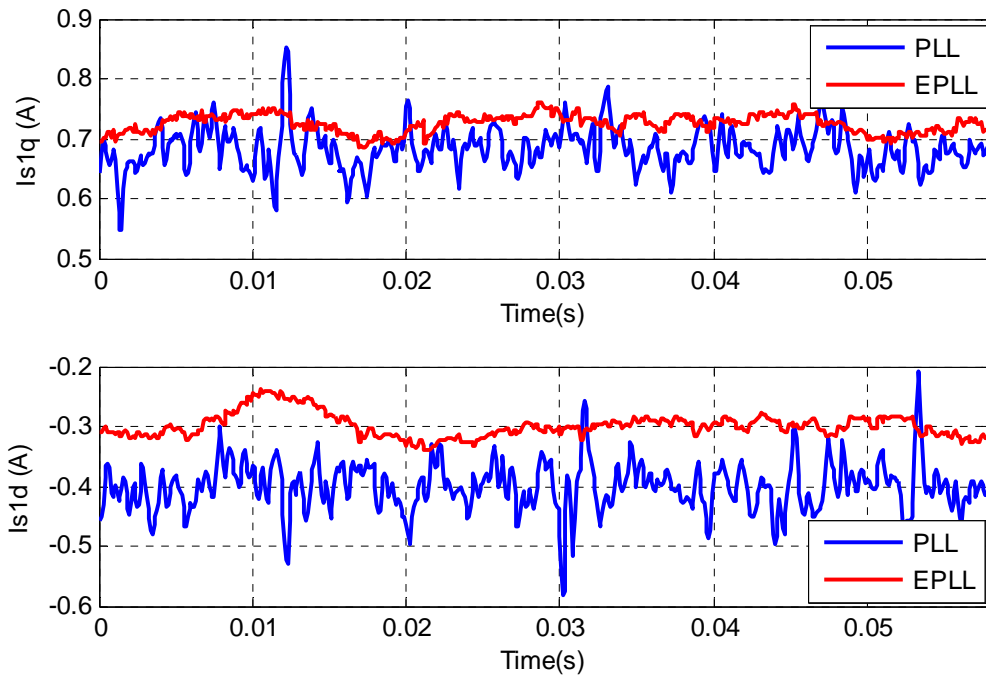


Figure 5.67 Experimental qd-axis voltage output of PLL and EPLL

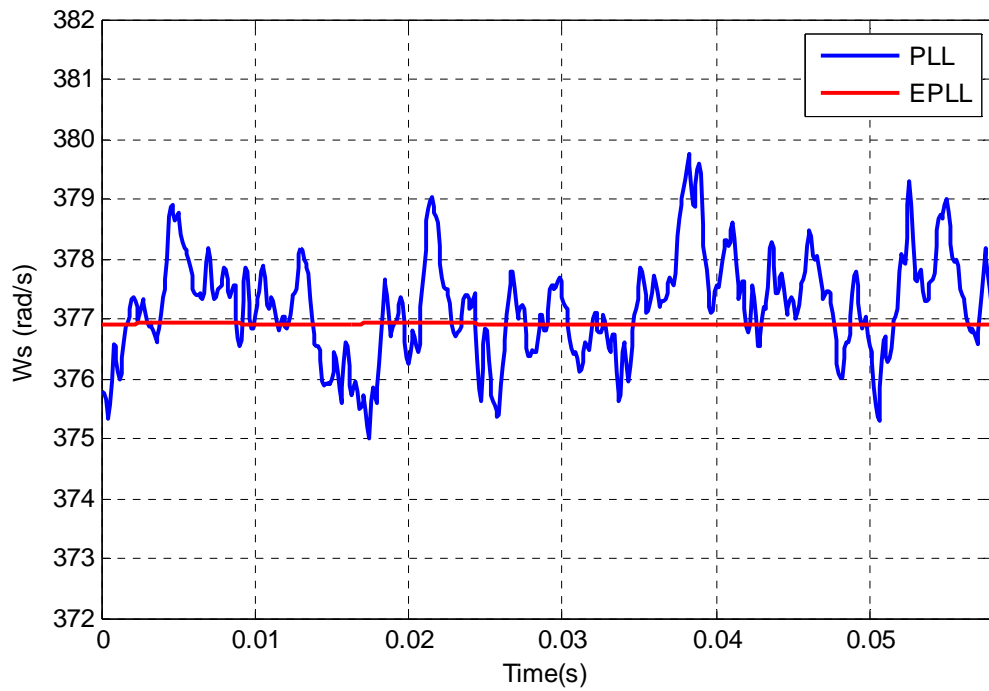


Figure 5.68 Experimental voltage frequency output of PLL and EPLL

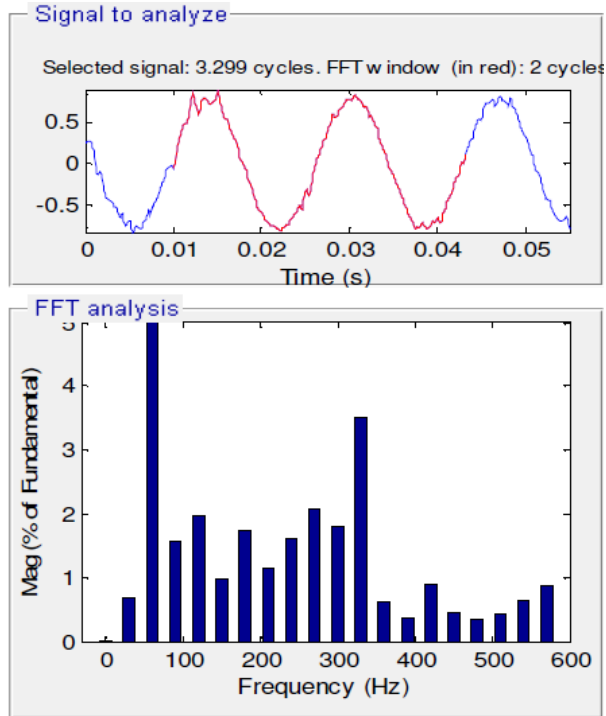


Figure 5.69 Harmonic spectrum of phase current of the digital filter for PLL, fundamental frequency is 20 times reduced scale.

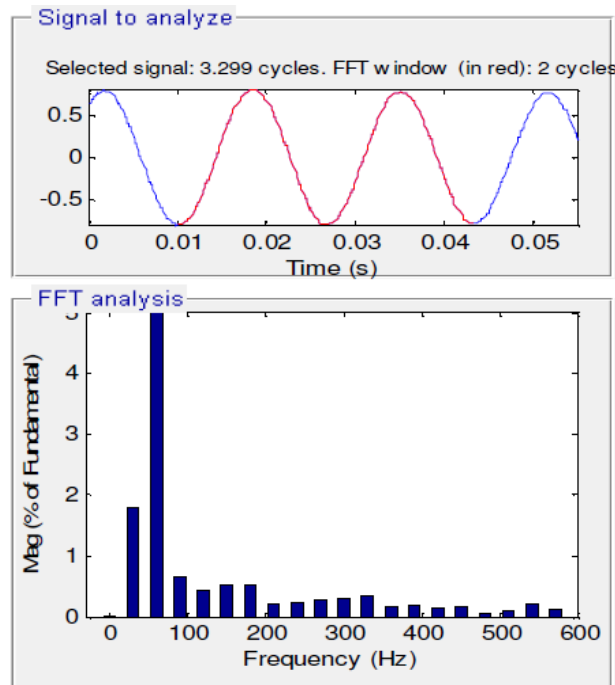


Figure 5.70 Harmonic spectrum of output phase current of EPLL, fundamental frequency is 20 times reduced scale.

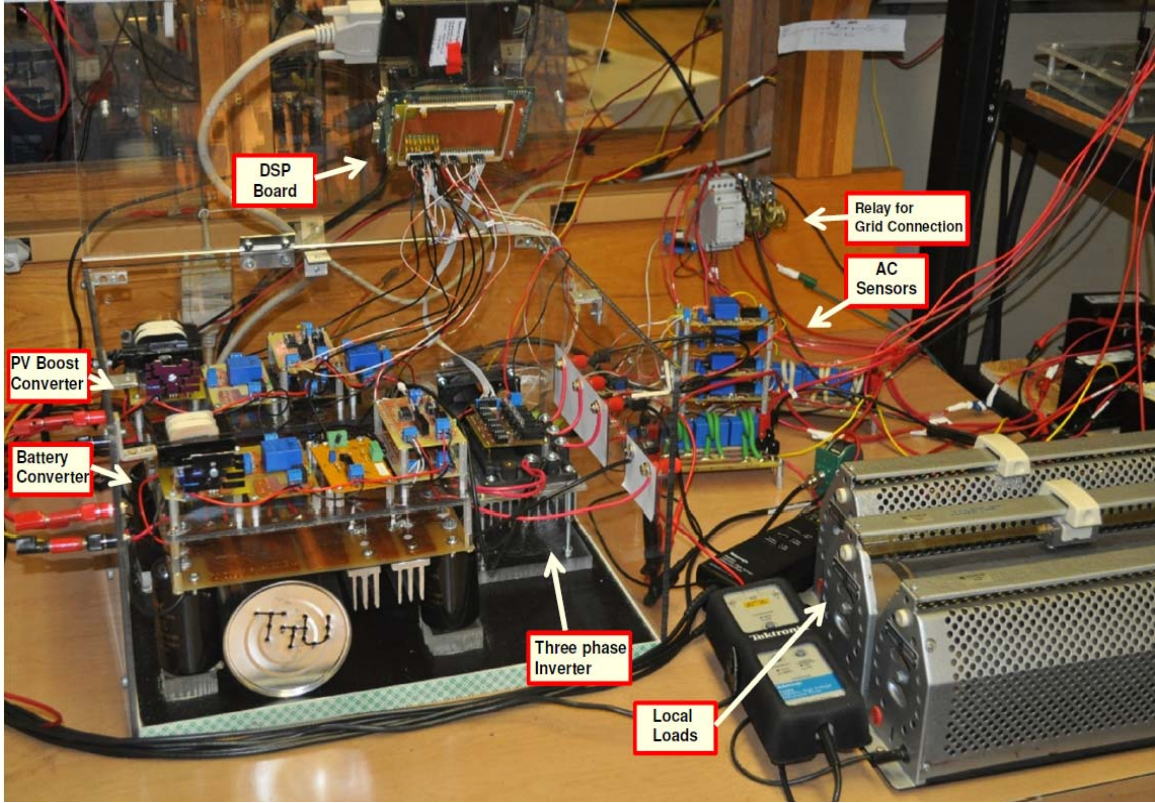


Figure 5.71 Hardware experimental setup

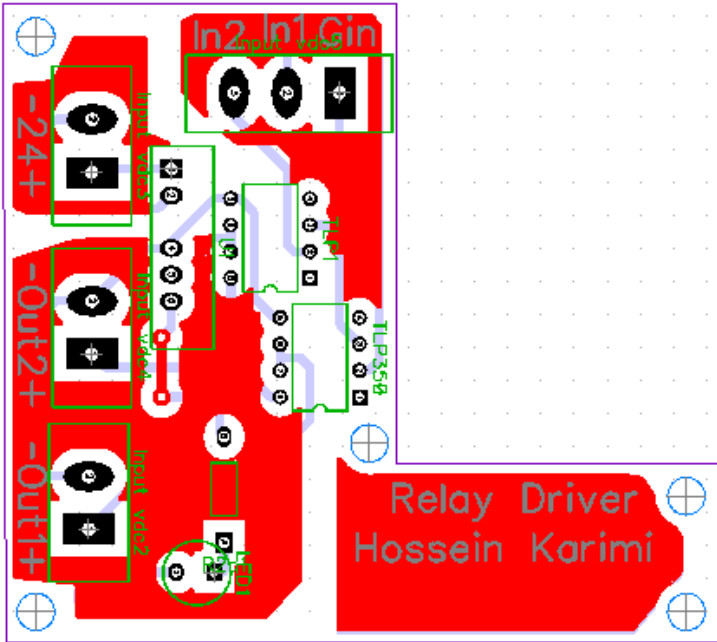


Figure 5.72 Relay driver PCB board

5.9 Connection of the PV, Battery and Three Phase Inverter

Most part of the experimental setup is shown in Figure 5.71. The configuration is like Figure 3.1 with three different converters, LC filter and local loads. An automatic relay connects the system to the main grid. As shown in Figure 5.72, an interface circuit is designed to close the relay from DSP in a specific programmed moment. Before connection of the system to the main grid, the synchronization process is investigated. As shown in Figure 5.73, the channel one of the oscilloscope shows the reference line to line grid voltage and the channel three presents the output voltage of the inverter after the LC filter at the point of common coupling (PCC). The reference of the qd-axis of inverter is changed from 0.85pu to 1 pu. The objective is to verify to different responses, at first the speed response of the voltage controller for tracking the reference, secondly the operation of the EPLL in tracking the angle and frequency of the main grid voltage. As shown in the zoomed graph, the inverter voltage tracks the references in less than one cycle and due to the precise operation of the EPLL, it matches the grid voltage and is ready to be connected. The system under local load is operated autonomously. The system dynamic behavior is investigated in different situations from autonomous operation to grid connected mode operation. At three different instants, the operation condition is changed. As shown in Figure 5.74 and Figure 5.75 at the system is working in autonomous mode before 0.1s. The Figure 5.74 shows the output active and reactive power of the inverter. In this mode, the just the inverter is feeding the local load and the power of the grid is zero in Figure 5.75. From 0.1s to 0.22s is the synchronization process and the system is

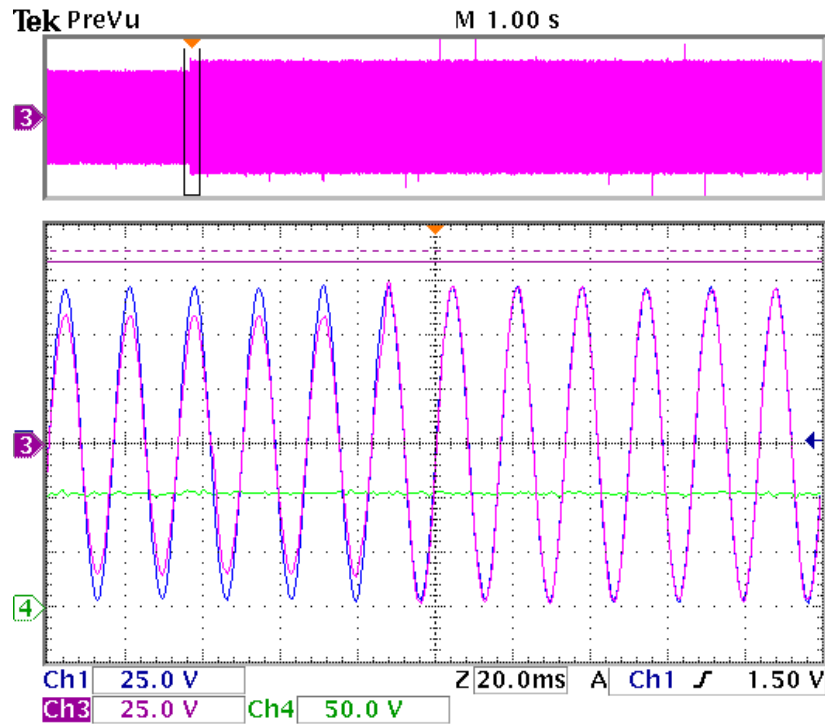


Figure 5.73 Experimental closed loop inverter voltage and current controller response

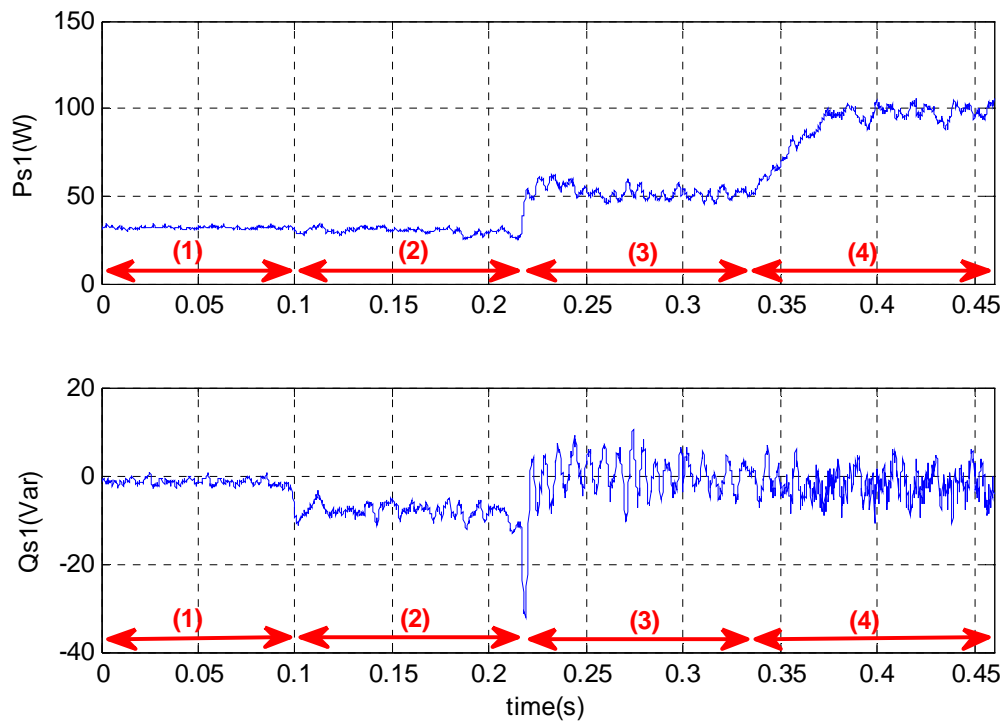


Figure 5.74 Experimental active and reactive power of the inverter in both autonomous and grid connected modes.

connected to the main grid. Still the active and reactive powers of the grid are almost zero. Due to the change of the voltage exactly synchronized to the grid with zero d-axis voltage in Figure 5.77 there is a slight change in the output reactive power of the inverter. At the instant of the 0.22s the droop controller is transferring the maximum power of the PV source to the local load and the main grid which is 50W. To transfer the maximum power of the PV and also to operate in unity power factor and keep the output reactive power of the inverter zero the voltage angle and frequency from the active power droop control and the voltage magnitude from the reactive power droop control are varied. Therefore there is slight change in the power of the voltage dependent local load in Figure 5.76. The excessive power of the inverter flows into the main grid in Figure 5.75. In addition at 0.33s the irradiation level of the sun is changed and maximum power of the PV source also varies to 100W. The reactive power is kept constant. Due to almost constant load, the active power flows into the grid is increase corresponding to the PV source output.

The output current of the inverter are tracking the references in Figure 5.78. The line to line voltage and phase current of the inverter are shown in Figure 5.79. In the moment of the change of PV irradiation level and its maximum power, change of the output current is obvious. Moreover the change of the output power causes a slight fluctuation in the DC-link voltage. The controller part of the bidirectional converter returns the DC link voltage to its reference (100V) very fast in Figure 5.80.

To show the charging mode of the battery in autonomous mode, the AC load is reduced suddenly at 2s. As it is shown in Figure 5.81 since the irradiation level of the sun

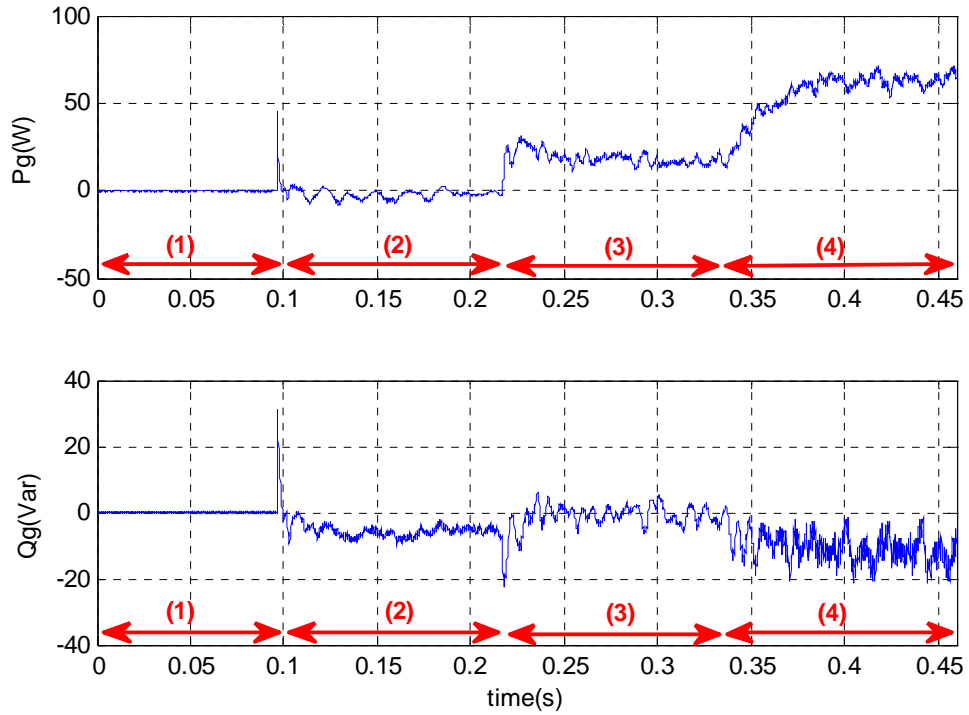


Figure 5.75 Experimental active and reactive power of the grid in both autonomous and grid connected modes.

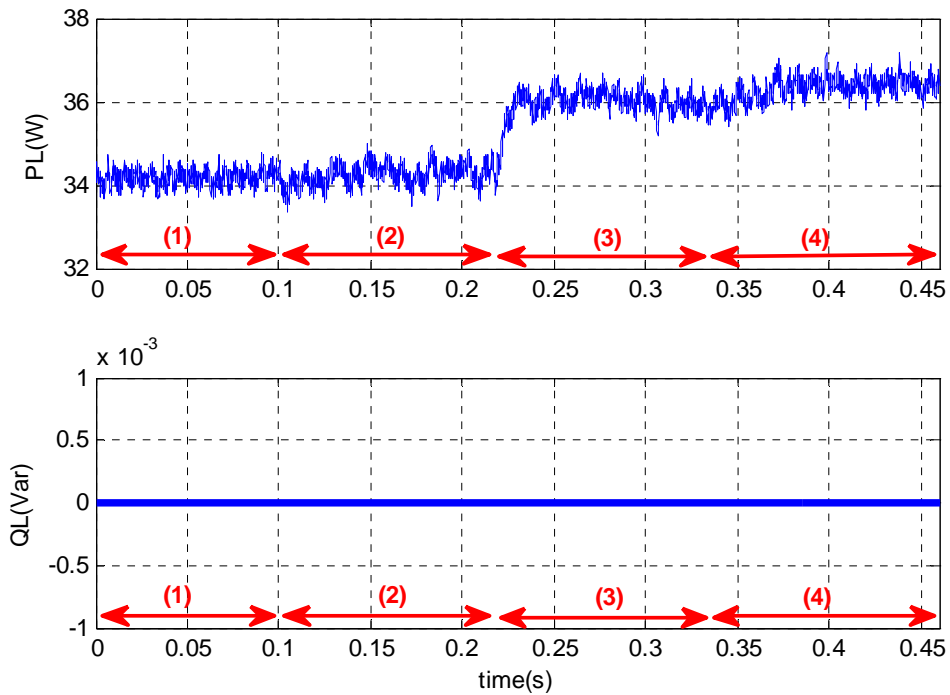


Figure 5.76 Experimental active and reactive power of the grid in both autonomous and grid connected modes.

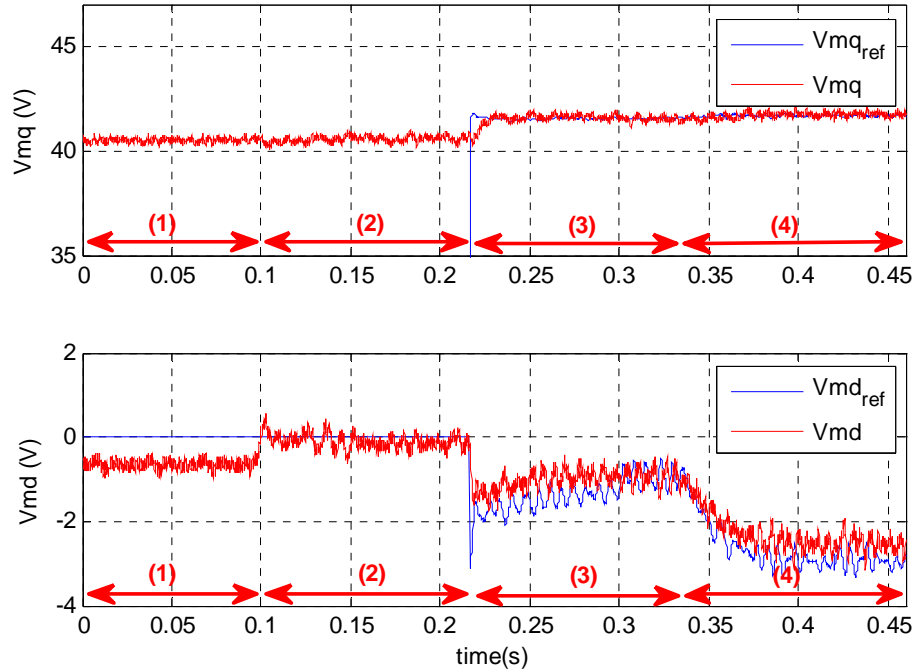


Figure 5.77 Experimental qd-axis load voltages in both autonomous and grid connected modes.

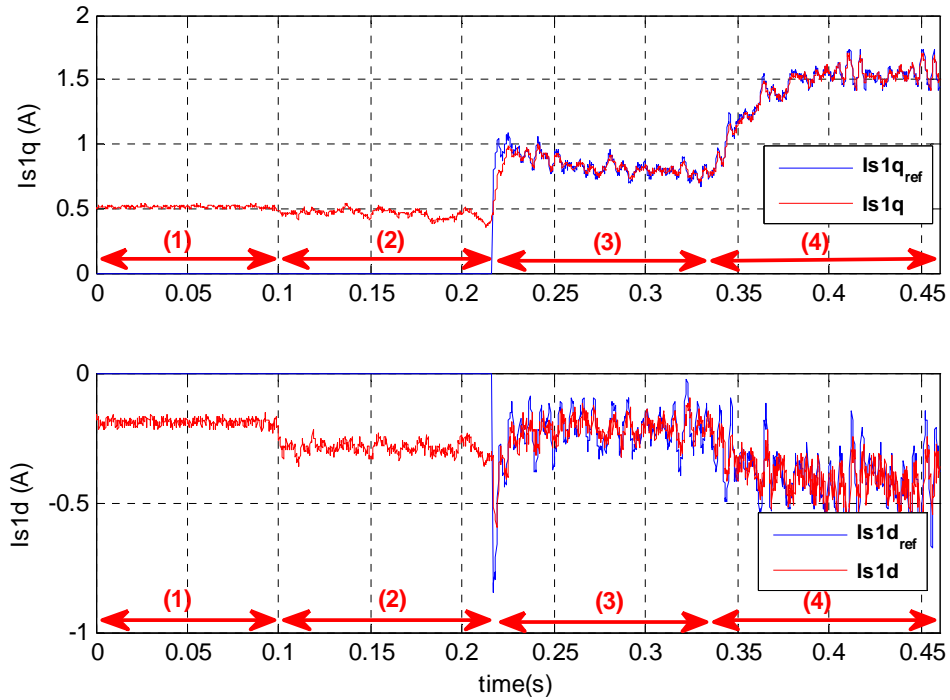


Figure 5.78 Experimental qd-axis inverter currents in both autonomous and grid connected modes.

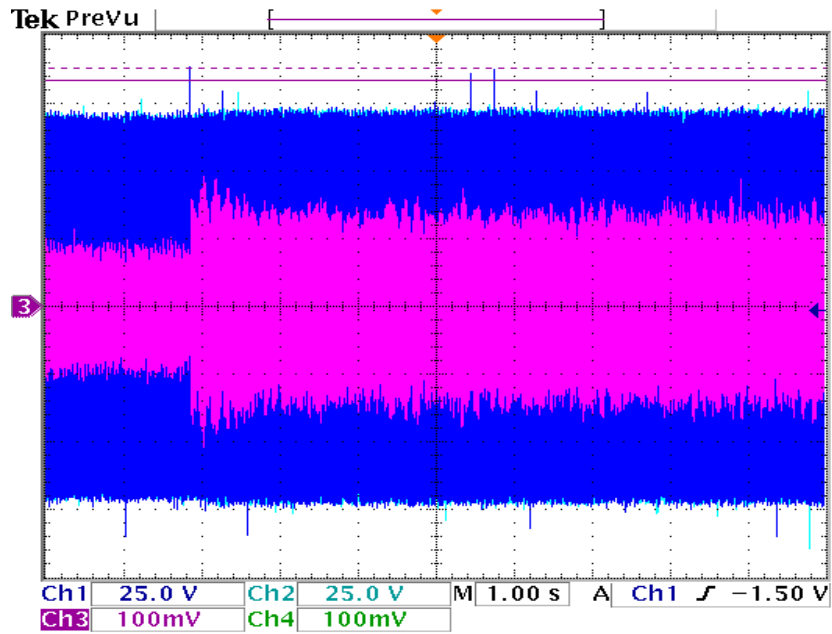


Figure 5.79 Experimental voltage and current of the inverter with changing of the PV source in grid connected mode, Ch1: V_{mab} , Ch3: I_{s1a}

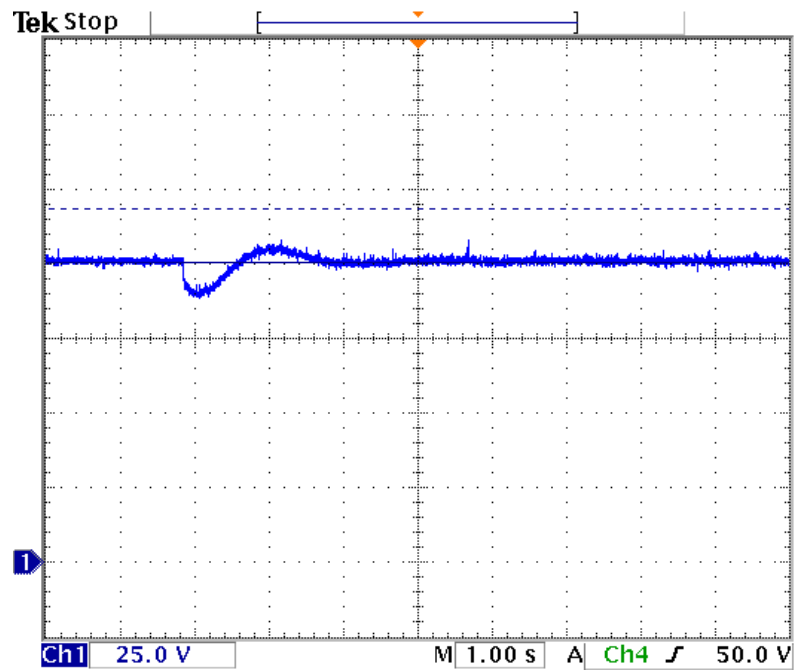


Figure 5.80 Experimental DC-link voltage after connection to the grid and change of reference power

is constant, the PV output voltage and current remain the same. Figure 5.82 illustrates the DC-link voltage and the output current of the battery. When the load is reduced in the constant PV source output, to fulfill the power balance, the excessive current flows into the battery therefore, the mode of the battery in the bidirectional DC-DC converter changes from discharging to charging mode. In addition, the battery converter controller keeps the DC-link voltage constant.

5.10 Conclusions

In this chapter the experimental setups are designed and tested to verify the proposed system structure and controller design. Due to the complexity of the system, the whole system is separated into different sections. The design process for each section is explained in detail and tested autonomously. Then the combined system results are analyzed. In the first section a 3kW, 50kHz boost converter is designed. Based on the designed parameters, the appropriate equipment pieces are chosen from the market. The high frequency inductor is designed and built using ferrite core and Litz wire to reduce the eddy current effect in high frequencies. The power circuit of the boost converter is designed in PCB and has been built and soldered. The open loop test in different duty ratios is applied and sampled with a duty ratio of 0.6 and 68 V as input voltage is shown. The output voltage after capacitor filter is DC with the lowest fluctuation and the expected voltage magnitude

The closed loop control of the PV source using a DC/DC boost converter is applied. A programmable DC source power supply with nonlinear characteristics is

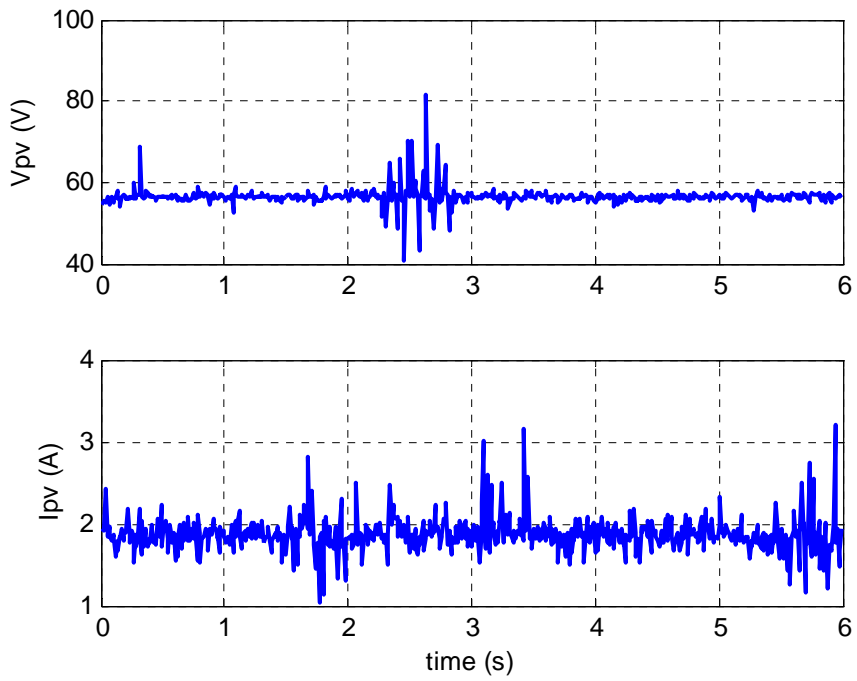


Figure 5.81 Experimental output voltage and current of the PV source

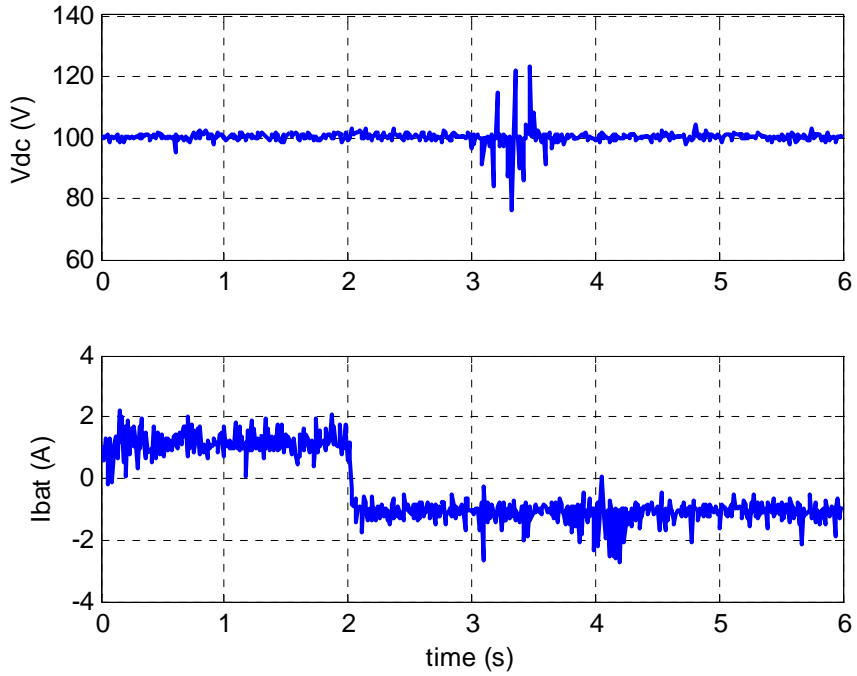


Figure 5.82 Experimental output voltage and current of the battery source

connected to an autonomous resistive load through the boost converter. The driver circuit, DC voltage sensor and DC current sensor boards are designed. The observation and perturbation method is used to get maximum possible power from the source. For the control part, the ezDSPF28335 is used and the entire program is written using C language inside the DSP. Two closed loop tests are applied to show the dynamic and steady state behavior of the system. The results show that the control algorithm can find the maximum power point in a few seconds which seems to be a satisfactory response for a PV source which usually doesn't change very fast.

In the next step, the three phase inverter and its interface isolator board is designed. Three phase sinusoidal pulse with modulation (SPWM) signals are produced inside the DSPF28335. The zero sequence is added to the typical SPWM signals. A look up table for sinusoidal waveform with 512 samples is used to be compared with an isosceles triangle carrier waveform of 5KHz. The continuous switching signals and output inverter voltage under a fixed 60Hz modulation index is produced even with a modulation index bigger than unity. An interface circuit is designed to connect the DSP to the three phase inverter module and gate drivers. The output open loop results under the resistive and under RL load with the 200V input DC link voltage are presented. The output voltage and current waveforms prove the performance of the written programs in the DSP for added zero sequence SPWM three phase inverter to increase the linear modulation region.

The phase lock loop (PLL) software for a three phase system is programmed DSP. After tuning the voltage sensor, the PLL program is tested experimentally using the operation of a three phase inverter based on the measured frequency and phase angle of

the grid voltage. The results show that the output voltage of the inverter follows the frequency and angle of the grid precisely.

For synchronization process, the effects of dead time and filter delay are considered. After the synchronization process the inverter with constant input DC source is connected to the grid. Using the measured signals, a closed loop PI controller is designed inside DSP to control reference active and reactive power and also current references.

At higher voltages, the current has a fifth harmonic causing disturbance in the power. The harmonic spectrum of the inverter output voltage and currents are shown. Attenuation of the harmonic voltage was attempted with synchronous PWM modulation. The switching frequency is chosen to be an integer multiple of $3f_s$, where f_s is the grid frequency. The experimental results show how the actual powers are tracking the references after successful synchronization and connection of the DG unit to the main grid.

Along with the PLL, the enhanced phase lock loop (EPLL) also is designed and the experimental results of both systems are compared. EPLL is used to define the reference frequency and angle of the load voltage. It also operates as a band pass filter for the other parameters like the inverter and grid currents. The outputs of EPLL have lower noise and therefore EPLL tracks the magnitudes, angles and frequencies of the actual input signals more precisely.

CHAPTER 6

DYNAMIC OPERATION AND CONTROL OF GRID CONNECTED INTERIOR PERMANENT MAGNET WIND TURBINE GENERATOR

6.1 Introduction

Recently, the development amount of the renewable energies such as photo voltaic (PV), geothermal, and wind energy has been increased significantly. Remarkable developments have been made with wind turbines during the last decade as a pollution free and renewable source to supplement other electricity generations.

Most of the wind turbines are variable speed to get more power from the same wind regime in comparison with fixed speed wind turbines. They also mostly use either doubly fed induction generator or synchronous generator.

Permanent magnet (PM) machines are one of the most popular kinds of synchronous machines in wind turbine applications because without the need for excitation, they offer several interesting features including maintenance-free operation, high efficiency and reliability, high power factor, and low inertia [119]. Permanent magnet synchronous machines with approximately sinusoidal back electromotive force can be broadly categorized into two types; 1) interior (or buried) permanent magnet machines (IPM) and 2) surface-mounted permanent magnet machines (SPM).

In the interior permanent magnet structure, the equivalent air gap is not uniform and it makes the saliency effect obvious. The quadrature-axis synchronous inductance of

IPM is usually larger than its direct-axis inductance [120], i.e., $L_{sq} > L_{sd}$, which significantly changes the torque production mechanism. Therefore, both magnetic and reluctance torque can be produced by the IPM machine [121]. In the second category, the magnets are mounted on the surface of the rotor. Because the magnets have high reluctance, the SPM machine can be considered to have a large and uniform effective air gap. This property makes the saliency effect negligible. Thus the quadrature-axis synchronous inductance of the SPM machine is equal to its direct-axis inductance, i.e., $L_{sq} = L_{sd}$ [122]. As a result, only magnet torque can be produced by the SPM machine, which arises from the interaction of the magnet flux and the quadrature-axis current component of stator currents (I_{sq}). Compared to the SPM machine, the IPM machine has a mechanically robust and solid structure since the magnets are physically contained and protected. It also contains both reluctance and magnetic torque which causes higher efficiency and operation in a wider speed range.

In this chapter the dynamic model of interior permanent magnet machine as a wind turbine generator is studied. An AC-DC-AC converter connects the wind turbine to the main grid [123]. Control parts are designed to get maximum power from the wind, keep DC link voltage constant, and guarantee unity power factor operation. Loss minimization of the generator is also included. The proportional-integral (PI) controllers are used for the voltage, speed and inner current control loops. The system is simulated in MATLAB/Simulink software and the results presented including the most important state variables and parameters.

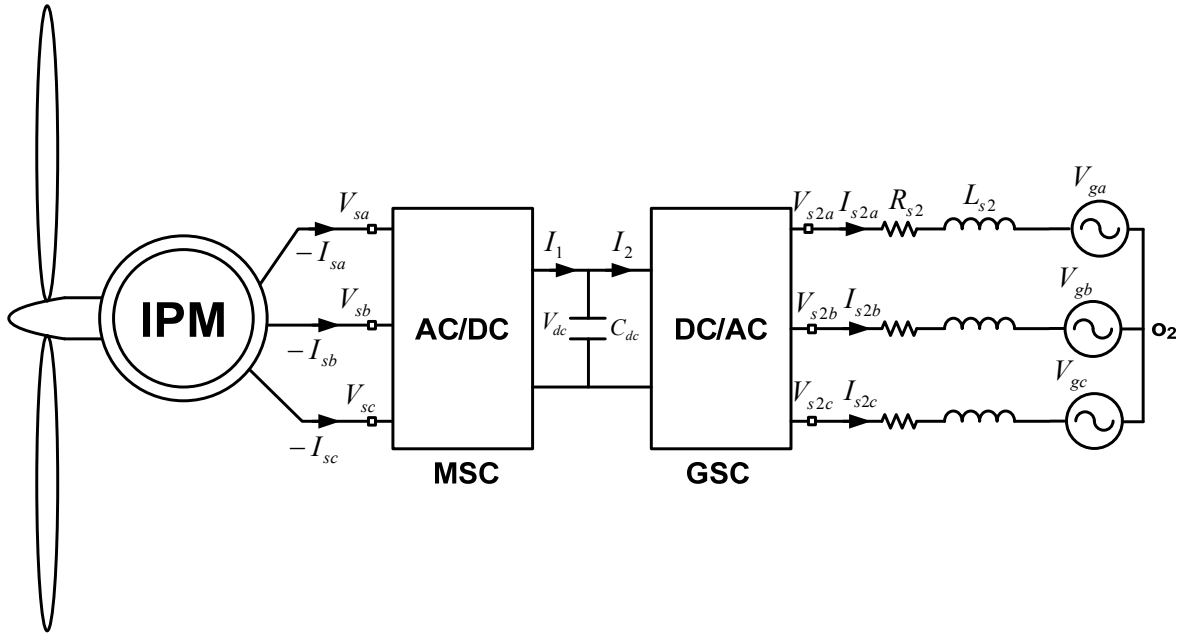


Figure 6.1 Schematic diagram of IPM wind turbine connected to the main grid

6.2 Study System

Figure 6.1 shows the configuration of the studied system including a wind turbine, interface converters, and the network. The wind turbine simply consists of blades, generator and power electronic converters. As shown in Figure 6.1, the wind turbine is connected to the main grid. A three blade horizontal wind turbine is considered. In the studied system an IPM machine converts mechanical power of the wind turbine to electric energy. A full back to back AC-DC-AC converter connects the wind turbine to the main network. It consists of the machine side converter (MSC) and the grid side converter (GSC). The machine side converter controls generator rotor speed to track maximum power point of wind turbine and it minimizes the generator loss simultaneously. The grid side converter controls reactive power flow to the grid and also

it keeps DC link voltage at a constant value. A voltage source is considered as the main grid which is connected to the converters through a transmission line. The resistance of the line also includes the converter switching loss.

6.3 Wind Turbine Model

The power and torque extracted from the wind using wind turbine can be calculated as follows [121]

$$P_T = \frac{1}{2} \rho A C_p(\lambda, \beta) V_w^3 \quad (6.1)$$

$$T_T = \frac{1}{2\omega_T} \rho A C_p(\lambda, \beta) V_w^3 \quad (6.2)$$

$$\lambda = \frac{R\omega_T}{V_w} \quad (6.3)$$

$$C_p = 0.5(\lambda - 0.022\beta^2 - 5.6)e^{(-0.17\lambda)} \quad (6.4)$$

where ρ is the air density, $A(=\pi R^2)$ is area swept by the rotor, C_p is the power coefficient, V_w is the wind speed, λ is tip speed ratio, β is rotor blade pitch angle, R is the turbine rotor radius and ω_T is angular speed of the turbine shaft. Table 6.1 shows parameters of wind turbine.

Table 6.1 Wind turbine parameters

ρ	1.225 Kg/m ³	β	0 deg
R	5.5 m	n_{gear}	6
$V_{w-rated}$	10 m/s	$P_{T-rated}$	24kW

At a particular wind velocity, the amount of power generated by the turbine depends upon the speed of the turbine, turbine parameters, and the air density. The air density is usually assumed to be constant. Turbine parameters are determined by its design and are constant; so for a fixed blade pitch angle, the output power of the turbine is mainly dependent on the turbine speed. In Figure 6.2 power coefficient versus tip speed ratio of the wind turbine at zero pitch angle is illustrated. To get maximum power in a constant pitch angle, we should choose maximum power coefficient ($C_{pmax} = 0.418$ at $\beta = 0$) which corresponds to $\lambda = 11.48$.

Figure 6.3 shows the nonlinear power–speed characteristics of the turbine. The characteristic shifts as the wind speed (V_w) varies. Each power–speed curve is characterized by a unique turbine speed (ω_{rMPP}) corresponding to the maximum power point (MPP) for that wind speed. In addition, for a given wind speed, the maximum power can be extracted if the turbine is rotated at ω_{rMPP} . Mechanical model of the turbine is as follows:

$$J\left(\frac{2}{p}\right)s\omega_r = T_t - T_e \quad (6.5)$$

where p , J and ω_r are the number of poles, inertia and electrical angular rotor velocity of generator respectively. T_t and T_e are wind turbine torque and generator electromechanical torque.

6.3.1 Defining MPP in Wind Turbine

To define maximum power point extracted from each wind speed [124]

$$\frac{dP_T}{d\omega_T} = \frac{1}{2} \rho A V_w^3 \frac{dC_p(\lambda, \beta)}{d\lambda} \frac{d\lambda}{d\omega_T} = 0 \quad (6.6)$$

where $\omega_r = n_{gear} \omega_T$ and $\frac{d\lambda}{d\omega_T} = \frac{R}{V_w}$, therefore

$$(1 - 0.17(\lambda - 0.022\beta^2 - 5.6)) = 0 \quad (6.7)$$

Thus in maximum power point

$$\lambda_{MPP} = \frac{1}{0.17} + 0.022\beta^2 + 5.6 \quad (6.8)$$

$$C_{pMPP} = 0.5(\lambda_{MPP} - 0.022\beta^2 - 5.6)e^{(-0.17\lambda_{MPP})} \quad (6.9)$$

$$\omega_{TMPP} = \frac{\omega_{rMPP}}{n_{gear}} = \frac{\lambda_{MPP} V_w}{R} \quad (6.10)$$

$$P_{TMPP} = k_{opt1} \omega_{TMPP}^3 = k_{opt2} \omega_{r_opt}^3 \quad (6.11)$$

where

$$k_{opt1} = \frac{1}{2} \rho A C_{pMPP} (R / \lambda_{MPP})^3 \quad (6.12)$$

$$k_{opt2} = \frac{k_{opt1}}{n_{gear}^3} \quad (6.13)$$

$$T_{TMMP} = \frac{P_{TMMP}}{\omega_{rMMP}} = k_{opt2} \omega_{rMMP}^2 \quad (6.14)$$

Therefore in any wind speed and pitch angle we will define the optimum rotor speed of the generator as reference value for speed control part

$$\omega_{rMMP} = n_{gear} \frac{\lambda_{MPP} V_w}{R} \quad (6.15)$$

As shown in Figure 6.2 and Figure 6.3, at each pitch angle and wind speed we can define power coefficient, tip speed ratio and generator speed with which we can extract maximum power from the wind.

6.3.2 Pitch Angle Effect

Using (6.4), we can show the effect of pitch angle on power coefficient of wind turbine. Based on (6.1) and (6.4) in a special wind speed and input power

$$C_p = \frac{P_T}{0.5 \rho A V_w^3} \quad (6.16)$$

Moreover, if $xe^x = y \Leftrightarrow x = W(y)$ and W is the Lambert function.

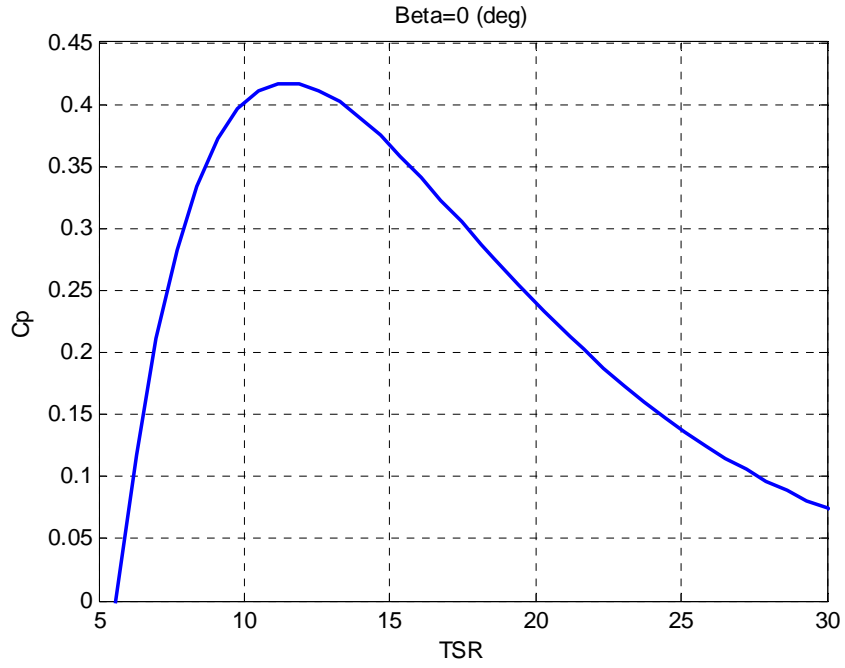


Figure 6.2 Power coefficient versus tip speed ratio at zero pitch angle

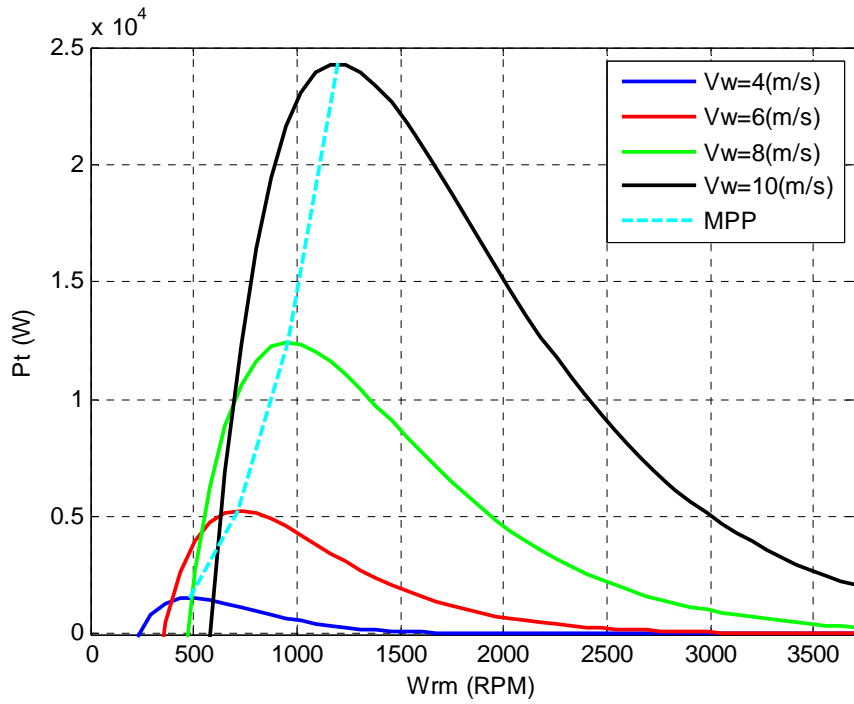


Figure 6.3 Power coefficient versus tip speed ratio at zero pitch angle

$$W(y) = \sum_{n=1}^{\infty} \frac{(-n)^{n-1}}{n!} x^n = x - x^2 + \left(\frac{3}{2}\right)x^3 - \left(\frac{8}{3}\right)x^4 + \dots \quad (6.17)$$

$$C_p = 0.5(\lambda - 0.022\beta^2 - 5.6)e^{(-0.17\lambda)} \quad (6.18)$$

If $C_p = C_{px}$

$$C_{px} = 0.5(\lambda + c_1)e^{(-c_2\lambda)} \quad (6.19)$$

$$\text{where } \begin{cases} c_1 = -0.022\beta^2 - 5.6 \\ c_2 = 0.17 \end{cases}$$

$$(-c_2\lambda - c_1c_2)e^{(-c_2\lambda - c_1c_2)} = -c_2 \frac{C_{px}}{0.5} e^{(-c_1c_2)} \quad (6.20)$$

$$-c_2\lambda - c_1c_2 = W\left(-c_2 \frac{C_{px}}{0.5} e^{(-c_1c_2)}\right) \quad (6.21)$$

$$\lambda = \frac{W\left(-c_2 \frac{C_{px}}{0.5} e^{(-c_1c_2)}\right) + c_1c_2}{-c_2} \quad (6.22)$$

Therefore in any special wind speed and power demand we can define different combinations of pitch angle and tip speed ratio or pitch angle and wind turbine rotor speed.

Figure 6.4 and Figure 6.5 show that with increase of pitch angle, maximum power coefficient reduces which causes a lower output power in a constant wind speed. In

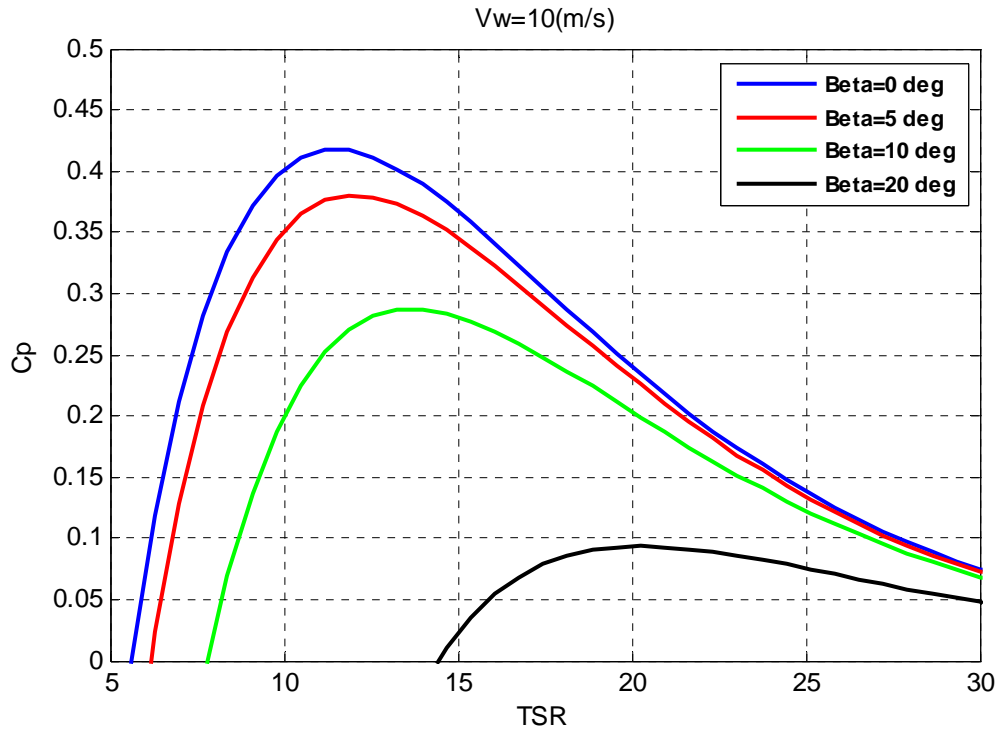


Figure 6.4 Tip speed ratio versus power coefficient at different pitch angle

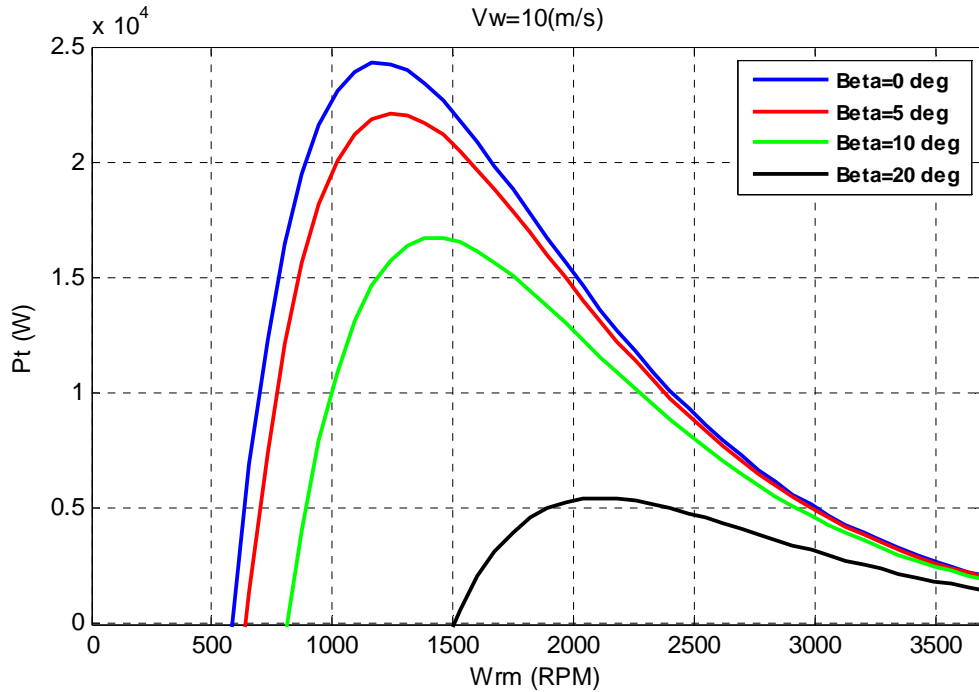


Figure 6.5 Output power of wind turbine versus generator rotor speed at different pitch angle and $V_w = 10 \text{ m/s}$

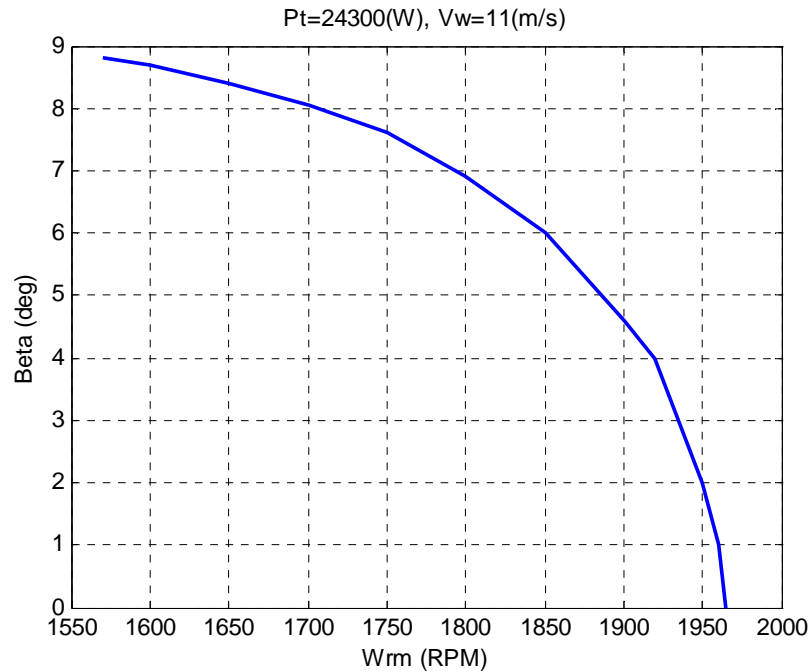


Figure 6.6 Pitch angle versus generator rotor speed at constant turbine power and wind speed

Figure 6.6, if we want to have constant power at a constant wind speed (usually rated power after rated speed) we will have different combination of generator speed and pitch angle to choose from; the higher the pitch angle, the lower the generator speed. Figure 6.7 illustrates changes of the pitch angle at a constant generator speed and constant output active power. Based on the parameters of the wind turbine, at rated speed besides mechanical issues of wind turbine, theoretically we can't increase wind speed more than 19.5 (m/s) in which pitch angle comes back to zero.

6.4 Dynamic Model and Steady State Operation region

The dynamic equations of the system in abc reference frame are as follows:

Stator voltage

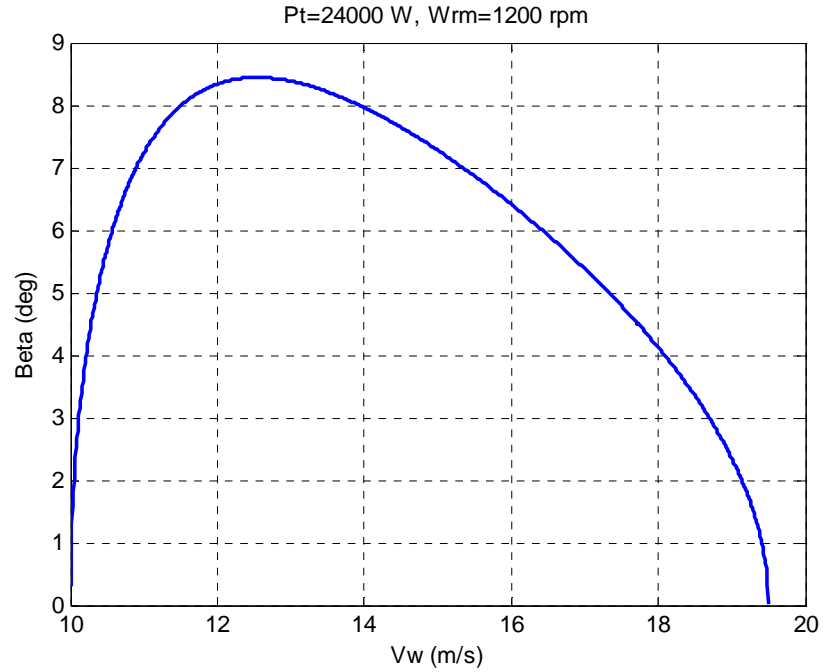


Figure 6.7 Wind speed versus pitch angle at the rated output power and rated rotor speed

$$\begin{cases} V_{sa} = R_s I_{sa} + p \lambda_{sa} \\ V_{sb} = R_s I_{sb} + p \lambda_{sb} \\ V_{sc} = R_s I_{sc} + p \lambda_{sc} \end{cases} \quad (6.23)$$

Stator flux

$$\begin{cases} \lambda_{sa} = L_s I_{sa} + \lambda_{ma} \\ \lambda_{sb} = L_s I_{sb} + \lambda_{mb} \\ \lambda_{sc} = L_s I_{sc} + \lambda_{mc} \end{cases} \quad (6.24)$$

Rotor voltage

$$\begin{cases} V_{ra} = R_r I_{ra} + p \lambda_{ra} \\ V_{rb} = R_r I_{rb} + p \lambda_{rb} \\ V_{rc} = R_r I_{rc} + p \lambda_{rc} \end{cases} \quad (6.25)$$

Rotor flux

$$\begin{cases} \lambda_{ra} = L_r I_{ra} + \lambda_{ma} \\ \lambda_{rb} = L_r I_{rb} + \lambda_{mb} \\ \lambda_{rc} = L_r I_{rc} + \lambda_{mc} \end{cases} \quad (6.26)$$

Machine side converter equations

$$\begin{cases} V_{sa} = V_{an} + V_{no} = \frac{V_{dc}}{2}(2s_{ap1} - 1) + V_{no} \\ V_{sb} = V_{bn} + V_{no} = \frac{V_{dc}}{2}(2s_{bp1} - 1) + V_{no} \\ V_{sc} = V_{cn} + V_{no} = \frac{V_{dc}}{2}(2s_{cp1} - 1) + V_{no} \end{cases} \quad (6.27)$$

$$V_{no} = \frac{1}{3}(V_{sa} + V_{sb} + V_{sc}) - \frac{1}{3}(V_{an} + V_{bn} + V_{cn}) \quad (6.28)$$

$$\begin{cases} s_{ap1} = \frac{1}{2}(1 + M_{ap1}) \\ s_{bp1} = \frac{1}{2}(1 + M_{bp1}) \\ s_{cp1} = \frac{1}{2}(1 + M_{cp1}) \end{cases} \quad (6.29)$$

Capacitor voltage

$$C_{dc} p V_{dc} = I_1 - I_2 = (-s_{ap1} I_{sa} - s_{bp1} I_{sb} - s_{cp1} I_{sc}) - (s_{ap2} I_{La} + s_{bp2} I_{Lb} + s_{cp2} I_{Lc}) \quad (6.30)$$

Grid side converter equations

$$\begin{cases} V_{s2a} = \frac{V_{dc}}{2}(2s_{ap2} - 1) = R_L I_{La} + L_L p I_{La} + V_{ga} + V_{no2} \\ V_{s2b} = \frac{V_{dc}}{2}(2s_{bp2} - 1) = R_L I_{Lb} + L_L p I_{Lb} + V_{gb} + V_{no2} \\ V_{s2c} = \frac{V_{dc}}{2}(2s_{cp2} - 1) = R_L I_{Lc} + L_L p I_{Lc} + V_{gc} + V_{no2} \end{cases} \quad (6.31)$$

$$V_{no2} = \frac{1}{3}(V_{s2a} + V_{s2b} + V_{s2c}) \quad (6.32)$$

$$\begin{cases} s_{ap2} = \frac{1}{2}(1 + M_{ap2}) \\ s_{bp2} = \frac{1}{2}(1 + M_{bp2}) \\ s_{cp2} = \frac{1}{2}(1 + M_{cp2}) \end{cases} \quad (6.33)$$

The core loss can be considered as a resistance as follows:

$$R_c = K_{Rc} \omega_r \quad (6.34)$$

where K_{Rc} is a constant coefficient.

If we choose rotor reference frame (ω_r), the transformed dynamic equations of the system to qd-axis reference frame are as follows:

Stator voltages

$$\begin{cases} V_{sq} = R_s I_{sq} + p \lambda_{sq} + \omega_r \lambda_{sd} \\ V_{sd} = R_s I_{sd} + p \lambda_{sd} - \omega_r \lambda_{sq} \end{cases} \quad (6.35)$$

Rotor voltages

$$\begin{cases} V_{rq} = R_r I_{rq} + p \lambda_{rq} \\ V_{rd} = R_r I_{rd} + p \lambda_{rd} \end{cases} \quad (6.36)$$

Stator flux

$$\begin{cases} \lambda_{sq} = L_{sq} I'_{sq} + L_{mq} I'_{rq} \\ \lambda_{sd} = L_{sd} I'_{sd} + L_{md} I'_{rd} + \lambda_m \end{cases} \quad (6.37)$$

Rotor flux

$$\begin{cases} \lambda_{rq} = L_{rq} I_{rq} + L_{mq} I_{sq} \\ \lambda_{rd} = L_{rd} I_{rd} + L_{md} I_{sd} + \lambda_m \end{cases} \quad (6.38)$$

Torque equation

$$T_e = \frac{3P}{4} (\lambda_{sd} I'_{sq} - \lambda_{sq} I'_{sd}) \quad (6.39)$$

In permanent magnet machine, the dynamic of the rotor can be neglected since the permanent magnet is a poor electrical conductor and the eddy currents that flow in the nonmagnetic materials securing the magnets demagnetization. Therefore

$$\begin{cases} I_{rq} = 0 \\ I_{rd} = 0 \end{cases} \quad (6.40)$$

$$\begin{cases} \lambda_{sq} = L_{sq} I'_{sq} = L_{sq} (I_{sq} - I_{cq}) \\ \lambda_{sd} = L_{sd} I'_{sd} + \lambda_m = L_{sd} (I_{sd} - I_{cd}) + \lambda_m \end{cases} \quad (6.41)$$

Substituting (6.41) into (6.35)

$$\begin{cases} V_{sq} = R_s I_{sq} + L_{sq} p(I_{sq} - I_{cq}) + \omega_r L_{sd} (I_{sd} - I_{cd}) + \omega_r \lambda_m \\ V_{sd} = R_s I_{sd} + L_{sd} p(I_{sd} - I_{cd}) - \omega_r L_{sq} (I_{sq} - I_{cq}) \end{cases} \quad (6.42)$$

or

$$\begin{cases} V_{sq} = R_s I_{sq} + L_{sq} p I'_{sq} + \omega_r L_{sd} I'_{sd} + \omega_r \lambda_m \\ V_{sd} = R_s I_{sd} + L_{sd} p I'_{sd} - \omega_r L_{sq} I'_{sq} \end{cases} \quad (6.43)$$

Currents of core loss resistance are

$$\begin{cases} I_{cq} = I_{sq} - I'_{sq} = \frac{\omega_r L_{sd} I'_{sd} + \omega_r \lambda_m}{R_c} = \frac{\omega_r \lambda_{sd}}{R_c} = \frac{V_{sq} - R_s I_{sq}}{R_c} \\ I_{cd} = I_{sd} - I'_{sd} = \frac{-\omega_r L_{sq} I'_{sq}}{R_c} = \frac{-\omega_r \lambda_{sq}}{R_c} = \frac{V_{sd} - R_s I_{sd}}{R_c} \end{cases} \quad (6.44)$$

so

$$\begin{cases} I_{sq} = \frac{\omega_r L_{sd} I'_{sd} + \omega_r \lambda_m}{R_c} + I'_{sq} \\ I_{sd} = \frac{-\omega_r L_{sq} I'_{sq}}{R_c} + I'_{sd} \end{cases} \quad \text{Or} \quad \begin{cases} I'_{sq} = \frac{R_c^2 I_{sq} - R_c \omega_r \lambda_m - R_c \omega_r L_{sd} I_{sd}}{R_c^2 + \omega_r^2 L_{sd} L_{sq}} \\ I'_{sd} = \frac{R_c^2 I_{sd} - \omega_r^2 L_{sq} \lambda_m + \omega_r L_{sq} R_c I_{sq}}{R_c^2 + \omega_r^2 L_{sd} L_{sq}} \end{cases} \quad (6.45)$$

Rewriting the torque and voltage equations

$$T_e = \frac{3P}{4} (\lambda_m I'_{sq} + (L_{sd} - L_{sq}) I'_{sq} I'_{sd}) \quad (6.46)$$

$$\begin{cases} V_{sq} = R_s I'_{sq} + L_{sq} p I'_{sq} + \omega_r L_{sd} I'_{sd} + \omega_r \lambda_m \frac{L_{sq}}{L_{sq}} \\ V_{sd} = R_s I'_{sd} + L_{sd} p I'_{sd} - \omega_r L_{sq} I'_{sq} \end{cases} \quad (6.47)$$

If we use the Thevenin circuit we can also write

$$\begin{cases} V'_{sq} = R'_s I_{sq} + L_{sq} p I_{sq} + \omega_r L_{sd} I_{sd} + \omega_r \lambda_m \\ V'_{sd} = R'_s I_{sd} + L_{sd} p I_{sd} - \omega_r L_{sq} I_{sq} \end{cases} \quad (6.48)$$

where

$$R'_s = \frac{R_s R_c}{R_s + R_c} \quad (6.49)$$

$$V'_{sq} = \frac{V_{sq} R_c}{R_s + R_c} \quad (6.50)$$

$$V'_{sd} = \frac{V_{sd} R_c}{R_s + R_c} \quad (6.51)$$

$$L_{sqc} = \frac{L_{sq} (R_s + R_c)}{R_c} \quad (6.52)$$

$$L_{sdc} = \frac{L_{sd} (R_s + R_c)}{R_c} \quad (6.53)$$

$$L_{sq} = L_{ls} + L_{mq} \quad \text{and} \quad L_{sd} = L_{ls} + L_{md} \quad (6.54)$$

The equivalent circuit of the IPM machine is shown in Figure 6.8. Its Parameters are presented in Table 6.2

The dynamic equations of the power system and converters are

Machine side converter equations

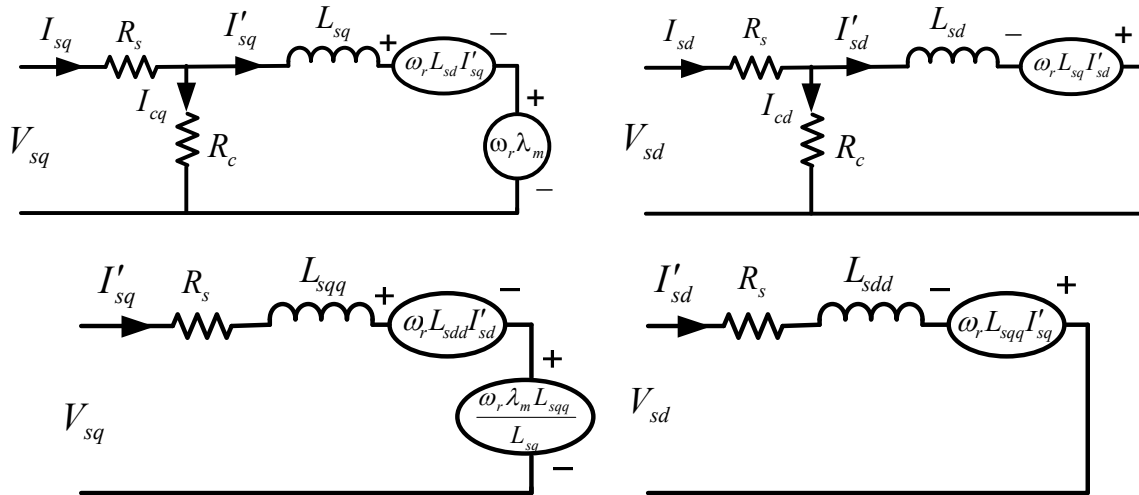


Figure 6.8 Equivalent circuits of IPM Machine

Table 6.2 Parameters of the IPM machine and the grid

$V_{m-rated}$	380 V	$I_{m-rated}$	66.87 A
$\omega_{m-rated}$	1200 rpm	P (no of poles)	6
R_s	0.1764 Ω	λ_m	0.246 Wb
L_{sd}	6.24 mH	L_{sq}	20.582 mH
C_{dc}	$10e^{-3}$ F	V_g	$350 \angle 0^\circ$ V
R_{s2}	0.01 Ω	L_{s2}	0.4 mH

$$\begin{cases} V_{sq} = \frac{M_{q1}}{2} V_{dc} \\ V_{sd} = \frac{M_{d1}}{2} V_{dc} \end{cases} \quad (6.55)$$

Capacitor equations

$$C_{dc} p V_{dc} = I_1 - I_2 = -\frac{3}{4} (M_{q1} I_{sq} + M_{d1} I_{sd}) - \frac{3}{4} (M_{q1} I_{Lq} + M_{d1} I_{Ld}) \quad (6.56)$$

Inverter equations

$$\begin{cases} V_{s2q} = \frac{M_{q2}}{2} V_{dc} = R_L I_{Lq} + L_L p I_{Lq} + \omega_r L_L I_{Ld} + V_{gq} \\ V_{s2d} = \frac{M_{d2}}{2} V_{dc} = R_L I_{Ld} + L_L p I_{Ld} - \omega_r L_L I_{Lq} + V_{gd} \end{cases} \quad (6.57)$$

To define minimum loss operation point

Copper loss equation

$$P_{copper} = \left(\frac{3}{2}\right) R_s (I_{sq}^2 + I_{sd}^2) = 1.5 R_s \left(\left(\frac{\omega_r L_{sd} I'_{sd} + \omega_r \lambda_m}{R_c} + I'_{sq} \right)^2 + \left(\frac{-\omega_r L_{sq} I'_{sq}}{R_c} + I'_{sd} \right)^2 \right) \quad (6.58)$$

$$P_{copper} = \left\{ \begin{aligned} &1.5 R_s (I_{sq}^2 + I_{sd}^2) + 1.5 R_s \frac{\omega_r^2}{R_c^2} (L_{sd}^2 I_{sd}'^2 + L_{sq}^2 I_{sq}'^2) + 1.5 R_s \frac{\omega_r^2 \lambda_m^2}{R_c^2} \\ &+ 3 R_s \frac{\omega_r^2 L_{sd} \lambda_m I'_{sd}}{R_c^2} + 3 R_s \frac{\omega_r I'_{sd} I'_{sq}}{R_c} (L_{sd} - L_{sq}) + 3 R_s \frac{\omega_r \lambda_m I'_{sq}}{R_c} \end{aligned} \right\} \quad (6.59)$$

Core loss equation

$$P_{core} = \left(\frac{3}{2}\right) R_c (I_{cq}^2 + I_{cd}^2) = 1.5 R_c \left(\left(\frac{\omega_r L_{sd} I'_{sd} + \omega_r \lambda_m}{R_c} \right)^2 + \left(\frac{-\omega_r L_{sq} I'_{sq}}{R_c} \right)^2 \right) \quad (6.60)$$

$$P_{core} = 1.5 \frac{\omega_r^2}{R_c} (L_{sd}^2 I_{sd}'^2 + L_{sq}^2 I_{sq}'^2) + 1.5 \frac{\omega_r^2 \lambda_m^2}{R_c} + 3 \frac{\omega_r^2 L_{sd} \lambda_m I'_{sd}}{R_c} \quad (6.61)$$

Thus the total loss is

$$P_{loss} = P_{copper} + P_{core} \quad (6.62)$$

$$P_{loss} = \left\{ \begin{aligned} &1.5R_s(I'_{sq}{}^2 + I'_{sd}{}^2) + 1.5\frac{\omega_r^2}{R_c}(R_s + R_c)(L_{sd}{}^2 I'_{sd}{}^2 + L_{sq}{}^2 I'_{sq}{}^2) + 1.5(R_s + R_c)\frac{\omega_r^2 \lambda_m^2}{R_c^2} \\ &+ 3(R_s + R_c)\frac{\omega_r^2 L_{sd} \lambda_m I'_{sd}}{R_c^2} + 3R_s \frac{\omega_r I'_{sd} I'_{sq}}{R_c} (L_{sd} - L_{sq}) + 3R_s \frac{\omega_r \lambda_m I'_{sq}}{R_c} \end{aligned} \right\} \quad (6.63)$$

The output active power of generator

$$P_e = \frac{3}{2}(V_{sq} I_{sq} + V_{sd} I_{sd}) \quad (6.64)$$

$$P_e = \left\{ \frac{3}{2} \left(\left(R_s I'_{sq} + \omega_r L_{sdd} I'_{sd} + \omega_r \lambda_m \frac{L_{sqq}}{L_{sq}} \right) \left(\frac{\omega_r L_{sd} I'_{sd} + \omega_r \lambda_m + I'_{sq}}{R_c} \right) + \left(R_s I'_{sd} - \omega_r L_{sqq} I'_{sq} \right) \left(\frac{-\omega_r L_{sq} I'_{sq}}{R_c} + I'_{sd} \right) \right) \right\} \quad (6.65)$$

Derivative of output active power versus q-axis stator current

$$\frac{\partial P_e}{\partial I'_{sq}} = \frac{3}{2} \left\{ \begin{aligned} &R_s \left(\frac{\omega_r L_{sd} I'_{sd} + \omega_r \lambda_m + I'_{sq}}{R_c} \right) + \left(R_s I'_{sq} + \omega_r L_{sdd} I'_{sd} + \omega_r \lambda_m \frac{L_{sqq}}{L_{sq}} \right) \\ &-\omega_r L_{sqq} \left(\frac{-\omega_r L_{sq} I'_{sq}}{R_c} + I'_{sd} \right) - \frac{\omega_r L_{sq}}{R_c} (R_s I'_{sd} - \omega_r L_{sqq} I'_{sq}) \end{aligned} \right\} \quad (6.66)$$

Derivative of output active power versus d-axis stator current

$$\frac{\partial P_e}{\partial I'_{sd}} = \frac{3}{2} \left\{ \begin{aligned} &\omega_r L_{sdd} \left(\frac{\omega_r L_{sd} I'_{sd} + \omega_r \lambda_m + I'_{sq}}{R_c} \right) + \frac{\omega_r L_{sd}}{R_c} \left(R_s I'_{sq} + \omega_r L_{sdd} I'_{sd} + \omega_r \lambda_m \frac{L_{sqq}}{L_{sq}} \right) \\ &+ R_s \left(\frac{-\omega_r L_{sq} I'_{sq}}{R_c} + I'_{sd} \right) + (R_s I'_{sd} - \omega_r L_{sqq} I'_{sq}) \end{aligned} \right\} \quad (6.67)$$

Derivative of total loss versus q-axis stator current

$$\frac{\partial P_{loss}}{\partial I'_{sq}} = \left\{ 3R_s I'_{sq} + 3 \frac{\omega_r^2}{R_c} (R_s + R_c) L_{sq}^2 I'_{sq} + 3R_s \frac{\omega_r I'_{sd}}{R_c} (L_{sd} - L_{sq}) + 3R_s \frac{\omega_r \lambda_m}{R_c} \right\} \quad (6.68)$$

Derivative of total loss versus d-axis stator current

$$\frac{\partial P_{loss}}{\partial I'_{sd}} = \left\{ 3R_s I'_{sd} + 3 \frac{\omega_r^2}{R_c} (R_s + R_c) L_{sd}^2 I'_{sd} + 3(R_s + R_c) \frac{\omega_r^2 L_{sd} \lambda_m}{R_c^2} + 3R_s \frac{\omega_r I'_{sq}}{R_c} (L_{sd} - L_{sq}) \right\} \quad (6.69)$$

For minimum loss (optimization) the following determinant should be zero

$$\gamma = \begin{vmatrix} \frac{\partial P_e}{\partial I'_{sq}} & \frac{\partial P_e}{\partial I'_{sd}} \\ \frac{\partial P_{loss}}{\partial I'_{sq}} & \frac{\partial P_{loss}}{\partial I'_{sd}} \end{vmatrix} = 0 \quad (6.70)$$

Moreover due to the use of motor equations, calculated power is negative therefore

$$-P_e = - \left\{ \frac{3}{2} \left(\left(R_s I'_{sq} + \omega_r L_{sdd} I'_{sd} + \omega_r \lambda_m \frac{L_{sq}}{L_{sq}} \right) \left(\frac{\omega_r L_{sd} I'_{sd} + \omega_r \lambda_m}{R_c} + I'_{sq} \right) + \left(R_s I'_{sd} - \omega_r L_{sq} I'_{sq} \right) \left(\frac{-\omega_r L_{sq} I'_{sq}}{R_c} + I'_{sd} \right) \right) \right\} = P_T - P_{copper} \quad (6.71)$$

Therefore in each wind speed with defining output wind power as follows:

$$\begin{cases} P_T = P_{TMPP} & \omega_r \leq \omega_b \\ P_T = P_b & \omega_r > \omega_b \end{cases} \quad (6.72)$$

And using (6.70) and (6.71) we will have two equations and two variables (I'_{sq}, I'_{sd}) which will define the steady state operation region of wind turbine.

6.4.1 Steady State Operation under Constant Generator Speed after Nominal Wind Speed

To keep generator speed or wind turbine speed constant after rated wind speed, pitch angle should be increased based on Figure 6.7. Figure 6.9 shows after nominal wind speed (10 (m/s)), with increase of pitch angle, wind turbine rotor speed remains constant at rated value (1200 rpm). In Figure 6.10, due to constant DC-link voltage, the modulation index of the converter increases based on the voltage magnitude and it is always less than unity. In Figure 6.11, magnitudes of qd-axis stator currents are shown. They are defined in a way that prepare minimum total loss and follow maximum power point of wind turbine characteristics. Current direction is negative because the motor equation is used for the generator. Figure 6.12 illustrates output voltage and current magnitude behavior of the stator. Before rated wind speed, both current and voltage magnitudes increase then remain constant. Figure 6.13 presents maximum power point tracking of the wind turbine characteristic and keeping output power constant at rated value after nominal wind speed using pitch angle control. The small difference between the input power from wind turbine and the output power of the generator is due to total loss which is always minimized. In Figure 6.14 efficiency of the generator for total loss minimization in different wind speeds is shown. With increase of wind speed, efficiency first decreases and then starts to increase. Total deviation of efficiency is less than 3% and after nominal wind speed it is fixed at around 95%.

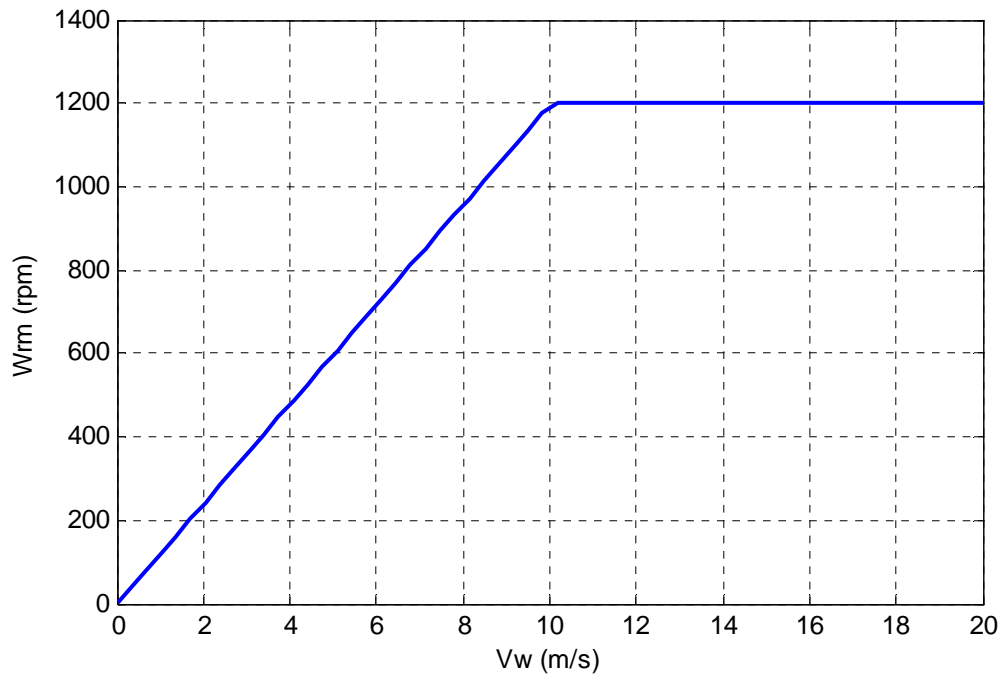


Figure 6.9 Wind turbine speed versus wind speed

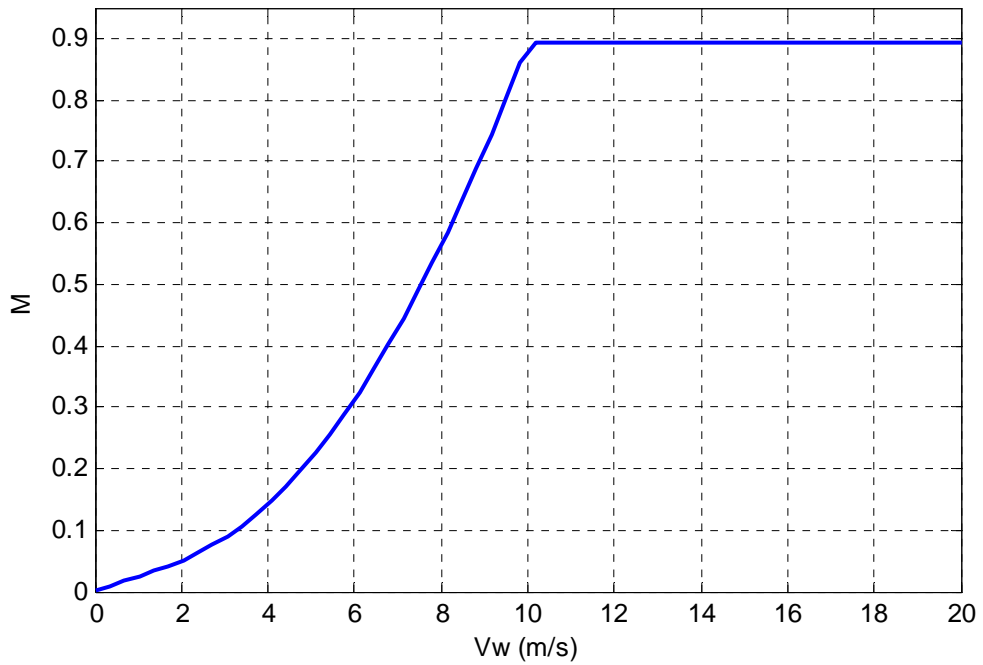


Figure 6.10 Machine side converter modulation index versus wind speed

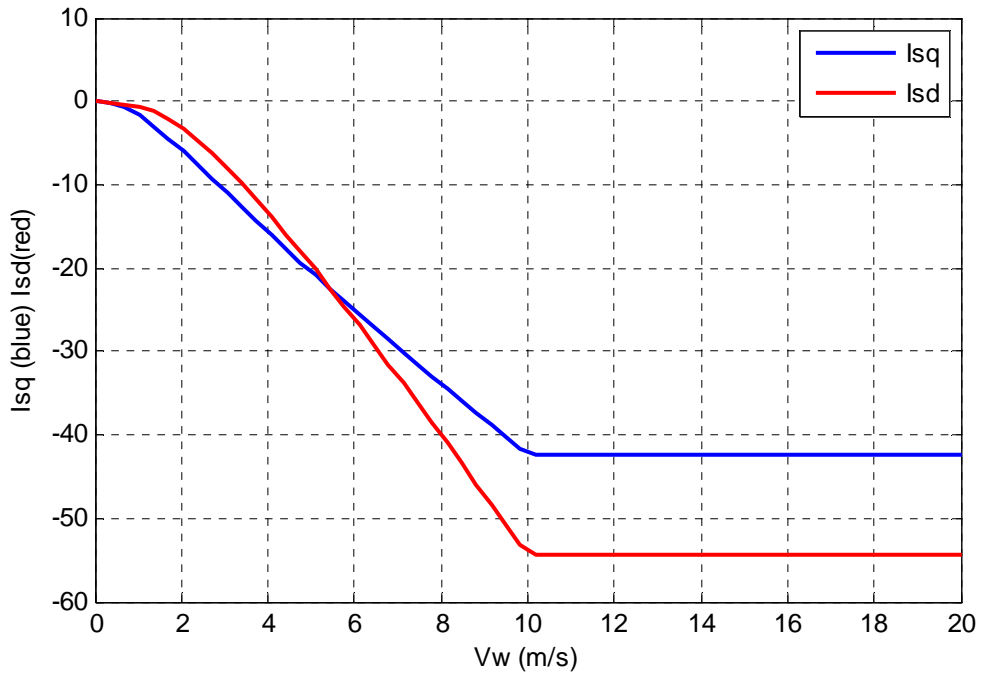


Figure 6.11 qd-axis stator current magnitudes versus wind speed

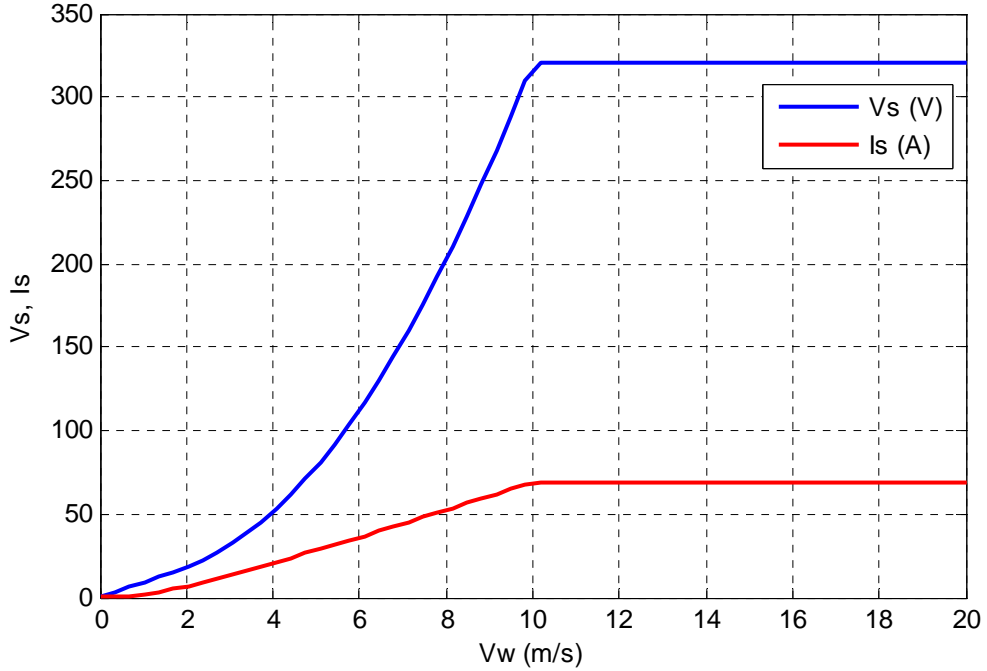


Figure 6.12 Stator voltage and current magnitude versus wind speed

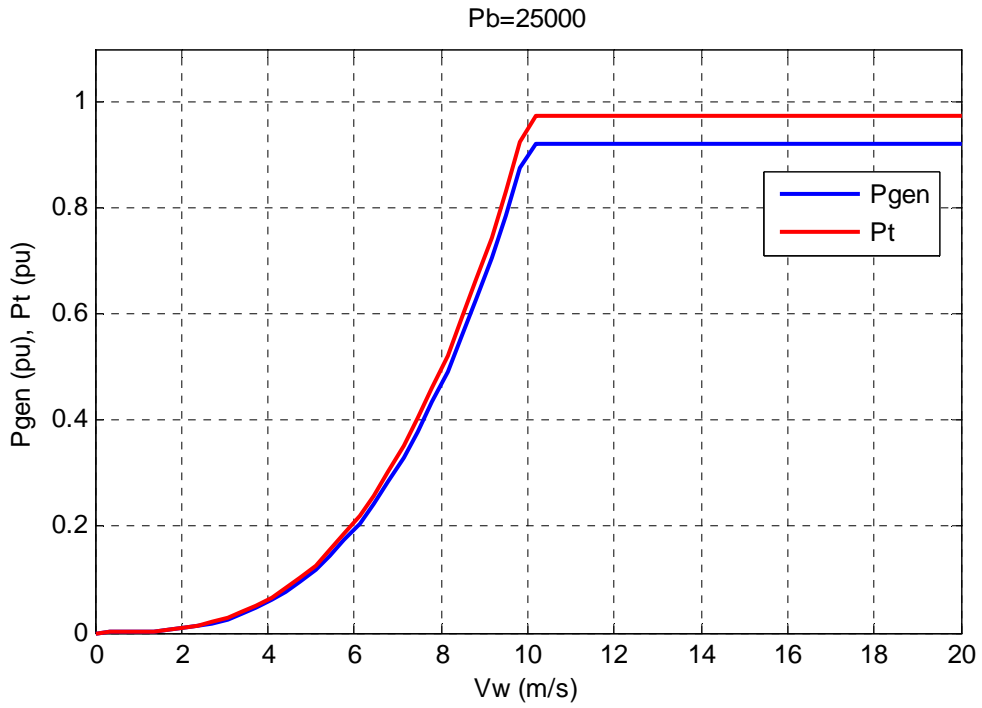


Figure 6.13 Power of wind turbine and output active power of generator versus wind speed

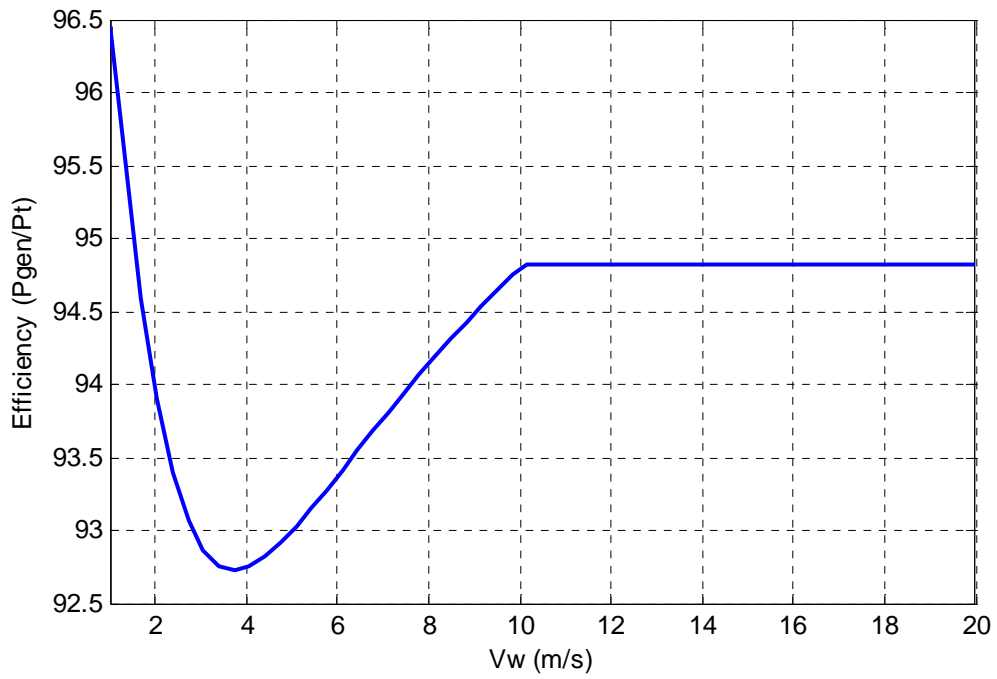


Figure 6.14 Efficiency versus wind speed

6.4.2 Steady state operation under constant pitch angle

In this section, pitch angle is kept constant at zero (pitch angle control is ignored). With increase of wind speed in constant pitch angle, wind turbine rotor speed increases gradually as illustrated in Figure 6.15. Difference of this condition is after rated wind speed at which because of loss minimization, instead of constant current and voltage magnitude, current starts to decrease and voltage increases in Figure 6.16 to keep the output power constant. Due to increase of voltage output magnitude in the same DC-link voltage, the modulation index of converter goes beyond unity after a rotor speed of around 1750 rpm as shown in Figure 6.17. Like the previous case, efficiency first decrease and then increases, however after rated rotor speed efficiency still increases as shown in Figure 6.19, which make this case more efficient after rated speed than the previous case if we ignore over speed of wind turbine and overflow of modulation index or choose a bigger DC-link voltage.

6.5 Operation Regions of the Permanent Magnet Machine

In general a permanent magnet (PM) machine can operate as either a motor or generator in both rotating directions. A common synchronous machine has two operation regions. Before nominal speed it is usually working at constant torque as illustrated in Figure 6.20. In this region, output power increases based on mechanical speed.

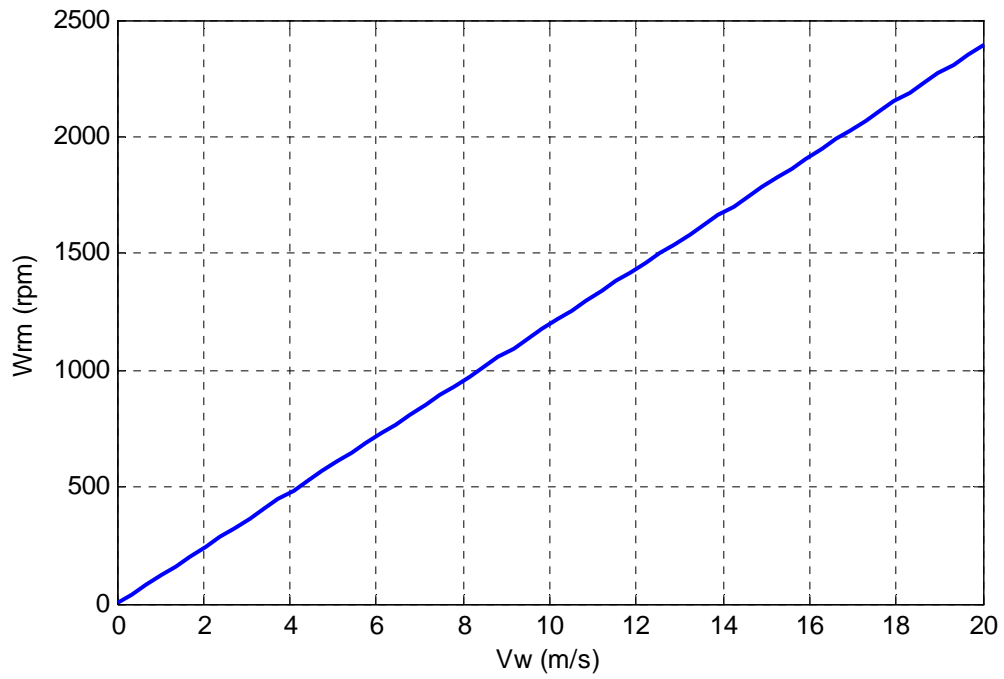


Figure 6.15 Wind turbine speed versus wind speed

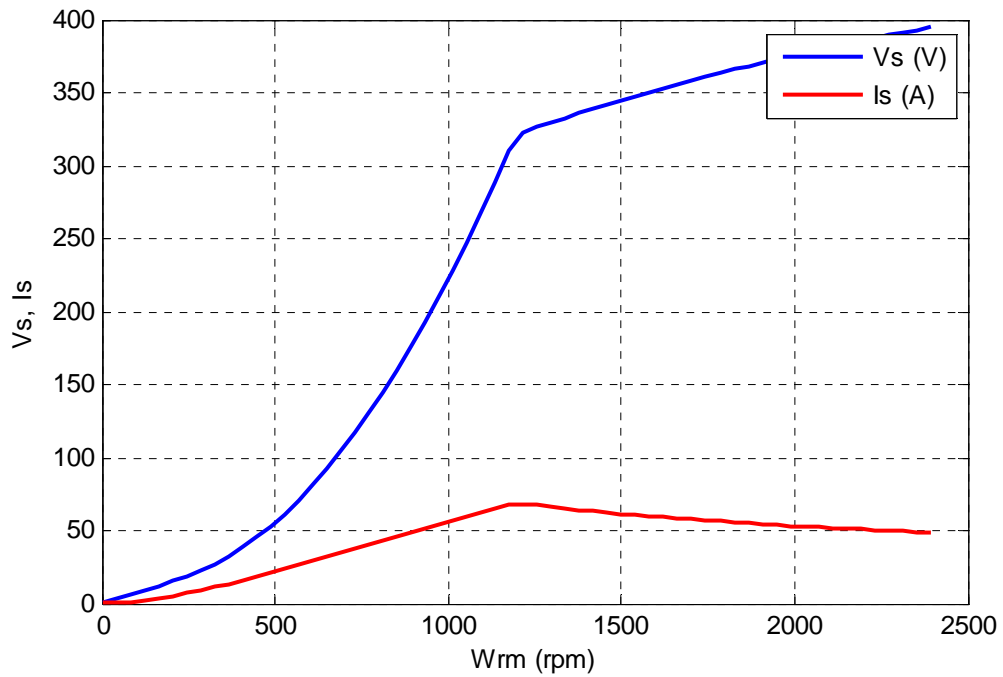


Figure 6.16 Stator voltage and current magnitude versus wind speed

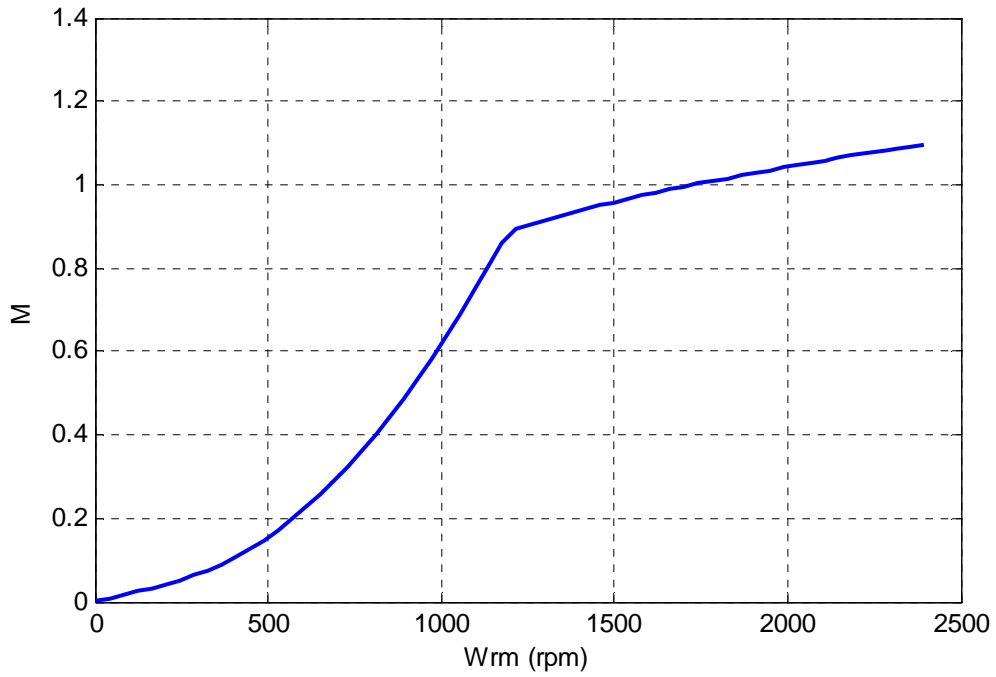


Figure 6.17 Converter modulation index versus wind speed

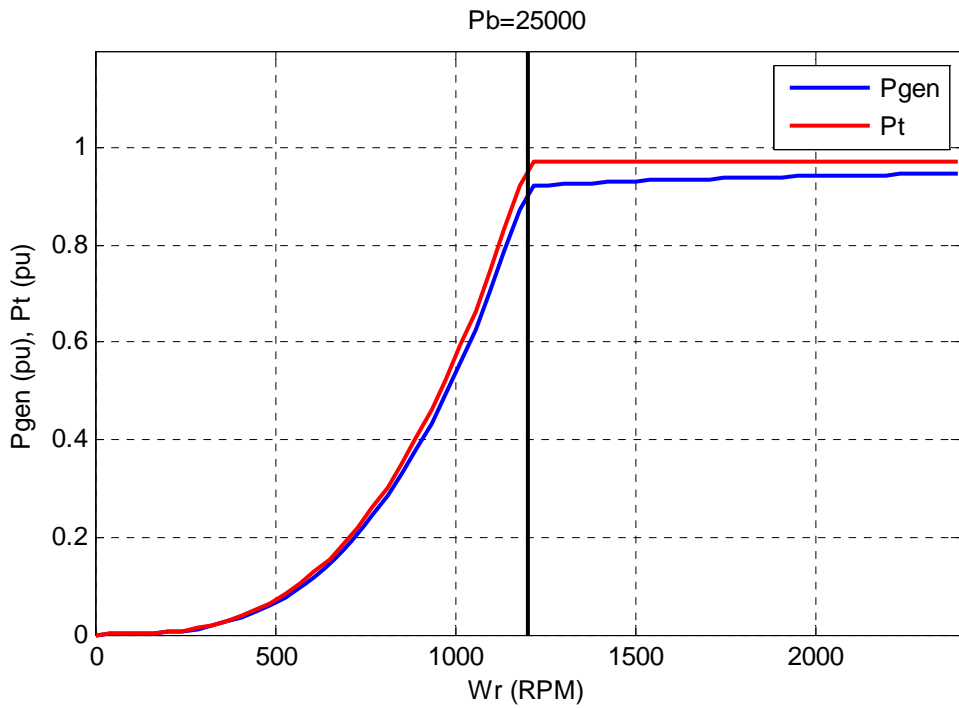


Figure 6.18 Power of wind turbine and output active power of generator versus wind speed

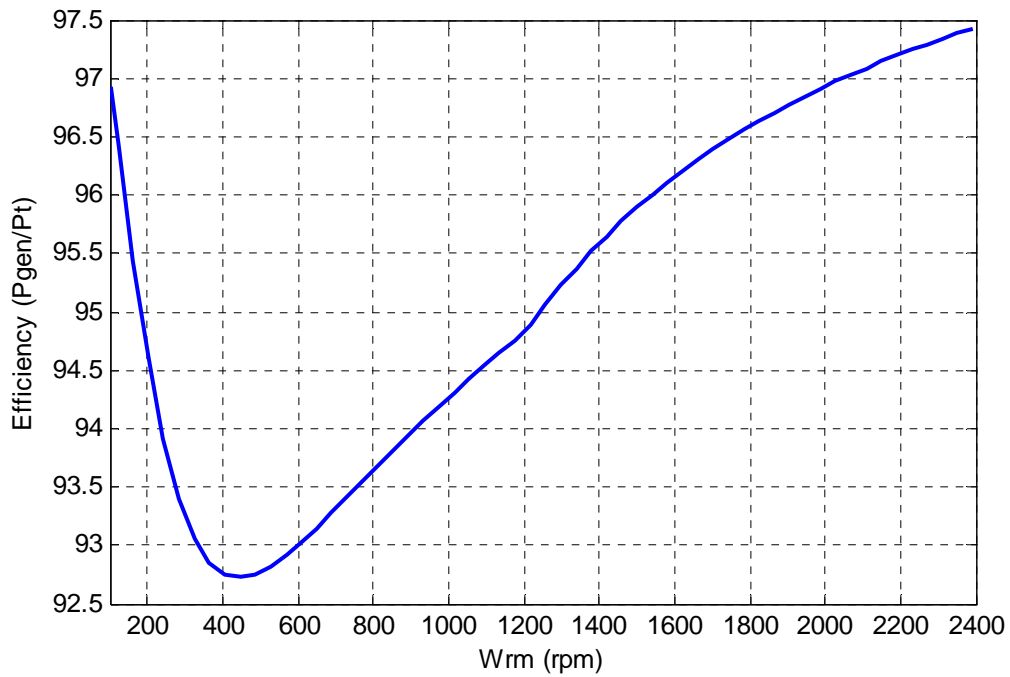


Figure 6.19 Efficiency versus wind speed

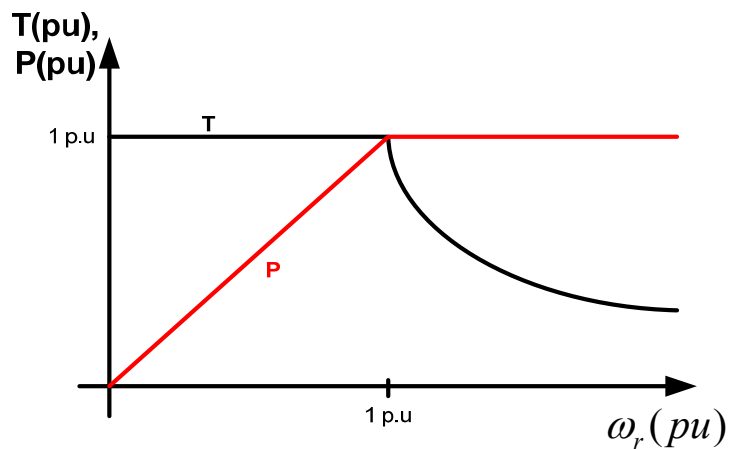


Figure 6.20 Power and torque characteristics of PM machine

Once the machine reaches its rated speed, output power remains constant at nominal value and the torque starts to decrease.

In a permanent magnet synchronous machine, to extend operating speed range, demagnetizing phase currents are generally applied to weaken the air-gap flux. This is

known as flux-weakening control and thus the motor is operated in the flux-weakening region.

6.5.1 Voltage and Current Constraints of PM Machine

In normal operation, with the speed of the PM motors increasing, the voltage applied to the motor must increase accordingly in order to counteract the speed-proportional induced back EMF in the stator windings. When the speed reaches the rated value, eventually, the voltage applied to the PMSM cannot be further increased to maintain the current required by torque production. On the other hand, considering the current capability, the maximum stator current is limited by the current rating of inverter as well as the thermal rating of stator windings.

Therefore, the maximum output torque and power developed by the PM machine is ultimately determined by the maximum current and voltage of the machine or the inverter connected to the machine.

Assume that the voltage applied to the PM machine reaches its limit. The maximum stator voltage, $V_{s\max}$, is determined as

$$V_{sq}^2 + V_{sd}^2 \leq V_{s\max}^2 \quad (6.73)$$

Hence, at high speeds, the voltage vector should remain on the locus of a circle with radius $V_{s\max}$ for maximum-power output.

Neglecting the ohmic voltage drop of stator resistance for high-speed operation, the limit by the maximum stator voltage is expressed in terms of steady-state currents as

$$(-\omega_r L_{sq} I_{sq})^2 + (\omega_r L_{sd} I_{sd} + \omega_r \lambda_m)^2 \leq V_{s \max}^2 \quad (6.74)$$

It can be seen that the current vector trajectories in the rotor reference frame are constrained by an ellipse at a specific speed in qd-axis stator current plane. Referring to the IPM, of which the quadrature-axis stator inductance is larger than the direct-axis inductance, i.e., $L_q > L_d$, the minor axis of the ellipse will be in the q-axis current direction.

Figure 6.21 shows the voltage-limited ellipses with respect to different operating speeds in the flux-weakening region. As illustrated, the voltage constraint determines a series of nested ellipses, i.e., concentration ellipses, centered at Point A $(-\lambda_m / L_{sd}, 0)$ in the qd-axis stator current plane. As the maximum voltage $V_{s \max}$ is fixed, the ellipse shrinks inversely with rotor speed ω_r . It should be noted that the shape of the ellipses depends upon the saliency ratio, which is defined as L_q/L_d . For all nonsaliency PM machines, e.g., surface-mounted PM motors, the voltage-limited ellipses change to circles and the corresponding equation is

$$L_{sq} = L_{sd} = L_s \quad (6.75)$$

$$(-\omega_r L_s I_{sq})^2 + (\omega_r L_s I_{sd} + \omega_r \lambda_m)^2 \leq V_{s \max}^2 \quad (6.76)$$

On the other hand, the current I_{sq} and I_{sd} must satisfy

$$I_{sq}^2 + I_{sd}^2 \leq I_{s \max}^2 \quad (6.77)$$

where $I_{s \max}$ is the allowable maximum stator current. This expression represents a current-limited circle centered at the origin and with the radius of $I_{s \max}$ as shown in Figure 6.21b.

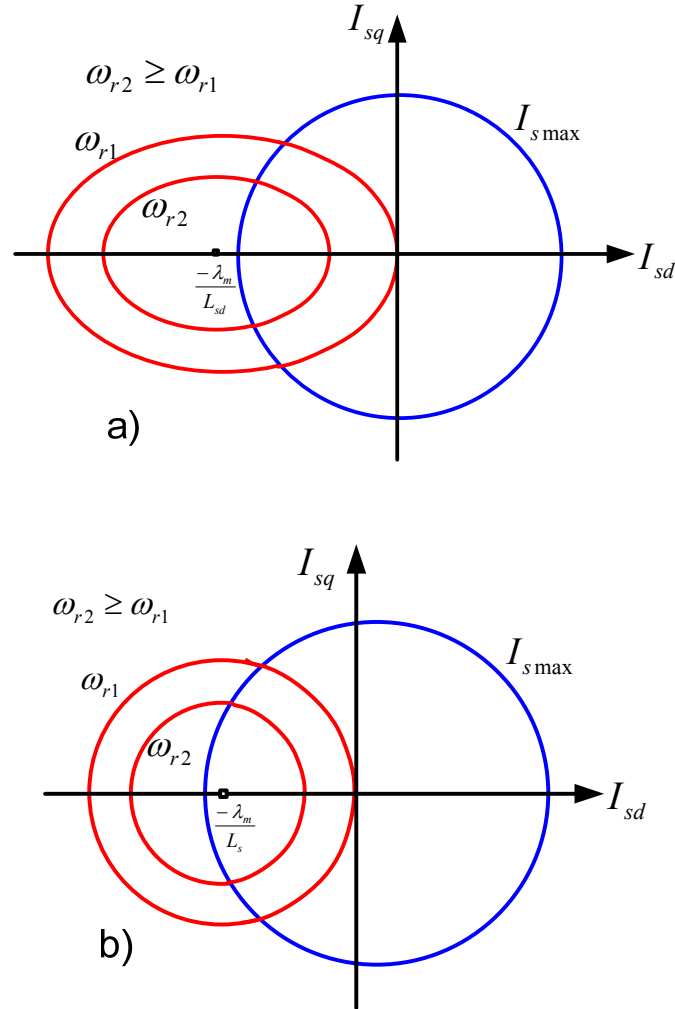


Figure 6.21 Voltage and current constraints characteristics a) Interior permanent magnet machine b) Surface mounted permanent magnet machine

It should be noticed that this current-limited circle remains constant for any speed and the instantaneous current I_{sq} and I_{sd} must comply with the maximum current constraint. In the qd -axis stator current plane, any combination of values of current component I_{sq} and I_{sd} generates a directed current vector from the origin. To a given rotor speed, the current vector can reach anywhere inside or on the boundary of the overlap area between the associated voltage-limited ellipse/circle and the current-limited circle during steady-state operation but not outside it. The overlap area becomes smaller

and smaller and even disappears when the rotor speed keeps increasing, indicating progressively smaller ranges for the current vector in the flux-weakening region.

6.5.2 Maximum Torque per Ampere (MTPA) Operation ($\omega \leq \omega_b$)

The maximum electromagnetic torque and output power developed by the PM machine is ultimately dependent on the allowable current rating and the maximum output voltage.

In a PM machine, which operates at a given speed and torque, optimal efficiency can be obtained by the application of an optimal voltage that minimizes power losses. At low speeds, this optimum will coincide with the condition of maximum torque per stator ampere, assuming the core losses to be negligible. Such operation leads to minimal copper losses of stator windings and power losses of semiconductor switches in the power inverter. Furthermore, minimization of the stator current for the given maximum torque results in a lower current rating of the inverter and thus the overall cost of the PMSM drive system is reduced; therefore, in most cases, the MTPA control mode is preferred for the constant-torque operation of PM machines. As presented previously in (6.46) the electromagnetic torque consists of

- a) Magnet torque, which is proportional to the product of the magnet flux linkage (i.e., rotor flux in the rotor reference frame) and the quadrature-axis stator current (i.e., torque producing stator current component).

b) Reluctance torque only for PM machines with saliency, which is dependent on the saliency ratio $\left(\frac{L_q}{L_d}\right)$ and the product of the direct-axis the quadrature-axis stator current components. Hence the electromagnetic torque of PMSM can be controlled instantaneously through controlling the stator currents in the rotating reference frame to meet load torque requirements.

If the stator currents are set to their maximum permissible value then, from (6.46), it is easy to see the maximum torque of SPM motors

$$T_{e\max} = \frac{3P}{4} \lambda_m I_{s\max} \quad (6.78)$$

where the quadrature-axis current component I_{sq_maxT} equals the maximum current $I_{s\max}$ while the direct-axis component I_{sd_maxT} is kept zero as

$$\begin{cases} I_{sd_maxT} = 0 \\ I_{sq_maxT} = I_{s\max} \end{cases} \quad (6.79)$$

As for IPM motors, in contrast, the maximum torque is produced when the stator current reaches its maximum but both its direct-axis and quadrature-axis component, I_{sd_maxT} and I_{sq_maxT} respectively, have values in agreement with torque optimization. It can be calculated as follows:

Torque equation based on stator phase current magnitude and its phase angle

$$T_e = \frac{3P}{4} (\lambda_m I_{sq} + (L_{sd} - L_{sq}) I_{sq} I_{sd}) \text{ and } \begin{cases} I_{sq} = I_{sa} \cos \beta \\ I_{sd} = -I_{sa} \sin \beta \end{cases} \quad (6.80)$$

$$T_e = \frac{3P}{4} \left(\lambda_m I_{sa} \cos \beta + (L_{sd} - L_{sq})(I_{sa} \cos \beta)(-I_{sa} \sin \beta) \right) \quad (6.81)$$

$$T_e = \frac{3P}{4} \left(\lambda_m I_{sa} \cos \beta + \frac{1}{2} (L_{sq} - L_{sd}) I_{sa}^2 \sin 2\beta \right) \quad (6.82)$$

For maximum torque per ampere (MTPA)

$$\frac{dT_e}{d\beta} = \frac{3P}{4} \left(-\lambda_m I_{sa} \sin \beta + (L_{sq} - L_{sd}) I_{sa}^2 \cos 2\beta \right) = 0 \quad (6.83)$$

$$-\lambda_m I_{sa} \sin \beta + (L_{sq} - L_{sd}) I_{sa}^2 (\cos^2 \beta - \sin^2 \beta) = 0 \quad (6.84)$$

$$\lambda_m I_{sd} + (L_{sq} - L_{sd}) I_{sq}^2 - (L_{sq} - L_{sd}) I_{sd}^2 = 0 \quad (6.85)$$

Relationship between qd-axis stator current in MTPA condition

$$I_{sq} = \pm \sqrt{I_{sd}^2 - \frac{\lambda_m}{(L_{sq} - L_{sd})} I_{sd}} \quad (6.86)$$

$$I_{sd} = \frac{-\lambda_m \pm \sqrt{\lambda_m^2 + 4(L_{sq} - L_{sd})^2 I_{sq}^2}}{-2(L_{sq} - L_{sd})} \Rightarrow I_{sd} = \frac{\lambda_m - \sqrt{\lambda_m^2 + 4(L_{sq} - L_{sd})^2 I_{sq}^2}}{2(L_{sq} - L_{sd})} \quad (6.87)$$

To find the angle of current at MTPA

$$-\lambda_m I_{sa} \sin \beta + (L_{sq} - L_{sd}) I_{sa}^2 (\cos^2 \beta - \sin^2 \beta) = -\lambda_m I_{sa} \sin \beta + (L_{sq} - L_{sd}) I_{sa}^2 (1 - 2 \sin^2 \beta) = 0 \quad (6.88)$$

$$-2(L_{sq} - L_{sd}) I_{sa}^2 \sin^2 \beta - \lambda_m I_{sa} \sin \beta + (L_{sq} - L_{sd}) I_{sa}^2 = 0 \quad (6.89)$$

$$-2(L_{sq} - L_{sd})I_{sa} \sin^2 \beta - \lambda_m \sin \beta + (L_{sq} - L_{sd})I_{sa} = 0 \quad (6.90)$$

$$\sin \beta = \frac{\lambda_m \pm \sqrt{\lambda_m^2 + 8(L_{sq} - L_{sd})^2 I_{sa}^2}}{-4(L_{sq} - L_{sd})I_{sa}} \quad (6.91)$$

$$\beta = \sin^{-1} \left(\frac{\lambda_m - \sqrt{\lambda_m^2 + 8(L_{sq} - L_{sd})^2 I_{sa}^2}}{-4(L_{sq} - L_{sd})I_{sa}} \right) \quad (6.92)$$

and $\begin{cases} I_{sq} = I_{sa} \cos \beta \\ I_{sd} = -I_{sa} \sin \beta \end{cases}$ therefore

qd-axis stator current at MTPA ($I_{sa} = I_{s\max}$)

$$I_{sd_maxT} = -I_{sa} \sin \left(\sin^{-1} \left(\frac{\lambda_m - \sqrt{\lambda_m^2 + 8(L_{sq} - L_{sd})^2 I_{sa}^2}}{-4(L_{sq} - L_{sd})I_{sa}} \right) \right) = \frac{\lambda_m - \sqrt{\lambda_m^2 + 8(L_{sq} - L_{sd})^2 I_{sa}^2}}{4(L_{sq} - L_{sd})} \quad (6.93)$$

$$I_{sq_maxT} = -\sqrt{I_{sa}^2 - I_{sd}^2} \quad (6.94)$$

Another way to calculate qd-axis stator current at MTPA

$$T_e = \frac{3P}{4} (\lambda_m I_{sq} + (L_{sd} - L_{sq}) I_{sq} I_{sd}) = \frac{3P}{4} (\lambda_m \sqrt{I_{sa}^2 - I_{sd}^2} + (L_{sd} - L_{sq}) I_{sd} \sqrt{I_{sa}^2 - I_{sd}^2}) \quad (6.95)$$

$$\frac{dT_e}{dI_{sd}} = \frac{3P}{4} \left(\frac{-\lambda_m I_{sd}}{\sqrt{I_{sa}^2 - I_{sd}^2}} - \frac{(L_{sd} - L_{sq}) I_{sd} I_{sd}}{\sqrt{I_{sa}^2 - I_{sd}^2}} + (L_{sd} - L_{sq}) \sqrt{I_{sa}^2 - I_{sd}^2} \right) = 0 \quad (6.96)$$

$$\frac{dT_e}{dI_{sd}} = -2(L_{sd} - L_{sq}) I_{sd}^2 - \lambda_m I_{sd} + (L_{sd} - L_{sq}) I_{sa}^2 = 0 \quad (6.97)$$

$$I_{sd_maxT} = \frac{\lambda_m \pm \sqrt{\lambda_m^2 + 8(L_{sd} - L_{sq})^2 I_{sa}^2}}{-4(L_{sd} - L_{sq})} \Rightarrow I_{sd_maxT} = \frac{\lambda_m - \sqrt{\lambda_m^2 + 8(L_{sq} - L_{sd})^2 I_{sa}^2}}{4(L_{sq} - L_{sd})} \quad (6.98)$$

$$I_{sq_maxT} = -\sqrt{I_{sa}^2 - I_{sd}^2} \quad (6.99)$$

Base speed of the synchronous machine at MTPA

$$\omega_b = \frac{V_{smax}}{\sqrt{(\lambda_m + L_{sd} I_{sd_maxT})^2 + (L_{sq} I_{sq_maxT})^2}} \quad (6.100)$$

6.5.3 Maximum Torque per Voltage (MTPV) Operation (Flux Weakening)

$$(\omega_b \leq \omega \leq \omega_{c1})$$

At high speeds (more than nominal speed) in the flux weakening region, maximum output power is achievable by means of the Maximum Torque per Voltage (MTPV) control. For a given speed, the maximum torque under both current and voltage constraints leads to the maximum output power. The current vector trajectory of maximum torque control in the qd-axis stator current plane is selected as follows:

$$\begin{cases} V_{sa}^2 = V_{smax}^2 = (\omega \lambda_m + \omega L_{sd} I_{sd})^2 + (\omega L_{sq} I_{sq})^2 \\ I_{sa}^2 = I_{smax}^2 = I_{sq}^2 + I_{sd}^2 \end{cases} \quad (6.101)$$

$$I_{sq2} = \frac{\sqrt{\left(L_{sd}^2 V_{sa}^2 - L_{sq}^2 V_{sa}^2 - I_{sa}^2 L_{sd}^4 \omega^2 + \lambda_m^2 L_{sq}^2 \omega^2 + \lambda_m^2 L_{sd}^2 \omega^2 + I_{sa}^2 L_{sq}^2 L_{sd}^2 \omega^2 \right)}}{\omega(L_{sd}^2 - L_{sq}^2)} \quad (6.102)$$

$$I_{sd2} = \frac{\sqrt{-I_{sa}^2 L_{sq}^2 L_{sd}^2 \omega^2 + I_{sa}^2 L_{sq}^4 \omega^2 + \lambda_m^2 L_{sq}^2 \omega^2 + L_{sd}^2 V_{sa}^2 - L_{sq}^2 V_{sa}^2 - \lambda_m L_{sd} \omega}}{\omega(L_{sd}^2 - L_{sq}^2)} \quad (6.103)$$

or from (6.101)

$$\left(\frac{V_{sa}}{\omega}\right)^2 = (\lambda_m + L_{sd} I_{sd})^2 + L_{sq}^2 (I_{sa}^2 - I_{sd}^2) \quad (6.104)$$

$$I_{sd}^2 (L_{sd}^2 - L_{sq}^2) + 2\lambda_m L_{sd} I_{sd} + \left(L_{sq}^2 I_{sa}^2 + \lambda_m^2 - \left(\frac{V_{sa}}{\omega}\right)^2 \right) = 0 \quad (6.105)$$

$$I_{sd} = \frac{-\lambda_m L_{sd} \pm \sqrt{\lambda_m^2 L_{sd}^2 - (L_{sd}^2 - L_{sq}^2) \left(L_{sq}^2 I_{sa}^2 + \lambda_m^2 - \left(\frac{V_{sa}}{\omega}\right)^2 \right)}}{(L_{sd}^2 - L_{sq}^2)} \quad (6.106)$$

$$I_{sq} = \pm \sqrt{I_{sa}^2 - I_{sd}^2} \quad (6.107)$$

6.5.4 Flux Weakening with Stator Current Operation ($\omega \geq \omega_{c1}$)

Figure 6.22 illustrates three different operation regions of a permanent magnet machine. In an interior permanent magnet machine if $\lambda_m / L_{sd} \leq I_{s\max}$, we can extend the speed operation region with flux weakening along with current reduction of stator in the third region. In this condition, the machine is working under nominal voltage ($V_{s\max}$) but current is decreasing therefore it doesn't operate under maximum power. The equations are as follows:

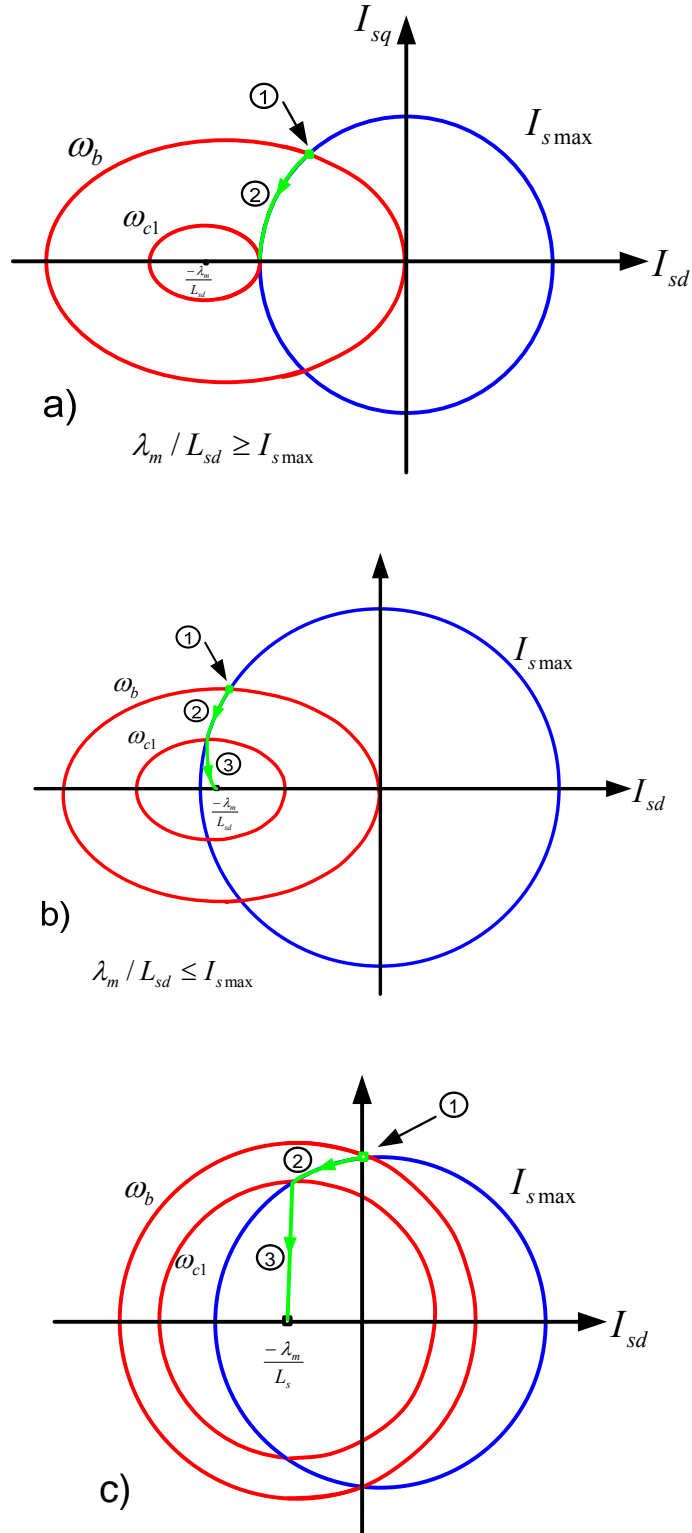


Figure 6.22 Operation region of PM machine a) Interior permanent magnet machine ($\lambda_m / L_{sd} \geq I_{s \max}$), b) Interior permanent magnet machine ($\lambda_m / L_{sd} \leq I_{s \max}$), c) Surface mounted permanent magnet machine.

$$\begin{cases} V_{sd}^2 = V_{smax}^2 = (\omega\lambda_m + \omega L_{sd}I_{sd})^2 + (\omega L_{sq}I_{sq})^2 \\ T_e = \frac{3P}{4}I_{sq}(\lambda_m + (L_{sd} - L_{sq})I_{sd}) \end{cases} \quad (6.108)$$

Thus

$$I_{sq} = \pm \frac{1}{L_{sq}} \sqrt{\left(\frac{V_{smax}}{\omega}\right)^2 - (\lambda_m + L_{sd}I_{sd})^2} \quad (6.109)$$

$$T_e = \pm \frac{3P}{4} \frac{1}{L_{sq}} (\lambda_m + (L_{sd} - L_{sq})I_{sd}) \sqrt{\left(\frac{V_{smax}}{\omega}\right)^2 - (\lambda_m + L_{sd}I_{sd})^2} \quad (6.110)$$

$$\frac{dT_e}{dI_{sd}} = 0 \quad (6.111)$$

$$\frac{dT_e}{dI_{sd}} = (L_{sd} - L_{sq}) \sqrt{\left(\frac{V_{smax}}{\omega}\right)^2 - (\lambda_m + L_{sd}I_{sd})^2} + \frac{(\lambda_m + (L_{sd} - L_{sq})I_{sd})(-L_{sd}(\lambda_m + L_{sd}I_{sd}))}{\sqrt{\left(\frac{V_{smax}}{\omega}\right)^2 - (\lambda_m + L_{sd}I_{sd})^2}} = 0 \quad (6.112)$$

$$\frac{dT_e}{dI_{sd}} = \left(\begin{array}{l} (L_{sd} - L_{sq}) \left(\left(\frac{V_{smax}}{\omega}\right)^2 - (\lambda_m + L_{sd}I_{sd})^2 \right) \\ + (\lambda_m + (L_{sd} - L_{sq})I_{sd})(-L_{sd}(\lambda_m + L_{sd}I_{sd})) \end{array} \right) = 0 \quad (6.113)$$

$$\frac{dT_e}{dI_{sd}} = \left(\begin{array}{l} -I_{sd}^2 (2L_{sd}^2 (L_{sd} - L_{sq})) - I_{sd} (4\lambda_m L_{sd}^2 - 3\lambda_m L_{sq} L_{sd}) \\ - 2\lambda_m^2 L_{sd} + \lambda_m^2 L_{sq} + \left(\frac{V_{smax}}{\omega}\right)^2 (L_{sd} - L_{sq}) \end{array} \right) = 0 \quad (6.114)$$

$$I_{sd} = \frac{-4\lambda_m L_{sd} + 3\lambda_m L_{sq} \pm \sqrt{(\lambda_m L_{sq})^2 + 8(L_{sd} - L_{sq})^2 \left(\frac{V_{s \max}}{\omega}\right)^2}}{4L_{sd}(L_{sd} - L_{sq})} \quad (6.115)$$

Based on the operation region the correct selection is

$$I_{sd} = \frac{-4\lambda_m L_{sd} + 3\lambda_m L_{sq} + \sqrt{(\lambda_m L_{sq})^2 + 8(L_{sd} - L_{sq})^2 \left(\frac{V_{s \max}}{\omega}\right)^2}}{4L_{sd}(L_{sd} - L_{sq})} \quad (6.116)$$

$$I_{sq} = -\frac{1}{L_{sq}} \sqrt{\left(\frac{V_{s \max}}{\omega}\right)^2 - (\lambda_m + L_{sd} I_{sd})^2} \quad (6.117)$$

For defining ω_{c1}

$$I_{sa}^2 = I_{s \max}^2 = I_{sq3}^2 + I_{sd3}^2 \quad (6.118)$$

$$\omega_{c1} = \frac{V_{s \max}}{2L_{sq}} \sqrt{\frac{-6\lambda_m^2 L_{sd}^3 - 8I_{s \max}^2 L_{sq}^3 L_{sd}^2 + 8I_{s \max}^2 L_{sq}^2 L_{sd}^3 - 2L_{sd}^2 \lambda_m^2 L_{sq} + 8L_{sd}^5 I_{s \max}^2 + 8L_{sq}^2 \lambda_m^2 L_{sd}}{-8I_{s \max}^2 L_{sq} L_{sd}^4 - 4L_{sq}^3 \lambda_m^2} \sqrt{\frac{22\lambda_m^4 L_{sd}^5 L_{sq} + 4\lambda_m^2 L_{sd}^8 I_{s \max}^2 - 51\lambda_m^4 L_{sd}^4 L_{sq}^2 + 36\lambda_m^4 L_{sd}^3 L_{sq}^3}{-128\lambda_m^2 L_{sd}^5 I_{s \max}^2 L_{sq}^3 + 92\lambda_m^2 L_{sd}^6 I_{s \max}^2 L_{sq}^2 - 32\lambda_m^2 L_{sd}^7 I_{s \max}^2 L_{sq}} + 124\lambda_m^2 L_{sd}^4 I_{s \max}^2 L_{sq}^4} - 96\lambda_m^2 L_{sd}^3 I_{s \max}^2 L_{sq}^5 + 36\lambda_m^2 L_{sd}^2 I_{s \max}^2 L_{sq}^6 - 3\lambda_m^4 L_{sd}^6}}{\sqrt{\left(4I_{s \max}^4 L_{sd}^5 - 4L_{sd}^4 I_{s \max}^4 L_{sq}\right) \left(-7L_{sd}^3 I_{s \max}^2 \lambda_m^2 + 5\lambda_m^2 L_{sd}^2 I_{s \max}^2 L_{sq} + 3\lambda_m^4 L_{sd} - \lambda_m^4 L_{sq}\right)}}} \quad (6.119)$$

The parameters of the IPM generator with change of the rotor speed are shown in Figure 6.23 to Figure 6.25. These figures illustrate three different operation regions. The

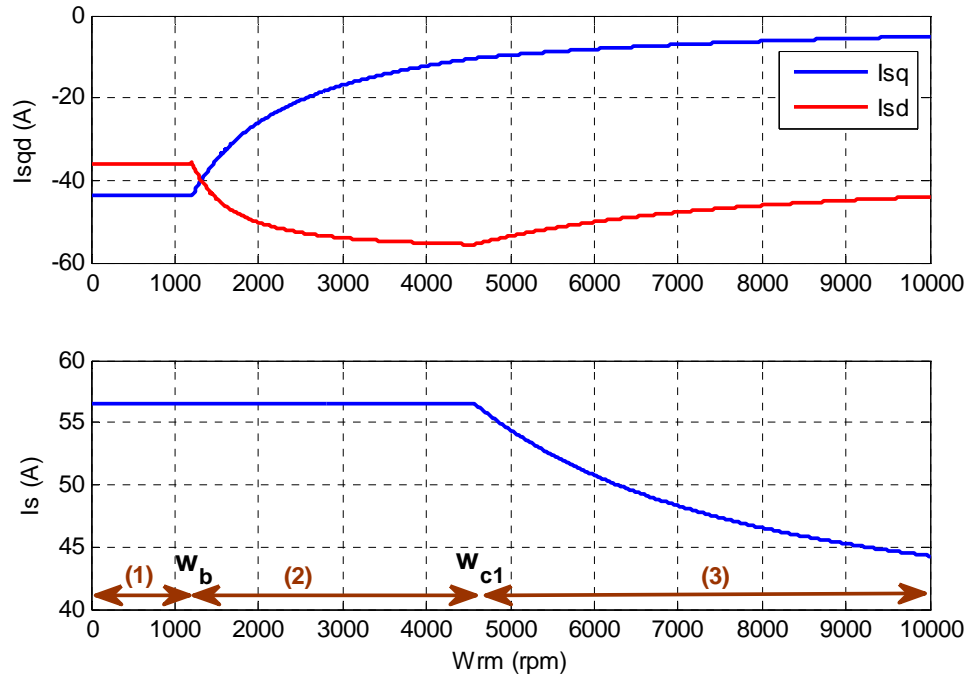


Figure 6.23 The qd-axis and magnitude of the IPM stator current

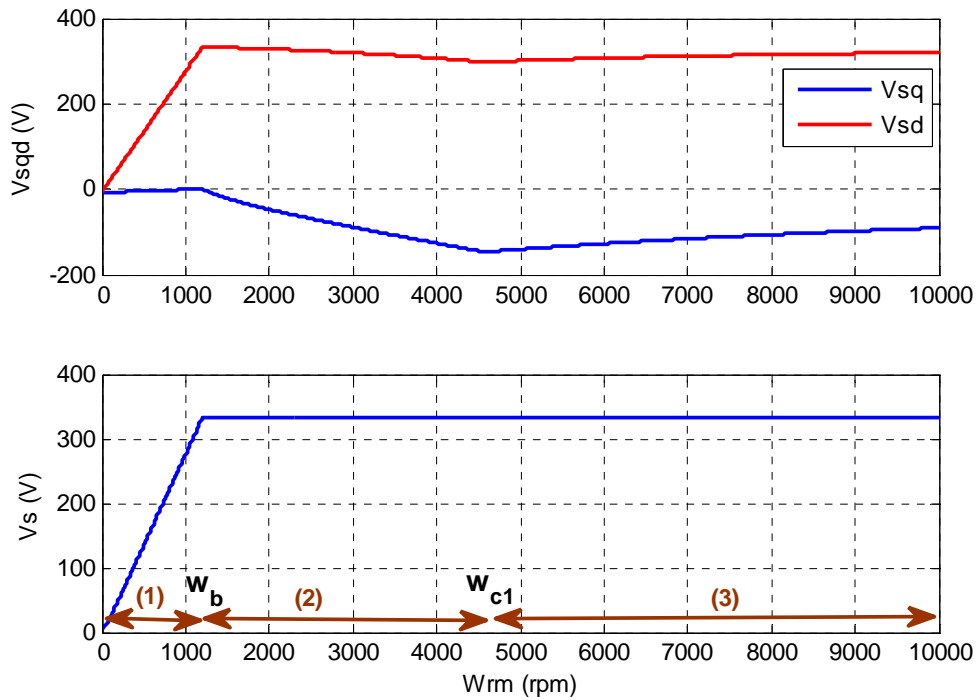


Figure 6.24 The qd-axis and magnitude of the IPM stator voltage

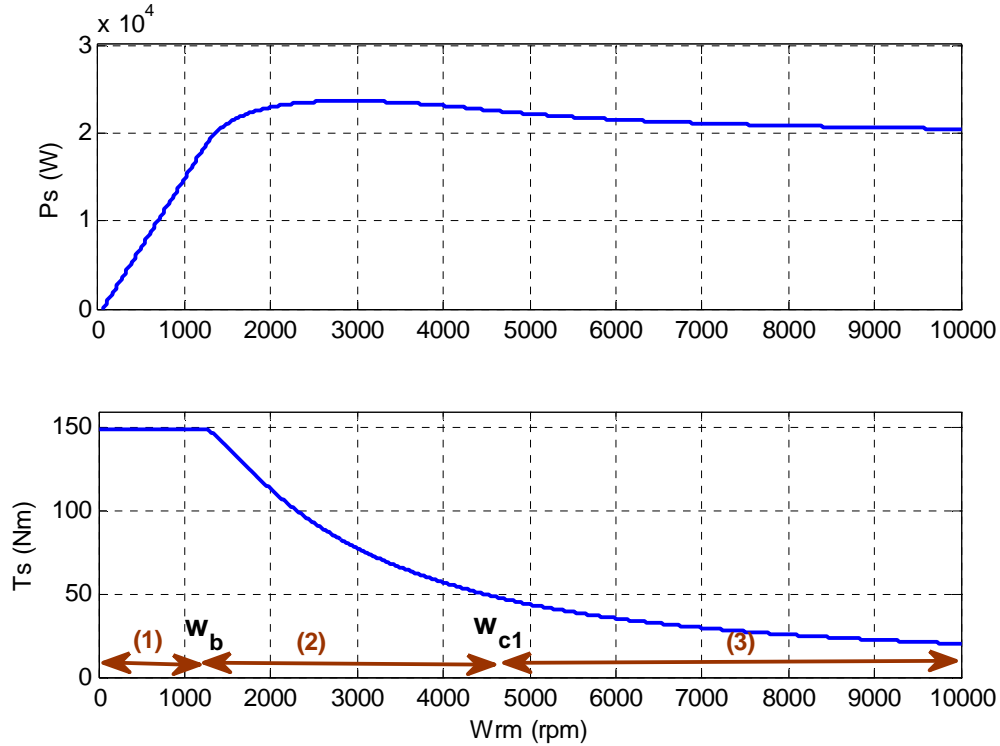


Figure 6.25 The output power and torque of the IPM generator

first region is up to the rated speed. The second region is the flux weakening region 1 and then the third region is the second flux weakening region.

6.6 Machine Side Converter Controller Design

In connection of the IPM machine to the wind turbine, the base objective is to get maximum power from the wind. Based on the parameters of wind turbine, we may have different conditions. First if wind turbine design exactly matches the generator, both maximum power of the generator and the wind turbine at nominal wind speed are in the same point as the nominal speed of the generator. Otherwise in other cases, maximum power happens either before or after nominal speed of generator [119]. Both generator and wind turbine are assumed to be matched.

In interior permanent magnet machine, if we don't consider the core loss of the machine, the dynamic equations in rotor reference frame, are as follows:

Stator voltages

$$V_{sq} = R_s I_{sq} + p\lambda_{sq} + \omega_r \lambda_{sd} = M_{q1} \frac{V_{dc}}{2} \quad (6.120)$$

$$V_{sd} = R_s I_{sd} + p\lambda_{sd} - \omega_r \lambda_{sq} = M_{d1} \frac{V_{dc}}{2} \quad (6.121)$$

where V_{sqd} , I_{sqd} and λ_{sqd} are qd-axis voltages, currents and flux linkages of the stator.

M_{qd1} and V_{dc} are qd-axis modulation index of machine side converter and DC link voltage respectively. R_s is the stator resistance.

Rotor voltages

$$V_{rq} = R_r I_{rq} + p\lambda_{rq} \quad (6.122)$$

$$V_{rd} = R_r I_{rd} + p\lambda_{rd} \quad (6.123)$$

where R_r and I_{rqd} are resistance and qd-axis currents of the rotor.

Stator flux

$$\lambda_{sq} = L_{sq} I_{sq} + L_{mq} I_{rq} \quad (6.124)$$

$$\lambda_{sd} = L_{sd} I_{sd} + L_{md} I_{rd} + \lambda_m \quad (6.125)$$

Rotor flux

$$\lambda_{rq} = L_{rq}I_{rq} + L_{mq}I_{sq} \quad (6.126)$$

$$\lambda_{rd} = L_{rd}I_{rd} + L_{md}I_{sd} + \lambda_m \quad (6.127)$$

Torque equation

$$T_e = \frac{3P}{4}(\lambda_{sd}I_{sq} - \lambda_{sq}I_{sd}) \quad (6.128)$$

$$\lambda_{sq} = L_{sq}I_{sq} \quad (6.129)$$

$$\lambda_{sd} = L_{sd}I_{sd} + \lambda_m \quad (6.130)$$

$$M_{q1} \frac{V_{dc}}{2} = R_s I_{sq} + L_{sq} p I_{sq} + \omega_r L_{sd} I_{sd} + \omega_r \lambda_m \quad (6.131)$$

$$M_{d1} \frac{V_{dc}}{2} = R_s I_{sd} + L_{sd} p I_{sd} - \omega_r L_{sq} I_{sq} \quad (6.132)$$

Capacitor equation

$$C_{dc} p V_{dc} = I_1 - I_2 = -\frac{3}{4}(M_{q1}I_{sq} + M_{d1}I_{sd}) - I_2 \quad (6.133)$$

The dynamic equations of the main grid and grid side converter are

$$\frac{M_{q2}}{2} V_{dc} - V_{gq} = R_{s2} I_{s2q} + L_{s2} s I_{s2q} + \omega_e L_{s2} I_{s2d} \quad (6.134)$$

$$\frac{M_{d2}}{2} V_{dc} - V_{gd} = R_{s2} I_{s2d} + L_{s2} s I_{s2d} - \omega_e L_{s2} I_{s2q} \quad (6.135)$$

The machine side converter objective is to control the rotor speed in order to obtain maximum power from the wind and minimize the generator loss simultaneously and is illustrated in Figure 6.26.

6.6.1 Loss Minimization and Rotor Speed Control

The total loss of the generator is the copper loss due to the stator resistance and the core loss. We can consider core loss as a resistance (R_c) in the model of the IPM machine as illustrated in Figure 6.8. The total loss is

$$P_{loss} = P_{copper} + P_{core} \quad (6.136)$$

where P_{copper} and P_{core} are copper loss and core loss respectively.

$$P_{loss} = \left\{ \begin{array}{l} 1.5R_s (I'_{sq}{}^2 + I'_{sd}{}^2) + 1.5 \frac{\omega_r^2}{R_c^2} (R_s + R_c) (L_{sd}{}^2 I'_{sd}{}^2 + L_{sq}{}^2 I'_{sq}{}^2) + 1.5(R_s + R_c) \frac{\omega_r^2 \lambda_m^2}{R_c^2} \\ + 3(R_s + R_c) \frac{\omega_r^2 L_{sd} \lambda_m I'_{sd}}{R_c^2} + 3R_s \frac{\omega_r I'_{sd} I'_{sq}}{R_c} (L_{sd} - L_{sq}) + 3R_s \frac{\omega_r \lambda_m I'_{sq}}{R_c} \end{array} \right\} \quad (6.137)$$

And output power of generator is (the current directions are for motor and reversed)

$$-P_e = -\frac{3}{2} (V_{sq} I_{sq} + V_{sd} I_{sd}) = P_T - P_{copper} \quad (6.138)$$

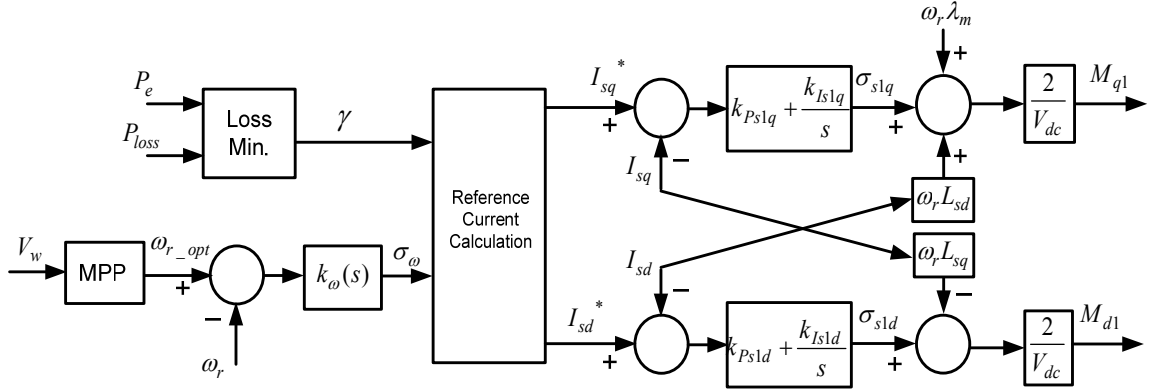


Figure 6.26 Machine side converter controller

$$-P_e = -\left\{ \frac{3}{2} \left[\left(R_s I'_{sq} + \omega_r L_{sdd} I'_{sd} + \omega_r \lambda_m \frac{L_{sq}}{L_{sq}} \right) \left(\frac{\omega_r L_{sd} I'_{sd} + \omega_r \lambda_m + I'_{sq}}{R_c} \right) + \left(R_s I'_{sd} - \omega_r L_{sq} I'_{sq} \right) \left(\frac{-\omega_r L_{sq} I'_{sq}}{R_c} + I'_{sd} \right) \right] \right\} = P_T - P_{copper} \quad (6.139)$$

where

$$\begin{cases} P_T = P_{TMPP} & \omega_r \leq \omega_b \\ P_T = P_b & \omega_r > \omega_b \end{cases} \quad (6.140)$$

If we ignore core loss and consider R_c is very big, the only loss is copper loss.

Thus the total loss of the generator is the copper loss due to the stator resistance.

$$P_{loss} = R_s (I_{sq}^2 + I_{sd}^2) \quad (6.141)$$

And

$$T_e = \frac{3P}{4} (\lambda_m I_{sq} + (L_{sd} - L_{sq}) I_{sq} I_{sd}) \quad (6.142)$$

For loss minimization the following requirement should be met [125]

$$\gamma = \begin{vmatrix} \frac{\partial T_e}{\partial I_{sq}} & \frac{\partial T_e}{\partial I_{sd}} \\ \frac{\partial P_{loss}}{\partial I_{sq}} & \frac{\partial P_{loss}}{\partial I_{sd}} \end{vmatrix} = f(I_{sq}, I_{sd}) = 0 \quad (6.143)$$

$$\gamma = \left(\frac{9P}{4} \right) \left(R_s (L_{sd} - L_{sq}) I_{sq}^2 - R_s (L_{sd} - L_{sq}) I_{sd}^2 - R_s \lambda_m I_{sd} \right) \quad (6.144)$$

From the dynamic of generator rotor speed

$$J \left(\frac{2}{P} \right) s \omega_r = T_t - T_e = k_\omega(s) (\omega_r^* - \omega_r) = \sigma_\omega \quad (6.145)$$

$$\frac{\omega_r}{\omega_r^*} = \frac{k_\omega(s)}{J \left(\frac{2}{P} \right) s + k_\omega(s)} = \frac{1}{1 + \tau_\omega s} = \frac{1}{1 + \frac{J}{p} \frac{2s}{k_\omega(s)}} \quad (6.146)$$

Using PI controller

$$k_\omega(s) = J \frac{2}{\tau_\omega P} = k_{P\omega} + \frac{k_{I\omega}}{s} \quad (6.147)$$

$$\begin{cases} k_{P\omega} = J \frac{2}{\tau_\omega P} \\ k_{I\omega} = 0 \end{cases} \quad (6.148)$$

For fast rotor speed control response, we choose rotor speed controller time constant as

[126]

$$\tau_\omega = \frac{1}{0.1 * 2\pi f_{swi}} \quad (6.149)$$

where f_{swi} is the switching frequency of the converter (5kHz).

6.6.2 Current Control

From the speed control and loss minimization

$$\begin{cases} T_t - \left(-\frac{3P}{4} (\lambda_m I_{sq} + (L_{sd} - L_{sq}) I_{sq} I_{sd}) \right) = \sigma_\omega \\ \gamma = \left(\frac{9P}{4} \right) R_s \left((L_{sd} - L_{sq}) I_{sq}^2 - (L_{sd} - L_{sq}) I_{sd}^2 - \lambda_m I_{sd} \right) = 0 \end{cases} \quad (6.150)$$

We have two equations and two variables (I_{sq}, I_{sd})

$$I_{sq} = \frac{\sigma_\omega - T_t}{\frac{3P}{4} (\lambda_m + (L_{sd} - L_{sq}) I_{sd})} \quad (6.151)$$

$$a_4 I_{sd}^4 + a_3 I_{sd}^3 + a_2 I_{sd}^2 + a_1 I_{sd} + a_0 = 0 \quad (6.152)$$

where

$$\begin{cases} a_4 = -(L_{sd} - L_{sq})^3 \\ a_3 = -(3\lambda_m (L_{sd} - L_{sq})^2) \\ a_2 = -(3\lambda_m^2 (L_{sd} - L_{sq})) \\ a_1 = -\lambda_m^3 \\ a_0 = \left(\frac{4}{3P} \right)^2 (L_{sd} - L_{sq}) (\sigma_\omega - T_t)^2 \end{cases} \quad (6.153)$$

So I_{sq} and I_{sd} have four solutions in which one pairs those produce the highest torque at

the lowest stator current magnitude are I_{sq}^* and I_{sd}^* . From the dynamic equations of the generator in laplace format

$$R_s I_{sq} + L_{sq} s I_{sq} = M_{q1} \frac{V_{dc}}{2} - \omega_r L_{sd} I_{sd} - \omega_r \lambda_m \quad (6.154)$$

$$R_s I_{sd} + L_{sd} s I_{sd} = M_{d1} \frac{V_{dc}}{2} + \omega_r L_{sq} I_{sq} \quad (6.155)$$

$$R_s I_{sq} + L_{sq} s I_{sq} = k_{s1q}(s)(I_{s1q}^* - I_{s1q}) = \sigma_{s1q} \quad (6.156)$$

$$R_s I_{sd} + L_{sd} s I_{sd} = k_{s1d}(s)(I_{s1d}^* - I_{s1d}) = \sigma_{s1d} \quad (6.157)$$

Using PI controller for both current controllers

$$\begin{cases} k_{s1q}(s) = k_{ps1q} + \frac{k_{Is1q}}{s} \\ k_{s1d}(s) = k_{ps1d} + \frac{k_{Is1d}}{s} \end{cases} \quad (6.158)$$

$$\frac{I_{sq}}{I_{sq}^*} = \frac{k_{s1q}(s)}{sL_{sq} + R_s + k_{s1q}(s)} = \frac{1}{1 + \tau_{s1}s} = \frac{1}{1 + \frac{sL_{sq} + R_s}{k_{s1q}(s)}} \quad (6.159)$$

$$\frac{I_{sd}}{I_{sd}^*} = \frac{k_{s1d}(s)}{sL_{sd} + R_s + k_{s1d}(s)} = \frac{1}{1 + \tau_{s1}s} = \frac{1}{1 + \frac{sL_{sd} + R_s}{k_{s1d}(s)}} \quad (6.160)$$

$$k_{s1q}(s) = \frac{sL_{sq} + R_s}{\tau_{s1}s} = k_{ps1q} + \frac{k_{Is1q}}{s} \quad (6.161)$$

$$k_{s1d}(s) = \frac{sL_{sd} + R_s}{\tau_{s1}s} = k_{Ps1d} + \frac{k_{Is1d}}{s} \quad (6.162)$$

So the coefficients of controllers are

$$\left\{ \begin{array}{l} k_{Ps1q} = \frac{L_{sq}}{\tau_{s1}} \\ k_{Is1q} = \frac{R_s}{\tau_{s1}} \end{array} \right. \text{ and } \left\{ \begin{array}{l} k_{Ps1d} = \frac{L_{sd}}{\tau_{s1}} \\ k_{Is1d} = \frac{R_s}{\tau_{s1}} \end{array} \right. \quad (6.163)$$

For faster inner current controller, the time constant is chosen to be twice that of the time constant of outer speed controller.

$$\tau_{s1} = \frac{1}{0.2 * 2\pi f_{swi}} \quad (6.164)$$

The designed parameters of controllers are presented in Table 6.3. The modulation indices of the machine side converter as the outputs of the control part can be defined as

$$M_{q1} = \frac{2}{V_{dc}} (\sigma_{s1q} + \omega_r L_{sd} I_{sd} + \omega_r \lambda_m) \quad (6.165)$$

$$M_{d1} = \frac{2}{V_{dc}} (\sigma_{s1d} - \omega_r L_{sq} I_{sq}) \quad (6.166)$$

6.7 Grid Side Converter Controller Design

As illustrated in Figure 6.27, the grid side converter controls the DC link voltage magnitude and the reactive power flows into the main grid. It consists of four separate PI controllers. The outputs of the DC voltage and the reactive power controllers produce references for inner current controllers where modulation indices of grid side converter will be produced.

6.7.1 DC Link Voltage and Reactive Power Control

From the active power relationship between two converters

$$\frac{1}{2}C_{dc}sV_{dc}^2 = P_1 - \frac{3}{2}(V_{s2q}I_{s2q} + V_{s2d}I_{s2d}) \quad (6.167)$$

$$\frac{1}{2}C_{dc}sV_{dc}^2 = k_{dc}(s)(V_{dc}^{*2} - V_{dc}^2) = \sigma_{dc} \quad (6.168)$$

So

$$\frac{V_{dc}^2}{V_{dc}^{*2}} = \frac{k_{dc}(s)}{sC_{dc} + k_{dc}(s)} \quad (6.169)$$

If we choose a PI controller

$$k_{dc}(s) = k_{Pdc} + \frac{k_{Idc}}{s} \quad (6.170)$$

Table 6.3 Designed parameters of the controllers

$k_{P\omega}$	1256.6	$k_{I\omega}$	0
k_{Ps1q}	129.3	k_{Is1q}	1108.4
k_{Ps1d}	39.2	k_{Is1d}	1108.4
k_{Pdc}	31.41	k_{Idc}	0
k_{Ps2}	25.1	k_{Is2}	628.3

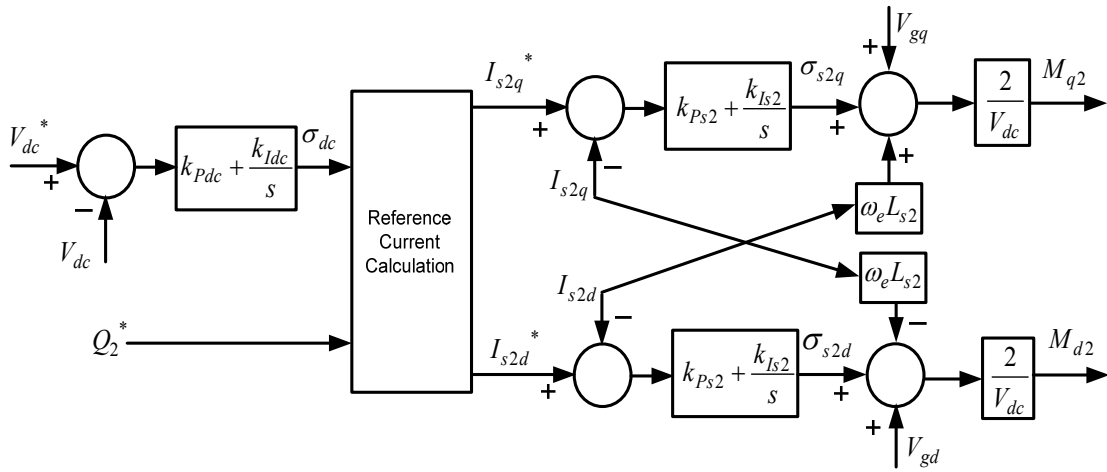


Figure 6.27 Grid side converter controller

$$\frac{V_{dc}^2}{V_{dc}^{2*}} = \frac{k_{dc}(s)}{sC_{dc} + k_{dc}(s)} = \frac{1}{1 + \tau_{dc}s} = \frac{1}{1 + \frac{sC_{dc}}{k_{dc}(s)}} \quad (6.171)$$

$$k_{dc}(s) = \frac{C_{dc}}{\tau_{dc}} = k_{Pdc} + \frac{k_{Idc}}{s} \quad (6.172)$$

The coefficients of the DC link PI controllers are

$$\begin{cases} k_{Pdc} = \frac{C_{dc}}{\tau_{dc}} \\ k_{Idc} = 0 \end{cases} \quad (6.173)$$

Like MSC control part we can choose DC link voltage controller time constant as

$$\tau_{dc} = \frac{1}{0.1 * 2\pi f_{swi}} \quad (6.174)$$

Furthermore to control output reactive power and therefore power factor

$$Q_2^* = \frac{3}{2} (V_{s2q} I_{s2d} - V_{s2d} I_{s2q}) \quad (6.175)$$

Thus from the two control parts

$$(V_{s2q} I_{s2q} + V_{s2d} I_{s2d}) = \frac{2}{3} (P_1 - \sigma_{dc}) \quad (6.176)$$

$$(V_{s2q} I_{s2d} - V_{s2d} I_{s2q}) = \frac{2}{3} Q_2^* \quad (6.177)$$

We can define qd-axis reference currents as the outputs of outer controller

$$\begin{cases} I_{s2q}^* = \frac{2 (P_1 - \sigma_{dc}) V_{s2q} - Q_2^* V_{s2d}}{3 (V_{s2q}^2 + V_{s2d}^2)} \\ I_{s2d}^* = \frac{2 (P_1 - \sigma_{dc}) V_{s2d} + Q_2^* V_{s2q}}{3 (V_{s2q}^2 + V_{s2d}^2)} \end{cases} \quad (6.178)$$

6.7.2 Current Control

To control the currents of grid side converter, from its output voltage equations

$$R_{s2}I_{s2q} + L_{s2}sI_{s2q} = \frac{M_{q2}}{2}V_{dc} - V_{gq} - \omega_e L_{s2}I_{s2d} \quad (6.179)$$

$$R_{s2}I_{s2d} + L_{s2}sI_{s2d} = \frac{M_{d2}}{2}V_{dc} - V_{gd} + \omega_e L_{s2}I_{s2q} \quad (6.180)$$

$$R_{s2}I_{s2q} + L_{s2}sI_{s2q} = k_{s2q}(s)(I_{s2q}^* - I_{s2q}) = \sigma_{s2q} \quad (6.181)$$

$$R_{s2}I_{s2d} + L_{s2}sI_{s2d} = k_{s2d}(s)(I_{s2d}^* - I_{s2d}) = \sigma_{s2d} \quad (6.182)$$

Both resistance and inductance of the current equation are the same, thus we can choose the same PI controllers as

$$k_{s2q}(s) = k_{s2d}(s) = k_{Ps2} + \frac{k_{Is2}}{s} \quad (6.183)$$

$$\frac{I_{s2q}}{I_{s2q}^*} = \frac{k_{s2q}(s)}{sL_{s2} + R_{s2} + k_{s2q}(s)} = \frac{1}{1 + \tau_{s2}s} = \frac{1}{1 + \frac{sL_{s2} + R_{s2}}{k_{s2q}(s)}} \quad (6.184)$$

$$\frac{I_{s2d}}{I_{s2d}^*} = \frac{k_{s2d}(s)}{sL_{s2} + R_{s2} + k_{s2d}(s)} = \frac{1}{1 + \tau_{s2}s} = \frac{1}{1 + \frac{sL_{s2} + R_{s2}}{k_{s2d}(s)}} \quad (6.185)$$

$$k_{s2q}(s) = k_{s2d}(s) = \frac{sL_{s2} + R_{s2}}{\tau_{s2}s} = k_{Ps2} + \frac{k_{Is2}}{s} \quad (6.186)$$

$$k_{Ps2} = \frac{L_{s2}}{\tau_{s2}} \text{ and } k_{Is2} = \frac{R_{s2}}{\tau_{s2}} \quad (6.187)$$

From the output of current controllers, the modulation indices of the grid side converter can be defined

$$\begin{cases} M_{q2} = \frac{2}{V_{dc}} (\sigma_{s2q} + V_{mq} + \omega_e L_{s2} I_{s2d}) \\ M_{d2} = \frac{2}{V_{dc}} (\sigma_{s2d} + V_{md} - \omega_e L_{s2} I_{s2q}) \end{cases} \quad (6.188)$$

In addition the inner GSC current controller time constant is chosen to be two times faster than the outer controllers

$$\tau_{s2} = \frac{1}{0.2 * 2\pi f_{swi}} \quad (6.189)$$

6.8 Simulation Results

To verify the performance of the designed controllers and study dynamic behavior of the system, a variable wind speed is applied to the wind turbine. The optimum rotor speed is calculated based on maximum power point algorithm. Figure 6.28 shows the wind speed, reference rotor speed and actual rotor speed of the generator. Rotor speed follows the optimum reference value to get maximum power from the wind in variable speed mode operation region. Output active power of the IPM generator changes, based on the wind speed at optimum value. Stator current precisely follows the reference to get maximum power from the wind and simultaneously minimize the generator loss. At 3s the average wind speed increases from 8 to 11 (m/s). After rated wind speed (10 (m/s))

the generator rotor speed, output active power and stator current remain constant at rated value. In spite of reference rotor speed change at the instant of change of wind speed, due to the inertia the actual rotor speed of the generator takes about 0.2 s to reach to the reference as a ramp function. In this period the output power and current magnitude of the generator reduces to make the rotor speed reaches to the reference as fast as possible.

Figure 6.29 shows the pitch angle and power coefficient of the wind turbine, before and after rated wind speed. To get optimum power from the wind, before rated wind speed the pitch angle is kept zero and the power coefficient is constant at maximum value. Above rated wind speed, pitch angle increases and changes based on wind speed value, for protection of the turbine from over speeding and keep the power under rated value. The higher pitch angle causes a lower power coefficient and lower output power. As illustrated in Figure 6.30, due to the fast response of grid side converter controllers, during both variable speed and constant rotor speed regions the DC link voltage and reactive power are kept constant. The DC link has a small voltage swell but reaches to the rated value in less than 50ms. The output reactive power is zero to guarantee unity power factor. The output current always follows the reference.

6.9 Conclusions

In this chapter, dynamic equations of the permanent magnet machine wind turbine connected to the grid are derived. Operation regions of the permanent magnet machine are also studied. In general, a permanent magnet machine has three different operation regions. The first region ($\omega \leq \omega_b$) is a point in which maximum torque per ampere is

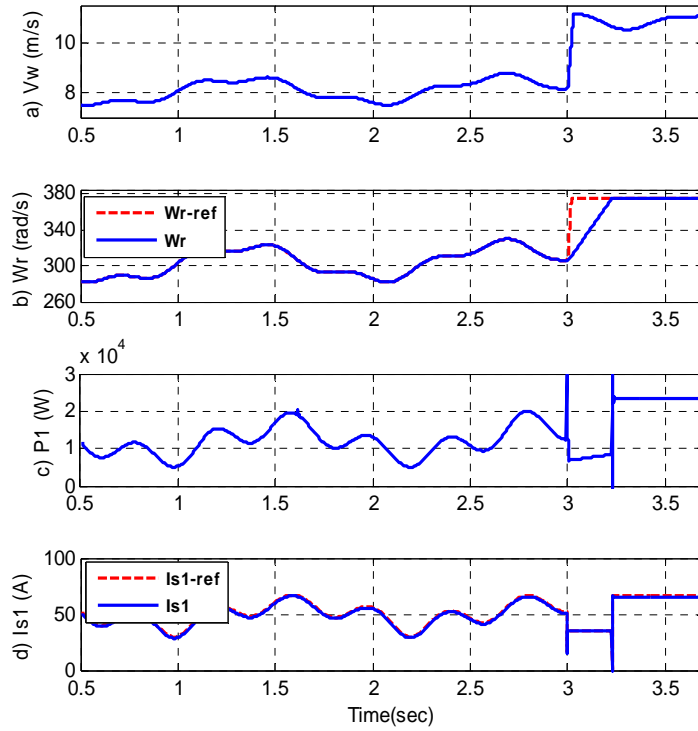


Figure 6.28 Dynamic operation of generator and MSC. a) wind speed, b) generator rotor speed, c) output active power, d) stator current magnitude

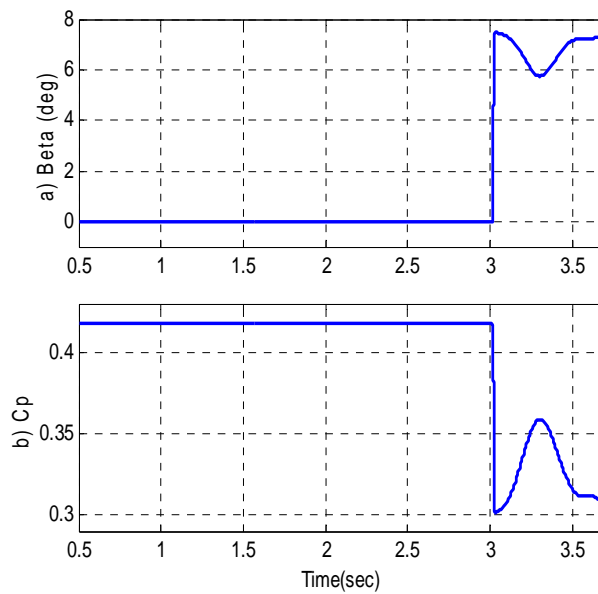


Figure 6.29 Pitch angle and power coefficient of wind turbine. a) pitch angle, b) power coefficient

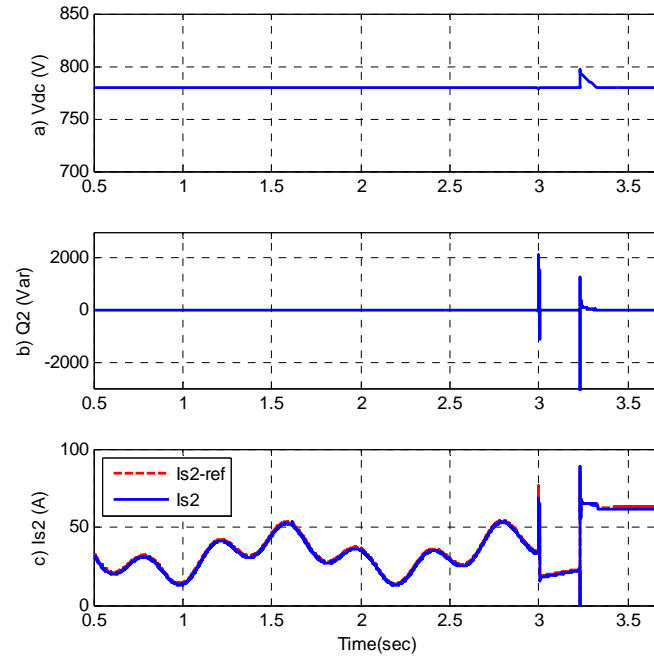


Figure 6.30 Dynamic operation of grid side converter. a) Dc link voltage, b) output reactive power, c) GSC output current magnitude

applied to minimize copper loss. In the second region ($\omega_b \leq \omega \leq \omega_{c1}$), the machine is working in both maximum current and maximum voltage, therefore with increasing generator speed, flux linkage is reduced. Thus in flux weakening region both maximum torque and maximum power are met. If $(\lambda_m / L_{sd}) \leq I_{s\max}$, we can extend generator speed in the third region until $I_{sq} = -\lambda_m / L_{sd}$ and $I_{sd} = 0$.

The controllers are designed for loss minimization and maximum power point tracking of the interior permanent magnet machine as a wind turbine generator. Both copper loss and core loss are considered. Effect of pitch angle on the operation region of generator is investigated. The whole system is connected to the main grid. The steady state operation regime of IPM generator in a wind turbine application based on total loss minimization and maximum power point tracking of wind turbine is presented. Until

rated wind speed the output power of the generator changes and the wind turbine gets maximum power from the wind. After rated wind speed the reference of the active power and rotor speed are kept constant and pitch angle control protects the wind turbine from over speed and over current phenomenon. The PI controllers are used. The controller parameters are designed based on the required speed response and the system parameters. Simulation results prove that fast speed response of the grid side converter keeps DC link voltage constant. For unity power factor, the output reactive power is zero.

CHAPTER 7

CONTROLLABILITY ANALYSIS OF RENEWABLE ENERGY SOURCES CONNECTED TO THE GRID

7.1 Introduction

In the recent years, there has been accelerated development of renewable energy sources such as the photo voltaic (PV) and wind energy to meet increasing energy demands of growing populations. Most of the installed wind turbines are variable speed turbines actuating doubly fed induction generators or synchronous generators in the kW and MW range [127-129]. Since many of the big wind turbines will be located off-shore, there is the need to find robust machine and converter technologies which will require little maintenance. Since doubly fed induction and synchronous machines use brushes and commutators, which require frequent maintenance and replacement, new electric machine structures to replace wind generators are being investigated. The interior permanent magnet (IPM) machine is one of the machines with considerable potential for wind power generation. This is because, brushes and commutators are not required and there is no field winding copper loss since the excitation permanent magnet is buried in the rotor. The IPM also has a better efficiency compared to other machines, although it is more expensive.

It is anticipated that Micro-grid systems comprised of many renewable energy sources, including IPM generators driven by wind turbines, serving autonomous loads or connected to the grid will become common place. The IPM generator will be required to

supply an active power to the grid under minimum generator loss condition at a controllable grid power factor. For a desired power rating, the IPM generator, the rectifier, inverter, and the topology of the filter connecting the inverter output to the grid must also be selected as well as the values of its inductors and capacitors. Then controllers will be designed to ensure system stability, robustness and high dynamic performance under all operating conditions. This sequential method of system design (structural (plant) design, control system design) has long been confirmed to problematize the optimal static and dynamic operations of complex and nonlinear engineering and biological systems. In particular, controllers can be limited by system characteristics induced by nonlinearity, such as input/output multiplicities, open-loop instability and right half plane zeros or non-minimum phase phenomenon which limits achievable controller bandwidth.

A micro-grid consisting of different types of renewable sources and loads is best conceived as a nonlinear system. The dynamic models of the sources are nonlinear and some of the loads are modeled as non-linearly voltage and/or current dependent. The main focus of research so far has been on the control of micro-grid systems aimed at achieving maximum power extraction from renewable sources, the sharing of real and reactive powers between parallel sources, and the seamless transition between autonomous and grid connected modes of operation. Another area of great exertion is the design of the interface filters between the grid and the energy sources to meet steady-state filtering requirements to prevent converter induced harmonics from flowing into the grid, while not provoking instabilities due to the variations in operating conditions and system parameters. Although there is an emerging consensus that the LCL filter is the best,

research is on-going to find the controller structure for the system, the state variables to be fed back and the selection of the filter parameters [130-132].

In order to elucidate the apparent difficulties in arriving at the optimal control structure for the LCL filter, this chapter appeals to the concept of system controllability to highlight the inherent characteristics of the system. Controllability is originally defined as the ability of a system to move fast move smoothly from one operating condition to another and deal effectively with disturbances [133]. Controllability analysis gives insights into the inherent characteristics and phase behavior of the system, which should inform our system design and the selection of controller architecture [134-136].

From the control viewpoint of a linear system, in a stable system all the real parts of the poles should be in left hand side of the s-plane. In addition a minimum phase system has all the real parts of the zeros of its characteristic equation transfer function are in the left hand plane. Therefore using the poles and zeros we can study or predict the response of the system to any input, moreover the type of the controller needed to improve its response can be selected more clearly.

Most of the electrical power systems and the micro-grid are highly complex and nonlinear systems. They are also multi input and multi output systems which makes their analysis even more complex. Unlike the linear systems, their characteristic equations cannot be defined, and in many cases their stability can only be defined locally over the steady state operation points using the eigenvalues of the linearized characteristic equations. For defining the minimum/non-minimum phase of the nonlinear system the concept of the zero dynamics has been used [136]. The unstable zero dynamics may cause problems for both dynamic and steady state response. From the dynamic point of

view, it causes inverse response in which the response spends part of its time going in the wrong direction. Hence, it reduces the bandwidth of the controller, causes a delay in reaching to the steady state value and limits the degree of achievable control quality [137-139]. The problem of a non-minimum phase system in steady state is called input multiplicity in which the same output can be obtained from the combinations of different inputs and output variables. It is therefore possible to have an unobservable transition from one steady state output to another one.

This chapter therefore investigates the controllability of an IPM wind turbine generator connected to the grid using the analysis of its open-loop stability and zero phase behaviors. The zero dynamics of the grid connected IPM generator using either the L or the LCL filter are investigated. The wind turbine is working at the maximum power point tracking scenario and other operational objectives include generator loss minimization, the control of the grid reactive power, and the converter DC link voltage. The effect of filter structure on the inherent characteristics of the grid-connected generator determined through the study of the zero dynamics constitutes the main theme of this chapter. It is also observed that the use of feedback linearization methodology for controller design where the stability of the zero dynamics permits the use of static controller gains is becoming privileged in the design of controllers for energy systems.

7.2 Zero Dynamics of the Nonlinear System

The definition of a nonlinear system with m number of inputs and outputs is

$$\begin{cases} \frac{\partial x}{\partial t} = f(x) + \sum_{j=1}^m g_j(x)u_j(x) \\ y_i = h_i(x), \quad i = 1, \dots, m \end{cases} \quad (7.1)$$

The number of the derivations (differentiations) of the output is needed to see the input in its equation (explicit relation between input and output) is called the relative order of the output. In a multi input multi output system (MIMO), the relative order is the sum of all relative orders of the outputs.

Another way to define the relative order of any output is to fulfill the following condition:

$$L_g L_f^{r_i-1} h_i(x) = [L_{g_1} L_f^{r_i-1} h_i(x), L_{g_2} L_f^{r_i-1} h_i(x), \dots, L_{g_m} L_f^{r_i-1} h_i(x)] \neq [0, 0, \dots, 0] \quad (7.2)$$

where the lie derivative definition is

$$L_f h(x) = \frac{\partial h}{\partial x} f(x) \quad (7.3)$$

$$L_f^2 h(x) = L_f L_f h(x), \quad L_g L_f h(x) = L_g \left(\frac{\partial h}{\partial x} f(x) \right) \quad (7.4)$$

The relative order of the multi input multi output (MIMO) system is

$$r = r_1 + r_2 + \dots + r_m \quad (7.5)$$

If the relative order of the system is less than the order of the system (number of dynamic states), part of the system is unobservable and there are internal dynamics. Internal dynamic states are not reflected during the process of feedback linearization and control design of the system; therefore their stability must be ascertained. The zero

dynamics is a special case of the internal dynamics and are defined to be the internal dynamics of the system when the selected system outputs are set to zero by the input. There are two methods to isolate the zero dynamics [140-141].

7.2.1 First Method

In the first method [140] for finding the zero dynamics, after defining the number of internal dynamics ($n - \sum r_i$), all the outputs should be made equal to zero. In this case some dynamic states will be removed, leaving the internal dynamics which are independent of the input variables.

It should be noted that if the purpose for checking the stability of the zero dynamics is to use the input/output linearization method for the controller design we define the characteristic matrix as

$$C_h(x) = \begin{bmatrix} L_{g1}L_f^{r_1-1}h_1 & \cdots & L_{gm}L_f^{r_1-1}h_1 \\ \vdots & & \vdots \\ L_{g1}L_f^{r_m-1}h_m & \cdots & L_{gm}L_f^{r_m-1}h_m \end{bmatrix} \quad (7.6)$$

Non-singularity of the characteristic matrix in a MIMO system is a sufficient condition for input/output linearization to be achievable through static state feedback. For systems for which this condition is not satisfied, controllers with dynamic contents can be employed to transform them to new equations satisfying the characteristic matrix [138].

7.2.2 Second Method

In the second method based on [141], a new co-ordinate system with $t(x)$ is generated in which the elements of the following matrix are linearly independent:

$$\eta = \begin{bmatrix} \eta^{(0)} \\ \eta^{(1)} \\ \vdots \\ \eta^{(m)} \end{bmatrix} = \begin{bmatrix} t_1(x) \\ \vdots \\ t_{n-\sum r_i}(x) \\ \hline h_1(x) \\ L_f h_1(x) \\ \vdots \\ L_f^{r_1-1} h_1(x) \\ \hline \vdots \\ h_m(x) \\ L_f h_m(x) \\ \vdots \\ L_f^{r_m-1} h_m(x) \end{bmatrix} \quad (7.7)$$

The original dynamic equations of the system are now converted to the new coordinates in which the input variables have been eliminated. For a MIMO system the following can be defined:

$$\begin{cases} F_i = L_f t_i(x) & i = 1, \dots, (n - \sum_{i=1}^m r_i) \\ G_i = [L_{g1} t_i \quad \dots \quad L_{gm} t_i] & i = 1, \dots, (n - \sum_{i=1}^m r_i) \\ C_i = [L_{g1} L_f^{r_i-1} h_i(x) \quad \dots \quad L_{gm} L_f^{r_i-1} h_i(x)] & i = 1, \dots, m \\ W_i = L_f^{r_i} h_i(x) & i = 1, \dots, m \end{cases} \quad (7.8)$$

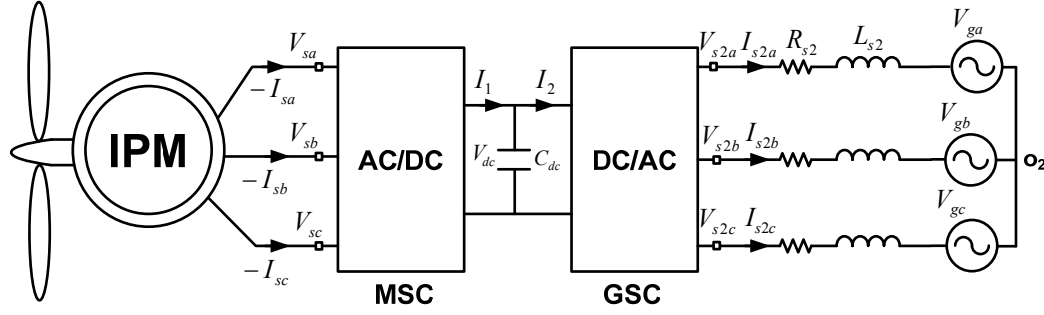


Figure 7.1 Schematic diagram of IPM wind turbine connected to the main grid with L type filter.

The zero dynamics after converting the matrices to the new coordinates (the output variables will be either zero or at their steady state values) are defined as follows:

$$\frac{d\eta_{n-\sum r_i}^{(0)}}{dt} = F_{n-\sum r_i}(\eta) - G_{n-\sum r_i}(\eta) \begin{bmatrix} C_1(\eta) \\ \vdots \\ C_m(\eta) \end{bmatrix}^{-1} [W_1(\eta) \cdots W_m(\eta)] \quad (7.9)$$

7.3 Controllability of Wind Turbine Connected through L filter to the Grid

As illustrated in Figure 7.1, in the study system, an interior permanent magnet generator driven by a wind turbine supplies power to the grid. A back to back AC/DC/AC inverter converts the AC generator output voltage to a DC voltage and then to another three-phase AC voltage. The grid side inverter is interfaced to the grid through the L type filter.

In the interior permanent magnet machine, the dynamic of the rotor can be neglected because the permanent magnet is a poor electrical conductor. Ignoring the core

Table 7.1 Parameters of the IPM machine for controllability analysis

$V_{m-rated}$	180 V	$I_{m-rated}$	5.5 A
$\omega_{m-rated}$	1800 rpm	P (no of poles)	4
R_s	1.5 Ω	λ_m	0.21 Wb
L_{sd}	0.035 H	L_{sq}	0.11 H
C_{dc}	600e ⁻⁶ F	J	0.089 kg/m ²
V_{gq}	170 V	V_{gd}	0 V
R_{s2}	0.01 Ω	L_{s2}	0.4 mH

loss of the machine the dynamic equations of the generator are as follows:

$$M_{q1} \frac{V_{dc}}{2} = V_{sq} = R_s I_{sq} + L_{sq} p I_{sq} + \omega_r L_{sd} I_{sd} + \omega_r \lambda_m \quad (7.10)$$

$$M_{d1} \frac{V_{dc}}{2} = V_{sd} = R_s I_{sd} + L_{sd} p I_{sd} - \omega_r L_{sq} I_{sq} \quad (7.11)$$

The converter DC Capacitor equation is given as

$$C_{dc} p V_{dc} = I_1 - I_2 = -\frac{3}{4} (M_{q1} I_{sq} + M_{d1} I_{sd}) - I_2 \quad (7.12)$$

where V_{sqd} , I_{sqd} are the complex qd-axis voltages and currents of the stator. M_{qd1} and V_{dc} are the complex qd-axis modulation index of machine side converter and DC link voltage respectively. R_s is the stator resistance. L_{sqd} and λ_m are qd-axis stator inductance and

magnetization flux of the generator.

The dynamic equations of the main grid with L type filter and grid side converter are

$$\frac{M_{q2}}{2} V_{dc} - V_{gq} = R_{s2} I_{s2q} + L_{s2} p I_{s2q} + \omega_e L_{s2} I_{s2d} \quad (7.13)$$

$$\frac{M_{d2}}{2} V_{dc} - V_{gd} = R_{s2} I_{s2d} + L_{s2} p I_{s2d} - \omega_e L_{s2} I_{s2q} \quad (7.14)$$

Parameters of the IPM machine and the grid are presented in Table 7.1. For generator copper loss minimization the following requirement should be met [125]

$$\gamma = \begin{vmatrix} \frac{\partial T_e}{\partial I_{sq}} & \frac{\partial T_e}{\partial I_{sd}} \\ \frac{\partial P_{loss}}{\partial I_{sq}} & \frac{\partial P_{loss}}{\partial I_{sd}} \end{vmatrix} = f(I_{sq}, I_{sd}) = 0 \quad (7.15)$$

$$\gamma = \left(\frac{9P}{4} \right) \left(R_s (L_{sd} - L_{sq}) I_{sq}^2 - R_s (L_{sd} - L_{sq}) I_{sd}^2 - R_s \lambda_m I_{sd} \right) \quad (7.16)$$

7.3.1 Steady State and Stable Operation Region

Under steady state operating conditions the derivatives of the states in (7.10) to (7.14) are set to zero. The resulting equations with the algebraic equation defining the reference grid reactive power and the condition for minimum generator loss (7.16) are used to determine the steady state operation. The known variables are

$$\left[V_{gq} \quad V_{gd} \quad Q_g \quad (\omega_r \Leftrightarrow T_t) \quad V_{dc} \right] \quad (7.17)$$

And the unknown variables are

$$\begin{bmatrix} I_{sq} & I_{sd} & M_{q1} & M_{d1} & I_{s2q} & I_{s2d} & M_{q2} & M_{d2} \end{bmatrix} \quad (7.18)$$

The rotor speed and the DC capacitor voltage are varied (ω_r and V_{dc}) to solve the steady-state equations given as

$$\begin{cases} -M_{q1} \frac{V_{dc}}{2} + R_s I_{sq} + \omega_r L_{sd} I_{sd} + \omega_r \lambda_m = 0 \\ -M_{d1} \frac{V_{dc}}{2} + R_s I_{sd} - \omega_r L_{sq} I_{sq} = 0 \\ -M_{q2} \frac{V_{dc}}{2} + V_{gq} + R_{s2} I_{s2q} + \omega_e L_{s2} I_{s2d} = 0 \\ -M_{d2} \frac{V_{dc}}{2} + V_{gd} + R_{s2} I_{s2d} - \omega_e L_{s2} I_{s2q} = 0 \\ -\frac{3}{4}(M_{q1} I_{sq} + M_{d1} I_{sd}) - \frac{3}{4}(M_{q2} I_{s2q} + M_{d2} I_{s2d}) = 0 \\ T_t - \left(\frac{3P}{4}\right)(\lambda_m I_{sq} + (L_{sd} - L_{sq}) I_{sq} I_{sd}) = 0 \\ \gamma = \left(\frac{9P}{4}\right)(R_s (L_{sd} - L_{sq}) I_{sq}^2 - R_s (L_{sd} - L_{sq}) I_{sd}^2 - R_s \lambda_m I_{sd}) = 0 \\ -Q_g + \left(\frac{3}{2}\right)(V_{gq} I_{s2d} - V_{gd} I_{s2q}) = 0 \end{cases} \quad (7.19)$$

The steady state operation regions of the generator system are illustrated in Figure 7.2. In this figure the output active and reactive power of the IPM generator are shown. The stator current and voltage of the machine are presented in parts Figure 7.2b and Figure 7.2c respectively. The steady state parameters of the machine are just related to the input wind power or rotor speed which is directly related to it with MPP algorithm. The modulation index of the machine side converter is related to both rotor speed and DC link voltage and it is always in the linear region below unity. Because all the power

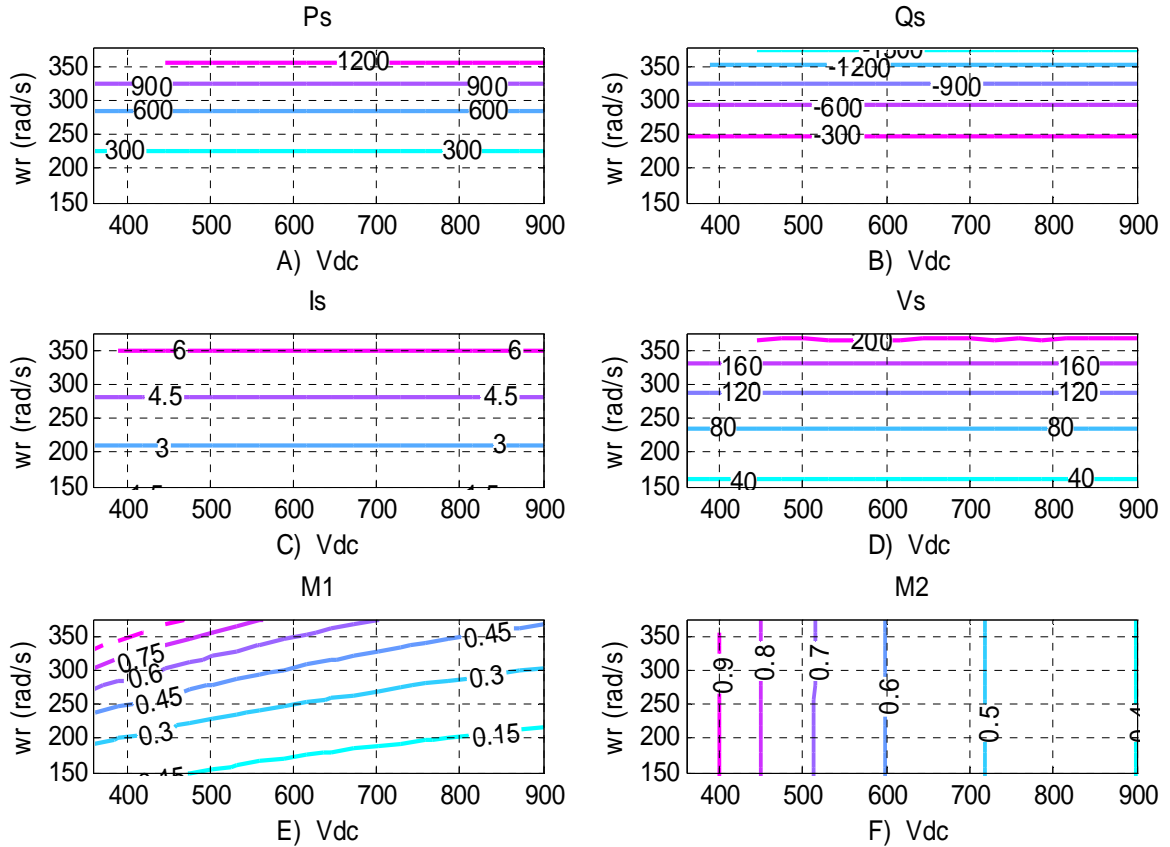


Figure 7.2 Steady state operation region of the system. a) output active power of the generator (W), b) output reactive power of the generator (Var), c) stator current (A), d) stator voltage (V), e) modulation index magnitude of machine side converter f) modulation index magnitude of grid side converter

coming from the wind on the other side is transmitting to the grid and the voltage of the grid is constant, the modulation index of the grid side converter in Figure 7.2 is just related to the DC link voltage magnitude.

To study the stability region of the system in all feasible operation regions, the model equations of the electrical subsystem is linearized and its characteristic equation is defined as a sixth order equation

$$\left\{ \begin{array}{l}
p\Delta I_{sq} = \frac{1}{L_{sq}} \left(M_{q1} \frac{\Delta V_{dc}}{2} - R_s \Delta I_{sq} - \omega_{r0} L_{sd} \Delta I_{sd} - L_{sd} I_{sd0} \Delta \omega_r - \Delta \omega_r \lambda_m \right) \\
p\Delta I_{sd} = \frac{1}{L_{sd}} \left(M_{d1} \frac{\Delta V_{dc}}{2} - R_s \Delta I_{sd} + \omega_{r0} L_{sq} \Delta I_{sq} + L_{sq} I_{sq0} \Delta \omega_r \right) \\
p\Delta I_{s2q} = \frac{1}{L_{s2}} \left(M_{q2} \frac{\Delta V_{dc}}{2} - R_{s2} \Delta I_{s2q} - \omega_e L_{s2} \Delta I_{s2d} \right) \\
p\Delta I_{s2d} = \frac{1}{L_{s2}} \left(M_{d2} \frac{\Delta V_{dc}}{2} - R_{s2} \Delta I_{s2d} + \omega_e L_{s2} \Delta I_{s2q} \right) \\
p\Delta V_{dc} = -\frac{3}{4C_{dc}} (M_{q1} \Delta I_{sq} + M_{d1} \Delta I_{sd} + M_{q2} \Delta I_{s2q} + M_{d2} \Delta I_{s2d}) \\
p\Delta \omega_r = \left(\frac{3p^2}{8J} \right) (\lambda_m \Delta I_{sq} + (L_{sd} - L_{sq}) I_{sq0} \Delta I_{sd} + (L_{sd} - L_{sq}) I_{sd0} \Delta I_{sq})
\end{array} \right. \quad (7.20)$$

$$\left[\begin{array}{l}
p\Delta I_{sq} \\
p\Delta I_{sd} \\
p\Delta I_{s2q} \\
p\Delta I_{s2d} \\
p\Delta V_{dc} \\
p\Delta \omega_r
\end{array} \right] = \left[\begin{array}{cccccc}
-\frac{R_s}{L_{sq}} & -\frac{\omega_{r0} L_{sd}}{L_{sq}} & 0 & 0 & \frac{M_{q1}}{2L_{sq}} & -\frac{L_{sd} I_{sd0} + \lambda_m}{L_{sq}} \\
\frac{\omega_{r0} L_{sq}}{L_{sd}} & -\frac{R_s}{L_{sd}} & 0 & 0 & \frac{M_{d1}}{2L_{sd}} & \frac{L_{sq} I_{sq0}}{L_{sd}} \\
0 & 0 & -\frac{R_{s2}}{L_{s2}} & -\omega_e & \frac{M_{q2}}{2L_{s2}} & 0 \\
0 & 0 & \omega_e & -\frac{R_{s2}}{L_{s2}} & \frac{M_{d2}}{2L_{s2}} & 0 \\
-\frac{3M_{q1}}{4C_{dc}} & -\frac{3M_{d1}}{4C_{dc}} & -\frac{3M_{q2}}{4C_{dc}} & -\frac{3M_{d2}}{4C_{dc}} & 0 & 0 \\
\frac{3p^2(\lambda_m + (L_{sd} - L_{sq}) I_{sd0})}{8J} & \frac{3p^2(L_{sd} - L_{sq}) I_{sq0}}{8J} & 0 & 0 & 0 & 0
\end{array} \right] \left[\begin{array}{l}
\Delta I_{sq} \\
\Delta I_{sd} \\
\Delta I_{s2q} \\
\Delta I_{s2d} \\
\Delta V_{dc} \\
\Delta \omega_r
\end{array} \right] \quad (7.21)$$

$$|\mathcal{M} - A| = a_6 \lambda^6 + a_5 \lambda^5 + a_4 \lambda^4 + a_3 \lambda^3 + a_2 \lambda^2 + a_1 \lambda + a_0 = 0 \quad (7.22)$$

The coefficients of (7.22) are presented in Appendix A. Using the Routh–Hurwitz criteria

$$\begin{array}{l|cccc}
\lambda^6 & a_6 & a_4 & a_2 & a_0 \\
\lambda^5 & a_5 & a_3 & a_1 & \\
\lambda^4 & b_1 = \frac{a_4 a_5 - a_3 a_6}{a_5} & b_2 = \frac{a_2 a_5 - a_1 a_6}{a_5} & a_0 & \\
\lambda^3 & c_1 = \frac{a_3 b_1 - a_5 b_2}{b_1} & c_2 = \frac{a_1 b_1 - a_5 a_0}{b_1} & & \\
\lambda^2 & d_1 = \frac{b_2 c_1 - b_1 c_2}{c_1} & a_0 & & \\
\lambda^1 & e_1 = \frac{c_2 d_1 - c_1 a_0}{d_1} & & & \\
\lambda^0 & a_0 & & &
\end{array} \tag{7.23}$$

The requirements for stability of the system

$$\begin{cases} a_6 > 0, a_5 > 0, a_4 > 0, a_3 > 0, a_2 > 0, a_1 > 0, a_0 > 0 \\ b_1 > 0, c_1 > 0, d_1 > 0, e_1 > 0 \end{cases} \tag{7.24}$$

As shown in Figure 7.3 only the coefficient a_0 affects the stability region in which operation above a particular rotor speed, the system is unstable.

7.3.2 Zero Dynamic Analysis

To analyze the zero dynamics of the system, the first method is adopted. The four inputs and four outputs are

$$Y = [\gamma \quad \omega_r \quad V_{dc} \quad Q_g]^T, \quad U = [M_{q1} \quad M_{d1} \quad M_{q2} \quad M_{d2}]^T \tag{7.25}$$

With differentiating the outputs to define the relative orders

$$\begin{cases} r_1 = 1, & r_2 = 2 \\ r_3 = 1, & r_4 = 1 \end{cases} \quad \text{and} \quad r = \sum_{i=1}^4 r_i = 5 \tag{7.26}$$

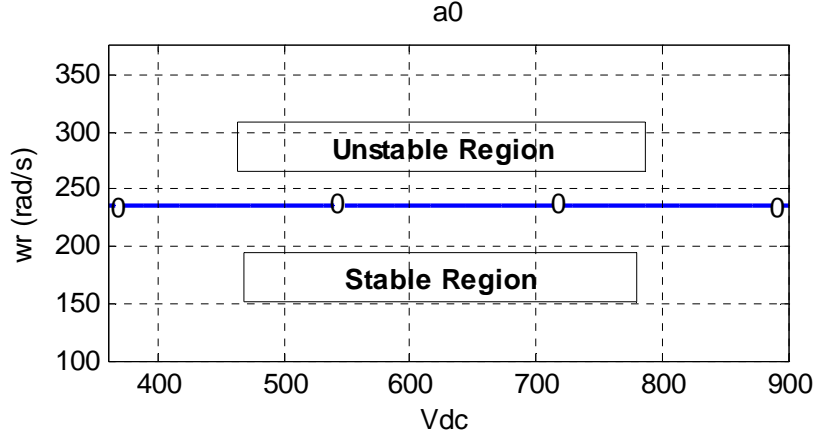


Figure 7.3 Stability region based on Routh–Hurwitz criteria. The last coefficient of the characteristic equation.

Therefore the system has one $(n - \sum r_i)$ internal dynamic. The zero dynamics is obtained when all the output variables are set to zero. With the grid voltage taken as the reference for the qd synchronous reference frame transformation and aligning the grid voltage in the q-axis ($V_{gq} = V_g, V_{gd} = 0$)

$$\begin{cases} C_{dc} p V_{dc} = 0 = -\frac{3}{4}(M_{q1} I_{sq} + M_{d1} I_{sd}) - \frac{3}{4}(M_{q2} I_{s2q} + M_{d2} I_{s2d}) \\ p \omega_r = 0 = T_t - \left(\frac{3P}{4}\right)(\lambda_m I_{sq} + (L_{sd} - L_{sq}) I_{sq} I_{sd}) \\ Q_g = 0 = \frac{3}{2}(V_{gq} I_{s2d} - V_{gd} I_{s2q}), \quad \omega_r = 0, \quad V_{dc} = 0 \\ \gamma = 0 = \left(\frac{9P}{4}\right)(R_s (L_{sd} - L_{sq}) I_{sq}^2 - R_s (L_{sd} - L_{sq}) I_{sd}^2 - R_s \lambda_m I_{sd}) \end{cases} \quad (7.27)$$

then

$$I_{sq} = -\frac{M_{d1} I_{sd}}{M_{q1}} \quad (7.28)$$

and the only remaining dynamic, the zero dynamic of the system, is

$$R_s I_{sd} + L_{sd} p I_{sd} = 0 \quad (7.29)$$

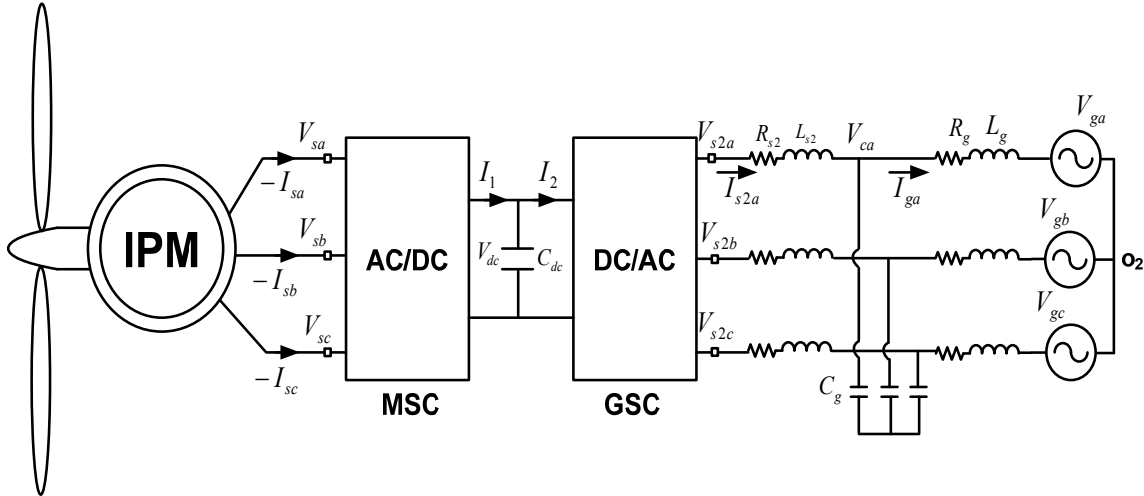


Figure 7.4 The IPM machine as a wind turbine generator connected through LCL filter.

Hence for positive resistance and inductance of the generator, the zero dynamics is always stable, declaring the nonlinear generator connected the grid system through L type filter to be minimum phase.

7.4 Controllability of Wind Turbine Connected through LCL filter to the Grid

The LCL filter shown in Figure 7.4 is a third-order filter which provides a much better ripple and harmonic attenuation over the higher frequency range using smaller passive elements. Therefore, they are more suited for high-power conversion systems and have already been widely employed in wind farms of over hundreds of kilowatts [142-145]. The second inductance represents the inductance of the filter, the grid and isolating transformer. The resistances also include the copper loss of the grid, transformer and switching loss of the grid side converter.

7.4.1 Steady State and Stable Operation Region

The total dynamic equations of the system with the LCL filter are

$$\left\{ \begin{array}{l}
 M_{q1} \frac{V_{dc}}{2} = R_s I_{sq} + L_{sq} p I_{sq} + \omega_r L_{sd} I_{sd} + \omega_r \lambda_m \\
 M_{d1} \frac{V_{dc}}{2} = R_s I_{sd} + L_{sd} p I_{sd} - \omega_r L_{sq} I_{sq} \\
 M_{q2} \frac{V_{dc}}{2} - V_{cq} = R_{s2} I_{s2q} + L_{s2} p I_{s2q} + \omega_e L_{s2} I_{s2d} \\
 M_{d2} \frac{V_{dc}}{2} - V_{cd} = R_{s2} I_{s2d} + L_{s2} p I_{s2d} - \omega_e L_{s2} I_{s2q} \\
 V_{cq} - V_{gq} = R_g I_{gq} + L_g p I_{gq} + \omega_e L_g I_{gd} \\
 V_{cd} - V_{gd} = R_g I_{gd} + L_g p I_{gd} - \omega_e L_g I_{gq} \\
 p V_{cq} = \frac{1}{C_g} (I_{s2q} - I_{gq} - \omega_e C_g V_{cd}) \\
 p V_{cd} = \frac{1}{C_g} (I_{s2d} - I_{gd} + \omega_e C_g V_{cq}) \\
 C_{dc} p V_{dc} = I_1 - I_2 = -\frac{3}{4} (M_{q1} I_{sq} + M_{d1} I_{sd}) - \frac{3}{4} (M_{q2} I_{s2q} + M_{d2} I_{s2d}) \\
 p \omega_r = \left(\frac{p}{2J} \right) (T_t - T_e) = \left(\frac{p}{2J} \right) T_t - \left(\frac{p}{2J} \right) \left(\frac{3P}{4} \right) (\lambda_m I_{sq} + (L_{sd} - L_{sq}) I_{sq} I_{sd})
 \end{array} \right. \quad (7.30)$$

In steady state the derivative parts are zero so we can solve eight equations including six dynamic equations in steady state condition along with the two algebraic equations of reactive power and loss minimization. Therefore there are

The known variables

$$[V_{gq} \quad V_{gd} \quad Q_2 \quad (\omega_r \Leftrightarrow T_t) \quad V_{dc}] \quad (7.31)$$

The unknown variables

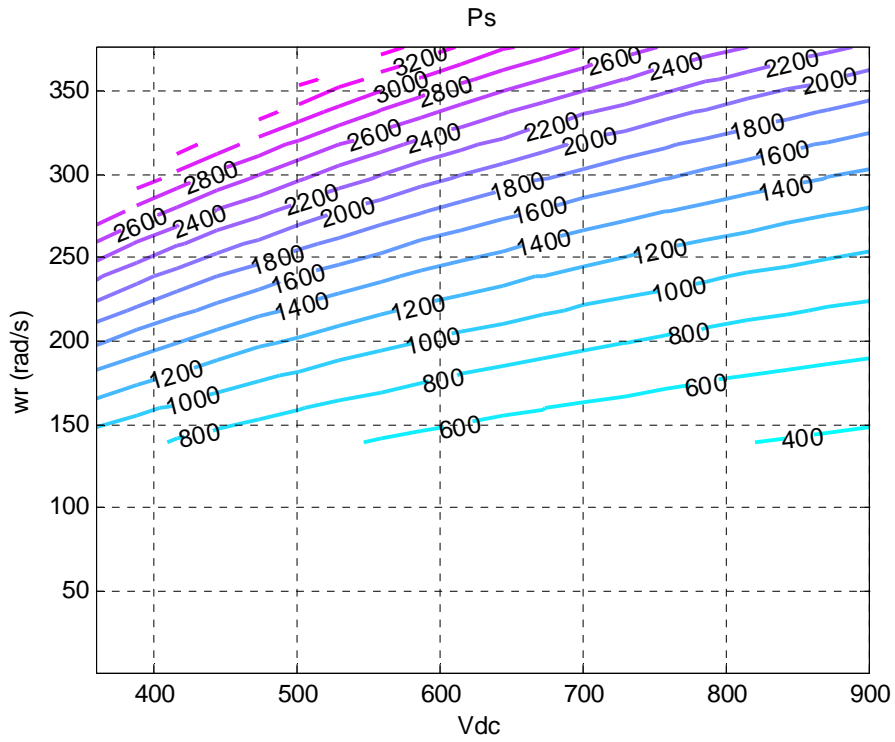


Figure 7.5 Output active power of IPM generator.

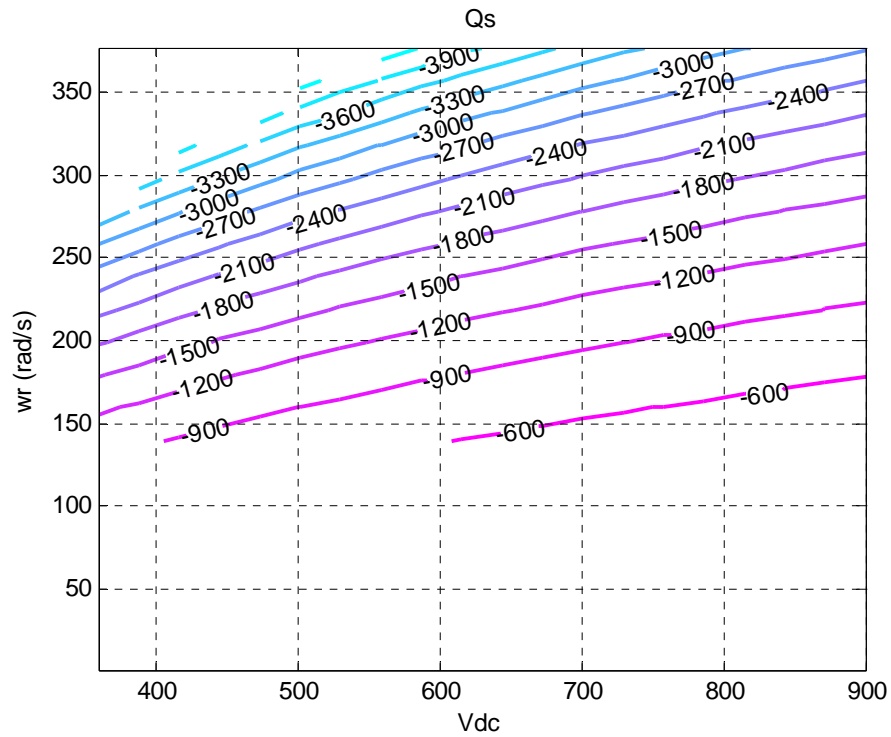


Figure 7.6 Output reactive power of IPM generator.

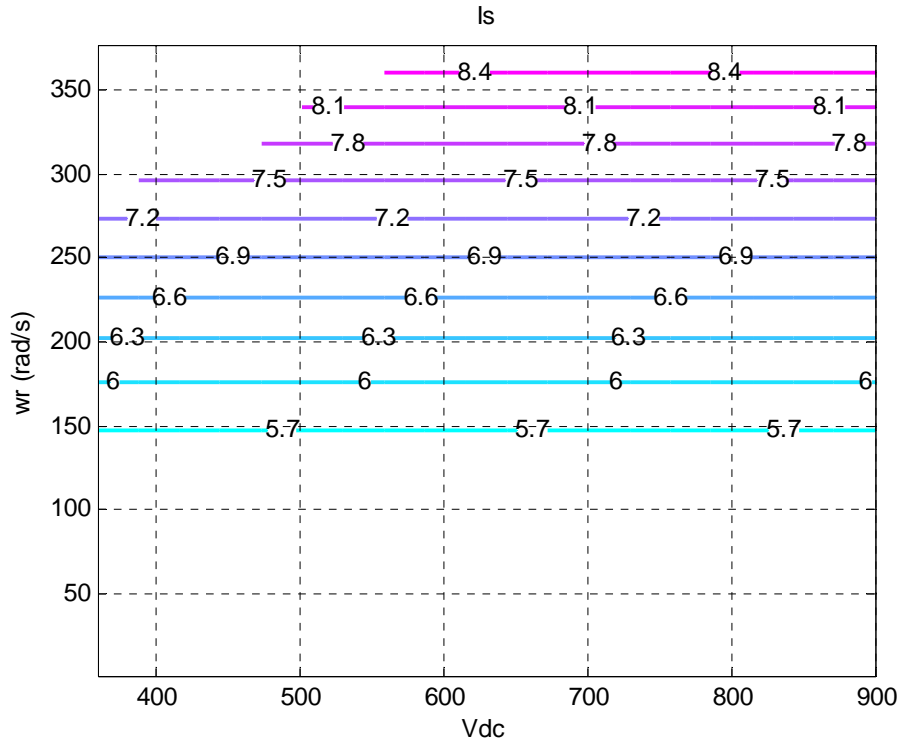


Figure 7.7 Stator current magnitude of IPM generator.

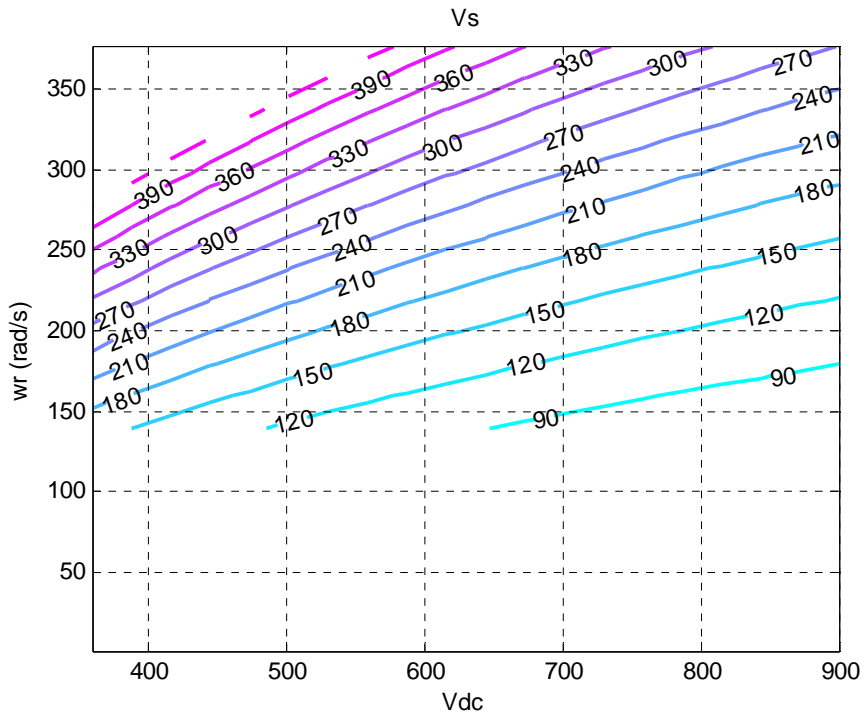


Figure 7.8 Stator voltage magnitude of IPM generator.

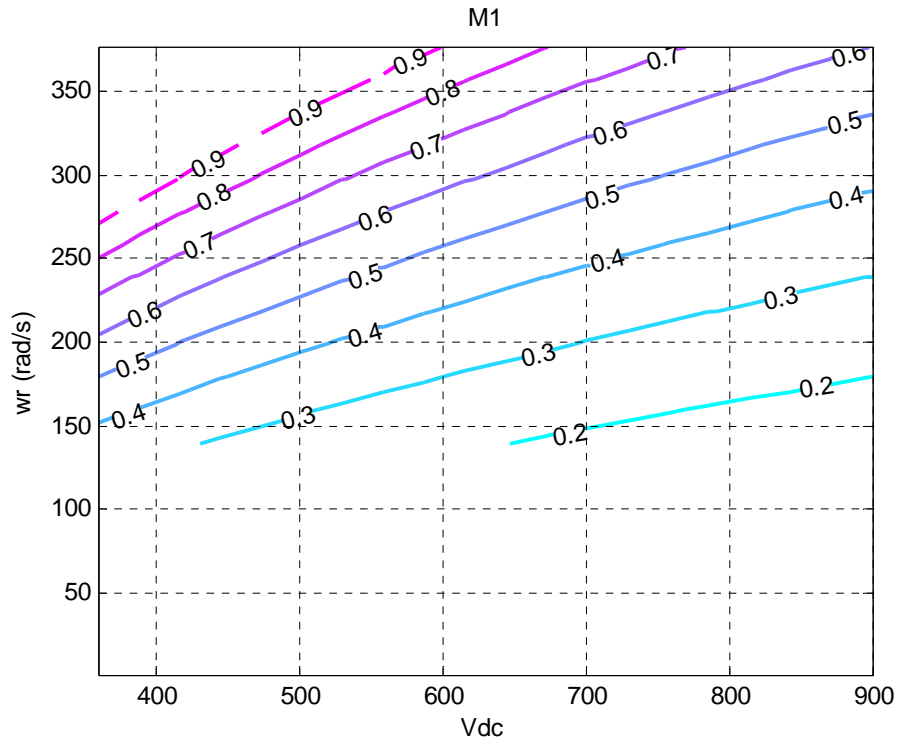


Figure 7.9 Modulation index magnitude of the machine side inverter.

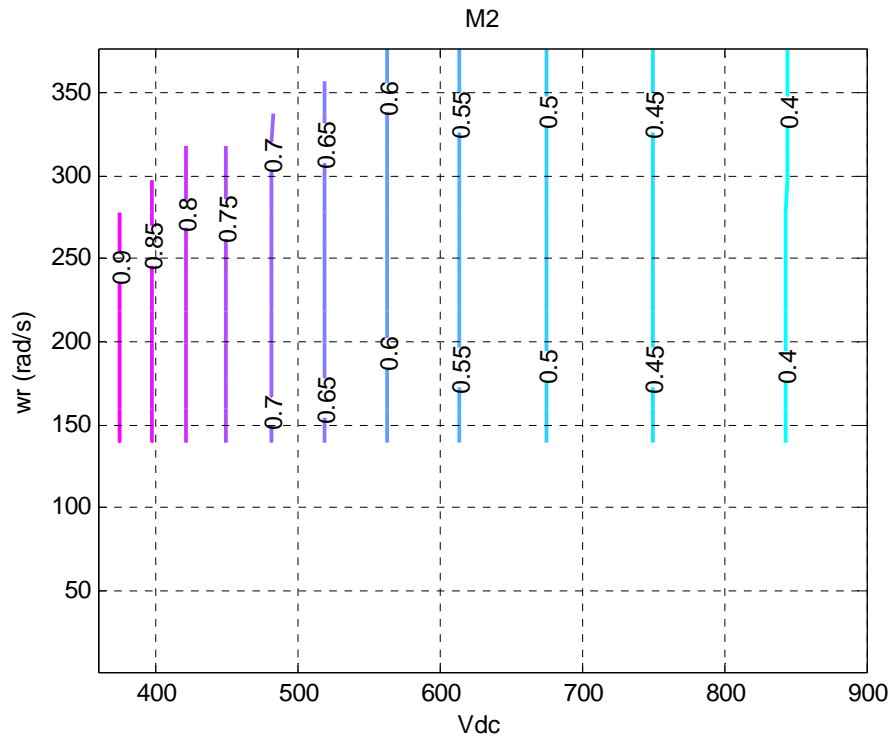


Figure 7.10 Modulation index magnitude of the grid side inverter.

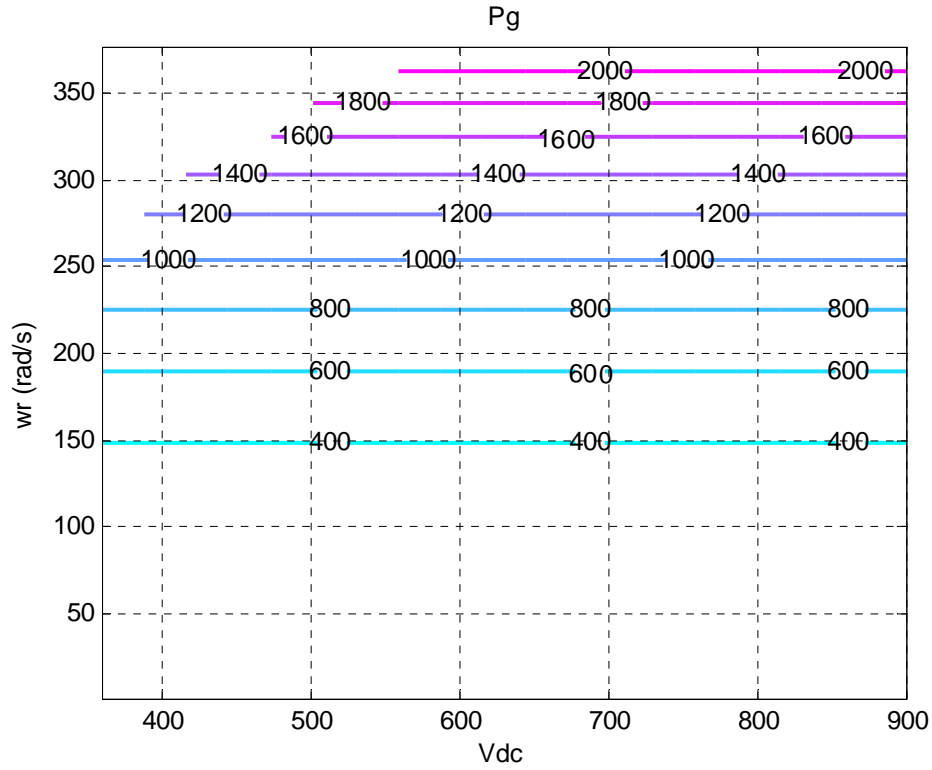


Figure 7.11 Active power flowing into the grid.

$$\left[I_{sq} \quad I_{sd} \quad M_{q1} \quad M_{d1} \quad I_{s2q} \quad I_{s2d} \quad M_{q2} \quad M_{d2} \quad I_{gq} \quad I_{gd} \quad V_{cq} \quad V_{cd} \right] \quad (7.32)$$

So we can vary ω_r and V_{dc} to calculate the other twelve variables. The results are illustrated in Figure 7.5 to Figure 7.11.

We can study the stability region of this system using the small signal analysis in any steady state point. We can define the eigenvalues of the system in that point and check for stability.

$$\left\{ \begin{array}{l}
p\Delta I_{sq} = \frac{1}{L_{sq}} \left(M_{q1} \frac{\Delta V_{dc}}{2} - R_s \Delta I_{sq} - \omega_{r0} L_{sd} \Delta I_{sd} - L_{sd} I_{sd0} \Delta \omega_r - \Delta \omega_r \lambda_m \right) \\
p\Delta I_{sd} = \frac{1}{L_{sd}} \left(M_{d1} \frac{\Delta V_{dc}}{2} - R_s \Delta I_{sd} + \omega_{r0} L_{sq} \Delta I_{sq} + L_{sq} I_{sq0} \Delta \omega_r \right) \\
p\Delta I_{s2q} = \frac{1}{L_{s2}} \left(M_{q2} \frac{\Delta V_{dc}}{2} - \Delta V_{cq} - R_{s2} \Delta I_{s2q} - \omega_e L_{s2} \Delta I_{s2d} \right) \\
p\Delta I_{s2d} = \frac{1}{L_{s2}} \left(M_{d2} \frac{\Delta V_{dc}}{2} - \Delta V_{cd} - R_{s2} \Delta I_{s2d} + \omega_e L_{s2} \Delta I_{s2q} \right) \\
p\Delta I_{gq} = \frac{1}{L_g} \left(\Delta V_{cq} - R_g \Delta I_{gq} - \omega_e L_g \Delta I_{gd} \right) \\
p\Delta I_{gd} = \frac{1}{L_g} \left(\Delta V_{cd} - R_g \Delta I_{gd} + \omega_e L_g \Delta I_{gq} \right) \\
p\Delta V_{cq} = \frac{1}{C_g} \left(\Delta I_{s2q} - \Delta I_{gq} - \omega_e C_g \Delta V_{cd} \right) \\
p\Delta V_{cd} = \frac{1}{C_g} \left(\Delta I_{s2d} - \Delta I_{gd} + \omega_e C_g \Delta V_{cq} \right) \\
p\Delta V_{dc} = -\frac{3}{4C_{dc}} \left(M_{q1} \Delta I_{sq} + M_{d1} \Delta I_{sd} + M_{q2} \Delta I_{s2q} + M_{d2} \Delta I_{s2d} \right) \\
p\Delta \omega_r = \left(\frac{3p^2}{8J} \right) \left(\lambda_m \Delta I_{sq} + (L_{sd} - L_{sq}) I_{sq0} \Delta I_{sd} + (L_{sd} - L_{sq}) I_{sd0} \Delta I_{sq} \right)
\end{array} \right. \quad (7.33)$$

$$\begin{bmatrix} p\Delta I_{sq} \\ p\Delta I_{sd} \\ p\Delta I_{s2q} \\ p\Delta I_{s2d} \\ p\Delta I_{gq} \\ p\Delta I_{gd} \\ p\Delta V_{cq} \\ p\Delta V_{cd} \\ p\Delta V_{dc} \\ p\Delta \omega_r \end{bmatrix} = A \begin{bmatrix} \Delta I_{sq} \\ \Delta I_{sd} \\ \Delta I_{s2q} \\ \Delta I_{s2d} \\ \Delta I_{gq} \\ \Delta I_{gd} \\ \Delta V_{cq} \\ \Delta V_{cd} \\ \Delta V_{dc} \\ \Delta \omega_r \end{bmatrix} \quad (7.34)$$

The characteristic equation

$$|\lambda I - A| = a_{10}\lambda^{10} + a_9\lambda^9 + a_8\lambda^8 + a_7\lambda^7 + a_6\lambda^6 + a_5\lambda^5 + a_4\lambda^4 + a_3\lambda^3 + a_2\lambda^2 + a_1\lambda + a_0 = 0 \quad (7.35)$$

Using the Routh–Hurwitz criteria we can check for stability. Because all eigenvalues in all operation regions are negative, the system is always stable.

7.4.2 Zero Dynamic Analysis

The dynamic equation of the system with the LCL filter in the nonlinear format

$$\dot{X} = f(x) + g_1u_1 + g_2u_2 + g_3u_3 + g_4u_4 \quad (7.36)$$

Where

$$f(x) = \begin{bmatrix} -\frac{R_s x_1}{L_{sq}} - \frac{x_{10} L_{sd} x_2}{L_{sq}} - \frac{x_{10} \lambda_m}{L_{sq}} \\ -\frac{R_s x_2}{L_{sd}} + \frac{x_{10} L_{sq} x_1}{L_{sd}} \\ -\frac{x_7}{L_{s2}} - \frac{R_{s2} x_3}{L_{s2}} - \frac{\omega_e L_{s2} x_4}{L_{s2}} \\ -\frac{x_8}{L_{s2}} - \frac{R_{s2} x_4}{L_{s2}} + \frac{\omega_e L_{s2} x_3}{L_{s2}} \\ \frac{x_7}{L_g} - \frac{V_{gq}}{L_g} - \frac{R_g x_5}{L_g} - \frac{\omega_e L_g x_6}{L_g} \\ \frac{x_8}{L_g} - \frac{V_{gd}}{L_g} - \frac{R_g x_6}{L_g} + \frac{\omega_e L_g x_5}{L_g} \\ \frac{x_3}{C_g} - \frac{x_5}{C_g} - \frac{\omega_e C_g x_8}{C_g} \\ \frac{x_4}{C_g} - \frac{x_6}{C_g} + \frac{\omega_e C_g x_7}{C_g} \\ 0 \\ \left(\frac{p}{2J} \right) T_t - \left(\frac{3P^2}{8J} \right) (\lambda_m x_1 + (L_{sd} - L_{sq}) x_1 x_2) \end{bmatrix} \quad (7.37)$$

$$g_1(x) = \begin{bmatrix} \frac{x_9}{2L_{sq}} \\ 0 \\ 0 \\ 0 \\ 0 \\ 0 \\ 0 \\ 0 \\ \frac{3x_1}{4C_{dc}} \\ 0 \end{bmatrix}, g_2(x) = \begin{bmatrix} 0 \\ \frac{x_9}{2L_{sd}} \\ 0 \\ 0 \\ 0 \\ 0 \\ 0 \\ 0 \\ \frac{3x_2}{4C_{dc}} \\ 0 \end{bmatrix}, g_3(x) = \begin{bmatrix} 0 \\ 0 \\ \frac{x_9}{2L_{s2}} \\ 0 \\ 0 \\ 0 \\ 0 \\ 0 \\ \frac{3x_3}{4C_{dc}} \\ 0 \end{bmatrix}, g_4(x) = \begin{bmatrix} 0 \\ 0 \\ 0 \\ \frac{x_9}{2L_{s2}} \\ 0 \\ 0 \\ 0 \\ 0 \\ \frac{3x_4}{4C_{dc}} \\ 0 \end{bmatrix} \quad (7.38)$$

The Output equations

$$Y = \begin{bmatrix} h_1(x) \\ h_2(x) \\ h_3(x) \\ h_4(x) \end{bmatrix} = \begin{bmatrix} \left(\frac{9P}{4}\right)(R_s(L_{sd} - L_{sq})x_1^2 - R_s(L_{sd} - L_{sq})x_2^2 - R_s\lambda_m x_2) \\ x_{10} \\ x_9 \\ \frac{3}{2}(V_{gq}x_6 - V_{gd}x_5) \end{bmatrix} \quad (7.39)$$

Where

$$X = [I_{sq} \quad I_{sd} \quad I_{s2q} \quad I_{s2d} \quad I_{gq} \quad I_{gd} \quad V_{cq} \quad V_{cd} \quad V_{dc} \quad \omega_r] \quad (7.40)$$

The new states and inputs are

$$U = [M_{q1} \quad M_{d1} \quad M_{q2} \quad M_{d2}] \quad (7.41)$$

With the same output variables in the new ten order system with LCL filter defined in (7.39) the relative orders defined as

$$\begin{cases} r_1 = 1, & r_2 = 2 \\ r_3 = 1, & r_4 = 3 \end{cases} \quad \text{and} \quad r = \sum_{i=1}^4 r_i = 7 \quad (7.42)$$

Therefore there are three $(n-\sum r_i)$ internal dynamics. In this system, the second method has been use for defining the zero dynamics. In the first step, based on (7.7), the new coordinates of the system are

$$\eta = \begin{bmatrix} \eta^{(0)} \\ \eta^{(1)} \\ \vdots \\ \eta^{(m)} \end{bmatrix} = \begin{bmatrix} t_1(x) \\ t_2(x) \\ t_3(x) \\ \dots \\ \left(\frac{9P}{4}\right)(R_s(L_{sd}-L_{sq})x_1^2 - R_s(L_{sd}-L_{sq})x_2^2 - R_s\lambda_m x_2) \\ \dots \\ x_{10} \\ \left(\frac{p}{2J}\right)T_t - \left(\frac{3P^2}{8J}\right)(\lambda_m x_1 + (L_{sd}-L_{sq})x_1 x_2) \\ \dots \\ x_9 \\ \dots \\ \frac{3}{2}(V_{gq}x_6 - V_{gd}x_5) \\ \left(\frac{3V_{gd}R_g + V_{gq}\omega_e L_g}{2L_g}\right)x_5 + \left(\frac{3V_{gd}\omega_e L_g - V_{gq}R_g}{2L_g}\right)x_6 - \frac{3V_{gd}}{2L_g}x_7 + \frac{3V_{gq}}{2L_g}x_8 \\ \dots \\ \left\{ \begin{aligned} &-\frac{3V_{gd}}{2L_g C_g}x_3 + \frac{3V_{gq}}{2L_g C_g}x_4 + \frac{3}{2}\left(\frac{V_{gd}}{L_g C_g} - \frac{V_{gd}R_g^2 + V_{gq}\omega_e L_g R_g}{L_g^2} + \frac{V_{gd}\omega_e^2 L_g^2 - V_{gq}\omega_e L_g R_g}{L_g^2}\right)x_5 \\ &+ \frac{3}{2}\left(-\frac{V_{gq}}{L_g C_g} - \frac{V_{gd}\omega_e L_g R_g + V_{gq}\omega_e^2 L_g^2}{L_g^2} - \frac{V_{gd}\omega_e L_g R_g - V_{gq}R_g^2}{L_g^2}\right)x_6 + \frac{3}{2}\left(\frac{V_{gd}R_g + 2V_{gq}\omega_e L_g}{L_g^2}\right)x_7 \\ &+ \frac{3}{2}\left(\frac{2V_{gd}\omega_e L_g - V_{gq}R_g}{L_g^2}\right)x_8 + \left(\frac{3V_{gd}R_g + V_{gq}\omega_e L_g}{2L_g}\right)\left(-\frac{V_{gq}}{L_g}\right) + \left(\frac{3V_{gd}\omega_e L_g - V_{gq}R_g}{2L_g}\right)\left(-\frac{V_{gd}}{L_g}\right) \end{aligned} \right\} \end{bmatrix} \quad (7.43)$$

$$\eta = \begin{bmatrix} \eta^{(0)} \\ \eta^{(1)} \\ \vdots \\ \eta^{(m)} \end{bmatrix} = \begin{bmatrix} \eta_1^{(0)} \\ \eta_2^{(0)} \\ \eta_3^{(0)} \\ \eta_1^{(1)} \\ \eta_1^{(2)} \\ \eta_2^{(2)} \\ \eta_1^{(3)} \\ \eta_1^{(4)} \\ \eta_2^{(4)} \\ \eta_3^{(4)} \end{bmatrix} = \begin{bmatrix} t_1(x) \\ t_2(x) \\ t_3(x) \\ \dots \\ a_1 x_1^2 + b_1 x_2^2 + c_1 x_2 \\ \dots \\ x_{10} \\ \dots \\ a_2 x_1 + b_2 x_1 x_2 + c_2 \\ \dots \\ x_9 \\ \dots \\ a_3 x_6 + b_3 x_5 \\ \dots \\ a_4 x_5 + b_4 x_6 + c_4 x_7 + d_4 x_8 \\ \dots \\ a_5 x_3 + b_5 x_4 + c_5 x_5 + d_5 x_6 + e_5 x_7 + h_5 x_8 + i_5 + j_5 \end{bmatrix} \quad (7.44)$$

where $t(x)$ is chosen as

$$t_1(x) = x_5, t_2(x) = x_4, t_3(x) = x_3 \quad (7.45)$$

With $t(x)$ given in (7.45), the linearized matrix of η will be

$$\Delta\eta = \begin{bmatrix} \Delta\eta^{(0)} \\ \Delta\eta^{(i)} \\ \vdots \\ \Delta\eta^{(m)} \end{bmatrix} = \begin{bmatrix} 0 & 0 & 0 & 0 & 1 & 0 & 0 & 0 & 0 & 0 \\ 0 & 0 & 0 & 1 & 0 & 0 & 0 & 0 & 0 & 0 \\ 0 & 0 & 1 & 0 & 0 & 0 & 0 & 0 & 0 & 0 \\ 2a_1x_{1o} & 2b_1x_{2o} + c_1 & 0 & 0 & 0 & 0 & 0 & 0 & 0 & 0 \\ 0 & 0 & 0 & 0 & 0 & 0 & 0 & 0 & 0 & 1 \\ a_2 + b_2x_{2o} & b_2x_{1o} & 0 & 0 & 0 & 0 & 0 & 0 & 0 & 0 \\ 0 & 0 & 0 & 0 & 0 & 0 & 0 & 0 & 1 & 0 \\ 0 & 0 & 0 & 0 & b_3 & a_3 & 0 & 0 & 0 & 0 \\ 0 & 0 & 0 & 0 & a_4 & b_4 & c_4 & d_4 & 0 & 0 \\ 0 & 0 & a_5 & b_5 & c_5 & d_5 & e_5 & h_5 & 0 & 0 \end{bmatrix} \quad (7.46)$$

In which the determinant of the linearized matrix $\eta(x)$ is not equal to zero

$$\det(\Delta\eta) = -(2b_2x_{1o}^2 a_1 - 2b_1x_{2o} a_2 - 2b_1x_{2o}^2 b_2 - c_1 a_2 - c_1 b_2 x_{2o})(c_4 h_5 - e_5 d_4) a_3 \neq 0$$

$$c_4 h_5 - e_5 d_4 = -\frac{9 V_{gd}^2 \omega_e L_g + V_{gq}^2 \omega_e L_g}{2 L_g^3} \neq 0 \quad (7.47)$$

Therefore all elements of the matrix are linearly independent. The system equations in the new coordinates are given as

$$\begin{bmatrix} x_1 \\ x_2 \\ x_3 \\ x_4 \\ x_5 \\ x_6 \\ x_7 \\ x_8 \\ x_9 \\ x_{10} \end{bmatrix} = \begin{bmatrix} f_{x1}(\eta_1^{(1)}, \eta_2^{(2)}) \\ f_{x2}(\eta_1^{(1)}, \eta_2^{(2)}) \\ \eta_3^{(0)} \\ \eta_2^{(0)} \\ \eta_1^{(0)} \\ f_{x6}(\eta_1^{(0)}, \eta_1^{(4)}) \\ f_{x7}(\eta_1^{(0)}, \eta_2^{(0)}, \eta_3^{(0)}, \eta_1^{(4)}, \eta_2^{(4)}, \eta_3^{(4)}) + C_{x7} \\ f_{x8}(\eta_1^{(0)}, \eta_2^{(0)}, \eta_3^{(0)}, \eta_1^{(4)}, \eta_2^{(4)}, \eta_3^{(4)}) + C_{x8} \\ \eta_1^{(3)} \\ \eta_1^{(2)} \end{bmatrix} \quad (7.48)$$

The zero dynamics are determined by setting the output variables to either zero or the steady-state values

$$\begin{cases} h_1(x) = \eta_1^{(1)} = \gamma^{ss} = 0 \\ h_2(x) = \eta_1^{(2)} = \omega_{r_ref} \\ h_3(x) = \eta_1^{(3)} = V_{dc_ref} \\ h_4(x) = \eta_1^{(4)} = Q_{2_ref} \end{cases} \quad (7.49)$$

and their derivatives

$$\begin{cases} \eta_2^{(2)} = 0 \\ \eta_2^{(4)} = 0 \\ \eta_3^{(4)} = 0 \end{cases} \quad (7.50)$$

With equation (7.50), the new equations are given in (7.51) which are constant.

$$\begin{cases} x_1 = a_{x1} \\ x_2 = a_{x2} \end{cases} \quad (7.51)$$

Using (7.8) the following can be calculated

$$\begin{cases} F_1 = L_f t_1 = \frac{x_7}{L_g} - \frac{V_{gq}}{L_g} - \frac{R_g x_5}{L_g} - \frac{\omega_e L_g x_6}{L_g} \\ F_2 = L_f t_2 = -\frac{x_8}{L_{s2}} - \frac{R_{s2} x_4}{L_{s2}} + \frac{\omega_e L_{s2} x_3}{L_{s2}} \\ F_3 = L_f t_3 = -\frac{x_7}{L_{s2}} - \frac{R_{s2} x_3}{L_{s2}} - \frac{\omega_e L_{s2} x_4}{L_{s2}} \end{cases} \quad (7.52)$$

The other matrices are defines as

$$\begin{cases} G_1 = [L_{g1}t_1 & L_{g2}t_1 & L_{g3}t_1 & L_{g4}t_1] = [0 & 0 & 0 & 0] \\ G_2 = [L_{g1}t_2 & L_{g2}t_2 & L_{g3}t_2 & L_{g4}t_2] = \begin{bmatrix} 0 & 0 & 0 & \frac{x_9}{2L_{s2}} \end{bmatrix} \\ G_3 = [L_{g1}t_3 & L_{g2}t_3 & L_{g3}t_3 & L_{g4}t_3] = \begin{bmatrix} 0 & 0 & \frac{x_9}{2L_{s2}} & 0 \end{bmatrix} \end{cases} \quad (7.53)$$

To substitute the input variables with the states, we need to define the equations of $C(x)$ and $W(x)$ as

$$\begin{cases} C_1 = \left(\frac{9P}{4}\right) \begin{bmatrix} (R_s(L_{sd} - L_{sq})x_1) \frac{x_9}{2L_{sq}} & (-2R_s(L_{sd} - L_{sq})x_2 - R_s\lambda_m) \frac{x_9}{2L_{sd}} & 0 & 0 \end{bmatrix} \\ C_2 = -\left(\frac{3P^2}{8J}\right) \begin{bmatrix} (\lambda_m + (L_{sd} - L_{sq})x_2) \frac{x_9}{2L_{sq}} & (L_{sd} - L_{sq})x_1 \frac{x_9}{2L_{sd}} & 0 & 0 \end{bmatrix} \\ C_3 = -\frac{3}{4C_{dc}} [x_1 \quad x_2 \quad x_3 \quad x_4] \\ C_4 = \begin{bmatrix} 0 & 0 & -\frac{3}{4} \frac{V_{gd}}{L_g C_g L_{s2}} x_9 & \frac{3}{4} \frac{V_{gq}}{L_g C_g L_{s2}} x_9 \end{bmatrix} \end{cases} \quad (7.54)$$

$$\begin{cases} W_{11} = \left(\frac{9P}{4}\right) \begin{pmatrix} 2R_s(L_{sd} - L_{sq})x_1 \left(-\frac{R_s x_1}{L_{sq}} - \frac{x_{10} L_{sd} x_2}{L_{sq}} - \frac{x_{10} \lambda_m}{L_{sq}} \right) \\ -(2R_s(L_{sd} - L_{sq})x_2^2 + R_s \lambda_m) \left(-\frac{R_s x_2}{L_{sd}} + \frac{x_{10} L_{sq} x_1}{L_{sd}} \right) \end{pmatrix} \\ W_{21} = -\left(\frac{3P^2}{8J}\right) \begin{pmatrix} (\lambda_m + (L_{sd} - L_{sq})x_2) \left(-\frac{R_s x_1}{L_{sq}} - \frac{x_{10} L_{sd} x_2}{L_{sq}} - \frac{x_{10} \lambda_m}{L_{sq}} \right) \\ + (L_{sd} - L_{sq})x_1 \left(-\frac{R_s x_2}{L_{sd}} + \frac{x_{10} L_{sq} x_1}{L_{sd}} \right) \end{pmatrix} \\ W_{31} = 0 \\ W_{41} = a_5 f_{31} + b_5 f_{41} + c_5 f_{51} + d_5 f_{61} + e_5 f_{71} + h_5 f_{81} \end{cases} \quad (7.55)$$

The above equations are transformed to the new coordinates to yield the equations of the zero dynamics given below:

$$\left\{ \begin{array}{l} \dot{\eta}_1^{(0)} = A_{z1}\eta_1^{(0)} + B_{z1}\eta_2^{(0)} + C_{z1}\eta_3^{(0)} + D_{z1} \\ \dot{\eta}_2^{(0)} = \left(\frac{A_{z2}\eta_1^{(0)} + B_{z2}\eta_2^{(0)} + C_{z2}\eta_3^{(0)} + M_{z2} + (D_{z2}\eta_1^{(0)3} + E_{z2}\eta_1^{(0)2} + F_{z2}\eta_1^{(0)} + G_{z2}\eta_1^{(0)}\eta_2^{(0)} + H_{z2}\eta_3^{(0)}\eta_1^{(0)})}{\eta_1^{(0)}V_{gq} + \eta_2^{(0)}V_{gd}} \right) \\ \dot{\eta}_3^{(0)} = \left(\frac{A_{z3}\eta_1^{(0)} + B_{z3}\eta_2^{(0)} + C_{z3}\eta_3^{(0)} + M_{z3} + (D_{z3}\eta_1^{(0)2}\eta_2^{(0)} + E_{z3}\eta_1^{(0)}\eta_2^{(0)} + F_{z3}\eta_2^{(0)2} + G_{z3}\eta_3^{(0)}\eta_2^{(0)} + H_{z3}\eta_2^{(0)})}{\eta_1^{(0)}V_{gq} + \eta_2^{(0)}V_{gd}} \right) \end{array} \right. \quad (7.56)$$

The equations of the zero dynamics are nonlinear and hence the stability can be checked using the corresponding linearized equations. The characteristic equation of the zero dynamics is a cubic equation given as

$$z^3 + n_2z^2 + n_1z + n_0 = 0 \quad (7.57)$$

The Routh–Hurwitz criteria for the stability of this characteristic equation is given as

$$\left\{ \begin{array}{l} n_2 > 0, \quad n_1 > 0, \quad n_0 > 0 \\ (n_1n_2 - n_0) > 0 \end{array} \right. \quad (7.58)$$

Figure 7.12 shows how the signs of two coefficients of (7.57) and (7.58) are influenced by the values of the rotor speed and the DC capacitor voltage. The zero dynamics is unstable for the operating regions considered which leads to the conclusion that the IPM generator system has unstable zero dynamics and is non-minimum phase for all operating conditions. For the selected controlled variables, there is an inherent structural constraint that adversely affects the controller design.

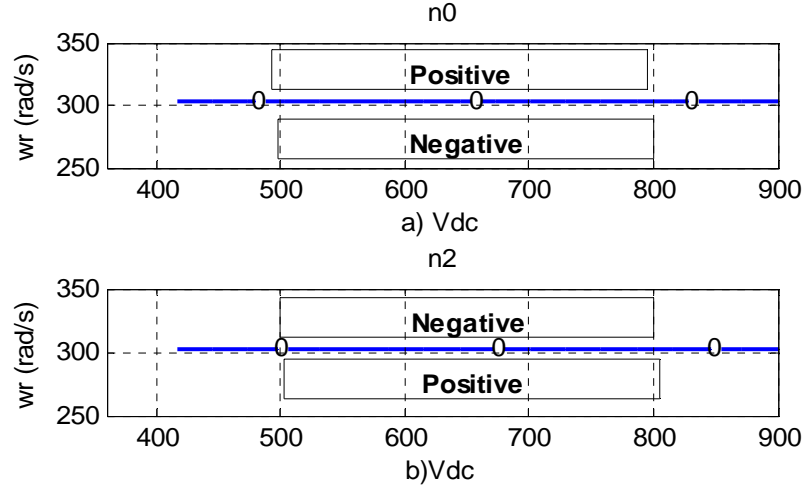


Figure 7.12 Two of the coefficients of the linearized zero dynamics characteristic equation (46). (a) the last coefficient (n_0), (b) second coefficient (n_2).

7.5 Controllability and Stability Analysis of PV System Connected to Current Source Inverter

As illustrated in Figure 7.13, in the study system, a PV system is connected to the grid through a current source inverter. The nonlinear characteristic equation of the PV system relating the PV voltage to its output current is as follows:

$$I_{pv} = n_p I_{ph} - n_p I_{rs} \left[\exp\left(\frac{q}{k \theta} \frac{V_{pv}}{A n_s}\right) - 1 \right] \quad (7.59)$$

$$I_{ph} = \left[I_{src} + k_\theta (\theta - \theta_r) \right] \frac{S}{100} \quad (7.60)$$

Equations (7.59) and (7.60) define the steady-state equation relating the current flowing out of the PV and the terminal voltage. In the equations, I_{rs} and θ are the reverse saturation current and the temperature of $p-n$ junction. I_{src} is the short-circuit

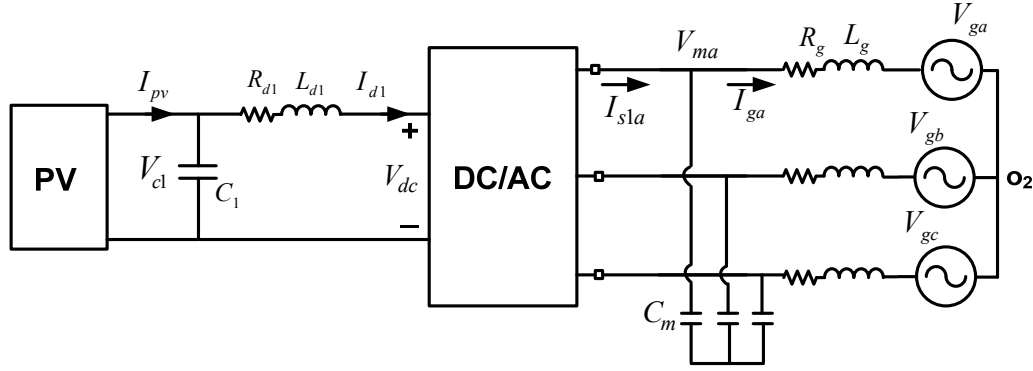


Figure 7.13 An IPM machine as a wind turbine generator connected through LCL filter.

current of one PV cell, n_s and n_p are the number of series and parallel PV cells in a string, respectively. A is the ideality factor and S is solar irradiation level. θ_r is the cell reference temperature and k_θ is the temperature coefficient. $q(=1.602e^{-19}C)$ and $k(=1.38e^{-23}J/K)$ are the unit electric charge and Boltzmann's constant. Table I shows parameters of PV system. The dynamic equations of the grid is

$$\begin{cases} V_{mq} - V_{gq} = R_g I_{gq} + L_g p I_{gq} + \omega_e L_g I_{gd} \\ V_{md} - V_{gd} = R_g I_{gd} + L_g p I_{gd} - \omega_e L_g I_{gq} \end{cases} \quad (7.61)$$

where V_{gqd} and I_{gqd} are the qd-axis grid voltage and current. The inverter and DC side dynamic equations are as follows:

$$\begin{cases} I_{s1q} = \frac{M_q}{2} I_{d1} \\ I_{s1d} = \frac{M_d}{2} I_{d1} \\ V_{dc} = \frac{3}{4} (M_q V_{mq} + M_d V_{md}) \end{cases} \quad (7.62)$$

$$\begin{cases} \frac{M_q}{2} I_{d1} - I_{gq} = C_m p V_{mq} + \omega_e C_m V_{md} \\ \frac{M_d}{2} I_{d1} - I_{gd} = C_m p V_{md} - \omega_e C_m V_{mq} \end{cases} \quad (7.63)$$

$$V_{c1} - \frac{3}{4} (M_q V_{mq} + M_d V_{md}) = R_{d1} I_{d1} + L_{d1} p I_{d1} \quad (7.64)$$

$$C_1 p V_{c1} = I_{pv} - I_{d1} \text{ and } V_{c1} = V_{pv} \quad (7.65)$$

To control the input current of the inverter and the reactive power following into the grid

$$\begin{cases} R_{d1} I_{d1}^2 + \frac{1}{2} L_{d1} p I_{d1}^2 = V_{d1} I_{d1} - \frac{3}{2} \left(\frac{M_q}{2} I_{d1} V_{mq} + \frac{M_d}{2} I_{d1} V_{md} \right) \\ Q_g = \frac{3}{2} (V_{gq} I_{gd} - V_{gd} I_{gq}) \end{cases} \quad (7.66)$$

If we align the grid voltage to the q-axis reference frame ($V_{gd} = 0$) and operate the system under unity power factor

$$Q_g = \frac{3}{2} V_{gq} I_{gd} = 0 \quad (7.67)$$

7.5.1 Steady State and Stability Analysis of the System

Under steady state operating conditions the derivatives of the states are set to zero. The resulting equations with the algebraic equation defining the reference grid

reactive power and operating under maximum power point of PV are used to determine the steady state operation. The known variables are

$$\left[V_{gq} \quad V_{gd} \quad Q_g \quad I_{pv} \quad V_{pv} \right] \quad (7.68)$$

And the unknown variables are

$$\left[M_q \quad M_d \quad I_{gq} \quad I_{gd} \quad V_{mq} \quad V_{md} \quad I_{d1} \right] \quad (7.69)$$

The irradiation of the sun is varied (S_1) and the PV voltage and current based on maximum power point operation are calculated to solve the steady-state equations given as

$$\begin{cases} V_{mq} - V_{gq} - R_g I_{gq} - \omega_e L_g I_{gd} = 0 \\ V_{md} - V_{gd} - R_g I_{gd} + \omega_e L_g I_{gq} = 0 \\ \frac{M_q}{2} I_{d1} - I_{gq} - \omega_e C_m V_{md} = 0 \\ \frac{M_d}{2} I_{d1} - I_{gd} + \omega_e C_m V_{mq} = 0 \\ V_{d1} - \frac{3}{4} (M_q V_{mq} + M_d V_{md}) - R_{d1} I_{d1} = 0 \\ I_{pv} - I_{d1} = 0 \\ Q_g = \frac{3}{2} V_{gq} I_{gd} = 0 \end{cases} \quad (7.70)$$

To study the stability region of the system in all feasible operation regions, the model equations of the electrical subsystem are linearized. The output, input and state variables of the system

$$h(x) = \begin{bmatrix} I_{d1}^2 \\ Q_g \end{bmatrix}, \quad U = \begin{bmatrix} M_q \\ M_d \end{bmatrix}, \quad X = \left[V_{mq} \quad V_{md} \quad I_{gq} \quad I_{gd} \quad I_{d1} \quad V_{pv} \right] \quad (7.71)$$

To define the number of internal dynamics

$$\begin{cases}
p\Delta I_{gq} = \frac{1}{L_g}(\Delta V_{mq} - R_g\Delta I_{gq} - \omega_e L_g \Delta I_{gd}) \\
p\Delta I_{gd} = \frac{1}{L_g}(\Delta V_{md} - R_g\Delta I_{gd} + \omega_e L_g \Delta I_{gq}) \\
p\Delta V_{mq} = \frac{1}{C_m} \left(\frac{M_{qo}}{2} \Delta I_{d1} + \frac{I_{d1o}}{2} \Delta M_q - \Delta I_{gq} - \omega_e C_m \Delta V_{md} \right) \\
p\Delta V_{md} = \frac{1}{C_m} \left(\frac{M_{do}}{2} \Delta I_{d1} + \frac{I_{d1o}}{2} \Delta M_d - \Delta I_{gd} + \omega_e C_m \Delta V_{mq} \right) \\
p\Delta I_{d1} = \frac{1}{L_{d1}} \left(\Delta V_{pv} - \frac{3M_{qo}}{4} \Delta V_{mq} - \frac{3V_{mqo}}{4} \Delta M_q - \frac{3M_{do}}{4} \Delta V_{md} - \frac{3V_{mdo}}{4} \Delta M_d - R_{d1} \Delta I_{d1} \right) \\
p\Delta V_{pv} = -\frac{qn_p I_{rs}}{C_1 k \theta A n_s} \exp\left(\frac{q}{k \theta A} \frac{V_{pv}}{n_s}\right) \Delta V_{pv} - \frac{1}{C_1} \Delta I_{d1}
\end{cases} \quad (7.72)$$

$$A = \begin{bmatrix}
-\frac{R_g}{L_g} & -\omega_e & \frac{1}{L_g} & 0 & 0 & 0 \\
\omega_e & -\frac{R_g}{L_g} & 0 & \frac{1}{L_g} & 0 & 0 \\
-\frac{1}{C_m} & 0 & 0 & -\omega_e & \frac{M_{qo}}{2C_m} & 0 \\
0 & -\frac{1}{C_m} & \omega_e & 0 & \frac{M_{do}}{2C_m} & 0 \\
0 & 0 & -\frac{3M_{qo}}{4L_{d1}} & -\frac{3M_{do}}{4L_{d1}} & -\frac{R_{d1}}{L_{d1}} & \frac{1}{L_{d1}} \\
0 & 0 & 0 & 0 & -\frac{1}{C_1} & -\frac{qn_p I_{rs}}{C_1 k \theta A n_s} \exp\left(\frac{q}{k \theta A} \frac{V_{pv}}{n_s}\right)
\end{bmatrix} \quad (7.73)$$

The characteristic equation is defined as a sixth order equation

$$|\lambda I - A| = a_6 \lambda^6 + a_5 \lambda^5 + a_4 \lambda^4 + a_3 \lambda^3 + a_2 \lambda^2 + a_1 \lambda + a_0 = 0 \quad (7.74)$$

The coefficients of (7.74) are presented in Appendix B. Using the Routh–Hurwitz, the criteria for stability is as

$$\begin{cases}
a_6 > 0, a_5 > 0, a_4 > 0, a_3 > 0, a_2 > 0, a_1 > 0, a_0 > 0 \\
b_1 > 0, c_1 > 0, d_1 > 0, e_1 > 0
\end{cases} \quad (7.75)$$

The parameters of (7.75) are defined using (7.23).

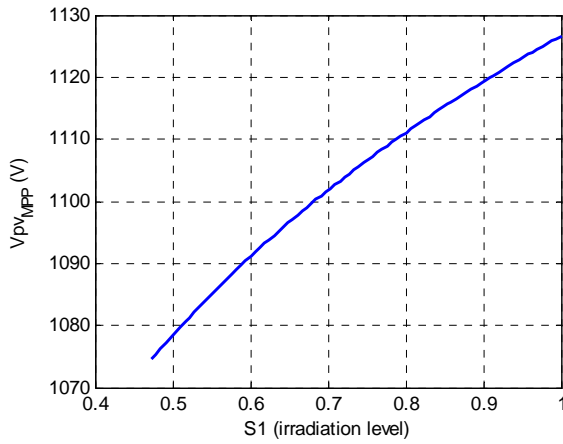


Figure 7.14 PV output voltage at MPP with in different irradiation level

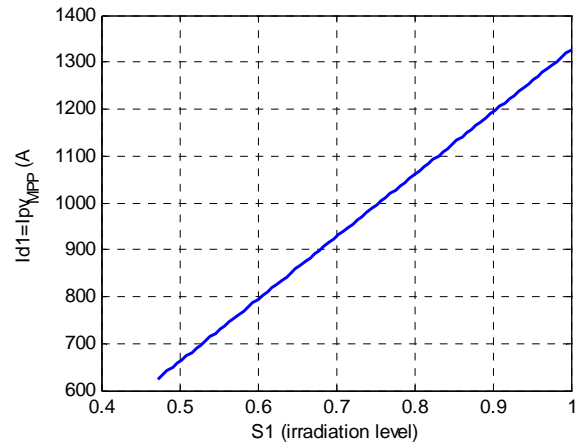


Figure 7.15 PV output current at MPP with in different irradiation level

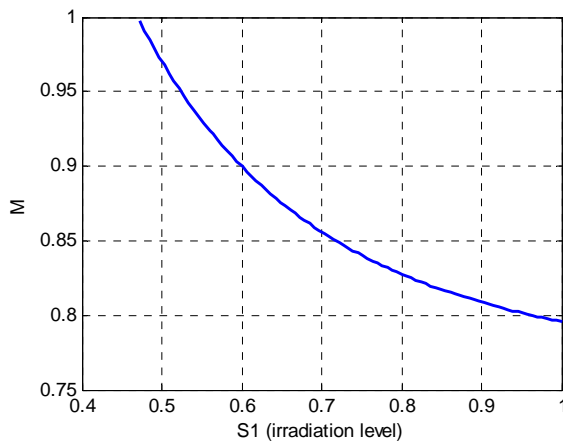


Figure 7.16 Inverter modulation index magnitude at different irradiation level

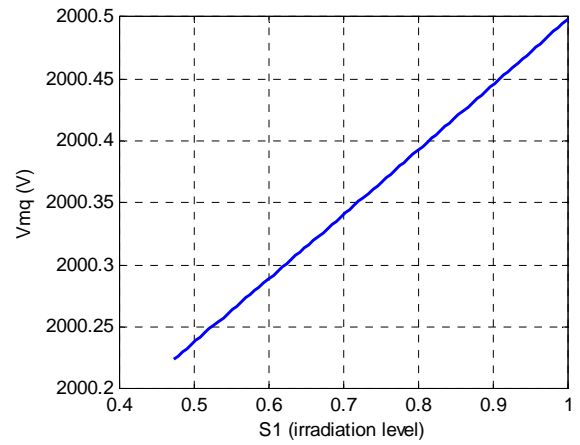


Figure 7.17 q-axis capacitor voltage at different irradiation level

After applying the steady state parameters, the system is stable in the whole operation region.

7.5.2 Zero Dynamics Analysis of PV

To analyze the zero dynamics of the system the two inputs and two outputs are

$$h(x) = \begin{bmatrix} I_{d1}^2 & Q_g \end{bmatrix}^T, U = \begin{bmatrix} M_q & M_d \end{bmatrix}^T \quad (7.76)$$

Differentiate the outputs to define the relative orders the results are

$$\begin{cases} r_1 = 1, \\ r_2 = 2, \end{cases} \quad \text{and} \quad r = \sum_{i=1}^2 r_i = 3 \quad (7.77)$$

Therefore the system has three $(n - \sum r_i)$ internal dynamics.

The dynamic equations of the system in nonlinear format are as

$$\dot{X} = f(x) + g_1(x)u_1 + g_2(x)u_2 \quad (7.78)$$

$$\begin{bmatrix} \dot{x}_1 \\ \dot{x}_2 \\ \dot{x}_3 \\ \dot{x}_4 \\ \dot{x}_5 \\ \dot{x}_6 \end{bmatrix} = \begin{bmatrix} \frac{x_3}{L_g} - \frac{V_{gq}}{L_g} - \frac{R_g}{L_g} x_1 - \omega_e x_2 \\ \frac{x_4}{L_g} - \frac{R_g}{L_g} x_2 + \omega_e x_1 \\ -\frac{x_1}{C_m} - \omega_e x_4 \\ -\frac{x_2}{C_m} + \omega_e x_3 \\ \frac{x_6}{L_{d1}} - \frac{R_{d1}}{L_{d1}} x_5 \\ \frac{I_{pv}}{C_1} - \frac{x_5}{C_1} \end{bmatrix} + \begin{bmatrix} 0 \\ 0 \\ \frac{x_5}{2C_m} \\ 0 \\ \frac{3x_3}{4L_{d1}} \\ 0 \end{bmatrix} u_1 + \begin{bmatrix} 0 \\ 0 \\ 0 \\ \frac{x_5}{2C_m} \\ \frac{3x_4}{4L_{d1}} \\ 0 \end{bmatrix} u_2 \quad (7.79)$$

$$Y = \begin{bmatrix} h_1(x) \\ h_2(x) \end{bmatrix} = \begin{bmatrix} x_5^2 \\ \frac{3}{2} V_{gq} x_2 \end{bmatrix} \quad (7.80)$$

The new coordinates of the system are

$$\eta = \begin{bmatrix} \eta^{(0)} \\ \eta^{(1)} \\ \vdots \\ \eta^{(m)} \end{bmatrix} = \begin{bmatrix} t_1(x) \\ t_2(x) \\ t_3(x) \\ \cdots \\ x_5^2 \\ \cdots \\ \frac{3}{2}V_{gq}x_2 \\ \cdots \\ \frac{3}{2}V_{gq}\left(\frac{x_4}{L_g} - \frac{R_g}{L_g}x_2 + \omega_e x_1\right) \end{bmatrix} \quad (7.81)$$

If we choose

$$t_1(x) = x_1, t_2(x) = x_3, t_3(x) = x_6 \quad (7.82)$$

$$\Delta\eta = \begin{bmatrix} \Delta\eta^{(0)} \\ \Delta\eta^{(1)} \\ \vdots \\ \Delta\eta^{(m)} \end{bmatrix} = \begin{bmatrix} 1 & 0 & 0 & 0 & 0 & 0 \\ 0 & 0 & 1 & 0 & 0 & 0 \\ 0 & 0 & 0 & 0 & 0 & 1 \\ 0 & 0 & 0 & 0 & 2x_{5_0} & 0 \\ 0 & \frac{3}{2}V_{gq} & 0 & 0 & 0 & 0 \\ \frac{3V_{gq}\omega_e}{2} & -\frac{3V_{gq}R_g}{2L_g} & 0 & \frac{3V_{gq}}{2L_g} & 0 & 0 \end{bmatrix} \begin{bmatrix} x_1 \\ x_2 \\ x_3 \\ x_4 \\ x_5 \\ x_6 \end{bmatrix} \quad (7.83)$$

$$\det(\Delta\eta) = \frac{9V_{gq}^2}{2L_g} x_{5_0} \neq 0 \quad (7.84)$$

With $t(x)$ given in (7.82), the determinant of the linearized matrix $\eta(x)$ is not equal to zero, in which case all the elements of $\eta(x)$ are linearly independent. The system equations in the new coordinates are given as

$$\begin{bmatrix} x_1 \\ x_2 \\ x_3 \\ x_4 \\ x_5 \\ x_6 \end{bmatrix} = \begin{bmatrix} \eta_1^{(0)} \\ \frac{2}{3V_{gq}} \eta_1^{(2)} \\ \eta_2^{(0)} \\ \frac{2L_g}{3V_{gq}} \eta_2^{(2)} - \omega_e L_g \eta_1^{(0)} + \frac{2R_g}{3V_{gq}} \eta_1^{(2)} \\ \sqrt{\eta_1^{(1)}} \\ \eta_3^{(0)} \end{bmatrix} \quad (7.85)$$

The following can be calculated

$$\begin{cases} F_1 = L_f t_1 = \frac{x_3}{L_g} - \frac{V_{gq}}{L_g} - \frac{R_g}{L_g} x_1 - \omega_e x_2 \\ F_2 = L_f t_2 = -\frac{x_1}{C_m} - \omega_e x_4 \\ F_3 = L_f t_3 = \frac{I_{pv}}{C_1} - \frac{x_5}{C_1} \end{cases} \quad (7.86)$$

The other matrices are defines as

$$\begin{cases} G_1 = [L_{g1} t_1 \quad L_{g2} t_1] = [0 \quad 0] \\ G_2 = [L_{g1} t_2 \quad L_{g2} t_2] = \left[\frac{x_5}{2C_m} \quad 0 \right] \\ G_3 = [L_{g1} t_3 \quad L_{g2} t_3] = [0 \quad 0] \end{cases} \quad (7.87)$$

To substitute the input variables with the states we need to define the equations of $C(x)$ and $W(x)$ as

$$\begin{cases} C_1 = [L_{g1} h_1 \quad L_{g2} h_1] = \left[-\frac{3x_5 x_3}{2L_{d1}} \quad -\frac{3x_5 x_4}{2L_{d1}} \right] \\ C_2 = [L_{g1} L_f h_2 \quad L_{g2} L_f h_2] = \left[0 \quad \frac{3V_{gq} x_5}{4C_m L_g} \right] \end{cases} \quad (7.88)$$

$$\left\{ \begin{array}{l} W_{11} = L_f h_1 = \frac{2x_5 x_6}{L_{d1}} - \frac{2R_{d1}}{L_{d1}} x_5^2 \\ W_{21} = L_f h_2 = \frac{3V_{gq}}{2} \left(\frac{x_4}{L_g} - \frac{R_g}{L_g} x_2 + \omega_e x_1 \right) \\ W_{31} = L_f^2 h_2 = \left(\begin{array}{l} \frac{3V_{gq} \omega_e}{2} \left(\frac{x_3}{L_g} - \frac{V_{gq}}{L_g} - \frac{R_g}{L_g} x_1 - \omega_e x_2 \right) \\ - \frac{3V_{gq} R_g}{2L_g} \left(\frac{x_4}{L_g} - \frac{R_g}{L_g} x_2 + \omega_e x_1 \right) + \frac{3V_{gq}}{2L_g} \left(-\frac{x_2}{C_m} + \omega_e x_3 \right) \end{array} \right) \end{array} \right. \quad (7.89)$$

For calculation of zero dynamics, we should put outputs either zero or as their steady state value. Thus their derivative will be zero. Therefore

$$\left\{ \begin{array}{l} h_1(x) = \eta_1^{(1)} = I_{d1_ref}^2 \\ h_1(x) = \eta_1^{(2)} = Q_{g_ref} \Rightarrow \eta_2^{(2)} = 0 \end{array} \right. \quad (7.90)$$

From the above results, during the calculation of zero dynamics we can consider

$$\left\{ \begin{array}{l} x_2 = a_{x2} = \frac{2Q_{g_ref}}{3V_{gq}} = cte \\ x_5 = a_{x5} = I_{d1_ref} = cte \end{array} \right. \quad (7.91)$$

and there is no need for their conversion to new coordinates.

$$\begin{bmatrix} x_1 \\ x_2 \\ x_3 \\ x_4 \\ x_5 \\ x_6 \end{bmatrix} = \begin{bmatrix} \eta_1^{(0)} \\ a_{x2} \\ \eta_2^{(0)} \\ -\omega_e L_g \eta_1^{(0)} + \frac{2R_g Q_{g-ref}}{3V_{gq}} \\ a_{x5} \\ \eta_3^{(0)} \end{bmatrix} \quad (7.92)$$

If we convert the matrices F_i , G_i , C_i , W_i to new coordinates

$$\begin{cases} F_1 = L_f t_1 = \frac{\eta_2^{(0)}}{L_g} - \frac{V_{gq}}{L_g} - \frac{R_g}{L_g} \eta_1^{(0)} - \omega_e a_{x2} \\ F_2 = L_f t_2 = -\frac{\eta_1^{(0)}}{C_m} + \omega_e^2 L_g \eta_1^{(0)} - \frac{\omega_e 2R_g Q_{g-ref}}{3V_{gq}} \\ F_3 = L_f t_3 = \frac{I_{pv}}{C_1} - \frac{a_{x5}}{C_1} \end{cases} \quad (7.93)$$

$$\begin{cases} G_1 = [L_{g1} t_1 \quad L_{g2} t_1] = [0 \quad 0] \\ G_2 = [L_{g1} t_2 \quad L_{g2} t_2] = \begin{bmatrix} \frac{a_{x5}}{2C_m} & 0 \end{bmatrix} \\ G_3 = [L_{g1} t_3 \quad L_{g2} t_3] = [0 \quad 0] \end{cases} \quad (7.94)$$

$$\begin{cases} C_1 = [L_{g1} h_1 \quad L_{g2} h_1] = \begin{bmatrix} -\frac{3a_{x5} \eta_2^{(0)}}{2L_{d1}} & -\frac{3a_{x5}}{2L_{d1}} \left(-\omega_e L_g \eta_1^{(0)} + \frac{2R_g Q_{g-ref}}{3V_{gq}} \right) \end{bmatrix} \\ C_2 = [L_{g1} L_f h_2 \quad L_{g2} L_f h_2] = \begin{bmatrix} 0 & \frac{3V_{gq} a_{x5}}{4C_m L_g} \end{bmatrix} \end{cases} \quad (7.95)$$

$$\left\{ \begin{array}{l} W_{11} = L_f h_1 = \frac{2a_{x5}\eta_3^{(0)}}{L_{d1}} - \frac{2R_{d1}}{L_{d1}} a_{x5}^2 \\ W_{21} = L_f^2 h_2 = \left(\frac{3V_{gq}\omega_e}{2} \left(\frac{\eta_2^{(0)}}{L_g} - \frac{V_{gq}}{L_g} - \frac{R_g}{L_g} \eta_1^{(0)} - \omega_e a_{x2} \right) + \frac{3V_{gq}}{2L_g} \left(-\frac{a_{x2}}{C_m} + \omega_e \eta_2^{(0)} \right) \right) \\ \quad - \frac{3V_{gq}R_g}{2L_g} \left(\frac{\left(-\omega_e L_g \eta_1^{(0)} + \frac{2R_g Q_{g-ref}}{3V_{gq}} \right)}{L_g} - \frac{R_g}{L_g} a_{x2} + \omega_e \eta_1^{(0)} \right) \end{array} \right. \quad (7.96)$$

$$\left\{ \begin{array}{l} \dot{\eta}_1^{(0)} = \frac{\eta_2^{(0)}}{L_g} - \frac{V_{gq}}{L_g} - \frac{R_g}{L_g} \eta_1^{(0)} - \frac{2\omega_e Q_{g-ref}}{3V_{gq}} \\ \dot{\eta}_2^{(0)} = a_{21} + a_{22}\eta_1^{(0)} + \frac{a_{23}}{\eta_2^{(0)}} + \frac{a_{24}\eta_1^{(0)2}}{\eta_2^{(0)}} + \frac{a_{25}\eta_1^{(0)}}{\eta_2^{(0)}} + \frac{a_{26}\eta_3^{(0)}}{\eta_2^{(0)}} \\ \dot{\eta}_3^{(0)} = \frac{I_{pv}}{C_1} - \frac{I_{d1-ref}}{C_1} \end{array} \right. \quad (7.97)$$

$$\left\{ \begin{array}{l} \dot{\eta}_1^{(0)} = a_{11} + a_{12}\eta_1^{(0)} + a_{13}\eta_2^{(0)} \\ \dot{\eta}_2^{(0)} = a_{21} + a_{22}\eta_1^{(0)} + \frac{a_{23}}{\eta_2^{(0)}} + \frac{a_{24}\eta_1^{(0)2}}{\eta_2^{(0)}} + \frac{a_{25}\eta_1^{(0)}}{\eta_2^{(0)}} + \frac{a_{26}\eta_3^{(0)}}{\eta_2^{(0)}} \\ \dot{\eta}_3^{(0)} = a_{31} \end{array} \right. \quad (7.98)$$

$$\begin{bmatrix} \Delta \dot{\eta}_1^{(0)} \\ \Delta \dot{\eta}_2^{(0)} \\ \Delta \dot{\eta}_3^{(0)} \end{bmatrix} = \begin{bmatrix} 0 & a_{12} \\ a_{22} + \frac{2a_{24}\eta_1^{(0)} + a_{25}}{\eta_2^{(0)}} & -\frac{1}{\eta_2^{(0)2}} (a_{23} + a_{24}\eta_1^{(0)2} + a_{25}\eta_1^{(0)} + a_{26}\eta_3^{(0)}) \\ 0 & 0 \end{bmatrix} \begin{bmatrix} a_{13} \\ \frac{a_{26}}{\eta_2^{(0)}} \\ 0 \end{bmatrix} \begin{bmatrix} \Delta \eta_1^{(0)} \\ \Delta \eta_2^{(0)} \\ \Delta \eta_3^{(0)} \end{bmatrix} \quad (7.99)$$

$$|SI - A| = s(s^2 + b_1 s + b_0) \quad (7.100)$$

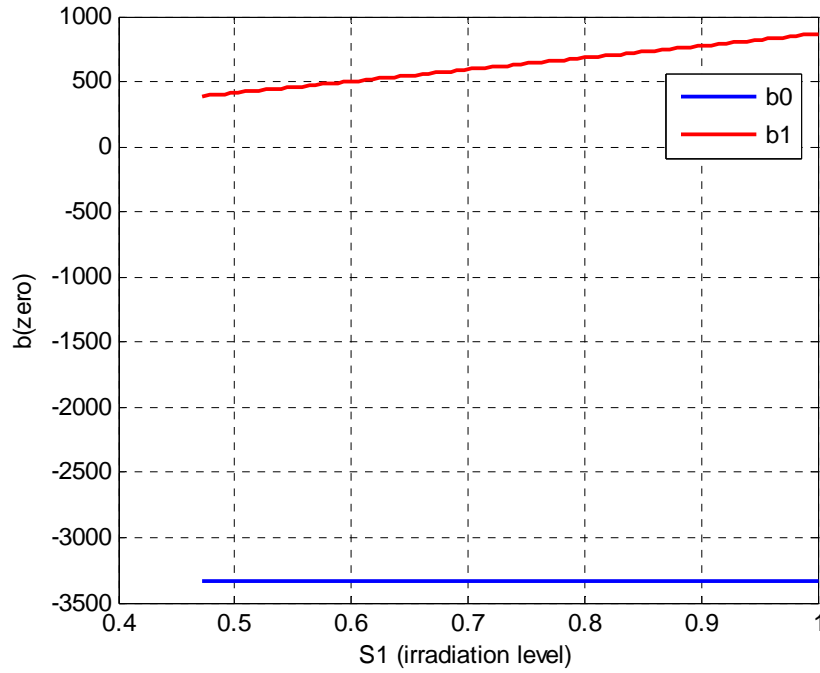


Figure 7.18 Two of the coefficients of the linearized PV zero dynamics characteristic

$$\begin{cases} b_1 = \frac{1}{\eta_{2o}^{(0)^2}} \left(a_{23} + a_{24} \eta_{1o}^{(0)^2} + a_{25} \eta_{1o}^{(0)} + a_{26} \eta_{3o}^{(0)} \right) \\ b_0 = - \left(a_{12} a_{22} + \frac{2a_{12} a_{24} \eta_{1o}^{(0)} + a_{12} a_{25}}{\eta_{2o}^{(0)}} \right) \end{cases} \quad (7.101)$$

The coefficients of (7.101) are presented in Appendix C. The Routh–Hurwitz criteria for the stability of this characteristic equation

$$\begin{cases} b_1 > 0 \\ b_0 > 0 \end{cases} \quad (7.102)$$

$$\begin{cases} \eta_{1o}^{(0)} = x_1 = I_{gqo} \\ \eta_{2o}^{(0)} = x_3 = V_{mqo} \\ \eta_{3o}^{(0)} = x_6 = V_{pvo} \end{cases} \quad (7.103)$$

Therefore besides one of the characteristic equation poles at origin ($S = 0$), second coefficient of Routh–Hurwitz criteria (b_0) in all operating region is negative. It means the PV system connected to the current source inverter is non-minimum phase in its all operation region.

7.6 Conclusions

This chapter investigated the controllability analysis of the wind turbine driven interior permanent magnet (IPM) generator interfaced to the grid using either an L or LCL filter. The stability regions of the operation based on maximum power point tracking of the wind turbine and loss minimization of the generator were shown. With the aid of two methods used for the extraction of the zero dynamics, it was shown that the generator fitted with the L filter has a stable zero dynamics, possesses a minimum phase characteristics which ensures that no structural limitation is imposed on the design of the controllers. When the generator is grid-interfaced using the LCL filter, the zero dynamics is unstable for all operating points, and in the small, the system is non-minimum phase. There is a structural constraint (such as limited current regulator bandwidth and response time) on any controller to be designed for the system. Also, the nonlinear controller design using the method of feedback state linearization cannot be applied to the control of the four specified variables of the IPM generator with LCL filter. Modest dynamic performance can however be achieved by using higher order controllers and/or high gain observers.

The controllability analysis for the IPM generator system suggests that the topological structure of the interface filter and the controlled variables have significant effects on the phase behavior of the system, the agility of any controller used, and hence the static and dynamic performance of the controlled generator system. This chapter provides an explanation as to why designing controllers for renewable energy systems with LCL interfaces with the grid has continued to be a challenge. Appropriate selection of controlled variables, states to be estimated using high gain observers and using high order controllers point the way for designing controllers that will deliver good static and dynamic performance.

CHAPTER 8

CONCLUSION AND FUTURE WORKS

8.1 Introduction

The previous works that have been done related to this area are detailed in chapter 1. The conclusions and contributions of this dissertation are summarized in this chapter. A short summary of each section is presented to discuss the proposed topics and approaches of this dissertation and the overall point of view is explained. Future works are also discussed.

8.2 Conclusions

State space modeling, stability analysis and dynamic behavior of a small Microgrid in both autonomous mode and grid connected mode are presented. The main objective of this investigation is to improve the control of Microgrid for both autonomous and grid conned modes. The droop control is applied to the maintain voltage and frequency. Frequency droops against output active power of converter while voltage magnitude droops against reactive power. The PI load voltage control and inner current control of the system are designed based on the dynamic equations in complex form. Along with considering both modes of operation, the locally available control parameters of each DG unit are used, so that communication among DG units is avoided in order to improve the system reliability and reduce the costs. The three phase PLL is designed and

added to each converter in order to measure instantaneous local frequency used for the qd-axis transformation. The system is simulated using MATLAB software to validate the design. The controllers share the power based on the related power for different sources with different rated power and different impedance connections to the network.

Instead of a constant DC source for the input of the inverter, in this dissertation a photovoltaic source with its nonlinear characteristic is used. The DG unit is connected to the main grid through the three phase inverter. The load voltage magnitude and frequency are adapted from the main grid. The DC link voltage is controlled for maximum power point operation of the PV. For unity power factor operation the second reference has been considered as output reactive power of the three phase inverter. With the change of irradiation level, DC link voltage and reactive power controllers follow their references precisely. Even during sudden change of the loads, the actual parameters of the system are still tracking their references well due to the fast response of the controllers. The DG unit is always operating in unity power factor and the modulation indices of the inverter even during transients are less than unity.

In autonomous operation of the microgrid, due to the limitation of the DG power for feeding the loads is included. A battery with a bidirectional DC-DC converter is added. Simulation results show that the battery discharges when total load is more than the maximum power of PV system. Under a lower irradiation level, the maximum power of PV system decreases, thus the battery discharges even under reduced load demand. When the inverter modulation index magnitude is reduced while keeping the load voltage constant, the input DC link voltage and the duty ratios of the two boost converters interfacing the sources are increased.

To verify the proposed controllers, the laboratory scale experiment is implemented in addition to the dynamic simulation of the system. The designed experimental system consists of a microgrid with two different sources, a nonlinear PV source and a battery source. A programmable DC source is used to emulate the nonlinear PV source characteristic. Three different power electronic converters, a unidirectional DC-DC boost converter, a bidirectional buck and boost converter and a three phase inverter are built. Each converter has its own controller signals coming from different control structures, drivers, sensor boards and digital signal processor (DSP) unit. The process of the design and test of each section are explained in detail. All the controllers, analog to digital conversions and PWM signal generation are implemented inside the ezDSPF28335. The maximum power point tracking of the PV source, active and reactive power control of the three phase inverter and charging and discharging control of the battery are applied. The experimental results are presented in both autonomous mode and grid connected mode after synchronization and connection of the system to the main network.

Along with the programmed PLL, the enhanced phase lock loop (EPLL) also is designed and the experimental results of both systems are compared. EPLL is used to define the reference frequency and angle of the load voltage. It is operated as a band pass filter for the other parameters such as the inverter and the grid currents. EPLL results have the lowest noise and therefore it tracks the magnitudes, angles and frequencies of the actual input signals more precisely.

Wind energy, as one of the most popular renewable sources in Microgrid, is also studied. In the interior permanent magnet structure, the equivalent air gap is not uniform and it makes the saliency effect obvious. In the IPM machine, both magnetic and reluctance torque can be produced. Compared to the surface mounted permanent magnet

(SPM) machine, the IPM machine has a mechanically robust and solid structure since the magnets are physically contained and protected. It contains both reluctance and magnetic torque which increases the efficiency and speed range operation. In this dissertation the dynamic model of interior permanent magnet machine as a wind turbine generator is studied. An AC-DC-AC converter connects the wind turbine to the main grid. The steady state operation regime of IPM generator in wind turbine application based on total loss minimization and maximum power point tracking of the wind turbine is presented. The proposed controllers in dynamic operation are designed to get maximum power from the wind, keep DC link voltage constant and guarantee unity power factor operation. At higher than rated wind speeds the reference of the active power and rotor speed are kept constant and pitch angle controlled to protect the wind turbine from over speed and over current phenomenon.

Finally, the controllability analysis of the wind turbine driven interior permanent magnet (IPM) generator interfaced to the grid using either an L or LCL filter is presented. The stability regions of its operation based on maximum power point tracking of the wind turbine and loss minimization of the generator are analyzed. With the aid of two methods used for the extraction of the zero dynamics, it is shown that the generator fitted with the L filter has a stable zero dynamics, possesses a minimum phase characteristics which ensures that no structural limitation is imposed on the design of the controllers. When the generator is grid-interfaced using the LCL filter, the zero dynamics is unstable for all operating points and the system is non-minimum phase. There are structural constraints (such as limited current regulator bandwidth and response time) on any controller to be designed for the system. Also, the nonlinear controller design using the method of

feedback state linearization cannot be applied to the control of the IPM generator with LCL filter. Modest dynamic performance can however be achieved by using higher order controllers and/or high gain observers.

8.3 Future Work

The concept of microgrid and renewable energies is relatively new compared to conventional power plants. In this dissertation, the two most popular renewable sources including photovoltaic (PV) and wind energy are studied. The structure of the PV system in both grid connected and autonomous operation are both simulated and verified experimentally. Some future work that can be done is to experimentally validate the proposed topologies for the interior permanent magnet machine based wind turbine.

The programmable source is used as a PV source. This system is not very accurate and due to the needed time for communication between the hardware DC source and the computer, it sometimes loses the tracking and behaves like a normal voltage source. Therefore the designed setup can be connected to a real PV solar cell array to test the maximum power point tracking.

The operation of a two DG unit system is investigated and the proposed controller for sharing the load can be applied to multi DG unit systems. Due to hardware limitations such as the number of the ports on the DSP, this work could not be extended. Almost ninety percent of the analog to digital conversion ports and pwm ports are used. So using a more powerful DSP or combination of FPGA and DSP can extend the system to a multi-DG unit with different types of sources.

Most electrical power systems are nonlinear and complex. The explained controllability analysis is a useful methodology that can be applied to other structures to study their characteristics and have an overall point of view about their responses without linearization which is what relates the analysis to the selected operation point. It will also help in the design process of the controllers.

REFERENCES

- [1] T. C. Green and M. Prodanovic', "Control of inverter-based microgrids," *Journal of Elect. Power Syst. Research*, vol. 77, no. 9, pp. 1204–1213, Jul. 2007.
- [2] J. M. Guerrero, J. C. Vasquez, J. Matas, M. Castilla and L.G.Vicuna, "Control Strategy for Flexible Microgrid Based on Parallel Line-Interactive UPS Systems" *IEEE Trans. on Industrial Electronics*, Vol. 56, Issue 3, pp. 726 – 736, March 2009.
- [3] F. Katiraei and M. R. Iravani, "Power Management Strategies for a Microgrid with Multiple Distributed Generation Units" *IEEE Trans. on Power Systems*, Vol. 21, Issue 4, pp. 1821 – 1831, Nov. 2006.
- [4] C. K. Sao and P. W. Lehn, "Control and Power Management of Converter Fed Microgrids" *IEEE Trans. on Power Systems*, Vol. 23, Issue 3, pp. 1088 – 1098, Aug. 2008.
- [5] J. C. Vasquez, J. M. Guerrero, A. Luna, P. Rodriguez and R.Teodorescu, "Adaptive Droop Control Applied to Voltage-Source Inverters Operating in Grid-Connected and Islanded Modes" *IEEE Trans. on Industrial Electronics*, Vol. 56, Issue 10, pp. 4088 – 4096, Oct. 2009.
- [6] M. C. Chandorkar, D. M. Divan, and R. Adapa, "Control of parallel connected inverters in standalone ac supply systems," *IEEE Trans. Ind. Appl.*, vol. 29, no. 1, pp. 136–143, Jan./Feb. 1993.
- [7] J. Holtz and K.-H. Werner, "Multi-inverter UPS system with redundant load sharing control," *IEEE Trans. Ind. Electron.*, vol. 37, no. 6, pp. 506–513, Dec. 1990.
- [8] J.-F. Chen and C.-L. Chu, "Combination voltage controlled and currentcontrolledPWMinverters for UPS parallel operation," *IEEE Trans. Power Electron.*, vol. 10, no. 5, pp. 547–558, Sep. 1995.
- [9] H. Van Der Broeck and U. Boeke, "A simple method for parallel operation of inverters," in *Proc. IEEE Telecommunications Energy Conference*, 1998, pp. 143–150.
- [10] T. Kawabata and S. Higashino, "Parallel operation of voltage source inverters," *IEEE Trans. Ind. Appl.*, vol. 24, no. 2, pp. 281–287, Mar./Apr. 1988.
- [11] H. Hanaoka, "Development of a novel parallel redundant UPS," in *Proc. IEEE Telecommunications Energy Conference*, 2003, pp. 493–498.
- [12] M. C. Chandorkar, D. M. Divan, Y. Hu, and B. Banerjee, "Novel architecture and control for distributed UPS systems," in *Proc. IEEE APEC*, 1994, pp. 683–689.

- [13] M. Arias, D. G. Lamar, M. Rodriguez, M. Hernando, and A. Fernandez, “Simple droop voltage control system for parallel operation of UPS,” in *Proc. IEEE APEC*, 2004, pp. 1946–1951.
- [14] W. Yao, M. Chen, J. Chen, and Z. Qian, “An improved multiple-loop controller for parallel operation of single-phase inverters with no control interconnections,” in *Proc. IEEE PESC*, 2007, pp. 448–452.
- [15] K. De Brabandere, B. Bolsens, J. Van den Keybus, A. Woyte, J. Driesen, and R. A. Belmans, “Voltage and frequency droop control method for parallel inverters,” *IEEE Trans. Power Electron.*, vol. 22, no. 4, pp. 1107–1115, Jul. 2007.
- [16] Y. W. Li and C. Kao, “An accurate power control strategy for power electronics interfaced distributed generation units operating in a low voltage multibus microgrid,” *IEEE Trans. Power Electron.*, vol. 24, no. 12, pp. 2977–2988, Dec. 2009.
- [17] L. Mihalache, “Paralleling control technique with no intercommunication signals for resonant controller-based inverters,” in *Conf. Rec. IEEE IAS Annu. Meeting*, 2003, vol. 3, pp. 1882–1889.
- [18] U. Borup, F. Blaabjerg, and P. N. Enjeti, “Sharing of nonlinear load in parallel-connected three-phase converters,” *IEEE Trans. Ind. Appl.*, vol. 37, no. 6, pp. 1817–1823, Nov./Dec. 2001.
- [19] S. J. Chiang and J. M. Chang, “Parallel control of the UPS inverters with frequency-dependent droop scheme,” in *Proc. IEEE PESC*, 2001, pp. 957–961.
- [20] K. Jaehong, J.M. Guerrero, P. Rodriguez, R. Teodorescu and N. Kwanghee, “Mode Adaptive Droop Control With Virtual Output Impedances for an Inverter-Based Flexible AC Microgrid,” *IEEE Trans. on Power Electronics*, vol.26, no.3, pp.689-701, March 2011.
- [21] C. Trujillo, F. Velasco, D. G. Garcera, E. Figueres and J.Guacaneme, “Reconfigurable control scheme for a PV microinverter working in both grid connected and island modes” *IEEE Trans. on Industrial Electronics*, 2012.
- [22] S. V. Iyer, M. N. Belur and M. C. Chandorkar, “Analysis and Mitigation of Voltage Offsets in Multi-inverter Microgrids” *IEEE Trans. on Energy Conversion*, Vol. 26, Issue 1, pp. 354 – 363, March 2011.

- [23] J. C. Vasquez, R. A. Mastromauro, J. M. Guerrero and M. Liserre, "Voltage Support Provided by a Droop-Controlled Multifunctional Inverter" *IEEE Trans. on Industrial Electronics*, Vol. 56, Issue 11, pp. 4510 – 4519, Nov. 2009.
- [24] C. Chen, Y. Wang, J. Lai, Y. Lee and D. Martin, "Design of Parallel Inverters for Smooth Mode Transfer Microgrid Applications" *IEEE Trans. on Power Electronics*, Vol. 25, Issue 1, pp. 6 – 15, Jan. 2010.
- [25] A. Tuladhar, H. Jin, T. Unger, and K. Mauch, "Control of parallel inverters in distributed ac power systems with consideration of the line impedance effect," in *Proc. APEC*, vol. 1, Feb. 1998, pp. 321–328.
- [26] C. K. Sao and P. W. Lehn, "Autonomous Load Sharing of Voltage Source Converters" *IEEE Trans. on Power Delivery*, Vol. 20, Issue 2, pp. 1009 – 1016, April 2005.
- [27] R. Majumder, B. Chaudhuri, A. Ghosh, R. Majumder, G. Ledwich and F. Zare, "Improvement of Stability and Load Sharing in an Autonomous Microgrid Using Supplementary Droop Control Loop" *IEEE Trans. on Power Systems*, Vol. 25, Issue 2, pp. 796 – 808, May 2010.
- [28] R. Majumder, A. Ghosh, G. Ledwich and F.Zare, "Power Management and Power Flow Control with Back-to-Back Converters in a Utility Connected Microgrid" *IEEE Trans. on Power Systems*, Vol. 25, Issue 2, pp. 821 – 834, May 2010.
- [29] R. Majumder, A. Ghosh, G. Ledwich and F.Zare, "Angle Droop versus Frequency Droop in a Voltage Source Converter Based Autonomous Microgrid" *In Proc. of Power & Energy Society General Meeting*, pp.1 – 8, 2009.
- [30] J. M. Guerrero, L. G. Vicuna, J. Matas, M. Castilla, and J. Miret, "Output impedance design of parallel-connected UPS inverters with wireless load-sharing control," *IEEE Trans. Ind. Electron.*, vol. 52, pp. 1126–1135, Aug. 2005.
- [31] J. M. Guerrero, J. Matas, L. G. Vicuna, M. Castilla, and J. Miret, "Decentralized control for parallel operation of distributed generation inverters using resistive output impedance," *IEEE Trans. Ind. Electron.*, vol. 54, pp. 994–1004, Apr. 2007.
- [32] F. Blaabjerg, Z. Chen, and S. B. Kjaer, "Power electronics as efficient interface in dispersed power generation systems," *IEEE Trans. Power Electron.*, vol. 19, pp. 1184–1194, Sep. 2004.

- [33] R. Majumder, A. Ghosh, G. Ledwich and F. Zare, "Load sharing and power quality enhanced operation of a distributed microgrid," *IET Renewable Power Generation.*, vol. 3, no. 2, pp. 109–119, June 2009.
- [34] A. Engler, "Applicability of droops in low voltage grids," *DER Journal*, vol. 1, pp. 1-5, Jan. 2005.
- [35] J. M. Guerrero, L. G. Vicuna, J. Matas, M. Castilla, and J. Miret, "A wireless controller to enhance dynamic performance of parallel inverters in distributed generation systems," *IEEE Trans. Power. Electron.*, vol. 19, no. 5, pp. 1205–1213, Sep. 2004.
- [36] Y. Li and Y. W. Li, "Power Management of Inverter Interfaced Autonomous Microgrid Based on Virtual Frequency-Voltage Frame" *IEEE Trans. on Smart Grid*, Vol. 2, Issue 1, pp.30 – 40, March 2011.
- [37] Y. Li and Y. W. Li, "Decoupled power control for an inverter based low voltage microgrid in autonomous operation," in *Proc. IEEE IPEMC*, 2009, pp. 2490–2496.
- [38] D. De and V. Ramanarayanan, "Decentralized Parallel Operation of Inverters Sharing Unbalanced and Non-linear Loads" *IEEE Trans. on Power Electronics*, Vol. 25, Issue 12, pp. 3015 – 3025, Dec. 2010.
- [39] E. Rokrok and M. E. H. Golshan, "Adaptive voltage droop scheme for voltage source converters in an islanded multibus microgrid" *IET Generation, Transmission & Distribution*, Vol. 4, Issue 5, pp. 562 – 578, March 2010.
- [40] S. Yang, Q. Lei, F. Z. Peng and Z. Qian, "A Robust Control Scheme for Grid-Connected Voltage-Source Inverters" *IEEE Trans. on Industrial Electronics*, Vol. 58, Issue 1, pp. 202 – 212, Jan. 2011
- [41] M. Vidyasagar, "Optimal rejection of persistent bounded disturbances," *IEEE Trans. Autom. Control*, vol. AC-31, no. 6, pp. 527–534, Jun. 1986.
- [42] W. M. Haddad and V. Chellaboina, "Mixed-norm H₂/L₁ controller synthesis via fixed-order dynamic compensation: A Riccati equation approach," in *Proc. 36th Conf. Decision Control*, Dec. 1997, pp. 452–457.
- [43] V. S. Chellaboina, W. M. Haddad, and J. H. Oh, "Fixed-order dynamic compensation for linear systems with actuator amplitude and rate saturation constraints," *International Journal of Control*, vol. 73, no. 12, pp. 1087–1103, Aug. 2000.

- [44] I. Y. Chung, W. Liu, D. A. Cartes, E. G. Collins and S. Moon, “Control Methods of Inverter-Interfaced Distributed Generators in a Microgrid System” *IEEE Trans. on Industry Applications*, Vol. 46, Issue 3, pp. 1078 – 1088, May 2010.
- [45] R. C. Dugan, M. F. McGranaghan, and H. W. Beaty, *Electrical Power Systems Quality*. New York: McGraw-Hill, 2002.
- [46] Y. W. Li, D. M. Vilathgamuwa and P. C. Loh, “Robust Control Scheme for a Microgrid With PFC Capacitor Connected” *IEEE Trans. on Industry Applications*, Vol. 43, Issue 5, pp. 1172 – 1182, Sept. 2007.
- [47] M. A. Hassan and M. A. Abido, “Optimal Design of Microgrids in Autonomous and Grid-Connected Modes Using Particle Swarm Optimization” *IEEE Trans. on Power Electronics*, Vol. 26, Issue 3, pp. 755 – 769, March 2011.
- [48] N. Pogaku, M. Prodanovic and T. C. Green, “Modeling, Analysis and Testing of Autonomous Operation of an Inverter-Based Microgrid” *IEEE Trans. on Power Electronics*, Vol. 22, Issue 2, pp. 613 – 625, March 2007.
- [49] E. Barklund, N. Pogaku, M. Prodanovic, C. Aramburo, and T. Green, “Energy management in autonomous microgrid using stability-constrained droop control of inverters,” *IEEE Trans. Power Electron.*, vol. 23, no. 5, pp. 2346–2352, Sep. 2008.
- [50] Y. Mohamed and E. Saadany, “Adaptive decentralized droop controller to preserve power sharing stability of paralleled inverters in distributed generation microgrids,” *IEEE Trans. Power Electron.*, vol. 23, no. 6, pp. 2806–2816, Nov. 2008.
- [51] S.V. Iyer, M. N. Belur and M. C. Chandorkar, “A Generalized Computational Method to Determine Stability of a Multi-inverter Microgrid” *IEEE Trans. on Power Electronics*, Vol. 25, Issue 9, pp. 2420 – 2432, Sept. 2010.
- [52] M. Z. Kamh and R.Iravani, “Unbalanced Model and Power-Flow Analysis of Microgrids and Active Distribution Systems” *IEEE Trans. on Power Delivery*, Vol. 25, Issue 4, pp.2851 – 2858, Oct. 2010.
- [53] M. Illindala and G. Venkataramanan, “Control of distributed generation systems to mitigate load and line imbalances,” in *Proc. 33rd Annu. IEEE PESC*, 2002, pp. 2013–2018.
- [54] P. Hsu and M. Behnke, “A three-phase synchronous frame controller for unbalanced load,” in *Proc. 29th Annu. IEEE PESC*, 1998, pp. 1369–1374.

- [55] Y. Li, D. M. Vilathgamuwa, and L. P. Chiang, "Microgrid power quality enhancement using a three-phase four-wire grid-interfacing compensator," *IEEE Trans. Ind. Appl.*, vol. 41, no. 6, pp. 1707–1719, Nov./Dec. 2005.
- [56] H. S. Song and K. H. Nam, "Dual current control scheme for PWM converter under unbalanced input voltage conditions," *IEEE Trans. Ind. Electron.*, vol. 46, no. 5, pp. 953–959, Oct. 1999.
- [57] W. C. Lee, T. K. Lee, and D. S. Hyun, "A three-phase parallel active power filter operating with PCC voltage compensation with consideration for an unbalanced load," *IEEE Trans. Power Electron.*, vol. 17, no. 5, pp. 807–814, Sep. 2002.
- [58] Y. Li, D. M. Vilathgamuwa, and P. C. Loh, "A grid-interfacing power quality compensator for three-phase three-wire Microgrid applications," *IEEE Trans. Power Electron.*, vol. 21, no. 4, pp. 1021–1031, Jul. 2006.
- [59] M. Hojo, Y. Iwase, T. Funabashi, and Y. Ueda, "A method of three phase balancing in microgrid by photovoltaic generation systems," in *Proc. Power Electron. and Motion Cont. Conf. (EPE-PEMC)*, pp. 2487–2491, Sept. 2008.
- [60] P. T. Cheng, C. Chen, T. L. Lee, and S. Y. Kuo, "A cooperative imbalance compensation method for distributed-generation interface converters," *IEEE Trans. Ind. Appl.*, vol. 45, no. 2, pp. 805–815, Mar./Apr. 2009.
- [61] S. A. O. Da Silva, P. F. D. Garcia, P. C. Cortizo, and P. F. Seixas, "A three-phase line-interactive UPS system implementation with seriesparallel active power-line conditioning capabilities," *IEEE Trans. Ind. Appl.*, vol. 38, no. 6, pp. 1581–1590, Nov./Dec. 2002.
- [62] P. Pillay, and M. Manyage, "Definitions of voltage unbalance," *IEEE Power Eng. Review*, vol. 21, no. 5, pp. 49–51, May. 2001.
- [63] E. Barklund, N. Pogaku, M. Prodanovic', C. H. Aramburo, and T. C. Green, "Energy management in autonomous microgrid using stability-constrained droop control of inverters," *IEEE Trans. Power Electron.*, vol. 23, no. 5, pp. 2346–2352, Sept. 2008.
- [64] J. M. Guerrero, J. C. Vasquez, J. Matas, L. G. de Vicuña, and M. Castilla, "Hierarchical control of droop-controlled AC and DC microgrids—a general approach toward standardization," *IEEE Trans. Ind. Electron.*, vol. 58, no. 1, pp. 158–172, Jan. 2011.

- [65] M. Savaghebi, A. Jalilian, J. C. Vasquez and J. M. Guerrero, "Secondary Control Scheme for Voltage Unbalance Compensation in an Islanded Droop-Controlled Microgrid" *IEEE Trans. on Smart Grid*, , pp. 1 – 11, 2012.
- [66] M. Savaghebi, A. Jalilian, J. Vasquez and J. Guerrero, "Autonomous Voltage Unbalance Compensation in an Islanded Droop-Controlled Microgrid" *IEEE Trans. on Industrial Electronics*, 2012.
- [67] A. Mehrizi-Sani and R. Iravani, "Potential-Function Based Control of a Microgrid in Islanded and Grid-Connected Modes" *IEEE Trans. on Power Systems*, Vol. 25, Issue 4, pp.1883 – 1891, Nov. 2010.
- [68] I. J. Balaguer, U. Supatti,; L. Qin, C. Nam-Sup and F. Z. Peng, "Intelligent control for intentional islanding operation of microgrids" *In Proc. of Sustainable Energy Technologies Conference*, Vol. 24, Issue 1, pp. 898 – 903, 2008.
- [69] I. J. Balaguer, U. Supatti,; L. Qin, C. Nam-Sup and F. Z. Peng, "Control for Grid-Connected and Intentional Islanding Operations of Distributed Power Generation" *IEEE Trans. on Industrial Electronics*, Vol. 58, Issue 1, pp.147 – 157, Jan. 2011.
- [70] X. Q. Guo and W.Y. Wu, "Improved current regulation of three-phase grid-connected voltage-source inverters for distributed generation systems" *IET Renewable Power Generation*, Vol. 4, Issue 2, pp.101 – 115, 2010.
- [71] Z. Lidong, L. Harnefors and H. P. Nee, "Power-Synchronization Control of Grid-Connected Voltage-Source Converters" *IEEE Trans. on Power Systems*, Vol. 25, Issue 2, pp. 809 – 820, May 2010.
- [72] Z. Lidong, L. Harnefors and H. P. Nee, "Interconnection of Two Very Weak AC Systems by VSC-HVDC Links Using Power-Synchronization Control" *IEEE Trans. on Power Systems*, Vol. 26, Issue 1, pp. 344 – 355, Feb. 2011.
- [73] M. Popov, H. Karimi, H. Nikkhajoei and V. Terzija, "Dynamic Model and Control of a Microgrid with Passive Loads" *International Conference on Power Systems Transients*, June 2009.
- [74] H. Karimi, H. Nikkhajoei, R. Iravani, "Control of an Electronically-Coupled Distributed Resource Unit Subsequent to an Islanding Event" *IEEE Trans. on Power Delivery*, Vol. 23, Issue 1, pp. 493 - 501, Jan. 2008.

- [75] Q. Lei, S. Yang and F. Z. Peng, “Multi-loop control algorithms for seamless transition of grid-connected inverter” *In Proc. of Applied Power Electronics Conference and Exposition*, pp. 844 – 848, 2010.
- [76] O. Wasynczuk, “Dynamic behavior of a class of photovoltaic power systems,” *IEEE Trans. Power App. Syst.*, vol. PAS-102, no. 9, pp. 3031–3037, Sep. 1983.
- [77] N. Femia, G. Petrone, G. Spagnuolo, and M. Vitelli, “A technique for improving P&O MPPT performances of double-stage grid-connected photovoltaic systems,” *IEEE Trans. Ind. Electron.*, vol. 56, no. 11, pp. 4473–4482, Nov. 2009.
- [78] R. Alonso, P. Ibáñez, V. Martínez, E. Román, and A. Sanz, “An innovative perturb, observe and check algorithm for partially shaded PV systems,” *In proc. Power Electronics and Applications Conf.*, Spain, 2009, pp. 1-8.
- [79] W. T. Chee, T. C. Green, and A. H.-A. Carlos, “Analysis of perturb and observe maximum power point tracking algorithm for photovoltaic applications,” *In Proc. Power and Energy Conf.*, Malaysia, 2008, pp. 237-242.
- [80] C. W. Tan, T. C. Green, and C. A. Hernandez-Aramburo, “A current mode controlled maximum power point tracking converter for building integrated photovoltaics,” *In Proc. Power Electronics and Applications Conf.*, Denmark, 2007, pp. 1-10.
- [81] A. Pandey, N. Dasgupta, and A. K. Mukerjee, “High-performance algorithms for drift avoidance and fast tracking in solar MPPT system,” *IEEE Trans. Energy Convers.*, vol. 23, no. 2, pp. 681–689, Jun. 2008.
- [82] E. Koutroulis, K. Kalaitzakis, and N. C. Voulgaris, “Development of a microcontroller-based, photovoltaic maximum power point tracking control system,” *IEEE Trans. Power Electron.*, vol. 16, no. 1, pp. 46–54, Jan. 2001.
- [83] M. A. Elgendy, B. Zahawi and D. J. Atkinson, “Assessment of Perturb and Observe MPPT Algorithm Implementation Techniques for PV Pumping Applications” *IEEE Trans. on Sustainable Energy*, Vol. 3, Issue 1, pp. 21 – 33, Jan. 2012.
- [84] A. K. Abdelsalam, A. M. Massoud, S. Ahmed and P. N. Enjeti, “High-Performance Adaptive Perturb and Observe MPPT Technique for Photovoltaic-Based Microgrids” *IEEE Trans. on Power Electronics*, Vol. 26, Issue 4, pp. 1010 – 1021, April 2011.

- [85] N. Femia, G. Petrone, G. Spagnuolo and M. Vitelli, "Optimization of Perturb and Observe Maximum Power Point Tracking Method" *IEEE Trans. on Power Electronics*, Vol. 20, Issue 4, pp. 963 – 973, July 2005.
- [86] E. Koutroulis and F. Blaabjerg, "A New Technique for Tracking the Global Maximum Power Point of PV Arrays Operating Under Partial-Shading Conditions" *IEEE Journal of Photovoltaics*, Vol. 2, Issue 2, pp. 184 – 190, 2012.
<http://ieeexplore.ieee.org/xpl/RecentIssue.jsp?punumber=5503869>
- [87] G. Adinolfi, N. Femia, G. Petrone, G. Spagnuolo and M. Vitelli, "Design of dc/dc Converters for DMPPT PV Applications Based on the Concept of Energetic Efficiency" *Journal of Solar Energy Engineering*, Vol. 132, pp.1 – 10, May 2010.
- [88] G. Petrone, G. Spagnuolo, R. Teodorescu, M. Veerachary and M. Vitelli, "Reliability Issues in Photovoltaic Power Processing Systems" *IEEE Trans. on Industrial Electronics*, Vol. 55, Issue 7, pp. 2569 – 2580, July 2008.
- [89] S. B. Kjaer, J. K. Pedersen, and F. Blaabjerg, "A review of single-phase grid-connected inverters for photovoltaic modules," *IEEE Trans. Ind. Appl.*, vol. 41, no. 5, pp. 1292–1306, Sep./Oct. 2005.
- [90] Q. Li and P. Wolfs, "A review of the single phase photovoltaic module integrated converter topologies with three different DC link configurations," *IEEE Trans. Power Electron.*, vol. 23, no. 3, pp. 1320–1333, May 2008.
- [91] E. Ozdemir and F. Kavaslar, "A new multifunctional power converter for grid connected residential photovoltaic applications," *In Proc. IEEE Energy Conversion Congress and Exposition*, Sep. 2009, pp. 2650–2656.
- [92] L. Ma, K. Sun, R. Teodorescu, J. M. Guerrero, and X. Jin, "An integrated multifunction DC/DC converter for PV generation systems," *In Proc. IEEE Int. Symp. Industrial Electronics*, 2010, pp. 2205–2210.
- [93] Y. Gurkaynak and A. Khaligh, "Control and power management of a grid connected residential photovoltaic system with plug-in hybrid electric vehicle (PHEV) load," *In Proc. IEEE Appl. Power Electron. Conf.*, 2009, pp. 2086–2091.
- [94] G. M. Tina and F. Pappalardo, "Grid-connected photovoltaic system with battery storage system into market perspective," *In Proc. IEEE Power and Energy Society/Industry Application Society Conf.*, Sep. 2009, pp. 1–7.

- [95] T. Shimada, Y. Ueda, and K. Kurokawa, "Look-ahead equalizing charge planning for grid-connected photovoltaic systems with battery storages," *In Proc. IEEE Photovoltaic Spec. Conf.*, 2008, pp. 1–3.
- [96] F. Giraud and Z. M. Salameh, "Steady-state performance of a grid connected rooftop hybrid wind–photovoltaic power system with battery storage," *IEEE Trans. Energy Conversion*, vol. 16, no. 1, pp. 1–7, Mar. 2001.
- [97] R. Carbone, "Grid-connected photovoltaic systems with energy storage," in *Proc. Int. Conf. Clean Electrical Power*, Jun. 2009, pp. 760–767.
- [98] H. Valderrama-Blavi, J. M. Bosque-Moncusí, L. Marroyo, F. Guinjoan, J. A. Barrado, and L. Martínez-Salamero, "Adapting a low voltage PEM fuel-cell to domestic grid-connected PV system," in *Proc. IEEE Ind. Electron. Ann. Conf. Soc.*, 2009, pp. 160–165.
- [99] Z. Jiang and R. A. Dougal, "Hierarchical microgrid paradigm for integration of distributed energy resources," in *Proc. IEEE Power Energy Soc. Gen. Meeting*, Jul. 2008, pp. 1–8.
- [100] M. E. Glavin, P. K. W. Chan, and W. G. Hurley, "Optimization of autonomous hybrid energy storage system for photovoltaic applications," in *Proc. IEEE Energy Conversion Congress and Exposition*, 2009, pp. 1417–1424.
- [101] H. Nakayama, E. Hiraki, T. Tanaka, N. Koda, N. Takahashi, and S. Noda, "Stand-alone photovoltaic generation system with combined storage system using EDLC," in *Proc. IEEE Ind. Electron. Ann. Conf. Soc.*, 2009, pp. 883–888.
- [102] S. Yang, Q. Lei, Z. Peng and Z. Qian, "A Robust Control Scheme for Grid-Connected Voltage Source Inverters," *IEEE Trans. Industrial Electronics*, Issue. 99, 2010.
- [103] H. Karimi, H. Nikkhajoei and R. Iravani, "Control of an Electronically-Coupled Distributed Resource Unit Subsequent to an Islanding Event," *IEEE Trans. Power Delivery*, vol. 23, no. 1, pp. 493-501, Jan. 2008.
- [104] R. Majumder, B. Chaudhuri, A. Ghosh, G. Ledwich and F. Zare, "Improvement of Stability and Load Sharing in an Autonomous Microgrid Using Supplementary Droop Control Loop," *IEEE Trans. Power Systems*, vol. 25, no. 2, pp. 796-808, May. 2010.
- [105] J. A. P. Lopes, C. L. Moreira and A. G. Madureira, "Defining control strategies for MicroGrids islanded operation," *IEEE Trans. Industrial Electronics*, vol. 21, no. 2, pp. 916-924, May 2006.

- [106] N. Pogaku, M. Prodanovic and T. C.Green, "Modeling, Analysis and Testing of Autonomous Operation of an Inverter-Based Microgrid," *IEEE Trans. Power Electronics*, vol. 22, no. 2, pp. 613-625, March 2007.
- [107] Y. W. Li and C. Kao, "An Accurate Power Control Strategy for Power-Electronics-Interfaced Distributed Generation Units Operating in a Low-Voltage Multibus Microgrid," *IEEE Trans. Power Electronics*, vol. 24, no. 12, pp. 2977-2988, Dec. 2009.
- [108] C. K. Sao and P. W. Lehn, "Control and Power Management of Converter Fed Microgrids," *IEEE Trans. Power Systems*, vol. 24, no. 12, pp. 2977-2988, Dec. 2009.
- [109] S. V. Iyer, M. N. Belur and M. C. Chandorkar, "A Generalized Computational Method to Determine Stability of a Multi Inverter Microgrid," *IEEE Trans. Power Electronics*, Issue. 99, 2010.
- [110] A. Dhooge, W. Govaerts, Y. A. Kuznetsov, W. Maestrom, and B. Sautois, "MATCONT and CL MATCONT Continuation Toolboxes in MATLAB," Gent University and Utrecht University, 2006.
- [111] J. A. P. Lopes, C. L. Moreira and A. G. Madureira, "Defining control strategies for Micro-Grids islanded operation," *IEEE Trans. Industrial Electronics*, vol. 21, no. 2, pp. 916-924, May 2006.
- [112] H. Karimi, H. Nikkhajoei and R. Iravani, "Control of an Electronically-Coupled Distributed Resource Unit Subsequent to an Islanding Event," *IEEE Trans. Power Delivery*, Vol. 23 , Issue 1, pp. 493 - 501, Jan. 2008
- [113] A. Yazdani and P.P. Dash, "A Control Methodology and Characterization of Dynamics for a Photovoltaic (PV) System Interfaced With a Distribution Network," *IEEE Trans. Power Delivery*, Vol. 24, Issue 3, pp. 1538-1551, July 2009
- [114] D.P. Hohm, and M.E. Ropp. "Comparative study of maximum power point tracking algorithms using an experimental, programmable, maximum power point tracking test bed," *Photovoltaic Specialists Conference*, Sept. 2000, pp. 1699-1702.
- [115] F. Liu, Y. Kang, Y. Zhang, and S. Duan., "Comparison of P&O and hill climbing MPPT methods for grid-connected PV converter," *Trans. IEEE Industrial Electronics and Applications*, 2008, pp. 804-807.

- [116] K. Kobravi, W. Kinsner and S. Filizadeh, "Analysis of Bifurcation and Stability in a Simple Power System Using MATCONT," In Proc. of IEEE Canadian Conference on Electrical and Computer Engineering (CCECE), pp. 1150-1154, 2007.
- [117] O. Ojo, "The Generalized Discontinuous PWM Scheme for Three-Phase Voltage Source Inverters" *IEEE Trans. on Industrial Electronics*, Vol. 51, Issue 6, pp. 1280 – 1289, Dec. 2004.
- [118] M. Karimi-Ghartemani and M. Reza Iravani, "A Method for Synchronization of Power Electronic Converters in Polluted and Variable-Frequency Environments" *IEEE Transactions on Power Systems*, Vol. 19, No 1, pp. 1263-1270, 2004.
- [119] R. H. Moncada, R. A. Rodriguez, J. A. Tapia and T. M.Jahns, "Axial flux permanent-magnet machine under optimum control strategy for wind power generation" In Proc. of the IEEE International Electric Machines and Drives Conference (IEMDC), pp. 1065-1071, 2009.
- [120] R. H. Moncada, J. A. Tapia and T. M.Jahns, "Inverse-saliency PM motor performance under vector control operation" In Proc. of Energy Conversion Congress and Exposition (ECCE), pp. 2368-2373, 2009.
- [121] Q. Wei, Qu Liyan and R.G. Harley, "Control of IPM Synchronous Generator for Maximum Wind Power Generation Considering Magnetic Saturation" *IEEE Trans. on Industry Applications*, Vol. 45, Issue 3, pp. 1095-1105, 2009.
- [122] M. Chinchilla, S. Arnaltes and J.C. Burgos, "Control of permanent-magnet generators applied to variable-speed wind-energy systems connected to the grid" *IEEE Trans. on Energy Conversion*, Vol. 21, Issue 1, pp. 130-135, 2006.
- [123] A. Abedini, "Interaction of Permanent Magnet Synchronous Generator Wind Turbine into Power Grid," PhD dissertation, University of Wisconsin-Milwaukee, USA, 2008.
- [124] V. Agarwal, R.K. Aggarw, P. Patidar and C. Patki, "A Novel Scheme for Rapid Tracking of Maximum Power Point in Wind Energy Generation Systems" *IEEE Trans. on Energy Conversion*, Vol. 25, Issue 1, pp. 228-236, 2010.
- [125] O. Ojo, F. Osaloni, Wu Zhiqiao and M.Omoigui, "A control strategy for optimum efficiency operation of high performance interior permanent magnet motor drives" on Proc. Of IEEE Industry Applications Conference, Vol. 45, pp. 604-610, 2003.

- [126] A. Yazdani and R. Iravani, "A neutral-point clamped converter system for direct-drive variable-speed wind power unit" *IEEE Trans. on Energy Conversion*, Vol. 21 , Issue 2, pp. 596-607, 2006.
- [127] U. K. Madawala, T. Geyer, J. B. Bradshaw and D. M. Vilathgamuwa, "Modeling and Analysis of a Novel Variable-Speed Cage Induction Generator," *IEEE Trans. on Industrial Electronics*, vol. 59, no. 2, pp. 1020–1028, Feb. 2012.
- [128] V. Delli Colli, F. Marignetti and C. Attaianesi, "Analytical and Multiphysics Approach to the Optimal Design of a 10-MW DFIG for Direct-Drive Wind Turbines," *IEEE Trans. on Industrial Electronics*, vol. 59, no. 7, pp. 2791–2799, July 2012.
- [129] J. Sopenan, V. Ruuskanen, J. Nerg and J. Pyrhonen, "Dynamic Torque Analysis of a Wind Turbine Drive Train Including a Direct-Driven Permanent-Magnet Generator," *IEEE Trans. on Industrial Electronics*, vol. 58, no. 9, pp. 3859–3867, Sep. 2011.
- [130] M. Liserre, F. Blaabjerg, and S. Hansen, "Design and Control of an LCL-filter- Based Three-Phase Active Rectifier," *IEEE Trans. on Industry Applications*, vol. 41, no. 5, pp. 1281–1291, Sep./Oct. 2005.
- [131] M. Malinowski, S. Stynski, W. Kolomyjski, and M. P. Kazmierkowski, "Control of Three-Level PWM Converter Applied to Variable-Speed-Type Turbines," *IEEE Trans. on Industrial Electronics*, vol. 56, no. 1, pp. 69–77, Jan. 2009.
- [132] I. J. Gabe, V. F. Montagner, and H. Pinheiro, "Design and Implementation of a Robust Current Controller for VSI Connected to the Grid through an LCL-filter," *IEEE Trans. on Power Electronics*, vol. 24, no. 6, pp. 1444–1452, Jun. 2009.
- [133] S. Skogestad and I. Postlethwaite, **Multivariable Feedback Control**, John Wiley and Sons, September 2008.
- [134] Z. Yuan, N. Zhang, B. Chen, J. Zhao, "Systematic Controllability Analysis for Chemical Processes," *AIChE Journal*, pp. 1-14, Jan. 2012.
- [135] Z. Yuan, B. Chen and J. Zhao, "An Overview on Controllability Analysis of Chemical Processes," *AIChE Journal*, vol. 57, no. 5, pp. 1185-1201, May 2011.
- [136] Z. Yuan, B. Chen and J. Zhao, "Phase Behavior Analysis for Industrial Polymerization Reactors," *AIChE Journal*, vol. 57, no. 10, pp. 2795-2807, Oct 2011.
- [137] C. Panjapornpon, **Model-Based Controller Design for General Nonlinear Processes**, Ph.D Dissertation, Drexel University, USA, 2005.

- [138] M. Sh. Nazrulla, **Control of Non-Minimum Phase Systems Using Extended High-Gain Observers**, Ph.D Dissertation, Michigan State University, USA, 2010.
- [139] A. Kuhlmann¹ and I. D. L. Bogle, "Design of Nonminimum Phase Processes for Optimal Switchability," *Journal of Chemical Engineering and Processing*, vol. 43, pp. 655-662, March 2003.
- [140] J. Slotine and W. Li, **Applied Nonlinear Control**. New Jersey: Prentice Hall, 1991.
- [141] A. Isidor, **Nonlinear Control Systems**, 3rd ed. New York: Springer-Verlag, 1995.
- [142] J. P. da Costa, H. Pinheiro, T. Degner and G. Arnold, "Robust Controller for DFIGs of Grid-Connected Wind Turbines," *IEEE Trans. on Industrial Electronics*, vol. 58, no. 9, pp. 4023–4038, Sep. 2011.
- [143] M. A. Parker, N. Chong and Li Ran, "Fault-Tolerant Control for a Modular Generator–Converter Scheme for Direct-Drive Wind Turbines," *IEEE Trans. on Industrial Electronics*, vol. 58, no. 1, pp. 305–315, Jan. 2011.
- [144] H. Geng, D. Xu, B. Wu and G. Yang, "Active Damping for PMSG-Based WECS With DC-Link Current Estimation," *IEEE Trans. on Industrial Electronics*, vol. 58, no. 4, pp. 1110–1119, April 2011.
- [145] J A. A. Rockhill, M. Liserre, R. Teodorescu and P. Rodriguez, "Grid-Filter Design for a Multimegawatt Medium-Voltage Voltage-Source Inverter," *IEEE Trans. on Industrial Electronics*, vol. 58, no. 4, pp. 1205–1217, April. 2011.

APPENDIX

APPENDIX A

COEFFICIENTS OF THE CHARACTERISTIC EQUATION OF THE IPM

GENERATOR CONNECTED TO THE GRID

$$a_6=1$$

$$a_5 = \frac{(L_{sd} \cdot L_s^2 \cdot J \cdot C_{dc} \cdot R_s + 2 \cdot L_{sd} \cdot L_s \cdot R_s^2 \cdot J \cdot C_{dc} \cdot L_{sq} + R_s \cdot L_s^2 \cdot J \cdot C_{dc} \cdot L_{sq}) / L_{sq} / L_s}{L_s^2 / C_{dc} / J}$$

$$a_4 = \frac{(R_s^2 \cdot L_s^2 \cdot J \cdot C_{dc} + 3/8 \cdot L_{sd} \cdot M_q^2 \cdot L_{sq} \cdot J \cdot L_s + 3/4 \cdot L_{sd}^2 \cdot L_s^2 \cdot I_{sd} \cdot C_{dc} \cdot \text{pole}^2 \cdot \text{Lamdam} - 3/8 \cdot I_{sq}^2 \cdot \text{pole}^2 \cdot L_{sd} \cdot L_s^2 \cdot L_{sq}^2 \cdot C_{dc} - 3/8 \cdot I_{sd} \cdot L_{sd} \cdot \text{Lamdam} \cdot L_s^2 \cdot C_{dc} \cdot \text{pole}^2 \cdot L_{sq} + 3/8 \cdot M_{d1}^2 \cdot L_{sq} \cdot L_s^2 \cdot J + 3/8 \cdot L_{sd} \cdot L_s^2 \cdot M_{d2}^2 \cdot J \cdot L_{sq} + 2 \cdot R_s \cdot L_s \cdot R_s^2 \cdot J \cdot C_{dc} \cdot L_{sq} + 3/8 \cdot M_{q1}^2 \cdot L_{sd} \cdot L_s^2 \cdot J + 3/8 \cdot I_{sq}^2 \cdot \text{pole}^2 \cdot L_{sq}^3 \cdot L_s^2 \cdot C_{dc} + 2 \cdot L_{sd} \cdot L_s \cdot R_s^2 \cdot J \cdot C_{dc} \cdot R_s + L_{sd} \cdot \omega_e^2 \cdot L_s^2 \cdot J \cdot C_{dc} \cdot L_{sq} + 3/8 \cdot L_{sd}^3 \cdot L_s^2 \cdot I_{sd}^2 \cdot C_{dc} \cdot \text{pole}^2 - 3/8 \cdot I_{sd}^2 \cdot L_{sd}^2 \cdot L_s^2 \cdot C_{dc} \cdot \text{pole}^2 \cdot L_{sq} + \omega_r^2 \cdot L_{sd} \cdot L_s^2 \cdot J \cdot C_{dc} \cdot L_{sq} + 3/8 \cdot L_{sd} \cdot L_s^2 \cdot \text{Lamdam}^2 \cdot C_{dc} \cdot \text{pole}^2 + L_{sd} \cdot R_s^2 \cdot J \cdot C_{dc} \cdot L_{sq}) / L_{sq} / L_{sd} / L_s^2 / C_{dc} / J}$$

$$a_3 = \frac{(3/8 \cdot M_{d1}^2 \cdot J \cdot L_s^2 \cdot R_s + 3/8 \cdot M_{d1} \cdot L_{sq} \cdot \omega_r \cdot J \cdot M_{q1} \cdot L_s^2 + 3/8 \cdot I_{sd}^2 \cdot L_{sd}^2 \cdot L_s^2 \cdot C_{dc} \cdot \text{pole}^2 \cdot R_s - 3/8 \cdot M_{d1} \cdot \omega_r \cdot L_{sd} \cdot J \cdot M_{q1} \cdot L_s^2 + 3/4 \cdot I_{sd} \cdot I_{sq} \cdot L_{sq} \cdot \omega_r \cdot L_{sd}^2 \cdot L_s^2 \cdot C_{dc} \cdot \text{pole}^2 + 3/8 \cdot J \cdot M_{q1}^2 \cdot L_s^2 \cdot R_s + 3/8 \cdot \text{Lamdam}^2 \cdot L_s^2 \cdot C_{dc} \cdot \text{pole}^2 \cdot R_s -$$

$$\begin{aligned}
& 3/8 * \text{Isd} * \text{Lsq} * \text{Lamd} * \text{Ls}^2 * \text{Cdc} * \text{pole}^2 * \text{Rs} - \\
& 3/8 * \text{Isq} * \text{Lsq}^2 * \text{wr} * \text{Lamd} * \text{Ls}^2 * \text{Cdc} * \text{pole}^2 - \\
& 3/8 * \text{Isd}^2 * \text{Lsq} * \text{Lsd} * \text{Ls}^2 * \text{Cdc} * \text{pole}^2 * \text{Rs} + 3/8 * \text{Isq}^2 * \text{Lsq}^2 * \text{Ls}^2 * \text{Cdc} * \text{pole}^2 * \text{Rs} + \\
& 3/8 * \text{Lsd} * \text{Mq}^2 * \text{Rs} * \text{J} * \text{Ls}^2 + 3/4 * \text{Mq}^2 * \text{Lsd} * \text{Ls}^2 * \text{Rs}^2 * \text{J} + 3/4 * \text{Lsd}^3 * \text{Ls}^2 * \text{Rs}^2 * \text{Isd}^2 * \text{C} \\
& \text{dc} * \text{pole}^2 + 3/8 * \text{Lsd} * \text{Ls}^2 * \text{Md}^2 * \text{J} * \text{Rs} + 3/8 * \text{Rs}^2 * \text{Lsd} * \text{Md}^2 * \text{J} * \text{Lsq} + \text{Lsd} * \text{Rs}^2 * \text{J} * \text{Cd} \\
& \text{c} * \text{Rs} + 3/8 * \text{Lsd} * \text{Mq}^2 * \text{Lsq} * \text{J} * \text{Rs}^2 + \text{Lsd} * \text{we}^2 * \text{Ls}^2 * \text{J} * \text{Cdc} * \text{Rs} - \\
& 3/4 * \text{Lsd} * \text{Ls}^2 * \text{Rs}^2 * \text{Lamd} * \text{Cdc} * \text{pole}^2 * \text{Isd} * \text{Lsq} + 2 * \text{Rs}^2 * \text{Ls}^2 * \text{Rs}^2 * \text{J} * \text{Cdc} + \text{Rs} * \text{we}^2 * \\
& \text{Ls}^2 * \text{J} * \text{Cdc} * \text{Lsq} + 3/8 * \text{Rs} * \text{Mq}^2 * \text{Lsq} * \text{J} * \text{Ls}^2 + 3/4 * \text{Isd} * \text{Lsd} * \text{Lamd} * \text{Ls}^2 * \text{Cdc} * \text{pol} \\
& \text{e}^2 * \text{Rs} + 3/8 * \text{Rs} * \text{Ls}^2 * \text{Md}^2 * \text{J} * \text{Lsq} + \text{Rs} * \text{Rs}^2 * \text{J} * \text{Cdc} * \text{Lsq} - \\
& 3/4 * \text{Lsd}^2 * \text{Ls}^2 * \text{Rs}^2 * \text{Isd}^2 * \text{Cdc} * \text{pole}^2 * \text{Lsq} + 3/2 * \text{Lsd}^2 * \text{Ls}^2 * \text{Rs}^2 * \text{Isd} * \text{Cdc} * \text{pole}^2 * \text{La} \\
& \text{md} + 3/4 * \text{Lsd} * \text{Ls}^2 * \text{Rs}^2 * \text{Lamd}^2 * \text{Cdc} * \text{pole}^2 - \\
& 3/4 * \text{Isd} * \text{Isq} * \text{Lsq}^2 * \text{wr} * \text{Lsd} * \text{Ls}^2 * \text{Cdc} * \text{pole}^2 - \\
& 3/8 * \text{Isq}^2 * \text{Lsq} * \text{Lsd} * \text{Ls}^2 * \text{Cdc} * \text{pole}^2 * \text{Rs} + 3/4 * \text{Md}^2 * \text{Lsq} * \text{Ls}^2 * \text{Rs}^2 * \text{J} + 3/4 * \text{Isq} * \text{Lsq} \\
& * \text{wr} * \text{Lsd} * \text{Lamd} * \text{Ls}^2 * \text{Cdc} * \text{pole}^2 + 2 * \text{wr}^2 * \text{Lsd} * \text{Ls}^2 * \text{Rs}^2 * \text{J} * \text{Cdc} * \text{Lsq} - \\
& 3/4 * \text{Isq}^2 * \text{pole}^2 * \text{Lsd} * \text{Ls}^2 * \text{Rs}^2 * \text{Lsq}^2 * \text{Cdc} + 3/4 * \text{Isq}^2 * \text{pole}^2 * \text{Lsq}^3 * \text{Ls}^2 * \text{Rs}^2 * \text{Cdc} / \\
& \text{Lsq} / \text{Lsd} / \text{Ls}^2 / \text{Cdc} / \text{J}
\end{aligned}$$

$$\begin{aligned}
& a_2 = (-9/64 * \text{Lsd} * \text{Mq}^2 * \text{pole}^2 * \text{Isd} * \text{Lsq} * \text{Ls}^2 * \text{Lamd} - \\
& 9/64 * \text{Md}^2 * \text{pole}^2 * \text{Isd}^2 * \text{Lsq} * \text{Ls}^2 * \text{Lsd} + 3/4 * \text{Lsd}^2 * \text{we}^2 * \text{Ls}^2 * \text{Isd} * \text{Cdc} * \text{pole}^2 * \\
& \text{Lamd} - \\
& 3/8 * \text{Lsd}^2 * \text{we}^2 * \text{Ls}^2 * \text{Isd}^2 * \text{Cdc} * \text{pole}^2 * \text{Lsq} + 3/8 * \text{wr}^2 * \text{Lsd} * \text{Ls}^2 * \text{Md}^2 * \text{Lsq} * \text{J} + 3/ \\
& 4 * \text{Rs} * \text{Ls}^2 * \text{Rs}^2 * \text{Lsd}^2 * \text{Isd}^2 * \text{Cdc} * \text{pole}^2 + \text{Rs}^2 * \text{we}^2 * \text{Ls}^2 * \text{J} * \text{Cdc} - \\
& 3/4 * \text{Rs} * \text{Ls}^2 * \text{Rs}^2 * \text{Lsd} * \text{Isd}^2 * \text{Cdc} * \text{pole}^2 * \text{Lsq} -
\end{aligned}$$

$$\begin{aligned}
& 3/4 * wr * Lsd * Mq1 * Ls2 * Rs2 * J * Md1 + 3/4 * Mq1^2 * Rs * Ls2 * Rs2 * J + wr^2 * Lsd * Rs2^2 * J * C \\
& dc * Lsq + 3/4 * Rs * Ls2 * Rs2 * Lamdam^2 * Cdc * pole^2 + 3/8 * Rs * Rs2 * Md2^2 * J * Lsq + 9/64 * L \\
& sd * Mq2^2 * pole^2 * Lamdam^2 * Ls2 - \\
& 9/64 * Isq^2 * pole^2 * Lsd * Ls2 * Lsq^2 * Md2^2 + 3/2 * Rs * Ls2 * Rs2 * Lsd * Isd * Cdc * pole^2 * L \\
& amdam - \\
& 3/4 * Rs * Ls2 * Rs2 * Lamdam * Cdc * pole^2 * Isd * Lsq + 3/4 * Md1 * wr * Lsq * Mq1 * Ls2 * Rs2 * J - \\
& 9/64 * Mq1 * Isq * pole^2 * Lsd^2 * Ls2^2 * Md1 * Isd - \\
& 3/8 * Isq^2 * pole^2 * Lsd * Rs2^2 * Lsq^2 * Cdc - \\
& 3/8 * Lsd * we^2 * Ls2^2 * Lamdam * Cdc * pole^2 * Isd * Lsq + 3/8 * Md1^2 * Lsq * we^2 * Ls2^2 * J \\
& + 3/8 * Isq^2 * pole^2 * Lsq^3 * Rs2^2 * Cdc + 9/32 * Lsd^2 * Mq2^2 * pole^2 * Lamdam * Ls2 * Isd - \\
& 9/64 * Mq1^2 * Isq^2 * pole^2 * Lsd * Ls2^2 * Lsq - \\
& 3/4 * Isq * pole^2 * Lsq^2 * Ls2 * Rs2 * Cdc * wr * Lamdam + 3/2 * wr * Lsd^2 * Ls2 * Rs2 * Lsq * Isq * \\
& Cdc * pole^2 * Isd + 3/8 * Isq^2 * pole^2 * Lsq^3 * we^2 * Ls2^2 * Cdc + 9/32 * Md1^2 * pole^2 * La \\
& mdam * Ls2^2 * Lsd * Isd + 3/4 * Md1^2 * Rs * Ls2 * Rs2 * J + 3/4 * Isq^2 * pole^2 * Lsq^2 * Ls2 * Rs2 \\
& * Cdc * Rs + 3/2 * wr * Lsd * Ls2 * Rs2 * Lsq * Isq * Cdc * pole^2 * Lamdam - \\
& 9/64 * Md1 * pole^2 * Isd * Lsq^2 * Mq1 * Ls2^2 * Isq + 3/8 * Rs * Mq2^2 * Lsq * J * Rs2 + 9/64 * Lsd^ \\
& 3 * Mq2^2 * pole^2 * Isd^2 * Ls2 + 9/64 * Isq^2 * pole^2 * Lsq^3 * Ls2 * Md2^2 - \\
& 3/8 * Isq^2 * pole^2 * Lsd * we^2 * Ls2^2 * Lsq^2 * Cdc + wr^2 * Lsd * we^2 * Ls2^2 * J * Cdc * Lsq - \\
& 9/64 * Md1^2 * pole^2 * Isd * Lsq * Ls2^2 * Lamdam + 9/32 * Mq1 * Isq * pole^2 * Lsq * Ls2^2 * Md \\
& 1 * Lsd * Isd + 9/64 * Md1^2 * pole^2 * Lsd^2 * Isd^2 * Ls2^2 + 9/64 * Mq1^2 * Isq^2 * pole^2 * Lsq^ \\
& 2 * Ls2^2 - \\
& 3/4 * Isq^2 * pole^2 * Lsd * Ls2 * Rs2 * Lsq * Cdc * Rs + 9/64 * Isq^2 * pole^2 * Lsq^3 * Mq2^2 * Ls2 + \\
& 9/32 * Mq1 * Isq * pole^2 * Lsq * Ls2^2 * Md1 * Lamdam + 3/8 * Lsd * we^2 * Ls2^2 * Lamdam^2 *
\end{aligned}$$

$$\begin{aligned}
& Cdc \cdot pole^2 - 9/64 \cdot Isq^2 \cdot pole^2 \cdot Lsd \cdot Mq2^2 \cdot Lsq^2 \cdot Ls2 - \\
& 3/2 \cdot wr \cdot Lsd \cdot Ls2 \cdot Rs2 \cdot Lsq^2 \cdot Isq \cdot Cdc \cdot pole^2 \cdot Isd - \\
& 9/64 \cdot Mq1 \cdot Isq \cdot pole^2 \cdot Lsd \cdot Ls2^2 \cdot Md1 \cdot Lamdam + 3/8 \cdot Mq1^2 \cdot Lsd \cdot Rs2^2 \cdot J + 3/8 \cdot Rs^2 \\
& \cdot Ls2 \cdot Md2^2 \cdot J + Rs^2 \cdot Rs2^2 \cdot J \cdot Cdc + 3/8 \cdot Rs^2 \cdot Mq2^2 \cdot J \cdot Ls2 + 3/8 \cdot Md1^2 \cdot Lsq \cdot Rs2^2 \\
& \cdot J + 9/64 \cdot Md1^2 \cdot pole^2 \cdot Lamdam^2 \cdot Ls2^2 + 3/8 \cdot wr^2 \cdot Lsd \cdot Mq2^2 \cdot Lsq \cdot J \cdot Ls2 + 3/8 \cdot Ls \\
& d^3 \cdot we^2 \cdot Ls2^2 \cdot Isd^2 \cdot Cdc \cdot pole^2 + 3/8 \cdot Mq1^2 \cdot Lsd \cdot we^2 \cdot Ls2^2 \cdot J + 9/32 \cdot Lsd^2 \cdot Ls \\
& 2 \cdot Md2^2 \cdot pole^2 \cdot Lamdam \cdot Isd + 9/64 \cdot Lsd \cdot Ls2 \cdot Md2^2 \cdot pole^2 \cdot Lamdam^2 + 9/64 \cdot Lsd^3 \\
& \cdot Ls2 \cdot Md2^2 \cdot pole^2 \cdot Isd^2 - 9/64 \cdot Isd^2 \cdot Lsd^2 \cdot Ls2 \cdot Md2^2 \cdot pole^2 \cdot Lsq - \\
& 9/64 \cdot Lsd \cdot Ls2 \cdot Md2^2 \cdot pole^2 \cdot Isd \cdot Lsq \cdot Lamdam + 3/8 \cdot Rs2 \cdot Lsd \cdot Md2^2 \cdot J \cdot Rs - \\
& 3/8 \cdot Isd^2 \cdot Rs2^2 \cdot Lsd^2 \cdot Cdc \cdot pole^2 \cdot Lsq + 3/4 \cdot Lsd^2 \cdot Rs2^2 \cdot Isd \cdot Cdc \cdot pole^2 \cdot Lamda \\
& m + 3/8 \cdot Lsd^3 \cdot Rs2^2 \cdot Isd^2 \cdot Cdc \cdot pole^2 - \\
& 3/8 \cdot Isd \cdot Rs2^2 \cdot Lsd \cdot Lamdam \cdot Cdc \cdot pole^2 \cdot Lsq + 3/8 \cdot Lsd \cdot Rs2^2 \cdot Lamdam^2 \cdot Cdc \cdot pole \\
& ^2 + 3/8 \cdot Lsd \cdot Mq2^2 \cdot Rs \cdot J \cdot Rs2 - \\
& 9/64 \cdot Lsd^2 \cdot Mq2^2 \cdot pole^2 \cdot Isd^2 \cdot Lsq \cdot Ls2) / Lsq / Lsd / Ls2^2 / Cdc / J
\end{aligned}$$

$$\begin{aligned}
a1 = & (9/32 \cdot Rs \cdot Ls2 \cdot Md2^2 \cdot pole^2 \cdot Lamdam \cdot Lsd \cdot Isd + 3/4 \cdot wr \cdot Lsd^2 \cdot we^2 \cdot Ls2^2 \cdot Lsq \cdot \\
& Isq \cdot Cdc \cdot pole^2 \cdot Isd - \\
& 9/64 \cdot Isq^2 \cdot pole^2 \cdot Lsd \cdot Rs2 \cdot Lsq^2 \cdot Md2^2 + 3/4 \cdot wr \cdot Lsd \cdot we^2 \cdot Ls2^2 \cdot Lsq \cdot Isq \cdot Cdc \cdot p \\
& ole^2 \cdot Lamdam + 3/8 \cdot Md1^2 \cdot Rs \cdot we^2 \cdot Ls2^2 \cdot J + 9/32 \cdot Lsd^2 \cdot Rs2 \cdot Md2^2 \cdot pole^2 \cdot Lam \\
& dam \cdot Isd - 9/64 \cdot Lsd^2 \cdot Rs2 \cdot Md2^2 \cdot pole^2 \cdot Isd^2 \cdot Lsq - \\
& 9/64 \cdot Rs \cdot Ls2 \cdot Md2^2 \cdot pole^2 \cdot Isd \cdot Lsq \cdot Lamdam - \\
& 9/64 \cdot Lsd \cdot Mq2^2 \cdot pole^2 \cdot Isd \cdot Lsq \cdot Rs2 \cdot Lamdam - \\
& 9/64 \cdot Lsd \cdot Rs2 \cdot Md2^2 \cdot pole^2 \cdot Isd \cdot Lsq \cdot Lamdam + 3/4 \cdot Rs \cdot Rs2^2 \cdot Lsd \cdot Isd \cdot Cdc \cdot pole^2
\end{aligned}$$

$$\begin{aligned}
& *Lamdam+9/64*Rs*Mq2^2*pole^2*Lsd^2*Isd^2*Is2- \\
& 3/8*Isq*pole^2*Lsq^2*Rs2^2*Cdc*wr*Lamdam+3/8*Isq^2*pole^2*Lsq^2*we^2*Is2^2 \\
& 2*Cdc*Rs- \\
& 3/8*wr*Lsd*Mq1*we^2*Is2^2*J*Md1+9/64*Lsd*Mq2^2*pole^2*Lamdam^2*Rs2- \\
& 3/4*wr*Lsd*Rs2^2*Lsq^2*Isq*Cdc*pole^2*Isd- \\
& 3/8*Rs*Rs2^2*Lamdam*Cdc*pole^2*Isd*Lsq+3/4*wr*Lsd^2*Rs2^2*Lsq*Isq*Cdc*pol \\
& e^2*Isd+3/8*Rs*Rs2^2*Lsd^2*Isd^2*Cdc*pole^2+3/8*Rs^2*Mq2^2*J*Rs2+3/8*Md1^ \\
& 2*Rs*Rs2^2*J+3/8*Rs*Rs2^2*Lamdam^2*Cdc*pole^2- \\
& 9/32*wr*Lsd*Is2*Lsq^2*Isq*Md2^2*pole^2*Isd+9/64*Rs*Mq2^2*pole^2*Lamdam^2 \\
& *Is2+9/64*Rs*Is2*Md2^2*pole^2*Lsd^2*Isd^2- \\
& 9/64*Rs*Mq2^2*pole^2*Isd^2*Lsq*Is2*Lsd- \\
& 9/64*Rs*Mq2^2*pole^2*Isd*Lsq*Is2*Lamdam \\
& +9/64*Isq^2*pole^2*Lsq^3*Mq2^2*Rs2- \\
& 3/8*Isq*pole^2*Lsq^2*we^2*Is2^2*Cdc*wr*Lamdam+9/64*Lsd^3*Rs2*Md2^2*pole^ \\
& 2*Isd^2+9/64*Isq^2*pole^2*Lsq^3*Rs2*Md2^2+9/32*wr*Lsd*Is2*Lsq*Isq*Md2^2*p \\
& ole^2*Lamdam+9/32*wr*Lsd^2*Mq2^2*pole^2*Isd*Lsq*Isq*Is2+9/64*Lsd^3*Mq2^2 \\
& *pole^2*Isd^2*Rs2+9/32*Lsd^2*Mq2^2*pole^2*Lamdam*Rs2*Isd- \\
& 9/64*Lsd^2*Mq2^2*pole^2*Isd^2*Lsq*Rs2+9/32*wr*Lsd^2*Is2*Lsq*Isq*Md2^2*pol \\
& e^2*Isd-9/64*Rs*Is2*Md2^2*pole^2*Isd^2*Lsq*Lsd- \\
& 3/8*Rs*Rs2^2*Lsd*Isd^2*Cdc*pole^2*Lsq+9/64*Rs*Is2*Md2^2*pole^2*Lamdam^2+ \\
& 9/32*Rs*Mq2^2*pole^2*Lamdam*Is2*Lsd*Isd+9/64*Isq^2*pole^2*Lsq^2*Mq2^2*Rs \\
& *Is2+3/8*wr^2*Lsd*Rs2*Md2^2*Lsq*J- \\
& 9/64*Isq^2*pole^2*Lsd*Is2*Lsq*Md2^2*Rs+3/4*wr*Lsd*Rs2^2*Lsq*Isq*Cdc*pole^
\end{aligned}$$

$$\begin{aligned}
& 2*\text{Lamdam}+9/32*wr*\text{Lsd}*Mq2^2*pole^2*\text{Lamdam}*\text{Lsq}*\text{Isq}*\text{Ls2}+3/8*\text{Md1}*wr*\text{Lsq}*M \\
& q1*\text{Rs2}^2*J-3/8*\text{Isq}^2*pole^2*\text{Lsd}*\text{Rs2}^2*\text{Lsq}*Cdc*\text{Rs}- \\
& 9/32*wr*\text{Lsd}*Mq2^2*pole^2*\text{Isd}*\text{Lsq}^2*\text{Isq}*\text{Ls2}- \\
& 3/8*\text{Rs}*we^2*\text{Ls2}^2*\text{Lsd}*\text{Isd}^2*Cdc*pole^2*\text{Lsq}+3/8*\text{Rs}*we^2*\text{Ls2}^2*\text{Lsd}^2*\text{Isd}^2* \\
& Cdc*pole^2- \\
& 3/8*wr*\text{Lsd}*Mq1*\text{Rs2}^2*J*\text{Md1}+3/8*wr^2*\text{Lsd}*Mq2^2*\text{Lsq}*J*\text{Rs2}+3/8*\text{Isq}^2*pole^2 \\
& *\text{Lsq}^2*\text{Rs2}^2*Cdc*\text{Rs}-9/64*\text{Isq}*\text{pole}^2*\text{Lsq}^2*\text{Ls2}*\text{Md2}^2*wr*\text{Lamdam}- \\
& 9/64*\text{Isq}*\text{pole}^2*\text{Lsq}^2*Mq2^2*wr*\text{Ls2}*\text{Lamdam}- \\
& 3/8*\text{Isq}^2*pole^2*\text{Lsd}*we^2*\text{Ls2}^2*\text{Lsq}*Cdc*\text{Rs}- \\
& 9/32*Mq1*\text{Isq}*\text{pole}^2*\text{Lsd}^2*\text{Ls2}*\text{Rs2}*\text{Md1}*\text{Isd}+3/8*Mq1^2*\text{Rs}*\text{Rs2}^2*J+3/8*\text{Rs}^2* \\
& \text{Rs2}*\text{Md2}^2*J+3/8*\text{Rs}*we^2*\text{Ls2}^2*\text{Lamdam}^2*Cdc*pole^2- \\
& 9/32*Mq1^2*\text{Isq}^2*pole^2*\text{Lsd}*\text{Ls2}*\text{Rs2}*\text{Lsq}+3/4*\text{Rs}*we^2*\text{Ls2}^2*\text{Lsd}*\text{Isd}*Cdc*pol \\
& e^2*\text{Lamdam}-9/32*Mq1*\text{Isq}*\text{pole}^2*\text{Lsd}*\text{Ls2}*\text{Rs2}*\text{Md1}*\text{Lamdam}+ \\
& 9/64*\text{Lsd}*\text{Rs2}*\text{Md2}^2*pole^2*\text{Lamdam}^2+9/16*Mq1*\text{Isq}*\text{pole}^2*\text{Lsq}*\text{Ls2}*\text{Rs2}*\text{Md1}* \\
& \text{Lsd}*\text{Isd}+3/8*Mq1^2*\text{Rs}*we^2*\text{Ls2}^2*J+9/16*Mq1*\text{Isq}*\text{pole}^2*\text{Lsq}*\text{Ls2}*\text{Rs2}*\text{Md1}*L \\
& amdam-3/4*wr*\text{Lsd}*we^2*\text{Ls2}^2*\text{Lsq}^2*\text{Isq}*Cdc*pole^2*\text{Isd}+ \\
& 9/32*Mq1^2*\text{Isq}^2*pole^2*\text{Lsq}^2*\text{Ls2}*\text{Rs2}+ \\
& 9/64*\text{Isq}^2*pole^2*\text{Lsq}^2*\text{Ls2}*\text{Md2}^2*\text{Rs}- \\
& 9/64*\text{Isq}^2*pole^2*\text{Lsd}*Mq2^2*\text{Lsq}^2*\text{Rs2}- \\
& 9/64*\text{Isq}^2*pole^2*\text{Lsd}*Mq2^2*\text{Rs}*\text{Lsq}*\text{Ls2}- \\
& 9/32*\text{Md1}^2*pole^2*\text{Isd}^2*\text{Lsq}*\text{Ls2}*\text{Rs2}*\text{Lsd}- \\
& 9/32*\text{Md1}^2*pole^2*\text{Isd}*\text{Lsq}*\text{Ls2}*\text{Rs2}*\text{Lamdam}- \\
& 9/32*\text{Md1}*\text{pole}^2*\text{Isd}*\text{Lsq}^2*Mq1*\text{Ls2}*\text{Rs2}*\text{Isq}+9/16*\text{Md1}^2*\text{pole}^2*\text{Lamdam}*\text{Ls2}^*
\end{aligned}$$

$$Rs2 * Lsd * Isd + 9/32 * Md1^2 * pole^2 * Lamdam^2 * Ls2 * Rs2 + 9/32 * Md1^2 * pole^2 * Lsd^2 * I$$

$$sd^2 * Ls2 * Rs2 + 3/8 * Md1 * wr * Lsq * we^2 * Ls2^2 * Mq1 * J -$$

$$3/8 * Rs * we^2 * Ls2^2 * Lamdam * Cdc * pole^2 * Isd * Lsq) / Lsq / Lsd / Ls2^2 / Cdc / J$$

$$a0 = (-9/64 * Mq1 * Isq * pole^2 * Lsd^2 * we^2 * Ls2^2 * Md1 * Isd$$

$$+ 9/64 * Rs * Rs2 * Md2^2 * pole^2 * Lsd^2 * Isd^2 + 9/64 * Rs * Mq2^2 * pole^2 * Lamdam^2 * Rs2$$

$$+ 9/64 * Md1^2 * pole^2 * Lsd^2 * Isd^2 * we^2 * Ls2^2 +$$

$$9/32 * Rs * Rs2 * Md2^2 * pole^2 * Lamdam * Lsd * Isd -$$

$$9/64 * Rs * Rs2 * Md2^2 * pole^2 * Isd^2 * Lsq * Lsd$$

$$+ 9/32 * wr * Lsd^2 * Rs2 * Lsq * Isq * Md2^2 * pole^2 * Isd -$$

$$9/64 * Isq * pole^2 * Lsq^2 * Rs2 * Md2^2 * wr * Lamdam + 9/32 * Md1^2 * pole^2 * Lamdam * we^2$$

$$* Ls2^2 * Lsd * Isd + 9/64 * Mq1^2 * Isq^2 * pole^2 * Lsq^2 * we^2 * Ls2^2 + 9/64 * Md1^2 * pole^2$$

$$* Lamdam^2 * Rs2^2 - 9/64 * Md1 * pole^2 * Isd * Lsq^2 * we^2 * Ls2^2 * Mq1 * Isq -$$

$$9/64 * Md1 * pole^2 * Isd * Lsq^2 * Mq1 * Rs2^2 * Isq -$$

$$9/64 * Md1^2 * pole^2 * Isd * Lsq * Rs2^2 * Lamdam -$$

$$9/64 * Rs * Mq2^2 * pole^2 * Isd^2 * Lsq * Rs2 * Lsd -$$

$$9/64 * Mq1 * Isq * pole^2 * Lsd * we^2 * Ls2^2 * Md1 * Lamdam -$$

$$9/64 * Mq1 * Isq * pole^2 * Lsd^2 * Rs2^2 * Md1 * Isd + 9/32 * wr * Lsd^2 * Mq2^2 * pole^2 * Isd * Ls$$

$$q * Isq * Rs2 + 9/32 * wr * Lsd * Mq2^2 * pole^2 * Lamdam * Lsq * Isq * Rs2 -$$

$$9/64 * Rs * Rs2 * Md2^2 * pole^2 * Isd * Lsq * Lamdam + 9/32 * Rs * Mq2^2 * pole^2 * Lamdam * Rs$$

$$2 * Lsd * Isd + 9/64 * Isq^2 * pole^2 * Lsq^2 * Mq2^2 * Rs * Rs2 -$$

$$9/64 * Isq * pole^2 * Lsq^2 * Mq2^2 * wr * Rs2 * Lamdam + 9/64 * Isq^2 * pole^2 * Lsq^2 * Rs2 * Md$$

$2^2 * R_s -$

$9/64 * M_d1^2 * pole^2 * Isd^2 * Lsq * R_s2^2 * Lsd + 9/32 * M_q1 * Isq * pole^2 * Lsq * R_s2^2 * M_d1 * Lsd * Isd + 9/32 * wr * Lsd * R_s2 * Lsq * Isq * M_d2^2 * pole^2 * Lamdam + 9/64 * M_q1^2 * Isq^2 * pole^2 * Lsq^2 * R_s2^2 -$

$9/64 * Isq^2 * pole^2 * Lsd * M_q2^2 * R_s * Lsq * R_s2 + 9/64 * M_d1^2 * pole^2 * Lamdam^2 * we^2 * Ls2^2 -$

$9/64 * M_d1^2 * pole^2 * Isd^2 * Lsq * we^2 * Ls2^2 * Lsd + 9/64 * R_s * M_q2^2 * pole^2 * Lsd^2 * Isd^2 * R_s2 -$

$9/64 * M_d1^2 * pole^2 * Isd * Lsq * we^2 * Ls2^2 * Lamdam + 9/32 * M_q1 * Isq * pole^2 * Lsq * we^2 * Ls2^2 * M_d1 * Lsd * Isd - 9/32 * wr * Lsd * M_q2^2 * pole^2 * Isd * Lsq^2 * Isq * R_s2 -$

$9/32 * wr * Lsd * R_s2 * Lsq^2 * Isq * M_d2^2 * pole^2 * Isd + 9/64 * M_d1^2 * pole^2 * Lsd^2 * Isd^2 * R_s2^2 -$

$9/64 * M_q1 * Isq * pole^2 * Lsd * R_s2^2 * M_d1 * Lamdam + 9/32 * M_q1 * Isq * pole^2 * Lsq * we^2 * Ls2^2 * M_d1 * Lamdam - 9/64 * Isq^2 * pole^2 * Lsd * R_s2 * Lsq * M_d2^2 * R_s -$

$9/64 * R_s * M_q2^2 * pole^2 * Isd * Lsq * R_s2 * Lamdam + 9/64 * R_s * R_s2 * M_d2^2 * pole^2 * Lamdam^2 -$

$9/64 * M_q1^2 * Isq^2 * pole^2 * Lsd * we^2 * Ls2^2 * Lsq + 9/32 * M_q1 * Isq * pole^2 * Lsq * R_s2^2 * M_d1 * Lamdam -$

$9/64 * M_q1^2 * Isq^2 * pole^2 * Lsd * R_s2^2 * Lsq + 9/32 * M_d1^2 * pole^2 * Lamdam * R_s2^2 * Lsd * Isd) / Lsq / Lsd / Ls2^2 / Cdc / J$

APPENDIX B

COEFFICIENTS OF THE CHARACTERISTIC EQUATION OF THE PV

SOURCE

$$a_6=1$$

$$a_5 = \frac{1}{8} * (8 * C_m^2 * L_g^2 * R_{d1} * C_1 - 8 * C_m^2 * L_g^2 * L_{d1} * C_1 * a_{111} + 16 * C_m^2 * L_g * L_{d1} * R_g * C_1) / L_g^2 / C_m^2 / L_{d1} / C_1$$

$$a_4 = \frac{1}{8} * (8 * C_m^2 * R_g^2 * L_{d1} * C_1 + 16 * w_e^2 * C_m^2 * L_g^2 * L_{d1} * C_1 - 8 * C_m^2 * L_g^2 * R_{d1} * C_1 * a_{111} + 3 * M_d^2 * C_m * L_g^2 * C_1 + 16 * C_m^2 * L_g * R_{d1} * R_g * C_1 + 8 * C_m^2 * L_g^2 + 3 * M_q^2 * C_m * L_g^2 * C_1 + 16 * L_{d1} * C_m * L_g * C_1 - 16 * C_m^2 * L_g * L_{d1} * R_g * C_1 * a_{111}) / L_g^2 / C_m^2 / L_{d1} / C_1$$

$$a_3 = \frac{1}{8} * (16 * w_e^2 * C_m^2 * L_g * L_{d1} * R_g * C_1 + 16 * L_{d1} * C_m * R_g * C_1 - 16 * w_e^2 * C_m^2 * L_g^2 * L_{d1} * C_1 * a_{111} + 16 * C_m^2 * L_g * R_g + 16 * R_{d1} * C_m * L_g * C_1 - 3 * M_d^2 * C_m * L_g^2 * C_1 * a_{111} + 16 * w_e^2 * C_m^2 * L_g^2 * R_{d1} * C_1 - 8 * C_m^2 * R_g^2 * L_{d1} * C_1 * a_{111} - 3 * M_q^2 * C_m * L_g^2 * C_1 * a_{111} - 16 * C_m^2 * L_g * R_{d1} * R_g * C_1 * a_{111} + 8 * C_m^2 * R_g^2 * R_{d1} * C_1 + 6 * M_q^2 * C_m * L_g * R_g * C_1 - 16 * L_{d1} * C_m * L_g * C_1 * a_{111} + 6 * M_d^2 * C_m * L_g * R_g * C_1) / L_g^2 / C_m^2 / L_{d1} / C_1$$

$$\begin{aligned}
a_2 = & 1/8 * (16 * C_m * L_g - 16 * L_{d1} * C_m * R_g * C_1 * a_{111} - \\
& 16 * w_e^2 * C_m^2 * L_g^2 * R_{d1} * C_1 * a_{111} + 16 * w_e^2 * C_m^2 * L_g^2 - \\
& 16 * L_{d1} * w_e^2 * C_m * L_g * C_1 + 8 * w_e^2 * C_m^2 * R_g^2 * L_{d1} * C_1 + 8 * L_{d1} * C_1 - \\
& 8 * C_m^2 * R_g^2 * R_{d1} * C_1 * a_{111} - \\
& 16 * R_{d1} * C_m * L_g * C_1 * a_{111} + 8 * w_e^4 * C_m^2 * L_g^2 * L_{d1} * C_1 + 3 * M_d^2 * C_m * w_e^2 * L_g^2 * \\
& C_1 + 16 * R_{d1} * C_m * R_g * C_1 - \\
& 6 * M_q^2 * C_m * L_g * R_g * C_1 * a_{111} + 16 * w_e^2 * C_m^2 * L_g * R_{d1} * R_g * C_1 + 3 * M_d^2 * L_g * C_1 + 3 * \\
& M_q^2 * w_e^2 * C_m * L_g^2 * C_1 - \\
& 16 * w_e^2 * C_m^2 * L_g * L_{d1} * R_g * C_1 * a_{111} + 3 * M_d^2 * C_m * R_g^2 * C_1 - \\
& 6 * M_d^2 * C_m * L_g * R_g * C_1 * a_{111} + 3 * M_q^2 * L_g * C_1 + 8 * C_m^2 * R_g^2 + 3 * M_q^2 * C_m * R_g^2 * \\
& C_1) / L_g^2 / C_m^2 / L_{d1} / C_1
\end{aligned}$$

$$\begin{aligned}
a_1 = & 1/8 * (-16 * R_{d1} * w_e^2 * C_m * L_g * C_1 + 16 * C_m * R_g - \\
& 8 * L_{d1} * C_1 * a_{111} + 3 * M_d^2 * R_g * C_1 + 8 * w_e^2 * C_m^2 * R_g^2 * R_{d1} * C_1 + 8 * w_e^4 * C_m^2 * L_g^2 * \\
& R_{d1} * C_1 - 8 * w_e^4 * C_m^2 * L_g^2 * L_{d1} * C_1 * a_{111} + 16 * L_{d1} * w_e^2 * C_m * L_g * C_1 * a_{111} - \\
& 3 * M_d^2 * C_m * w_e^2 * L_g^2 * C_1 * a_{111} - 8 * w_e^2 * C_m^2 * R_g^2 * L_{d1} * C_1 * a_{111} - \\
& 16 * R_{d1} * C_m * R_g * C_1 * a_{111} - 16 * w_e^2 * C_m^2 * L_g * R_{d1} * R_g * C_1 * a_{111} - \\
& 3 * M_d^2 * L_g * C_1 * a_{111} - 3 * M_q^2 * w_e^2 * C_m * L_g^2 * C_1 * a_{111} + 8 * R_{d1} * C_1 - \\
& 3 * M_d^2 * C_m * R_g^2 * C_1 * a_{111} + 3 * M_q^2 * R_g * C_1 + 16 * w_e^2 * C_m^2 * L_g * R_g - \\
& 3 * M_q^2 * C_m * R_g^2 * C_1 * a_{111} - 3 * M_q^2 * L_g * C_1 * a_{111}) / L_g^2 / C_m^2 / L_{d1} / C_1
\end{aligned}$$

$$\begin{aligned}
a_0 = & \frac{1}{8} (8 - 3M_q^2 R_g C_1 a_{111} - 8w_e^2 C_m^2 R_g^2 R_{d1} C_1 a_{111} - \\
& 16w_e^2 C_m L_g + 16R_{d1} w_e^2 C_m L_g C_1 a_{111} + 8w_e^4 C_m^2 L_g^2 - \\
& 3M_d^2 R_g C_1 a_{111} - 8R_{d1} C_1 a_{111} - \\
& 8w_e^4 C_m^2 L_g^2 R_{d1} C_1 a_{111} + 8w_e^2 C_m^2 R_g^2) / L_g^2 / C_m^2 / L_{d1} / C_1
\end{aligned}$$

APPENDIX C

COEFFICIENTS OF THE ZERO DYNAMICS CHARACTERISTIC EQUATION

OF THE PV SOURCE

$$a_{11} = -\frac{2}{3} \cdot \omega_e \cdot Q_{g_ref} / V_{gq} - V_{gq} / L_g$$

$$a_{12} = -R_g / L_g$$

$$a_{13} = 1 / L_g$$

$$a_{21} = -\frac{2}{3} \cdot \omega_e \cdot R_g \cdot Q_{g_ref} / V_{gq} + \frac{4}{3} \cdot R_g \cdot \omega_e \cdot Q_{g_ref} / V_{gq}$$

$$a_{22} = (\omega_e^2 \cdot L_g - 1 / C_m - 2 \cdot \omega_e^2 \cdot L_g)$$

$$a_{23} = (4/9 \cdot R_g \cdot Q_{g_ref} \cdot L_g / V_{gq}^2 \cdot (3/2 \cdot V_{gq} \cdot \omega_e / L_g \cdot (-V_{gq} - 2/3 \cdot \omega_e \cdot L_g \cdot Q_{g_ref} / V_{gq}) - 1/L_g \cdot Q_{g_ref} / C_m) - 2/3 / C_m \cdot L_{d1} \cdot R_{d1} \cdot I_{d1_f}^2 / L_{d1})$$

$$a_{24} = (\omega_e^2 \cdot L_g \cdot R_g)$$

$$a_{25} = (-2/3 * R_g^2 * Q_{g_ref} / V_{gq} * \omega - 2/3 * \omega * L_g^2 / V_{gq} * (3/2 * V_{gq} * \omega / L_g * (-V_{gq} - 2/3 * \omega * L_g * Q_{g_ref} / V_{gq}) - 1 / L_g * Q_{g_ref} / C_m))$$

$$a_{26} = (2/3 / C_m * L_{d1} * I_{d1_f} / L_{d1})$$

$$a_{31} = I_{pv} / C_1 - I_{d1_f} / C_1$$

PUBLICATIONS

- Hossein Karimi-Davijani and Olorunfemi Ojo, " Dynamic Operation and Control of a Multi-DG Unit Standalone Microgrid," *In Proc. of IEEE Innovative Smart Grid Technologies (ISGT 2011) Conference*, Anaheim, CA, pp. 1-7, January 2011.
- Hossein Karimi-Davijani and Olorunfemi Ojo, " Modeling and Steady-State Analysis of a Stand-Alone, Photo-Voltaic -Three Phase Inverter Power System," *In Proc. of IEEE Applied Power Electronics Conference (APEC 2011)*, Fort Worth, TX, pp. 1259-1266, March, 2011.
- Hossein Karimi-Davijani and Olorunfemi Ojo, " Optimum Control of Grid Connected Interior Permanent Magnet Wind Turbine Generator," *In Proc. of IEEE Energy Conversion Congress Conference (ECCE 2012)*, Raleigh, NC, Sept, 2012.
- Hossein Karimi-Davijani and Olorunfemi Ojo, " Controllability Analysis of IPM Generator Connected Through LCL filter to the Grid," *In Proc. of IEEE Annual Conference of Industrial Electronics Society (IECON 2012)*, Montreal, Canada, Oct, 2012.

VITA

Hossein Karimi-Davijani received his Bachelor and Master of Science degree in Electrical Engineering from Mazandaran University, Iran in 2006 and 2009 respectively. He joined the PhD program at Tennessee Technological University in September, 2009. His main research interests include power electronics application in power system and renewable energy.